NBS SPECIAL PUBLICATION 669

U.S. DEPARTMENT OF COMMERCE/National Bureau of Standards

Laser Induced Damage in Optical Materials: 1982

BOULDER DAMAGE SYMPOSIUM

ASTM

STP 847

NATIONAL BUREAU OF STANDARDS

The National Bureau of Standards[1] was established by an act of Congress on March 3, 1901. The Bureau's overall goal is to strengthen and advance the Nation's science and technology and facilitate their effective application for public benefit. To this end, the Bureau conducts research and provides: (1) a basis for the Nation's physical measurement system, (2) scientific and technological services for industry and government, (3) a technical basis for equity in trade, and (4) technical services to promote public safety. The Bureau's technical work is performed by the National Measurement Laboratory, the National Engineering Laboratory, and the Institute for Computer Sciences and Technology.

THE NATIONAL MEASUREMENT LABORATORY provides the national system of physical and chemical and materials measurement; coordinates the system with measurement systems of other nations and furnishes essential services leading to accurate and uniform physical and chemical measurement throughout the Nation's scientific community, industry, and commerce; conducts materials research leading to improved methods of measurement, standards, and data on the properties of materials needed by industry, commerce, educational institutions, and Government; provides advisory and research services to other Government agencies; develops, produces, and distributes Standard Reference Materials; and provides calibration services. The Laboratory consists of the following centers:

Absolute Physical Quantities[2] — Radiation Research — Chemical Physics — Analytical Chemistry — Materials Science

THE NATIONAL ENGINEERING LABORATORY provides technology and technical services to the public and private sectors to address national needs and to solve national problems; conducts research in engineering and applied science in support of these efforts; builds and maintains competence in the necessary disciplines required to carry out this research and technical service; develops engineering data and measurement capabilities; provides engineering measurement traceability services; develops test methods and proposes engineering standards and code changes; develops and proposes new engineering practices; and develops and improves mechanisms to transfer results of its research to the ultimate user. The Laboratory consists of the following centers:

Applied Mathematics — Electronics and Electrical Engineering[2] — Manufacturing Engineering — Building Technology — Fire Research — Chemical Engineering[2]

THE INSTITUTE FOR COMPUTER SCIENCES AND TECHNOLOGY conducts research and provides scientific and technical services to aid Federal agencies in the selection, acquisition, application, and use of computer technology to improve effectiveness and economy in Government operations in accordance with Public Law 89-306 (40 U.S.C. 759), relevant Executive Orders, and other directives; carries out this mission by managing the Federal Information Processing Standards Program, developing Federal ADP standards guidelines, and managing Federal participation in ADP voluntary standardization activities; provides scientific and technological advisory services and assistance to Federal agencies; and provides the technical foundation for computer-related policies of the Federal Government. The Institute consists of the following centers:

Programming Science and Technology — Computer Systems Engineering.

---

[1] Headquarters and Laboratories at Gaithersburg, MD, unless otherwise noted;
mailing address Washington, DC 20234.

[2] Some divisions within the center are located at Boulder, CO 80303.

Laser Induced Damage In Optical Materials: 1982

Proceedings of a Symposium Sponsored by:
National Bureau of Standards
American Society for Testing and Materials
Office of Naval Research
Department of Energy
Defense Advanced Research Project Agency
Air Force Office of Scientific Research

November 16-17, 1982
NBS, Boulder, Colorado 80303

Edited by:

Harold E. Bennett
Naval Weapons Center
China Lake, California 93555

Arthur H. Guenther
Air Force Weapons Laboratory
Kirtland Air Force Base, New Mexico 87117

David Milam
Lawrence Livermore National Laboratory
Livermore, California 94550

Brian E. Newnam
Los Alamos National Laboratory
Los Alamos, New Mexico 87545

BOULDER DAMAGE SYMPOSIUM

U.S. DEPARTMENT OF COMMERCE, Malcolm Baldrige, Secretary
NATIONAL BUREAU OF STANDARDS, Ernest Ambler, Director

Issued January 1984

Library of Congress Catalog Card Number: 83:600625

National Bureau of Standards Special Publication 669
Natl. Bur. Stand. (U.S.), Spec. Publ. 669, 499 pages (Jan. 1984)
CODEN: XNBSAV

U.S. Government Printing Office
Washington: 1984

For sale by the Superintendent of Documents, U.S. Government Printing Office, Washington, DC 20402

Foreword

The Proceedings contain the papers presented at the Fourteenth Symposium on Optical Materials for High Power Lasers held at the National Bureau of Standards (NBS) in Boulder, Colorado, on November 16-17, 1982. The Symposium was jointly sponsored by the National Bureau of Standards, the American Society for Testing and Materials, the Office of Naval Research, the Defense Advanced Research Projects Agency, the Department of Energy, and the Air Force Office of Scientific Research. The Symposium was attended by approximately 200 scientists from the United States, the United Kingdom, Japan, France, West Germany, and the USSR. It was divided into sessions devoted to the following topics: Materials and Measurements, Mirrors and Surfaces, Thin Films, and finally Fundamental Mechanisms. The Symposium Co-Chairmen were Dr. Harold E. Bennett of the Naval Weapons Center, Dr. Arthur H. Guenther of the Air Force Weapons Laboratory, Dr. David Milam of the Lawrence Livermore National Laboratory, and Dr. Brian E. Newnam of the Los Alamos National Laboratory. They also served as editors of this report. Dr. Alexander J. Glass of KMS Fusion acts as Conference Treasurer with Aaron A. Sanders of the National Bureau of Standards as the Conference Coordinator.

The editors assume full responsibility for the summary, conclusions, and recommendations contained in the report and for the summaries of discussion found at the end of each paper. The manuscripts of the papers presented at the Symposium have been prepared by the designated authors, and questions pertaining to their content should be addressed to those authors. The interested reader is referred to the bibliography at the end of the summary article for general references to the literature of laser damage studies. The Fifteenth Annual Symposium on this topic will be held in Boulder, Colorado, from November 14-16, 1983. A concerted effort will be made to ensure closer liaison between the practitioners of high peak power and the high average-power community.

The principal topics to be considered as contributed papers in 1983 do not differ drastically from those enumerated above. We expect to see a continuing transfer of information from research activities to industrial practice. New sources at shorter wavelengths continue to be developed, and a corresponding shift in emphasis to short wavelength and repetitively pulsed damage problems is anticipated. Fabrication and test procedures will continue to be developed together with an improved understanding of defect-dominated damage mechanisms.

The purpose of these symposia is to exchange information about optical materials for high power lasers. The editors will welcome comment and criticism from all interested readers relevant to this purpose, and particularly relative to our plans for the Fifteenth Annual Symposium.

H. E. Bennett, A. H. Guenther,
D. Milam, and B. E. Newnam
Co-Chairmen

DISCLAIMER

CONTENTS

Materials and Measurements

Mirrors and Surfaces

Thin Films

Fundamental Mechanisms

SYMPOSIUM WELCOME

David Milam
Lawrence Livermore National Laboratory
Livermore, CA 94550

I and my fellow chairmen, Hal Bennett, Art Guenther and Brian Newnam, welcome you to the fourteenth Boulder Damage Symposium. Our program contains 45 papers. The authors represent 15 universities, 5 government agencies, and 5 companies in the U.S., and government agencies, universities and companies in 5 foreign countries. In size and composition, this conference is comparable to those of the last few years. Part of this continued interest in laser damage arises from the fact that the interaction of light and matter is an important physics problem. However, most damage studies are driven and funded by the need for damage-resistant laser components. Even if the problems of yesterday had all been solved, design and fabrication of tomorrow's lasers would require additional damage experiments. These future needs, combined with the unsolved problems at hand, insure that damage studies (and a forum for discussing damage) will be necessary for many years.

The conference has six sponsors: the American Society for Testing and Materials, the Air Force Office of Scientific Research, the Defense Advanced Research Projects Agency, the Department of Energy, the National Bureau of Standards and the Office of Naval Research. Alex Glass of KMS Fusion served as treasurer and Aaron Sanders of NBS as coordinator. Ms. Susie Rivera of NBS is the conference secretary. The contributions of these agencies and individuals are sincerely appreciated.

We have a continuing problem in preparation of the conference report. It is a majority opinion of the conference chairmen that each paper presented at the conference should be included in the report. However, some papers are arriving many months after the conference. This greatly delays and complicates the completion of editing, so we ask each author to be prompt in supplying a manuscript.

Having completed these administrative announcements, I wish to comment briefly on a general problem within the damage community. The Q-switched and mode-locked lasers with which I am familiar emit pulses with durations that are typically less than 50 ns, at wavelengths between 250 nm and 1000 nm. The safe operating level for these lasers is less than 20 J/cm^2, and usually less than 10 J/cm^2. The safe fluence is determined by laser damage except for lasers emitting pulses with durations well under 1 ns, for which self-focusing is the limiting mechanism. By contrast, damage studies conducted with these same laser pulses sometime result in threshold values which are more than 10 times greater than the operating levels in current lasers.

In some instances these large thresholds are observed in scientific studies of materials which do not damage in operating lasers. For example, we are not surprised to find that the bulk threshold for fused silica is much greater than safe operating fluences.

It is, however, more difficult to understand the significance of oversize thresholds measured in direct support of the development of a particular laser. I can think of only two explanations. Either we are studying a component which is not limiting laser performance, or we are using a measurement that does not provide data directly applicable to laser design. Valid data on nonlimiting problems may be of value once present limitations are removed. Inappropriate measurements may hinder component improvement by indicating incorrect paths for the development.

The importance of performing experiments that provide absolute thresholds (independent of local relative standards) has been discussed by many speakers at this conference. The measurement capability within the damage community has steadily improved. We are now able to provide experimental answers for many questions. I believe our results would have increased significance if we would compare measured threhsolds with current operating levels to insure that our questions are relevant.

Boulder Damage Symposium 1982

ASTM Welcome

John A. Detrio
University of Dayton
Dayton, Ohio 45469

Welcome to the Fourteenth Annual Boulder Damage Symposium. Sustaining excellence over 14 years is a challenging task. It is a credit to the organizers of this meeting, Hal Bennett, Art Guenther, David Milam, Brian E. Newnam, Aaron A. Sanders and to the authors and participants of the Boulder Damage Symposium that this meeting continues to attract international attention, and to be the forum for presenting the state-of-the-art of optical materials for high power lasers.

Each year the contents of the Symposium's program gives some insight into trends in the science and technology of high power laser optical components. This year's program contains work which continues trends begun at earlier meetings toward measurements of repetitively pulsed damage mechanisms, and the influence of preparation and environmental factors on damage mechanisms with emphasis on surface and coating preparation methods. These trends are indications of the maturation of laser technology and the increased practical application of pulsed lasers. The relatively rapid transition from laser science to laser technology is just one more example of the accelerated pace of technology and its effect on our lives.

The demand for reliable, long lived optical components for high power lasers is a certain sign that these components are expected to perform over an extended useful life in practical situations. These applications include chemical and materials processing, manufacturing, energy research and production, and medical applications. The practical application of a technology does not put an end to scientific or theoretical research. In fact, the development of more carefully controlled materials properties and more precise measurements permit more sensitive tests of theories now than ever before.

The attempts to understand and control the failure mechanisms in optical components has required a reexamination of the materials themselves, their preparation and fabrication, and the careful testing and characterization of these materials. It is in this role of testing and evaluating materials that ASTM, the American Society for Testing and Materials, supports and endorses the Boulder Damage Symposium. ASTM is a non-profit, volunteer organization dedicated to the development of standards for materials and test methods.

Being a non-profit agency, ASTM provides primarily moral support to the symposium. For example, the proceedings of earlier damage symposia are available from ASTM. This activity fulfills ASTM's secondary role of helping in the spread of scientific knowledge. We are pleased to participate in the damage symposium.

Once again, let me say welcome to the Boulder Damage Symposium with a special warm welcome to our many guests from overseas. We are very happy that you could come and share your work with us. Your attendance confirms my sentiments about the value and importance of the Boulder Damage Symposium.

Laser-Induced Damage in Optical Materials
Fourteenth ASTM Symposium
November 16-17, 1982

The Fourteenth Annual Symposium on Optical Materials for High Power Lasers (Boulder Damage Symposium) was held at the National Bureau of Standards in Boulder, Colorado, November 16-17, 1982. The Symposium was held under the auspices of ASTM Committee F-1, Subcommittee on Laser Standards, with the joint sponsorship of NBS, the Defense Advanced Research Project Agency, the Department of Energy, the Office of Naval Research, and the Air Force Office of Scientific Research. Approximately 200 scientists attended the Symposium, including representatives of the United Kingdom, France, Japan, West Germany, and the USSR. The Symposium was divided into sessions concerning Materials and Measurements, Mirrors and Surfaces, Thin Films and finally Fundamental Mechanisms. As in previous years, the emphasis of the papers presented at the Symposium was directed toward new frontiers and new developments. Particular emphasis was given to materials for high power apparatus. The wavelength range of prime interest was from 10.6 μm to the uv region. Highlights included surface characterization, thin film-substrate boundaries, and advances in fundamental laser-matter threshold interactions and damage mechanisms. Harold E. Bennett of the Naval Weapons Center, Arthur H. Guenther of the Air Force Weapons Laboratory, David Milam of the Lawrence Livermore National Laboratory, and Brian E. Newnam of the Los Alamos National Laboratory were co-chairmen of the Symposium. The Fifteenth Annual Symposium is scheduled for November 14-16, 1983 at the National Bureau of Standards, Boulder, Colorado.

Key words: laser damage; laser interaction; optical fabrication; optical materials and properties; thin film coatings.

1. Introduction

The Fourteenth Annual Symposium on Optical Materials for High Power Lasers (Boulder Damage Symposium) was held, as in previous years, at the National Bureau of Standards in Boulder, Colorado, November 16-17, 1982. The Symposium was held under the auspices of the ASTM Committee F-1, Subcommittee on Laser Standards, with the joint sponsorship of NBS, the Defense Advanced Research Projects Agency, the Department of Energy, the Office of Naval Research, and the Air Force Office of Scientific Research. Working sessions of the Committee F-1 Subcommittee on Lasers were held on Monday, November 15. Approximately 200 scientists attended the Symposium, including representatives of the United Kingdom, France, Japan, West Germany, and the USSR. The Symposium was divided into sessions concerning Materials and Measurements, Mirrors and Surfaces, Thin Films and finally Fundamental Mechanisms. In all, approximately 45 technical presentations were made. Harold E. Bennett of the Naval Weapons Center, Arthur H. Guenther of the Air Force Weapons Laboratory, David Milam of the Lawrence Livermore National Laboratory, and Brian E. Newnam of the Los Alamos National Laboratory were co-chairmen of the Symposium. Alexander J. Glass of KMS Fusion, is Conference Treasurer and Aaron A. Sanders of the National Bureau of Standards acts as Conference Coordinator.

The purpose of these symposia is to exchange information about optical materials for high power lasers. The authors will welcome comments and criticism from all interested readers relevant to this purpose and particularly relative to our plans for the Fifteenth Annual Symposium, scheduled for November 14-16, 1983, at the National Bureau of Standards, Boulder, Colorado.

2. Principal Conclusions

Various surface effects received considerable attention this year. It was shown that water, hydrogen, oxygen and OH^- contribute in a multitude of ways to the laser-damage process. For example, surface absorption in germanium is believed to be caused primarily by the presence of a hygroscopic oxide layer which results from surface treatment. However, polishing with diamond on a tin lap is one way to reduce the effect. Many other materials also exhibit surface effects. Spatially localized variations, of orders of magnitude, in water-related contaminant levels have been found and correlated with low damage thresholds.

Laser cleaning (or laser-induced desorption) appears to passivate the surface, reducing its affinity for water. More vigorous laser treatment, i.e. raising the surface to near melting, increases the damage threshold even further, as is understandable from the laser absorption studies, reported last year, which showed that some water-related contaminants are so tightly bound that very high surface temperatures are required to drive them off. It is interesting to note that improvement in damage threshold is not restricted to regions of strong water-band absorption. Beneficial gains at 1.06 μm are significant, for example, even though no appreciable water band exists at that wavelength.

Polishing procedures as well as laser annealing affect the surface and presumably the laser damage threshold. New finishing techniques such as float polishing and mechanochemical polishing offer various degrees of promise in reducing the subsurface damage resulting from conventional polishing techniques while still producing surfaces with excellent optical figures and low surface micro-roughness levels. Scratch standards for specifying optical surfaces are not the answer.

As regards measurements, the keys continue to be absorption and the determination of other thermally related properties. As such, materials measurements are being reported at cryogenic temperatures. One anticipated conclusion is that the thermal properties of crystalline materials will tend to improve as the temperature is reduced. There is expected to be little improvement for glassy materials, however. Metals, on the other hand, will improve their optical performance at low temperatures, particularly in the infrared.

In the area of damage testing, new facilities are still being reported, and damage testing is being carried out at wavelengths as short as 193 nm. The importance of multiple-pulse testing is finally being realized and, although the reason for the degradation in materials after being exposed to repeated laser pulses is often obscure, some progress was reported. For example, the fact that the 1.06 μm bulk threshold of germanium at 100 Hz was only 15% of that measured at 1 Hz was attributed to the additional free carriers present at the higher pulse rate, while laser-induced slip is suggested as the dominant mechanism for metal mirrors used in multiple-pulse applications.

Application is the final test and the system is the final application. Of necessity, then, systems analyses continue to be developed. A technique for obtaining a first cut of a cooled mirror design for a proposed laser train, without recourse to a large computer, has been developed, an adaptive optics mirror design which does not require actuators was presented, and the adequacy of normal incidence tolerances for turning flats used at large angles of incidence was verified.

As the Symposium turned to the vital area of thin film research and development, recent progress with non-standard coating deposition techniques was emphasized. The primary goal is to produce coatings of higher quality than available by use of the commercially-standard techniques involving electron guns and resistive heating. In contrast to the polycrystalline films usually produced by these standard techniques, ion-beam-deposited coatings of TiO_2, Ta_2O_5, as well as SiO_2 were found to be nearly amorphous and in a compressive state of stress. At the other structural extreme, molecular-beam epitaxy of certain classes of compounds produces single-crystal films in high vacuum. It offers the possibility of reduced absorption of energy by electrons in low-energy states and reduced probability of electron avalanche breakdown. However, deposition of wide-bandgap dielectrics of interest for high-power laser optics has yet to be demonstrated by this method.

In pursuit of coatings having the very desirable diamond-like properties, hydrogenated amorphous carbon films were produced in an rf-excited glow discharge of benzene vapors. Especially low absorption was attained at 2.8 and 3.8 μm (15 and 25 cm^{-1}, respectively) which is only a few times greater than that of crystalline diamond. Finally, as an economical alternative to physical vapor deposition processes, gradient-index antireflection (AR) coatings produced with the Neutral Solution Process were shown to be scalable to very large-diameter glass optics without any reduction in damage threshold.

Coating damage studies were concentrated in the ultraviolet this year. The average multiple-shot damage thresholds for state-of-the-art multilayer reflectors are 3, 5, and 8 J/cm^2 at 248, 308, and 351 nm, respectively, for 10-ns pulses. Using non-quarterwave thickness designs, 25% to 50% higher thresholds are obtained. As a valuable diagnostic tool in multiple-shot damage testing, real-time video monitoring has proven itself in observing and recording the onset and evolution of coating damage.

From a survey of the damage thresholds of single-layer and multilayer reflectors for 248 nm, several interesting trends were observed. High-index films had lower thresholds than low-index films, thresholds correlated inversely with extinction coefficient and uv bandedge, but no correlation with film stress was apparent. For reflectors using a given low-index material, higher thresholds were obtained with high-index layers with minimum absorption. For a fixed high-index component, higher thresholds resulted from use of the low-index component with minimum refractive index. The physical basis for this last result is not understood.

Coating designs using halfwave-thick overcoats on reflectors and undercoats with AR coatings consistently have had higher damage resistance on the order of 50%. However, one study this year found these designs to be ineffective for subnanosecond-pulse laser radiation at 351 nm.

Pre-irradiation of optical components with subthreshold laser intensities was shown again to increase the damage threshold of wide-bandgap dielectrics. For the case of AR coatings produced by the Neutral Solution Process, the surface threshold was increased by a factor of two by this treatment.

Under the subheading of thin film diagnostics, the capability of two techniques to detect localized absorbing film contaminants or impurity sites was demonstrated. Internal reflectance spectroscopy applied to the problem of water contamination in ThF_4 films lead to the conclusion that the origin of the water may well be in the starting material rather than entering during or after deposition. The application of photothermal deflection microscopy likewise identified many coating defects not revealed by Nomarski microscopy.

Passing to fundamental damage mechanisms, this year's contributions included aspects pertinent to each of bulk, surface, and thin-film damage phenomena. Of special interest to all laser users was a review of ocular damage mechanisms which are based on either thermal, photochemical, or high-field strength interactions. Eye damage is not necessarily a prompt reaction to laser radiation. In particular, photochemical effects may manifest long after exposure, and lenticular cataracts may be delayed by years. The most dangerous spectrum for retinal injury is 400-500 nm.

The spot-size dependence of laser damage has been a controversial issue at these symposia for many years. This year a physical model was presented which, at least for thin-film coatings, demonstrated that the conventional definition of damage threshold (average of the lowest laser fluence causing damage and the highest fluence producing no damage) is inherently spot-size dependent. A new threshold definition was proposed: the maximum fluence for which no damage was observed over a sufficient number of test sites. That this conservative definition is independent of laser spot size was supported by abundant test results involving optical coatings.

Although a number of experimental studies have concluded that absorbing defects are the initial sites of damage in optical coatings, a relative ordering of damage resistance of the various coating materials has been observed in numerous studies. A significant analytical result presented this year demonstrated that the threshold scales with the thermal properties of the host coating material with insignificant dependence on those of the impurity.

A study dealing with geometric surface defects demonstrated experimentally that linear defects oriented perpendicular to the laser electric field have increased absorption and reduced damage threshold. This observation explains the unequal damage resistance of diffraction gratings when alternatly irradiated with S- or P-orientations of the electric field.

A number of multiple-shot studies at this and at previous symposia have revealed the accumulation nature of damage for some materials. Among the list of materials which have exhibited this phenomenon are silicon, KD^*P, NaCl, fused silica, Cu mirrors, and optical polymers. In each case, the number of laser shots required to produce observable damage monotonically increased with decreasing laser fluence.

Finally, a new damage mechanism, unipolar arcing, was introduced to the laser-damage community. Occurring only after generation of a plasma at a surface, pits and craters result from electrical current arcs between the optical element and the adjacent plasma.

3.0 Summary of Papers

The subject matter of the Fourteenth Annual Boulder Damage Symposium consisted broadly of four topics: (1) Materials and Measurements, (2) Mirrors and Surfaces, (3) Thin Films and (4) Fundamental Mechanisms for Laser Damage. In this section a concise summary of each paper is given. Our intention here is only to provide the reader with an overview and critique of the Symposium and to identify the authors and institutions which contributed to it. The interested reader is referred to the papers themselves for further details. Each topical area is introduced with a brief commentary on the status of the underlying problems addressed, and comments are often made about the import of the paper in our view.

3.1 Materials and Measurements

Materials are a primary concern of the Symposium, and an assessment of the status of materials applicable to a given type of laser or spectral range is a valuable contribution to both the Symposium and the field.

R. Harris, D. Dempsey, D. O'Quinn, and M. Gangl of the University of Dayton Research Center and W. Knecht of the Materials Laboratory at Wright-Patterson Air Force Base presented measurements of the summed bulk and surface absorption at 1.3 µm and the thermo-optic coefficient, dn/dT, in a variety of crystals and glasses. Their stated goal was the assessment of window materials for the 1.315-µm iodine laser. However, their technique for measuring absorption did not appear to give an unambiguous ranking of the various candidate materials. In their words, "The use of larger, non-standard size samples for several of these materials resulted in larger measured absorption coefficients than obtained for the same materials measured earlier with the standard 38-mm diameter samples." Further, their reported absorptions (generally 10^{-4} to 10^{-3} cm^{-1}) were comparable to, or slightly greater than, the expected surface absorptions which were included in the measurements, so the data may not be truly representative of the various materials. Some values of dn/dT given by these authors were, within experimental uncertainty, equal to values quoted by the manufacturers, but a general comparison of their results with previous measurements was not provided.

Other thermal properties of materials are also of great interest in connection with laser effects. The origin of these properties can often be best understood by low temperature determinations. K. McCarthy and H. Sample of Tufts University measured the thermal conductivity of a fluorozirconate glass (ZBLAN, 57.7 percent ZrF_4, 1.14 percent BaF_2, 5.8 percent LaF_3, 4.0 percent AlF_3, and 20.1 percent NaF) and of TeO_2 crystals over the temperature range from 1.5° to 100°K. The thermal conductivity of the glass (10^{-3} W cm^{-1} $°K^{-1}$ at 4°K) increased with increasing temperature, a behavior that is typical of other glasses. The conductivity of the TeO_2 crystals reached a maximum, 10 W $cm^{-1}$$°K^{-1}$ at 5°K, and then decreased with increasing temperature. For both materials, the estimated conductivity at 300°K was approximately 10^{-2} W cm^{-1} $°K^{-1}$. The authors pointed out that low-temperature operation may be more useful in crystals, where thermal conductivities tend to increase with decreasing temperature, than in glasses where conductivities usually decrease with decreasing temperature.

One important crystalline infrared material is germanium and R. Wood, S. Sharma, and P. Waite of the GEC Research Laboratories in Wembley, England reviewed its optical characteristics. At 10.6 μm, absorption in the bulk of germanium is due to free-carrier absorption. Simple theories were presented which adequately describe the variation in free-carrier concentration with temperature and the absorption coefficient as a function of both temperature and impurity level. Minimum absorption at 10.6 μm was obtained by using n-type doping to produce a resistivity of 9 Ω-cm. The authors measured the absorption in crystals of varied length. The data indicated that surface absorption contained a contribution whose magnitude (0.05 - 0.7 percent) varied with sample preparation, and a major contribution (up to 0.7 percent) was believed to be caused by the presence of hygroscopic germanium oxide surface layers. Surfaces polished with diamond on a tin lap, and tested in vacuum, had the least absorption.

In a companion paper, the same authors reported laser-damage thresholds of a germanium crystal irradiated with pulses from a TEA CO_2 laser operating at pulse repetition rates of 1, 10, 50, and 100 Hz. Thresholds decreased monotonically with pulse rate; at 100 Hz the threshold was only 15 percent of that measured at 1 Hz. The relative decrease of threshold with repetition rate was correctly modeled by assuming that damage resulted from free-carrier absorption which increased as the sample temperature increased. Therefore, thresholds were lower at high repetition rates at which the sample did not cool sufficiently during the interpulse interval.

Laser damage thresholds in silicates are of continuing interest and L. Merkle, M. Bass, and R. Swimm of the University of Southern California focused 21-ns, 1064-nm pulses and 15-ns, 532-nm pulses into the bulk of crystalline quartz and fused silica and measured the number of shots required to produce damage as a function of pulse intensity. The diameters of the focal spots were about 14 μm at 1064 nm and 7 μm at 532 nm. For each shot they measured the absorption of the laser pulse and the relative scattering by the focal volume. For the pulse which caused a detectable change in scattering, they recorded the waveforms of the incident and transmitted laser pulse. For all samples, damage could be produced by irradiating the sample with many pulses at intensities ranging from 55 to 90 percent of the single-shot threshold suggesting that multiple-shot damage was cumulative. However, they were unable to detect any change in scattering or absorption prior to damage. Further, the fluence levels in the tiny focal volumes, up to 10^3 J/cm^2, were so large relative to operating levels in lasers that it is difficult to use their results to predict lifetimes for optical elements.

Another class of compounds of continuing interest are the alkali halides. F. Faizullov and V. Kovalev of the Lebedev Physical Institute and J. Janszky and R. Voszka from the Laboratory on Crystal Physics in Budapest used 150-ns, 10.6-μm pulses to test ultrapure crystals of KCl and NaCl that had been doped with either calcium or lead. The most surprising result was that the bulk damage threshold of KCl increased from 0.3 GW/cm^2 to 1.3 GW/cm^2 as the calcium dopant level was increased from 10^{-8} to 10^{-3} mol/mol. The authors believe that the insertion of divalent calcium into a potassium site forms a cation vacancy which tends to trap excess potassium and reduce the probability of formation of colloidal clusters of potassium.

For many years, a group at the Center for Laser Studies at the University of Southern California under the direction of S. Allen has been studying laser-assisted coating deposition. Additionally, surface effects have been under study for a comparable length of time at Michelson Laboratory, Naval Weapons Center. It is thus not suprising that these combined efforts would lead to the related field of laser-induced desorption (LID). This year S. Allen, together with J. Porteus, W. Faith, and J. Franck of the Michelson Laboratory, evaluated this technique for its use in the analysis of optical surfaces for contaminants and defects. Principal emphasis was given to a study of water and other contaminants on normally transparent substrates. Detection and identification was made by use of an ionizer and a standard quadrupole mass analyzer. Spot sizes ranged from 120 to 380 μm. A variation in contaminant concentration of several orders of magnitude in some cases was noted when various regions of a sample were scanned. This localized variation was attributed to defects. It is gratifying to note that there was a strong correlation between sites affording higher levels of desorbed material and sites having a low damage threshold. One last comment worth mentioning is that laser-cleaned surfaces evidenced little affinity for water indicating a potential passivation of the surface.

Absorption is often (but not always) related to reduced laser damage thresholds, and this year M. Itoh of the Institute of Chemical and Physical Research in Saitama and I. Ogura of the University of Tokyo described a somewhat novel interferometric technique for measuring absorption. The samples were placed in one arm of an interferometer and heated by an intense beam propagating through the sample along a path at right angles to the interferometric probe beam. Fringe patterns recorded at intervals during heating indicated the local temperature distribution in the sample. The surface absorption and bulk absorption coefficient were computed by comparing solutions to the heat flow equation with the observed fringe shifts. For KCl, the measured surface absorption and bulk absorption coefficients at 10.6 μm were, respectively, 1.1×10^{-3} and 1.0×10^{-3} cm^{-1}, values that are in reasonable agreement with data reported in previous symposia. However, Itoh and Ogura reported a very large bulk absorption at 488 nm in quartz, 9.5×10^{-2} cm^{-1}. The magnitude of this absorption could be peculiar to their quartz sample (the exact type of quartz was unspecified), but it might also indicate a systematic difficulty in the absolute calibration of their instrument.

Extrinsic absorption of CVD ZnSe at 10.6 μm was the subject of research by K. Lewis of the Royal Signals and Radar Establishment, Malver, United Kingdom, and G. Arthur of the Atomic Weapons Research Establishment, Aldermaston, United Kingdom. Surface absorption, measured by attenuated total reflectivity (ATR), was dominated by the presence of water and hydrocarbons. The water thickness was estimated to be 100 Å. Cleaning of surfaces with trichloroethane and acetone reduced surface absorption by an order of magnitude. In stoichiometric ZnSe, the absorption coefficient at frequencies near 10.6 μm was about 0.003 cm^{-1}, a value not corrected for surface absorption. In ZnSe grown in a Zn-rich environment, the absorption coefficients ranged from 0.007 to 0.107 cm^{-1}. This increased absorption in Zn-rich material was attributed to free-carrier absorption thought to be caused by the presence of impurities which form acceptors (Cu or Na substituted in Zn sites) and donors (possibly In in Zn sites). Annealing in an inert gas environment effectively reduced this absorption by several orders of magnitude, possibly by impurity diffusion from grain boundary sites.

A new laser damage facility assembled at the Loughborough University of Technology was described by S. Wiseall and D. Emmony. Some preliminary results at 193 nm and 249 nm were also reported. Unfortunately, in these initial measurements the authors varied the intensity by moving the sample beyond the focus. As B. Newnam pointed out in the question period, possible spurious effects of air breakdown at focus and the possible influence of diffraction effects caused by beam truncation earlier in the optical train make the beam profile at the damage site quite uncertain. The spot size also varies, but as the authors correctly pointed out, the spot-size dimensions (2-5 mm) were large enough so that little spot-size dependence would be anticipated. Measurements were reported at 193 nm on several alkali and alkaline-earth fluorides, and a decrease in damage level with increasing refractive index was observed as expected. Multilayers of unknown design or composition were tested at 249 nm on one pyrex and several fused quartz substrates. Those films not designed for exposure to a fluorine atmosphere exhibited when exposed, low damage thresholds. No comparison was made to other results in this wavelength range reported in the literature, possibly because so little was known about the present samples. One should not draw firm conclusions from this work about the damage thresholds of uv multilayers until more carefully controlled and documented experiments are performed. The facility at Loughborough presents the opportunity for performing further research and is particularly welcome for tests at 193 nm.

In a display of the validity of the principles of physical optics, T. Wiggins, T. Saito, and J. Hosken of the Air Force Academy placed hole gratings ahead of the focusing lens in their damage experiment to obtain an array of small focal spots whose relative amplitudes and sizes were predictable by Fourier analysis. In examples of multiple-site damage induced on diamond-turned metal surfaces by pulses from a Nd:glass laser, the severity of damage was well correlated with the relative amplitudes in the array of foci.

It has become increasingly evident that as far as laser inertial confinement fusion is concerned, short wavelengths are the way to go. There are two approaches, direct production through short wavelength lasers or by frequency multiplication of longer wavelength systems. The latter approach allows one to employ presently-available, well-engineered, high-intensity, solid-state glass laser systems. The principle engineering problem is the production of large-aperture, efficient, frequency conversion assemblies which are damage resistant. To this end, R. Bossert, S. Jacobs, and L. Lund, of the Laboratory for Laser Energetics at the University of Rochester have reported on the design, assembly, and operation of a 6-cm aperture monolithic cell for up-converting 1.06 μm radiation to a 0.351 μm output. The cell employs an efficient polarization mismatch scheme of KDP Type II crystals useful at high energies. Specifics of the construction are given together which details on the utility of various damage-resistant, constant index matching fluids. (Koolase was the final choice).

3.2 Mirrors and Surfaces

Surfaces are a key concern in any large, multi-element laser optical train. Techniques that improve surface damage threshold, by reducing surface absorption, scattered light, or wavefront distortion (making it possible to focus the laser beam to a high intensity spot), are of interest to the entire laser community.

For many years now, we have been waiting in anticipation concerning the potential of laser polishing or laser annealing of optical surfaces as a means of raising their damage threshold. In the continuing saga of this developing story, P. Temple, S. Seitel, and D. Cate of the Michelson Laboratory, Naval Weapons Center, discussed the recent progress in the CO_2 laser polishing of fused silica. While previous emphasis was on assessing the pulsed 1.06 μm damage resistance of such heated surfaces, recent efforts concentrated on determining the rate of sublimation, surface removal vs. surface modification, desorption and, most importantly, surface figure modification. This work, together with that reported on LID, suggests that the most important problems may be surface preparation for coating and protection against environmental degradation. The authors stated that very little material was removed during the surface treatment process.

Another technique for producing very high quality surfaces with minimum surface distortion may be float polishing. Y. Namba, recently at the University of New Mexico, discussed a new float polishing machine developed in Japan to produce very flat optical components with ultra-low surface microroughness. Optical figures as good as a twentieth of a visible wavelength peak-to-peak on small samples were reported. The surface microroughness was measured to be 2 Å rms and subsurface damage was minimal. Unfortunately, the polishing mechanism is not well understood.

Another paper dealing with fused silica surfaces and the effect of various surface polishing techniques on laser-damage sensitivity was given by H. Vora of the Honeywell Corporate Technology Center with W. Lowdermilk and J. Swain of the Lawrence Livermore National Laboratory. Samples were polished mechanochemically using $SrCO_3$, a MgO and NiO slurry, colloidal silica, as well as sapphire. The latter was thought to introduce scratches and subsurface microfractures. All such polished samples were tested using 1-nsec, 1.06 µm laser pulses. Damage levels ranged between 9 and 17 J/cm^2. Unfortunately, no measurements of surface roughness were given or laser spot size mentioned. It was concluded that subsurface microfracture is not by itself an important mechanism in lowering the pulsed laser-induced damage threshold, an observation previously well documented.

Conventional polishing techniques remain the most widely-used surface finishing technique. Such surfaces often contain observable scratches which may reduce the laser damage threshold. M. Young of the National Bureau of Standards at Boulder indicated that current scratch standards are not appropriate for predicting the relative laser damage threshold of optical components. Scratch standards are not specified in terms of width, but in terms of visual appearance, a qualitative cosmetic parameter not easily quantified. There was some correlation in measurements performed at the Bureau of Standards between near-angle scattered intensity and scratch number, but close to half of the scratches could just as easily have been given the next higher or lower scratch classification. Also, currently available scratch standards do not have a reliable relation to scratch widths, although the widths of most of the standard scratches, denoted as between 10 and 80, are between 1 µm and 10 µm. The width of a #10 scratch is often expected to be 1 µm, a #60 scratch 6 µm and so on. The author concluded that, "If I were buying parts for a high power laser, I would hate to rely on such a loose standard for avoiding catastrophic damage to my components." Unanswered was the question, directed from the audience, as to what more pertinent laser surface specification should be used.

The single-shot ultraviolet damage thresholds at 248 nm of uv-transmitting silicate glasses, fluorides, halides, alkaline earths and KDP and its isomorphs were reported by F. Rainer, W. Lowdermilk, and D. Milam of Lawrence Livermore National Laboratory. Pulses 20 ns in length were used. For the silicate glasses, damage thresholds were 5 to 9 J/cm^2 first appearing primarily at the rear surface. Color centers formed in UVFK54 glass at less than 2 J/cm^2. Improvements in rear-surface damage threshold for these glasses are probably possible but were not realized. In LiF, the bulk and rear-surface damage thresholds were nearly the same, about 10 J/cm^2 or more. Thresholds for CaF_2 were similar, while those for MgF_2 and NaF were in the 17 to 18 J/cm^2 region. KDP, KD^*P, and ADP had entrance-surface thresholds in the 3 to 9 J/cm^2 region. Nonlinear absorption produced transmission losses as great as 30 to 50 percent in these latter materials, so rear-surface damage did not occur. These results suggest that the 248 nm, two-photon absorption coefficients are larger than published values at 266 nm by a factor of 2 to 10.

The effect of ambient electronegative gases on damage threshold was investigated by J. Kardach of the Air Force Institute of Technology and A. Stewart and A. Guenther of the Air Force Weapons Laboratory. A 1.06 µm laser having a pulse length of 5 ns and a focused spot size of 176 µm ($1/e^2$ radius) was used for these experiments. Gas compositions of nitrogen, Freon 14 (CF_4), and SF_6 at pressures from 5×10^{-6} torr to 2 atmospheres were used. Half-wave thick films of ZrO_2, various sol gel coatings, diamond-turned copper, uncoated fused silica, ARG-2 glass, and porous surface layers of ARG-2 glass were tested. No detectable variations in threshold damage with ambient gas type or its pressure were found. These results suggest that damage in the cases tested occurred just beneath the surface of the sample where damage initiation is not affected by the sample surroundings. Eron'ka, et. al., previously observed a variation in damage threshold, defined as spark generation, with changes in ambient gas. This result is not in disagreement with present results since "damage threshold" is defined differently. Spark thresholds are generally higher than "first detectable permanent damage" and would be sensitive to electron rate-controlling factors present in avalanches.

Laser damage to metals at cryogenic temperatures was reported by D. Decker, J. Franck, W. Faith, and J. Porteus of the Naval Weapons Center. Measurements were made at 139°K and 276°K on diamond-turned gold samples and at 133°K and 300°K on diamond-turned copper samples. The increase in observed damage threshold at cryogenic temperature was about 1.3 to 1.5X and is in good agreement with that calculated from the Drude theory at a wavelength of 2.7 μm. The onset of selective damage scaled in the same ratio, suggesting that localized thermal defects such as those caused by a crack, void or grain boundary, rather than absorbing particles, may be the origin of localized defect damage.

N. Koumvakalis, C. Lee, and M. Bass of the Center for Laser Studies, University of Southern California investigated the relationship of single- and multiple-pulse damage thresholds in diamond-turned copper and silver-coated mirrors as a function of wavelength and spot size. They concluded that the single-pulse damage threshold can be explained as defect initiated and will be independent of spot size above a critical value which depends on defect density. Multiple pulse damage was found to occur at lower irradiance levels than the single-shot threshold but approached the single-shot threshold as the spot size increased. The authors suggested that the multiple-shot threshold is an intrinsic process related to laser-induced slip and is defect dependent only in the upper limit. This paper provides a mechanism for multiple-shot damage which suggests that beam uniformity may be very important in establishing the damage thresholds for the optics in multipulse systems.

J. Palmer of TRW presented a comprehensive analysis of a first-cut technique for designing a heat exchanger mirror which does not require the use of a large computer program. First, the optical, structural and thermal properties of the mirror performance are estimated as an output. Then the reflectance requirements on the mirror surface, the decision as to whether to use single, double, or triple coolant channels for the mirror design, bending of the mirror surface under thermal and structural loading and maximum defect size on the mirror surface which can be tolerated are estimated. Once this process is completed the boundaries of the mirror design are known and detailed design can begin.

In a paper presented by title only, V. Apollonov, S. Chyetkin, V. Khomich, and A. Prokhorov of the Lebedev Physical Institute continued their discussion of porous heat exchanger mirror structures. They suggested extending their use to adaptive optics. In their proposed design the force correcting the surface figure is not applied through mechanical actuators as is normally the case, but rather through control of pressure on segments of the heat exchanger. While this technique may not have use in high band-pass situations, it could be very useful in optimizing or controlling high energy cw, or high average power laser systems.

The objective of many laser systems is to focus radiation on a target. In addition to the decrease in focused intensity caused by catastrophic laser-induced damage of any of the optical components, wavefront distortion will decrease the peak focal intensity. At these annual symposia, H. Bennett of the Naval Weapons Center has frequently presented various analyses of the effects of imperfect surfaces on beam focusability. This year he compared the influences of random surface figure irregularities and sphericity of otherwise flat reflecting surfaces when used at nonnormal incidence. Not surprisingly, he found that wavefront distortion due to random irregularities is a maximum at normal incidence and decreases monotonically as the cosine of the angle of incidence. However, sphericity, which introduces astigmatism, produces zero wavefront distortion at normal incidence but grows with angle as $\sin^2\theta$ up to 55°, after which there is a diminishing effect. Additionally, sphericity causes a small focal shift which, in most applications, can be either compensated or tolerated. Comparing the relative magnitudes of the two figure imperfections at any angle of incidence, it was determined that the distortion introduced by sphericity, which meets a prescribed peak-to-valley figure specification, will be less than that from random figure errors.

3.3 Thin Films

As in past years more papers were presented in the general area of thin film technology than in any other subject area, presumably because there is room for considerable improvement. There are two principal schools of thought regarding the most expeditious scientific approach to realize more damage-resistant optical coatings. One group suggests investigation of new coating deposition techniques while the other prefers to understand the damage mechanisms and relate them to film characteristics and the deposition process variables— obviously, both should be pursued.

A strong candidate for a "new" deposition technique, proposed because of our present understanding of the film structure/ damage interplay, is Molecular Beam Epitaxy. This film growth technique was the subject of a paper by M. Rona and P. Sullivan of the Arthur D. Little Co. Emphasis was on the deposition of single-crystal films produced in ultra high vacuum (10^{-10} torr). For the semiconductor industry, films with rms surface roughness of <5 Å (determined by crystal structure, not substrate) with <1 percent variation in thickness over a 5-cm diameter have been grown. It is expected that films grown by this technique will exhibit reduced absorption by electrons in low energy states and reduced probability of electron avalanche breakdown as a result of longer electron mean free paths. All that is needed is someone with enough courage ($) to contaminate an MBE apparatus for developing hard, wide-band gap, laser coatings.

Another new deposition process which is being pursued vigorously is ion-beam sputtering. J. Sites, P. Gilstrap, and R. Rujkorakarn of Colorado State University have been depositing layers of SiO_2, Ta_2O_5 and TiO_2 using beams of 500-1200 eV argon and oxygen ions which are neutralized by an equal number of electrons. A second beam at lower energy is used for stress modification and pre-deposition sputter cleaning of the substrate. Films deposited in this manner are mechanically stable, nearly amorphous, relatively dense, and extremely adherent, with a beneficial compressive internal stress. Values of absorption coefficients ranged from 2.5 to 18 cm^{-1} for half-wave thick films of SiO_2 and TiO_2, respectively. Damage tests performed at the Air Force Weapons Laboratory gave thresholds of 15 to 40 J/cm^2 for 114-μm radius (1/e intensity), 5-ns FWHM pulses at 1.06 μm for single-layer films and only slightly less for a three-layer structure. This latter result is significant in that it may indicate low interlayer absorption. The only impurity that could be identified was carbon (<1%).

Hard carbon coatings are a very promising thin film development and B. Dischler, A. Bubenzer, P. Koidl, G. Brandt, and O. Schirmer from the Fraunhofer-Institute for Applied Solid State Physics in West Germany have now attained absorption coefficients as low as 15 cm^{-1} at 2.8 μm for hydrogenated material by exciting an rf discharge in benzene vapors. This value is only a few times higher than that of crystalline diamond. The films were hard, chemically inert, amorphous and had a relatively high index of refraction, 1.93. The substrates used were Ge, Si, and glass. The possible dependence of short wavelength absorption on dangling-bond density was also discussed.

The preceding three papers involved physical vapor deposition of optical coatings. However, coatings produced by chemical processes at moderately-low temperatures are also being evaluated for large optical components. Motivated by the high damage resistance and economy of the Neutral-Solution Process (NSP) for borosilicate laser optics, G. Wirtenson and N. Brown of Lawrence Livermore National Laboratory and L. Cook of Schott Optical Glass, Inc., developed procedures and equipment to obtain antireflective surfaces on large-diameter glass optics up to 90 cm. Typically, the peak transmittance realized was 99.2 to 99.5 percent through two surfaces after a processing time of two to four days, depending on the wavelength of interest. The surfaces were found to be extremely fragile so that cleaning by drag wiping should be avoided. Further, contamination by hydrocarbon particulates, e.g., dioctyl phthalate, could increase the surface reflectance over a period of time to the initial 4 percent level. Fortunately, simple flushing with ethyl alcohol restored the surfaces to their initial post-process state. The high damage resistance of 12 J/cm^2 measured for small NSP-process witness pieces was also obtained on a 46-cm lens.

Extending from 248 nm to 1064 nm, the next five papers reported results of damage tests on a wide variety of coating materials. The ultraviolet laser damage test facility now in operation at Los Alamos National Laboratory was described in detail by S. Foltyn, L. Jolin, and B. Newnam, and a summary of damage data for uv reflectors and crystalline materials was presented. The system employs in-line beam diagnostics and a real-time video monitoring system. Three excimer wavelengths are available, and testing is performed at 35 pps using a nominal 10-ns pulsewidth and a spot-size diameter of 600 µm. The best multiple-shot thresholds consistently obtained for multilayer reflectors have been 3 J/cm^2 at 248 nm, 5 J/cm^2 at 308 nm and 8 J/cm^2 at 351 nm. Nonquarterwave designs have resulted in significantly higher (25-50%) thresholds, particularly at the shorter wavelengths. At 248 nm, thresholds for single-crystal and press-forged LiF windows were 6 and 3.5 J/cm^2, respectively. Of special interest was the dependence of the threshold of KD*P crystals on the number of laser pulses: 3 J/cm^2 after 7000 shots or 8 J/cm^2 after 500 shots.

The objective of a coating damage survey at 248 nm by F. Rainer, W. Lowdermilk, and D. Milam of Lawrence Livermore National Laboratory and C. Carniglia, T. Hart and T. Lichtenstein of Optical Coating Laboratory, Inc. was to determine the relationships between damage thresholds and the physical properties of various film materials which might serve as a guide to selecting optimum coating combinations. Half-wave thick layers of 15 oxide and fluoride films were deposited by electron-gun evaporation at OCLI onto fused silica substrates polished by the bowl-feed process. Damage thresholds for these coatings, using 20-ns pulses, ranged from 0.3 J/cm^2 for ZrO_2 to 25 J/cm^2 for ThF_4. Not unexpectedly, high-index films had lower thresholds than low-index films in agreement with previous studies reported at these symposia. Further, thresholds correlated inversely with extinction coefficient k and the uv band edge, and no general relationship with film stress was apparent. Thirteen different high reflectors composed of 15 layers plus a half-wave overcoat of the low-index component of the above materials on BK-7 substrates also were tested and ranked in order of threshold. Values ranged from 0.5 J/cm^2 for the ZrO_2/YF_3 combination up to 8 J/cm^2 for MgO/LiF. For reflectors made of a given high-index material, pairing with a film having the lowest refractive-index realized the highest threshold. Using a given low-index film, thresholds correlated with use of high-index film materials having the lowest absorption.

The use of ultraviolet laser drivers for inertial confinement fusion experiments has made the wavelength 351 nm especially interesting since it is produced by both the XeF excimer and frequency-tripled Nd:glass lasers. In their damage experiments of coated optics for this wavelength, J. Abate, R. Roides, S. Jacobs, W. Piskorowski, and T. Chipp of the Laboratory of Laser Energetics surveyed the influences of substrate type, polish, and post treatment on over- and under-coated damage thresholds of optical thin films. Materials studied were Ta_2O_5/SiO_2, Sc_2O_3/SiO_2, Al_2O_3/MgF_2, and Y_2O_3/SiO_2 pairs. Films intended for use as dichroic elements (1064 and 351 nm) were tested at the two wavelengths with pulses of 0.4 and 1 ns over large areas (5 mm in diameter). To quote the authors, "What is striking about the data ....is that thresholds are consistently between 2 and 3 J/cm^2 and that the methods that seem to markedly affect the damage thresholds of optical coatings at 1.06 µm seem to have little or no effect at 351 nm."

Multiple-shot irradiation just below the single-shot damage threshold has been reported by several laboratories to significantly raise the damage resistance of optical coatings, surfaces and the bulk interior of crystals. As further evidence of the benefit of subthreshold conditioning, J. Swain, W. Lowdermilk, and D. Milam of Lawrence Livermore National Laboratory reported an impressive factor of two increase in the single-shot threshold of Schott's Neutral-Solution Processed BK-7 surfaces. Without pre-irradiation, large-diameter optics with this gradient-index antireflecting surface have a mean threshold of 12 J/cm^2 for single 1-ns pulses at 1064 nm. Irradiated by 6 to 8 shots below threshold until laser-induced light emission ceased, a 25 J/cm^2 threshold was measured on both surfaces. Further, this factor of two improvement was obtained over the entire range of 1 to 20 ns for which the threshold increased as the square root of the pulsewidth.

In support of the upgraded eight-beam Octal glass laser fusion facility at the Centre d'Etudes de Limeil, France, the damage resistance of antireflection coatings and reflectors produced by three French coating firms (MATRA, MTO, and CILAS) was measured. The results of these tests involving nearly 500 samples and 200 components were summarized by D. Friart, M. Novari, and F. Garaude of the Commissariat a l'Energie Atomique, B. Geenen, A. Malherbes, and J. Guerain of the Societé MATRA, J. Rome, M. Buffenoir, and P. Perbal of M. T. O., S. A. and M. Soulié of CILAS. Using 3-ns pulses focused to a 1.8-mm diameter spot size, damage thresholds ranged between 3 to 6 J/cm^2 for coatings of ZrO_2/SiO_2, TiO_2/SiO_2 and single-layer MgF_2. Coatings with ZrO_2 as the high-index component damaged earlier than those using TiO_2, and large-diameter components had slightly lower thresholds than the smaller test samples. These thresholds and trends are in essential agreement with those determined over the past decade at the several American laser fusion laboratories.

The remaining four papers concerned with thin films involved measurements of coating imperfections, contaminants and stability in hostile gaseous environments.

The problem of water in thorium fluoride films was addressed by G. Hansen, D. Lund, A. D'Agostino, and W. Hansen of Utah State University using internal reflectance spectroscopy. Using this nondestructive technique, monolayer amounts of water can be identified quantitatively and their position at the film surface or in the bulk of the film can be determined by modifying the position of the standing wave produced when the critical angle is exceeded. The ThF_4 films were deposited on ZnSe or Ge substrates at the Air Force Weapons Laboratory and some had overlayers of CeF_3 or ZnSe and underlayers of SiO. The observed water level varied greatly from film to film but was unaffected by the presence of a capping layer. The lability of the water was studied by heating the films and by immersing them in water and in D_2O, where the isotope shift observed indicated how easily ion exchange occurred. The authors concluded that (1) the water in many cases is very tightly bound (in agreement with the conclusions of J. Porteus, et. al. at last year's conference), (2) overlayers did not reduce the H_2O presence in the films examined but that some films were more porous than others, and (3) films which had little water initially or after being heated did not reabsorb water. For the ThF_4 films studied, they suggested that water was present in the starting material before evaporation rather than entering them during or after film preparation. The internal reflectance technique was again demonstrated to be a very powerful tool, and it is to be hoped that these authors will use it on films in which the starting material and deposition conditions are more carefully controlled.

The effect on multilayer high-reflectance coatings of errors in thickness or index of refraction of individual layers was revisited by R. Ruykorakarn, R. Hannum, and J. Sites of Colorado State University. They pointed out that thickness errors affect the secondary minima more than the reflectance maximum. The reverse is true for increases in absorption coefficient. The reflectance maximum is also more sensitive to changes in index of refraction than it is to thickness errors.

The environmental stability of thin, single- and multilayer-dielectric coatings was investigated by J. Palmer of TRW. Thin film coatings of Al_2O_3, Si, ZnS, MgF_2, CeO, ZrO_2, and Y_2O_3 were deposited on substrates of silver-coated float glass, molybdenum, gold, copper, and aluminum. The test samples were exposed to hostile environments of 95-percent relative humidity at 35°C, 95-percent saturated ethanol vapor at 35°C, and 10 percent by volume HF and H_2S. Considerable effort clearly went into this survey, but unfortunately it is difficult to extract much fundamental information from the results.

We continue to look for meaningful yet facile indicators of damage sensitivity. Nowhere is this more desirable than in the thin-film optics area. With this objective, W. Mundy and R. Hughes of Pacific Union College and C. Carniglia of Optical Coating Laboratory, Inc., investigated the sensitivity of photothermal deflection microscopy. This microprocessor-controlled technique, although simple, provides high spatial resolution and identification of low-level absorption areas. The system employs a chopped Ar-ion laser (514.5 nm) as the heat source while a HeNe laser is used for the probe. The sample was scanned in 4-μm steps. Interestingly, many coating defects not identified by Normaski microscopy were discovered. The most obvious area to be investigated is a correlation of the sites so covered with their damage sensitivity. If this proves fruitful, then many more research applications will arise such as elemental analysis, calibration with absorption data, and time-dependent absorption studies.

3.4 Fundamental Mechanisms

While practical measurement of damage thresholds of materials, surfaces, and thin films is necessary to define the present state-of-the-art, many of the advances in producing better optical components have been the fruit of basic studies relating to fundamental damage mechanisms. This year, a wide range of topics was addressed, ranging from ocular damage susceptibility, scaling with laser and materials properties, damage precursors and accumulation with multiple-shot irradiation, first-principles calculation of the refractive index, and an electro-mechanical surface mechanism called unipolar arcing.

In the first laser biological effects paper to be presented at these symposia, D. Sliney of the U. S. Army Environmental Hygiene Agency, Aberdeen Proving Ground divided the various mechanisms for eye damage from laser radiation into three categories: (1) normal-thermal, (2) photochemical, and (3) high-field strength. Photochemical effects, in particular, may produce effects long after the event (hours or days) and lenticular cataracts may occur years after irradiation occurs. The most dangerous wavelength region for retinal injury is from 0.4 to 0.5 μm, but other wavelengths are also hazardous at higher fluences. High-field damage from subnanosecond exposure, particularly multiple-pulse exposure, is not yet well understood. Much remains to be done in all three areas of research.

The next three papers were concerned with scaling of damage susceptibility with laser parameters (spot-size and pulsewidth) and materials properties. In a very important paper by S. Foltyn of Los Alamos National Laboratory, a statistical theory was presented which predicts that single-shot damage thresholds can often be interpreted to make the resultant damage threshold independent of spot size. The conventional damage threshold determination, by contrast, leads to a spot-size dependence whose interpretation can be very confusing. The statistical procedure proposed should, in principle, make it possible to utilize well-controlled small lasers to determine damage thresholds which are equally valid when large areas of a component are irradiated using a large device. It was assumed that the damage process is defect related, only one type of defect was considered in the theory, and cumulative effects were ignored. Data for optical coatings was presented which showed that in many cases the assumptions are justified. The bottom line is that the intercept for threshold damage, i.e. maximum fluence at which no damage occurs for all irradiated sites, does not change as the spot size changes. Only the slope of the survivability curve (damage probability vs laser fluence) is affected.

Scaling the damage thresholds of optical coatings as a function of various material properties has been addressed several times at these symposia. This year, M. Lange and J. McIver of the University of New Mexico and A. Guenther and T. Walker of the Air Force Weapons Laboratory considered the relative roles of absorbing inclusions and the host material in determining the damage threshold. Beginning with the exact solution of the heat diffusion equation obtained thirty years ago by Goldenberg and Tranter, an approximate analytical solution was obtained. This solution clearly reveals that the damage threshold scales with the thermal properties of the host material as $T\sqrt{\rho C_p Kt}$, with an insignificant dependence on those of the impurity. (The factors in this formula are the melting temperature, density, specific heat, thermal conductivity and laser pulse width.) Comparison of their analytical result with an exact numerical solution was excellent.

M. Soileau, W. Williams, E. Van Stryland, T. Boggess, and A. Smirl of North Texas State University measured bulk thresholds in fused silica and NaCl crystals with both 0.53-μm and 1.05-μm pulses having durations from 4 to 200 ps focused to spot-size radii ranging from 3.9 to 14.2 μm. They observed that the threshold breakdown field E_b increased with decreasing pulse duration in functional agreement with M. Sparks' theory for avalanche breakdown. However, measured values of E_b were smaller at 0.53 μm than at 1.05 μm, and they increased with decreasing spot size, observations which are in conflict with avalanche theory. The authors believe the wavelength dependence could be explained by a theory invoking multiphoton-initiated avalanche breakdown, and that the spot-size scaling should be attributed to extrinsic effects. They reported data which indicated that self-focusing was not a relevant factor.

The ripple structure often associated with laser damage of surfaces was revisited by M. Soileau and E. Van Stryland of North Texas State University.

A model had been proposed by Soileau and Temple at the 1976 Boulder Damage Conference which related ripple formation to the presence of defects and correctly accounted for their spacing and polarization dependence. In the present paper, the dependence of absorption on orientation of the defects was verified experimentally both by determining the damage threshold of a grooved NaCl sample oriented in and perpendicular to the plane of polarization and by monitoring the absorption photoacoustically of a grating with spacing comparable to the wavelength, 10.6 μm. Reduced damage threshold and increased absorption occurred when the linear defects were aligned orthogonal to the laser field. A still unexplained anomaly is why the ripple spacing for metals and semiconductors is the free space wavelength λ whereas for wide-band gap dielectrics it is λ/n where n is the index of refraction.

The shifting emphasis from single-shot-per-site studies to multiple-shot, repetitively-pulsed laser damage has directed attention to precursor phenomena and accumulation of microdamage to detectable levels. In such a study, M. Becker, Y. Jhee, M. Bordelon, and R. Walser of the University of Texas discussed irradiation of p-type silicon with 1064-nm pulses having durations of 60-80 ps. The pulses were delivered at a rate of 13 Hz, and focused to a spot approximately 100 μm in diameter. The silicon samples were tested in vacuum (10^{-5} torr) which allowed collection of ions or electrons ejected from the surface and comparison of charge collection with observations of damage. Damage was observed after an "incubation" period whose duration varied with laser intensity. They believe the incubation period indicates accumulation of a "reversible excitation" other than temperature. Exoemission of charge, the primary topic of the paper, was not observed unless damage (detectable by scanning electron microscopy) was induced. The authors made no comment regarding how the proposed incubation period preceding damage might be related to exoemission of charge.

In a companion paper by the same authors, they reported that the multipulse damage threshold of single-crystal silicon for 1.06-μm pulses had no dependence on pulse repetition frequency. A simple thermal calculation indicated that there was adequate heat dissipation between pulses, in support of this observation.

Multiple-shot irradiation was also the test regime of the damage studies of organic and inorganic glasses reported by A. Manenkov, G. Matyushin, V. Nechitailo, A. Prokhorov, and A. Tsaprilov of the Lebedev Physical Institute. They reviewed literature which indicates that multiple-shot thresholds are less than single-shot thresholds, proposed a statistical framework for analysis of multiple-shot data, and presented results of recent experiments in which polymers were irradiated with either 1064-nm or 694-nm pulses. The experimental data showed that scattering from the focal volume increased steadily with repeated shots prior to damage, but that the intensity of laser-induced uv light emission remained at a constant low level until a few shots prior to damage. For spot sizes between 0.1 and 8 mm, the threshold measured with 200 shots was at least a factor of 10 below the single-shot threshold, but spot-size scaling was weaker in multiple-shot than in single-shot thresholds. The authors concluded that reduced multiple-shot thresholds resulted from accumulation of microdamages.

The index of refraction of a material is closely related to both its single and multiphoton damage threshold. B. Jensen and A. Torabi of Boston University presented a derivation which makes it possible to calculate the magnitude and spectral dependence of the index of refraction from first principles even near the band edge. The derivation was developed for compound semiconductors and depends on the Kane model of the band structure. Its applicability to wider bandgap materials has yet to be determined.

Different mechanisms of damage are manifest at various irradiation levels. While this series of meetings has principally been concerned with that regime around the threshold for the first observable, non-reversible damage, one can sometimes learn about threshold damage mechanisms by studying pre-catastrophic indicators, e.g., photoconductivity. A presentation by F. Schwirzke of the Naval Postgraduate School on unipolar arcing in metal mirrors fits into the above-threshold category. It was shown that, after the production of a plasma resulting from the interaction of a laser and a metallic surface, there are three principal interrelated damage mechanisms: thermal evaporation, ion sputtering, and unipolar arcing. The first two, being principally thermo-mechanical, are well known to the laser damage community. The third, unipolar arcing, being primarily an electrical interaction with thermal-mechanical aspects, is not. Results of such high-level, laser-induced interactions are pits and craters resulting from micro-arcs between the optical element and the adjacent laser heated plasma. When the plasma is not present, unipolar arc craters are not observed.

4. Recommendations

One of the clearest trends at the Fourteenth Annual Boulder Damage Symposium was the general realization that laser radiation in an actual system is going to strike a component surface more than once and that we should therefore understand the effects of multiple irradiations on component performance. Unexpected problems arise when a component is subjected to hundreds, thousands or millions of laser pulses and the physical processes behind these phenomena, although much clearer than previously, are still not well enough understood. More work on multipulse or multiexposure damage testing is therefore clearly desirable. Coupled with and closely related to the multipulse requirement is the move to study shorter wavelength laser effects. Many visible and ultraviolet lasers must be used in a pulsed mode. They bring in other new problems as well. In the infrared one is concerned with multiphonon effects and thermal heating of surfaces, coatings and coating defects. At shorter wavelengths an entirely different set of concerns becomes important. Electronic transitions suddenly become of primary importance and multiphoton effects must be understood. In addition, the light quantum now has enough energy that a range of effects in defects, impurities, etc., now becomes possible and photochemical as well as photothermal effects must be considered. Surface desorption or adsorption of contaminants must be considered, surface states must be determined in much finer detail and surface preparation processes need to be developed and perfected. The entire question of disturbed surface layers and surface microroughness takes on added importance at shorter optical wavelengths and more interactions with solid state and semiconductor physicists, who have been worrying the surface-interaction-with-electron problem for years, is recommended.

There is a question as to whether we can continue to tolerate the inadequate surface standards with which optics has been plagued for years. As we go to visible and ultraviolet wavelengths the absorption and scattering from surfaces is cursed by factors which are entirely unrelated to the "scratch-dig" surface standards by which optical surfaces are traditionally specified. The problem clearly is becoming acute and the ASTM, which was instrumental in initially starting this conference, together with the Optical Society of America and other technical organizations, such as the Quantum Electronics and Applications Section of the IEEE, are the logical organizations to resolve this situation.

To progress toward more perfect optical coatings, continued, thorough evaluation and optimization of novel deposition techniques is encouraged. Especially those capable of producing totally amorphous or single-crystal films should be compared with those resulting in polycrystalline structure. Molecular-beam epitaxy of wide-bandgap materials should be demonstrated, and ion beams should be exploited to determine if dense, water-free coatings are feasible.

To facilitate optimization of the coating deposition parameters in the pursuit of ultra-low loss multilayer reflectors, high-precision measurement techniques with four and five-decimal place resolution need to be utilized on a routine basis. Finally, finely-resolved spatial maps of coating absorption should be compared with similar maps of damage susceptibility.

A welcome trend is the realization that lasers and laser optical trains may not always operate at room temperature, and low temperature or cyclic performance in particular must be investigated. The sometimes slow but consistent progress in better understanding the engineering details of real systems should be encouraged. This Symposium is not the place to discuss detailed hardware designs but it is very appropriate to consider the general principles on which good hardware designs are based. Future papers in such areas are encouraged.

5. Acknowledgments

The editors would like to acknowledge the invaluable assistance of Mr. Aaron A. Sanders and the other involved staff members of the National Bureau of Standards in Boulder, Colorado, for their interest, support, and untiring efforts in the professional operation of the Symposium. Particular thanks to Ms. Susie Rivera for her part in the preparation and publication of the Proceedings and to Ms. Pat Whited of the Air Force Weapons Laboratory for conference coordination. We are also grateful to Commander Theodore Saito of the Air Force Academy and Dr. Kenneth Jungling of the University of New Mexico for serving as rapporteurs for the poster sessions.

6. References

[1] Glass, A. J.; Guenther, A. H., eds., Damage in laser glass, ASTM Spec. Tech. Publ. 469 (ASTM, Philadelphia, PA, 1969).

[2] Glass, A. J; Guenther, A. H., eds., Damage in laser materials, Nat. Bur. Stand. (U.S.) Spec. Publ. 341 (1970).

[3] Bloembergen, N., Fundamentals of damage in laser glass, National Materials Advisory Board Publ. NMAB-271 (National Academy of Sciences, Washington, D.C., 1970).

[4) Bloembergen, N., High power infrared laser windows, National Materials Advisory Board Publ. NMAB-356 (National Academy of Sciences, Washington, D.C., 1971).

[5] Glass, A. J.; Guenther, A. H., eds., Laser induced damage of optical materials: 1972, Nat. Bur. Stand. (U.S.) Spec. Publ. 372 (1972).

[6] Glass, A. J.; Guenther, A. H., eds., Laser induced damage in optical materials: 1973, Nat. Bur. Stand. (U.S.) Spec. Publ. 387 (1973).

[7] Glass, A. J.; Guenther, A. H., eds., Laser induced damage in optical materials, 1973: a conference report, Appl. Opt. 13, 74 (1974).

[8] Glass, A. J.; Guenther, A. H., eds., Laser induced damage in optical materials: 1974, Nat. Bur. Stand. (U.S.) Spec. Publ. 414 (1974).

[9] Glass, A. J.; Guenther, A. H., eds., Laser induced damage in optical materials: 6th ASTM symposium, Appl. Opt. 14, 698 (1975).

[10] Glass, A. J.; Guenther, A. H., eds., Laser induced damage in optical materials: 1975, Nat. Bur. Stand. (U.S.) Spec. Publ. 435 (1975).

[11] Glass, A. J.; Guenther, A. H., eds., Laser induced damage in optical materials: 7th ASTM symposium, Appl. Opt. 15, 1510 (1976).

[12] Glass, A. J.; Guenther, A. H., eds., Laser induced damage in optical materials: 1976, Nat. Bur. Stand. (U.S.) Spec. Publ. 462 (1976).

[13] Glass, A. J.; Guenther, A. H., eds., Laser induced damage in optical materials: 8th ASTM symposium, Appl. Opt. 16, 1214 (1977).

[14] Glass, A. J.; Guenther, A. H., eds., Laser induced damage in optical materials: 1977, Nat. Bur. Stand. (U.S.) Spec. Publ. 509 (1977).

[15] Glass, A. J.; Guenther, A. H., eds., Laser induced damage in optical materials: 9th ASTM symposium, Appl. Opt. 17, 2386 (1978).

[16] Glass, A. J.; Guenther, A. H., eds., Laser induced damage in optical materials: 1978, Nat. Bur. Stand. (U.S.) Spec. Publ. 541 (1978).

[17] Glass, A. J.; Guenther, A. H., eds., Laser induced damage in optical materials; 10th ASTM symposium, Appl. Opt. 18, 2112 (1979).

[18] Bennett, H. E.; Glass, A. J.; Guenther, A. H.; Newnam, B. E., eds., Laser induced damage in optical materials: 1979, Nat. Bur. Stand. (U.S.) Spec. Publ. 568 (1979).

[19] Bennett, H. E.; Glass, A. J.; Guenther, A. H.; Newnam, B. E., eds., Laser induced damage in optical materials: 11th ASTM symposium, Appl. Opt. 19, 2375 (1980).

[20] Bennett, H. E.; Glass, A. J.; Guenther, A. H.; Newnam, B. E., eds., Laser induced damage in optical materials: 1980, Nat. Bur. Stand. (U.S.) Spec. Publ. 620 (1981).

[21] Bennett, H. E.; Glass, A. J.; Guenther, A. H.; Newnam, B. E., eds., Laser induced damage in optical materials: 12th ASTM symposium, Appl. Opt. 29, 3003 (1981).

[22] Bennett, H. E.; Guenther, A. H.; Milam, D.; Newnam, B. E., eds., Laser induced damage in optical materials: 1981, Nat. Bur. Stand. (U.S.) Spec. Publ. 638 (1983).

[23] Bennett, H. E.; Guenther, A. H.; Milam, D.; Newnam, B. E., eds., Laser induced damage in optical materials: 13th ASTM symposium, Appl. Opt. 22, 3276 (1983).

1.3 μm Laser Window Materials Survey Continued

R. J. Harris, D. V. Dempsey, D. B. O'Quinn,
and M. E. Gangl
University of Dayton
Research Institute
Dayton, Ohio 45469

and

W. L. Knecht
Air Force Wright Aeronautical Laboratories,
Materials Laboratory
Wright-Patterson Air Force Base, Ohio 45433

This work represents a continuation of efforts to assess candidate window materials for use in the iodine laser operating at 1.315 μm. The results presented here are effective optical absorption coefficient, β_{eff}, as measured using laser rate calorimetry at 1.319 μm, spectral transmission from the ultraviolet through the infrared region, and thermo-optic coefficient, $\partial n/\partial T$, at four wavelengths in the visible and near infrared. The materials reported in this paper include fused silica, sapphire, water clear ZnS, LiF, MgF_2, stabilized cubic zirconia, undoped Q-98 glass from Kigre, and Schott IRG-3, LG-660, LG-670, LG-680, LG-750, LG-760, and LG-810 glasses.

Key Words: Al_2O_3; infrared materials; laser calorimetry; laser glass; LiF; MgF_2; optical absorption; SiO_2; thermo-optic coefficient; ZnS; ZrO_2

1. Introduction

The measurements reported here were performed as a part of the continuing effort to identify and assess candidate materials for use in the development of the iodine (I*) laser operating at 1.315 μm. This effort has been ongoing for the last three years and several materials properties were reported earlier [1,2,3]. Here we report properties of additional materials studied.

The optical absorption coefficients given here were obtained using laser rate calorimetry [4,5] using a Quantronix 114 Nd:YAG laser modified to operate at 1.319 μm. These values are the effective absorption coefficients, β_{eff}, calculated using the equation

$$\beta_{eff} = \frac{(1-R_b)}{(1+R_b)} \frac{P_A}{P_T} = \frac{2n}{1+n^2} \frac{mC_p}{\ell} \frac{\Delta T}{\Delta t} \frac{1}{P_T} \qquad (1)$$

where P_A is the power absorbed in the sample, P_T is the power transmitted, R_b is the reflection coefficient at the exit face, n is the refractive index, m is the mass of the sample, C_p is the heat capacity, ℓ is the sample thickness, and $(\Delta T/\Delta t)$ is the sum of the heating and cooling slopes.

The value reported is the sum of the bulk and surface absorption, whence the term "effective":

$$\beta_{eff} \equiv \beta_B + (1+x)\beta_s/\ell \qquad (2)$$

where β_B is the bulk absorption coefficient and β_s is the fractional absorption per surface. The x is a factor between 1 and n depending on the coherence conditions of the irradiating light [6].

Since the surface absorption is included in the measurement, any remarkable condition of the surface such as cloudiness or roughness is included in the sample descriptions given below.

Spectral transmission measurements were made using a Beckman 5270 and Perkin-Elmer 180 spectrophotometer with a combined spectral range of 0.25 to 50 μm. Transmission traces of some of the more uncommon materials will be presented below also.

Thermo-optic coefficient measurements were made using an interferometric technique described in detail in Reference 7. The method involves observing the temperature change necessary for a one fringe change in optical path for internal interference in the sample and then calculating the thermo-optic coefficient using the equation

$$\partial n/\partial T = \lambda/2\ell\Delta T - n\alpha$$

where λ is the wavelength of the laser used for the measurement, ΔT is the temperature change per fringe, α is the thermal expansion coefficient and the other quantities are as defined above. The measurements were made in the temperature range from 25 to 85 degrees C at 0.6328, 1.15, 1.319, and 3.39 μm.

2. Experimental Results

The results presented here are those obtained on materials studied since references 2 and 3. Spectral transmission traces are presented only for the glasses since the other materials have essentially featureless spectra in the high transmission region. For the $\partial n/\partial T$ data the values of the constants used in the calculation are presented in a separate table.

Two varieties of fused silica (SiO_2) were obtained for characterization, Suprasil W-1 from Heraeus-Amersil and Vitreosil IR-1 from Thermal American Fused Quartz Company. The samples were 70 mm in diameter by 13 mm thick. These dimensions are approximately twice the standard size sample we have been characterizing, so the calorimetric absorption cannot be directly compared with the materials of the standard size with confidence. Their greater thermal mass made the measurement difficult since it strained the capability of our equipment.

The Suprasil W-1 absorption coefficient was $0.364\times10^{-3}cm^{-1}$ which is nearly twice as high as that obtained in earlier measurements on smaller samples of $0.190\times10^{-3}cm^{-1}$, but it is still lower than other types of fused silica (see Ref. 2). It is unclear whether this difference is due to the difference in sample size or difference in batch. The spectral transmission is not significantly different from that of the smaller samples. The transmission curve is shown in Figure 1.

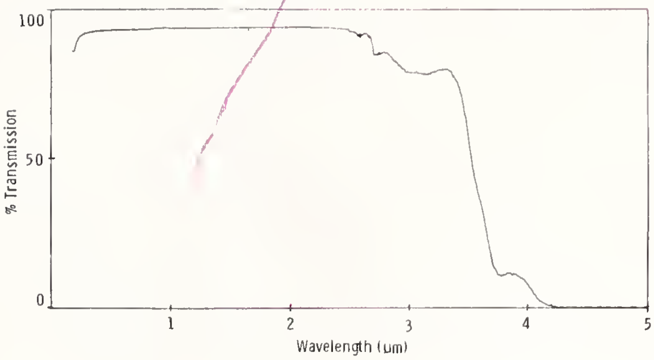

Figure 1. Spectral transmission of Suprasil W-1. Sample thickness is 13 mm.

The Vitreosil IR-1 showed considerable variation sample to sample for the absorption coefficient and one of the three showed very large variation as a function of location on the sample. There was also considerable difference in the strength of an absorption band near 2.7 μm, presumably the OH band, from sample to sample and in the one odd sample in the 1.3 μm absorption. The other two showed homogeneity to ±0.2% in transmission at 2.7 μm. The transmission spectra for the 2.5 to 5 μm spectral region are shown in Figure 2, and Figure 3 shows a map of transmission for the odd sample depicting the severe inhomogeneity. The absorption coefficient ranged from 0.4 to $0.73 \times 10^{-3} cm^{-1}$. Interferometry and Schlieren photography did not show conclusive evidence of inhomogeneity in refractive index for the odd sample.

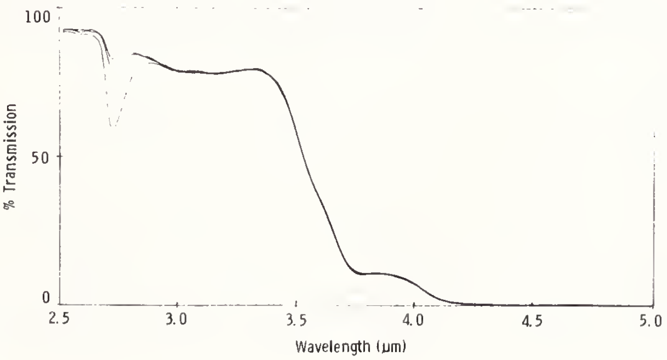

Figure 2. Spectral transmission of three different samples of Vitreosil IR-1 showing strong differences in the intensity of the absorption band at 2.7 μm. All samples are 13 mm thick.

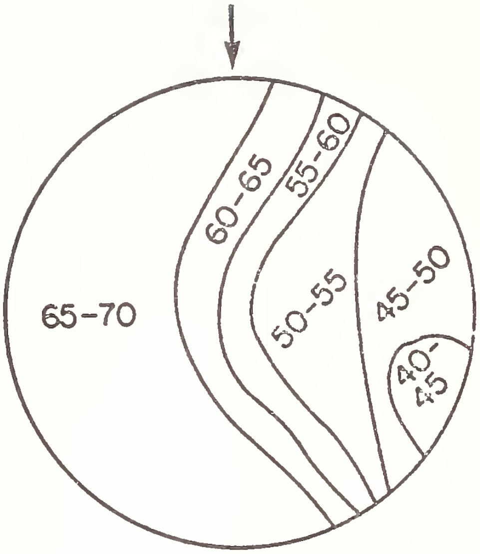

Figure 3. Transmission map of Vitreosil IR-1 sample #3949 showing approximate lines of constant transmittance. The sample was measured at 2.7 μm at various locations and showed the above extreme inhomogeneity.

Sapphire (Al_2O_3) samples were obtained from Crystal Systems and Union Carbide for measurements. The Crystal Systems samples were 70 mm diameter by 13 mm thick and as noted above may not be directly comparable to other sample measurements. The absorption coefficients for the three samples showed variability from 0.3 to $0.65\times10^{-3}cm^{-1}$ from sample to sample but little inhomogeneity on a particular sample. These values are somewhat higher than earlier measurements on Crystal Systems sapphire of $0.211\times10^{-3}cm^{-1}$ of the standard 38 mm diameter size (see Ref. 2).

The Union Carbide sapphire were standard size samples. The measured absorption coefficient for them was $0.359\times10^{-3}cm^{-1}$ which is approximately 50% higher than the best Crystal Systems material. All samples were oriented with the c-axis perpendicular to the face (0001).

Five 70 mm diameter by 7 mm thick LiF samples were received from Harshaw. The samples showed little sample to sample variation or inhomogeneity in individual samples. The absorption coefficient measured for these samples was $0.534\times10^{-3}cm^{-1}$ which is significantly higher than the earlier measurement of $0.133\times10^{-3}cm^{-1}$ on standard size samples. Again, this disparity may be due to sample size.

Harshaw also sent five 70 mm diameter by 7 mm thick MgF_2 samples. The samples were randomly oriented with only one of the five having the c-axis nearly perpendicular to the face as desired. The orientation of this sample was about five degrees off. The measured absorption coefficient for these samples was $0.710\times10^{-3}cm^{-1}$ with again little variation between samples or within a sample. This is again somewhat higher than earlier measurements of $0.307\times10^{-3}cm^{-1}$ on standard size samples.

A sample of RAYTRAN® water clear ZnS from a recent batch was sent from Raytheon for comparison with an older sample. The spectral transmission was not significantly different from the older material; however, the absorption coefficient was lower. The newer material had a measured absorption coefficient of $0.608\times10^{-3}cm^{-1}$ as compared with $1.23\times10^{-3}cm^{-1}$ for the older material.

A sample of stabilized cubic zirconia, ZrO_2 with 12.0 mol% Y_2O_3 was received from Ceres Corporation and polished by Adolph Meller. It was polished only to window shine specification so the surface was too uneven for transmission measurements. The measured absorption coefficient was $0.848 \times 10^{-3} cm^{-1}$.

Results from measurements on Kigre, Inc. Q-98 phosphate glass lightly doped with Nd were reported in Ref. 2 and Kigre made a special melt of the glass with Al substituted for the Nd dopant. Virtually all the absorption band features in the visible and near IR were removed, as can be seen in the comparison of the transmission spectra in Figures 4 and 5. There are three small residual bands in the visible which appear to be due to some residual Nd contamination in the melt. The measured absorption coefficient increased, however, from $0.360 \times 10^{-3} cm^{-1}$ for the Nd doped glass to $1.36 \times 10^{-3} cm^{-1}$ for the Al doped glass.

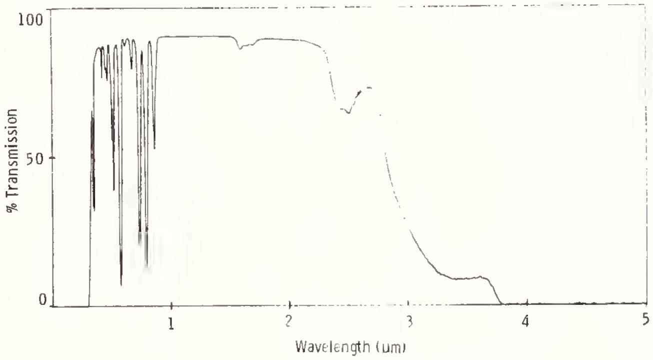

Figure 4. Spectral transmission of Nd doped Q-98 glass from Kigre. Sample thickness is 10 mm.

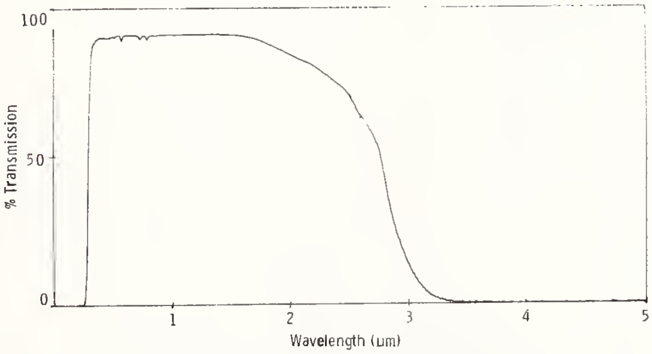

Figure 5. Spectral transmission of Al doped Q-98 glass from Kigre. The small structure in the visible corresponds to the strong bands in the Nd doped material and is probably due to residual Nd contamination in the melt. Sample thickness is 10 mm.

Several glasses were received from Schott Optical for characterization. These included IRG-3 dense lanthanum flint glass; three silicate glasses, LG-660, LG-670, and LG-680; two phosphate glasses, LG-750 and LG-760; and one fluorophosphate glass, LG-810. The LG series glasses are laser glasses and are doped with Nd. The transmission spectrum of IRG-3 is presented in Figure 6.

The laser glasses show several absorption bands in the visible and near IR, but are featureless in the neighborhood of 1.3 µm. The transmission spectrum of LG-670 is shown in Figure 7 as representative of the general nature of all the LG series. The absorption coefficients of these glasses fall in the range of 0.58 to $4.12\times10^{-3}cm^{-1}$ and are given in Table 1, which summarizes the results of all the materials measured. Two of the glasses, LG-670 and LG-680, were returned to Schott after their polish by Unertle Optical for hardening. This process involves an ion exchange of sodium for lithium in a hot salt bath and produces a clouded surface. Post hardening measurements were done on these samples and showed increased scattering at the surface and also increased absorption. The increased absorption may be due to the surface effects. The samples will be repolished and remeasured to more fully investigate the increase.

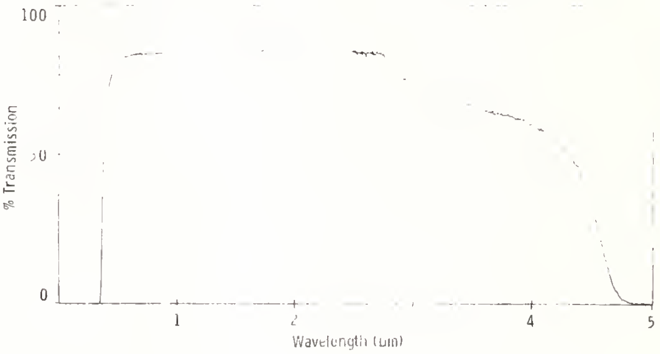

Figure 6. Spectral transmission of Schott IRG-3 glass. Sample thickness is 5 mm.

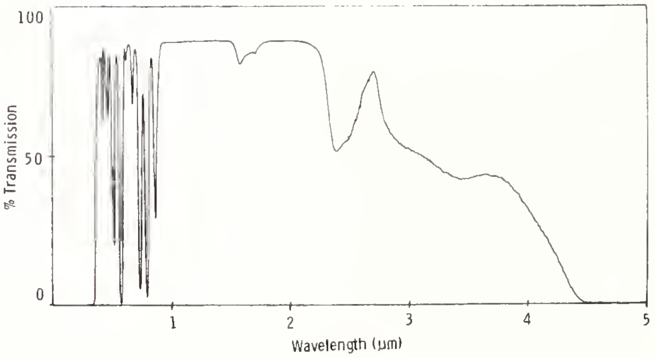

Figure 7. Spectral transmission of Schott LG-670 laser glass. The structure is due to Nd doping. Sample thickness is 7 mm.

Table 1. Summary of Calorimetric Absorption Results at 1.3 μm

Material (Source)	$\beta_{eff} \div 10^{-3} cm^{-1}$	Results
LiF (Harshaw)	0.534	
MgF_2 (Harshaw)	0.710	
RAYTRAN® ZnS (Raytheon)	0.608	
$ZrO_2:Y_2O_3$ (Ceres)	0.848	
Al_2O_3:		
(Union Carbide)	0.359	
(Crystal Systems)	0.293	Best
	0.647	Worst
	0.501	Average
Fused Silica:		
Suprasil W-1 (Heraeus Amersil)	0.364	
Vitreosil IR-1 (Thermal American Fused Quartz Co.)	0.406	Best
	0.727	Worst
	0.548	Average
LG-660 (Schott)	0.605	
LG-670 (Schott)	0.575	
	2.20	After hardening
LG-680 (Schott)	0.898	
	2.99	After hardening
LG-750 (Schott)	0.798	
LG-760 (Schott)	0.848	
LG-810 (Schott)	0.844	
Q-98, undoped (Kigre)	1.36	
IRG-3 (Schott)	4.12	

Measurements of $\partial n/\partial T$ were also made on several of the materials in the survey. The values obtained in the past year are presented in Table 2. The value for LiF is a correction of a value presented in Ref. 3. The values of the constants used in calculating the $\partial n/\partial T$ results are given in Table 3. The MgO was produced by Adolph Meller. The LiF was supplied by Harshaw. The CORTRAN samples are glass made by Corning and designated 9753 and 9754 by the manufacturers. The Fused Silica is Suprasil II made by Heraeus-Amersil. The Q-98 glass is a laser glass produced by Kigre, Inc. and was doped with aluminum instead of neodymium. Its $\partial n/\partial T$ value is slightly lower than its neodymium doped analog. The IRG- and LG- series glasses are from Schott Optical, IRG-3 is a lanthanum dense flint glass, IRG-N6 is a Ca Al silicate glass, IRG-7 is a lead silicate glass, and the LG-660 and LG-670 are neodymium doped silicate glasses.

Table 2. Summary of $\partial n/\partial T$ Results

	$\partial n/\partial T \div 10^{-5}/°C$			
Material	@.6328 μm	@1.15 μm	@1.32 μm	@3.39 μm
MgO	1.13±0.46	1.10±0.35	1.15±0.38	1.11±0.24
LiF	-2.00±0.37	-2.02±0.20	-2.10±0.19	----
Cortran 9753	0.41±0.25	0.48±0.25	0.39±0.15	0.60±0.15
Cortran 9754	0.88±0.43	0.75±0.32	0.74±0.20	1.17±0.44
Fused Silica	1.00±0.24	1.03±0.23	----	----
IRG-3	0.02±0.23	-0.21±0.12	-0.20±0.04	----
IRG-N6	0.39±0.14	0.34±0.13	0.39±0.25	----
IRG-7	-0.22±0.20	-0.29±0.12	-0.26±0.05	----
Undoped Q-98 Glass	0.05±0.15	-0.22±0.09	-0.27±0.10	Opaque
LG-660	-0.08±0.27	-0.16±0.34	-0.06±0.29	----
LG-670	-0.08±0.16	0.07±0.12	----	----

Table 3. Constants Used in $\partial n/\partial T$ Calculations

Material	$\alpha \div 10^{-6}/°C$	n@.6328 μm	n@1.15 μm	n@1.312 μm	n@3.39 μm
MgO	10.5	1.74	1.74	1.74	1.74
LiF	35.0	1.39	1.39	1.39	1.39
Cortran 9753	6.2	1.61	1.61	1.61	1.61
Cortran 9754	6.2	1.66	1.66	1.66	1.66
Fused Silica	0.49	1.45	1.45	1.45	1.41
IRG-3	8.1	1.84	1.81	1.81	1.78
IRG-N6	6.3	1.59	1.58	1.57	1.56
IRG-7	9.6	1.56	1.55	1.54	1.52
Undoped Q-98 Glass	8.2	1.55	1.59	1.59	Opaque
LG-660	10.7	1.52	1.51	1.51	1.51
LG-670	9.26	1.57	1.56	1.56	1.56

3. Conclusions

Optical absorption at 1.3 μm, spectral transmission, and the thermo-optic coefficient have been measured for a variety of glass and crystalline materials for possible use with the iodine laser. The use of larger, non-standard size samples for several of these materials resulted in larger measured absorption coefficient than obtained for the same materials measured earlier with the standard 38 mm diameter samples. This increase might be associated with difficulties in fabricating larger samples, but is more likely due to difficulties in making the calorimetric measurement on samples of large thermal mass. The most noteworthy of the large samples was the Vitreosil IR-1 which showed considerable inhomogeneity in absorption and also in transmission.

The Schott LG series glasses were consistently low in absorption, but none were as good as the Nd doped Q-98 laser glass from Kigre.

4. References

[1] Fernelius, Nils C., Dempsey, David V., Walsh, David A., O'Quinn, David B., and Knecht, Walter L., "Survey of 1.3 μm Window Materials," Proceedings of the Twelfth Symposium on Optical Materials for High Power Lasers, Boulder, Colorado (1980).

[2] Fernelius, Nils C., Dempsey, David V., O'Quinn, David B., Gangl, Michael E., and Knecht, Walter L., "Survey of 1.3 μm Window Materials Continued," Proceedings of the Thirteenth Symposium on Optical Materials for High Power Lasers, Boulder, Colorado (1981).

[3] Harris, Richard J. and Gangl, Michael E., "Thermo-Optic Coefficient of 1.3 μm Laser Window Materials," Proceedings of the Thirteenth Symposium on Optical Materials for High Power Lasers, Boulder, Colorado (1981).

[4] Pinnow, D. A. and Rich, T. C., Appl. Opt. 12, 984 (1973).

[5] Hass, M., Davisson, J. W., Klein, P. H., and Boyer, L. C., J. Appl. Phys. 45, 3959 (1974).

[6] Fernelius, Nils C. and Johnston, George T., "Discussion of a Theory of Analysis of Rate Calorimetry which Includes Coating Absorption," Proceedings of the Tenth Symposium on Optical Materials for High Power Lasers, Boulder, Colorado (1978).

[7] Harris, R. J., Johnston, George T., Kepple, G. A., Krok, P. C., and Mukai, H., Appl. Opt. 16, 436 (1977).

Thermal Conductivity of a Fluorozirconate Glass
and Tellurium Dioxide Single Crystals

Kathryn A. McCarthy and H.H. Sample

Physics Department, Tufts University, Medford, MA 02155

Measurements of the thermal conductivity of a fluorozirconate glass and two tellurium dioxide crystals have been made in the 1.5 - 100 K temperature range. The thermal conductivity of the glass increases linearly with temperature in the lowest temperature region, "plateaus" from 8 K to 20 K, and then increases again. These measurements are part of a continuing program to measure thermal conductivities of materials suitable for electro-optic devices and as transmitting materials in the visible and in the infrared, in the 1.5 to 400 K temperature range.

Keywords: Cryogenic; fluorozirconate glass; tellurium dioxide; thermal conductivity; thermo measurements.

Knowledge of the heat conduction rate in materials used with high power lasers is essential in the design of such systems. Here we report measurements of the thermal conductivities of a fluorozirconate glass (ZBLAN glass, see below) and of single crystals of tellurium dioxide (TeO_2), in the 1.5 - 100 K temperature range. The present data are part of a continuing program to measure the thermal properties of materials useful as infrared (IR) transmitting windows and/or for IR acousto-optic devices. The thermal conductivity measurements for these and other materials are currently being extended to T = 400 K.

Thermal conductivity was measured via the steady state method, utilizing a cryostat described previously [1]. Except as noted below, the absolute experimental accuracy of the measurements is better than 5% at all temperatures.

The ZBLAN glass specimen [2] had a composition (in mol%) as follows: $ZrF_4 = 55.7$, $BaF_2 = 14.4$, $LaF_3 = 5.8$, $AlF_3 = 4.0$, $NaF = 20.1$. It had a density $\rho = 4.26$ g/cm^3, index of refraction $n_D = 1.504$, and coefficient of linear expansion $\alpha = 174 \times 10^{-7}$ °C^{-1}. The specimen had dimensions 9.3 mm x 4.8 mm x 27.5 mm long and an etched surface.

The tellurium dioxide single crystals were obtained from two sources. Sample No. 1 [3] had dimensions 3.8 mm x 3.8 mm x 26 mm, with the long dimension (heat-flow direction) parallel to the c-axis of the crystal; the surface was optically polished and the crystal was of optical quality. Unfortunately, this sample cracked before a complete set of measurements was accomplished. Sample No. 2 [4] had dimensions 4.3 x 4.7 x 25 mm, cut so the heat-flow direction was along a (110) crystal direction (i.e. perpendicular to the c-axis). Its surface was not polished.

Figure 1 shows the thermal conductivity results for the ZBLAN specimen. The error bars at the highest temperatures are due to uncertainties in correcting for radiation heat losses [5]; otherwise measurement errors are smaller than the size of the data points. As can be seen, the thermal conductivity is in the 10^{-3} Watt cm^{-1} K^{-1} range, increases with increasing temperature, and shows a "plateau" in the 8 -20 K region. These features are similar to those observed in other amorphous systems [6-8]; for comparison we have included typical behavior for silica and borosilicate glasses [9]. At our lowest measurement temperatures, $K \propto T^{1.4}$, also similar to the temperature dependence for other glasses, at comparable temperatures.

While it is generally agreed that the existence of the plateau region in all glasses is due to an abrupt decrease in phonon mean free paths with increasing frequency, the exact cause of the decrease has not been completely resolved [6]. The similarity of the ZBLAN glass data to borosilicate glass data above 20 K leads us to believe that the conductivities of the two materials will also be similar at still higher temperatures. So, for example, a conductivity on the order of 10^{-2} W cm^{-1} K^{-1} is to be expected for ZBLAN glass at T = 300 K.

Figure 2 shows the thermal conductivity results for the two tellurium dioxide crystals. For these high conductivity specimens, it was necessary to use very small temperature gradients below T = 4 K ($0.1\% \lesssim \Delta T/T < 1\%$), resulting in rather large random measurement errors, shown by the error bars. Above 8 K, the errors are less than the size of the data points. As mentioned above,

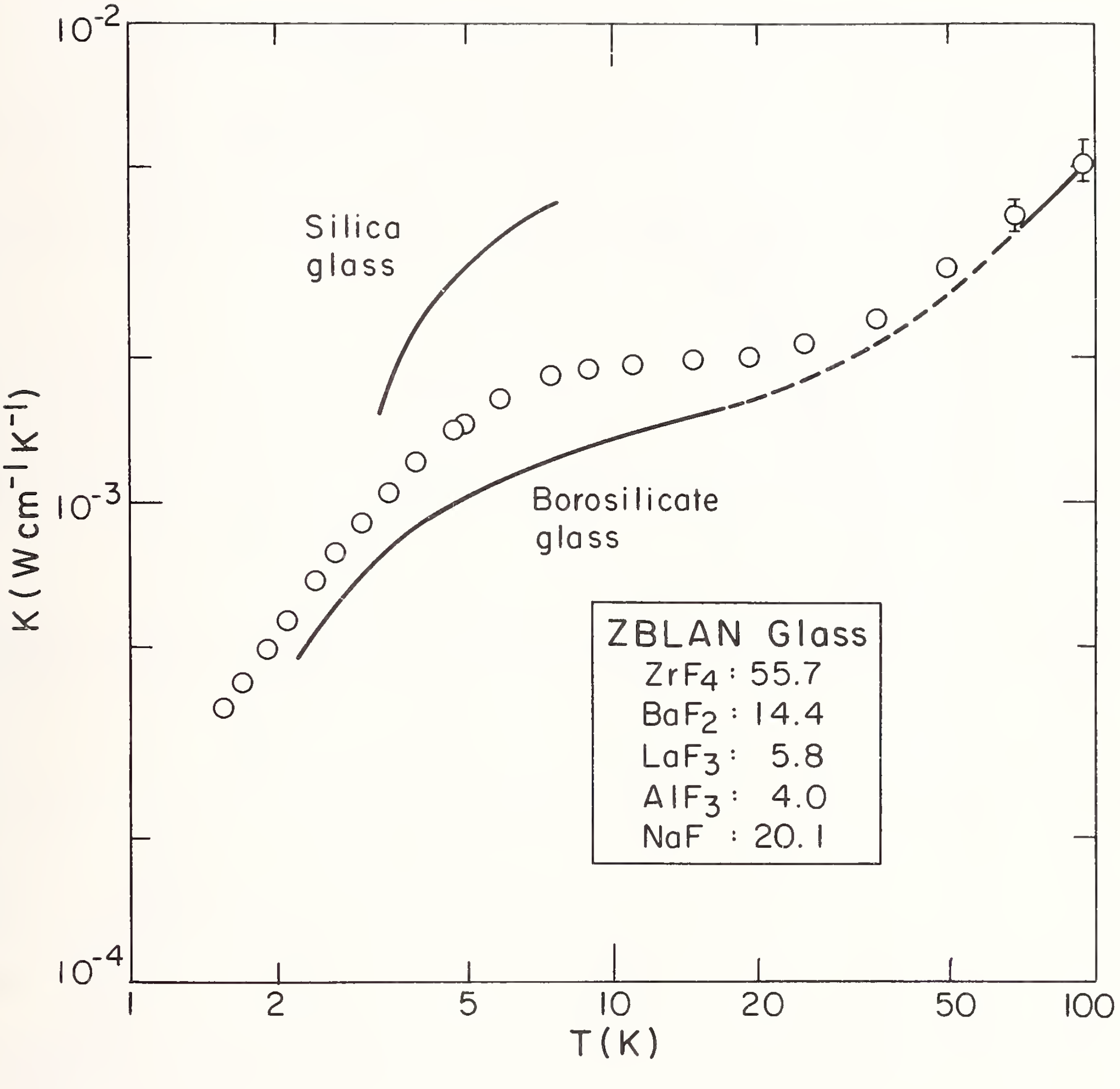

Figure 1. Thermal conductivity of a fluorozirconate (ZBLAN) glass.

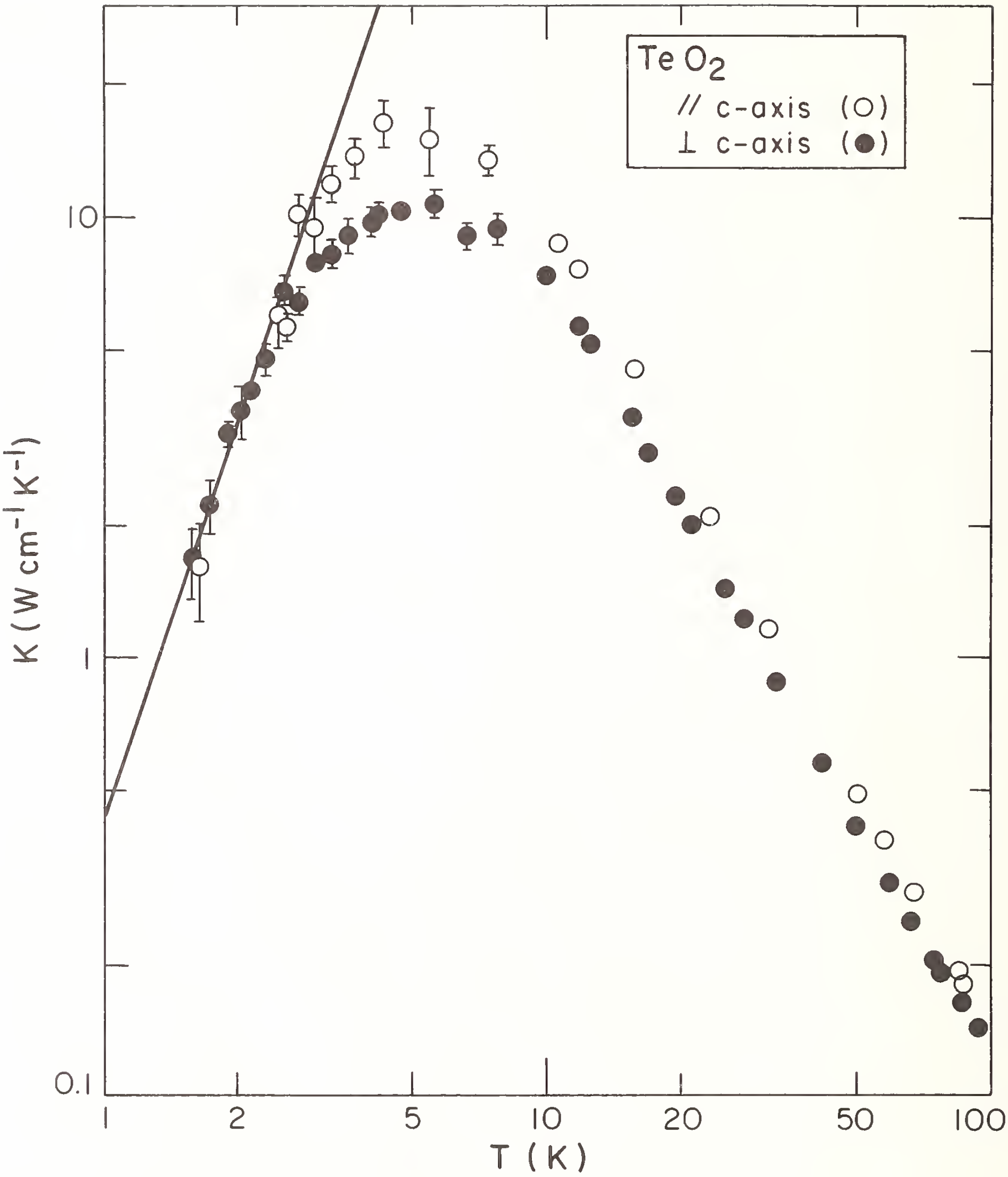

Figure 2. Thermal conductivities of tellurium dioxide single crystals: o, Sample No. 1 ($\dot{Q}$ parallel to c-axis); •, Sample No. 2 ($\dot{Q}$ perpendicular to c-axis). The solid line illustrates the T^3 dependence of K at low temperatures.

Sample No. 1 cracked before a complete set of measurements could be made, which explains the paucity of data for this specimen. The general features to be noted for the tellurium dioxide data are: 1) the T^3 dependence at low temperatures, shown by the solid line in Figure 2; 2) the high peak values of the conductivity at about 5 K (10-15 Watt cm^{-1} K^{-1}); 3) the rapid decrease of K with temperature for temperatures above the peak (typical of high conductivity crystalline insulators); and 4) the lower conductivity of Sample No. 2 ($\dot{Q} \perp$ c-axis) compared to Sample No. 1 ($\dot{Q}$ // c-axis), at higher temperatures.

The T^3 dependence of K at low temperatures can be used to calculate [10] a Debye temperature for TeO_2 of θ = 250 K, higher than the value (160 K) calculated from room-temperature elastic constant data [11]. The high peak value of K is due to the relatively low Debye temperatures (high specific heat) coupled with low specimen impurity and defect concentrations which would reduce (and smear out) the conductivity peak. We believe that the lower conductivity (by about 20%) of Sample No. 2 relative to Sample No. 1 is due to the intrinsic orientation dependence of K in this anisotropic material. However, the two crystals were from different suppliers, and the possibility that some of this difference is due to a higher impurity concentration in Specimen No. 2 cannot be ruled out. Finally, extrapolation of the TeO_2 data to higher temperatures leads us to estimate a conductivity of $(3\pm1) \times 10^{-2}$ W cm^{-1} K^{-1} at T = 300 K, in good agreement with the value quoted by the manufacturer [12], for Sample No. 1.

It is interesting to note that while these two types of IR materials have quite different conductivities at low temperatures, their room temperature conductivities are nearly the same. This fact may be important for the design of high power laser systems. If getting heat out of a window material or optical component is a problem, then operating the component at reduced temperatures can greatly improve the situation, for components constructed of high purity crystalline materials. This will not be the case for amorphous solids (glasses), whose conductivities generally decrease as the temperature is lowered.

The authors wish to thank M. Drexhage for supplying the ZBLAN glass sample, and both Crystal Technology Inc. and Itek Corporation for the loan of the TeO_2 specimens.

References

[1] R.A. Kashnow and K.A. McCarthy, J. Phys. Chem. Solids 30, 813 (1969); M. Jirmanus, K.A. McCarthy, H.H. Sample and J. Bulman (unpublished).

[2] Sample obtained from M. Drexhage, RADC/Hanscom Field, Bedford, MA.

[3] Crystal Technology Inc., 1035 East Meadow Circle, Palo Alto, CA.

[4] Sample prepared by S. Daigneault, Itek Corporation, 10 Maguire Rd., Lexington, MA.

[5] Our measurement technique automatically corrects for radiation losses to first order, so no "correction" has been explicitly applied to the data in figure 1. The error bars represent ±25% of the calculated effect of the radiated heat on the conductivity.

[6] M.P. Zaitlin and A.C. Anderson, Phys. Rev. B12, 4475 (1975).

[7] H. Böttger, Phys. Stat. Sol. B62, 9 (1974).

[8] R. Berman, Thermal Conduction in Solids (Clarendon Press, Oxford, 1976).

[9] Data tabulated in Thermophysical Properties of Matter, The Thermophysical Properties Research Center Data Series, edited by Y.S. Touloukian, R.W. Powell, C.Y. Ho and P.G. Klemens (IFI/Plenum, New York, 1970), Vol. 2. Silica: p. 922, curve 55; borosilicate: p. 922, curve 39.

[10] The relationship $K = 1/3\, c\, v\ell = 2\pi^2 k^4 T^3 \ell / 15\, \hbar^3 v^2$ (see Ref. 6) is used in conjunction with $v = (V/6\pi^2)^{1/3}(k\theta/\hbar)$ to extract the Debye temperature (θ), given the T^3 dependence of the conductivity (K), the volume per atom (V) of TeO_2 of 1.47×10^{-23} cm^3, and taking the phonon mean free path (ℓ) to be on the order of the cross-sectional dimensions of the crystal or $[4.3 \times 4.7]^{\frac{1}{2}} = 4.5$ mm.

[11] N. Uchida and Y. Ohmachi, J. Appl. Phys. 40, 4692 (1969).

[12] Assuming that the value of 30 μW cm^{-1} K^{-1} quoted in the manufacturer's [3] product information sheet is in error, and should actually be 30 mW cm^{-1} K^{-1}.

Optical characteristics of germanium at 10 microns

R M Wood, S K Sharma and P Waite

GEC Reserach Laboratories, Hirst Research Centre

Wembley, England, HA9 7PP

A review of the parameter values and an in-depth interpretation of the relevant properties of germanium has been made in order to produce a self-consistent theory of the factors determining the absorption properties of germanium windows in CO_2 laser systems.

Theoretically generated absorption coefficient versus temperature curves have been computed and compared with experimental results showing that within the wavelength and temperature range considered the simple free carrier absorption theory is quite adequate in predicting the behaviour of the bulk absorption in doped and intrinsic germanium. Resulting from the unequal absorption cross section of electrons and holes to 10.6 μm radiation it can be shown that the bulk absorption coefficient can be 'fine tuned' to provide different characteristics, in particular increased laser induced damage threshold. It will be shown that many of the beam handling problems found come from the surface component of absorption rather than the bulk. The source of surface absorption often lies in the polishing procedure with trapped polishing material and sub-surface damage. It has also been shown that the main source of residual surface absorption is in the growth of a hygroscopic oxide layer. The thickness of this layer has been studied by calorimetric, c.w. laser damage and gas drying techniques and good agreement has been gained. Water absorbed in this layer may be drawn off by placing the sample in a vacuum or by cleaning with IPA. The growth of the oxide layer has been studied and attempts made to passivate the surface.

Keywords: CO_2 lasers, Germanium, Absorption, Calorimetry

1 Introduction

Germanium is widely used in infra-red laser systems as a window material due to its low dispersion and its low absorption at room temperature in the wavelength range 2-12 μm. The lower of these two limits is defined by the bandgap of the material (figure 1). Decreasing the wavelength of radiation incident on a germanium window from 2 μm results in an absorption coefficient which increases exponentially [1]. There is usually additional structure superimposed on this exponential rise, brought about by exciton formation or the presence of defects and impurities in the crystal. At the long wavelength limit multiphonon infra-red absorption becomes the dominant process. This is a characteristic of the germanium lattice and the limit of 12-13 μm is defined by the fundamental LO phonon frequency associated with it. As the wavelength of incident radiation is increased beyond 12 μm the absorption coefficient increases as before. However, due to the selection rules governing the formation of phonons by the lattice, there is a great deal of structure associated with it [2,3]. This is shown in figure 2. Within the transparent wavelength region the residual absorption is a compound of the weak tails of the fundamental lattice and electronic absorptions, and the intrinsic carrier absorption (figure 3). In practice one would expect to see some contribution from impurities and defects to arise as well. In general, the absorption coefficient behaves according to the approximate relationship shown in equation (1) below [4,5,6].

$$\beta = Aw^{-2} \qquad \ldots(1)$$

β = absorption coefficient in cm^{-1}

A = constant of proportionality

w = frequency of incident radiation

This expression describes the excitation of free carriers into higher states of their host band. The constant, A, applies at a given temperature only.

2 Theory

2.1 Band structure of germanium

The first few conduction bands and the upper valence bands of germanium are reproduced in figure 1 (from reference 7).

The bands close to the intrinsic bandgap of germanium are shown semi-quantitatively in this figure. The valence bands are essentially the same as those in GaAs and Si, with a 'heavy hole' band maximising in energy at about (000). The conduction band does not reach its lowest energy at the zone centre as in the case of GaAs, but instead does so at eight locations on the zone boundary, giving the material an indirect bandgap of 0.67 eV at 300°K [8] and a direct bandgap of 0.803 eV at 300°K [9].

At lower temperatures the indirect path involving phonon co-operation will dominate, whereas at higher temperatures the direct path will contribute. An average activation energy for excitation of free carriers is therefore found to be 0.37 eV in the temperature range 300-1000°K [10]. The temperature coefficient is the same for both the direct and the indirect gap and has been found to be -4×10^{-4} eV $°K^{-1}$.

2.2 The effect of doping germanium

Doping can be either p or n type, depending on the dopant used. For resistivities below about 50 Ω-cm, n-type material has a lower bulk absorption coefficient than p-type at 10.6 μm. This arises because of the higher absorption cross-section of holes to this wavelength of light. Capron and Brill [11] studied the absorption coefficient of n and p type germanium as a function of the doping level and their findings are presented in figure 4.

These results were examined by Bishop and Gibson [12], who treated the problem of interpretation as follows:

The total absorption of a germanium sample can be expressed as:

$$A_{TOT} = \beta_L(T,W)+\alpha_e N_e(T,W)+\alpha_h N_h(T,W)+\beta_{II}(T,W)+\beta_s(T,W) \qquad \ldots(2)$$

where

A_{TOT} = total absorption

α_e = electron absorption cross-section

α_h = hole absorption cross-section

β_{II} = ionised impurity absorption

β_L = lattice absorption

N_e = concentration of electrons

N_h = concentration of holes

β_s = surface absorption

For a crystal in equilibrium we can write:

$$N_e N_h = N_i^2 \qquad \ldots(3)$$

where parameter N_i is the intrinsic carrier concentration.

Also

$$N_i = 2\,\underline{2\pi kT}^{\,3/2}\cdot(N_e N_h)^{3/4}\cdot\exp\{-E_g/2kT\} \qquad \ldots(4)$$

$$h^2 = N_e\ )\ \text{in the intrinsic case}$$

$$= N_h\ )\ \text{and}\ \sigma = e(N_e\mu_e+N_h\mu_h) \qquad \ldots(5)$$

where μ_e, μ_h are the mobilities of holes and electrons; σ is the conductivity in Ω^{-1} cm^{-1} and e is the value of the fundamental electronic charge in coulombs.

From equation (3):

$$N_h = N_i^2/N_e \qquad \ldots(6)$$

substituting equation (6) into equation (2):

$$A_{TOT} = \beta_L + \alpha_e N_{et} + \frac{\alpha_h N_i^2}{N_e} + \beta_{II} + \beta_s \qquad \ldots(7)$$

It has been shown that for low concentrations of dopant impurity, the contribution of the component β_{II} to the overall absorption coefficient, is completely independent of carrier concentration [2], as is the contribution deriving from the sample surfaces.

Therefore differentiating equation (7) with respect to N_e:

$$\frac{dA_{TOT}}{dN_e} = \alpha_e + (\alpha_h N_i^2/N_e^2)\cdot(-1)$$

$$dA_{TOT}/dN_e = \alpha_e - \alpha_h N_i^2/N_e^2 \qquad \ldots(8)$$

For minimum A_{TOT}, this differential must equate to zero.

$$\alpha_e = \alpha_h N_i^2/N_e^2$$

$$N_e = \frac{\alpha_h}{\alpha_e}^{1/2}\cdot N_i \qquad \ldots(9)$$

Substituting in values for electron and hole mobilities at 300°K [10,13] and values for α_e and α_h the absorption cross-sections [5,3,14], the minimum resistivity at room temperature can be calculated and compared to the results of Capron and Brill [11].

The values chosen to fit these data were as follows:

$\mu_h = 1850\ \text{cm}^2\text{V}^{-1}\text{s}^{-1}$

$\mu_e = 4000\ \text{cm}^2\text{V}^{-1}\text{s}^{-1}$

$\alpha_e = 0.15\cdot 10^{-16}\text{cm}^{-2}$

$\alpha_h = 6.50\cdot 10^{-16}\text{cm}^{-2}$

$N_i = 2.7\cdot 10^{13}\ \text{cm}^{-3}$

These give a value for the room-temperature minimum-absorption resistivity of 9 Ω-cm, and a theoretical fit to the data of Capron and Brill as shown in figure 4.

The effect of doping germanium p-type is such that the absorption coefficient increases with increasing concentration of holes in the valence band. For resistivities lower than 30 Ω-cm at room-temperature, heavy absorption occurs as shown in figure 4. Germanium doped n-type exhibits a minimum in the absorption coefficient as explained mathematically above. This arises because of the different absorption cross-sections of electrons and holes to 10.6 μm radiation. The electron cross-section derives from free carrier absorption and the hole cross-section from transitions within the valence band [15]. The minimum occurs when the concentrations of electrons and holes are such that each population has the same absorption; $\alpha_e N_e = \alpha_h N_h$.

The value of the resistivity when this criterion is fulfilled is governed by the respective absorption cross section values and by the intrinsic carrier concentration of the material.

The effect of doping on the thermal conductivity of germanium has been investigated [16]. For doping concentrations of $\leqslant 10^{15}\ \text{cm}^{-3}$ the effect on this transport property is negligible. However, heavily doping the material with impurities such as tin can give decreases of up to 50%.

2.3 Temperature dependences

2.4 Specific heat

Studies have shown that in germanium, the specific heat rises steadily in the region of interest (300-450°K) [17]. From these results, however, it will be noted that the specific heat value changes by only 8% in this temperature range.

2.5 Absorption and transmission

At 10.6 μm, a wavelength at which germanium appears transparent, the absorption tails due to the lattice and the bandgap, are negligible. In this region the absorption can be attributed to the free carriers present in the crystal. As a result, the absorption characteristics of germanium are very strongly dependent on the population density and nature of any impurities present, and the temperature dependence of the absorption coefficient is thus linked to the temperature dependence of the free carrier concentrations.

By using ideas discussed in Section 2.2 and expressions found in the literature [10,12], theoretical curves for the carrier concentration variation as a function of temperature (figure 5) and absorption coefficient variation as a function of both temperature and impurity level (figures 6,7,8) can be produced.

Figure 5 shows how carrier concentrations increase with increasing temperature in the intrinsic régime according to equation (10):

$$N_i = N_e = N_h = 1.76*10^{16}*T^{3/2}\exp\{-4550\cdot 7/kT\} \qquad \ldots(10)$$

where

N_i = intrinsic carrier concentration

N_e = electron concentration

N_h = hole concentration

T = temperature in °K

k = $1.38*10^{-23}$J°K^{-1}

When germanium is doped n-type or p-type, the simple exponential behaviour in equation (10) is destroyed. The additional curves in figure 5 show the behaviour of a series of germanium samples containing differing donor concentrations. There is a range of temperature within which the conduction band is swamped by carriers provided by the shallow donors in the forbidden gap. This region is called the 'exhaustion range' and usually corresponds to the range of temperature inside which most semiconductor devices are designed to operate. Devices operating under such conditions have the advantage of being largely insensitive to fluctuations in temperature, due to the majority carrier concentration remaining the same. With regard to figure 6 and referring to the work of Young [6], undoped (50 Ω-cm) germanium begins to absorb appreciably at temperatures in excess of about 325°K when thermal runaway is initiated. Very approximately, this corresponds to an absorption of 0.1 cm^{-1} (see figure 6). The intrinsic sample of germanium, as can be seen from figure 5 will never have a region of temperature-independent carrier concentration and as is provided by doping. If the sections of electrons and holes were equal in germanium, one could never achieve an absorption coefficient lower than that found for intrinsic germanium at any given temperature by doping the material. The two absorption cross-sections are, however, unequal as stated earlier in 2.2. This state of affairs should allow a certain amount of 'fine tuning' to be undertaken as far as absorption characteristics are concerned. From the paper by Capron and Brill [11] and Bishop and Gibson [12] as well as the curves in figures 6 and 7, it can be seen that by doping germanium n-type, the absorption coefficient can be artifically lowered by depression of the hole population, with its correspondingly larger absorption per carrier. This gives an 'ideal' sample as being that possessing a room temperature resistivity of 9 Ω-cm. However, it can be shown that for a sample doped in such a way, the onset of thermal runaway will be close to that of the intrinsic material, ie. ≈325°K. If a larger margin for error is required, the material should be made more strongly n-type to increase the high temperature limit of the exhaustion range of the sample. A sample, for instance, of 3.1 Ω-cm (figure 6) has an absorption which stays below the value of 0.1 cm^{-1} until ~350°K; this is 20-25°K later than the point at which the corresponding absorption occurs in 9 Ω-cm material.

3 Experimental measurements

3.1 Apparatus

A differential calorimeter system has been developed capable of being used to make measurements of absorptions down to 10^{-6} with ±1% repeatability. A feature of this system is the provision of a vacuum cell in which the sample (and sample standard) can be inserted (see figure 9). Use of this system allows measurements to be made under laboratory ambient conditions, under vacuum and under controlled atmospheric conditions.

3.2 Measurements

Results of transmittance measurements are shown in figure 10 where the transmittance of an undoped germanium sample was monitored as the sample was warmed over the range 290-360°K, which agrees with the value of 309°K taken from the computer-generated plot in figure 8. This figure was shown to be reproducible with no hysteresis.

Measurements of absorption have been made on a series of well characterised germanium substrates under ordinary laboratory ambient conditions. These values agreed well with those previously measured [11] (see figure 11). However, it was realised that there was an appreciable surface contribution to be allowed for (of the order of 0.3% surface).

This was proved because of measurements made on thin (0.4 cm) and thick (1 and 2.2 cm) samples. It should be noted that the Capron and Brill [11] measurements were made on 1 cm thick samples with no allowance for surface absorption. For this reason a correction should be made to the absorption versus resistivity graph and this is shown in figure 11.

Further measurements made on the germanium substrates in the vacuum calorimeter proved that the surface absorption can be modified by the surface state and the ambient atmosphere. Figure 12 shows that for any given substrate there is an appreciable removable absorption which can be replaced by exposure to air. The removable surface absorption was proposed as being due to both hydrocarbon and water layers, depending on the previous handling and cleaning procedures and the ambient conditions.

The measured removable surface contributions varied from 0.05% to 0.7% per surface. There was also an apparent variable non-removable absorption of up to 0.7%. The maximum estimated surface absorption was 0.94%.

Subsequent measurements made on the same samples [18] showed that the non-removable absorption was directly due to the polishing processes. The original polishing was done with alumina. When the surfaces were treated to a Syton polish the non-removable absorption was reduced to about 0.1% and after final polishing with diamond powder on a tin lap to 0.05% per surface. The different polishing processes altered the removable surface contributions and the best surfaces showed average removable surface contributions of 0.15% per surface.

Estimates of the surface absorption were made by two other techniques. The first of these gave support to the view that the absorption was due to water by the accurate weighing of a molecular seive which had been arranged to catch water vapour removed from the surface of a heated germanium substrate. In all, 16.9 μm^3 of water was found to have evaporated from a 25 mm dia 4 mm thick sample. This corresponded to a lyer of water 1.3×10^{-6} cm thick yielding an absorption contribution of 0.13% surface based on the known absorption of water at 10.6 μm.

The total surface absorption was also measured by irradiating a pair (2 and 4 mm thick) of germanium substrates with a 400 W CO_2 laser beam. The samples cracked after 14.9 s and 27.8 s exposures respectively. If it is assumed that the samples were approximately identical then it follows that the absorption that led to damage must be largely associated with the surface and a simple thermal analysis yields the result that the surface absorption was approximately 0.65% per surface.

3.3 Discussion

In the theory developed a surface absorption, β_s, was defined but subsequently assumed to be negligible

$$A_{TOT} >> \beta_s(T,W)$$

This is only satisfactory in the cases where the total absorption is high compared to the total absorption,

(a) in the case of a thick sample,

(b) in the case of a high absorbing sample (i.e. p-type or n-type with $3<\rho<50$.

It is also possible to circumvent it by making comparative measurements on thick and thin samples.

In the case of most laser windows the surface contribution may not be negligible and can lead to anomolous results.

It can be shown that badly prepared or damaged surfaces totally negate a low bulk absorption coefficient and greatly increase the risk of thermal runaway. It has been shown that the surface absorptance varies both with the surface state and with the ambient atmosphere. Even apparently well polished surfaces have been shown, by X-ray topography (see figure 13) to contain several micron thick polycrystalline layers [19], the legacy of the original cutting process. Most of this absorption is attributable to water vapour which is absorbed on to the sample surfaces when it is left standing in air.

The amount of the surface absorption is conditional on the surface finish. For example, an Al^2O^3 polished surface can have a high non-easily removable absorption. This polycrystalline layer can be substantially removed by Syton polishing without removing the absorption. When, however, that surface is dried (with IPA or under vacuum) a much lower absorption may be measured. The IPA treated surface may take two or three days to recover its absorption but a vacuum dried surface will recover virtually instantaneously on the re-admittance of the atmosphere or of water vapour. Repeated Syton polishing gradually leads to both a lower total absorption and a lower removable water absorption. Other surface finishing techniques, e.g. ion-beam etching, HF etching, diamond turning and diamond polishing have been shown to give temporarily lower absorption. It is thought that the source of the absorption is a hygroscopic germanium oxide layer. This would explain th difference in behaviour as cleaning with IPA or HF would remove most of the oxide layer. Work is at present being undertaken to verify this.

4 Conclusions

A review of some of the relevant properties of germanium was provided in Section 2. The various components which go to make up the total absorption coefficient of a germanium sample were discussed, with emphasis upon the importance of the concentration of free carriers in the transparent wavelength range. A review, together with an in-depth interpretation was provided, of the work done by Capron and Brill [11] and Bishop and Gibson [12] on doped germanium. From the results presented in these publications, it can be shown that the bulk absorption coefficient can be 'fine tuned' to provide different characteristics. This arises from the unequal absorption cross-sections of electrons and holes to 10.6 μm radiation; holes absorb 43 times as much as electrons at this wavelength.

A germanium sample which exhibits a room temperature resistivity of about 9 Ω cm has a bulk absorption coefficient corresponding to the minimum. However, considering thermal runaway probabilities, a greater margin of safety can be allowed by doping the material such that at room temperature the resistivity is about 3 Ω cm, involving a relatively small trade-off in an increased bulk absorption coefficient.

The work of Morin and Maita [10] was used together with that of the authors mentioned earlier to provide a means of theoretically generating absorption coefficient versus temperature curves. Comparison of the resulting expressions with experimental results (figure 8) were very favourable, showing that, within the wavelength and temperature ranges considered, the simple free-carrier absorption theory is quite adequate in predicting the behaviour of the bulk absorption in germanium.

It has been shown in Section 3 that the surface component of absorption is more problematic, and is consequently less tractable in solution. Work is currently being done to discover how the surface of a germanium sample degrades with time and how to protect it from doing so. It has been shown that the source of the surface absorption is due to water adsorbed on the sample surface and that this may be drawn off by placing the sample in a vacuum or by cleaning with IPA or HF.

5 Acknowledgement

This work has been carried out with the support of Procurement Executive, Ministry of Defence, sponsored by DCVD.

6 References

[1] F Urbach
The long wavelength edge of photographic sensitivity and of the electronic absorption of solids
Phys Rev 92, 1324, (1953)

[2] R J Collins and H Y Fan
Infrared lattice absorption bands in germanium silicon an diamond
Phys Rev 93, (4), 674, (1953)

[3] H Y Fan, W Spitzer and R J Collins
Infrared absorption in n-type germanium
Phys Rev 101, (2), 566, (1956)

[4] Semiconductors and Semimetals
Vol 3, p 409. Acad. P. N.Y. (1967)

[5] W Kaiser, R J Collins and H Y Fan
Infra-red absorption in p-type germanium
Phys Rev 91, (6), 1380, (1954)

[6] P A Young
Thermal runaway in germanium laser windows
Appl Opt 10, (3), 638, (1971)

[7] F Herman et al
Quantum theory of atoms, molecules, and the solid state
Ed P O Lowdin (Acad. P., 1966) p 381

[8] S J Fray, F A Johnson, J E Quarrington and N Williams
Lattice bands in germanium
Proc Phys Soc 85, 153, (1965)

[9] S Zwerdling and B Lax
Oscillatory magneto-absorption of the direct transition in germanium
Phys Rev 106, 51, (1957)

[10] F J Morin and J P Maita
Conductivity and Hall effect in the intrinsic range of germanium
Phys Rev 94, (6), 1525, (1954)

[11] E D Capron and O L Brill
Absorption coefficient as a function of resistance for optical germanium at 10.6 μm
Appl Opt., 12, (3), 569, (1973)

[12] J Bishop and A F Gibson
Absorption coefficient of germanium at 10.6 μm
Appl Opt 12, (11), 2549, (1973)

[13] P P Debye and E M Conwell
Electrical properties of n-type germanium
Phys Rev 93, 693, (1954)

[14] A H Kahn
Theory of the infrared absorption of carriers in germanium and silicon
Phys Rev 97, (6), 1647, (1955)

[15] M Hass and B Bendow
Residual absorption in infreared materials
Appl Opt 16, (11), 2882, (1977)

[16] A V Ioffe
Effect of various impurities on the thermal conductivity of the germanium lattice
Sov Phys Sol State, 9, (8), 1914, (1968)

[17] D Gerlich, B Abeles and R E Miller
High temperature specific heats of Ge, Si, and Ge-Si alloys
J Appl Phys, 36, (1), 76, (1965)

[18] C J Hutchinson, C Lewis, J A Savage and A Pitt
Surface and bulk absorption in germanium at 10.6 μm
App Opt 21, (8), 1490, (1982)

[19] J Foley, S K Sharma and R M Wood
Absorption calorimetry and laser induced damage threshold measurements on germanium and zinc selendie
Boulder Damage Symposium, NBS Special Publication 620, 248 (1980)

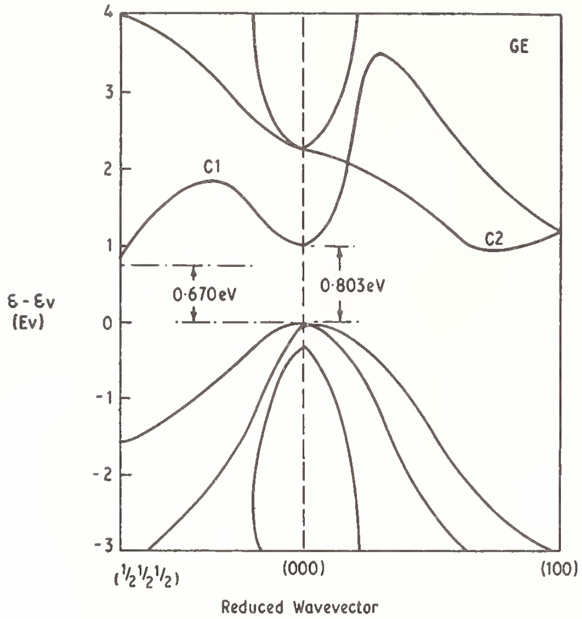

Figure 1 : The band structure of germanium

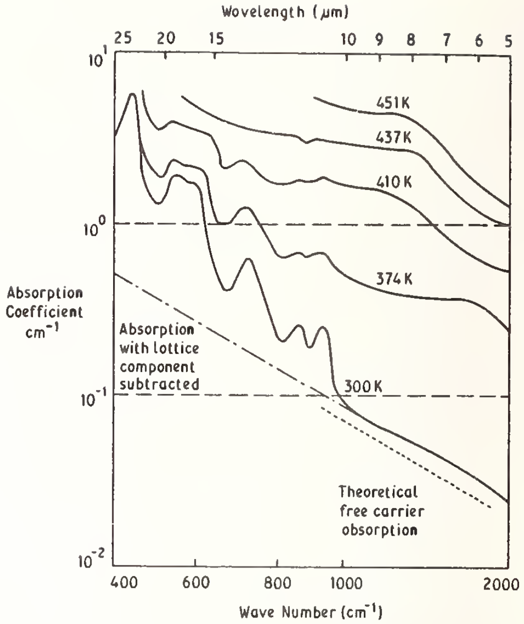

Figure 2 : Variation of the absorption coefficient of n-type (60 Ω cm) germanium with temperature and wave number

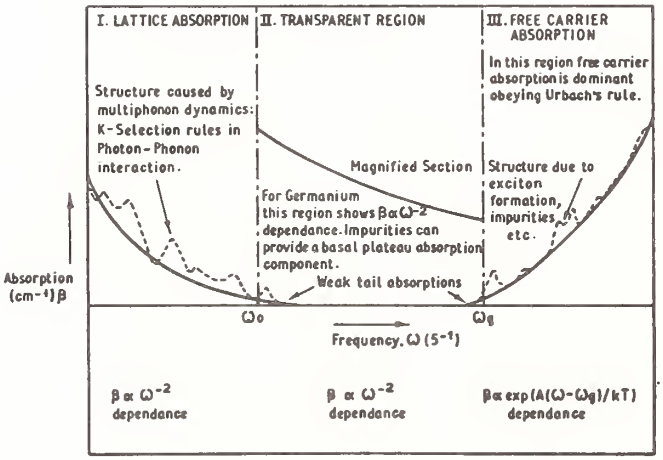

The three basic regions of absorption in Germanium. I. Lattice dominated. II. Transparent region in which free carrier concentration has a large part in the determination of the absorption coefficient and III. strong exponential rise in absorption due to inter-band transitions. ω_g determined by the activation energy.

Figure 3 : Absorption in germanium

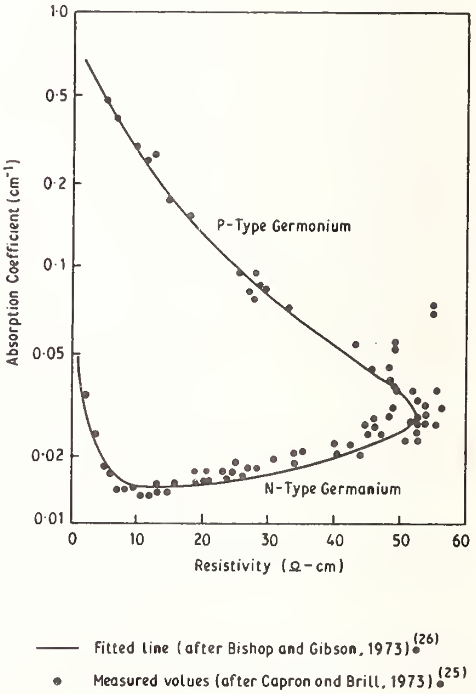

Figure 4 : Absorption coefficient of germanium at 10.6 μm

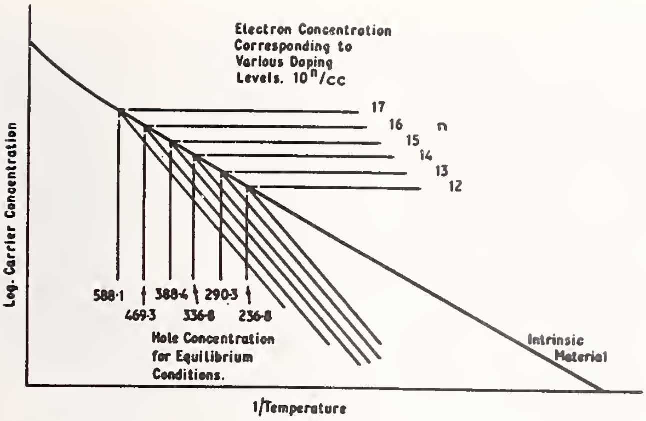

Figure 5 : Germanium carrier concentration versus temperature

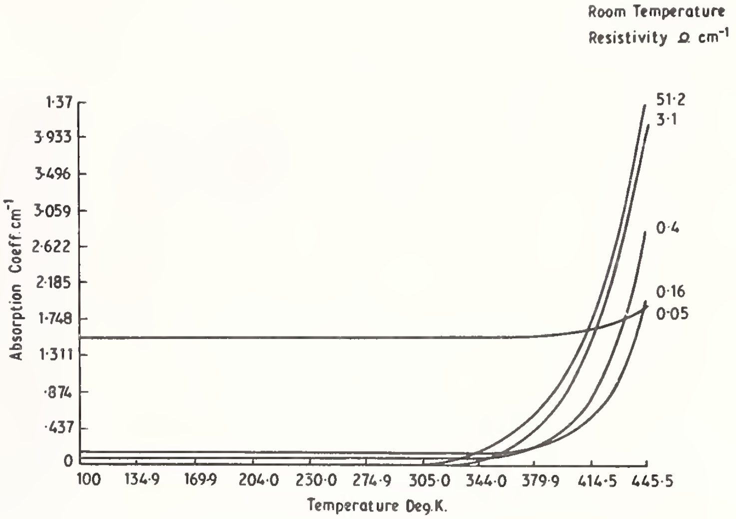

Figure 6 : Absorption coefficient of n-type germanium versus temperature and dopant levels

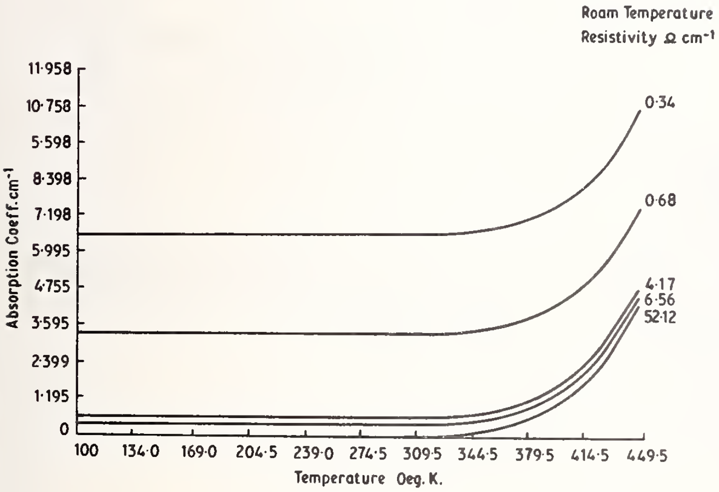

Figure 7 : Absorption coefficient of p-type germanium versus temperature and dopant levels

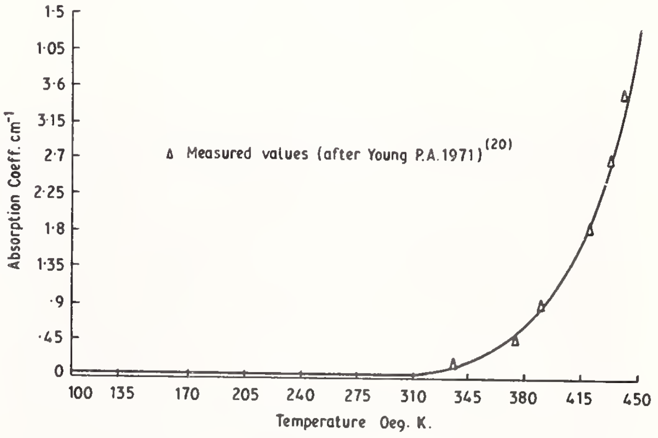

Figure 8 : Absorption coefficient of intrinsic germanium versus temperature

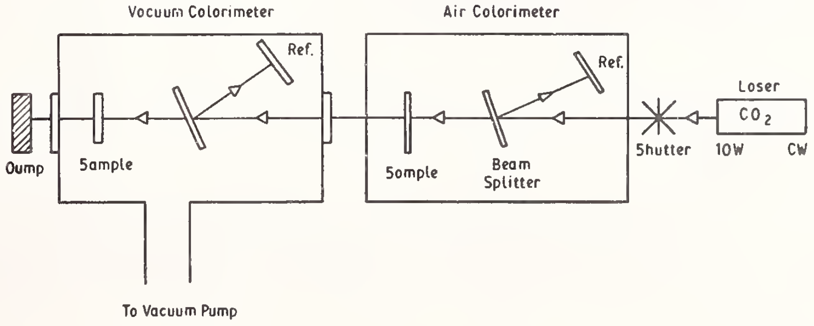

Figure 9 : Schematic of differential calorimeter system

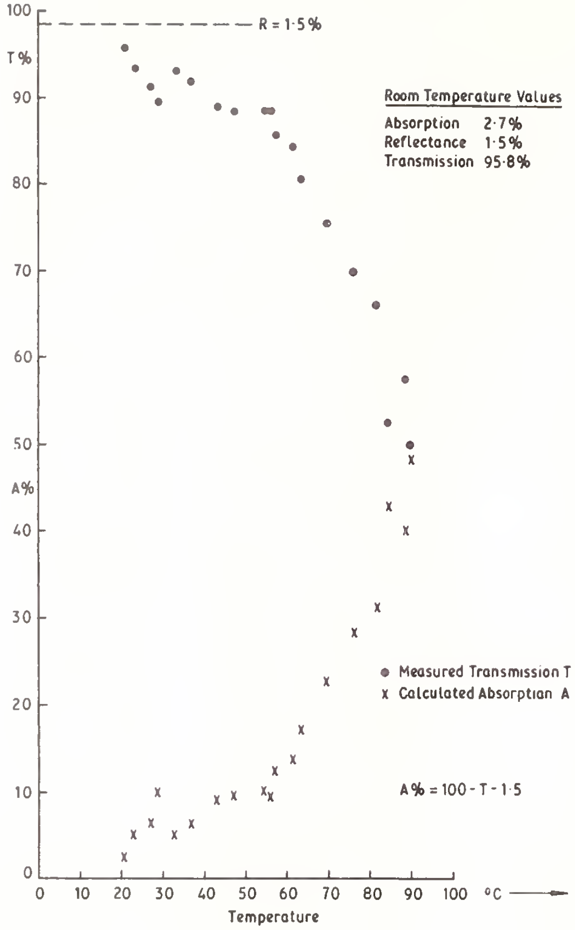

Figure 10 : Measured transmission and calculated absorption versus temperature

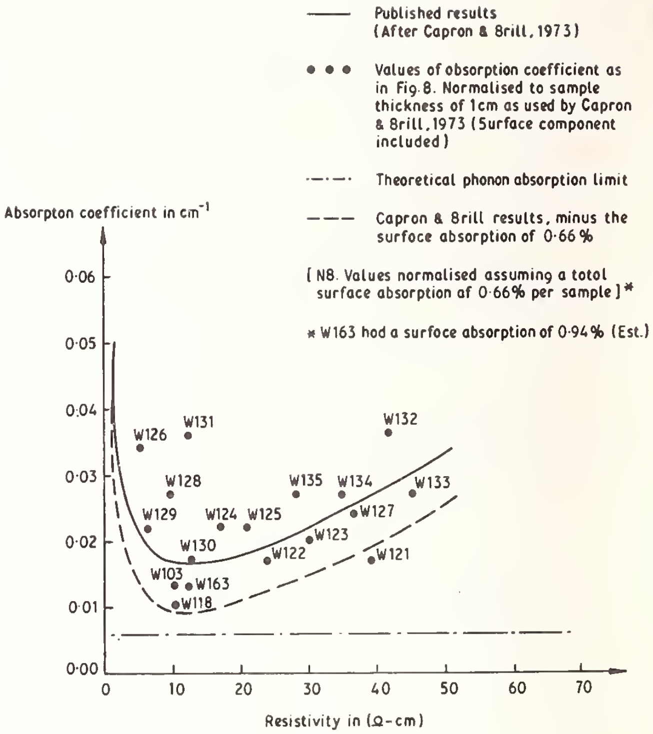

Figure 11 : Measured absorption coefficient of n-type germanium as a function of resistivity

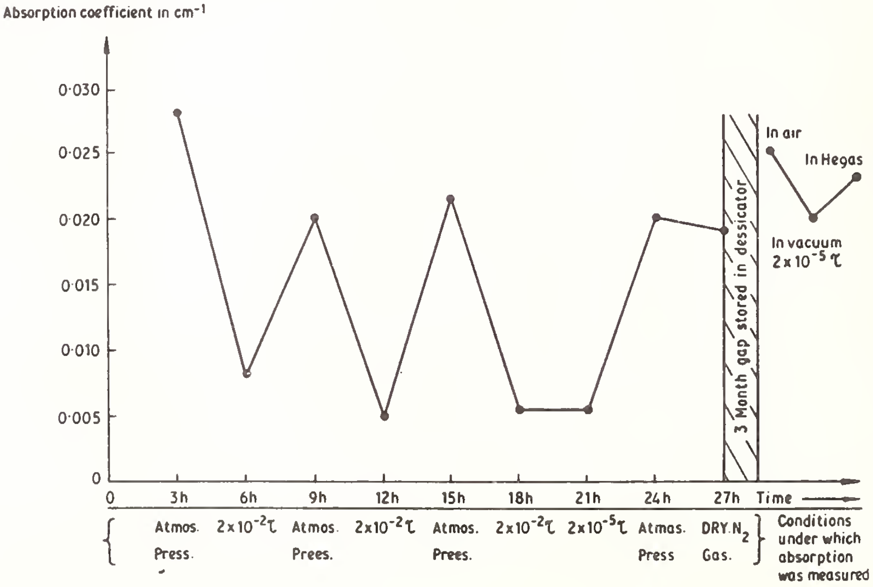

Figure 12 : Behaviour of the absorption coefficient of a 4 mm thick germanium sample under various conditions in a vacuum calorimeter

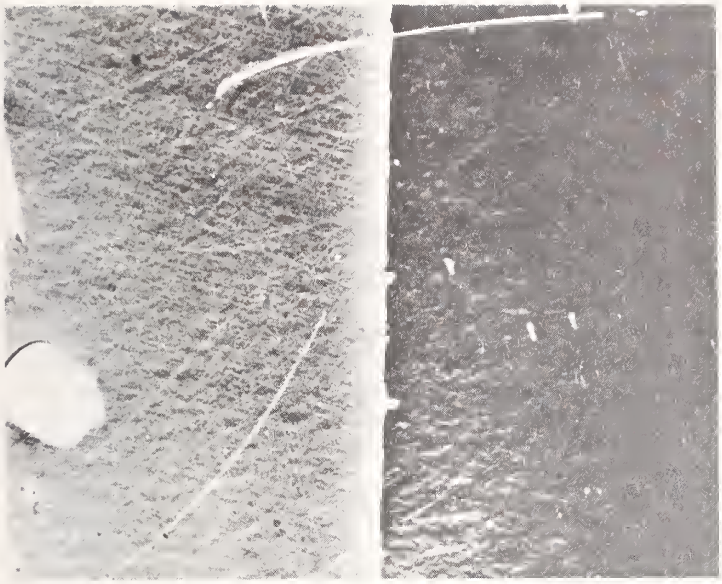

unetched etched

(a) surface topograph (0.5 μm penetration)

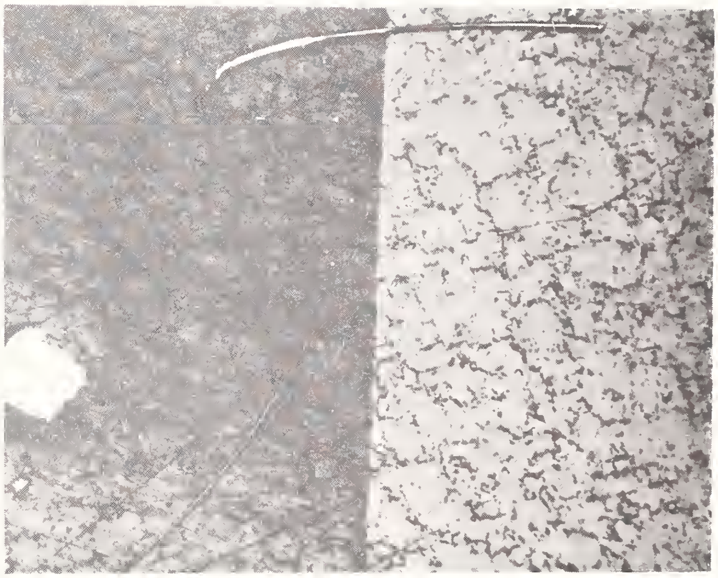

unetched etched

(b) topograph (10 μm penetration)

Figure 13 : X-ray topographs of germanium

Variation of Laser Induced Damage Threshold with Laser Pulse Repetition Frequency

R M Wood, S K Sharma and P Waite

GEC Research Laboratories, Hirst Research Centre
Wembley, England, HA9 7PP

Laser induced damage threshold studies have been made on single crystal germanium window substrates at 10.6 μm using a pulsed TEA laser at prf's from single shot to 100 Hz. These measurements have been made using a system employing real time transmittance and surface inspection. The reflectance and transmittance of the component under test is monitored via an energy integration network and minicomputer and the real time transmittance (using storage scopes) and the surface morphology are monitored simultaneously using a split video system.

These studies have shown that the LIDT of germanium drops markedly with prf, the 100 Hz value being about 1/10th that of the single shot value. It has been shown that this behaviour is consistent with the analysis of free carrier absorption in intrinsic and n-type doped germanium which leads to thermal runaway.

Keywords: Laser damage, CO_2, Lasers, prf, Germanium, Thermal runaway, TEA laser, Non-linear absorption

1 Introduction

The laser induced damage threshold of single crystal germanium is dominted by the electrical and thermal properties of the crystal rather than by dielectric breakdown. Since the absorption coefficient at 10.6 μm in germanium has been shown to be non-linear, thermal runaway is expected to occur and the LIDT should be dependent on resistivty.

Experiments have been performed using a new repetition-rate TEA laser system and the LIDT results have been found to be prf dependent, the 100 Hz value being 15% of the single-shot value. Preliminary theoretical calculations, using an exponential model of sample cooling with time, have shown a reasonable agreement between the normalised calculated and measured prf LIDT values.

2 Apparatus

A new pulsed laser induced damage threshold measurement apparatus based around a 100 Hz pulsed TEA laser has been set up and both prf dependent and cumulative damage measurements have been made.

The laser is a pulsed hybrid TEA laser. This laser can be operated at upto 100 Hz. A schematicof the system is shown in figure 1. The CW section smoothes the TEA pulse and allows a clean TEM_{00} pulse to be extracted. The pulse length can be tuned from 50 ns to at least 1 μs by changing and controlling the gas mix.

The measurement system consists of three simultaneous measurements. The surface morphology of the sample under test is viewed directly using a sensitive video camera with a suitable zoom lens (x 12). This allows the spot at which the samples is placed to be both viewed and recorded. The reflectance and transmittance of the component under test is monitored via an energy meter, integration network and subsequently recorded in a micro-computer. The real time transmittance or reflectance can also be measured, using the same energy meters and high speed storage oscilloscopes (the outputs of these can also be stored via a separate video recorder or even on the same screen as the surface morphology using a split screen video technique). The video system, the computer and the oscilloscopes are all slaved to the laser and the data obtained from each laser pulse can be recorded. After laser damage has been induced either the laser is switched off or the sample moved to a new site and the experiment repeated.

After the experiments have been completed the records are played back and the frames containing the laser damage is abstracted and analysed.

The use of these three measurment techniques is extremely useful when prf or cumulative studies are being made. The reflectance and transmittance measurements are extremely sensitive ways of detecting the onset of laser induced damage. The video recording technique allows any changes that occur in the sample surface to be recorded, and it also records the formation of the laser damage plasma spark.

3 Measurements

Multiple pulse irradiation experiments are being made on a range of CO_2 laser components and materials. This paper summarises the results which have been made on uncoated germanium substrates using a 100 ns pulse duration. These substrates were first cleaned and characterised and then set at the focus of a 50 mm lens. First of all the single-shot damage threshold was found by irradiating a clear area at successively higher power levels until damage occurred. This measurement was made on a number of adjacent areas. The laser was then run at 10 Hz and the power level gradually increased until damage occurred. The power was varied about this level on adjacent areas and the number of pulses required to cause damage was recorded. This procedure was repeated at 50 Hz and 100 Hz prf settings. A plot of the LIDT values against the number of pulses required to cause damage is presented in figure 2.

4 Observation of damage

It will be seen from figure 2 that each repetition rate has its own multi-pulse LIDT. With repeated irradiation at levels 10% below these levels no damage was observed to at least 10^5 pulses. These measurements were repeated on several different samples of germanium and although the specific LIDTs varied the fractional drop with respect to the single-shot value remained approximately constant (see table 1).

Inspection of the video film of the sample surface and the laser energy meter records showed that the laser damage at the prf threshold took place over about three shots. At these levels the plasma spark was initiated, grew and finally diminished. The transmitted beam gradually fell to a minimum. Under continued irradiation no further damage took place. At irradiation levels above the 'prf thresholds' the damage was more catastrophic and generally drilled through the sample. At the 'prf threshold' levels the damage occurred at the peak of the power pulse whilst at higher power levels the damage was initiated earlier in the pulse.

5 Discussion

Laser induced damage to germanium is mainly due to the limitation and the continuation of thermal runaway. Taking the simplified case of an unfocussed beam and ignoring the contribution due to dielectric breakdown at scratches and similar surface damage sites, we find that for a normal, thin germanium window, the energy αE_0 is absorbed in a cylinder of radius r and length h (i.e. in a volume $\pi r^2 h$), where α is the absorption coefficient (cm^{-1}) and E_0 is the total amount of incident energy. Unless beam size is comparable to the diffusion length L, $(L=2(D\tau)\ )$, there is negligible lateral spread of the energy in the pulse time τ. The peak temperature rise at the centre of this cylinder is approximately given by the expression:

$$DT = T - T_0 = \frac{4\alpha E_0}{\rho C \pi r^2 h} \qquad \ldots (1)$$

assuming a Gaussian beam profile.

Taking normal parameter values:

$h = 4$ mm, $\rho = 5.46$ gm cm^{-3}, $C = 0.376$ $Jgm^{-1}{}^\circ K^{-1}$, $\alpha = 0.01$ cm^{-1}, $E_0 = 50$ mJ

then the temperature rise is 37.6°C for r = 50 μm and
0.15°C for r = 2.5 mm

This calculation has assumed a constant absorption α. Once the temperature rise is sufficient however, non-linear absorption takes place (figure 3) leading to thermal runaway. As a preliminary calculation to obtain the temporal temperature profiles as a function of incident power for a typical TEA pulse, the centre-weighted absorption coefficient was taken from figure 3 yielding the curves shown in figure 4. This figure illustrates the dominance of thermal runaway as a mechanism for laser induced damage in a non-linear absorber.

Extending the problem to the case of a window sample which is irradiated with a train of identical laser pulses, the situation becomes more complex. Suppose a second pulse, P2, is indicent before the effect of an initial pulse P1 is completely dissipated by the transport mechanisms operating in the sample. The initial conditions of the heat equation for P2 would then have to contain the 3-dimensional temperature profile created by P1. Each laser pulse therefore generates a step-like temperature-rise with a subsequent thermal-conductivity dependent decay (figure 5). For a specific prf there will be a range of peak powers and pulse energies where no damage will occur (except from probabilistic avalanche or cumulative laser degradation effects). The lowest pulse power/energy at which damage just occurs is termed the prf damage threshold.

An attempt has been made to quantify the prf damage thresholds as a function of prf using a simple model for the situation outlined above. Table 1 includes the calculated values for the prf damage threshold, normalised to the single shot level. These figures were calculated using a simple exponential cooling model with a characteristic time-constant of τ = 0.07 seconds (figure 6). It can be shown that for a given prf the damage threshold should be approximately constant if all the pulses are consistent in peak power and duration. There is only a slight variation which is dependent on specific sample parameters such as thermal diffusivity.

It is expected that all semiconductors should show approximately the same behaviour as long as thermal runaway dominates the LIDT. Materials with large band-gaps may be found to exhibit avalanche breakdown effects before non-linear thermal effects become operative.

Table 1 LIDT versus prf

prf (Hz)	Normalised prf	
	Experimental	Theoretically calc. (τ = 0.07)
Single Shot	1.0	1.0
10	0.75	0.76
50	0.50	0.51
100	0.15	0.13

Acknowledgement

This work has been carried out with the support of Procurement Executive, Ministry of Defence, sponsored by DCVD.

---

6 References

[1] R M Wood, S K Sharma and P Waite
Optical characteristics of germanium at 10.6 microns
Laser Damage Symposium NBS Boulder, Col USA, 1982

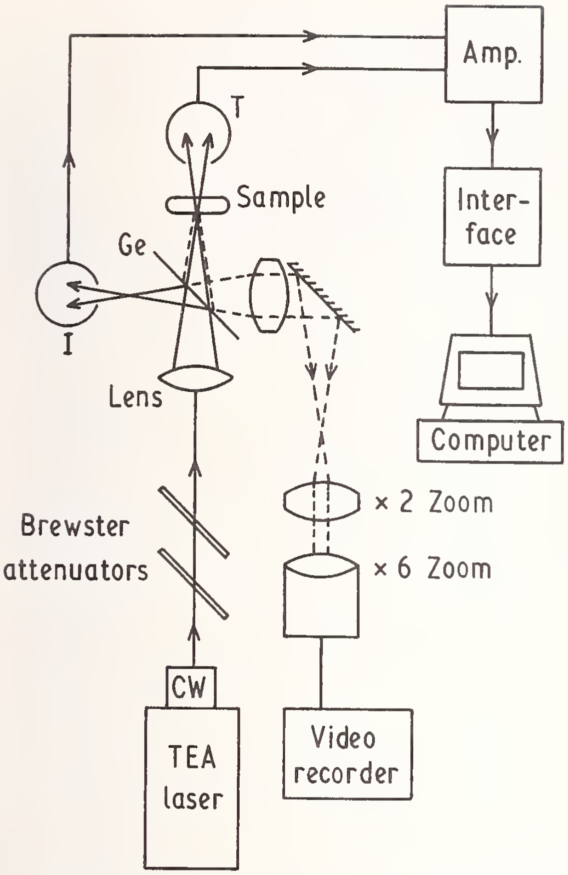

Figure 1 : Schematic of prf laser and LIDT monitoring apparatus

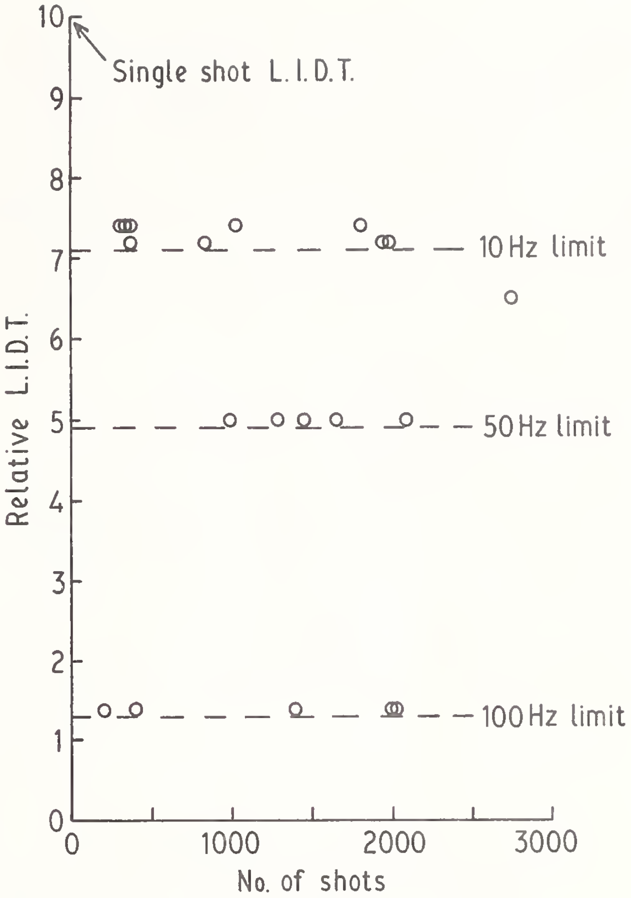

Figure 2 : Plot of prf LIDT vs number of shots for germanium

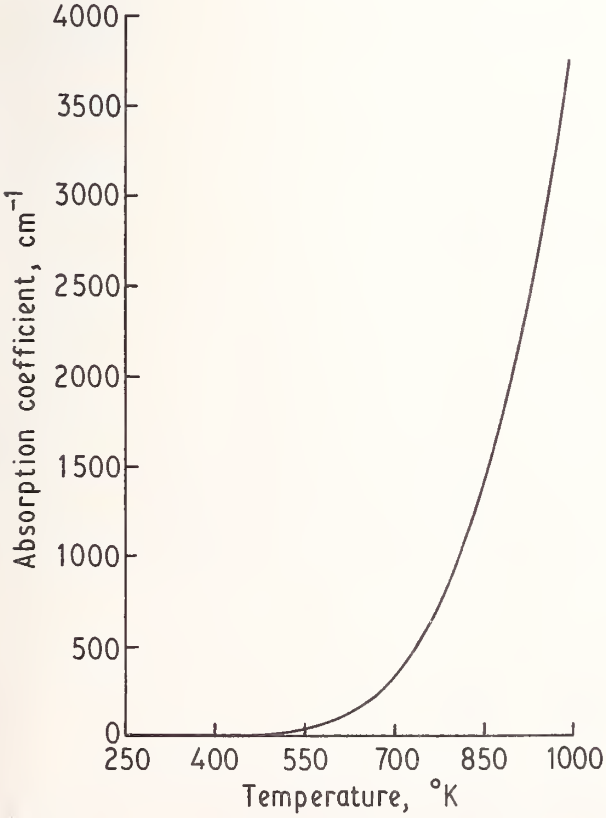

Figure 3 : Absorption coefficient of n-type germanium, 9 Ω cm, N-type

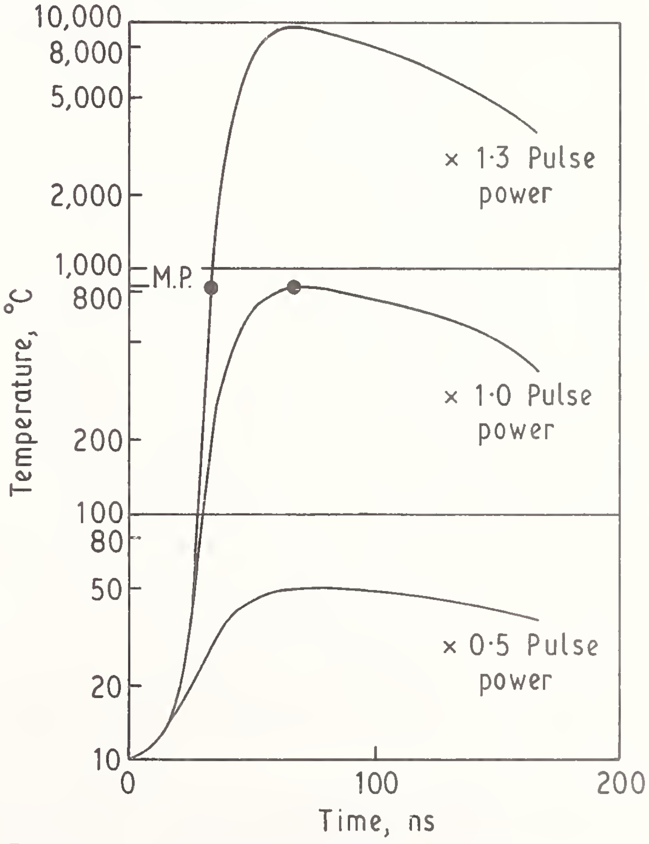

Figure 4 : Temperature rise of germanium during a TEA laser pulse

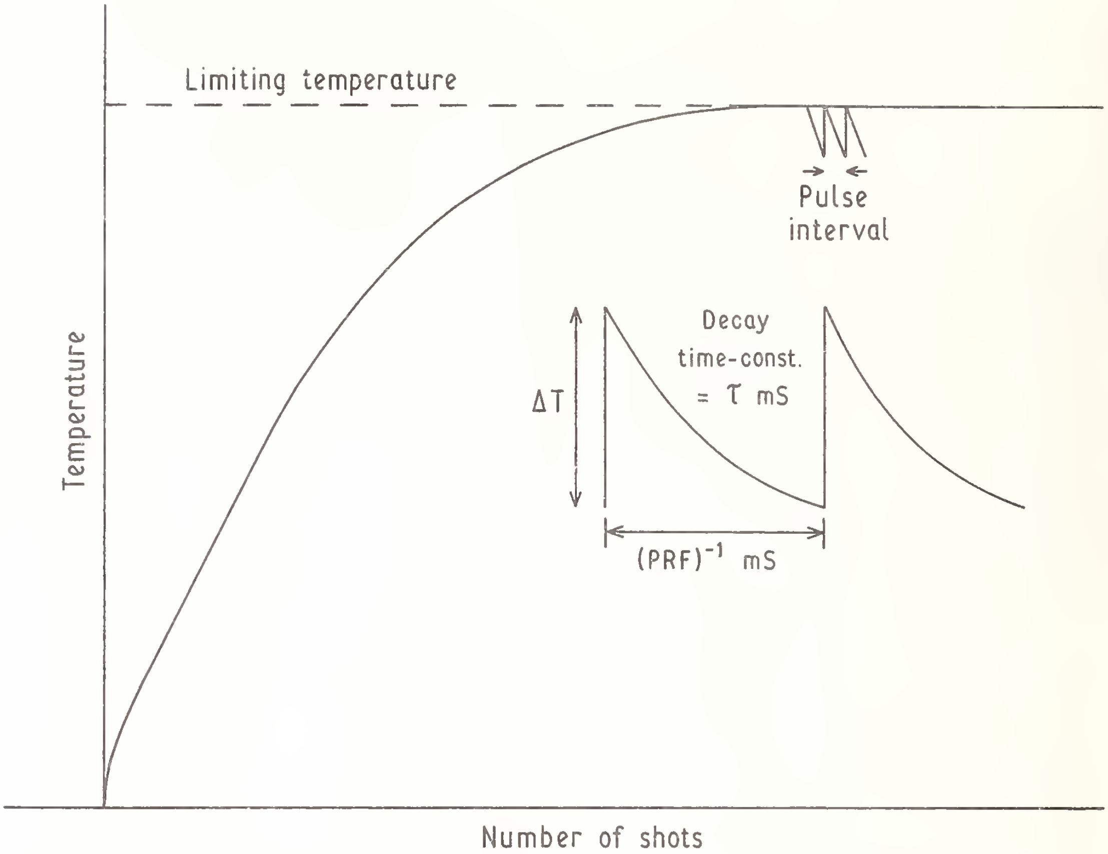

Figure 5 : Peak temperature at the centre of a sample under repeated irradiation

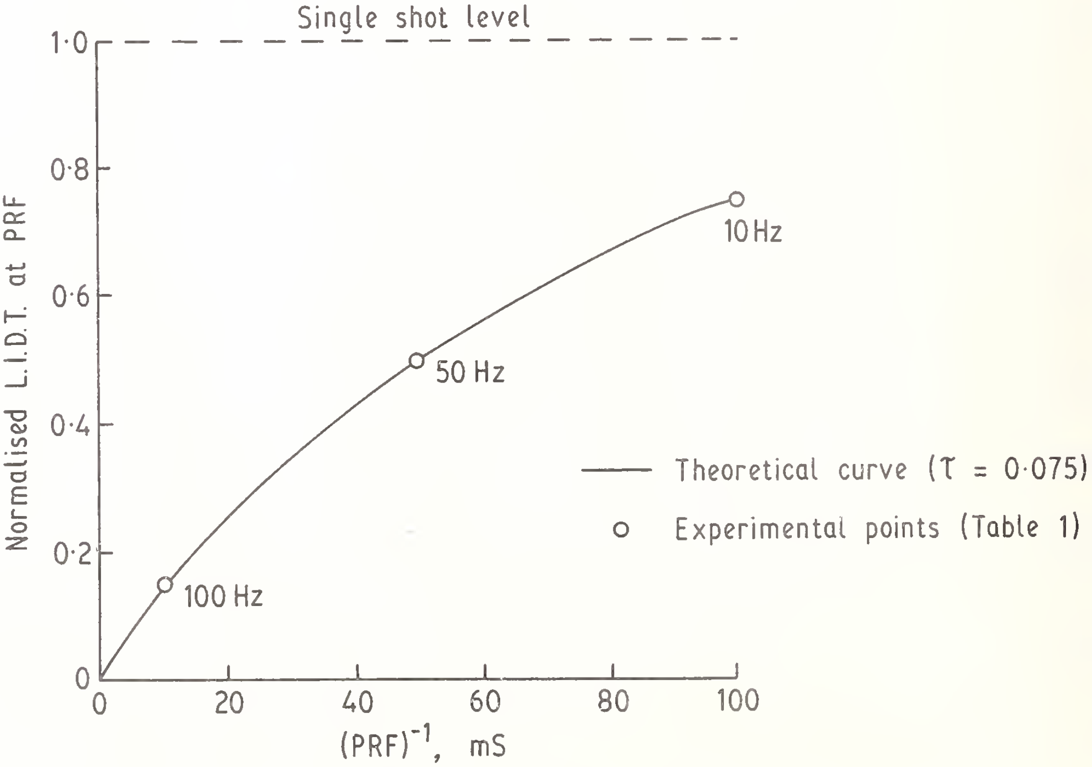

Figure 6 : Normalised LIDT values as a function of 1/PRF for prf values of 10, 50 and 100 Hz in germanium

Several questions and comments were stimulated concerning the physical processes leading to thermal runaway in germanium. The speaker cited previous studies that determined that free-carrier concentration, and thereby absorption, increase with temperature. Absorption leading to runaway was attributed to extrinsic defects or impurities, such as dopants, but the speaker asserted that even intrinsic absorption can produce thermal runaway. R. Walser, however, stated that intrinsic silicon cannot exhibit runaway. M. Soileau added that multiphoton absorption is dominant for semiconductors irradiated by short, ~100 ps, laser pulses. A. Manenkov suggested that repetitively pulsed laser calorimetry would prove conclusively whether or not temperature increases from pulse to pulse.

Multiple Pulse Laser-Induced Bulk Damage in Crystalline and Fused Quartz at 1.064 and 0.532 μm

Larry D. Merkle, Michael Bass and Randall T. Swimm

University of Southern California
University Park, DRB 17
Los Angeles, CA 90089-1112

We report bulk damage measurements on single crystal quartz and two types of fused silica under single and multiple pulse laser irradiation at 1.064 μm and 0.532 μm. Whereas the single pulse damage threshold varies little among the materials or with wavelength, the multiple pulse induced damage behavior depends strongly upon material and wavelength, with damage rarely occurring within a few thousand pulses except very near threshold in some samples, but always occurring within a few hundred pulses even below 60% of threshold in others. Laser calorimetry and measurements of light scattered during irradiation give no evidence of change prior to the pulse on which macroscopic damage occurs. However, the distribution of the number of pulses needed to produce macroscopic damage as a function of intensity is indicative of an accumulation process in which some minimum intensity is required to initiate the accumulation of microscopic damage.

Key words: cumulative; damage; fused silica; multiple pulse; single pulse; quartz.

1. Introduction

The subject of multiple pulse laser-induced damage to transparent optical materials at intensities too low to cause observable damage in one pulse has been less thoroughly studied than single pulse damage, and is certainly far from being well understood, though several interesting studies have been reported [1-10]. Not only is the subject of obvious practical importance for the prediction of the longterm survivability of laser optics, but the comparison of multiple pulse with single pulse damage may offer significant insights into the physical processes which cause laser-induced damage.

Multiple pulse induced damage may be of at least two distinct types. In some cases, the damage behavior indicates that the material has no "memory" of preceding laser pulses, but damages after many pulses simply because the probability of damage on any one pulse is less than unity [1,2]. In other cases, evidence is seen for changes in the sample properties prior to macroscopic damage indicative of the accumulation of microscopic damage leading to the catastrophic failure event [3-9].

We report here the results of a study of multiple pulse laser-induced bulk damage in single-crystal quartz and fused silica under 1.064 μm and 0.532 μm wavelength irradiation. Several techniques have been used to monitor parameters which can give information regarding the damage process and the presence or absence of microscopic changes prior to the macroscopic damage event. These include calorimetry, light scattering, observation of incident and transmitted damaging pulse waveforms, microscopy of damage sites and analysis of the variation with intensity of the number of pulses needed to obtain macroscopic damage. The experiments will be discussed more fully in Section 2.

The results of the experiments will be reported in Section 3 and discussed in Section 4. It will be shown that the observed macroscopic failure after many pulses must arise from the accumulation of microscopic changes in the material brought about by the earlier pulses, but that these microscopic changes are very subtle, eluding direct observation in these measurements. It will also be shown that the accumulation mechanism appears to require some minimum incident intensity to initiate or support the growth of the microscopic changes or damages. These and other conclusions will be discussed in Section 5.

2. Experiments

The experimental apparatus employed in this study was designed to allow the monitoring of several parameters during each experiment and is diagrammed in figure 1. The laser is Molectron MY-34 YAG laser with single axial mode configuration giving pulses of near-Gaussian spatial and temporal profile at a pulse repetition frequency of 10 pps [11]. The fundamental output at 1.064 μm has a pulse duration of 21 nsec FWHM, and was focused into the sample to give a focal spot radius (e^{-2}) of 13.8 μm in fused silica and 14.5 μm in crystalline quartz as measured in air and corrected for refraction at the sample surface. With second harmonic generation 0.532 μm output was produced having a pulse duration of 15 nsec FWHM and focal spot radius (e^{-2}) of 6.6 μm in fused silica and 7.0 μm in crystalline quartz. A beam splitter allowed monitoring of each pulse by a Laser Precision energy meter which was calibrated to give the incident energy in single-pulse experiments and the average incident energy in multiple-pulse experiments. Using other beam splitters, the incident and transmitted waveforms were monitored by Hewlett-Packard 5082-4207 PIN photodiodes and a Tektronix 7844 dual-trace oscilloscope with camera.

In multiple-pulse experiments only the damaging-pulse waveforms were recorded. In this work "damage" is defined by the appearance of a flash of light, the attenuation of the transmitted pulse, and the production of macroscopic zone of melted and cracked material, as observed by scatter of a coaxial He-Ne laser beam. This is the same definition of macroscopic damage widely used in the study of single pulse damage. These changes were always found to occur on the same pulse in these experiments, and it was convenient to use the flash of light, produced by plasma generated in the damage event and detected by a properly filtered RCA C31059 photomultiplier, to trigger the oscilloscope. The output from this PMT was also used to close a Uniblitz shutter to terminate the experiment after damage occurs.

Scattered pulsed laser light from a 2.5 mm diameter region of the sample centered on the focal spot was imaged by a lens and aperture onto a Hamamatsu R632 photomultiplier filtered to receive only the laser wavelength. The output of this PMT and of another PIN photodiode monitoring the incident energy were connected a LeCroy 2249SG analog to digital converter, which sent signals proportional to the incident and scattered energies to a Hewlett-Pakcard 9825A calculator. This allowed the counting of pulses and the detection of any change in scattering efficiency of the sample prior to macroscopic damage. It also provided a means to monitor laser stability, so that any experiment in which the pulse to pulse variability was significantly greater than the usual 5% could be rejected.

In some experiments, a thermocouple was attached to the sample, which was suspended by threads to minimize thermal contact with the sample chamber. In this way, a laser calorimetric measurement could be made to detect any increase in the absorption coefficient of the sample prior to macroscopic damage.

The single-crystal quartz samples used in this work were obtained from Sawyer Research Products. The fused silica samples were of two types: Suprasil-1 and UV grade Corning 7940. The crystalline quartz samples were oriented such that the beam propagated along the z-axis for the 1.064 μm experiments. Due to the ease of obtaining surface damage at 0.532 μm, it was necessary to turn the samples to obtain a longer path length at this wavelength, corresponding to beam propagation along the y-axis in quartz.

3. Experimental Results

The number of pulses needed to obtain macroscopic damage is plotted versus the fraction of single-pulse damage threshold intensity in figures 2 and 3 for crystalline quartz and fused silica. Figure 2 displays the results of 1.064 μm wavelength experiments, figure 3 the 0532 μm results. The single-pulse damage thresholds in this work were defined as the average of the intensity below which single-pulse damage was never obtained and that above which single-pulse damage was always observed. The single-pulse damage threshold intensities for the different materials and wavelengths are listed in table 1. Due to the width of the intensity range within which single-pulse damage only sometimes occurred (typically 10-15% of the threshold intensity), the damage thresholds of the three materials may be considered to be roughly equal at each wavelength. Note, however, that the multiple-pulse damage behavior of the crystalline quartz varies systematically from that of the fused silicas. At a given fraction of threshold intensity, the crystalline material tends to withstand more pulses before suffering macroscopic damage than do the fused silicas. Indeed, at 1.064 μm quartz requires more than 1000 pulses to damage below 90% of threshold, whereas the 1000 pulse intensity is about 80% of threshold for Suprasil-1, and about 75% for Corning 7940. Multiple-pulse damage is observed at smaller fractions of threshold at 0.532 μm, but with the exception of the solid circles in the crystalline quartz data, to be discussed below, the trend is similar. The intensity at which 1000 pulses are required to cause macroscopic damage is about 70% of threshold in crystalline quartz, about 60% in Suprasil-1 and about 55% in Corning 7940.

The solid circles in figure 3A represent experiments performed on sites in one portion of one crystalline quartz sample. Evidently this region damaged more easily than the majority of the material. On the other hand, microscopy and light scattering measurements have been unable to detect any significant differences between this region and the remainder of the sample. The material from which the quartz samples were cut did not include any seed material and the cause of the weakening is uncertain. Since these data came from only one contiguous region within one sample, they will not be considered further in this paper.

A recent study of multiple-pulse laser induced damage in alkali-halides found evidence of an increase in the absorption coefficient on the several pulses just preceding macroscopic damage, indicative of the growth of absorbing microscopic damage sites [6]. On some of the experiments at 1.064 μm in the present study laser calorimetric measurements were performed to search for changes in absorption prior to macroscopic failure. No such change has been detected. This indicates that if microdamage is accumulating on pulses prior to the observed damage flash, its size must be limited as follows. Based upon the observed noise in the calorimetry measurements, it is estimated that an increased absorption on the order of 0.4 μJ per pulse could be detected. If this energy were absorbed in one small spot, such as at an absorbing inclusion or microdamage from an earlier pulse, a region of material about five to six microns in diameter would be melted. This large size only weakly limits the size of microdamage sites which could escape detection by calorimetry. Also, the time required for diffusion of heat from the beam path to the thermocouple, especially in fused silica, may prevent detection of changes in the absorption coefficient in the last few pulses prior to macroscopic damage when irradiating at a 10 Hz repetition frequency.

The monitoring of scattered laser light represents a more sensitive means of detecting microdamage accumulation and was used in nearly all of the multiple-pulse experiments. Figure 4 shows the output of the incident and scattered light detectors, described in the previous section, for one particular experiment. This plot is representative of the data observed in all of the experiments, in that no increase in the scattered light signal relative to the incident energy could be detected prior to the pulse on which the macroscopic damage occurred. We estimate that a 10% increase in scattering could have been reliably detected. Based upon the capacity of the analog to digital converter, the approximate sensitivity of the photomultiplier tube and the losses in the optical train, the minimum detectable amount of energy scattered into the solid angle of the scattered light collecting lens is estimated to be about 1.6 picojoules per pulse in typical 1.064 μm experiments and 2.2 picojoules per pulse in typical 0.532 μm. From the Rayleigh law of scattering by one small object his would correspond, for the collection geometry and typical incident energies used, to detection limits of about

$$V\Delta n \doteq 7.7 \times 10^{-4}\ (\mu m)^3 \qquad (1)$$

in the 1.064 μm experiments and

$$V\Delta n \doteq 3.5 \times 10^{-4}\ (\mu m) \qquad (2)$$

in the 0.532 μm experiments. Here V is the volume of the scatterer and Δn is the absolute difference in index of refraction between the scatterer and the surrounding material.

The photography of the incident and scattered waveforms of damage-producing pulses provides additional information regarding the damage process. Figure 5 shows tracings of two oscillographs of damaging pulses, both from experiments on Corning 7940 with multiple-pulse 0.532 μm irradiation. Due to slight variations in detector alignment from day to day, the relative amplitudes are of less significance than the pulse shapes. The rather sudden truncation of the transmitted waveform (lower trace) in figure 5A is typical of all damage event waveform data, both single-pulse and multiple-pulse induced, at both wavelengths, except for 0.532 μm multiple-pulse damage events below about 70% of threshold intensity in fused silica. This sudden truncation generally occurs at or before the peak intensity point of the waveform, though sometimes it occurs within a few nanoseconds after the peak at intensities only slightly below maximum. This behavior is similar to that observed by Bass and Barrett [2], who interpreted it as evidence for electron avalanche initiated by a probabilistic mechanism. In the fused silica materials at intensities of 0.532 μm light below 70% of threshold, transmitted damaging-pulse waveforms like that shown in figure 5B were sometimes observed, becoming the predominant type of event in Corning 7940 below about 60% of threshold. In these damage events attenuation of the transmitted waveform begins in the trailing edge of the pulses and takes several nanoseconds to decrease to minimum transmission. Such distinctly different waveform truncation behaviors may indicate the operation of different damage mechanisms in the different intensity regions.

Micrographs of two damaged sites in Suprasil-1 are shown in figure 6. Both were caused by 0.532 μm irradiation, the damage in figure 6a by a single pulse just at threshold intensity, that in figure 6b by many pulses at 55 - 60% of threshold. The latter is a damage site caused by a slow-attenuation damage event of the type just discussed. Its far smaller size is not surprising in view of the fact that damage occurred late in the pulse so that little energy was available in the trailing edge to be absorbed by the damage site. Other than the size difference, there is no systematic difference in morphology between the slow-attenuation multiple-pulse damage sites and the fast-attenuation single-or multiple-pulse damage sites. Nearly all observed damage sites exhibit a spindle-shaped melted region which begins at or very near the focal plane and extends upstream a distance of about 300 µm for 1.064 µm -induced damage and up to about 200 µm for 0.532 µm - induced damage. This suggests that, with the exception of a very few anomalous sites, the melted region is controlled by the intensity distribution of the irradiating beam, not by the distribtuion of damageable defects.

4. Discussion of Results

The lack of an observable change in the absorption coefficient or the scattering efficiency prior to multiple-pulse induced macroscopic damage may indicate that no change in the material precedes the observed damage event or that such material changes do occur but are too subtle to be detected by the techniques used in this study. The statistics of the distribution of damage events with respect to the number of pulses needed to cause macroscopic damage can be used to distinguish between these types of mechanisms [1,2]. If no change in the material is caused by the pulses preceding the observed damage, that is if the material has no "memory" of preceding pulses, and if the laser is sufficiently stable (as could be verified in these experiments using the ADC to record pulse energy and the oscilloscope to monitor pulse shape,) then damage after many pulses must indicate that there is a constant nonzero probability of damage on any pulse. In such a case, the distribution f(N) of many experiments at constant intensity as a function of the number of pulses N needed to produce damage is expected to follow a binomial distribution [1,2]

$$f(N) = P_1(1-P_1)^{N-1} \tag{3}$$

where P_1 is the probability of damage on any one pulse. At any given intensity more damage events would be expected to occur in one pulse than two, more in two pulses than in three, and so on.

The data of figures 2 and 3 do not fit this description, excluding the data points from the "weak" region of crystalline quartz. Rather, at any given intensity below the single-pulse threshold the probability of damage appears to be quite small for the first few pulses, then becomes significant for larger numbers of pulses before dropping off again after many pulses. This behavior may be seen more clearly figure 7, a plot of the ditribution of damage events in Corning 7940 irradiated by 0.532 µm pulses in one narrow intensity range. The smooth curves compare eq. (3) with P_1 equal to the observed mean value of N and a Poisson ditribution of the same mean value. The data are too sparse to allow identification with any particular distribution function, and the Poisson ditribution is chosen only as an example of a peaked function. However, it is clear that a peaked distribution can describe the data far better than eq. (3).

Such a distribution, in which the probability of macroscopic damage is higher after several pulses than after one pulse, strongly indicates that the early pulses modify the material in some way. Thus the distribution of observed multiple-pulse damage events suggests an accumulation damage process even though no material changes prior to macroscopic failure have been detected.

Numerous types of accumulative changes in the material may be envisioned which could increase the probability of damage on subsequent laser pulses. Eron'ko, et.al., have proposed that multiple-pulse damage in insulators occurs by the accumulative breaking of bonds in the material to gradually create microscopic damage sites [4,5]. In their model, the average number of pulses needed to induce macroscopic damage varies as

$$N \propto \exp(-K\varepsilon) \tag{4}$$

where ε is the RMS electric field strength of the electromagnetic wave. The N versus intensity data for crystalline quartz and the 1.064 µ data for fused silica vary too strongly with intensity to allow meaningful comparison with eq. (4), but the data for fused silica at 0.532 µm do permit comparison. Figure 8 is a plot of log N versus the square root of the intensity for the Corning 7940 data. This should be linear if eq. (4) correctly describes the damage process. The data clearly do not follow a straight line, nor do the Suprasil-1 data at 0.532 µm when plotted similarly. Thus other mechanisms for the damage must be considered.

The behavior of the data in figure 3 for both types of fused silica could be fit by two straight lines. This would be indicative of two damage mechanisms operative in different intensity ranges which require a number of pulses to produce damage varying exponentially with intensity. However, such an interpretation would be unphysical, in that two damage mechanisms whose probability increases exponentially with intensity would add in such a way that the more strongly-varying function would dominate at higher intensities. This is exactly opposite to the behavior of the data.

The curvature of the data plots in figures 3B and 3C can more plausibly be interpreted as evidence for a damage mechanism driven by accumulative material changes which cannot occur below some minimum irradiation intensity or pulse energy. In such a case irradiation at intensities approaching the minimum intensity from above would require increasing numbers of pulse to achieve macroscopic damage. Below the minimum intensity, an infinite number of pulses would be needed. One possible functional form for the variation of N with intensity which gives this behavior is an hyperbola. This functional form arises in the case that the rate of accumulation of microscopic precursors to macroscopic damage is zero below some critical intensity and increases linearly with intensity above the critical intensity. The solid curves in figures 3B and 3C represent fits to the data by the hyperbolic forms

$$N(I)_{\text{Suprasil}} = \frac{1.225}{(I/I_t) - 0.625} - 2.266 \qquad (5)$$

$$N(I)_{\text{Corning}} = \frac{1.867}{(I/I_t) - 0.570} - 3.340 \qquad (6)$$

where I_t is the single pulse damage threshold intensity. The critical intensities $0.625I_t$ for Suprasil-1 and $0.57I_t$ for Corning-7940, are not intended to be precise, but the overall good fit supports the suggested existence of a critical intensity for the damage mechanism operative in fused silica under 0.532 μm irradiation in this intensity regime.

Whereas the exponential intensity dependence of the bond breaking model of Eron'ko et. al., [4,5] arises rather generally in physical processes based upon excitation or tunelling between quantized states of individual atoms or small groups of atoms, the hyperbolic dependence noted above is suggestive of cooperative phenomena. Examples of such phenomena include melting in which a minimum temperature must be reached to initiate the phase transition, and mechanical failure in which a minimum stress must be applied to induce plastic deformation. The lack of observable changes in absorption or scattering prior to macroscopic damage limits the size of any such melted or otherwise damaged regions but the intensity dependence, taken together with the distribution of damage events at any one intensity discussed earlier, gives evidence that such microscopic damage does occur.

The data presented here show that multiple pulse induced macroscopic damage occurs after fewer pulses at a given fraction of single pulse damage threshold intensity in fused silica than in single crystal quartz. It also occurs after fewer pulses at a given fraction of threshold intensity under irradiation at 0.532 μm than at 1.064 μm. The difference between the materials may suggest interaction of the light with already-existing microscopic structural defects or the generation of absorbing point defects such as color centers, as both are more prevalent in fused silica than in the crystalline material. The wavelength dependence is consistent with either mechanism, since shorter wavelengths interact more strongly with particles smaller than the wavelength and various point defects may exist with absorption bands in the visible but not in the near infrared.

5. Conclusions

We have presented a study of single and multiple pulse laser-induced bulk damage in crystalline and fused quartz at two wavelengths of irradiation. Parameters such as the absorption coefficient, the relative light scattering efficiency, the shapes of incident and transmitted laser pulse waveforms, and damage morphologies were studied as well as the variation with intensity of the number of pulses needed to cause macroscopic damage.

It has been found that, whereas the single pulse damage threshold intensities for the materials tested are very similar, fused silica suffers macroscopic damage after fewer subthreshold pulses than are typically required to damage crystalline quartz. Also, macroscopic damage occurs in fewer pulses under irradiation at a given fraction of threshold intensity at 0.532 μm than at 1.064 μm. These trends are in agreement with earlier studies [3,10,12].

At a given intensity of irradiation below the single pulse threshold, the probability of the occurrence of macroscopic damage is peaked about a number of pulses greater than one. This strongly suggests that macroscopic damage occurs by means of the accumulation of laser-produced microscopic changes in the material. In view of the above observations, possible mechanisms for this accumulation may involve the growth of small structural defects initially much smaller than the light wavelength, or the generation of point defects which absorb green light more strongly than near infrared.

The data presented here indicate the subtlety of the accumulation process. The lack of observable changes in the absorption coefficient or the efficiency of light scattering prior to macroscopic damage limits the size and nature of the microscopic changes which precede such damage.

In particular the light scattering experiment, which is the more sensitive of the two techniques, limits the volume V of any region in which the index of refraction varies from that of the unirradiated material by Δn to a value such at $V\Delta n$ is less than a few times 10^{-4} $(\mu m)^3$. The similarity of the damage sites created by multiple pulse irradiation to those created by a single pulse, and the conformity of the region of melted material to the beam path and focal plane suggest that the damage depends upon intrinsic material properties or upon rather common and homogeneously distributed defects.

The generation of macroscopic damage in these materials may be a rather complex phenomenon. The observation of distinct types of waveform truncation at damage and the different material dependences of single pulse and multiple pulse damage behavior suggest that two or more damage mechanisms may be operative in different intensity regions.

The variation of the number of pulses needed to produce macroscopic failure with intensity at 0.532 µm gives evidence that a minimum intensity or pulse energy may exist below which the observed damage processes are not operative. Of course, these data do not exclude the possibility that other mechanisms may cause damage at lower intensities after irradiation with larger numbers of pulses than were used in this study. However, it is interesting to note that the transparent optical elements in pulsed lasers typically suffer only coating failure, not bulk damage, even after 10^7 - 10^9 pulses. For example, the components of the laser used in this study have survived 10^8 pulses without bulk damage at intensities of about 100 MW/cm^2. This may itself suggest that a minimum intensity for the initiation of multiple pulse damage does indeed exist.

We are presently undertaking experiments using 0.355 µm wave length irradiation to extend the wavelength dependent aspect of the present study. The ability of the shorter wavelength photons to interact more strongly with very small defects and to access different resonant absorption transitions will provide further information on the damage process or processes operative in SiO_2.

Acknowledgement: This work was supported by Department of Energy project agreement number DE-AT03-81NE33080.

References

[1]. M. Bass and H. H. Barrett, NBS Spec. Publ. 356, 76 (1971).

[2]. M. Bass and H. H. Barrett, NBS Spec. Publ. 372, 58 (1972).

[3]. C. Y. She and D. F. Edwards, NBS Spec. Publ. 372, 11 (1972).

[4]. S. B. Eron'ko, S. N. Zhurkov and A. Chmel', Sov. Phys. Solid State 20(12), 2064 (1978).

[5]. S. N. Zhurkov, S. B. Eron'ko and A. Chmel', Sov. Phys. Solid State 22 (10), 1776 (1980).

[6]. S. -T. Wu and M. Bass, Appl. Phys. Lett. 39 (12), 948 (1981).

[7]. E. W. Van Stryland, W. E. Williams, M. J. Soileau and A. L. Smirl, Proc of 1982 Symposium on Laser Induced Damage, to be published.

[8]. M. F. Becker, Y. -K. Jhee, M. Bordelon and R. M. Walser, Proc. of 1982 Symposium on Laser Induced Damage, to be published.

[9]. A. A. Manenkov, G. A. Matyushin, B. S. Nechitailo, A. M. Prokhorov and A. A. Tsaprilov, Proc. of 1982 Symposium on Laser Induced Damage, to be published.

[10]. S. K. Balitskas and E. K. Maldutis, Sov. J. Quant. Elect. 11 (4), 541 (1981).

[11]. W. Fountain and M. Bass, IEEE J. Quant. Elect. QE-18, 432 (1982).

[12]. M. J. Soileau and M. Bass, IEEE J. Quant, Elect. QE-16 (8), 814 (1980).

Table 1. Single-pulse bulk damage threshold intensities for two wavelengths of irradiation

Material	$I_{threshold}$ at 1.064 μm	$I_{threshold}$ at 0.532 μm
Crystalline quartz	132 GW/cm^2	102 GW/cm^2
Suprasil-1	113 GW/cm^2	94 GW/cm^2
Corning 7940	113 GW/cm^2	111 GW/cm^2

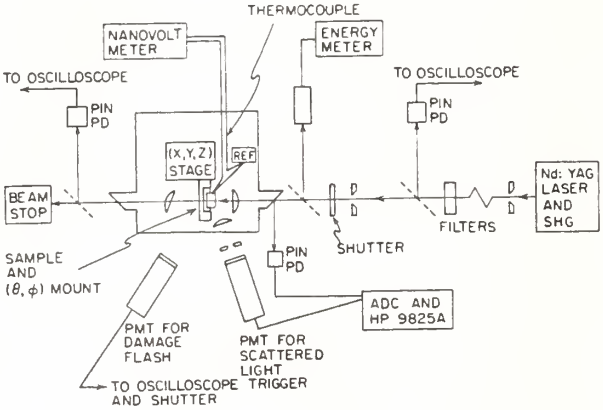

Figure 1. Experimental Appartus

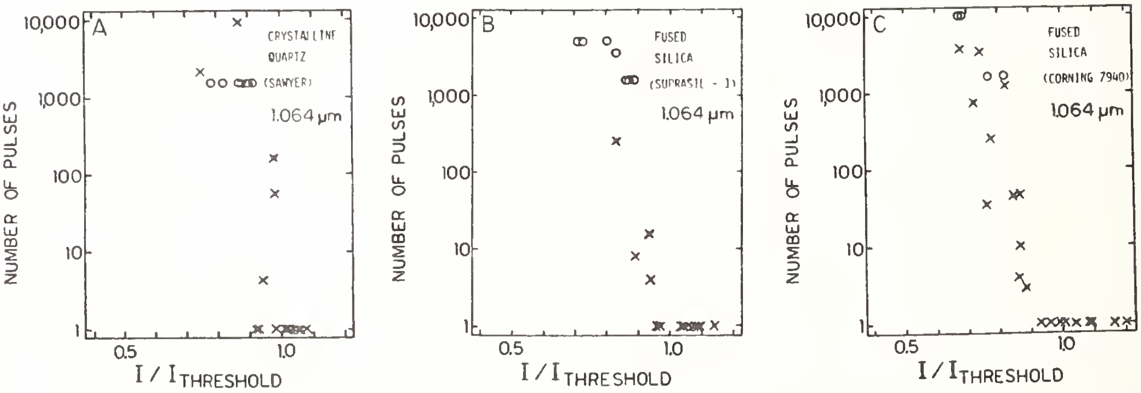

Figure 2. Number of pulses versus intensity for damage experiments using 1.064 μm wavelength irradiation. X's represent experiments in which macroscopic damage was observed after the number of pulses indicated. Open circles represent experiments which were terminated after the indicated number of pulses without macroscopic damage. The peak intensity is normalized to the corresponding single pulse threshold intensity in Table 1.

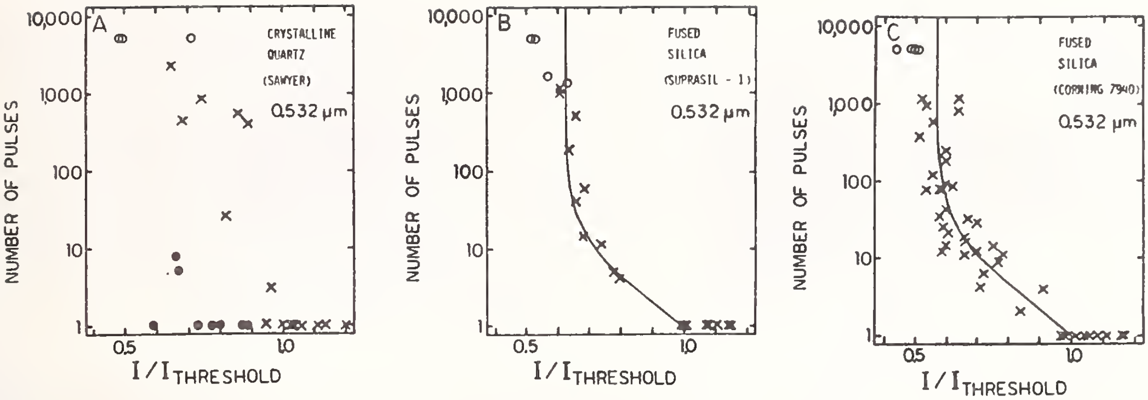

Figure 3. Number of pulses versus intensity for damage experiments using 0.532 μm wavelength irradiation. X's represent experiments on "normal" samples in which macroscopic damage was observed after the number of pulses indicated. Open circles represent experiments which were terminated after the indicated number of pulses without macroscopic damage. Filled circles in A represent damage-producing experiments on the "weak" sample discussed in the text. The peak intensity is normalized to the corresponding single pulse threshold intensity in Table 1. The curves in B and C represent equations (5) and (6).

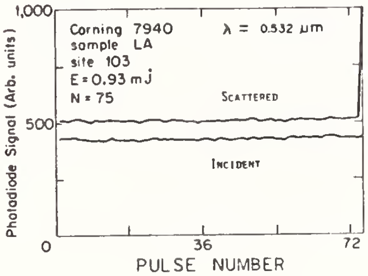

Figure 4. ADC output for a representative multiple pulse damage experiment. Upper trace: signal proportional to the energy of the scattered light on each pulse. Lower trace: signal proportional to the incident energy of each pulse. For this experiment I_{peak} ∿65 GW/cm^2 and macroscopic damage occurred on the 75th pulse.

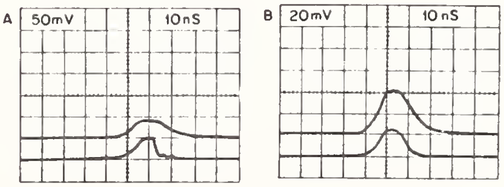

Figure 5. Damaging-pulse waveforms for 0.532 μm experiments on Corning 7940 fused silica. A: Typical waveforms for a "fast-attentuation" damage event. B: Typical waveforms for a "slow-attentuation" damage event. In each case the upper trace is the incident waveform and the lower trace is the transmitted waveform.

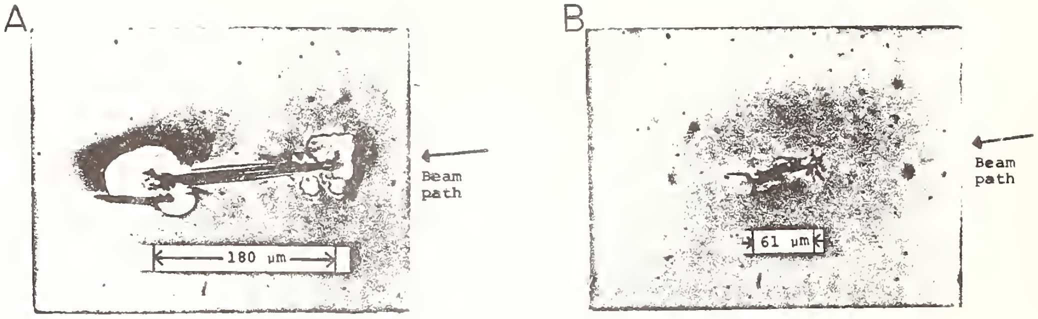

Figure 6. Damage sites in Suprasil-1 fused silica irradiated at 0.532 µm. A: Typical single pulse damage site. B: Typical mutiple pulse damage site for which the damaging pulse attenuation was "slow."

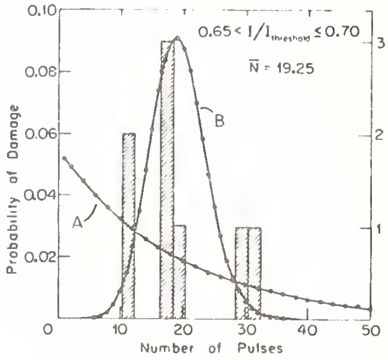

Figure 7. Distribution of damage events in one intensity range from the Corning 7940 data of Figure 3C. Curve A is binomial distribution, Equation (3), with $1/P_1=19.25$. Curve B is a Poisson distribution with a mean of 19.25.

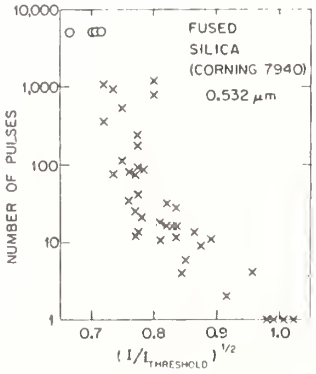

Figure 8. The data of figure 3C plotted versus the square root of the normalized intensity.

The paper attracted extensive questioning, during which the speaker stated (1) that the repetition rate during multiple-shot tests was 10 pps, (2) the spot sizes (e^{-1} in intensity) were about 14µm in 1064-nm tests and 6.6-7µm in 532-nm tests, and (3) the beam propagated along the Z axis in the crystalline quartz sample. A member of the audience suggested that "aluminum" platelets were present in some early samples of 7940 silica, and that the crystalline quartz probably contained sodium iron silicate. The speaker believed such platelets might influence damage, but thought sodium compounds were likely to be present as individual ions. He further stated that he believed it would be unwise to extrapolate his multiple-shot data to predict an absolutely safe fluence, and commented on preliminary data that suggested that thresholds at 1 pps might be slightly greater than those at 10 pps.

The Role of Ca and Pb Dopants in Pulsed 10,6 μm Bulk Damage of Superpure NaCl and KCl Crystals

F.S. Faizullov, V.I. Kovalev

P.N. Lebedev Physical Institute, USSR Academy of Sciences, Moscow, USSR

and

J. Janszky, R. Voszka

Research Laboratory on Crystal Physics, Hungarian Academy of Sciences,
Budapesht, Hungary

The study has shown considerable increase (about 3 times from 0,4 GW/cm^2) of the TEA CO$_2$-laser bulk damage threshold in superpure RAP grown NaCl and KCl crystals with dopping by divalent metals Ca and Pb. The dopants were added into the melt with concentrations 10^{-8}-10^{-3} mol/mol for KCl and 2•10^{-7}-10^{-4} mol/mol for NaCl. The concentration of contaminants (including OH) in samples under the test is less than 10^{-7} mol/mol.

It is known, that bulk damage threshold in optical materials is difined by absorbing microinclusions. These could be the metal colloid particles in superpure alkali halides. Physical explanation of the found phenomenon is based on the analogy of the colloid particles-F-centres system in crystals with the liquid-vapour system.

Key words: NaCl and KCl; TEA CO$_2$-laser; Bulk damage threshold; Divalent metals; Dopping; Colloid particles; F-centres.

1 Introduction

It is well known that absorbing microinclusions play the main role in the bulk optical damage of real optical materials. The ascertion of this fact, the investigation of microinclusion bulk damage principles, and the improvement of the optical materials technology made it possible to increase considerably the bulk optical damage thresholds /1,2/. The thresholds, nevertheless, remain two or three orders lower than a theoretical limit determined either by an avalanche or a multiphoton ionization /3,4/. As a result, one may conclude that the absorbing microinclusions play the main role in bulk optical damage of real optical materials. The dimensions of inclusions in modern laser optical materials are, however, too small to be discovered by traditional methods. Of course, this makes it difficult to identify the nature and composition of these inclusions. Respectively this impedes the interpretation of experimental results and the improvement of optical materials technology for highpower applications. The controlled insertion of any dopant into the test material would allow one to check the influence of a dopant chemical composition on the optical damage threshold. Obviously, the role of a dopant composition in any material would become apparent if the concentration of other contaminants appears to be considerably less that of the dopant under test.

In this work we investigated the effect of Ca and Pb dopant taken in a wide range of concentrations (10^{-8} to 10^{-3} mol /mol) in superpure NaCl and KCl crystals on the bulk optical damage under CO$_2$ laser pulsed irradiation.

2 Experimental procedure and test specimens

The optical damage threshold was measured by the method described earlier /5/. Laser pulses of 150 ns (FWHM) at P(20) line were emitted from a TEA CO$_2$ laser. The laser provided a TEM$_{00}$ mode beam. The beam was focused by NaCl lens of 55 mm F.L. into the bulk of samples under test. The effective cross-section of the laser beam in the focal plane of the lens was 2:10^{-4}cm^2. The accuracy of relative measurements was 10% and that of the absolute one - 20-25%.

Test specimens of NaCl and KCl were RAP grown in hermetic quartz crucibles with multiple zone-refining after growing. The concentration of monovalent metal contaminants was not more than 10^{-6} mol /mol , and that of the anion contaminants (including OH) - 10^{-7} mol /mol . Divalent metal dopants were added in melt with concentrations of 10^{-8} to 10^{-3} mol /mol in KCl and $2 \cdot 10^{-7}$ to 10^{-4} mol /mol in NaCl. The details of the growing process and contamination control methods are given in /6/.

3 Experimental results

Figures 1 and 2 represent the results of bulk damage threshold measurements (the average of 4-6 shots) in the samples under test. Vertical lines in Figures are the average dispersion of thresholds at different points of the sample. From Fig. 1 it is seen that the bulk damage threshold decreases markedly with the increasing of Pb concentration (C) in NaCl from 10^{-5} mol /mol which agree with /7/, and can be accounted for the precipitation of Pb and its salts for $C > 10^{-5}$ mol/mol.

The doping of NaCl by Ca decreases the bulk threshold as well, but not so strongly, as with doping by Pb at $C > 10^{-5}$ mol /mol . Moreover, the threshold decreases with decreasing of Ca concentration in NaCl. This effect is much more evident in KCl:Ca (Fig. 2). The threshold drops three times with decreasing of Ca concentration in KCl from 10^{-5} to 10^{-8} mol /mol . Besides, unlike NaCl, the threshold in KCl:Ca does not decrease at high concentration (more than 10^{-5} mol /mol).

4 Discussion

This result strange, as it may seem, can be explained in the following way. Alkali halide crystals always contain an overbalance of alkali metals or halides even after most improved methods of crystal growing and purification. As is known, the excess of an alkali metal is solved much easier than that of a halide. The excess of the alkali metal provokes two kinds of structure defects in crystals: F-centres, like point defects of the lattice, and macroscopic metal inclusions, the so called colloid particles. F-centre is the anion vacancy, which traps an overplus electron (Fig. 3a). The diffusion-like migration of anion vacances in the crystal lattice can lead to the case, when many anion vacances cluster together at one point of the lattice, and form a macroscopic defect-metal colloid particle. As a matter of fact, the F-centre is the minimal metal colloid particle of 1 nm size, which consists of 6 metal atoms (Fig. 3a). But in practice, the term colloid is extended to much larger sizes, in fact, more than ~ 5 nm /8/.

The system of metallic colloids and F-centres is an example of a condensed phase and dispersed solute in thermodynamic equilibrium in the crystal /8,9/. In other words, at crystal temperature T, a part of an overplus metal is in the F-centre form, and the remaining metal is in the colloid form. In this case the colloid particles would be "evaporated" by the increasing crystal temperature T. That is the effect /10/, which can explain the results of the increasing optical bulk damage by a factor of 5-10 of the alkali halide crystals with the help of thermal treatment (annealing) /11/.

From the analogy of colloid particles-F-centres and the liquid-vapour systems it follows that the colloid particles can be "evaporated" (bulk damage threshold of the crystal can be increased) without high-temperature annealing, if one succeeds in decreasing the concentration of the excess alkali metal (in other words, pumping out of the vapour at constant temperature). Such effects may take place, for example, in alkali halides by the divalent metal doping. In this case the cathion vacancy is formed near the divalent ion (Fig.3b). The electrical neutrality of a crystal is provided by a compensation of the cathion vacancy with the divalent ion. The cathion vacancy can trap excess alkali metal and decrease the probability of the F-centre formation at constant concentration of the excess alkali metal. This phenomenon should decrease the dimensions of colloid particles in the crystal (and increase the damage threshold).

Obviously, such effects can appear when the dopant is totally soluable in the crystal. Otherwise, the doping metal would precipitate and decrease the bulk damage threshold (NaCl with Ca and Pb concentrations $> 10^{-5}$ mol /mol). The absence of the threshold decreasing in KCl:Ca is probably due to a better soluability of Ca in KCl.

At the same time, it is necessary that the concentration of alkali metal was small enough for the compensation of alkali metal excess by the divalent metal doping without precipitation of the doping metal. The samples under test in our work were taken to fit these requirements. The increasing of point defects and colloids concentration in crystal can increase the yield stress and hardness by impending the dislocation motion /8,9/. However, the optical damage threshold would not be heightened as well, in accordance with a nonlinear model of microinclusions heating by pulsed laser radiation /13,14/ (which is more preferrable for pulsed damage than the linear model of Hopper and Uhlmann /15/). In accordance with the nonlinear model, the damage threshold of optical material is independent of mechanical properties, and is fully defined by absorbing defects characteristics. That is why the investigation of the initial cause of optical damage is the most important question.

Among the reasons why the observed dependence of the optical damage treshold had not been earlier discovered, one should note the important role of admixture of the hydroxil OH. The typical OH concentration in air-grown crystals is 10^{-3} mol /mol . The measurements in KCl with a special doping by 10^{-3} mol /mol concentration of OH show that the threshold intensity is 0.4 GW/cm^2 (Fig. 2). This value is lower than the damage thresholds of OH free samples under test (Fig. 2).

5 Summary

The study of the bulk damage thresholds in superpure NaCl and KCl crystals with the gain switched TEA CO_2-laser pulses has yielded a very important result. The effect of considerable damage threshold increasing with doping by divalent metals has been discovered in superpure NaCl and KCl crystals. We have suggested a physical explanation based on the analogy of colloid particles-F-centres with the liquid-vapour systems.

Although this work deals with colloids in ionic matrices only, our results may help to interpret any result on colloids in other superpure optical materials.

The authors are grateful to Drs A.V. Vinogradov from Lebedev Physical Institute and V.V. Nabatov from Shubnikov Crystallography Institute for their valuable discussions and assistance.

6 References

1 Danileiko Yu.K., Manenkov A.A., Prokhorov A.M., Khaimov-Mal'kov V.Y., JETP, 58, 31 (1970).
2. Aleshin I.V., Imas Y.A., Komolov V.L. Optical strength of low-absorbing materials (in Russian), Leningrad, 1974.
3 Epifanov A.S., Manenkov A.A., Prokhorov A.M. JETP, 70, 728 (1976).
4 Vinogradov A.V., Faisullov F.S. Sov. J. of QE, 7, 650 (1977).
5 Kovalev V.I., Morosov V.V., Faisullov F.S. Sov. J. of QE, 4, 1208 (1975).
6 Voszka R., Tarjan I., Berkes L., Krajsovsky J. Kristall und Technik, 1, 423 (1966); Raksanyi K., Voszka R. Kristall und Technik, 4, 227 (1969).
7 Nabatov V.V., Beliaev L.M., Dimenko N.N., Voszka R. Acta Phys. Acad. Sci.Hung., 47, 107 (1979).
8 Hughes A.F., Jain S.C. Adv. in Phys., 28, 717 (1979).
9 Seitz F. Rev. Mod. Phys., 26, 7 (1954).
10 Vinogradov An.V., Tribel'sky M.I. JTP Letters, 5, 595 (1979).
11 Gorshkov B.G., Danileiko Yu.K., Epifanov A.S., Lobachev V.A., Manenkov A.A., Sidorin A.V. JETP, 72, 1171(1977).
12 Kittel Ch. Introduction to solid state physics. Fourth Edition, New York, London, Sidnay, Toronto.
13 Danileiko Yu.K., Manenkov A.A., Nechitailo V.S., Prokhorov A.M., Khaimov-Mal'kov B.Y. JETP, 63, 1030 (1972).
14 Anisimov S.I., Makshantsev B.I. PhTT (Phys. Sol. Stat.), 15, 1090 (1973).
15 Hopper R.W., Uhlmann D.R. J. Appl. Phys., 41, 4023 (1970).

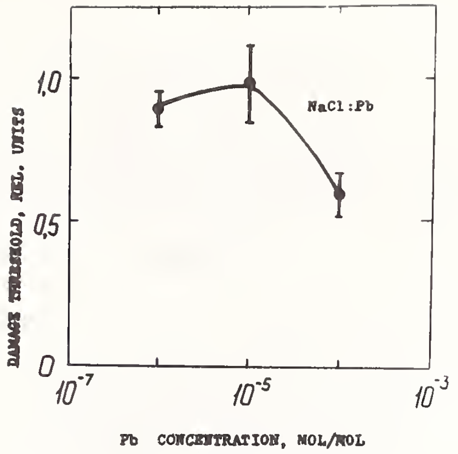

Fig. 1. Bulk damage threshold (relative units) in NaCl samples versus Pb concentration.

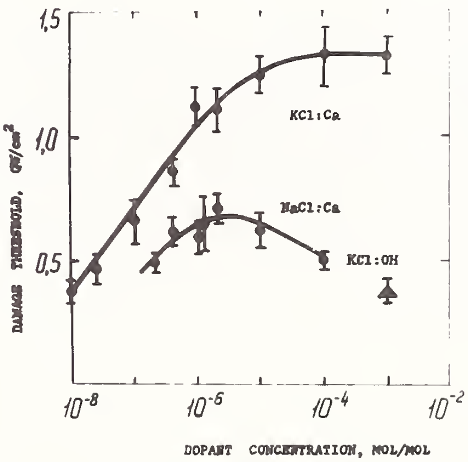

Fig. 2. Bulk damage threshold in NaCl and KCl samples versus Ca concentration. Triangle is the threshold for KCl-OH.

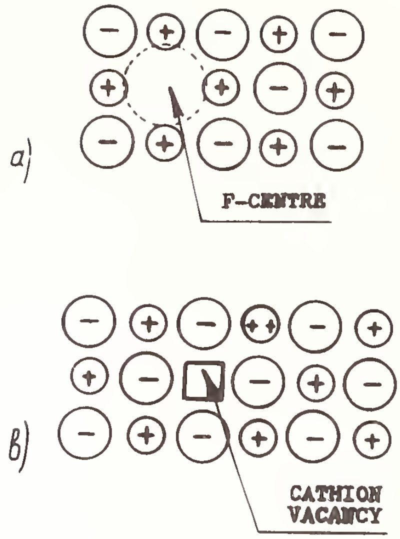

Fig. 3.a. Schematic model of an F-centre.

b. Cathion vacancy in alkali-halide lattice with a divalent metal dopant.

When asked why increased Ca doping reduced thresholds in NaCl, but increased thresholds in KCl, the speaker said Ca was less soluble in NaCl than in KCl, and that precipitates of Ca or of calcium salts occurred in NaCl crystals doped with $> 10^{-5}$ mol/mol of Ca. In answer to additional questions, the speaker stated (1) that the threshold of the undoped crystals was 0.4 GW/cm^2 for test beams 100-150μm in diameter, a value believed to be relatively low by several in the audience, and (2) that he had been unable to detect F centers in the crystals.

Contaminant and Defect Analysis of Optical Surfaces by Infrared Laser-Stimulated Desorption

S. D. Allen

Center for Laser Studies
University of Southern California, Los Angeles, California 90089-1112

J. O. Porteus, W. N. Faith, J. B. Franck

Michelson Laboratory, Physics Division
Naval Weapons Center, China Lake, California 93555

Infrared laser induced desorption (LID) has been demonstrated for water and other contaminants on nominally transparent substrates. The apparatus consists of a UHV chamber interfaced with several pulsed IR lasers. Detection of the desorbed fluence is via an ionizer and quadrupole mass analyzer. For the samples measured to date, the LID is defect dominated for both small (120 μm) and large (380 μm) spot sizes. For the larger spot sizes, the data for multiple irradiations of the same site (N/I) can be explained using a simple defect model. The LID fluence of water and other contaminants such as hydrocarbons can vary by orders of magnitude from site to site on the same sample. Similar variations were observed for average values of the desorption signal as a function of sample and substrate finish. The surface damage threshold of these materials correlates with the measured LID fluence of contaminants, i.e., samples and sites with high contaminant fluences damage at low thresholds. Samples investigated include: polished CaF_2 (two vendors), BaF_2, NaCl and etched CaF_2 and NaCl. A comparison of desorbed water and hydrocarbons at 2.8, 3.8 and 10.6 μm suggests that water may not provide the dominant mechanism for localized optical absorption and damage. Laser cleaned surfaces which were dosed with water at ~ -100°C showed no evidence of readsorbed water on subsequent LID testing, indicating a passivation of the surface.

Key words: surface contamination, laser induced damage, surface defect analysis, laser induced desorption.

Introduction

As materials for high power laser optics have improved, it has become increasingly true that failure occurs at surfaces and interfaces in the optical component where contamination is most probable. Last year at this conference we reported initial results from an experiment designed to quantitatively measure such contamination [1]. The experiment consists of an UHV chamber interfaced with a pulsed IR laser. The laser wavelength is chosen such that adsorbed molecules couple strongly to the laser field and absorb sufficient energy to cause desorption. The desorbed molecules are detected with a quadrupole mass analyzer. In most cases, the substrate is highly transparent to the laser wavelength. The advantage of this choice of experimental parameters is that large amounts of energy can be transferred to the adsorbed molecules at intensities significantly below the damage threshold of the substrate. Most other laser induced desorption (LID) experiments are conducted under conditions in which the substrate is highly absorbing [2].

The HF/DF and CO_2 TEA lasers with nominal wavelengths at 2.7, 3.8 and 10.6 μm respectively were used to irradiate samples of CaF_2, BaF_2, NaCl, KCl, Cu, Mo and several coatings. Most measurements were made with the HF laser as it is strongly absorbed by H_2O, a pervasive contaminant. Detected desorbed species include H_2O, OH and hydrocarbon fragments. Detection sensitivity for adsorbed H_2O scales with the laser spot size and is estimated at several percent of a monolayer using the present experimental geometry. (HF laser, D_{1/e^2} = 380 μm). Initial desorption experiments were carried out on polished and etched samples which had been subjected to an 8 hour bakeout at 250°C, as the tenacity of surface water and hydroxide ions at elevated temperatures is well known [3]. Measurements of desorption fluence as a function of laser energy density showed considerable data scatter which increased for smaller spot sizes D_{1/e^2} = 120 μm). As each data point was taken on a new site (1/1), there appeared to be a large site to site variation on approximately a 100 μm scale. This effect could be due to selective adsorption of contaminants at defect sites such as scratches, cracks, pits and pores.

LID Passivation

In order to overcome this experimental limitation, we used laser induced desorption to clean several "large" areas using multiple overlapping laser irradiations. These areas were then dosed with many Langmuirs of H_2O both at room temperature and -100°C in an attempt to obtain a uniform adsorbed layer. The sample was subsequently re-irradiated and no desorbed H_2O was detected. It was clear from the thermal desorption that occurred as the samples warmed, that water was deposited on the substrate at approximately -100°C, but none was detectable once the substrate had warmed up to slightly below room temperature. Unfortunately, we were unable with the current experimental apparatus to maintain the sample at reduced temperatures during the laser induced desorption. We can conclude from these results for CaF_2 (100) and (111), BaF_2 (111) and NaCl(100), that laser induced desorption causes changes in the surface which inhibit H_2O adsorption at room temperature. Similar surface passivation effects have been observed for chemically etched KCl surfaces [4]. SEM examination of such single crystal etched surfaces shows an essentially featureless surface with an occasional low angle grain boundary. A reasonable explanation, therefore, is that adsorption of H_2O takes place predominantly at defect sites and that LID somehow removes these sites. These results have obvious applications to surface preparation of high power laser optics . Further experiments such as SEM and TEM examination of LID cleaned surfaces should be conducted to determine what changes take place in the laser irradiated surface.

Simple Defect Model

In order to quantitatively analyze the defect mediated adosrption, a simple model was developed. As shown in Figure 1, we assume that the defect density and contaminant adsorption on the surface is uniform and that there is a single threshold laser intensity necessary for desorption. The assumption of a threshold intensity is a good approximation for a process which is undoubtedly governed by an activation energy whether it is strictly thermal or has some component of bond selective excitation. In addition, comparison of the desorption energy for H_2O on CaF_2, for example, with the available laser energy shows that two photons of 2.8 μm are necessary for each H_2O molecule desorbed. The LID is thus highly nonlinear in the laser intensity and can be reasonably approximated by an intensity threshold. Above the threshold, all adsorbed molecules are assumed to be desorbed. Using this model, the desorption fluence, ψ, is proportional to the irradiated area above the threshold intensity. For a gaussian beam, this becomes

$$\Psi = m\pi r_{TH}^2$$

$$\Phi_{TH} = \Phi_0 e^{-r_{TH}^2/\rho^2}$$

$$\Psi = m\pi\rho^2 \left[\ln\Phi_0 - \ln\Phi_{TH}\right]$$

If the desorbed fluence is plotted as a function of the natural logarithm of the axial energy density, Φ_0, the slope of the resulting straight line yields information on the defect density and size. The zero desorption intercept is the threshold intensity for the LID process.

An example of LID data for H_2O on etched CaF_2 using the HF laser (D_{1/e^2} = 380 μm) in a 1/1 experiment is given in Figure 2. The large data scatter indicates that this model is not applicable on the scale of several mm (the spacing between irradiated sites is 1 mm). If we similarly plot the data for a N/1 experiment for the same system, but use the cumulative desorbed H_2O fluence, we obtain a much improved signal to noise ratio as shown in Figure 3. Similar graphs have been plotted for many sites on CaF_2, both (100) and (111), BaF_2 and NaCl as shown in Figures 4, 5, 6 and 7. Although there is evidence of the site to site data scatter shown in Figure 2, the curves tend to group naturally into several types. As indicated by the site coordinates, given in mm, similar sites occur in areas separated by up to a centimeter. In some curves, e.g., Figure 3, two distinct straight lines are evident, implying an initial desorption from defects with a relatively low threshold intensity and subsequent appearance of a second type of defect with a higher threshold. Occasionally one site will show an unusually high LID signal. For example, sites 5,15 and 7,0 in Figures 5 and 6 respectively lie signficantly above the remaining data. In each case the anomalous curves are approximately parallel to but offset vertically from the other curves. A possible explanation is the occurrence of a particularly large, lower threshold desorption site within the initial irradiated area. If such defects are uncommon, e.g. foreign particles, they are not accounted for using the proposed model. A large signal will result on the first but not on subsequent shots if a large desorption site falls within the initially irradiated area.

In the absence of measurements at intensities near the indicated threshold and other gaps in the data, we have not attempted to draw any quantitative conclusions from either the measured thresholds or the density factors. What is remarkable is that the measured curves are so simple, implying in most cases, one or more types of defect sites uniformly distributed over an area several hundred microns in diameter.

A comparison with the previously reported data [1] shows that the 1/1 LID signal measured on CaF_2 (100) was more uniform from site to site and that the signals were more than an order of magnitude larger. The initially measured CaF_2 samples were polished and supplied by a different vendor. Independent damage measurements [5] of the two types of samples showed consistently lower damage thresholds for the material reported in reference 1. Poor quality, low damage threshold, high LID fluence surfaces are reproducibly bad from site to site, whereas good quality, high damage threshold surfaces exhibit low average LID fluences but large site to site variations. These observations are consistent with the proposed defect model.

Wavelength Dependence of LID

As shown in the previous paper [1] , the desorption efficiency of the DF laser for H_2O was less than that observed for the HF laser, but the disparity was not as large as would be expected on the basis of the absorption coefficients of H_2O at 2.7 and 3.8 μm. As shown in Table 1, H_2O absorbs strongly in the 2.7 μm region and virtually not at all at 3.8 μm [6]. This seeming contradiction is also seen in the few points in Figures 3, 5, 6 and 7 where N/1 data for the DF and CO_2 lasers does not differ significantly from the HF LID data. There are several explanations which should be explored. The simplest is that the particular HF laser wavelengths used in this experiment do not effectively couple to the adsorbed OH bonds. The dominant spectral components in the HF laser are 2.795 μm (34%); 2.71, 2.835, and 2.635 μm (20% each). The spectrum of H_2O adsorbed on CaF_2 powders [3] shows a broad spectral feature centered at 2.12 μm and extending from approximately 2.7 to 3.3 μm attributed to hydrogen bonded H_2O and a sharp absorption line at 2.72 μm ascribed to strongly held free H_2O molecules. In no case was there any absorption observed near 3.8 μm. An alternative explanation is that several contaminant species are co-adsorbed. As shown in Table 1, C-H bonds absorb in the DF laser region and C-C bonds in the CO_2 laser region. As alcohol is frequently used as a polishing vehicle and in the etching process for the surface preparation of the tested materials, it is reasonable to assume that some fraction of the adsorbed and surface occluded material is alcohol.

Sequential desorption measurements of CH_3 and H_2O were made at both HF and DF wavelengths. It was observed that on no site was one contaminant observed in the absence of the other. The ratios of desorbed fluence for first irradiation/second irradiation for the two components are given in Table 2. At 3.8 μm, the ratio of desorbed fluence for H_2O or CH_3 remains approximately the same whether H_2O or CH_3 is measured first. In contrast, similar measurements at the HF wavelengths yield a large change in ratio with change in observation order. A comparison of N/1 LID of the various suspect contaminants at closely spaced sites could quantify these apparent differences.

There is some evidence of cumulative heating effects for N/1 LID measurements in CaF_2 at 10.6 μm where the substrate is a bulk absorber. Water continues to be desorbed on sequential shots even when the energy density and therefore the irradiated area above threshold is fixed. An estimated temperature rise of at least several hundred ^{o}C due to the bulk absorption would lower the effective LID threshold in the heated area. As the area heated by bulk absorption and the substrate temperature increases, the LID also increases even for the same effective laser spot size. What is surprising in these experiments is the relatively high damage threshold observed in spite of the high bulk absorption. We were unable to damage the etched CaF_2 (111) in N/1 experiments up to 150 J/cm^2 measured for etched (111) NaCl (Fig. 7). This result emphasizes the importance of surface defect absorption versus bulk absorption in determining the laser damage theshold.

Conclusions

We have shown that for the surfaces considered, i.e., CaF_2, BaF_2, and NaCl, LID cleaning provides passivation for subsequent H_2O adsorption. These materials are representative of the ionic crystals used for high power infrared optics. The LID signal initially observed is, therefore, probably associated with adsorption of H_2O and other contaminants at native defects in the surface such as scratches, cracks, grain boundaries, etch pits, pores, etc. A simple defect model can explain the laser pulse energy dependence of the LID fluence if measurements are made at a single site (N/1). Site to site LID measurements can differ by orders or magnitude, but some areas on the order of mm^2 show similar behavior, suggesting the possibility of using LID for nondestructive mapping of contaminant concentrations. A series of experiments involving the measurement of LID as a function of wavelength and multiple species at a single site imply that contaminants other than H_2O may significantly influence laser damage of these surfaces.

Acknowledgments

The authors are pleased to acknowledge the support of the Office of Naval Research Special Research Opportunities Program and Navy Independent Research Funding.

References

[1] J. O. Porteus, W. N. Faith, and S. D. Allen, this conference, 1981;
S. D. Allen, J. O. Porteus and W. N. Faith, Appl. Phys. Lett. 41, 416 (1982).

[2a] Absorbing Substrates:
L. P. Levine, J. F. Ready and E. Bernal G., J. Appl. Phys. 38, 331 (1967).
H. F. Winters and E. J. Kay, Appl. Phys. 43, 789 (1972).
P. A. Temple, D. K. Burge, and J. M. Bennett, NBS Special Publ. 462, 195 (1976).
R. Gauthier and C. Guittard, Phys. Status Solidi A 38, 477 (1976).
J. P. Cowin, D. J. Auerbach, C. Becker, and L. Wharton Surf. Sci. 78, 545 (1978).

[2b] Low Absorption Substrates:
J. Heidberg, H. Stein, E. Riehl, and A. Nestmann, Z. Phys. Chem. Neue. Folge. 121, 145 (1980).
T. J. Chuang, J. Chem. Phys. 76, 3828 (1982).

[3] P. B. Barraclough and P. G. Hall, Surf. Sci. 46, 393 (1974); J. Chem. Soc. Faraday Trans. 171, 2266 (1975).

[4] S. D. Allen, M. Braunstein, C. Giuliano and V. Wang, NBS Special Publication 414, 66 (1974).

[5] J. O. Porteus, unpublished results.

[6] J. D. Roberts and M. C. Caserio, "Basic Principles of Organic Chemistry", W. A. Benjamin, NY (1965).

Table 1

COMPARISON OF H_2O AND HYDROCARBON SEQUENTIAL LID ON CaF_2 (100)

λ (μm)	CH_3/H_2O	H_2O/CH_3
3.8	0.4	2.4
2.8	0.3	14

Table 1. Ratio of desorbed H_2O and CH_3 fluence for first irradiation/second irradiation on the same site at both HF and DF wavelengths.

Table 2

CHROMOPHORE	ABSORPTION BANDS	LASER	EXAMPLES
O-H	2.7 - 2.8	HF	water, alcohols
O-H (hydrogen bonded)	2.9 - 3.1	HF	water, alcohols
C-H	3.0 - 3.7	DF	hydrocarbon, alcohols
C-0	7.7 - 11.0	CO_2	alcohols
C-C	8.0 - 12.0	CO_2	hydrocarbons

Table 2. Absorption bands of suspected contaminants on optically polished and/or etched surfaces.

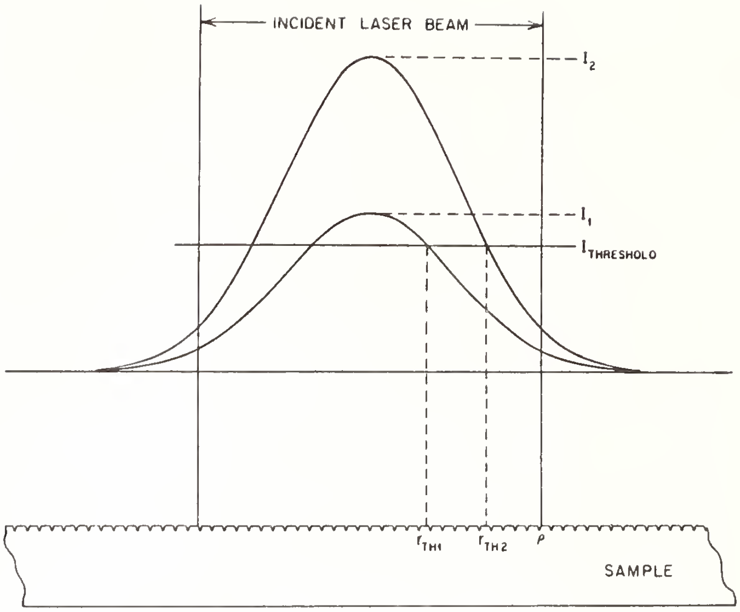

Fig. 1 Schematic diagram of the defect density model used. $I_2 = 2I_1$, ρ is the $1/e^2$ radius of the gaussian beam, and $I_{threshold}$ is the minimum intensity at which desorption takes place from the surface defects.

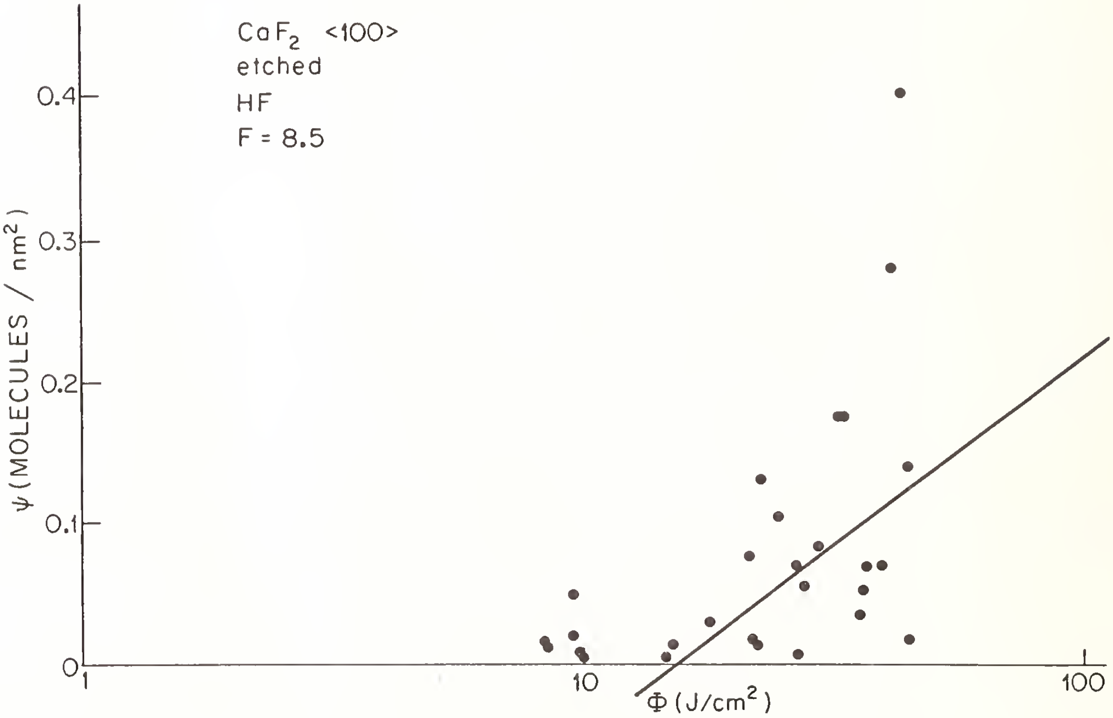

Fig. 2 LID fluence of mass 18 (H_2O) as a function of axial energy density for a 1/1 experiment on etched (100) CaF_2. D_{1/e^2} = 380 μm at HF.

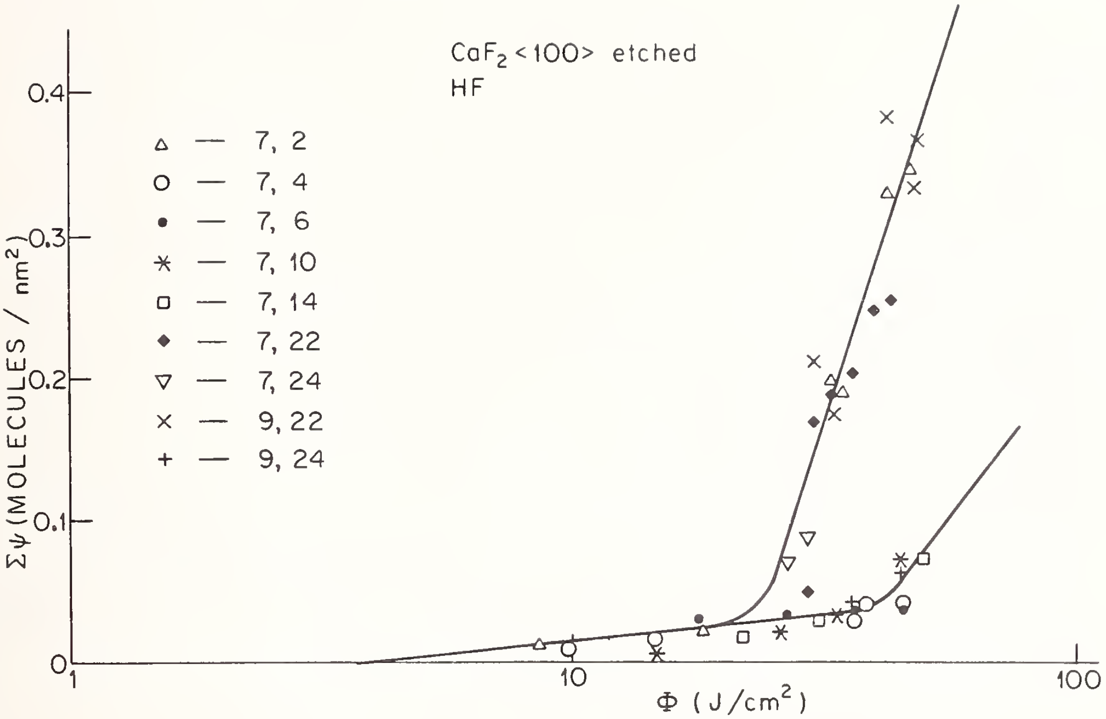

Fig. 3 Cumulative LID fluence of mass 18 (H_2O) as a function of axial energy density for a N/l experiment using the same system as Fig. 2. Each irradiated site is designated by its coordinates in mm.

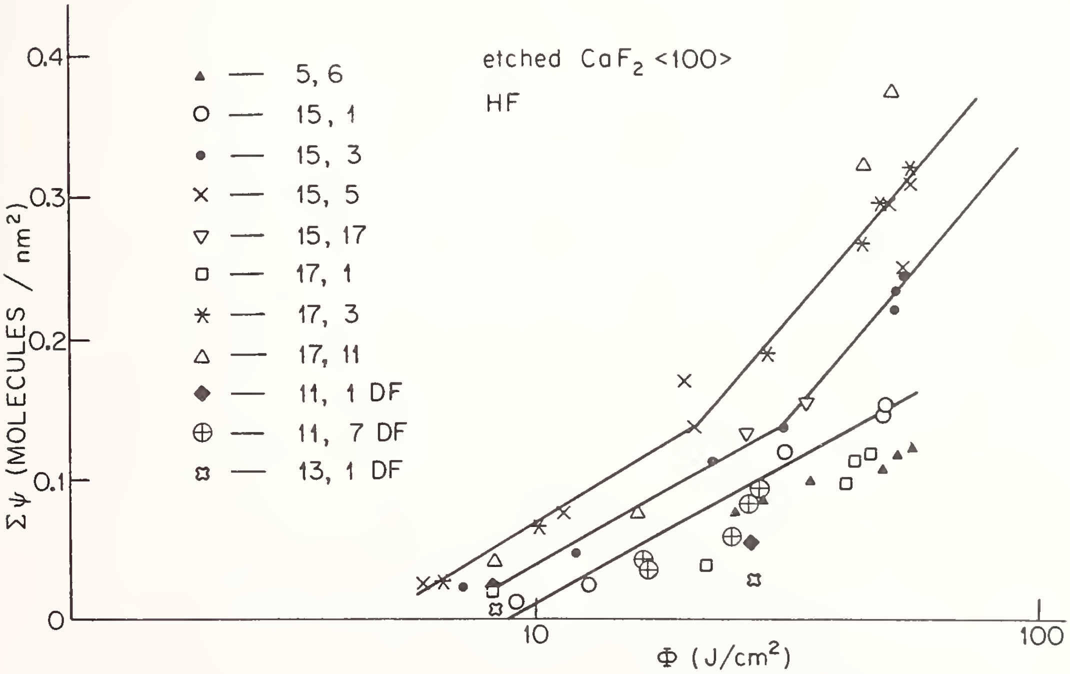

Fig. 4 Cumulative LID fluence of mass 18 (H_2O) as a function of axial energy density for an N/l experiment on (100) CaF_2. D_{1/e^2} = 380 μm at HF and DF. Irradiated sites are designated by their coordinates in mm.

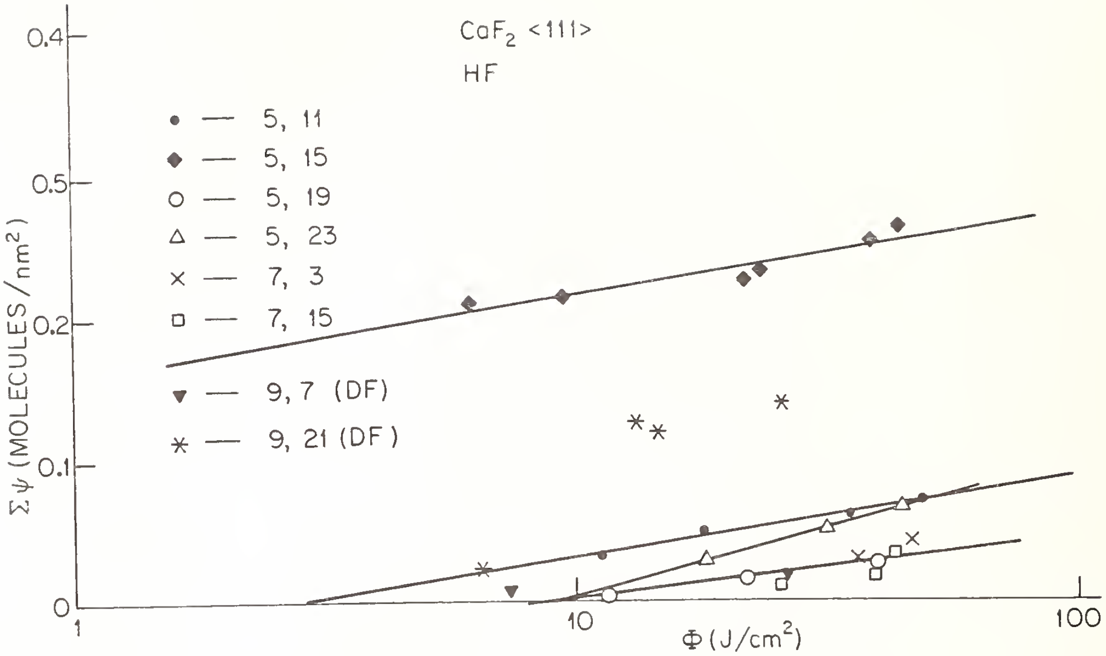

Fig. 5 Cumulative LID fluence of mass 18 (H_2O) as a function of axial energy density for an N/1 experiment on (111) BaF_2. D_{1/e^2} = 380 μm at HF and DF. Irradiated sites are designated by their coordinates in mm.

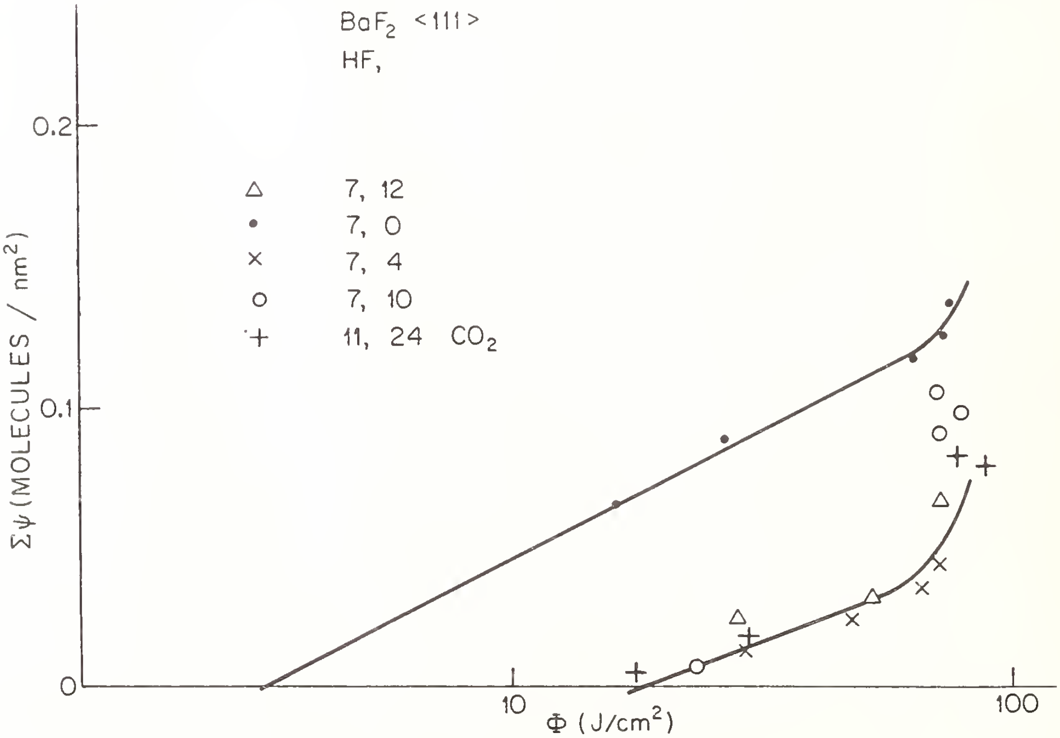

Fig. 6 Cumulative LID fluence of mass 18 (H_2O) as a function of axial energy density for an N/1 experiment on (111) BaF_2. $D_{1/e}{}^2$ = 380 μm at HF and CO_2. Irradiated sites are designated by their coordinates in mm.

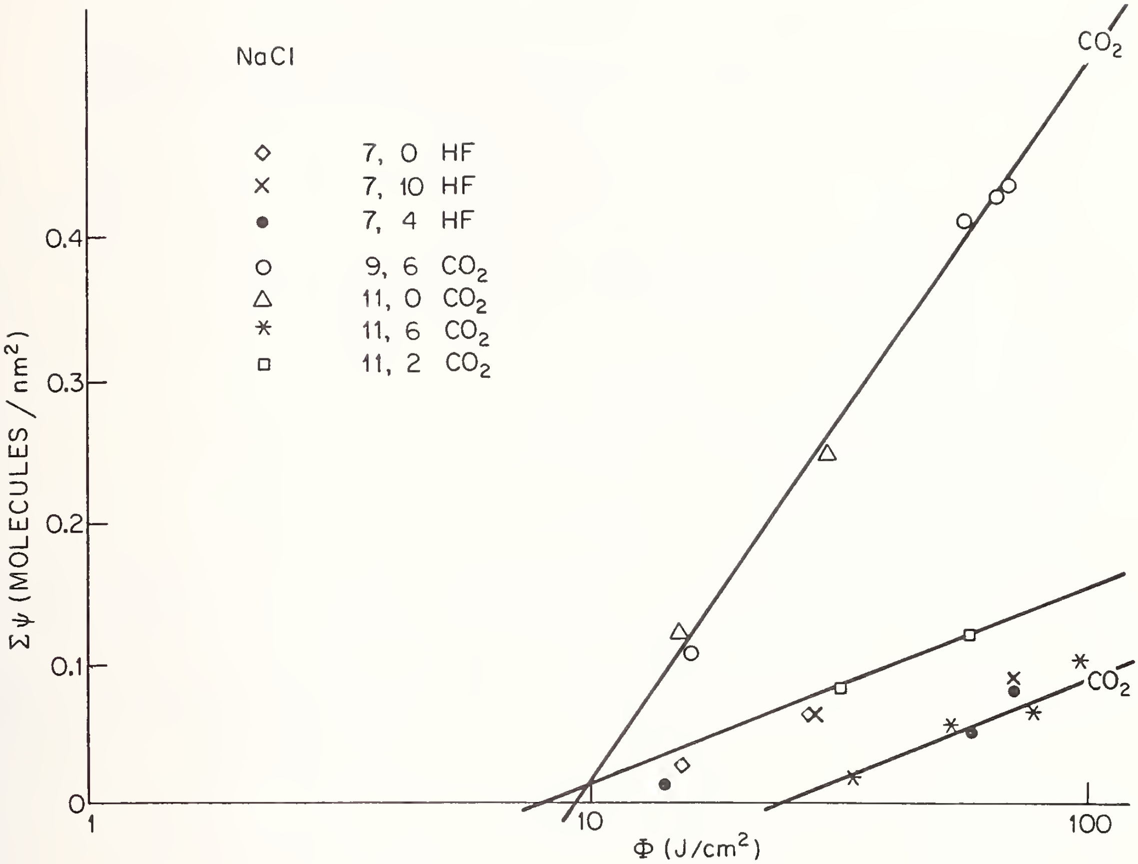

Fig. 7 Cumulative LID fluence of mass 18 (H_2O) as a function of axial energy density for an N/1 experiment on (100) NaCl. D_{1/e^2} = 380 μm at HF and CO_2. Irradiated sites are designated by their coordinates in mm. (Back surface damage at the CO_2 wavelength is indicated by the CO_2 notation on two graphs.)

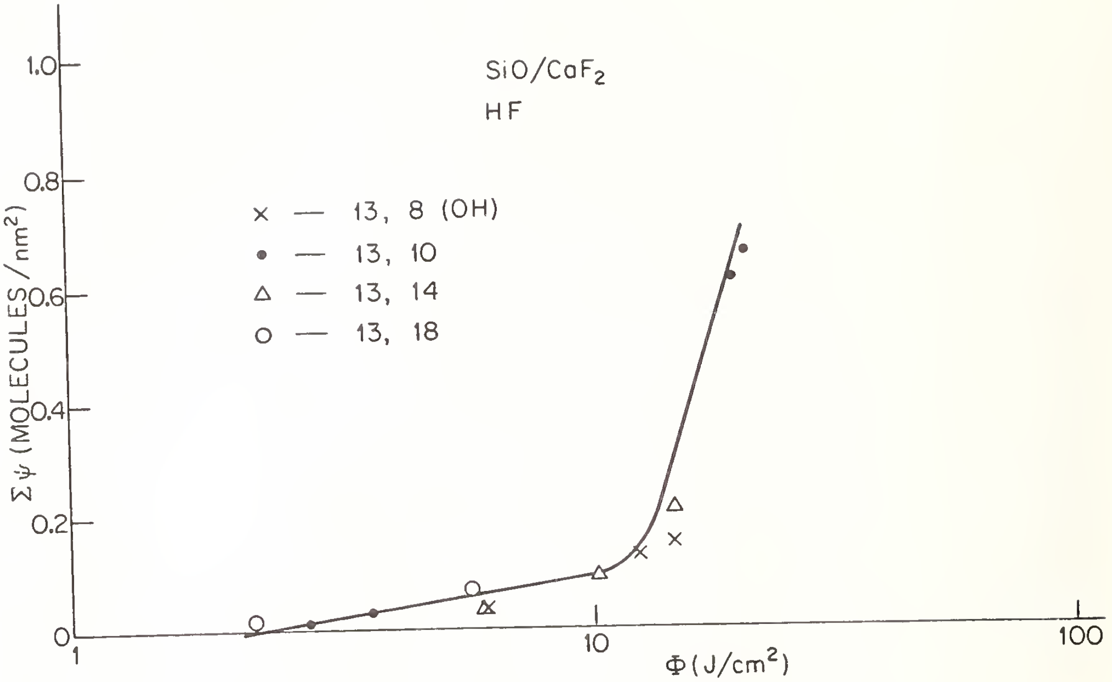

Fig. 8 Cumulative LID fluence of mass 18 (H_2O) as a function of axial energy density for an N/1 experiment on an SiO film on CaF_2. D_{1/e^2} = 380 μm at HF. Irradiated sites are designated by their coordinates in mm.

In answer to a comment that the input fluences in the experiment were high relative to the input at 2.7μm that should be needed to evaporate water, the speaker stated that the laser operated at both 2.7 and 2.8μm, and that there probably were spectral shifts in the absorption spectra of some surface bonded water. In response to further questions, the speaker cited two observations that suggested that most of the desorbed water had initially been trapped in the polished layer: (1) the amount of desorbed water varied for samples polished by different vendors, and (2) laser-cleaned areas that were exposed to water and retested did not show evidence of water contamination in subsequent desorption tests.

Low Optical Absorption Measurement of Laser Optical Materials by Interferometric Laser Calorimetry

Masahide ITOH

The Institute of Physical and Chemical Research,
Hirosawa, Wako-shi, Saitama, 351, Japan

and

Iwao OGURA

Institute of Industrial Science, University of Tokyo,
Roppongi, Minato-ku, Tokyo, 106, Japan

A calorimetric method for measuring the low absorption coefficients of laser optical materials is proposed. It uses the interferometer at 633 nm to measure the bulk and the surface absorption coefficients by the change of the optical path length due to the temperature rise caused by the absorption of CO_2 laser beam. Non-contact measurement as well as linear and rapid response of the absorption makes possible multi-point measurement with high time-resolution. The surface absorption can be separated from the bulk absorption. With the aid of digital technique, the bulk and the surface absorption coefficients of infra-red materials such as ZnSe, KCl, NaCl, etc. , are obtained with the range of $10^{-3}cm^{-1}$.

Key Words: interferometry; laser calorimetry; highly transparent materials; laser window; surface absorption; bulk absorption; KCl; ZnSe.

1. Introduction

The widespread use of high power lasers requires further studies of the very low loss optical materials. The progress in the technique of measuring small absorption coefficients has contributed to the development of such materials. Laser calorimetric method is one of the most powerful techniques of measuring the low optical absorption of the infrared laser window materials [1~5][1]. Especially, interferometric laser calorimetry has a merit of obtaining the inner temperature distribution of the transparent sample in multi-point in parallel because of non-contact measurements [6,7]. We will also propose some applications of this method.

2. Thermal Equation

The coordinate system of the interferometric laser calorimetry is shown in fig. 1. The CO_2 laser beam passes through the sample at right angle with He-Ne laser probe beam. The sample absorbs the CO_2 laser light proportional to its absorption coefficient. The heat gives rise to the change in optical path length. This change is observed as the movement of the fringe by the interferometers. Thermo-optic coefficient γ that is, the change rate of the optical path length versus the temperature, is written as:

$$\gamma \equiv \frac{dL}{dT} = (n-1)\frac{\partial d}{\partial T} + d\frac{\partial n}{\partial T} , \qquad (1)$$

---

[1] Figures in brackets indicate the literature reference at the end of this paper.

where L is the optical path length, T the temperature, d the thickness and n the refractive index.

The temperature distribution in the sample obeys the partial differential equation of heat conduction given by [8]

$$\frac{1}{\kappa}\frac{du}{dt} = \nabla^2 u + F \ . \tag{2}$$

Here u is the temperature difference between the sample and the ambient, and κ is the thermal diffusivity. The heat source term F is

$$F = \frac{P}{k}\frac{1}{(\pi w)^2}\exp\left(-\frac{(x-L_x/2)^2+(y-L_y/2)^2}{w^2}\right)$$

$$\times\left\{(1-\alpha)\beta e^{-\beta z}+\alpha\left[\delta(z)+(1-\alpha)e^{-\beta z}\delta(z-L_z)\right]\right\} , \tag{3}$$

where P is the power of the laser beam of the heating radiation source, w is the radius of the spot size, L_x, L_y, and L_z are the sample size, $\delta(z)$ is the delta function, and α and β are the bulk and surface absorption coefficients, respectively. We calculated the temperature u of x,y,z,t, under the boundary condition of the third kind with the Fourier method. The solution of the eq. (2) is

$$u = \sum_{i=0}^{\infty}\sum_{j=0}^{\infty}\sum_{k=0}^{\infty} A_{ijk}(t)\cdot g_i^x(x)\cdot g_j^y(y)\cdot g_k^z(z) , \tag{4}$$

where

$$A_{ijk} = \frac{f_{ijk}}{\mu_{ijk}}(1- e^{-\mu_{ijk}t}) ,$$

$$\mu_{ijk} = \kappa\left[(\lambda_i^x)^2+(\lambda_j^y)^2+(\lambda_k^z)^2\right] ,$$

$$F = \sum_{i=0}^{\infty}\sum_{j=0}^{\infty}\sum_{k=0}^{\infty} f_{ijk}\cdot g_i^x(x)\cdot g_j^y(y)\cdot g_k^z(z) .$$

The change in optical path length that we observed by the interferometer is proportional to the integral of the temperature between the sample thickness, as

$$U = \gamma\int_0^{L_y} u \ dy = \gamma L_y \sum_{i=0}^{\infty}\sum_{k=0}^{\infty}\frac{f_{i0k}}{\mu_{i0k}}(1- e^{\mu_{i0k}t})\cdot g_i^x(x)\cdot g_k^z(z) . \tag{5}$$

In the case of low optical absorption, change in the optical path length is the linear combination of the surface and the bulk absorption terms that we write U_s and U_b, respectively:

$$U = \alpha \ U_s + \beta \ U_b , \tag{6}$$

where

$$U_s = \sum_{k=0}^{\infty}\left[\frac{2}{L_z}R_{00k}\left(1-\frac{hL_z}{4}\right) + \sum_{i=1}^{\infty}\frac{4}{L_z}R_{2i,0,k}\left(1-\frac{1}{2}\frac{2i\pi kL_z}{(2i)^2\pi^2+2kL_z^2}\right)\right] ,$$

$$U_b = \sum_{k=0}^{\infty} R_{00k} ,$$

$$R_{i0k} = \frac{L_y}{\mu_{i0k}}(1- e^{\mu_{i0k}t})\cdot g_i^x\cdot g_k^z\cdot a_i ,$$

where a_i is the i-th expansion coefficient of the cross sectional (x-) component of the heat source F. U_s and U_b can be calculated with the constants of the sample, such as specific heat, density, thermal diffusion constant, heat transfer coefficient, etc. Figure 2 shows a distribution of the the optical path length that is proportional to the inner temperature of the transparent sample.

3. Experiments

We used the two types of interferometers. If the opposite surfaces of the sample are both optically flat, the interferometer of the Twiman-Green type is used (fig. 3(a)). Otherwise we have to use the holographic interferometer (fig. 3(b)). As probe laser beam, He-Ne laser is used, where the wavelength is 633 nm, and the power is 5 mW. The light source that induces temperature rise is continuous wave CO_2 laser. The the wavelength is 10.6 μm, the power 10 W and the spot-size is 1 mm. The cubic KCl samples are used, where its sides are 20 mm. Sample is set on the edges of the bakelite holder.

Figure 4 shows an example of the fringe movements using holographic interferometry. CO_2 laser beam passes through the center of the sample from right to left. We can see the temperature distribution inside the sample from this patterns. About 30 seconds after CO_2 laser turns off, the temperature in the sample becomes uniform. Using the change of optical path length after 30 seconds, we can obtain the thermo-optic coefficient γ.

The samples are two pieces of KCl where measuring wavelength is 10.6 μm. And we also measured the quartz and CaF_2 at 488 nm of the Ar laser. We read out the fringe movement at the center of the sample. For the calibration of the movement due to the interferometer, we subtract the outer movement of the fringe from the center. Intensity profile of the interference pattern is assumed to be sinusoidal. We first measure the peak to peak intensity of the fringe to move the one arm of the interferometer by piezo electric transducer, and obtain the change in the optical path length by interpolating the peak-to-peak intensity.

4. Results and Discussion

After we measure the optical path length change U of x,y,z,t, we can determine the surface absorption coefficient α, and the bulk absorption coefficient β by the least square method (fig. 5). Figure 6 is an example of the experimental data and the fitting line of two different of KCl's. We may say that experimental data are in good agreement with our method.

The surface and the bulk absorption coefficients are obtained (table 1). The errors of each value are about 10 %. We consider that this error is caused by the change of environmental condition during experiments, and the thermal stresses. On the other hand, internal stress effect may be obtained by measuring the stress birefringence with interferometers.

Table 1. Determined bulk and surface absorption coefficients.

Specimen	Wavelength	Bulk Absorption $\beta \times 10^3 (cm^{-1})$	Surface Absorption $\alpha \times 10^3$
Quartz	488 nm	95 ± 7	5.3 ± 0.3
CaF_2	488 nm	6.6 ± 0.5	4.0 ± 0.6
KCl(1)	10.6 μm	2.1 ± 0.2	1.1 ± 0.3
KCl(2)	10.6 μm	1.0 ± 0.2	1.1 ± 0.1

We also propose another application of the interferometric laser calorimetry that is to obtain the distribution of the bulk absorption. We can obtain the change in optical path length in multi-point in parallel. In this case we used the 1024 point linear image sensor as the detector, and processed the data with mini-computer (fig. 7).

The partial differential equation of heat conduction (eq. (2)) is rewritten into the difference equation:

$$\frac{1}{L_y}\ \frac{U_{i,j+1}-U_{ij}}{\Delta t} = \frac{U_{i+1,j}\ -\ 2U_{ij}\ +\ U_{i-1,j}}{(\Delta z)^2} + \frac{P}{\rho c}\ \beta_i \qquad (7)$$

Subscript i and j denote the spatial and temporal parameter respectively. If we measure the spatial distribution of the optical path length change with the short time repetition, we can obtain the distribution of the bulk absorption coefficient β_i .

The test experiments of measuring the bulk absorption distribution of ZnSe is shown in fig. 8. In this case, we assumed the only bulk absorption, and consequently, the increase of the absorption near the sample surface was observed. Connecting the interferometer with the micro-computer, we can not only get the surface and the bulk absorption coefficients separately, but also get the distribution of the absorption in the sample.

Laser interferometric calorimetry has the merit of high speed response to the temperature field. With the pulsed CO_2 laser, damage occurs within 100 ns. We have observed the stress and the thermal wave inside a ZnSe sample under the TEA CO_2 laser irradiation where the pulse duration is 100 ns and total power is 1 J. The surface and the bulk linear or nonlinear absorption will be obtained by analysing the wave form.

In the case that the sample does not have optical parallel, such as lenses, prisms or rough surface, we may use the Schlieren method. If we use the 2-nd harmonic wave of the Nd-YAG laser as the probe light we can observe few nano-second thermal or stress effect. With the use of double pulsed YAG laser, we may take a double exposed holography, and after development the hologram, the deformation less $\lambda/100$, that is, about few nano-meter can be measured by analysing the reconstructed holographic 3-dimentional image using digital fringe scanning technique.

5. Conclusion

We have developed a technique of measuring the surface and the bulk absorption coefficients separately using an interferometric laser calorimetry. It uses the interferometer at 633 nm to measure the bulk and the surface absorption coefficients separately by the change of the optical path length due to the temperature rise caused by the absorption of 10.6 μm CO_2 laser beam. We measured the bulk and the surface absorption coefficients of KCl's, and obtain 1.0×10^{-3} cm^{-1} and 1.1×10^{-3} , respectively. We also measured the distribution of the absorption inside the sample and observed the thermal and stress wave induced by the pulsed laser light. We believe that all optical measurements have some merits of high sensitivity and high time response to study the low optical absorption materials.

6. Acknowledgement

The authors acknowledge stimulating discussions with Dr. K. Kuroda. The authors also thank Dr. H. Saito and Prof. T. Ose for their encouragements.

7. References

[1] Temple, P. A., Examination of laser damage sites of transparent surface and films using total internal reflection microscopy; *Laser Induced Damage in Optical materials*; 1979, October 30-31 1979, NBS Boulder Co., eds. by H. E. Bennett, A. J. Glass, A. H. Guenther and B. E. Newnam, NBS Special Publication 568, U. S. Government Printing Office, Washington, D. C. 1980, p333.

[2] Wu, S.T.; Bass, M., Intensity dependent absorption of Alkali-halides at 10.6 μm; *Laser Induced Damage in Optical materials*; 1980, September 30-October 1 1980, NBS Boulder Co., eds. by H. E. Bennett, A. J. Glass, A. H. Guenther and B. E. Newnam, NBS Special Publication 620, U. S. Government Printing Office, Washington, D. C. 1981, p75.

[3] Braunstein, R.; Kim, R. R.; Braunstein, M., Wavelength modulation spectroscopy of laser window materials; *Laser Induced Damage in Optical materials*; 1980,

September 30-October 1 1980, NBS Boulder Co., eds. by H. E. Bennett, A. J. Glass, A. H. Guenther and B. E. Newnam, NBS Special Publication 620, U. S. Government Printing Office, Washington, D. C. 1981, p29.

[4] Rosenstock, H. B., Absorption Measurements by Laser Calorimetry, J. Appl. Phys. 50: 102-110 1970.

[5] Itoh, M.; Saito, H., Pulsed Photoacoustic Technique to Measure the Absorption Coefficients of the Highly Transparent Materials. Opt. Commun. 44: 229-231 1983.

[6] Itoh, M.; Ogura, I., Absorption Measurement of the Optical Materials by Real Time Holographic Interferometry. Opt. Commun. 33: 183-187 1980.

[7] Itoh, M.; Ogura, I., Absorption measurements of laser optical materials by interferometric calorimetry, J. Appl. Phys. 53: 5140-5145 1982.

[8] Carslaw, H. S.; Jaeger, J. C., *Conduction of Heat in Solids*. London; Oxford University Press; 1959.

8. Figures

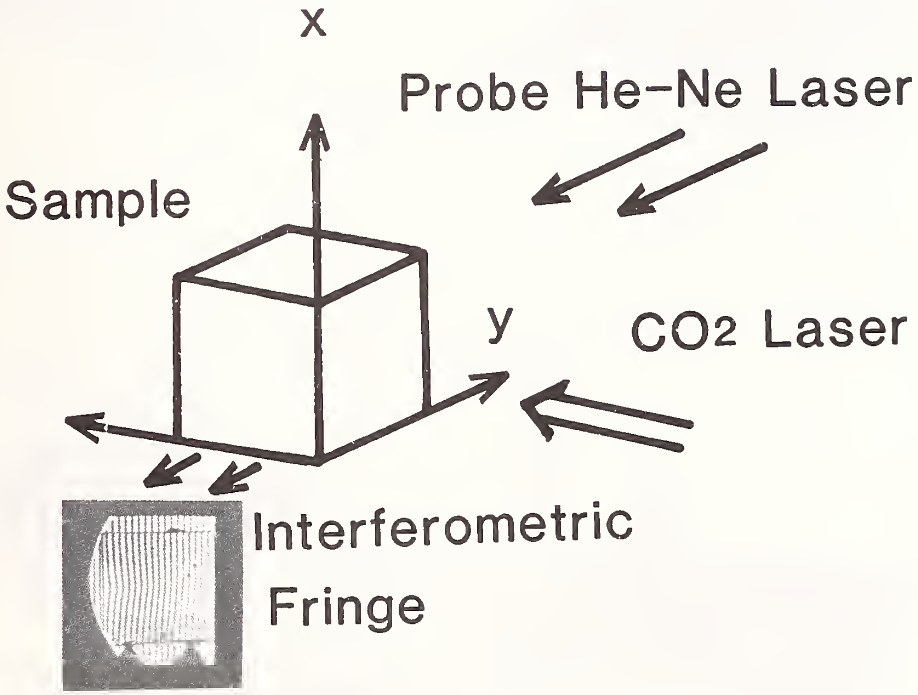

Figure 1. Coordinate system.

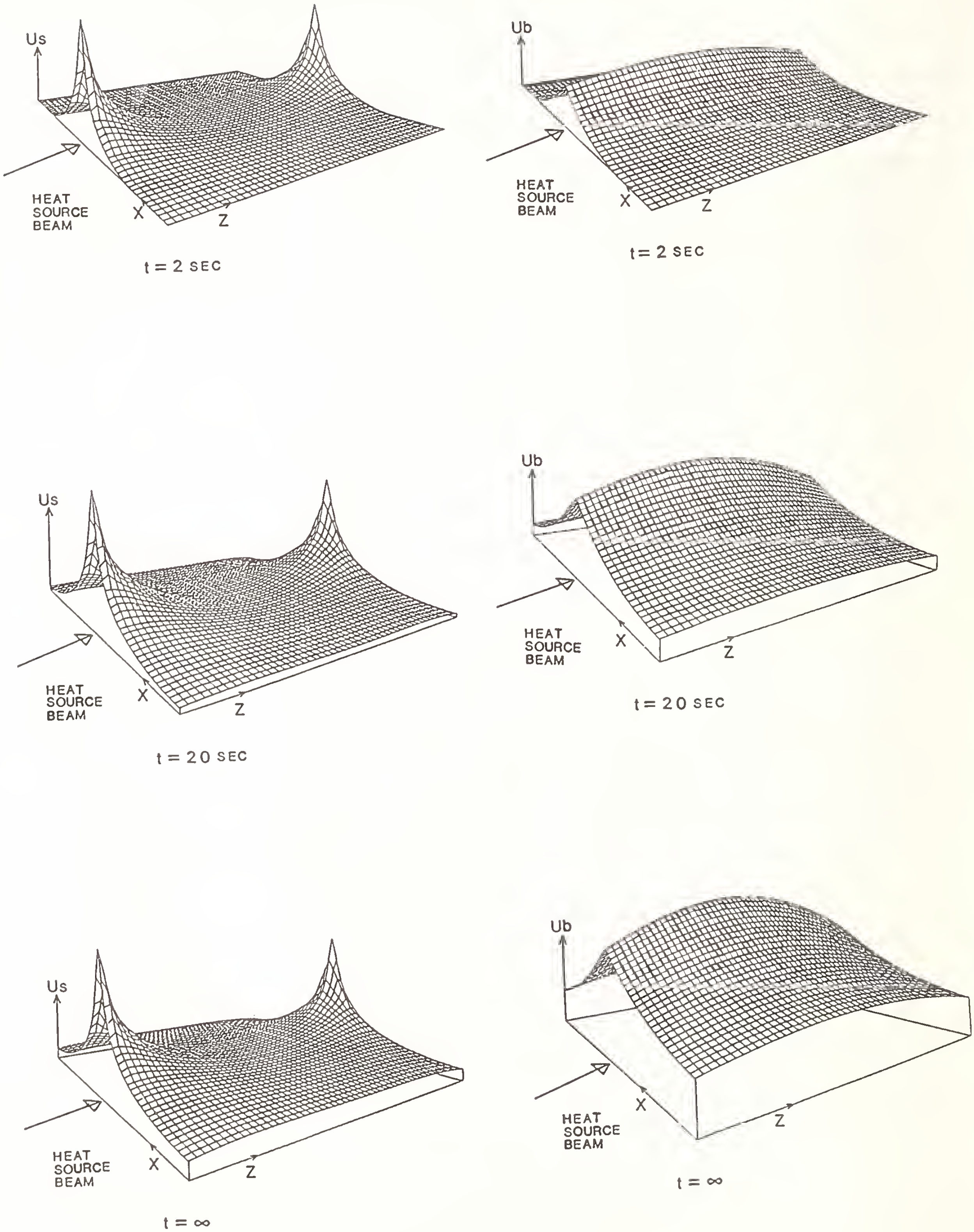

t = 2 SEC

t = 2 SEC

t = 20 SEC

t = 20 SEC

t = ∞

t = ∞

Figure 2. Distribution of the optical path length. The right side of the figure is due to the only surface absorption, and the left is due to the bulk absorption.

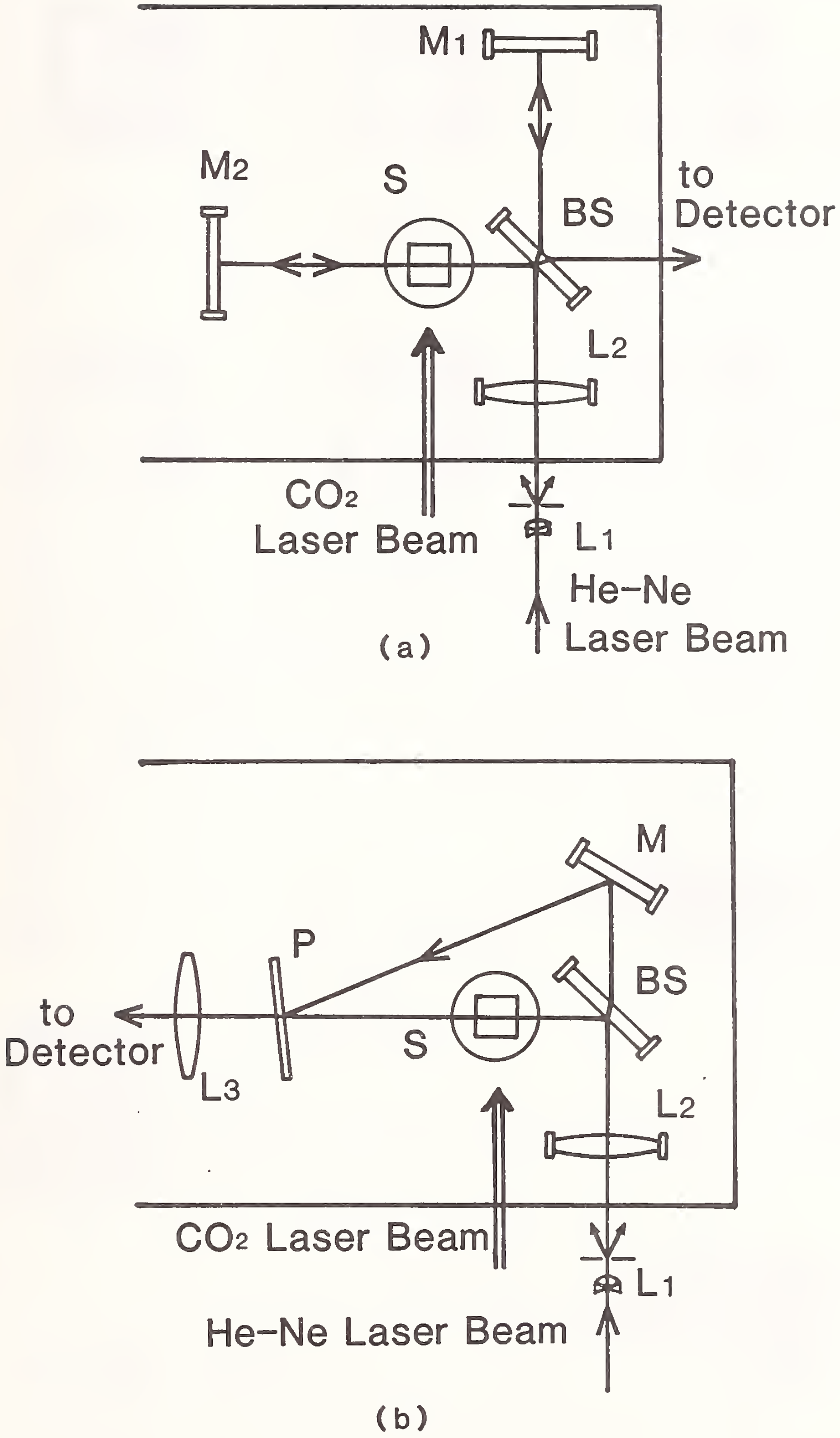

Figure 3. Schematic of Interferometers. (a) Twiman-Green type which is used if the opposite surface of the sample are both optically flat. (b) Holographic type which is used, otherwise

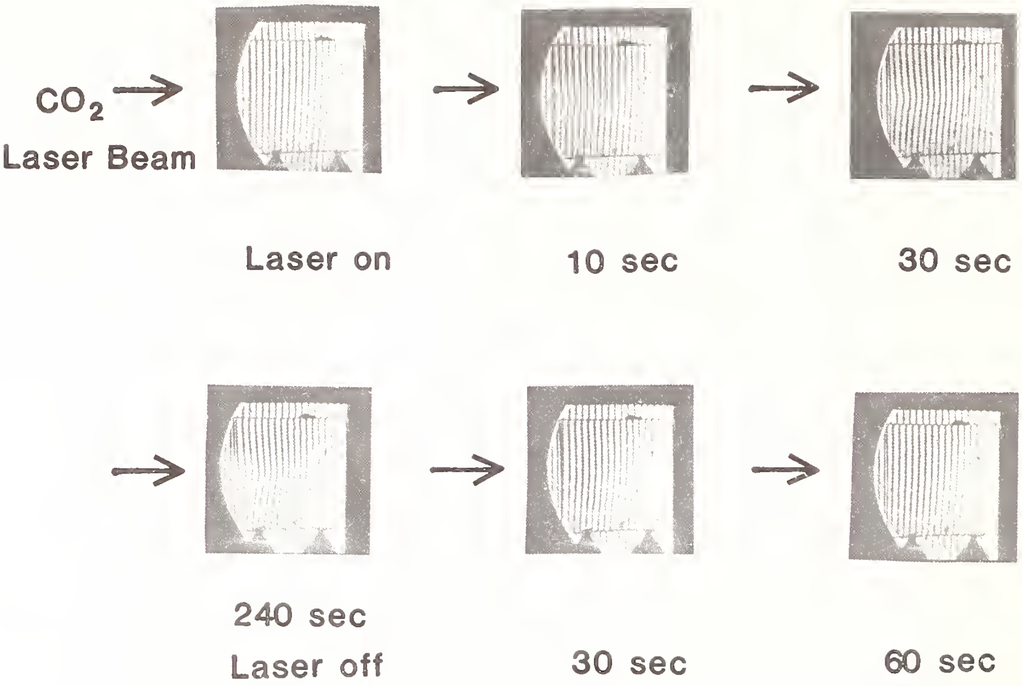

Figure 4. Example of the fringe movement observed by the holographic interferometer.

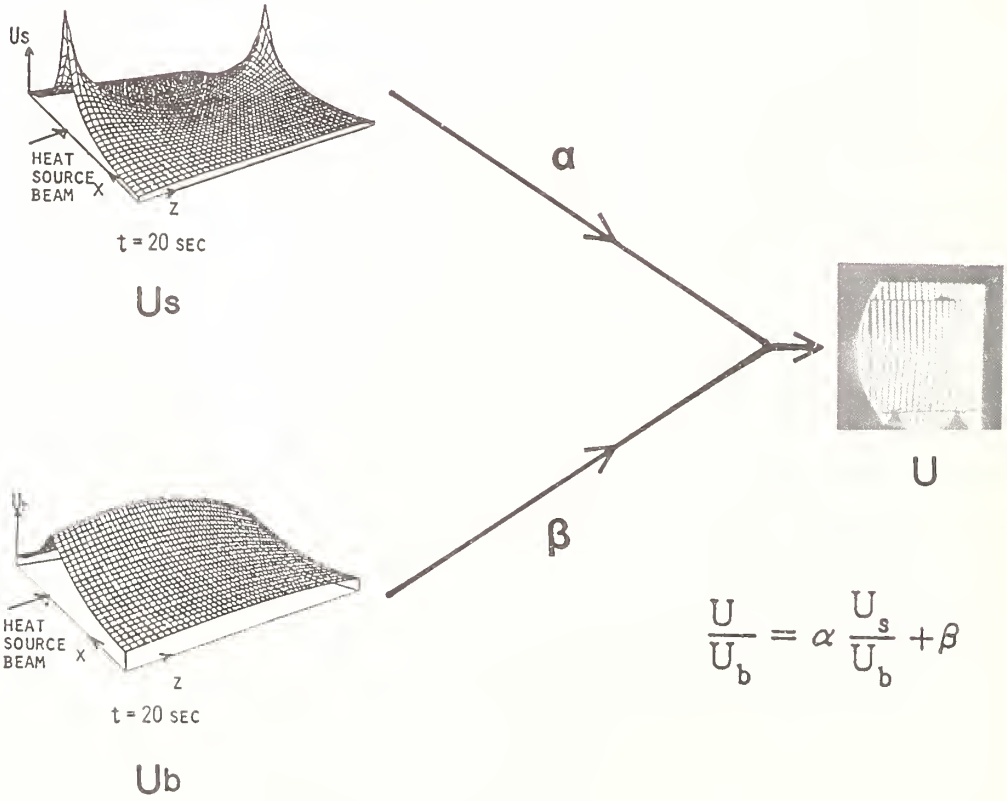

$$\frac{U}{U_b} = \alpha \frac{U_s}{U_b} + \beta$$

Figure 5. Procedure of measurements.

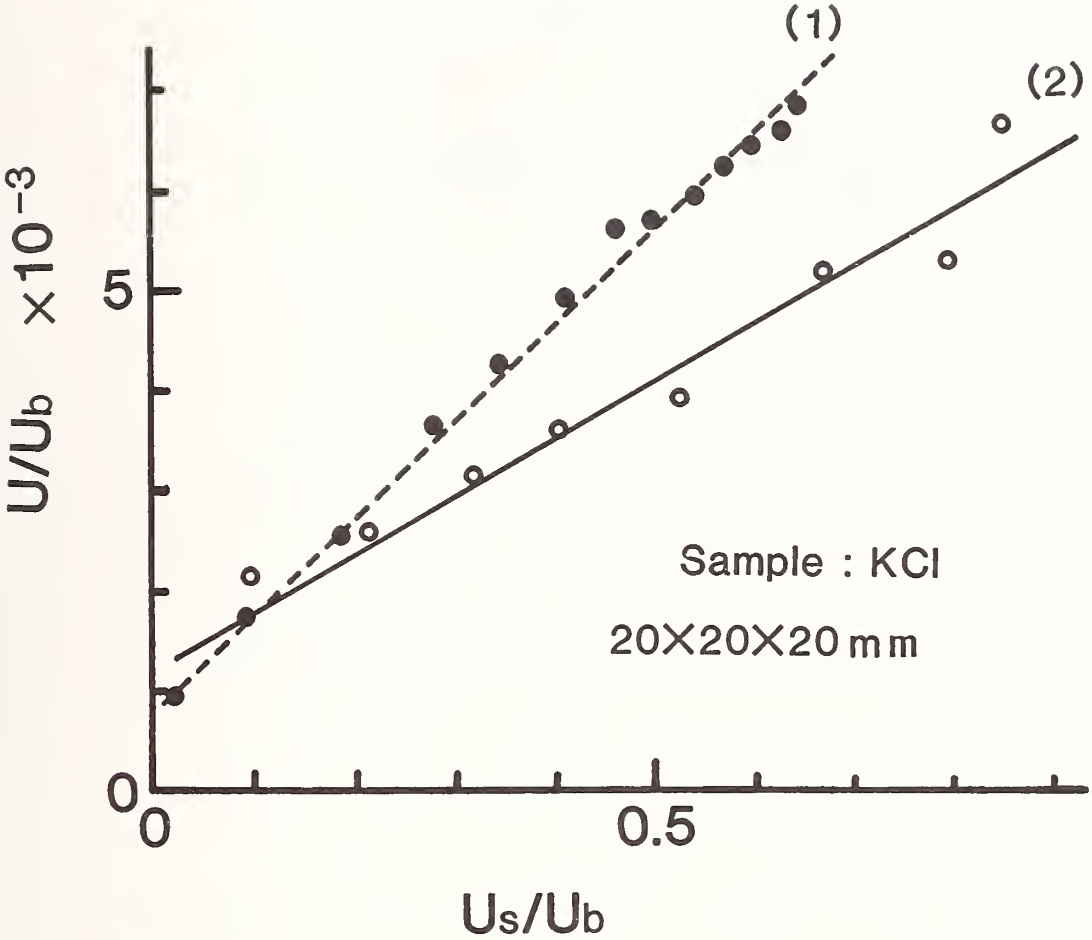

Figure 6. Plot of the ratio of U/U_b vs. U_s/U_b. U is the measuring optical path length (OPL), U_b is the calculating OPL due to the bulk absorption, and U_s is the calculating OPL due to the surface absorption.

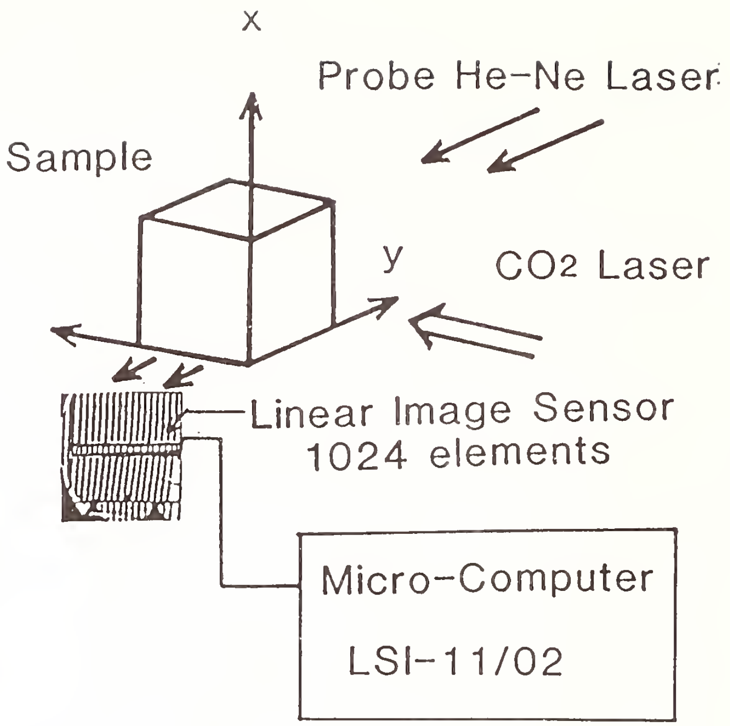

Figure 7. Experimental set up to obtain the distribution of the bulk absorption.

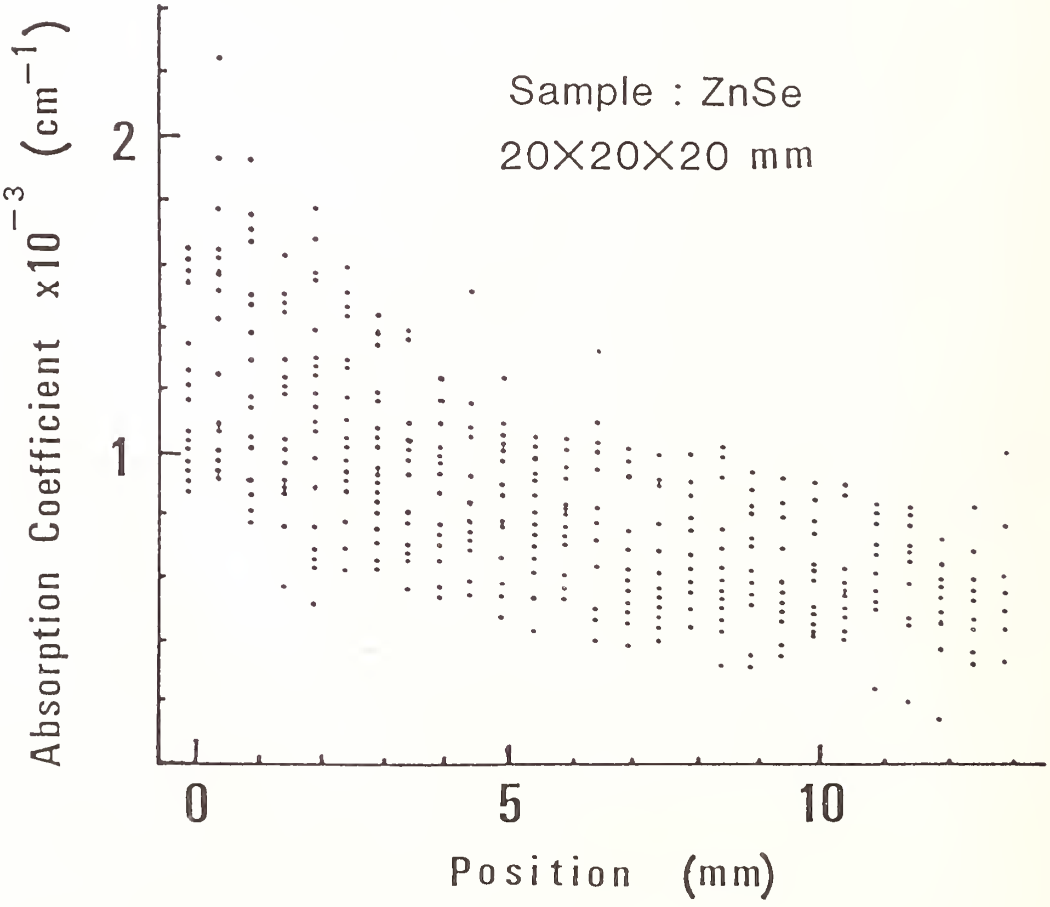

Figure 8. Distribution of the bulk absorption.

The accuracy of the reported absorption coefficients for alkali halide crystals was questioned. Reference was made to previous measurements on such crystals at 10 microns performed by B. Bendow and coworkers in the 1970's. In these, stress-induced changes in the optical path length (via thermal lensing), amounting to ~20-30 percent, had complicated the determination of the absorption coefficients.

Surface and Free Carrier Absorption Processes in CVD Zinc Selenide

K L Lewis

Royal Signals and Radar Establishment
St Andrews Road, Malvern, Worcs. WR14 3PS UK

and

G S Arthur

Atomic Weapons Research Establishment
Aldermaston, Berks. RG7 4PR UK

An investigation is reported of the effects of extrinsic absorption processes on the infra-red properties of ZnSe prepared by chemical vapour deposition. Surface absorption processes are discussed with reference to the absorption of water and hydrocarbon impurities from the atmosphere. Particular attention is paid in the case of bulk absorption to the effects of free carrier scattering processes which produce a wavelength dependence of the absorption coefficient of the type $\beta = \lambda^{\rho}$. In material free from second-phase inclusions, the intensity of infra-red absorption at 10.6 µm measured calorimetrically, has been found to be correlated with a red photoluminescence process produced under near band-gap irradiation. Detailed studies of the photoluminescence show that the electronic structure of the material is dominated by the presence of sodium and copper acceptors, together with a donor tentatively ascribed to indium. In well-compensated material, deeper centres appear to predominate.

The behaviour on annealing of material exhibiting face carrier absorption can be described by a model involving the diffusion of impurities such as Fe, Ni or Cr from grain boundary sites.

Keywords: Calorimetrically; free carrier absorption; photoluminescence;
surface absorption; zinc selenide.

1. Introduction

The II-VI semiconductor compound ZnSe is of current interest as an infra-red transmitting material. A combination of wide bandgap (2.7eV) and low lattice vibrational frequencies allows transmission over a wide wavelength range (0.5-22µm), covering most of the visible spectrum, two thermal imaging bands (3-5 and 8-12µm) and the operating frequencies of several infra-red lasers (HF, DF and CO_2). Production of such material by chemical vapour deposition (CVD) techniques avoids the difficulties that are likely to be encountered in the scale-up of melt growth or hot-pressing processes, and results in a polycrystalline product with a grain size of 50-100µm. The material is n-type with a DC resistivity of 10^{10}-10^{12}Ωcm. However, the electrical properties are set by the presence of potential barriers at the grain boundaries, preventing the application of conventional techniques of electrical assessment. Russell et al [1] have examined the material using Electron Beam Induced Current techniques and suggest that the electrical properties at the grain boundaries are a consequence of the segregation of hydride species or transition metal impurities.

The infra-red properties of ZnSe are a direct consequence of the impurity content and defect structure of the material. For example, Dutt, Kim and Spitzer [2], who studied aluminium-doped single crystal ZnSe, found that the intensity of infra-red absorption was dependent on the aluminium content and the conditions of annealing in zinc-rich atmospheres. It is believed that a self-compensation of charge carriers occurs in Al-doped ZnSe such that the shallow donor level of Al (E_A = 0.026eV) is compensated by the formation of a complex species (Al_{Zn}-V_{Zn}) which acts as a deep acceptor. Annealing of ZnSe:Al in zinc-rich atmospheres results in a suppression of the zinc-vacancy concentration and therefore reduces the self-compensation. This results in an increase in the free-carrier absorption effect. However, the local vibrational mode spectrum of such material contains two additional absorption bands which cannot be explained on the basis of this defect model, and the electronic structure may be complicated by the presence of other defects or impurities. Recently, Dean [3] has highlighted the role of impurities in providing shallow or deep centres which determine the electrical properties of II-VI materials, and emphasises the need for a greater degree of impurity control.

Kulakov and Grinev [4] have also examined melt-grown ZnSe:Al, and have found that it is necessary to reduce the free carrier concentration to less than $10^{12}cm^{-3}$ in order to achieve absorption coefficients at 10μm of less than $0.001cm^{-1}$.

Some impurities give rise to specific absorption bands in the infra-red. For example, SiO species give rise to a narrow band near 9.1μm [5], whilst Cu and Fe give rise to extremely broad features, centred at 2μm and 3.3μm respectively [6]. The Fe band has little effect on 10.6μm absorption, but the long wavelength end of the Cu band produces a significant absorption at 10.6μm. On the basis of the data of Kulakov et al [6], it is necessary to reduce the Cu content to less than 1 ppm in order to achieve absorption coefficients at 10.6μm of less than $0.001cm^{-1}$.

In a study of absorption processes in optical materials, it is also essential to ensure that differences in the properties of the bulk material are not affected by random differences in surface absorption effects, which may vary from sample to sample depending on surface preparation and cleaning conditions. This is of particular importance when the contribution of bulk absorption is small, and laser calorimetry is required for its accurate measurement. This work examines surface absorption and infra-red free carrier absorption (IRFCA) processes in CVD ZnSe using a variety of techniques.

IRFCA is produced in CVD ZnSe grown under Zn-rich conditions and results in an increase in 10.6μm absorption coefficient by several orders of magnitude, despite low levels of electrically active impurities. The origin of this effect is discussed in relation to the defect structure of the material.

2. Material Growth and Assessment

The ZnSe examined in this study was produced by chemical vapour deposition from mixtures of zinc vapour and H_2Se gas as previously described [7]. The zinc and H_2Se were of nominal 99.999% purity (Koch Light Ltd and British Oxygen Co. respectively), and were transported to the deposition zone within the furnace using an argon carrier stream of greater than 99.999% in purity, derived from a liquefied source. Impurity levels in the product were determined by atomic absorption spectroscopy and neutron activation analysis. Material was selected for study from batches of similar purity. Type 1 material was grown near stoichiometric conditions, whilst type 2 was grown under zinc-rich conditions. Table (1) shows that there are no significant differences in purity of the two materials. The inequality signs represent detection limits.

Samples for optical assessment were cut from the deposit and polished using diamond abrasive compounds. Infra-red absorption spectra were measured using a Perkin Elmer model 597 spectrophotometer, whilst absorption coefficients near 10.6μm were determined using a laser calorimeter [8]. The calorimetric system was used as previously described with the exception of the replacement of the laser by a 10W step-tu nable CO_2 laser (GTE Sylvannia model 950). Photoluminescence (PL) spectra were determined under Hg lamp excitation using a 1 metre monochromator (Bentham Instruments) and lock-in signal processing. Photoluminescence Excitation (PLE) spectra were recorded using conventional lamp/monochromator techniques but with a double-beam sampling system which automatically corrected for the spectral dependance of intensity produced by the lamp/monochromator source. Samples for PLE measurements were etched lightly with an aqueous solution of potassium ferricyanide/potassium hydroxide to remove the surface work-damaged layer. For low temperature measurements, samples were fixed onto the cold finger of a vacuum cryostat.

3. Surface Absorption Processes

The infra-red absorption properties of the ZnSe surfaces were examined using Attenuated Total Reflectivity (ATR) sampling. In this technique, the infra-red beam is propagated along a thin polished plate of material by a series of total internal reflections. At each reflection, the evanescent wave 'samples' a portion of the surface, and on passage along the plate, 25 to 50 such samplings occur. The ATR spectrum of a polished CVD ZnSe plate, which has been standing in the laboratory air for a few days is shown in figure (1). The spectrum is dominated by features due to O-H and $-CH_n$ vibrational modes. The OH species presumably arise from atmospheric moisture whilst the CH_n derive from hydrocarbon pollutants. The origin of the sharp band at $1540cm^{-1}$ is open to debate. It is not due to the bending vibrations of the $-CH_n$ groups since these give rise to the two weaker bands near 1390 and $1450cm^{-1}$. The sharpness of the band suggests that it may be due to -C=O species, with the shift in frequency from the usual 1650 - $1750cm^{-1}$ being a consequence of the electronic interaction with the bulk ZnSe, rather as in formates and organic acid salts of the type $(R\text{-}CO_2)^- M^+$ [9]. Indeed, Kirovskaya and Pimenova [10] have studied the adsorption of carbon dioxide on the related compound ZnTe, and suggest that the surface complex formed has the carboxylate ion structure.

Notably absent from figure (1) are any absorption features in the spectral range 900-1000cm^{-1}. However, the presence of the O-H band near 3300cm^{-1} shows that H_2O is present which would also give rise to a flat featureless absorption plateau in the range 900-1000cm^{-1}. In addition, the liquid water spectrum contains a broad absorption feature near 1550cm^{-1} which may be superimposed on the band attributed above to $-CO_2$ species. Laser calorimetric measurements on a sample of ZnSe (table 2) clearly demonstrate the effect of a surface layer of water, and using a value of bulk absorption coefficient for H_2O at 10.6μm of 10^3cm^{-1}, we estimate a water film thickness of 100Å.

Cleaning of samples using trichloroethane, followed by acetone, was found to reduce the intensity of the absorption features in figure (1) by an order of magnitude. Samples used for the absorption studies discussed in the following section were each subjected to this cleaning procedure.

4. Absorption Due to Free Charge Carriers

Samples of ZnSe produced under Zn-rich conditions have been found to exhibit IRFCA. Values of absorption coefficient β for several examples, including material grown near stoichmetric conditions, are listed in table (3). Despite the similarity in purity of the material (type 1 cf. type 2), variations in the magnitude of β extend over several orders of magnitude. The calorimetric measurements were carried out using several laser frequencies near 10.6μm in order to check whether the results were being influenced by optical resonance phenomena. Despite deliberate fabrication of the samples to be slightly wedge shaped, some resonance was detected in certain cases, and the values of absorption coefficient used for the purposes of the following discussion are mean values of the measurements at the different spectral lines of the CO_2 laser. No correction is applied for the effects of residual surface absorption.

The spectral dependence of absorption (measured using the spectrophotometer, figure (2)) reveals the free-carrier nature of the absorption processes, since β is related to wave length λ by an expression of the form

$$\beta = k\lambda^{\rho}$$

On the basis of the discussions of Dutt et al [2] and Jensen, [15] the value of the exponent ρ of 4.3 suggests that the absorption is dominated by contributions from an impurity scattering mechanism. Jensen [11] derives an expression for the absorption coefficient of the form

$$\beta = n_e \sigma \tag{1}$$

$$\text{where} \quad \sigma = \frac{\sigma_o}{x^4} \; \frac{H(x,r)}{(1+x)D(x,r)} \tag{2}$$

$$x = \frac{h\omega}{E_g} \tag{3}$$

$$\sigma_o = {}^2/_3 \, \frac{e^2}{nE_g^{\,3}} \cdot N_i \left(\frac{k^2}{2mnE_g}\right)\left(\frac{4\pi e^2}{e_o}\right)^2 \sqrt{\frac{E_g}{2m_n c^2}} \tag{4}$$

and H and D are complex functions of x and r. Other symbols are defined in table (4). In the limit of $r \rightarrow \infty$, equation (2) simplifies to

$$= \frac{2\sigma_o}{x^{3.5}} \tag{5}$$

for the case where the final electron state lies in the parabolic region of the conduction band,

$$\text{or } \sigma = \frac{\sigma_o}{x^5} \tag{6}$$

when the final electron state lies in the hyperbolic region of the conduction band.

Equations (5) and (6) therefore predict values of $\rho = 3.5$ for the parabolic limit, and $\rho = 5$ for the hyperbolic limit, since

$$\lambda = \frac{1.240}{h\nu}$$

Assuming that the density of charged impurities N_i is equal to the free carrier concentration n_e, values of n_e may be estimated from equation (1). Using the parameters listed in table (4), we obtained carrier concentrations of 0.9×10^{16} and $6.6 \times 10^{16} cm^{-3}$ for the two limits discussed above. This corresponds to a concentration of electrically active impurity of between 0.4 and 3 ppma. A comparison with the actual values listed for type 2 material in table (1) shows that several impurities are present at concentrations in this range, but it is not possible to state which is dominating the free-carrier absorption process.

5. Photoluminescent Properties and Electronic Structure

Samples exhibiting the IRFCA effect described above are characterised by a red photoluminescence centred at 1.97eV. Indeed, figure (3) shows that for several samples, the experimentally determined absorption coefficient at 10.6μm is correlated with the luminescence intensity at 1.97eV. The spectral distribution of the emission when excited by Hg light at 2.84eV is shown in figure (4). A similar emission spectrum is obtained under 3.40eV excitation, although the emission intensity is reduced by an order of magnitude.

The photoluminescence excitation PLE spectrum of the red emission is shown in figure (5). Two features are found; the first, at about 2.38eV is the characteristic excitation band for the 1.97eV process, whilst the second at 2.62eV is much narrower and is due to excitation processes occurring via shallow impurity states. These spectra are similar to those published by Jones and Woods [12] for copper-doped ZnSe, demonstrating the importance of Cu impurities in determining the photoluminescent (PL) properties of the CVD ZnSe. It is clear that the red emission is not due to the self-activated luminescence process since the PLE spectrum contains two maxima, and not just one peak near 2.7eV [12].

As the temperature of measurement is reduced, the narrower PLE band shifts to higher energy, also revealing some structure in the form of a sharp dip at 2.783eV. Such sharp features are characteristic of exciton processes, and in this case is probably the I_1^{deep} acceptor [3]. The PL spectra exhibit considerable structure at near band-gap energy when examined at liquid helium temperatures (figure 6). In samples exhibiting IRFCA, the bound-exciton spectral region contains lines due to I_1^y (sodium), I_1^{deep} and an unidentified donor (I_2^z) line [13]. On the basis of a comparison with single crystal ZnSe containing chlorine, the I_2^z line is about 0.55meV lower in energy suggesting that the donor may be In_{Zn} or F_{Se} according to the data of Merz et al [14]. Donor-acceptor pair (DAP) features are also found, especially the P(Na) series [3]. In material produced near stoichiometry, the I_1^y line is absent, to be replaced by an I_1^x (Lithium) line of reduced intensity. However, the most significant difference is the presence of a broad DAP-like feature at just below 2.60eV. It is thought, [21] that this may be the DAP band associated with the I_1^{deep} exciton.

Measurements of thermally-stimulated current and luminescence (TSC and TSL) carried out on a sample exhibiting strong IRFCA reveal the presence of two traps [15]. The first, at 0.1eV, is ascribed to the sodium acceptor, identified by the I_1^y line above. The second at 0.28eV is too deep to be associated with In_{Zn} or F_{se} ($E_D \sim 0.029$eV) and is probably due to a lattice vacancy or vacancy-impurity complex. Merz et al [16] suggest that the binding energy associated with the I_1^{deep} acceptor is about 0.2eV on the basis of Halsted and Avens [17] empirical rule. TSL measurements on a sample exhibiting weak IRFCA reveal two different trapping centres, with binding energies 0.38eV and 0.72eV. It is likely that these are the two centres associated with green and red PL in ZnSe : Cu [12,18].

The exact nature of the electronic structure of the material is dependent on the identification of the I_1^{deep} acceptor. Dean and Merz [19] suggested that the I_1^{deep} centre involves a Zn vacancy following a study of the effect of annealing of ZnSe in vacuum and in zinc vapour. The I_1^{deep} line is enhanced following annealing in vacuum, but reduced by the zinc vapour anneal, suggesting that the vacuum anneal favours the formation of zinc vacancies. We have examined the effect of annealing a CVD ZnSe sample exhibiting strong IRFCA in an atmosphere of high purity argon, and found that dramatic reductions in the magnitude of the IRFCA (figure 7) and 1.97eV PL occur. This evidence, together with the fact that IRFCA is only found in material grown under Zn-rich conditions, demonstrate the possible importance of the zinc vacancy. On the other hand, recent evidence discussed by Dean [3], suggests that I_1^{deep} is associated with Cu_{Zn} from a study of the Zeeman behaviour of the emission. Much of the effects previously ascribed to the formation of vacancies by annealing in vacuo may merely be a result of impurity diffusion processes, from sites such as grain boundaries or inclusions, whilst growth under Zn-rich conditions merely reduces the incidence of impurities on the zinc sublattice. Such a model has to be reconciled with the results of irradiation experiments on nominally undoped ZnSe. For example, Taguchi and Palmer [20] found that an I_1 emission line near 2.780eV was produced by 100keV proton irradiation at room temperature, and was ascribed, on the basis of a comparison with 5 MeV electron irradiation and EPR evidence, to a zinc vacancy. However, it is known that the dominant impurities in the CVD material are the transition metals (Fe, Ni, Cr) and a hydride species [1], and cathodoluminescent studies [1] suggest that these are segregated at grain boundary sites. The transition metals are well-known luminescence 'killers' [22] - a consequence of their ability to provide efficient shunt pathways for electron-hole recombination. Thus the impurity diffusion model described above is a likely explanation for the behaviour of CVD ZnSe on annealing.

The electronic structure of material exhibiting IRFCA which evolves from the above discussion is shown in schematic form in figure (8). The only donor species identified as being present is Z, and on the basis of a consideration of the residual impurity content of the feedstock used is tentatively ascribed to In_{Zn} ($E_D = 0.029$eV). The red emission of 1.97eV is due to a transition from this donor to the deep Cu_{Zn} acceptor ($E_A = 0.72$eV). The PLE maximum at 2.38eV occurs via the transition A to B whilst the narrow maximum of 2.62eV is probably due to a transition from the sodium acceptor to the donor level. The P(Na) emission series of low temperatures arise from transitions from the indium to the Na_{Zn}. Following Dean [3], the 0.38eV trap is attributed to a complex such as (Cu_{Zn}-$C\ell_{se}$). The origin of the 0.28eV trap is unclear; if it associated with the 0.1eV trap (Na_{Zn}), then it may involve a complex centre such as (Na_{Zn}-V_{se}).

The position of the Cu_{Zn} acceptor in figure (8) implies that the activation energy of quenching of the Cu-red emission at 1.97eV should be about 0.7eV. However, we determine a value (figure 9) nearer 0.1eV. In a study of many ZnSe:Cu samples, Jones and Woods [12] also report similar discrepancies. This suggests that a charge transfer process may be occurring between acceptor centres in the CVD ZnSe, possibly as a consequency of the presence of transition metal impurities.

The evidence provided by the results of the PL, TSC and TSL studies suggest that the free-carrier absorption is a consequence of the presence of shallow electronic states in the material. In the case where the dominating electronic states are deep (eg the 0.38 and 0.72eV traps), the magnitude of free-carrier absorption effects are very much reduced. From the point of view of material growth, this sets a requirement on the control of levels of impurities such as Al, Na, Li, Cl, In, Ga etc in order to achieve low values of photon absorption at 10.6μm.

6. Conclusions

A study has been carried out of optical absorption due to surface processes and free charge carriers in CVD ZnSe. Surface absorption is dominated by the presence of water and hydrocarbon impurities, but can be reduced by careful cleaning of the surface. Infra-red absorption due to free-carrier scattering processes has been found in ZnSe produced under zinc-rich conditions. The intensity of the absorption process has been found to be correlated with a photoluminescence at 1.97eV produced in the material under near band-gap irradiation. The electronic structure of the material is complex, and involves acceptors due to Cu_{Zn} and Na_{Zn} as well as a donor tentatively ascribed to In_{Zn}. Some of the PL and PLE phenomena can be explained on the basis of these impurities. The free-carrier absorption is reduced by several orders of magnitude following annealing under inert gas conditions. This may be a result of the diffusion of impurities such as transition metals and hydride species from grain boundary sites.

The authors are indebted to the support of the Chemical Analysis Group at AWRE, and to Drs P J Dean and M Skolnick at RSRE, Malvern for the low-temperature photoluminescence measurements.

7. References

[1] Russell, G.J., Waite, P., Woods, J. and Lewis, K.L. : Proc. Conf. on Microscopy of Semiconducting Materials, Oxford, April 1981. Inst Phys Conf Ser 60 (7) 371 (1981)

[2] Dutt, B.V., Kim, O.K. and Spitzer, W.G. : J Appl. Phys 48 2110 (1977).

[3] Dean, P.J. : Czech J Phys B30 272 (1980).

[4] Kulakov, M.P. and Grinev, V.I. : Inorg. Mat. 16 139 (1980) (from Izv. Akad. Nauk SSSR, Neorg. Mat. 16 223 (1980)).

[5] Lewis, K.L. and Hill, J.; Proc. 7th Inf. Conf. on CVD 629 (1979).

[6] Kulakov, M.P., Savtchenko, I.B. and Fadeev, A.V. : J Cryst. Growth 52 609 (1981).

[7] Lewis, K.L., Cook, D.J. and Roscoe, P.B. : J Cryst. Growth 56 614 (1982)

[8] Gibb, R. and Lewis, K.L. : J Phys E: Sci Inst. 11 304 (1978).

[9] Lee Smith, A. : 'Applied Infra-Red Spectroscopy' 54 "Chemical Analysis", Wiley.

[10] Kirovskaya, I.A. and Pimenova, L.N. : Inorg. Mat. 12 191 (1976) (from Izv. Akad. Nauk SSSR, Neorg Mat. 12 221 (1976)).

[11] Jensen, B. : J Phys Chem Solids 34 2235 (1973).

[12] Jones, G. and Woods, J. : J Lumin 9 389 (1974).

[13] Dean, P.J. : Private Communication.

[14] Merz, J.L., Kukimoto, H., Nassau, K. and Shiever, J.W. : Phys Rev. B6 545 (1972).

[15] Waite, P. : PhD Thesis, Durham University (to be published).

[16] Merz, J.L., Nassau, K. and Shiever, J.W. : Phys Rev B8 1444 (1973).

[17] Halstead, R.E. and Aven, M. : Phys Rev Lett 14 64 (1965).

[18] Stringfellow, G.B. and Bube, R.H. : Phys. Rev 171 903 (1968).

[19] Dean, P.J. and Merz, J.L. : Phys Rev. 178 1310 (1969).

[20] Taguchi, T. and Palmer, D.W. : Paper presented at 2nd BACG meeting on the Crystal Growth and Characterisation of II-VI Compounds. (1980)

[21] Dean, P.J. : Inst. Phys. Cont. Ser 46 100 (1979).

[22] Aven, M. and Prener, J.S. : 'Physics and Chemistry of II-VI Compounds'. North Holland (1967).

Table 1. Purity of Material Examined

Impurity	Type 1 ZnSe	Type 2 ZnSe
Cu	0.34	0.45
Fe	0.9	0.9
Mg	< 3	< 3
Ni	0.25	0.25
Cr	0.8	0.8
Co	< 0.6	< 0.6
Al	< 2.7	< 2.7
Mn	< 0.05	< 0.05
Cl	0.12	< 0.12
Br	< 0.05	< 0.05
I	< 0.03	< 0.03

Values are given in units of ppma.

In addition, traces of Ca were detected using semi-quantitative emission spectrographic techniques. Elements other than those listed above were not detected.

Table 2. Effect of Moisture on Absorption of ZnSe at 10.6μm

Sample State	Absorbance of 10.6μm
Sample diamond polished, rinsed in tichloroethane, acetone and finally water. Allowed to dry for 1 hour.	0.00356
Sample re-immersed in acetone, allowed to dry.	0.00149

(Sample thickness = 0.255cm)

Table 3. Absorption Coefficients of ZnSe Samples Near 10.6μm

(values are uncorrected for the effects of residual surface absorption)

Sample	Type	λ μm	β cm^{-1}
1	1	10.19	0.0032
		10.25	0.0031
		10.33	0.0025
		10.49	0.0026
		10.55	0.0026
		10.60	0.0025
		10.65	0.0029
		10.69	0.0026
		10.73	0.0034
2	2	10.30	0.011
		10.60	0.0080
		10.69	0.0073
3	2	10.49	0.026
		10.60	0.024
		10.76	0.031
4	2	10.19	0.025
		10.30	0.027
		10.49	0.029
		10.60	0.031
5	2	10.30	0.071
		10.49	0.060
		10.60	0.044
		10.76	0.054
6	2	10.19	0.107
		10.30	0.092
		10.49	0.106
		10.60	0.105

Table 4. Parameters Used for Estimation of Carrier Concentration

Symbol	Parameter	Value
$\hbar\omega$	Frequency	0.124 eV
β	Absorption Coefficient	0.11 cm^{-1}
E_g	Bandgap	2.67 eV (= 4.277×10^{-12} erg)
n	Refractive Index	2.4
e	Electronic Charge	4.8029×10^{-10} esu
e_o	Static Dielectric Constant	9.12
m_n	Effective Electron Mass	0.17 m
h	Planck Constant	6.624×10^{-27} erg s ($\hbar = h/2\pi$)
c	Velocity of Light	2.998×10^{10}cm S^{-1}
m	Electron rest mass	9.109×10^{-28}g
r	Spin-orbit splitting	∞

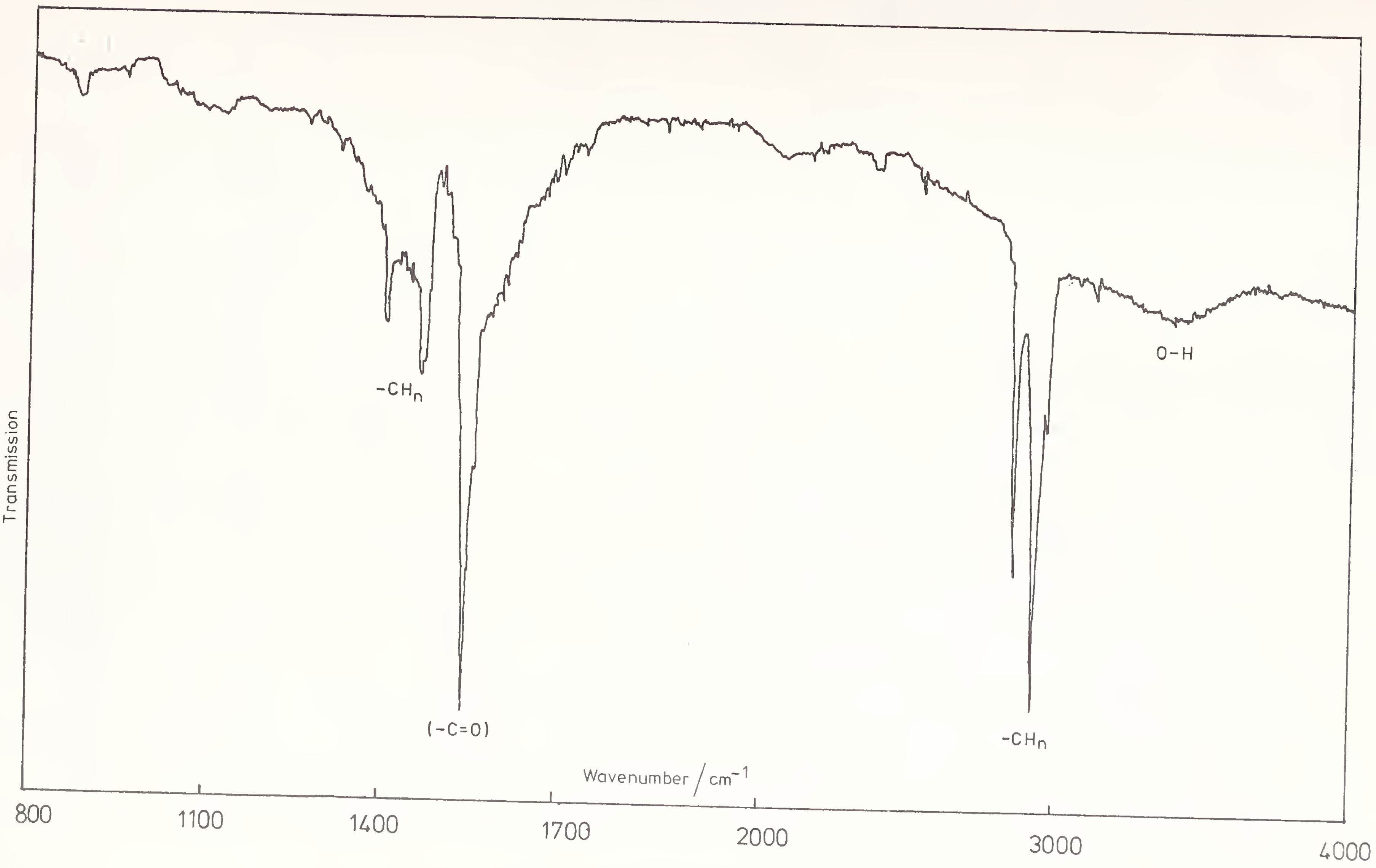

Fig 1. Attenuated Total Reflectivity Spectrum of Adsorbed Species on ZnSe.

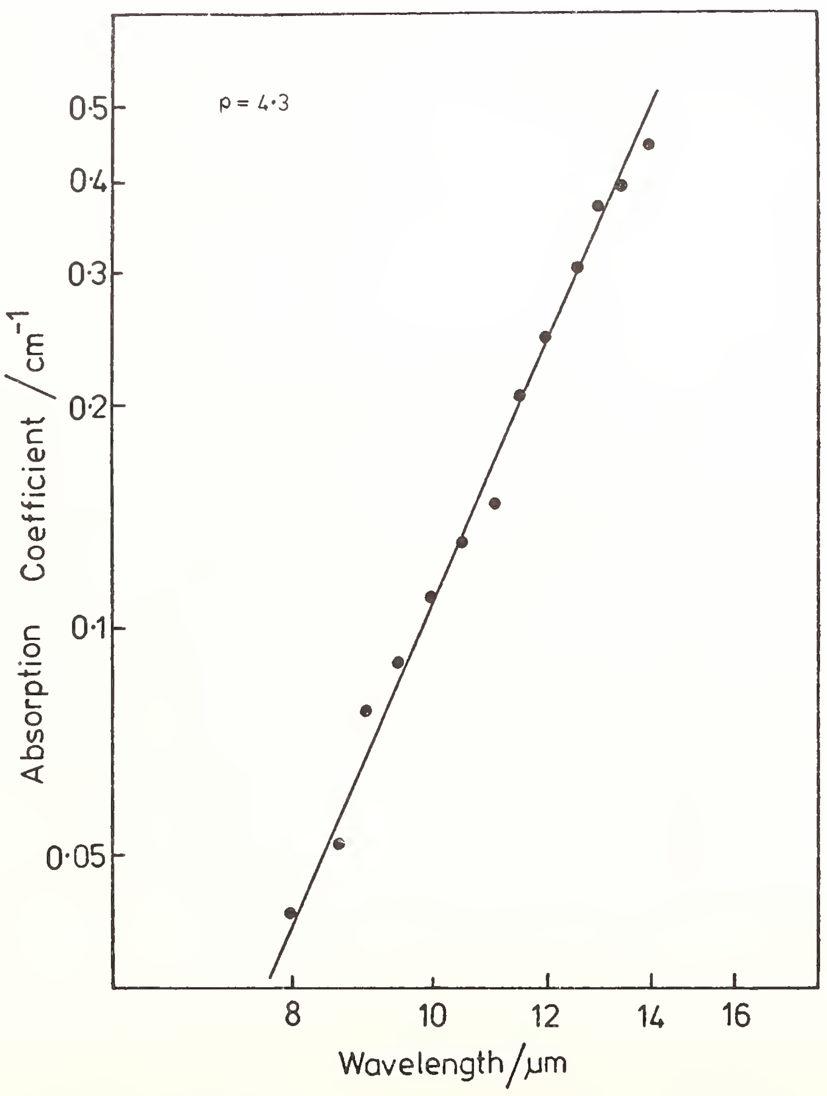

Fig 2. Free Carrier Infra-red Absorption in ZnSe Grown Under Zinc-rich Conditions.

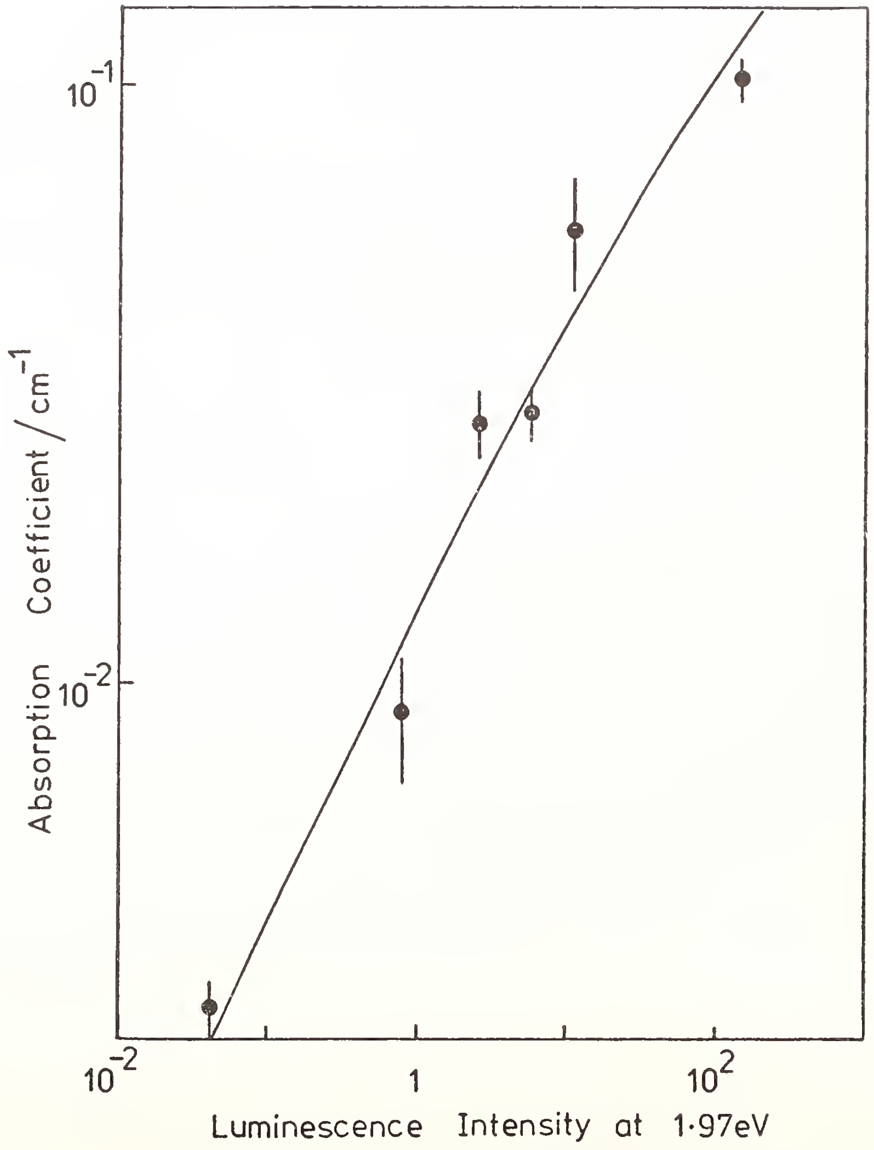

Fig 3. Relationship Between Absorption Coefficient at 10.6µm and Intensity of Luminescence at 1.97eV.

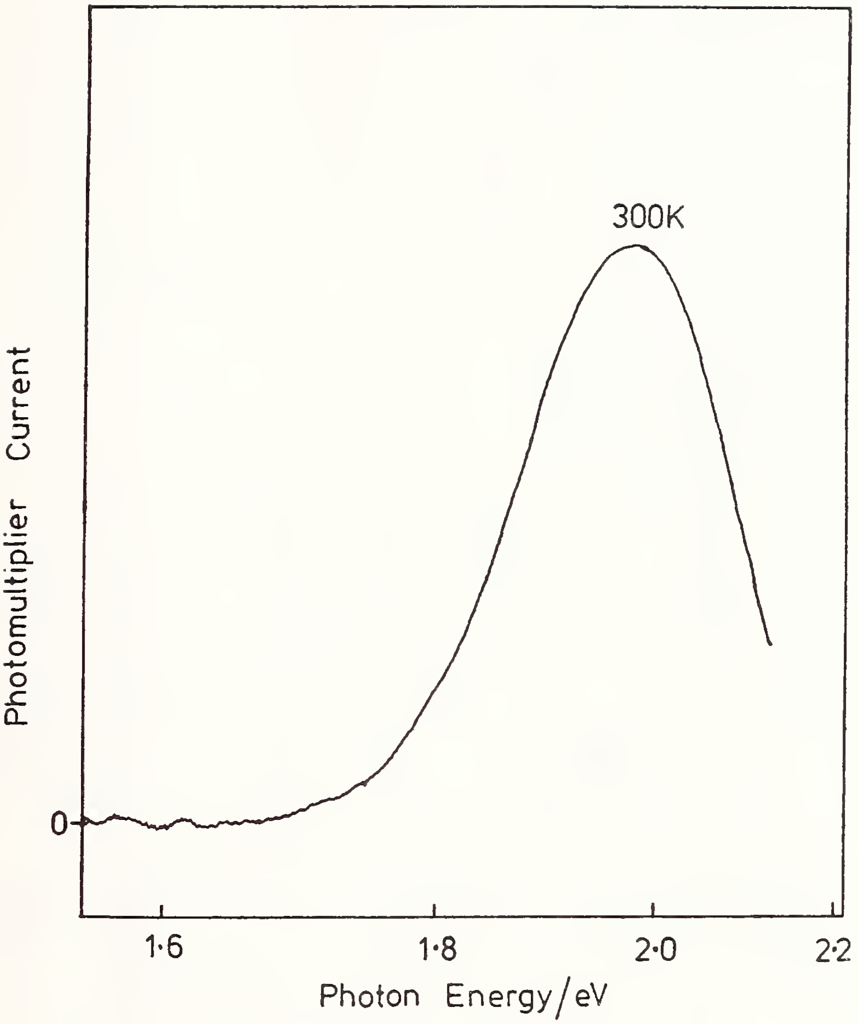

Fig 4. Spectral Distribution of Red Emission in Type 2 ZnSe.

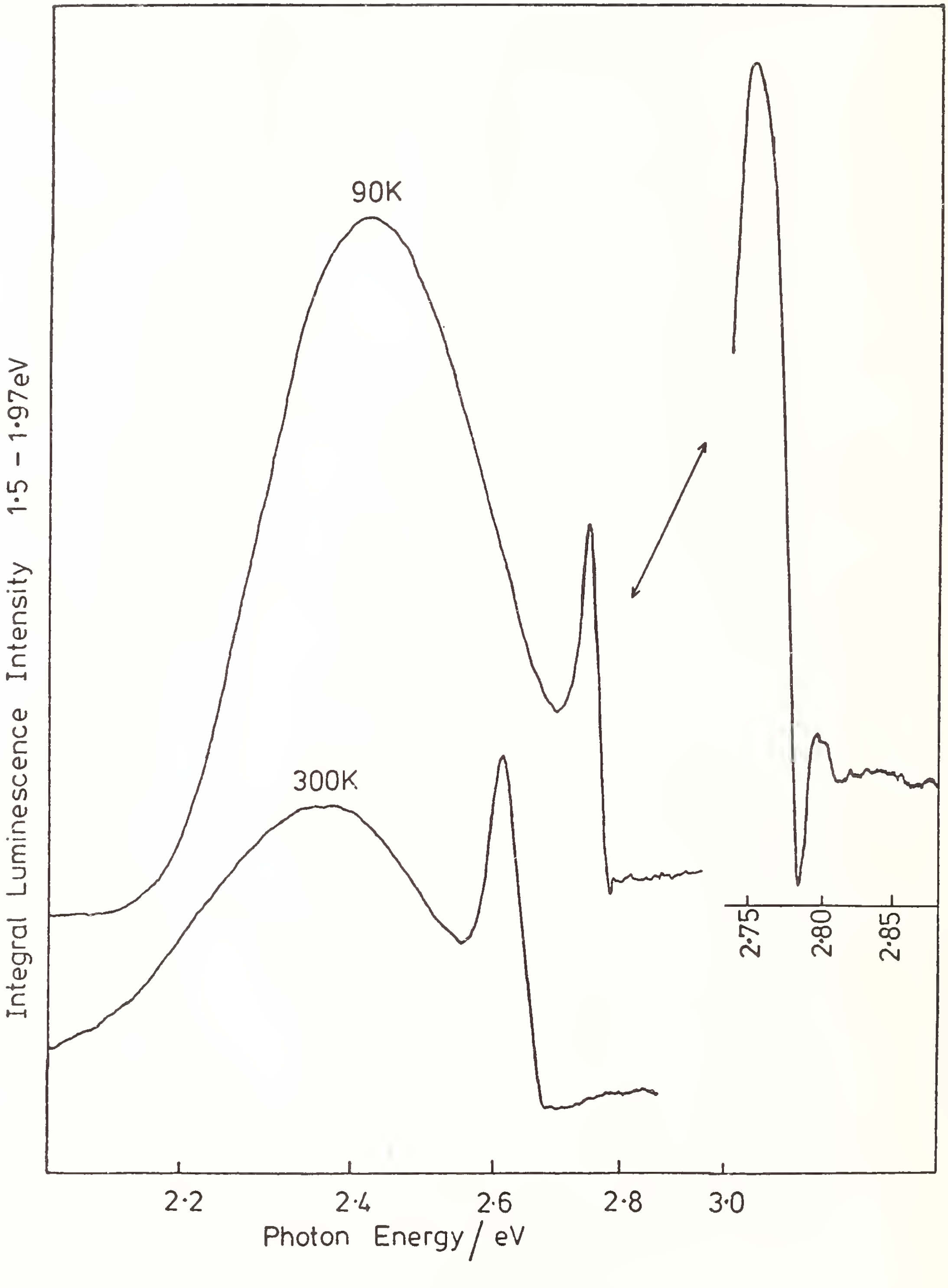

Fig 5. Photoluminescence Excitation Spectrum for Red Emission Process.

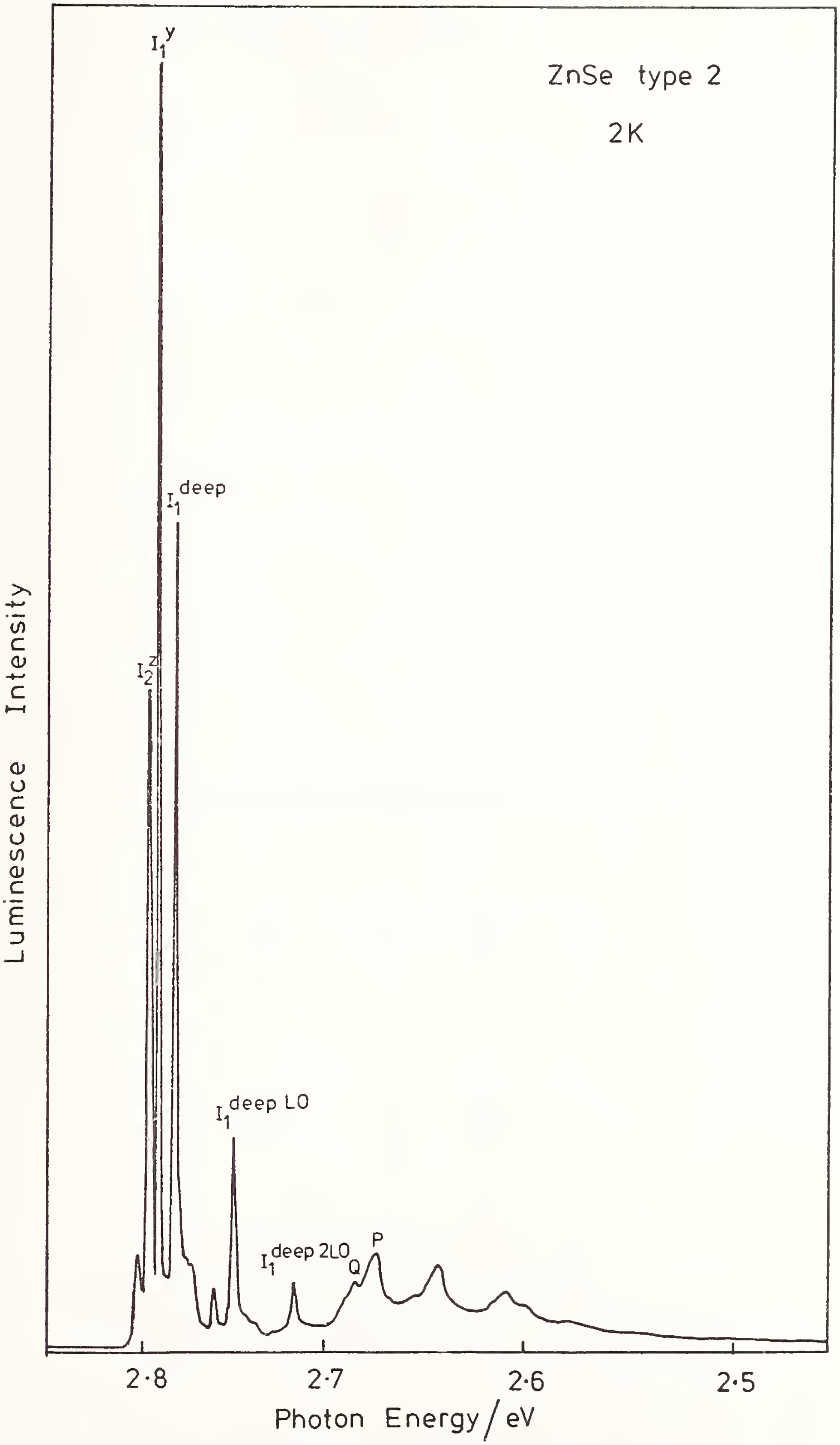

Fig 6. Photoluminescence Spectrum of Type 2 ZnSe Recorded at 2K Under UV Laser (3.44eV) Excitation. (Courtsey of Dr P J Dean, RSRE, Malvern).

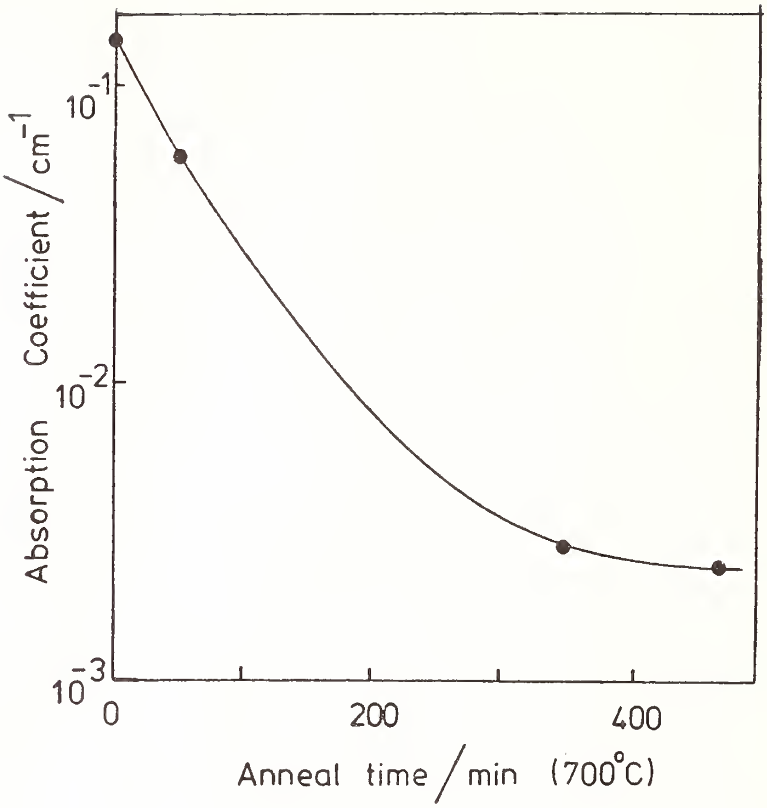

Fig 7. Variation of 10.6µm Absorption Coefficient of Type 2 ZnSe on Annealing in High Purity Argon Atmosphere.

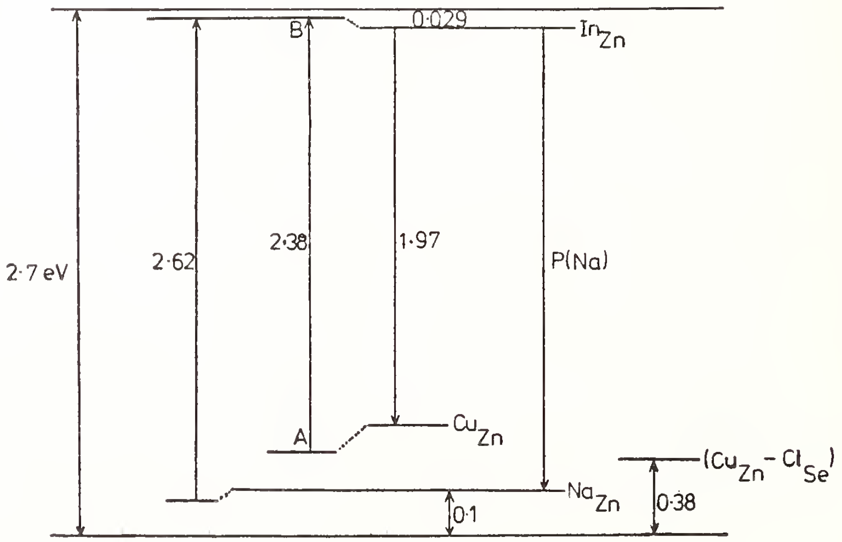

Fig 8. Proposed Electronic Structure of Type 2 ZnSe.
(the P(Na) transition is observed at liquid helium temperatures).

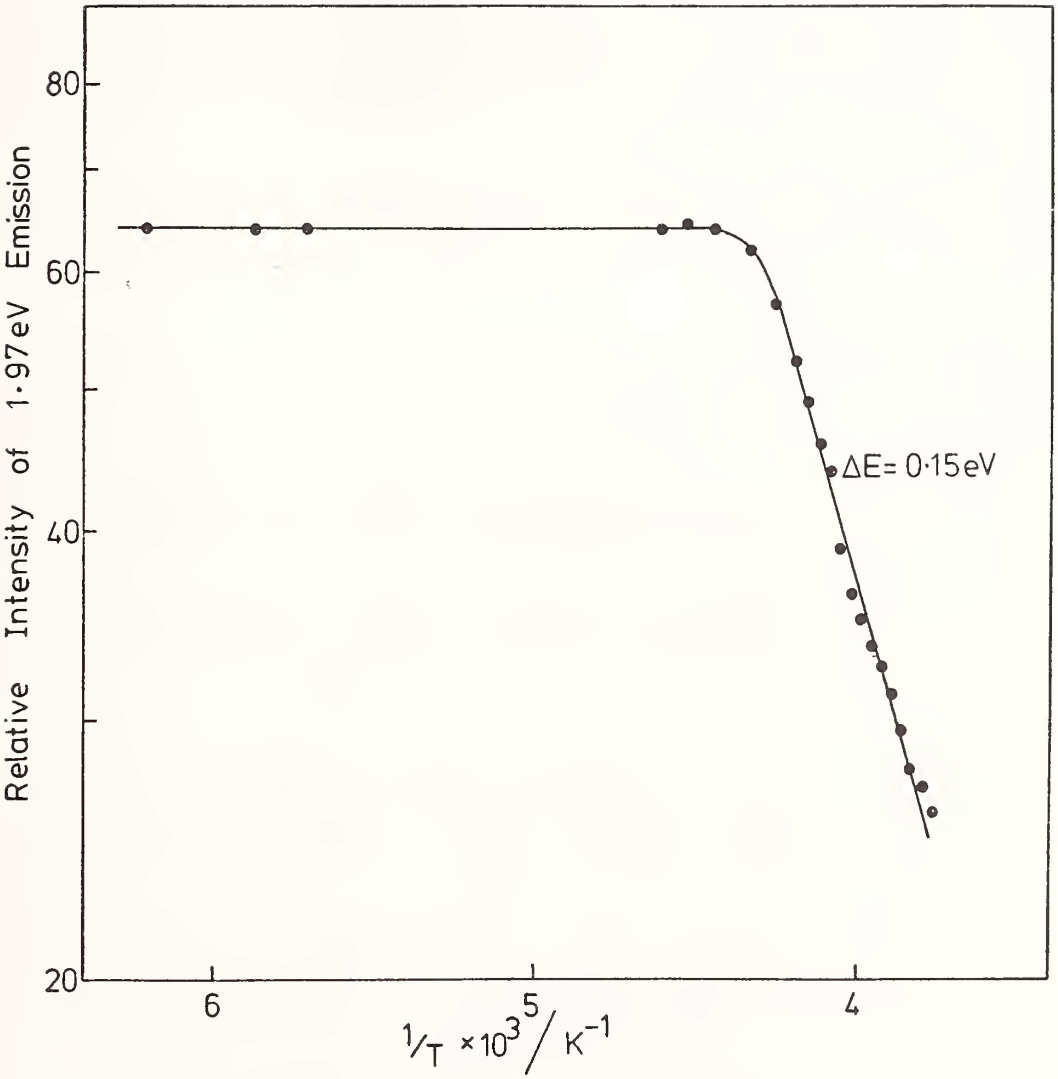

Fig 9. Thermal Quenching of Copper-red Emission at 1.97eV.

A Laser Damage Facility in the Ultra-Violet

S.S. Wiseall and D.C. Emmony

Department of Physics
Loughborough University of Technology
Loughborough, Leicestershire LE11 3TU
U.K.

A laser damage facility has been set up based on a one Joule KrF excimer laser. Damage threshold measurements at 193nm have been made on polished samples of LiF, MgF_2, and SrF_2 and cleaved samples of LiF, NaF, CaF_2, MgF_2, SrF_2 and BaF_2. Observations on the thresholds are discussed and some interesting aspects of the damage morphology described.

Damage threshold measurements have also been made at 249nm on a range of multilayer dielectric reflectors. The results indicate that Pyrex may be used as a substrate instead of fused silica without a reduction in the damage threshold and that the damage threshold of excimer mirrors exposed to a fluorine environment is substantially reduced over that of unused mirrors.

Key Words: excimer laser; fluoride crystals; laser damage; ultra-violet reflectors; thin films.

1. Introduction

One of the major limitations in the development of high energy excimer lasers is the relatively low damage threshold of the laser mirrors themselves. The purpose of this work was to provide the KrF laser development programme at the Rutherford Laboratories with a laser damage and diagnostic facility.

Preliminary damage threshold measurements at 193nm have been made on a range of fluoride crystals. The major excimer wavelength of interest is 249nm. Damage threshold measurements at this wavelength have been made on a number of multilayer dielectric reflectors.

2. Experimental Details

A schematic diagram of the experimental arrangement is shown in figure 1. The philosophy behind the experimental approach was to use a large beam area incident in the damage plane to simulate real tests on lasers with large beam diameters. This also enabled a large percentage of the area of the sample to be tested making identification of weak spots more probable.

The experimental arrangement is based on a Lambda Physik EMG 200 excimer laser that gives a maximum output of about one Joule at 249nm. The output energy at this wavelength was measured with a Laser Instrumentation Calorimeter and was stable, shot to shot, to about 5%. The temporal pulse profile illustrated in figure 1 was measured with a vacuum photodiode (EMI Gen-Com, PD1912 S5) and a Tektronix 466 oscilloscope. The temporal profile remained constant from shot to shot and had a half width of about 30ns. The energy density in the damage plane was varied by moving the sample away from the focus. Thus, a variable spot size was used in these damage threshold measurements. In the case of threshold damage caused by defects a spot size dependence has been observed at 10.6μm, 1.06μm and 248nm on metals, transparent dielectrics and thin films [1], [2], [3]. The spot size dependence occurs for the case where the beam dimensions are comparable to the spacing between the defects which are initiating the damage. In the tests reported here no spot size dependence is expected because effective spot diameters of 2-5mm were used. The spot size dependence of the damage threshold observed at 10.6μm and 1.06μm on copper mirrors was only observed for spot sizes less than 150μm [2]. Two methods were used to measure the beam size as a function of distance from the lens. The first involved burn patterns on the grey back side of instant polaroid film (Type 667, Coaterless Land Pack film). The burn area plotted as a function of the lens-sample distance is shown in figure 2. The threshold values were determined by measuring the pulse energy and the distance beyond the lens where damage occurred. The two main sources of error in the fluence value calculated using this approach were the accuracy of the measurement of the lens-sample plane distance and the measurement of the burn area, especially near the lens focus. The fluence values calculated in this way represent some average fluence and not necessarily the peak fluence. The second method investigated for measuring the beam size as a function of distance beyond the lens was to use Dylux 608 film [4]. This material turns blue on exposure to UV light near 250nm. The optical density of the blue image was measured by scanning with a helium neon laser. The reproducibility of the beam profile was checked on a shot to shot basis using the Dylux film and to within experimental error no differences were observed. The Dylux film was found to suffer from a number of disadvantages. The first is that the Dylux is not sensitive at 193nm. The peak optical density of the exposed film was found to be somewhat time-dependent, even though the film was stored in the dark. A decrease in optical density between 5-10% was observed in the first week. The main problem with the Dylux film was its limited dynamic range. A graph of the peak optical density of the Dylux exposure plotted as a function of the lens-sample distance is shown in figure 3. The horizontal section indicates saturation is occurring as the lens focus is approached. For these reasons the threshold values quoted in this paper were calculated using the burn area method.

Laser induced damage was defined as the observation of any physical change in the sample when observed through a X10 microscope. The formation of damage was observed as the shot was fired, the sample being illuminated with white light. The damage specimen was also observed when removed from the damage plane at a higher magnification. Threshold damage was often observed as the formation of several micropits ∿10μm in diameter; it was found that these were quite difficult to identify once the sample had been moved out of the damage plane.

Two damage thresholds were defined. The first definition was the minimum fluence to guarantee damage in a single shot. The second definition was the maximum fluence not to cause damage after 600 laser shots. This test was performed at a repetition rate of 2Hz. These two definitions seemed to be useful from the practical viewpoint.

3. Damage Thresholds at 193nm

Table 1 summarises the single shot and multishot thresholds of the fluoride crystals. Three polished samples were tested, LiF, MgF_2 and SrF_2, the rest were cleaved specimens. The LiF and CaF_2 were supplied in two purity grades, listed as IR grade and UV grade. The tests were performed at 0^o incidence. A maximum of three crystals of each type were tested, listed as No. 1, No. 2 and No. 3.

Threshold damage was observed on the entrance surface. All of the cleaved specimens had single shot damage thresholds in the range 1.5-2.5Jcm^{-2} except BaF_2. Polished samples of LiF and SrF_2 had single shot damage thresholds somewhat lower than their equivalent cleaved counterparts. This suggests that the polishing compound remaining in the surface is absorbing at 193nm and initiating damage. In support of this the polished sample of LiF fluoresced green and the cleaved samples fluoresced blue. The green fluorescence was particularly strong from surface scratches.

The cleaved surfaces of all of the crystals were 1-2 days old before damage measurements were made. The only exceptions are those marked with an asterisk in table 1. The single shot damage thresholds of the two NaF crystals and one LiF crystal were measured within several minutes of them being cleaved. The high damage threshold of these measurements can be accounted for by the high water solubility of these two crystals compared to the others.

The single shot damage threshold is about 2-4 times greater than the multishot level. Damage was generally observed within the first 10-30 shots of a multishot test. This probably means that damage is initiated in one shot at a lower level than we can detect with our present method. After 10-30 shots the damage has grown sufficiently to be observed.

Figure 4 shows a graph of these damage data plotted against refractive index. Apart from NaF, there appears to be a trend of higher index materials having lower damage thresholds. This trend has been observed previously at other wavelengths [5].

4. Damage Morphology at 193nm

4.1 Fluoride Crystals

Some interesting aspects of the damage morphology have been observed on the fluoride crystals. These are illustrated in figures 5-9.

Figure 5 shows the triangular surface pattern on a cleaved sample of SrF_2. A similar surface cleaved pattern, but rectangular, is shown in figure 6. Damage with the triangular form was only observed in the alkali-earth fluorides, the rectangular cleaving only being observed in NaF and LiF. The origin of the cleaving is probably thermal shock the surface experiences from the surface generated plasma. This type of phenomena has been observed in previous damage work at 1.06μm and 10.6μm on several crystalline materials [5], [6]. The ring structure shown in figure 7 was observed on LiF.

Rings were observed in experiments involving more than one laser shot. The number of concentric rings increases with shot number. Ring formation due to a plasma has been observed previously by Boling et. al at 1.06μm [5]. Bulk damage in LiF is shown in figure 8 and illustrated pictorially in figure 9. This type of damage was observed at only one site in the polished sample of LiF and the cleaved sample of SrF_2. The tail of the damage is not necessarily perpendicular to the entrance surface, but in all cases tapered away from it. In a few cases the tail was observed to be curved. The cause of this type of bulk damage is uncertain.

4.2. SiO Overcoated Aluminium Mirrors

Whilst setting up the damage facility the need arose for some relatively inexpensive aluminium beam steering mirrors. When the first of these was placed in the beam damage was immediately observed. The aluminium did not have a MgF_2 overcoat as expected but a 1/4μm SiO overcoat. The silicon monoxide absorbs strongly at 193nm. The interesting aspect of the damage was the diffraction colours observed from the damage region when illuminated with white light. The damage region was also illuminated with a helium neon laser and characteristic diffraction rings were observed. Analysis of the ring diameters gave a scattering centre dimension of 1.4μm.

An SEM replica picture of the surface is shown in figure 10. The surface consists of a distribution of uniform ripples or globules of diameter 1.5μm. The globule formation was observed to occur just above threshold at $0.2Jcm^{-2}$. The globule size was not dependent upon the angle of incidence of the laser light in the range 0-45°. The globule size was also independent of the shot number in the range 1-20 shots. The picture contrast though did improve somewhat with shot number.

In various parts of the damage area parallel and circular lines appear. These are illustrated more clearly in figures 11 and 12. The parallel ridges follow the scratch, the scratch width was typically in the range 0.1-0.3μm. The ridge spacing for the parallel lines and circular lines was the same as that of the background pattern.

Simple calculations show that at the incident energy density of $0.2Jcm^{-2}$ there is sufficient energy to melt the SiO. Ripple patterns on metals and semiconductors have been observed previously [7], [8]. Various models have been proposed and are often described by interference between the incident (and reflected) wave and a surface scattered evanescent wave [7]. These models predict a ripple periodicity dependent upon the angle of incidence with a periodicity equal to the laser wavelength at normal incidence. The parallel and circular patterns observed here also suggest an interference or wave phenomena. The issue is confused though because the diameter of the surface undulations does not appear to be angle dependent and the ripple periodicity is a factor of seven times the free space wavelength of the laser light.

5. Damage Thresholds at 249nm

Table 2 summarises the single shot damage thresholds of some multilayer dielectric reflectors listed as A, B and C. Their nominal reflectivity before testing was 99%. They all had fused silica substrates unless specified. The description 'used' means they had been operated in a fluorine environment as an excimer mirror before the tests were performed. The multishot threshold of these mirrors were also tested and found to be a consistent factor of 3-4 times less than the single shot threshold. The damage threshold of mirror B was previously determined by the Lawrence Livermore Laboratory. Their figure of $6Jcm^{-2}$ compares favourably with ours of $7.9Jcm^{-2}$. Three main points of interest arise from table 2.

(i) The first is the large difference between the threshold of mirror B at $7.9Jcm^{-2}$ and the unused samples of type C at about $2Jcm^{-2}$. Mirror B was designed for operation in a non-fluorine environment, whereas mirrors in C were all fluoride coatings made to improve their fluorine resistance.

(ii) The next point is the factor of six difference between the threshold of the unused reflectors in C and the Dynasil 4000 substrate used to produce them. This substrate had a single shot threshold of $12Jcm^{-2}$. This large difference illustrates the damage threshold limitation arising from thin film overcoatings.

(iii) The final point is the large reduction in the damage threshold of used mirrors compared to unused mirrors of the same kind. The used mirrors had a large number of milky blotches visible when illuminated in white light. This is presumably caused by fluorine attack on the multilayers and/or substrate. The used high reflector in table 2 with a Pyrex substrate suggests that as far as damage thresholds are concerned, there is no great advantage in using a fused silica substrate. Newnam et. al [9] have noticed a 10% improvement in multilayer dielectric reflector damage thresholds at 249nm when produced on a fused silica substrate compared to a BK-7 glass substrate.

6. Conclusions

In conclusion, we have set up a laser damage and diagnostic facility in the ultra-violet and have measured damage thresholds at 193nm and 249nm.

The damage thresholds of the fluoride crystals at 193nm were in the range 1-3Jcm^{-2}. A trend of lower damage thresholds for high index materials has been observed.

The damage threshold of the multilayer dielectric reflectors at 249nm suggests that Pyrex may be used instead of fused silica as a substrate material. The damage threshold of an excimer mirror exposed to a fluorine environment was found to be much less than that of an unexposed mirror.

The authors would like to thank the Science and Engineering Research Council for a research grant to carry out the work. We would also like to thank B.D.H. Chemicals Limited and Technical Optics Limited for some of the test samples and Dr. F. O'Neill of the Rutherford and Appleton Laboratory for his help and encouragement.

7. References

[1] C.S. Lee, N. Koumvakalis, M. Bass, Appl. Phys. Lett. 41(7), 1 October 1982.

[2] L.G. DeShazer, B.E. Newnam, K.M. Leung, Appl. Phys. Lett. 23, 11, 1 Dec. 1973.

[3] Foltyn, S.R.; Newnam, B.E.; Jolin, L.J. Laser damage results and analyses for UV reflectors under multiple-shot irradiation. Nat. Bur. Stand. (U.S.) Spec. Publ. 1981 Nov. Awaiting publication.

[4] M.W. Taylor, J. Goldhar, J.R. Murray, Appl. Opt. 21, 1, 1 Jan. 1982.

[5] Boling, N.L.; Dube, G.; Crisp, M.D. Laser surface damage studies on several glasses. Nat. Bur. Stand. (U.S.) Spec. Publ. 387, 1973.

[6] Reichelt, W.H.; Stark, E.E. Radiation induced damage to NaCl by 10.6μm fractional joule, nanosecond pulses. Nat. Bur. Stand. (U.S.) Spec. Publ. 387, 1973.

[7] D.C. Emmony, R.P. Howson, L.J. Willis, Appl. Phys. Lett. 23, 11, 598, 1 Dec. 1973.

[8] F. Keilmann, Y.H. Bai: J. Appl. Phys. A, 29, 9-18 (1982).

[9] Newnam, B.E.; Foltyn, S.R.; Jolin, L.J. Multiple-shot ultra-violet laser damage resistance of nonquarter wave reflector designs for 248nm. Nat. Bur. Stand. (U.S.) Spec. Publ. 1981, awaiting publication.

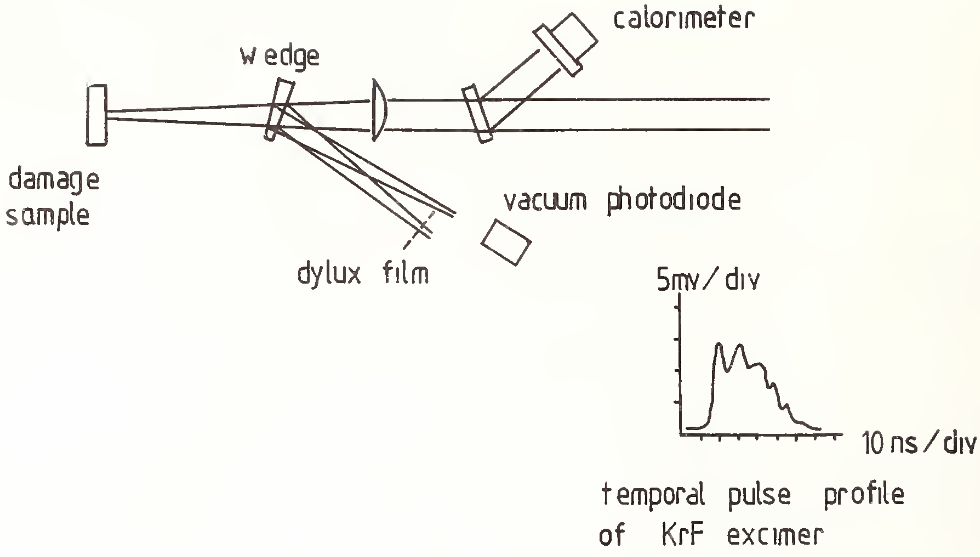

Figure 1. Experimental Arrangement.

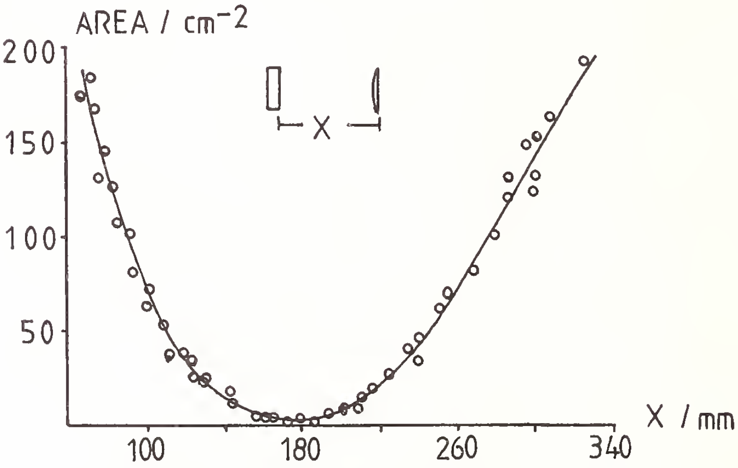

Figure 2. Burn area of polaroid film plotted against distance beyond the lens.

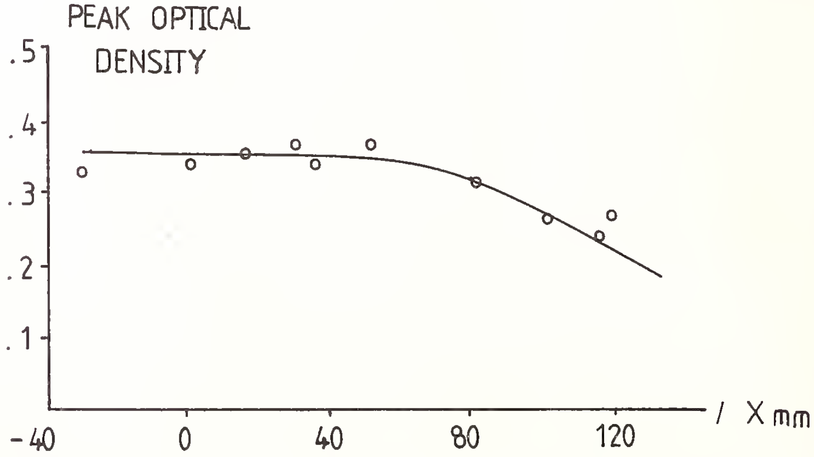

Figure 3. Peak optical density of Dylux film plotted against distance beyond the lens.

Table 1. Damage thresholds of fluoride crystals at 193nm.

crystal type		single shot threshold ±30% / Jcm^{-2}			multi-shot threshold ±30% / Jcm^{-2}	
	no.1	no.2	no.3	no.1	no.2	no.3
LiF I.R grade	3.9*	2.2	2.6			
U.V grade	2.4	3.3				
polished	1.8			1.0		
NaF cleaved	1.3	2.9*	3.0*			
CaF_2 I.R grade	2.1	1.9				0.5
U.V grade	2.5	2.6			0.65	
MgF_2 polished	2.6			2.8		
SrF_2 cleaved	1.6	2.2				
polished	1.3			0.5		
BaF_2 cleaved	1.2		1.0		0.6	

Table 2. Damage thresholds of multilayer dielectric reflectors at 249nm.

TYPE	DESCRIPTION	SINGLE SHOT THRESHOLD / Jcm^{-2}
A	USED	0.6
B	UNUSED	7.9
C	UNUSED	2.6
	UNUSED	2.0
	USED	0.3
	USED	0.3
	USED duran substrate	0.75
	fused silica substrate dynasil 4000	12.3

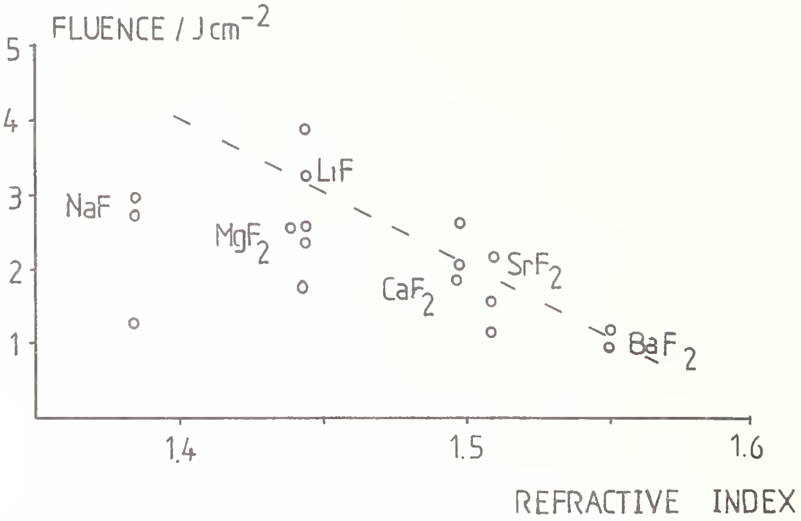

Figure 4. Single shot damage level plotted against refractive index.

Figure 5. Surface damage on SrF$_2$, 1 shot, fluence 4.2Jcm^{-2}.

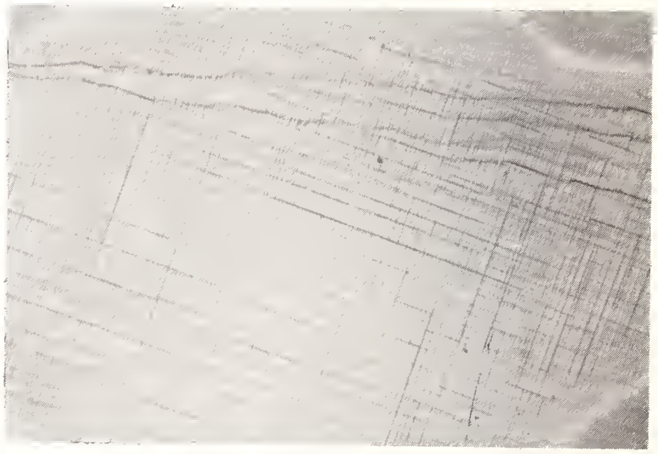

Figure 6. Surface damage on LiF, 100 shots, fluence 1.7Jcm^{-2}.

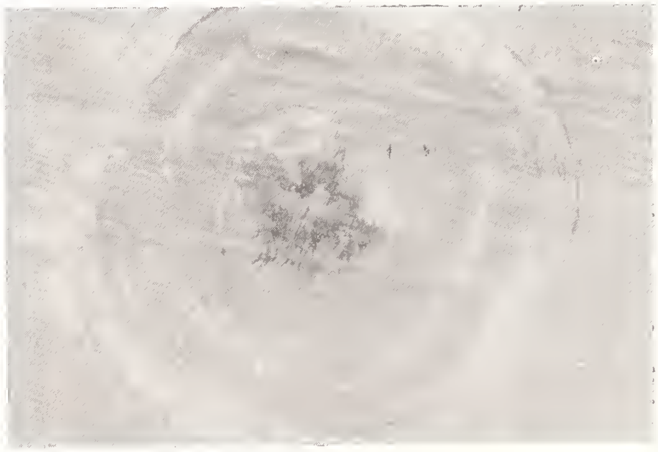

Figure 7. Surface damage on LiF, 25 shots, fluence 1.6Jcm^{-2}.

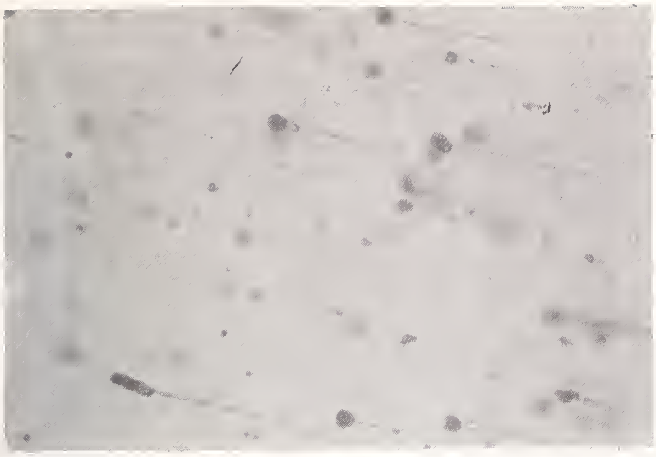

Figure 8. Bulk damage in LiF 3 shots, fluence 1.9Jcm^{-2}.

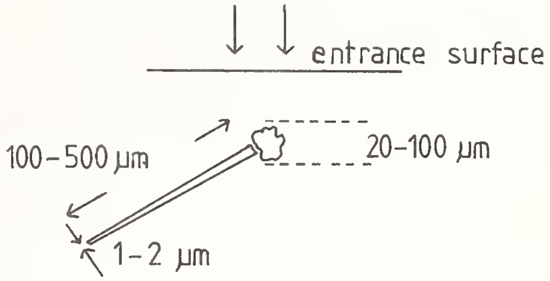

Figure 9. Geometry of bulk damage.

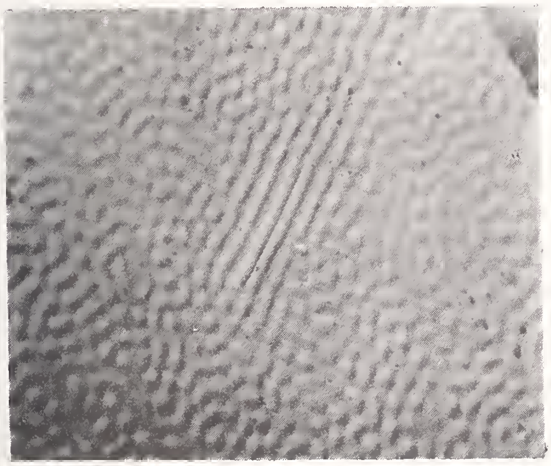

Figure 10. SiO overcoated Al mirror, 1 shot, 25^{0} incidence, fluence .18Jcm^{-2}, Mg X2000.

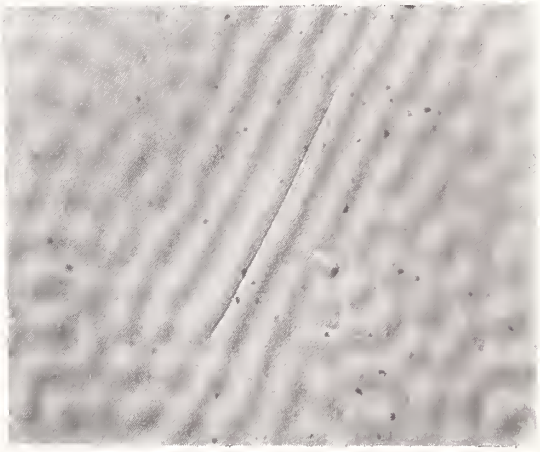

Figure 11. SiO overcoated Al mirror, 1 shot, 25^{0} incidence, fluence .18Jcm^{-2}, Mg X4000.

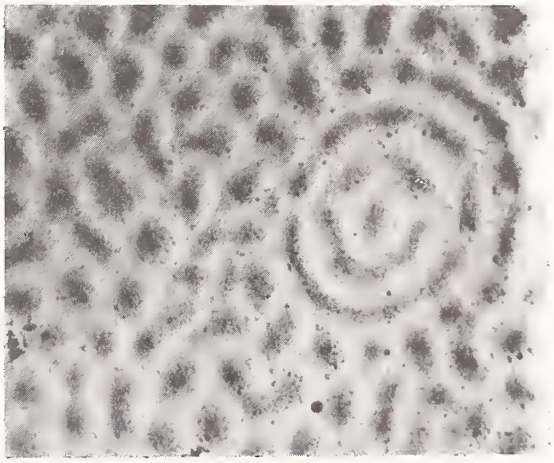

Figure 12. SiO overcoated Al mirror, 3 shots, 45^{0} incidence, fluence .18Jcm^{-2}, Mg X4000.

When asked about the coating materials used in the reflectors that were tested, the speaker replied that reflectors with "thresholds of about 2 J/cm^2" were made of unidentified fluorides. Materials in the remaining reflectors were unknown. The speaker commented that attempts were being made to use a model incorporating a surface acoustic disturbance to explain the circular fringe patterns observed on damage sites. A strong criticism from the audience was made of the placement of damage samples downstream of the beam waist in the damage experiment.

Use of Hole Gratings in Laser Damage Testing**

T. A. Wiggins,* T. T. Saito, and J. A. Hosken

United States Air Force Academy
Colorado 80840

Placing a metal plate with an array of round holes of radius a and separation d in front of a lens which focuses laser radiation for small-spot damage testing produces a set of intense spots of different intensities. The number of spots and their relative intensities depend upon the ratio d/a and the symmetry of the array. The $1/e^2$ size of each spot is negligibly larger than that due to the lens alone if a large number of holes is illuminated. The advantage of using a hole grating is that, if the intensity loss which depends on d/a is acceptable, damage data can be acquired more rapidly since identical spots having a wide range of intensities are produced from a single shot. Further, the role of defects or surface quality can be assessed since several spots receive equal intensities. Beam quality and sharpness of focus can also be more easily observed. Examples of damage to copper and nickel surfaces will be presented.

Key words: defects; hole grating; laser damage; small-spot damage

1. Introduction

In small-spot laser damage testing, it would be convenient to present a range of intensities to a sample in a single shot so that the threshold can be determined more easily than if a series of shots of different intensities are used. A method for doing this has been suggested [1]. However it has the disadvantage of providing an intensity variation in only one direction. A two-dimensional method is presented here.

If an array of round, equally-spaced apertures, a hole grating, is placed in front of the focussing element used in damage testing, the element will form a Fourier transform of the array, which is itself an array of regions of high intensity. This grating obviously produces a decrease in the intensity available for testing, due both to the transmission of the array, and because the transmitted energy is divided among several intense regions. There are, however, advantages in the use of a hole grating if the intensity loss does not preclude its use. They are: 1) several different intensities are available from a single shot; 2) except for the central one, more than one spot receives a given intensity; 3) the spacing of the spots can be adjusted by selection of the aperture spacing and focal length of the focussing element; 4) the locations of the spots are known so that they can be easily located to assess the extent of the damage produced; and 5) the effect of two or more adjacent simulataneous intense spots can be investigated.

2. Intensity Calculation

Designating the hole radii as a, their spacing d, and the number of holes in a single straight line that are uniformly illuminated as N, the intensity of a spot for a linear array can be written

$$I = I_0 \left[\frac{J_1(2xa)}{xa} \cdot \frac{\sin(Nxd)}{N \sin(xd)} \right]^2$$

where J_1 is a first order Bessel function and $x = \pi \sin\theta/\lambda$. An equation of similar form applies to a two-dimensional array. The half-intensity angle of each spot will be approximately 1/N of the spacing between spots.

**Supported in part by AFOSR through the SCEEE Summer Fellow Program.

*Permanent address, Department of Physics, The Pennsylvania State University, 104 Davey Laboratory, University Park, PA 16802

3. Experimental Results

Two hole gratings have been used to demonstrate their feasibility. They were selected area from screens produced by Buckbee-Mears, St. Paul, MN by photo-etching of stainless steel sheets. Enlargements of the hole gratings are shown in figure 1. The dimension of the gratings were $a = 1.1 \times 10^{-2}$ and $d = 5.6 \times 10^{-2}$ cm for the 60° array and $a = 1.1 \times 10^{-2}$ and $d = 4.0 \times 10^{-2}$ cm for the 90° array. Zero intensity occurs at an angle $\theta \approx 0.61\ \lambda/a$, the angular radius of the Airy disc. The diffraction patterns produced by these gratings are shown in figure 2 made using a beam-expanded He-Ne laser. The relative intensity of the central spot compared with that produced without the hole grating was measured using a pin-hole apertured photodiode and the He-Ne source. The results were 1:65 for the 60° and 1:31 for the 90° arrays. The values can be compared to the results 1:65 and 1:18 estimated from the calculated transmissions, $(2\pi/\sqrt{3})(a/d)^2$ and $(a/d)^2$, respectively and the ratios of the intensities of the central spots compared with the summations of the intensities of all the spots within the Airy discs. The agreement for the 60° array is very good. The discrepancy for the 90° array is probably due to variations in the hole radii resulting in a blurring of the Airy disc.

Relative intensities have been predicted for these cases and are shown in figure 3. They have been calculated from the values of $J_1(2xa)/xa$ for values of $x = m\lambda/d$, where m is an integer. It is noted that the largest order within the Airy disc is given by $m < 0.61\ d/a$. This is 3 for the 60° and 2 for the 90° array.

Damage testing on diamond turned metals was performed with a Nd:glass laser system. Figure 4 shows the result using the 60° array on nickel and the 90° on copper. The exact replication of damage for spots predicted to have the same intensities is remarkable. It is noted, however, that near threshold, differences can appear indicating the utility of this method for a study of defect-initiated damage.

Figure 5 which shows damage on a copper surface illustrates another use of the hole grating, that is in the observation of the alignment of a laser cavity. In a high gain medium such as Nd:glass, some misalignment will not prevent lasing. However, such a misaligned cavity will produce a highly divergent beam as evidenced by the damage shown in this figure. This information could of course be obtained without the use of a hole grating. However in this case, a series of shots of different intensities might be required to distinguish between the effects of the system and those due to scratches, dirt and defects on a surface.

It is noted that if the holes have different radii, in particular following a Poisson distribution, the Airy disc can be removed and a wider, smooth range of intensities obtained.

4. References

[1] Wiggins, T. A.; Walker, T. W.; Guenther, A. H. A novel technique for investigating impurity initiated short pulse laser damage in thin films. Bennett, H. E.; Glass, A. J.; Guenther, A. H.; Newman, B. E., ed. Laser Induced Damage in Optical Materials: 1980. Nat. Bur. Stand. Spec. Publ. 620; 1981 October. 277-281

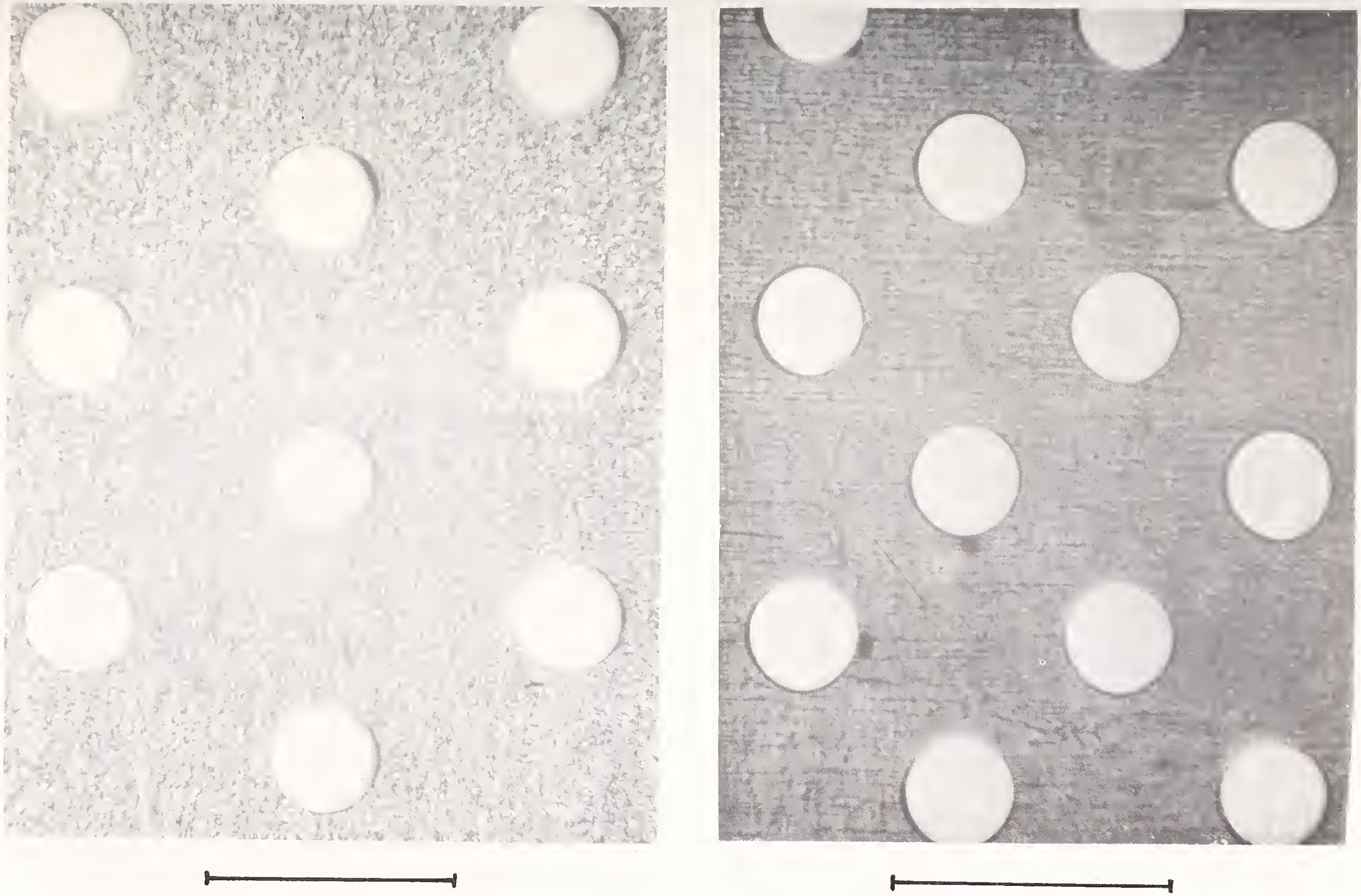

Figure 1. Reproductions of the 60° and 90° gratings used. The length of the bars represent 0.5 mm.

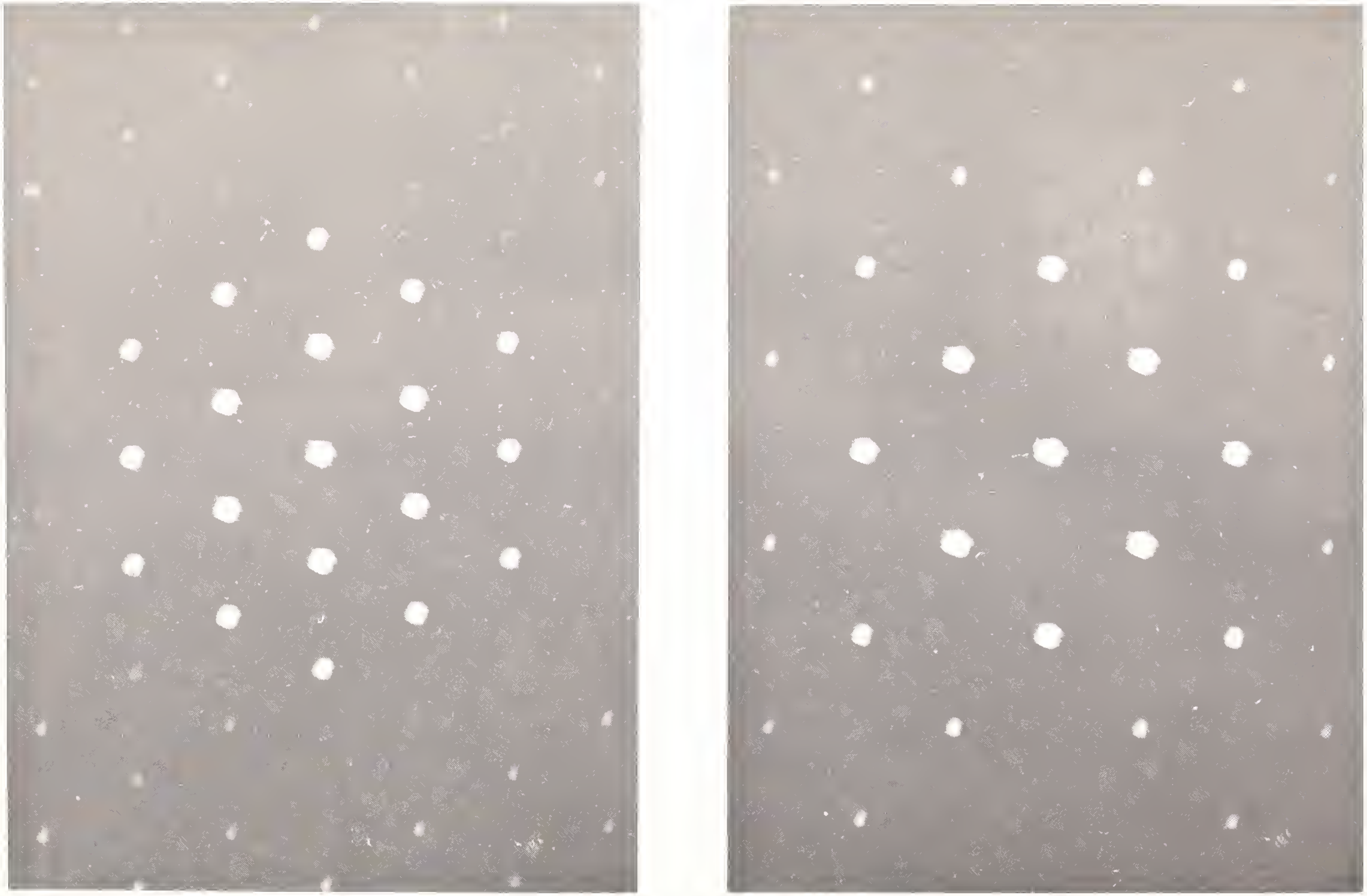

Figure 2. Diffraction patterns produced by the gratings using a He-Ne source.

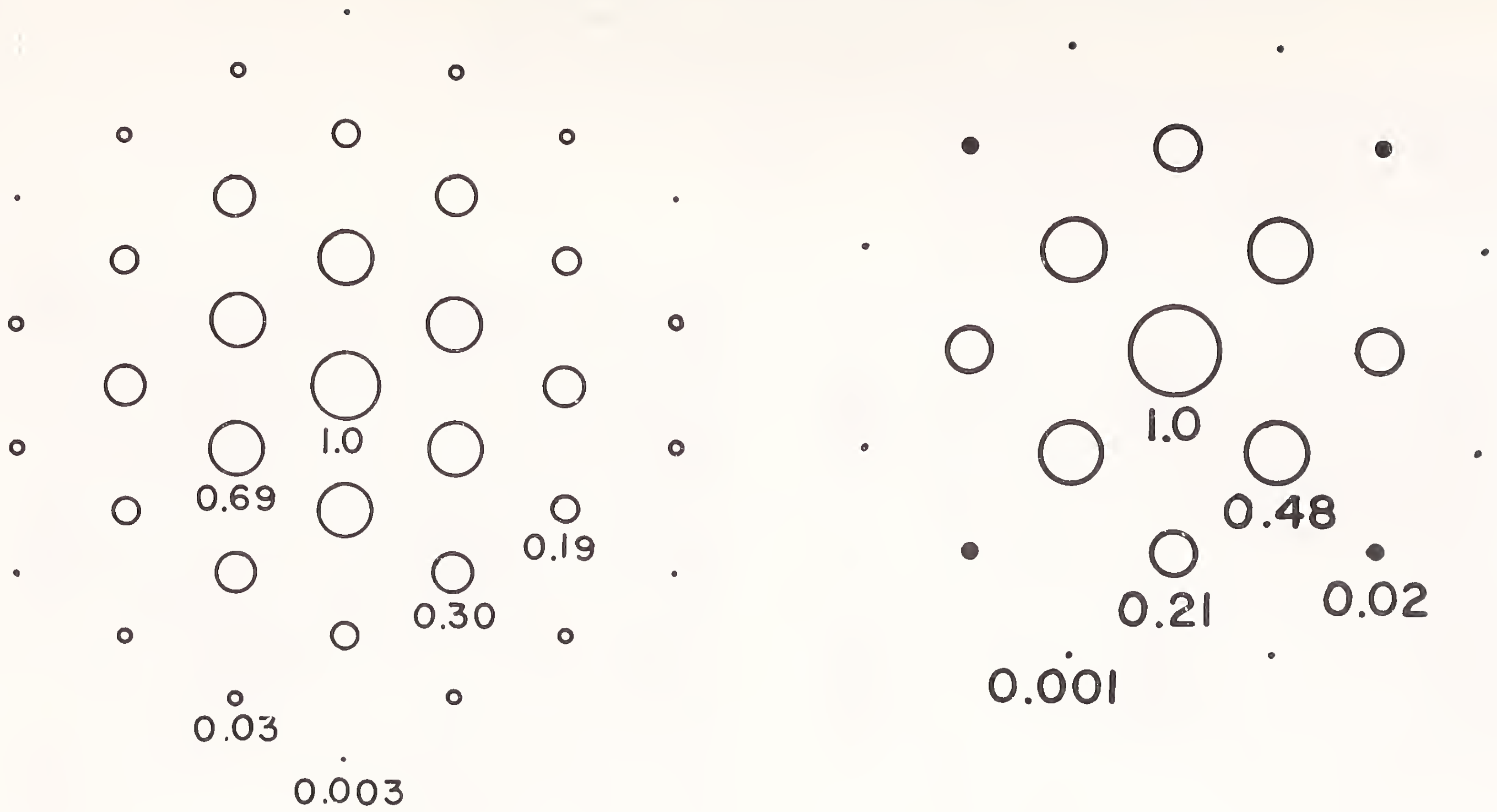

Figure 3. Intensities in the diffraction patterns. The areas of the circles are proportional to the calculated intensities indicated.

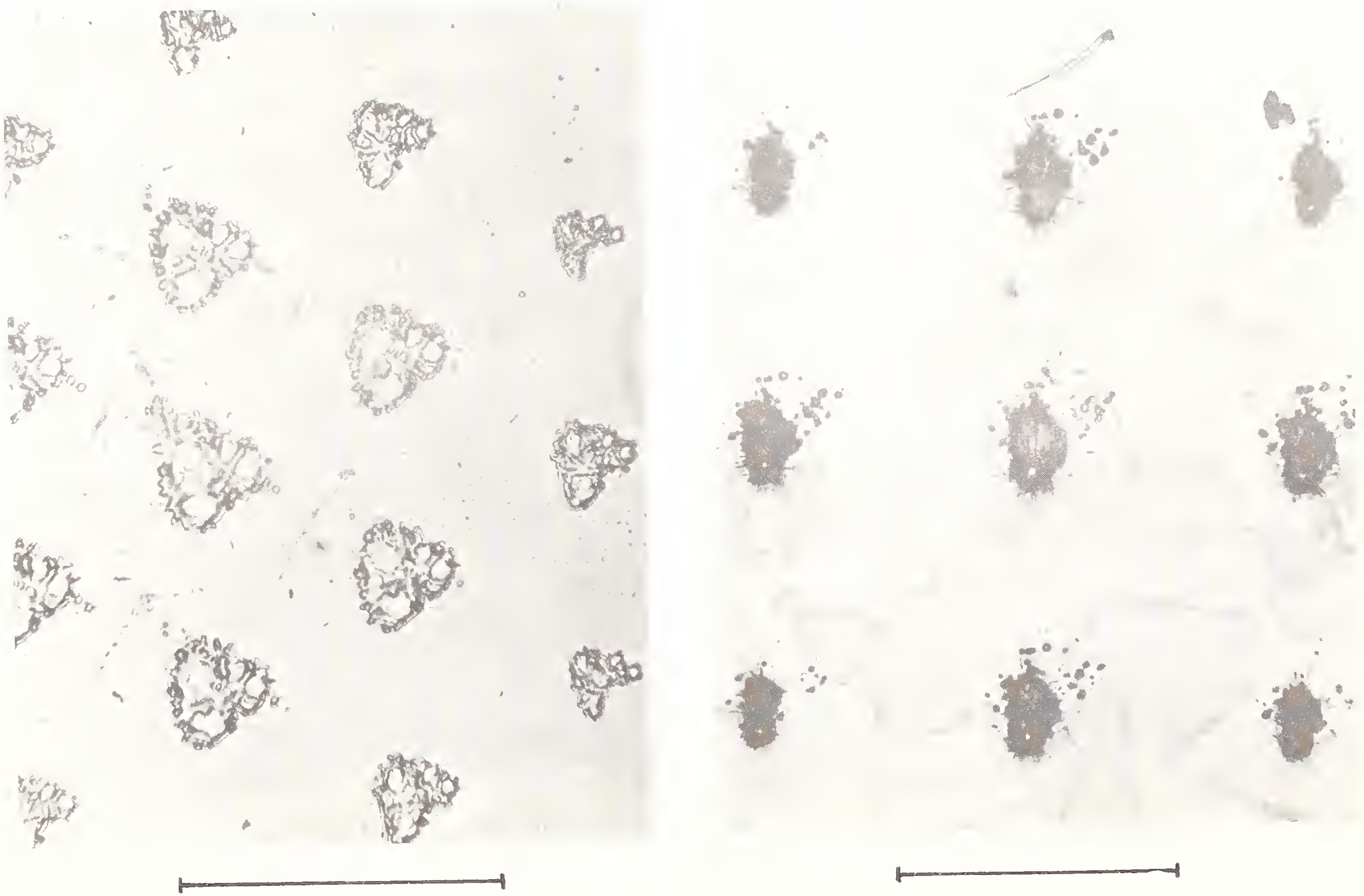

Figure 4. Damage produced on diamond-turned nickel with the 60° array and on copper with the 90° array. The length of the bars represent 0.5 mm on the sample.

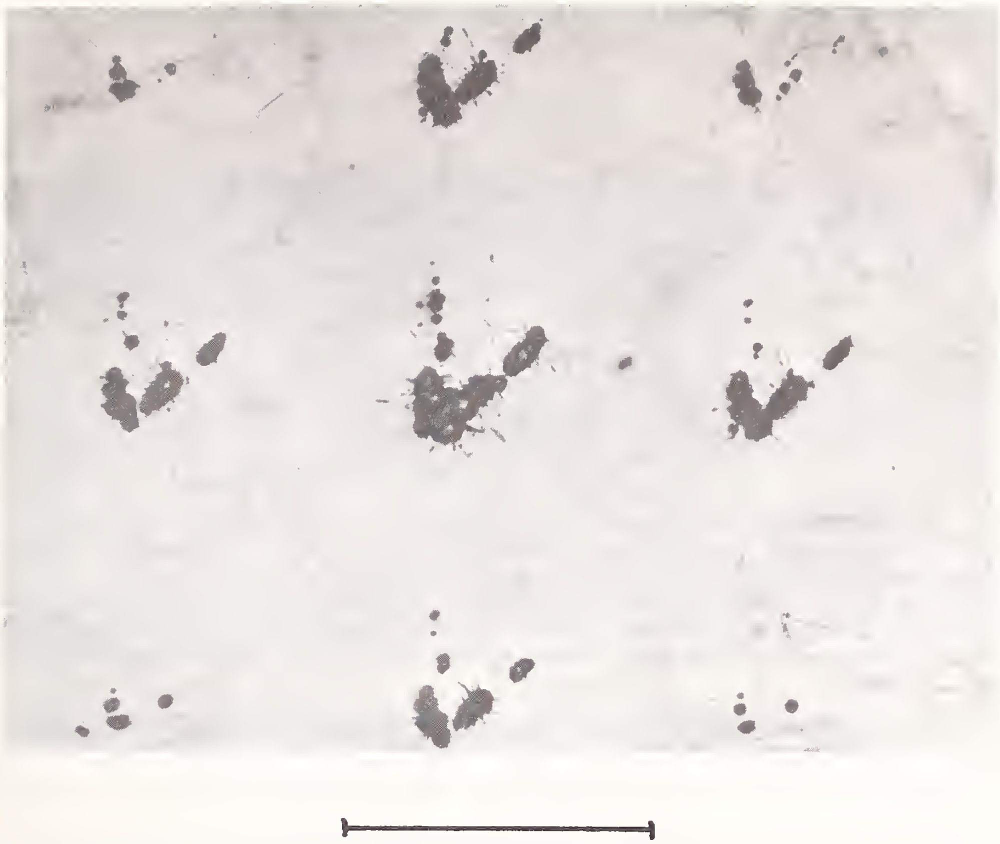

Figure 5. Damage produced on diamond turned copper with the 90° array using a poorly adjusted laser cavity. The length of the bar represents 0.5 mm on the sample.

MONOLITHIC CELL FOR FREQUENCY CONVERSION

R. Bossert, S. D. Jacobs, and L. Lund

Laboratory for Laser Energetics
University of Rochester
250 East River Road
Rochester, New York 14623

We report the successful design, assembly, and operation of a single cell for frequency conversion of Nd:glass laser radiation from λ = 1054 nm to λ = 351 nm. Our approach combines the highly energy-efficient "polarization mismatch" scheme previously conceived (1)[1] and developed (2) with the simplicity of the "tandem" crystal approach recently demonstrated (3). The resultant "monolithic" conversion cell consists of two KDP Type II crystals, assembled with tuning axes orthogonal and contained between a single pair of windows. An index-matching liquid is used to eliminate reflections from all internal surfaces.

In this paper we describe a simple birefringence-sensitive method for marking and orienting circular doubler and mixer crystals with tuning axes orthogonal to better than 60 seconds of arc. The monolithic cell design is described, with emphasis on the chemical compatibility of component materials (crystals, spacers, seals, and metal surfaces) with index-matching liquids. A comparison between Halocarbon (4,5) and Koolase (6) index-matching fluids, after several months of operation (greater than 400 shots), shows the latter to exhibit better long-term, photochemical stability.

The performance of the monolithic cell is superior to that of separate doubler and mixer cells. It exhibits better long-term pointing stability and produces a cleaner 3ω beam.

Key words: frequency conversion; Halocarbon; index-matching fluid; Koolase; KDP; Nd:glass; photochemical degradation; polarization mismatch; third harmonic; Type II crystal.

1. Introduction

The invention (1) of a scheme for highly-efficient energy conversion of Nd:glass laser radiation to its third harmonic (3ω = 351 nm), and the subsequent demonstration of the process using two bare crystals of Type II KDP (2), have provided the inertial fusion program with an attractive approach toward improving the performance of laser fusion targets. An overall energy-conversion efficiency, from 1ω (λ = 1054 nm) to 3ω (λ = 351 nm), of 80% has been predicted and demonstrated for Nd:glass systems using real beam temporal and spatial energy profiles, The actual deliverable 3ω energy, however, has fallen below 80% because of optical materials problems. Nonlinear loss processes at 2ω (λ = 527 nm) (4) and photochemically-induced degradation at 3ω (7) have impeded the use of index-matching liquids for the recovery of energy losses from Fresnal reflections at the conversion crystal surfaces.

In this paper we describe a frequency-conversion cell which successfully solves the 3ω photochemical degradation problem at moderate intensity levels and offers additional advantages over previous cell designs. In what follows, we briefly review (a) the "polarization mismatch" scheme for frequency conversion, (b) describe a monolithic conversion cell which combines both doubling and tripling crystals between a common pair of cell windows, (c) give fabrication and alignment guidelines for optimum cell assembly, and (d) discuss long-term cell performance, with special emphasis on the photochemical stability of "Koolase" — the index-matching liquid of choice for this design and our laser systems.

2. Concept

The "polarization mismatch" concept for frequency conversion is shown schematically in figure 1a. Both the KDP second-harmonic generator (SHG) and the KDP third-harmonic generator (THG) are Type II cut, such that the z-crystallographic axis (the crystal optic axis) makes an angle of approximately 59° with the polished optical surface normal of each crystal. 1ω laser radiation, incident on the SHG, is linearly polarized at 35° to the

---

[1] Numbers within parentheses indicate the literature references at the end of this paper.

o-direction of the doubler. Provided that the intensity of the incident laser radiation and the thickness of the SHG are appropriately matched (1,2), equal numbers of 1 ω and 2 ω photons emerge from the SHG, which is angle-tuned for phase matching. These photons are subsequently mixed in the THG to produce 3 ω radiation. As indicated in figure 1a, the THG is rotated with respect to the SHG by 90° about the system optical axis, and must therefore be angle-tuned in a plane orthogonal to that used to tune the SHG. The thickness of both crystals is chosen to be the same.

Figure 1b gives the overall third-harmonic, energy-conversion efficiency versus average 1 ω beam input intensity for crystals whose thickness is 20 mm. A maximum internal conversion efficiency approaching 80% is possible for real-beam (gaussian temporal and flattened gaussian spatial) input intensities of 0.7 GW/cm^2. The "polarization mismatch" scheme simultaneously provides high-conversion efficiencies and minimizes sensitivity to beam divergence and phase matching angle (1).

3. Monolithic Cell Design

The orthogonality of SHG and THG crystals in the "polarization mismatch" scheme described above, allows one to design a single frequency-conversion cell which contains both crystals. Angle tuning for proper phase matching can then be accomplished in a standard gimbal mount. This simplification was first demonstrated by Summers et al. (3).

The design shown in figure 2a incorporates the SHG and THG crystals between a common pair of fused silica windows. These four optical elements are gently, but firmly, held together by spring loaded plungers and swivel pads. Three sets of glass spacers separate the crystals from each other and the end windows, and enable index-matching liquid to coat all six internal optical surfaces. The two external surfaces of the cell possess dual wavelength 1 ω - 3 ω AR coatings. The characteristics of materials chosen for the construction and testing of a 60 mm clear aperture device are indicated by the code in figure 2a. The gimbal mounted device is shown in figure 2b. A thermistor temperature sensor, mounted within the cell body in close proximity to the crystals, controls current to an infrared heat lamp, which temperature stabilizies the cell to ±0.05°C. Temperature stabilization is required to decouple the cell from temperature fluctuations that occur in the GDL (Glass Development Laser) laser bay.

One obvious advantage to the monolithic cell design, when compared with separate SHG and THG designs, is that it requires fewer optical elements and AR coated surfaces. In addition, we have chosen to make the input and output windows identical to simplify spare parts inventory. The use of a single liquid for index matching of all internal surfaces is a mixed blessing (see section 5.0).

4. Assembly and Testing

It is fundemantal to the monolithic cell configuration that the SHG and THG crystals be installed with their o and e directions orthogonal, and that the o and e directions be distinguished from each other (see fig. 1a). Satisfying the former condition ensures that angle tuning one crystal in the gimbal mount is decoupled from angle tuning the second crystal. Satisfying the latter condition ensures that the SHG may be properly oriented with respect to the incoming 1 ω laser radiation.

By utilizing the uniaxial birefringence of KDP, it is possible to devise a simple, inexpensive method for orienting and marking SHG and THG crystals prior to loading and filling the monolithic cell. Figure 3 demonstrates the two procedures required. Rotation of a crystal through 360° around its optical surface normal, while between crossed polarizers, produces four intensity minimas in the lock-in detected HeNe signal. These minimas define the ordinary ray (o) and extraordinary ray (e) directions projected onto the polished crystal surface. These directions may be marked onto the crystal barrel. By orienting one of these directions at 45° to the incident HeNe polarization direction, the intensity between crossed polarizers versus angle of incidence can then be measured. If the axis of tilt and the o-direction coincide, a rapidly varying series of intensity maxima and minima , separated by about 0.7 mrad (depending on laser beam divergence), can be observed. If the axis of tilt and the e-direction coincide, very little intensity change over tens of mrad can be observed. Both conditions are depicted in figure 3. This orientation technique can define the o- and e-directions of an SHG or THG crystal to within 60 seconds of arc, and is presently more sensitive than our ability to mark and mechanically orient circular crystals in a cell.

The 60 mm clear-aperture, monolithic conversion cell, shown in figure 2b, has been operating in our UV thin-film, damage-testing facility (8,9) since July, 1982. Compared to the separate SHG/THG, two-cell method used prior to this date, the monolithic cell exhibits greatly improved, long-term pointing stability and has generated a cleaner 3ω beam. Figure 4 shows the improved spatial energy profile as measured at a CID camera in our thin-film, damage-testing facility. Also shown in this figure is the small-signal, phase-matched, angle-tuning curve for 3ω laser radiation. The monolithic cell has remained at the peak of the 3ω tuning curve since July 1982, whereas the separate cell configuration required monthly pointing corrections on the order of 1 mrad.

5. Index-Matching Liquid

"Koolase" is the refractive index-matching liquid of choice for our monolithic conversion cell. This proprietary azeotrope is composed of esters, heterocyclic, and primary hydroxyl compounds (6). It has a viscosity of 2 cst. at 21 °C, a refractive index of 1.44 at $\lambda = 337$ nm (7), and negligible optical absorption at $\lambda = 527$ nm and $\lambda = 1054$ nm. The linear absorption coefficient for Koolase at $\lambda = 351$ nm can be as good as 0.37 cm^{-1}, but this may vary depending on the batch. This fluid was developed as a non-toxic, non-hydroscopic, laser flash tube coolant, and is therefore photochemically stable under intense UV irradiation. We have determined that Koolase is compatible with KDP and a number of other materials. Table 1 gives the results of a thirteen-month, passive soak test, conducted at room temperature. Particulates may be removed from the 2.0 µm filtered, as purchased liquid, by additional filtering through a Nalge 0.20 µm nylon membrane filter using a glass syringe.

Table 1. Materials compatibility with Koolase

COMPATIBLE	NOT COMPATIBLE	WHY
• KDP	• Transparent mylar	Swelling
• Fused silica	• Dyed mylar	Bleeding
• Indium	• Vinyl tubing	Increased UV absorption
• Gold	• Tygon tubing	Increased UV absorption
• 6061 Aluminum	• Gum rubber tubing	Increased UV absorption
• Black anodized aluminum	• Polyflo tubing	Increased UV absorption
• 316 stainless steel	• Silicon tubing	Increased UV absorption
• Polypropylene	• Buna N O-ring	Increased UV absorption
• Nylon membrane filter	• Neoprene O-ring	Bleeding
• Viton	• Polyurthane O-ring	Increased UV absorption
• Red silicon oring	• Black delrin	Increased UV absorption
• White silicon oring	• Lexan	Increased UV absorption
• White delrin	• Teflon TFE	Increased UV absorption
• Teflon PFA	• Copper	Chemical reaction
• Teflon FEP		
• RTV 108		

In both our 60 mm monolithic cell and a separate 140 mm THG cell, over the past three to six months, Koolase has shown no long-term, photochemically-induced degradation to itself (see fig. 5) or to the KDP crystal surface. The number of laser shots taken and average 3ω fluences, during this time period, were 350 @ 0.2 J/cm^2 and 100 @ 0.75 J/cm^2, respectively, at a pulsewidth of 1 nsec. The passive absorption losses for 1ω, 2ω, 3ω laser radiation in the three 150 µm-thick, fluid gaps of the monolithic cell have remained below 1% total during this time period.

Halocarbon oil (4,5), another index-matching fluid that has been found effective and stable in a 140 mm SHG cell at $\lambda = 527$ nm, has not exhibited adequate photochemical stability in a 140 mm THG cell. Figures 6a and 6b indicate that, after two months and 200 shots @ 0.75 J/cm^2, Halocarbon oil showed an increase in UV absorption, accompanied by chemical attack to the KDP crystal surface.

6. Conclusion

In this paper we have described the design, construction, and performance of a monolithic cell for frequency conversion of moderate intensity, Nd:glass, laser radiation from λ = 1054 nm to λ = 351 nm. This design takes advantage of the highly energy-efficient "polarization mismatch" conversion scheme, wherein two Type II KDP crystals of equal thickness are orthogonally oriented between a common pair of cell windows. Long-term pointing stability and 3 ω beam quality are enhanced with the monolithic cell design. Long-term photochemical stability problems, associated with the use of a single index-matching liquid for laser radiation at 1 ω, 2 ω, 3 ω, have been solved.

The authors would like to thank Dr. J. A. Abate for providing the 3 ω CID photographs, Dr. S. Craxton for valuable suggestions concerning portions of the manuscript, and Eugene Kowaluk for typing the manuscript.

This work was supported in part by the Exxon Research and Engineering Company, General Electric Company, Northeast Utilities, New York State Energy Research and Development Authority, the Standard Oil Company (Ohio), the University of Rochester, and the Empire State Electric Research Corporation. This work was also supported by the U. S. Department of Energy Inertial Fusion Project under Contract DE-AC08-80DP40124.

7. References

(1) Craxton, R. S. Theory of high efficiency third harmonic generation of high power Nd:glass laser radiation. Opt. Comm. 34: 474-478; 1980 September.

(2) Seka, W.; Jacobs, S. D.; Rizzo, J. E.; Boni, R.; Craxton, R. S. Demonstration of high efficiency third harmonic conversion of high power Nd:glass laser radiation. Opt. Comm. 34: 469-473; 1980 September.

(3) Summers, M. A.; Boyd, R. D.; Eimerl, D.; Booth, E. M. Two-color frequency conversion system for high power lasers. Technical Digest - CLEO'81, OSA, 1981 June. p.30.

(4) Smith, W. Lee. High-intensity transmission properties of index-matching fluids for laser fusion applications. Technical Digest - CLEO'81, OSA, 1981 June. p.32.

(5) Available from Halocarbon Products Corp., 82 Burlews Court, Hackensack, NJ 07601.

6) Available from Kimball Associates, 846-B Rummell Road, St. Cloud, FL 32769.

7) Jacobs, S. D.; Abate, J. A. Compatibility of transmissive optical materials with high intensity 0.351 μm laser radiation. Technical Digest - CLEO'81, OSA, 1981 June. p.86.

8) Abate, J. A. Laser damage thresholds of optical coatings at 0.351 nm. Technical Digest - CLEO'81, OSA, 1981 June. p.86.

9) Abate, J. A.; Roides, R.; Jacobs, S. D.; Piskorowski, W.; Chipp, T. Laser damage thresholds of optical coatings at 351 nm. Presented at the 14th Annual Sympoisum on Optical Materials for High Power Lasers, Boulder, Colorado, 1982 November.

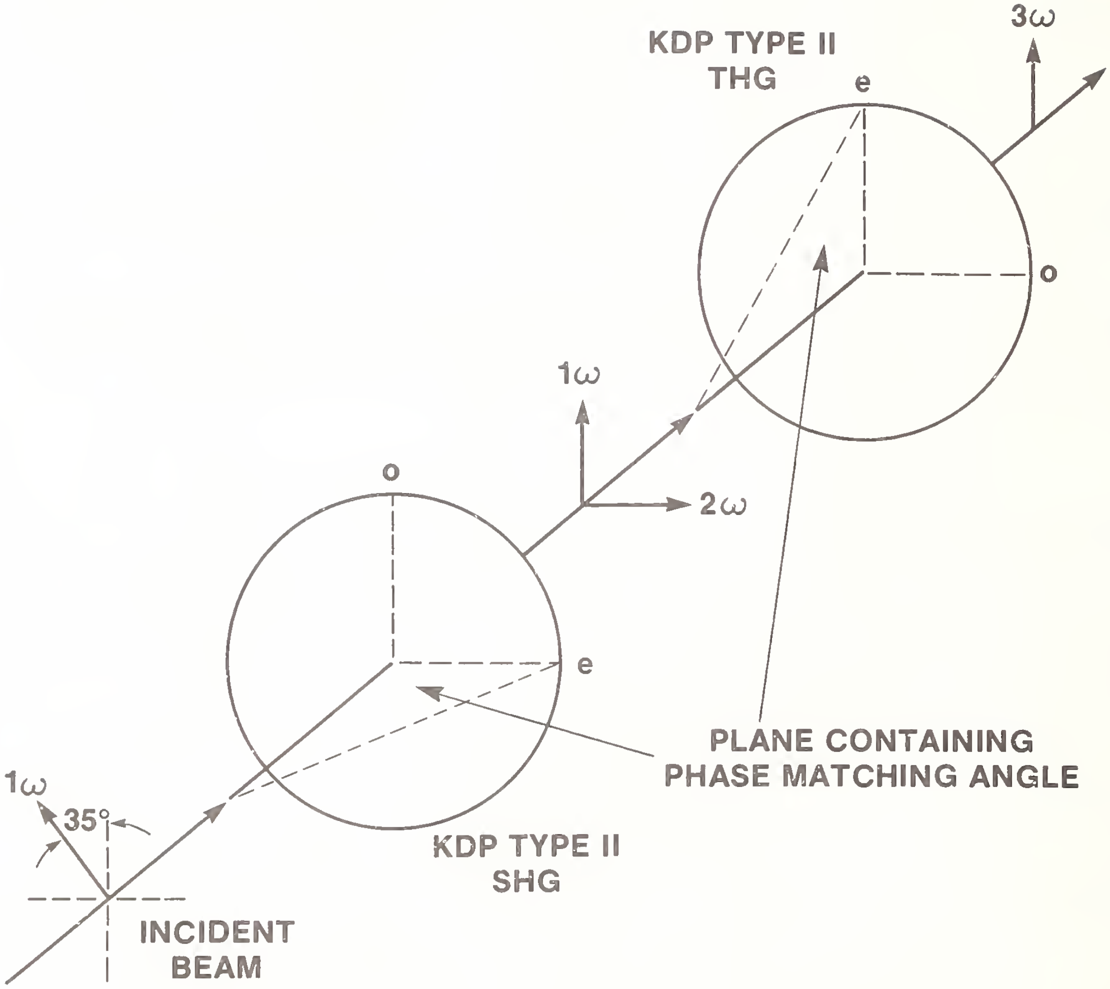

Figure 1a. Polarization mismatch frequency conversion scheme.

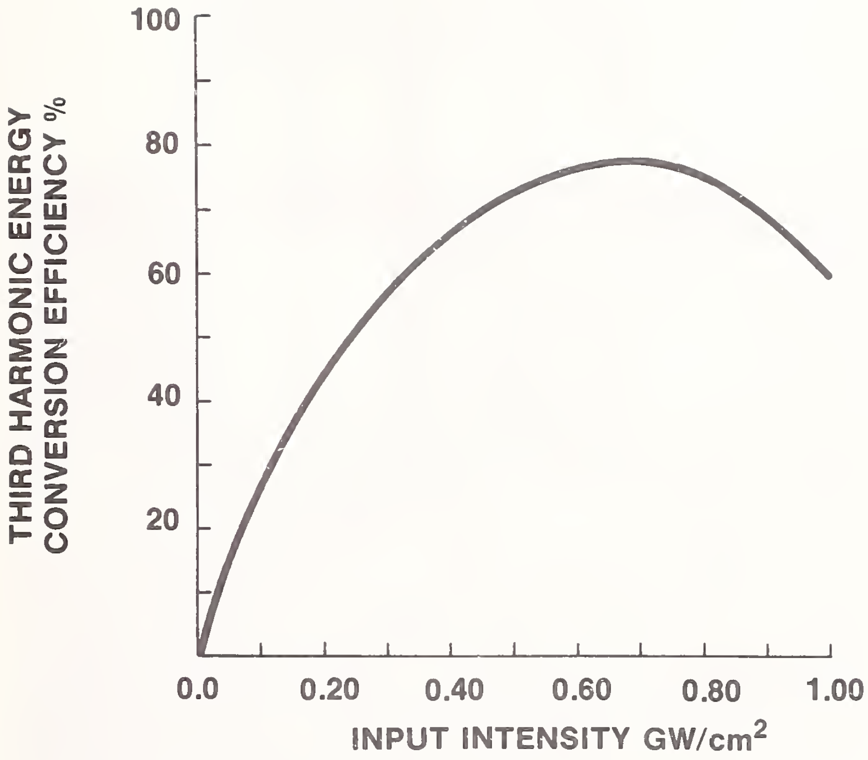

Figure 1b. 3ω conversion efficiency as a function of 1ω input intensity for two 20 mm thick KDP Type II crystals. Theoretical curve assumes gaussian temporal and flattened gaussian spatial laser beam profiles.

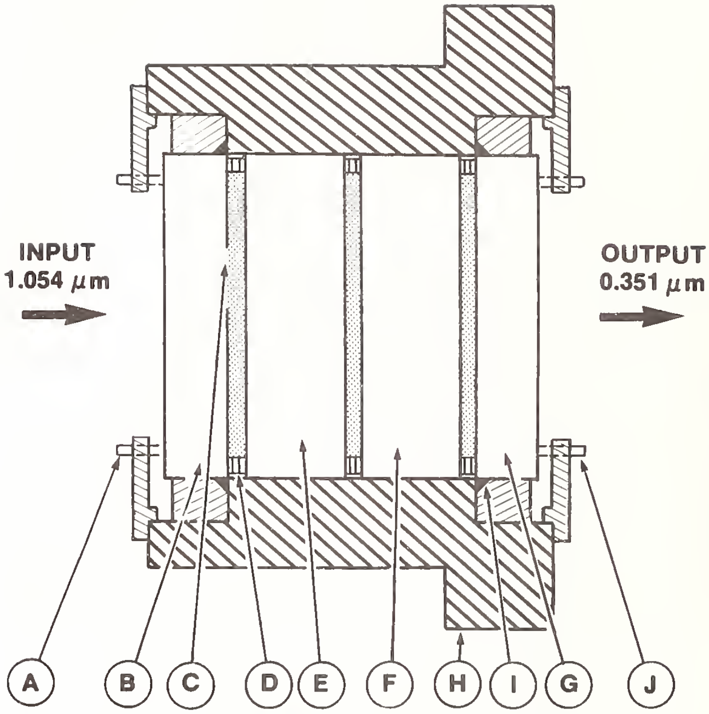

CODE	ITEM	DESCRIPTION
A	Swivel Pad	Solid Stop for Window
B	Input Window	Fused Silica with 1ω-3ω AR
C	Index Matching Liquid	Koolase 0.20 μm Filtered
D	Spacer	Glass, t = 150 μm
E	Type II KDP SHG	θ = 58.90°, t = 20 mm
F	Type II KDP THG	θ = 59.03°, t = 20 mm
G	Output Window	Fused Silica with 1ω-3ω AR
H	Cell Housing	Electroless Nickel Plated Aluminum 6061
I	Liquid Seal	Viton O-ring 75 Durometer
J	Spring Plunger	Stainless Steel

Figure 2a. Monolithic frequency conversion cell.

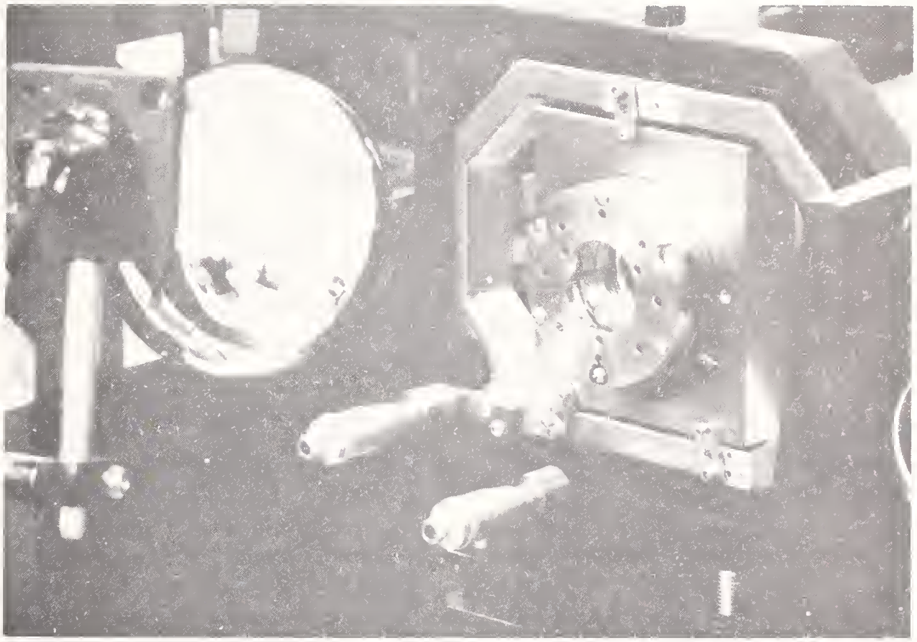

Figure 2b. 60 mm, clear-aperture, monolithic cell in a gimbal mount. Heat lamp in foreground is for temperature stabilization.

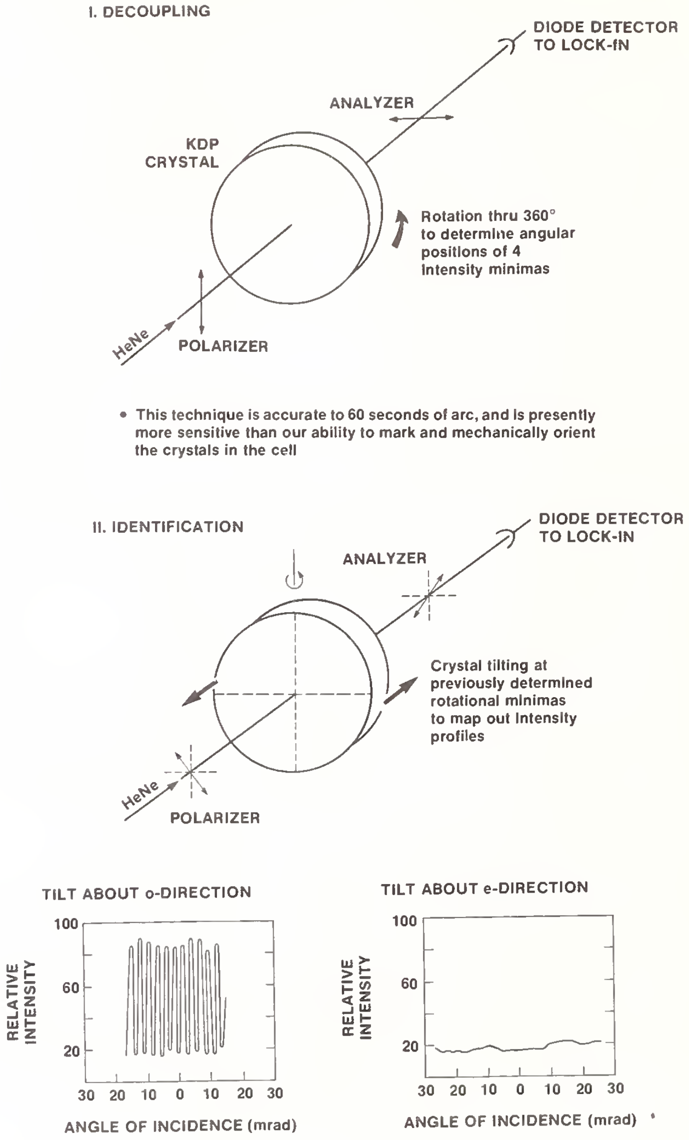

Rotation thru 360° to determine angular positions of 4 intensity minimas

- This technique is accurate to 60 seconds of arc, and is presently more sensitive than our ability to mark and mechanically orient the crystals in the cell

Crystal tilting at previously determined rotational minimas to map out intensity profiles

Figure 3. Method for identifying and marking ordinary ray (o) and extraordinary ray (e) directions projected onto the polished crystal surface.

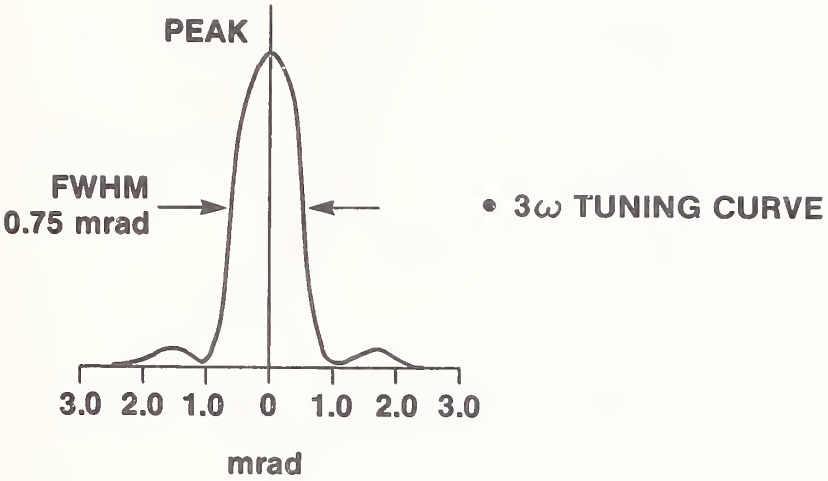

BEAM PROFILES USED FOR THE LLE 3ω DAMAGE TESTER

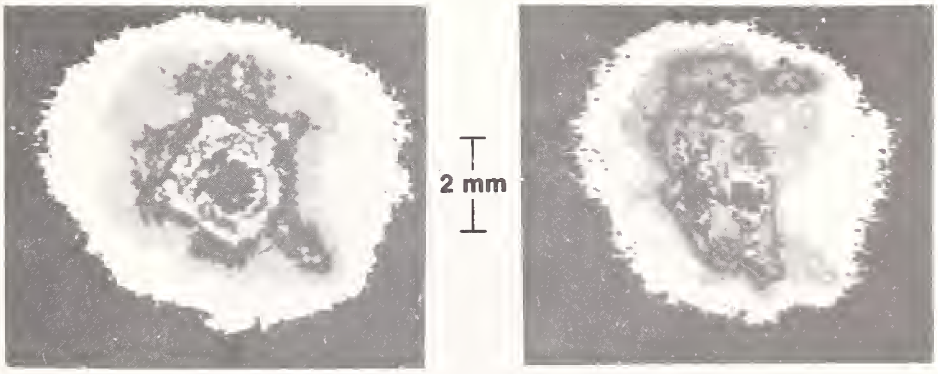

MONOLITHIC CELL

SEPARATE SHG AND THG

Figure 4. Tuning curve and CID camera processed, spatial-energy profiles of 3ω beam. Monolithic cell imparts better pointing stability and beam quality to the UV laser damage-testing facility.

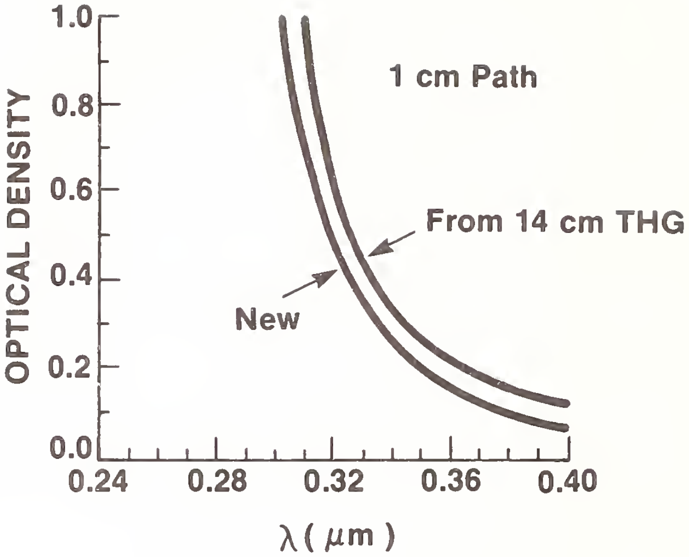

Figure 5. UV stability of Koolase after 3 months and 100 shots.

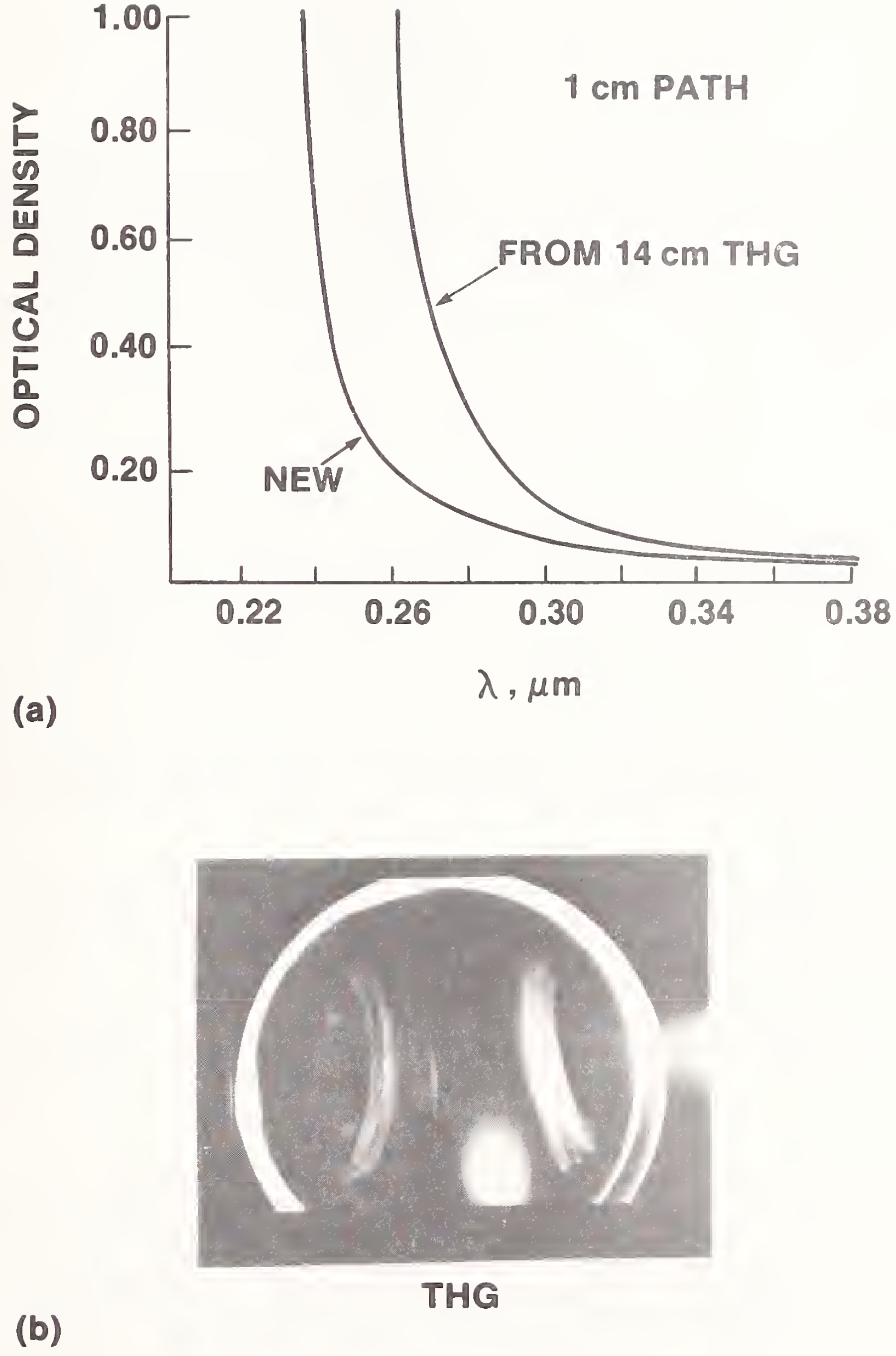

Figure 6. Compatibility of Halocarbon oil and UV radiation.

a) Degraded UV transmittance after 2 months and 200 shots.

b) Chemically attacked KDP crystal surface resulting from a).

CO_2 Laser Polishing of Fused Silica: Recent Progress

P. A. Temple, S. C. Seitel, and D. L. Cate*

Michelson Laboratory, Physics Division
Naval Weapons Center, China Lake, California 93555

A review of CO_2 laser polishing of fused silica for increased surface damage resistance to pulsed 1.064-μm radiation is presented. Discussed will be recent efforts which have concentrated on (1) determining the rate of sublimation of the surface during CO_2 laser treatment to address the question of surface removal vs surface modification, (2) Auger line shape and water desorption studies of mechanically polished vs CO_2 laser polished surfaces, and (3) efforts at figure retention of CO_2 laser polished surfaces using a new treatment apparatus which allows simultaneous CO_2 laser treatment of both sides of a sample.

Key words: fused silica; laser damage; laser desorption; laser polishing.

Introduction

In previous work we have reported improvement in the 1.064-μm pulsed laser damage threshold for surfaces of fused silica which have been polished by several minutes of surface exposure to an intense CO_2 (10.59 μm) CW laser beam [1-3].[1] That work did not answer the fundamental question of why the pulsed laser damage threshold increased with CO_2 laser treatment. In this paper we give evidence that large amounts of surface are not removed by the treatment process, indicating that the improvement is most likely due to either the removal of small amounts of impurity or the modification of the surface material itself, rather than the gross removal of large amounts of material to reveal undisturbed bulk material.

ESCA spectra of a silicon peak were taken of the fused silica surface before and after CO_2 laser treatment. These data indicated that the CO_2 treated surface exhibited a slightly higher binding energy, indicating that the silicon was more highly oxidized in the CO_2 treated surface.

Laser desorption spectra were also taken, using a pulsed 10.59-μm laser as stimulus. These data showed that surfaces which had been CO_2 polished evolved less water when illuminated atsubdamage threshold intensities than did the mechanically polished fused surface. When the 10.59-μm pulse strength was increased to cause damage, it was observed that water, which is normally present in bulk fused silica, was uniformly distributed around the damage site out to several millimeters from the damage site.

Lastly, a new apparatus is described which allows the simultaneous treatment of both sides of a fused silica substrate. This is an advantage when parts with minimum strain are desired.

Previous Work

Figures 1 through 3 show damage results presented previously [1-3]. Figure 1 is a bar graph showing the number of sites which survived 100 exposures at each of two intensities on four CO_2 laser polished samples and on a typical mechanically polished sample. The "treatment schedules" are of increasing CO_2 laser power. Figure 1 shows that a surface which only has been mechanically polished will damage on approximately one-half the exposures at Is and will damage on essentially all exposures at 1.81 Is. However, after CO_2 treatment using schedule 3, there was no damage after 100 exposures at Is and 100 exposures at 1.81 Is. Reference 3 describes in detail the schedules used to polish these parts.

Figure 2 shows the beam energy required to cause damage as a function of beam waist position in the vicinity of the sample surface. In these measurements, 9-nsec, 1064-nm pulses were focused

---

*D. L. Cate is a cadet at the U.S. Air Force Academy.

[1] Numbers in brackets indicate the literature references at the end of the paper.

to a 16.5-μm-radius spot size. The sample was positioned so the beam waist was well inside the sample. Several sites were tested to determine the input energy required to damage 50% of the bulk sites tested. The sample was then moved 0.25 mm further from the lens so the beam waist was closer to the surface, and the threshold was remeasured. This process was repeated to determine the damage threshold when the beam waist was (1) in the bulk material, (2) on the surface, and (3) in the air in front of the surface. The data shown in figure 2 are for a mechanically polished silica sample and for a silica part CO_2 polished by schedule 3. The position 0.0 corresponds to the sample surface being positioned in the beam waist. For the mechanically polished part, the input energy required to cause damage remained constant as the sample was moved to probe several bulk sites. The input energy reached a minimum when the waist was on the surface and then increased. The data for the CO_2 polished surface are similar, except that no dip in threshold was observed when the beam waist was on the surface. These data suggest that the schedule 3 CO_2 polished surface is as damage resistant as the bulk.

Figure 3 shows data from large-spot testing. Samples prepared by treatment schedule 3 had the highest thresholds: one survived repeated irradiation at approximately 60 J/cm^2. This is to be contrasted with a value of 16 to 23 J/cm^2 for the mechanically polished part which is identical except for not having been CO_2 laser polished as a final finishing step.

Mass Loss Measurements

Figure 4 shows the mass of a single fused silica sample as a function of repeated CO_2 laser irradiation. The 175-, 200-, and 225-watt laser powers correspond to schedules 1, 2, and 3, respectively, of figure 1. The balance used was a Mettler electronic balance with a manufacturer's repeatability specification of ±2.0 μg. This corresponds to a surface removal of ±135 Å over the 1.0 square-inch area which was irradiated with the CO_2 laser beam. By zeroing the instrument before each measurement, it was possible to stay well within this specification. Figure 4 shows that the sample mass changed by less than the ±135 Å uncertainty imposed by the manufacturer's specification. This indicates that the surface is not being removed in massive amounts, revealing "fresh" bulk-like fused silica with its anticipated bulk-like higher damage threshold. We are left with the possible removal of selected impurities by CO_2 heating or by modification of the silica surface as the reason for increased damage threshold.

ESCA Spectrum of Silicon in Fused Silica

Figure 5 shows ESCA spectra of a mechanically polished fused silica surface and a schedule 3 CO_2 polished surface. The data show a slight shift to higher binding energy in the CO_2 polished surface, indicating a possible increase in silicon oxidation state after CO_2 polishing.

Laser Desorption Studies

A mechanically polished part and a CO_2 polished part were examined by laser desorption using a 10.59-μm, 100-nsec pulsed laser as the activation source. The parts were placed in a UHV chamber which contained a residual gas analyzer, as described by Porteus et al. [4]. Masses 15, 16, and 18 were monitored for relative signal intensity. Masses 15 and 16 are hydrocarbon peaks and 18 is H_2O. The results are shown in figure 6. It can be seen that all three species are less prevalent in the laser polished parts than on the mechanically polished parts. In all cases, the same laser energy was used for all shots. The intensity was well below the 10.6-μm pulsed damage threshold for the silica surface. The reduced hydrocarbon concentration of the CO_2 polished parts was in agreement with Auger data, not shown.

When a sample was damaged by the 10.59-μm beam by intentionally increasing the laser energy, it was found that water was removed from the damage pit and distributed in a circular pattern about the damage pit. The pattern was several millimeters in radius. Figure 7 shows this effect. In figure 7 are shown mass 18 data for a region of the sample prior to damage. The site at 0.0 was then damaged with a single pulse. Water desorption data were then taken again along the same row and along an adjacent row displaced 0.5 mm from the first row. It is clear that the mass 18 signal has increased after damage. It is not clear if the water has been deposited after being ejected from the damage pit or if the sample surface has been modified, possibly by fracturing, near the site. In any case, these data indicate that damage data taken too near to existing damage sites may be modified by the previous damage. It should be noted that fused silica contains substantial amounts of water in the bulk material. The data also indicate that the amount of water present on a CO_2 polished surface is less than on a mechanically polished surface. Whether this plays any role in the 1064-nm damage threshold improvement is certainly not obvious.

New CO_2 Polishing Apparatus

Figure 8 is a schematic diagram of the CO_2 laser polishing apparatus. The device in the lower left, labeled mirror assembly, is designed to allow treatment of both sides of a sample simultaneously. Figure 9 shows in detail the mirror assembly [5]. Shown is the laser path of the rastered beam during one-half of its travel. During the other half, it strikes the two mirrors on the right side of the diagram and the right side of the sample. As the beam is raised and lowered as well as moved left and right by the "moving mirror" (fig. 8), the entire sample is swept by the laser beam. This device is small enough to be inserted into a vacuum chamber and will allow the simultaneous treatment of both faces of a sample in order to minimize the distortion described elsewhere [1-3].

Summary

Results of earlier measurements were presented which demonstrate the increased laser damage resistance of CO_2 polished fused silica surfaces. The possibility of surface sublimation resulting in gross removal of material was investigated by tracking the weight loss of a sample as it was treated with successively increasing CO_2 laser powers. No detectable weight loss was seen, indicating that the increase in pulsed damage threshold was due to some mechanism other than bulk removal of "disturbed" material. The ESCA spectra of mechanically polished and CO_2 polished surfaces indicate that there is some shift in peak position of a silicon line. This is an indication that silicon in CO_2 polished surfaces is more highly oxidized than in mechanically polished surfaces.

Laser desorption measurements were made on CO_2 polished and on mechanically polished surfaces. These measurements indicated that CO_2 polished surfaces release less water and masses 15 and 16 hydrocarbon than the mechanically polished surfaces. These results are consistent with Auger data. When a CO_2 polished surface was damaged, it was observed that a region of several millimeters radius now was capable of giving up large amounts of water when pulsed with subdamage 10.59-μm pulses. The origin of this effect was not determined, but it may have been splattered water-rich ejectorate, or the surface may have been altered to allow the release of water trapped just below the surface.

Finally, an apparatus designed to allow the polishing of both sides of a fused silica substrate was described. This apparatus makes use of four mirrors to redirect the rastered beam in a pattern which strikes first the left side and then the right side of the sample.

References

[1] Temple, P. A.; Milam, D.; Lowdermilk, W. H. "CO_2-laser polishing of fused silica surfaces for increased laser damage resistance at 1.06 micrometers," in Laser Induced Damage in Optical Materials: 1979, Bennett, H. E.; Glass, A. J.; Guenther, A. H.; Newnam, B. E., ed. 1979 October 30-31; Boulder, CO. Nat. Bur. Stand. (U.S.) Spec. Publ. 568; 1980 July. Pp. 229-236.

[2] Temple, P. A.; Soileau, M. J. "1.06 micrometer laser-induced breakdown of CO_2-laser-polished fused SiO_2," in Laser Induced Damage in Optical Materials: 1980, Bennett, H. E.; Glass, A. J.; Guenther, A. H.; Newnam, B. E., ed. 1980 September 30-October 1; Boulder, CO. Nat. Bur. Stand. (U.S.) Spec. Publ. 620; 1981 October. Pp. 180-188.

[3] Temple, P. A.; Lowdermilk, W. H.; Milam, D. "CO_2 laser polishing of fused silica surfaces for increased laser damage resistance at 1064 nm," Appl. Opt. 21; 3249-3255; 1982.

[4] Porteus, J. O.; Faith, W. N.; Allen, S. D. "Laser desorption analysis of H_2O and other contaminants from optical surfaces," presented at the 13th Annual Symposium on Optical Materials for High Power Lasers; Boulder, CO; 1981 November.

[5] Cate, D. L. A New Mirror Apparatus for Symmetric CO_2 Laser Polishing of Fused Silica, Naval Weapons Center, China Lake, CA; NWC Technical Memorandum 4896; 1982 September.

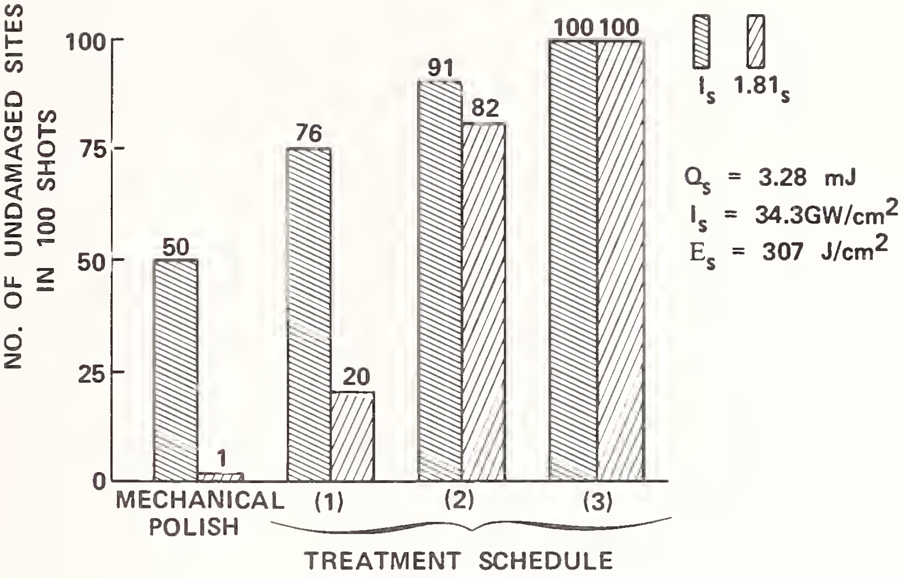

Figure 1. Bar graph showing the number of sites which survived 100 shots at each of two intensities on three multipass CO_2 polished samples and on a typical mechanically polished sample. The sites were illuminated on a 0.5-mm grid with only one exposure per site.

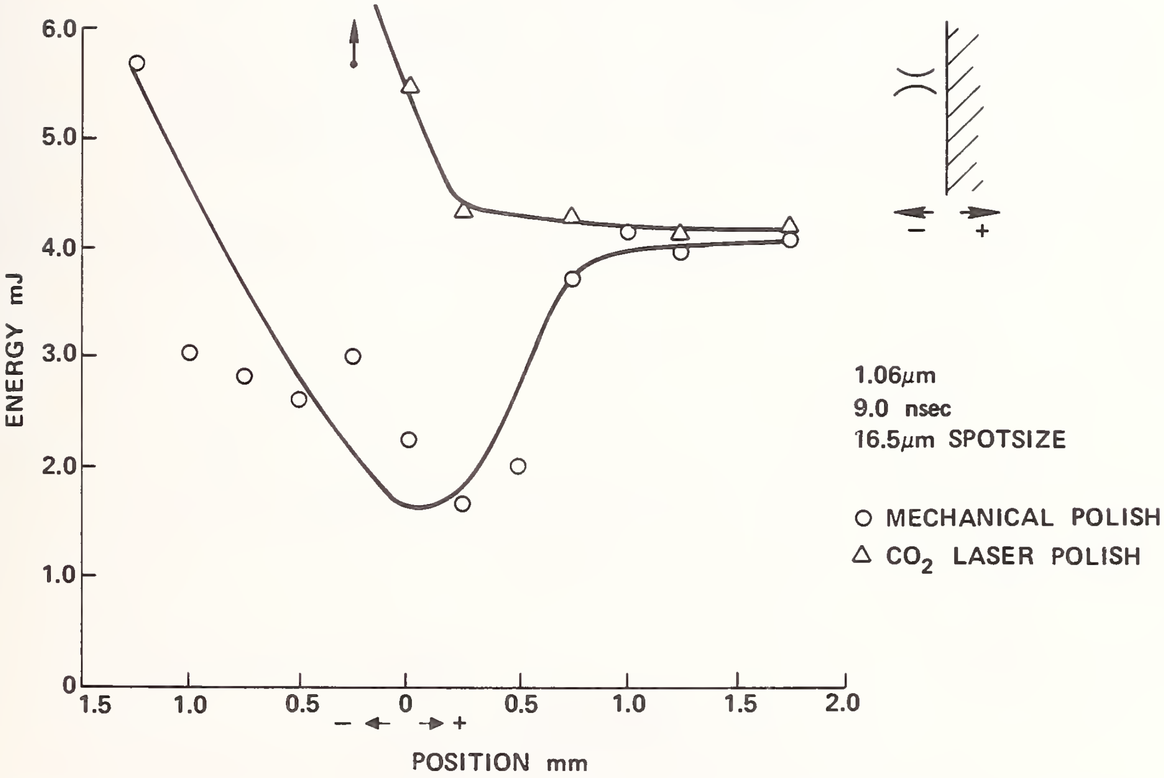

Figure 2. Beam energy required to cause damage as a function of beam waist position. The solid lines are not mathematical fits but are hand-sketched to aid in interpretation.

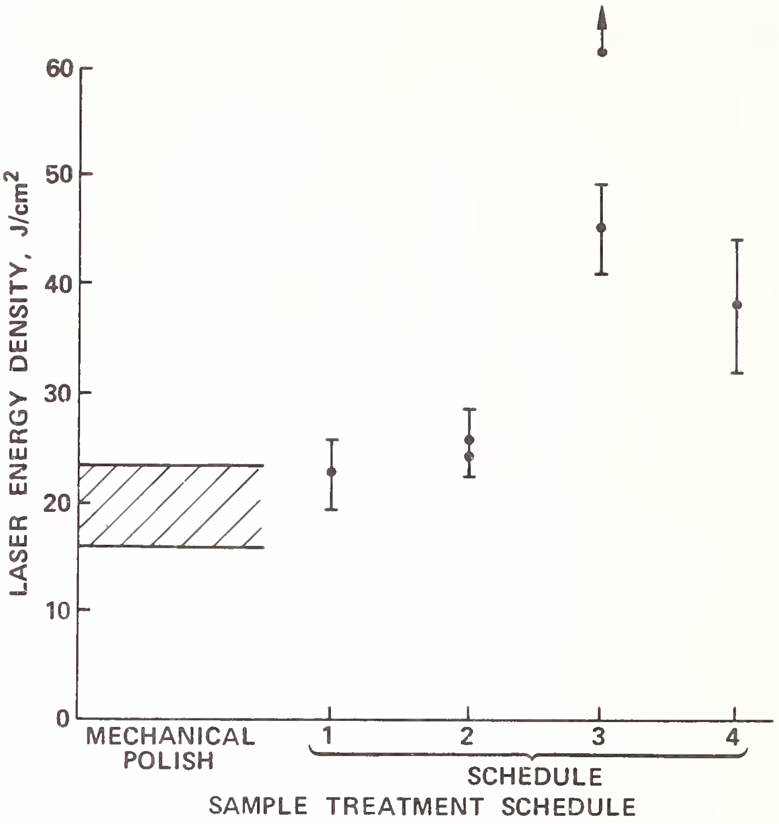

Figure 3. The 1064-nm, 1-nsec damage threshold on fused silica surfaces as a function of treatment schedule used in multipass CO_2 laser polish.

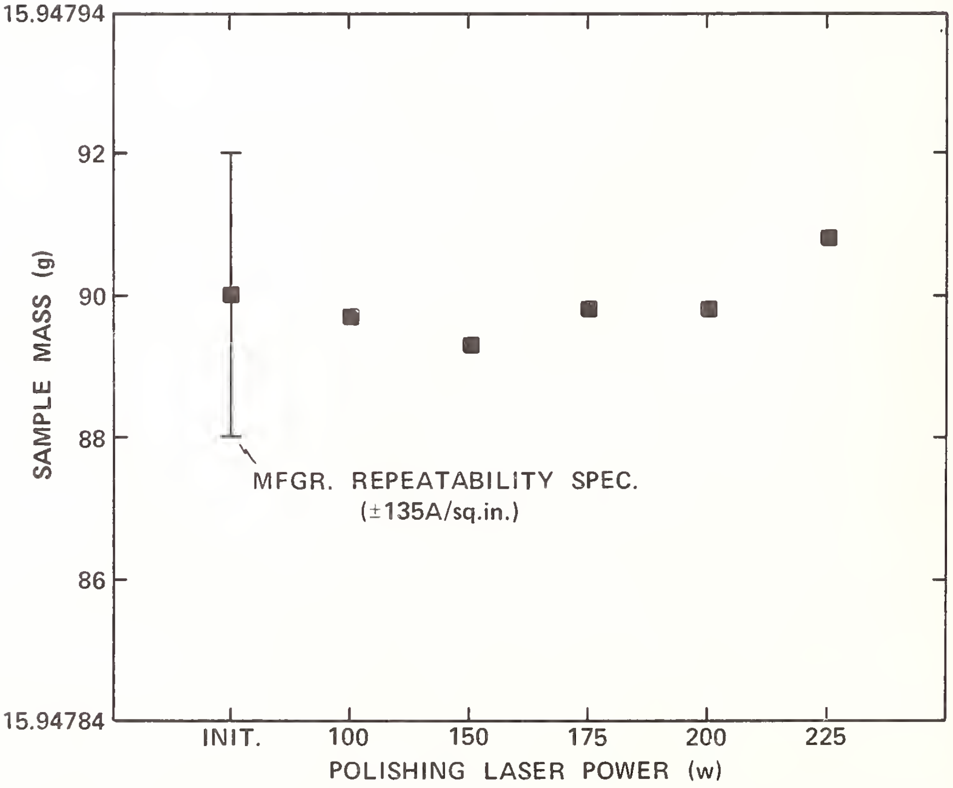

Figure 4. The mass of a sample of fused silica which was laser polished over a 1-inch-square area at successively higher laser intensities.

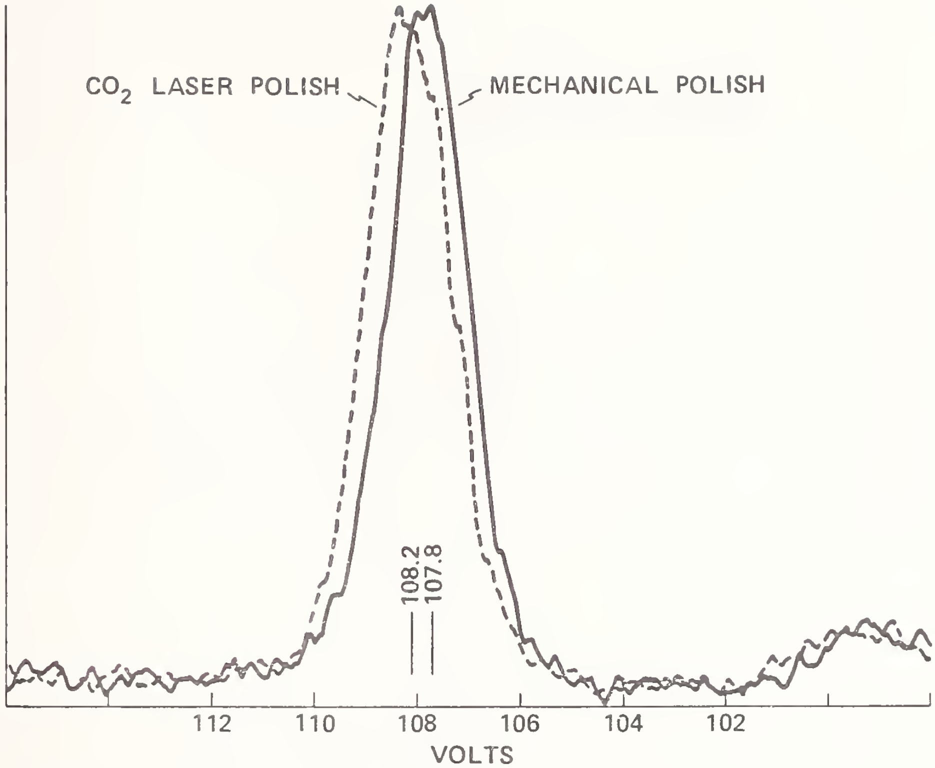

Figure 5. ESC spectrum of a silicon transition in a mechanically polished and a CO_2 laser polished spectrum.

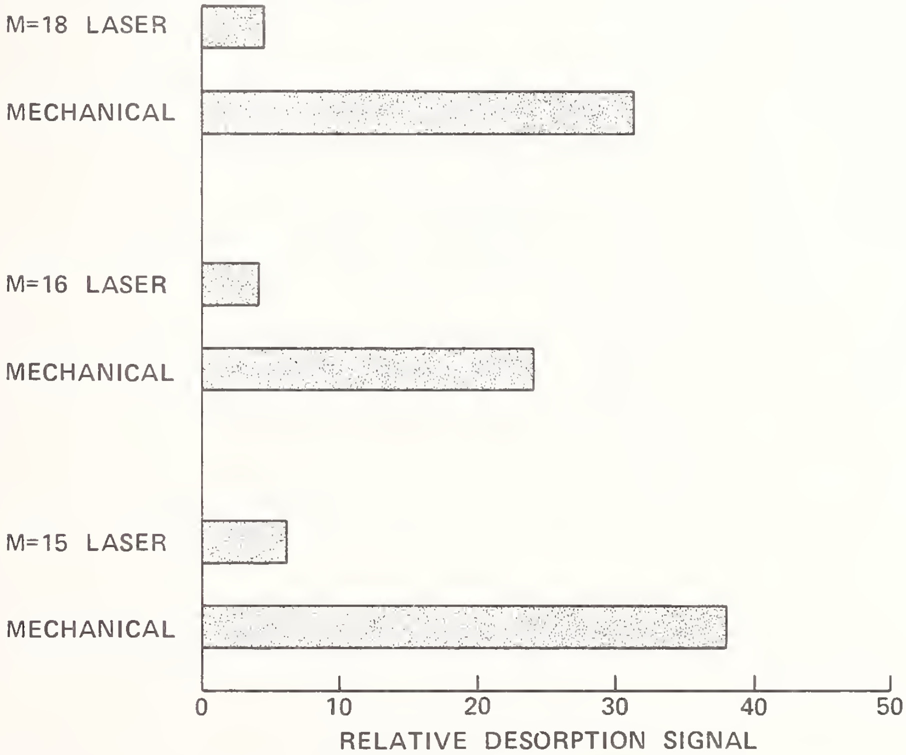

Figure 6. Relative desorption signals for masses 15, 16, and 18 for a mechanically and a CO_2 laser polished surface. The molecular desorption was stimulated by a 10.6-μm, 100-nsec laser pulse of subdamage threshold intensity.

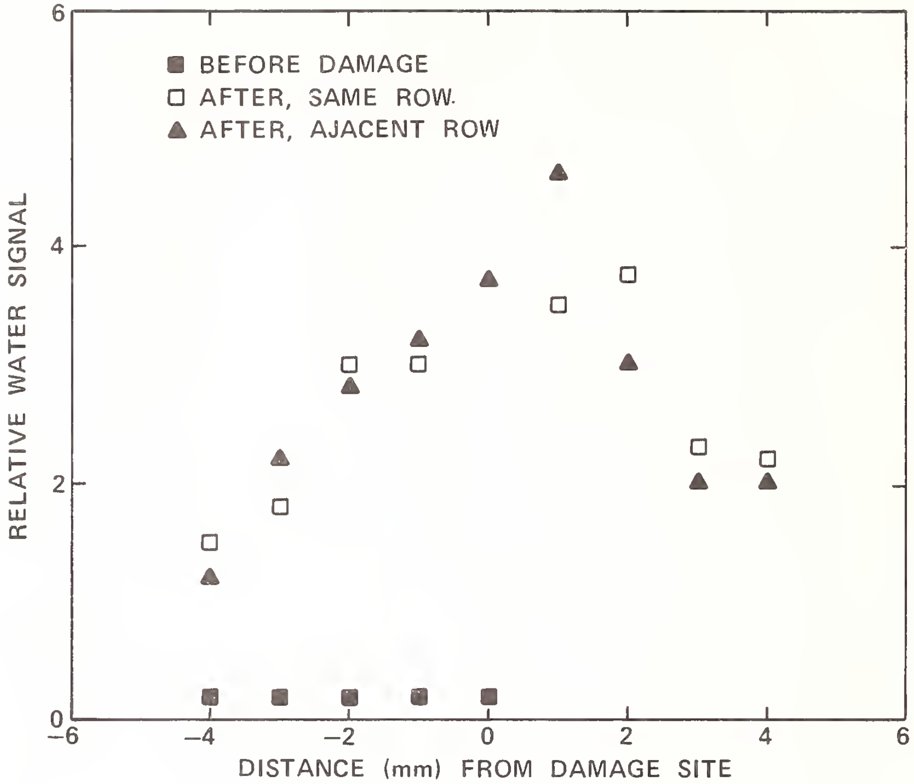

Figure 7. Desorption signal for mass 18 as a function of position. The signal which resulted from the single damage pulse at 0.0 mm is not shown.

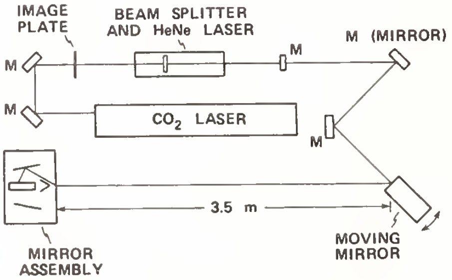

Figure 8. Diagram of the CO_2 laser polishing apparatus.

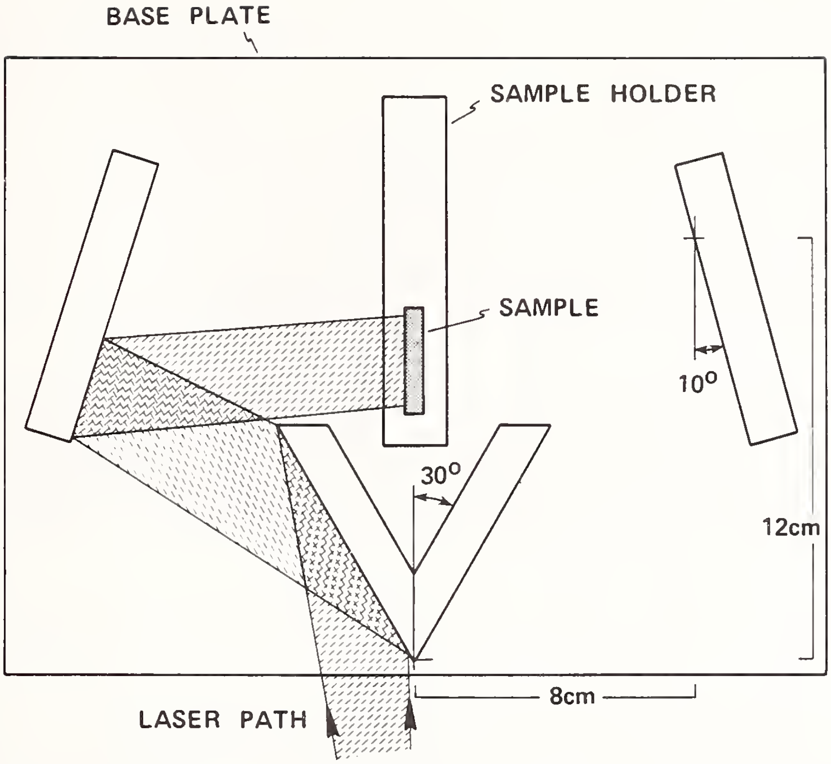

Figure 9. Top view of the two-sided polishing apparatus. The laser path shown sweeps one side of the sample. During actual use, the beam sweeps the entire front mirror, thus striking both sides of the sample.

Float Polishing and Defects of Fused Silica*

Yoshiharu Namba

Institute for Modern Optics
Department of Physics and Astronomy
The University of New Mexico
Albuquerque, New Mexico 87131

A float polishing machine has been newly developed to finish optical components. The machine has a rail head and a precise main spindle of both high rigidity and rotational accuracy, and can cut a tin lap of 460 mm in diameter to the degree of 1 μm in flatness. Very good flatness of 0.03 μm (λ/20) on BK-7 glass of 100 mm in diameter and extremely small surface roughness of 2.2 angstroms rms on fused silica were obtained by the machine. Defects of fused silica were examined by etching and Nomarski microscopy. Volume defects such as bubbles or inclusions in μm size seem to exist in fused silica.

Key words: Defect; flatness; float polishing; fused silica; laser damage; surface roughness.

1. Introduction

Both machining accuracy and productivity are the most important factors in the manufacturing of optical components. Moreover, higher surface damage thresholds are required on the optical components for high power lasers. Previous works reported that the threshold was a function of the surface conditions, such as surface roughness [1][1], pits, microcracks [2], entrapped polishing particles [3,4] or contamination [2] from polishing compounds and laps. Therefore, the surface of super-smooth, damage-free and no contamination is required for the optical components for high power lasers [5] in order to improve the laser-induced damage threshold on the polished surface and interface between the substrate and coating film. The properties of the interface and coating film seem to be affected by qualities of polished surface of the substrate.

The float polishing technology [6,7] was invented for polishing electronic materials ultrafinely without deformed layer. Sapphire and Mn-Zn ferrite single crystals were polished with various fine powders in distilled water on a tin lap, and super smooth surface finishes better than 10 angstroms Rz with crystallographic perfection were obtained [6,8]. Therefore, this technology seems to be useful for making high energy laser components.

In this paper, a newly developed float polishing machine for making optical components, some results of surface topography on the float-polished glasses, and examination of defects on fused silica samples polished by the state-of-the-art are described.

2. Development of Float Polishing Machine

The float polishing technology has been widely used in manufacturing magnetic heads for video cassette recorders in Japan and has improved the performance of the heads remarkably [9]. Very good flatness λ/20 = 0.03 μm on the area of 7x7 mm^2, excellent retention of edge geometry less than 100 angstroms in radius and extremely small surface roughness better than 10 angstroms Rz were obtained on single crystal surfaces by the float polishing [6-10].

A float polishing machine was newly designed as shown in Fig. 1 in order to use the float polishing technology for making optical components. This machine of double housing type looks like a diamond turning machine [11], and has a high accuracy vertical main spindle with hydrostatic bearing of both high rigidity and rotational accuracy, a cross rail with a rail head and work spindle, and a filter unit for ultra-clean air. The machine can cut a tin lap of 460 mm in diameter to the degree of 1 μm in flatness with a diamond tool as shown in Fig. 2. The key of making workpieces flat by polishing is the flatness of a lap, because the flatness is transferred on the work surfaces during

---

*Work supported by the Air Force Weapons Laboratory, Kirtland AFB, New Mexico, under contract F29601-82-K0017.

[1] Figures in brankets indicate the literature references at the end of this paper.

polishing process. The continuously dressed flat annular machines are widely used for polishing ultra-flat optical surfaces [12]. In this case it is the most important that the pitch surface wears uniformly, the flatness of which is indirectly monitored by measuring the flatness of the standard sample on the pitch surface periodically.

A spiral groove of 2 mm in pitch is cut on the commercially-pure tin lap with a cut-off tool of high speed steel as shown in Fig. 3. Chips are removed by vacuum during the cutting process. Then the tin lap surface is cut with a diamond tool as shown in Fig. 4, and the feed rate is 0.3 mm/rev. After cleaning up the lap with distilled water and putting a stainless steel ring on the base plate of stainless steel under the tin lap for making a vessel, the polishing fluid mixed with distilled water and 2 wt% SiO_2 powder (Aerosil 300, Degussa Corp.) of 70 angstroms in nominal diameter is poured into the vessel. Workpieces to be polished are put on the work holder, then the latter is mounted at the edge of the work spindle in order to make a universal joint.

Figure 5 shows the actual polishing condition. During the polishing process, the work spindle rotates the work holder of 180 mm in diameter, and the polishing pressure is applied on the workpieces only by the weights of the work holder and workpieces so as to maintain the stable movement of workpieces. The workpieces are floating in a stable state, or are suspended in the polishing fluid by the hydrodynamic behaviour of fluid between the workpieces and grooved tin lap. In this figure the tin lap and work holder are rotating at the same revolution of 80 rpm in the same direction.

3. Polishing of Glasses

The conventionally pitch-polished BK-7 glass of 100 mm in diameter and 30 mm in thickness was polished with the new float polishing machine as shown in Fig. 6. In this case, the diameter of the work holder was the same as the workpiece which was mounted under the work holder with a double-sticky tape in order to prevent the workpiece from the thermal deformation due to waxing process.

Figure 7 shows the flatness of the float-polished BK-7 glass sample, measured with Zygo Mark III, Phase Measuring Interferometer System. Before the measurement, the sample was left on the Zygo system in a temperature-controlled measuring room for more than 24 hours in order to eliminate thermal errors. The result shows that the peak-to-valley flatness is 0.049 x (wavelength) = $\lambda/20$ = 0.031 µm and rms flatness is 0.006 x (wavelength) = $\lambda/167$ = 0.0038 µm = 38 angstroms on the sample. In this connection, Zygo Mark III, Zapp System detected that the peak-to-valley flatness was 0.029 x (wavelength) = $\lambda/34$ = 0.018 µm and rms flatness was 0.006 x (wavelength) = $\lambda/167$ = 0.0038 µm = 38 angstroms on the same sample. The float-polished sample seems to be very flat beyond the measuring limit of the measuring machine.

Fumed silica named Aerosil 300 of Degussa Corporation has the very low stock removal power for polishing fused silica, however, it is too small in size to make any scratch on the fused silica surface and is very pure as same as silicon single crystals which are widely used in the semiconductor industry. Pure fumed silica composed of the same composition as fused silica seems to be useful for preventing the contamination during polishing [2,6]. J. M. Bennett measured the surface profile of float-polished fused silica samples of 38 mm in diameter with Talystep [13] as shown in Fig. 8. The measuring conditions were the stylus radius of 1 µm and loading of 2 mg. The figure shows 2.2 angstroms rms roughness in the measured length of 800 µm on polished fused silica, 1.9 angstroms rms in 60 µm length, 1.6 angstroms rms in 15 µm length, and the instrumental noise corresponds to 1.1 angstroms rms. From the previous experience of polishing single crystals [8], this surface roughness number of 2.2 angstroms rms may be considered to reduce to some extent by the successive experiment.

Colloidal silica of alkalinity has higher removal rate than the fumed silica powder which shows acidic in water, however, the rougher surface of fused silica is obtained by the float polishing with the colloidal silica than that with the fumed silica.

4. Defects of Fused Silica Surface

Polishing technology for fused silica has been developed to reduce the surface roughness and mechanically-damaged layer [1,14]. Sawed and ground glasses have numerous reticulate cracks under the surface [2]. Controlled grinding was performed to remove the surface damage, assuming if proper amounts of the surface were removed during each stage of grinding and polishing, the damage would be disappeared [14]. However, various defects were detected visually under the Nomarski interference microscope of Nikon Optiphot on all of the tested samples [1,14,15] by etching with hydrofluoric acid, and such defects have remarkably reduced with the times. Figure 9 shows typical defects on well-polished fused silica surface [1] after 5 minutes etching with 5 % HF. These defects are classified as follows; (1) a series of semicircular microcracks, (2) a hollow due to a semicircular microcracks, (3) a faint scratch, (4) a tiny pit due to bubble, inclusion or residual damage of pre-machining, (5) depression due to different phase. Most of the defects above-mentioned can be removed by careful polishing processes [14,15], but tiny pits of few micrometers in diameter were remained on all samples tested in this study.

Figure 10 is a Nomarski micrograph on the etched surface of fused silica after polishing by VTI, Inc. and laser irradiation by AFWL, and shows two black spots representing two separate pits and a laser damaged site. This sample was remarkably well-polished and very smooth. Only defects on the polished surface after etching were tiny pits and small number of depressions which were detected only on this sample. These small pits of few micrometers and sub-micrometers can be considered to be caused by bubbles and inclusions contained in the bulk material or by small cracks due to pre-machining. As the results of observing the birth and death process of tiny pits on the fused silica surface during the float polishing, it was detected that new pits appeared and pits previously existed were removed during polishing. Therefore, these pits seem to be caused by volume defects such as bubbles and inclusions contained in the bulk material. It is necessary to study such a small volume defects in fused silica in the future, and the total internal reflection microscopy [16] is one of the best method to detect the defect.

In order to study the effects of bulk material, surface and coated film on the laser damage threshold, fused silica has been used as bulk material because it is optically uniform and can be used for optical components in the range of visible and near infrared. However, the fused silica samples used in this experiment may be considered to contain volume defects which are not known in detail, so that in order to perform the basic research work on laser damage in optical materials it is recommended to replace fused silica with single crystal materials which still contain point and line defects, but rarely volume defects. Sapphire seems to be one of the best materials as such single crystals, and it is easy to polish without damage layer [6]. It is relatively easy both to detect various defects on the sapphire surface of good quality and to know the origin of laser damage of bulk surface by using various modern methods because of crystal.

Figure 11 shows a series of a laser damage site on the fused silica sample, taken with the Nomarski microscope of Nikon Optiphot. 7.6 angstroms rms surface roughness was measured by TIS measurement on the test surface before laser irradiation [14]. Most of the patterns caused by laser irradiation of 1.06 µm wavelength did not change the status even after etching with 5 % HF for 5 minutes and 25 % HF for 5 minutes. In the case of crystallographic materials, plastically-deformed region or area having residual stress can be revealed by etching because these areas are more active and have anisotropy of etching rate. Figure 11 shows that the slight laser damage on the front surface may be only changed topographically but not metallurgically, and the damage site did not change the condition after etching. This phenomenon seems to be unique existing only on the amorphous material, therefore the laser polishing can be considered to be effective for eliminating defects on the mechanically-polished fused silica [17,18].

5. Conclusions

From this paper the following conclusions may be drawn:

1) The flatness of λ/20 = 0.03 µm and rms flatness of λ/167 = 0.0038 µm on BK-7 glass sample of 100 mm in diameter and the surface roughness of 2.2 angstroms rms on fused silica sample of 38 mm in diameter were obtained by using the newly-developed float polishing machine.

2) Pits of few micrometers or sub-micrometers in size were appeared on all fused silica samples tested in this study after carefully-polishing and etching with HF. These pits seem to derive from volume defects such as bubbles and inclusions in the bulk.

3) The difference of metallurgical subsurface disorder between the polished surface and 1.06 µm laser damaged site on fused silica can not be observed by etching with 5 % and 25 % HF. This is the feature of amorphous material and the laser polishing seems to be available to get the higher damage threshold on conventionally-polished surfaces.

6. Acknowledgments

The author would like to thank Dr. A. H. Guenther of Air Force Weapons Laboratory and Prof. M. O. Scully of University of New Mexico for encouraging this work, Prof. K. C. Jungling of University of New Mexico and Dr. A. F. Stewart of Air Force Weapons Laboratory for helpful discussion, Dr. J. M. Bennett of Naval Weapons Center and Mr. W. E. Kunzler of Air Force Weapons Laboratory for measuring surface roughness, Mr. J. W. Bender of International Laser Systems, Inc. for various help to this experimental work, and Mr. S. F. Soares of University of New Mexico for the experimental work.

A part of the work to make the float polishing machine was supported by Grant-in-Aid for Developmental Scientific Research No. 485063 of the Japanese Ministry of Education.

7. References

[1] House, R. A., Bettis, J. R., Guenther, A. H. and Austin, R., Correlation of Laser-Induced Damage with Surface Structure and Preparation Techniques of Several Optical Glasses at 1.06 µm, Laser Induced Damage in Optical Materials: 1975, NBS Spec. Publ. 435, 305 (1976).

[2] Landingham, R. L., Casey, A. W. and Lindahl, R. O., Effects of Various Polishing Media and Techniques on the Surface Finish and Behavior of Laser Glasses, The Science of Ceramic Machining and Surface Finishing II, NBS Spec. Publ. 562, 231 (1979).

[3] Boling, N. L., Dubé, G. and Crisp, M. D., Laser Surface Damage Studies on Several Glasses, Laser Induced Damage in Optical Materials: 1973, NBS Spec. Publ. 387, 69 (1973).

[4] Leung, K. M. and DeShazer, L. G., Surface Defects on Crystals of TiO_2 and YVO_4 Studies by Laser-Induced Damage Effects, Laser Induced Damage in Optical Materials: 1974, NBS Spec. Publ. 414, 193 (1974).

[5] Bass, M., Leung, K. M. and Tang, C., Pulsed Laser Induced Damage at the DF Laser Wavelength, Laser Induced Damage in Optical Materials: 1976, NBS Spec. Publ. 462, 136 (1976).

[6] Namba, Y. and Tsuwa, H., Ultra-Fine Finishing of Sapphire Single Crystal, Annals of the CIRP, 26/1, 325 (1977).

[7] Namba, Y. and Tsuwa, H., Float Polishing of Mn-Zn Ferrites and Characteristics of Finished Surfaces, Proceedings of 4th International Conference on Production Engineering, 1017 (1980).

[8] Namba, Y. and Tsuwa, H., Mechanism and Some Applications of Ultra-Fine Finishing, Annals of CIRP, 27/1, 511 (1978).

[9] U. S. Patent 4,358,295 November 9, 1982. "Polishing Method".

[10] Namba, Y. and Tsuwa, H., Ultrafine Finishing of Ceramics and Metals by Float Polishing, Laser Induced Damage in Optical Materials: 1980, NBS Spec. Publ. 620, 171 (1981).

[11] Donaldson, R. R., Large Optics Diamond Turning Machine, LLL, UCRL-52812 (1979).

[12] Cooke, F., Brown, N. and Prochnow, E., Annular Lapping of Precision Optical Flatware, Optical Engineering, 15, 407 (1976).

[13] Bennett, J. M. and Dancy, J. H., Stylus Profiling Instrument for Measuring Statistical Properties of Smooth Optical Surfaces, Applied Optics, 20, 1785 (1981).

[14] Bordzol, L. and Kurdock, J. R., Dielectric Samples Program, Final Report, Report No. 14955, Contract No. F29650-80-C-009 (1980).

[15] Fused silica sample polished by VTI, Inc. (1982).

[16] Temple, P. A., Total Internal Reflection Microscopy: A Surface Inspection Technique, Applied Optics, 20, 2656 (1981).

[17] Temple, P. A., Milam, D. and Lowdermilk, W. H., CO_2-Laser Polishing of Fused Silica Surfaces for Increased Laser Damage Resistance at 1.06 µm, Laser Induced Damage in Optical Materials: 1979, NBS Spec. Publ. 568, 229 (1980).

[18] Temple, P. A. and Soileau, M. J., 1.06 µm Laser-Induced Breakdown of CO_2-Laser-Polished Fused SiO_2, Laser Induced Damage in Optical Materials: 1980, NBS Spec. Publ. 620, 180 (1981).

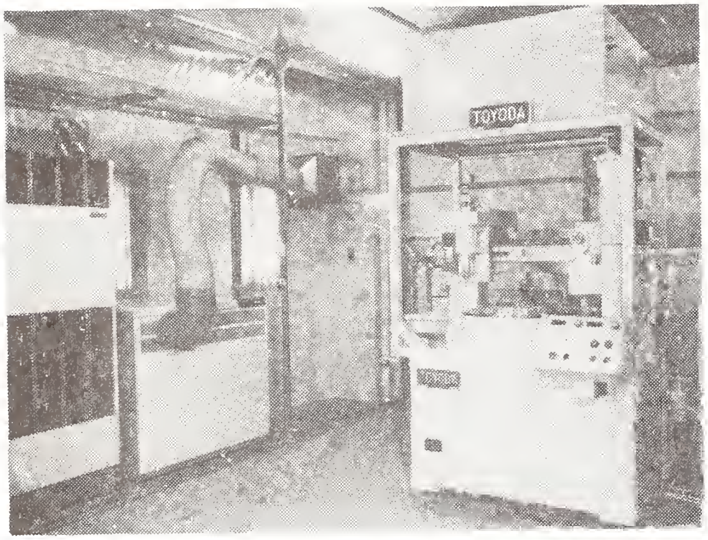

Figure 1. Newly developed float polishing machine in a clean room.

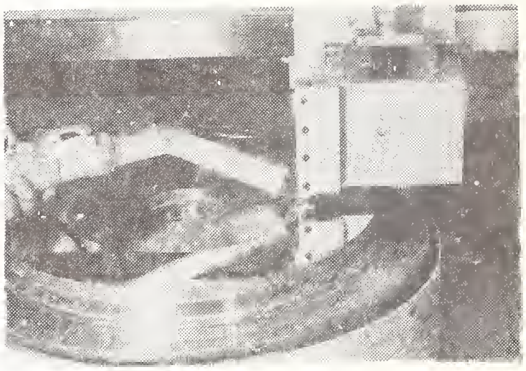

Figure 2. Diamond-turning of a tin plate like a mirror.

Figure 3. Cutting a spiral groove on a tin lap with a high speed steel tool.

Figure 4. Final cut of the tin lap with a diamond tool.

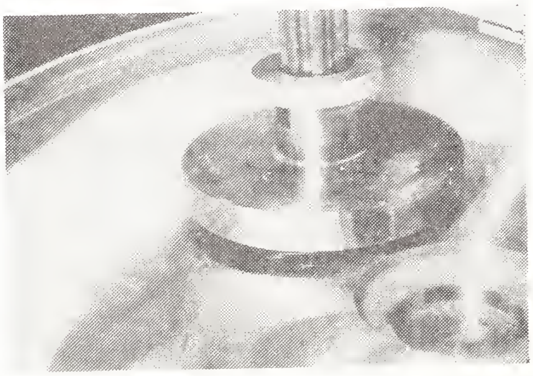

Figure 5. Actual condition of float polishing of 3 samples of 76 mm in diameter at a time.

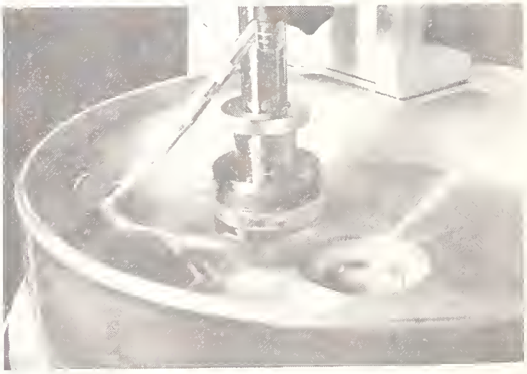

Figure 6. Actual condition of float polishing of a BK-7 glass sample of 100 mm in diameter.

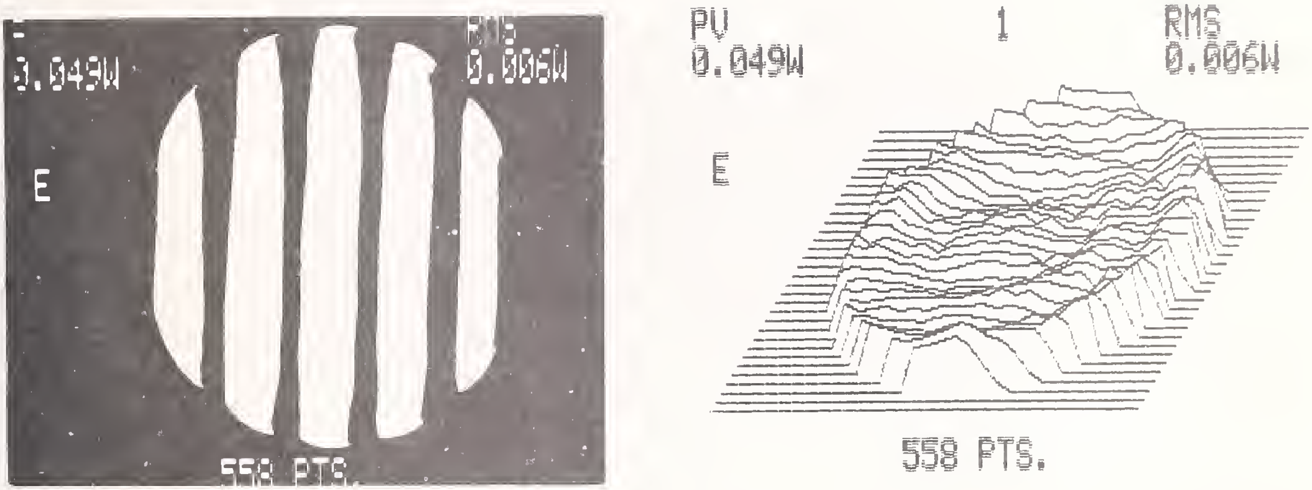

Figure 7. Flatness of a float-polished BK-7 glass sample of 100 mm in diameter, measured with Zygo Mark III, Phase Measuring Interferometer System.

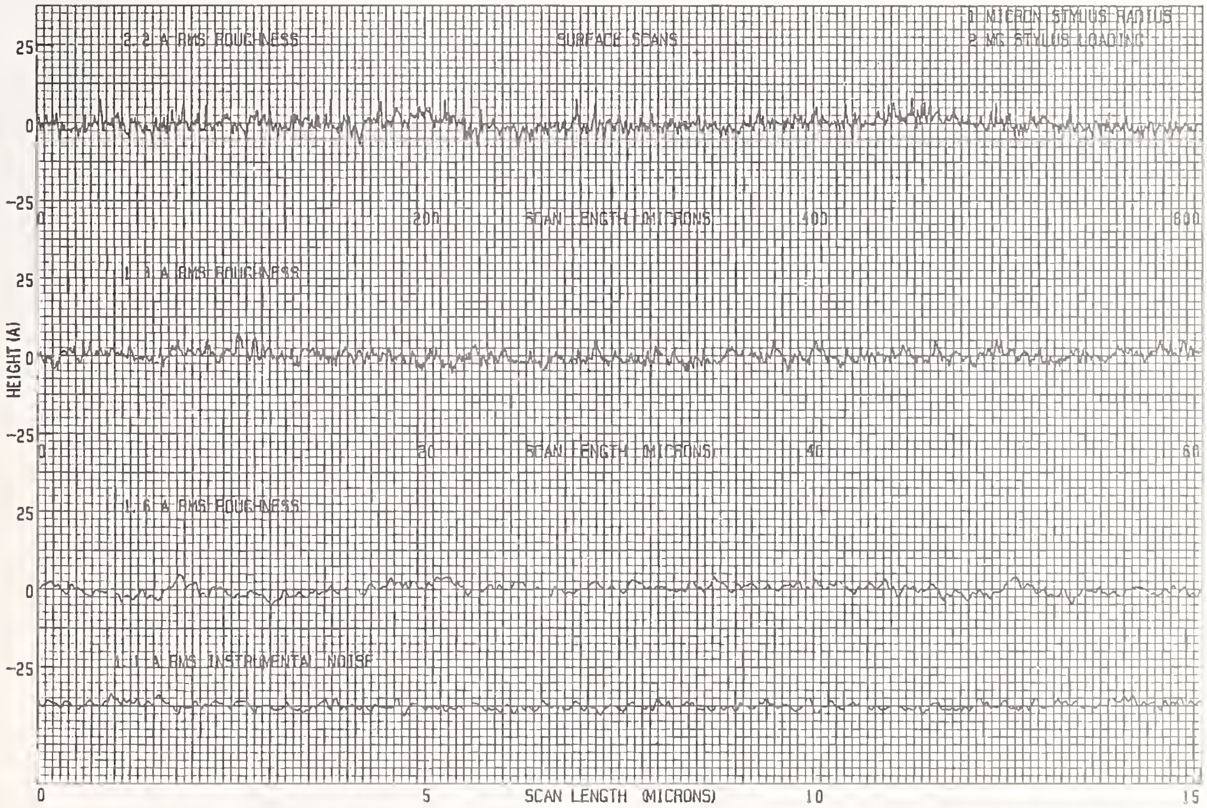

Figure 8. Surface profile of a float-polished fused silica sample, measured by J. M. Bennett with Talystep.

Figure 9. Nomarski micrograph of well-polished fused silica [1] after 5 minutes etching with 5 % HF.

Figure 10. Nomarski micrograph of laser damaged site on the fused silica sample polished by VTI, Inc., taken with Nikon Optiphot (Two arrows indicate pits after 5 minutes etching with 5 % HF).

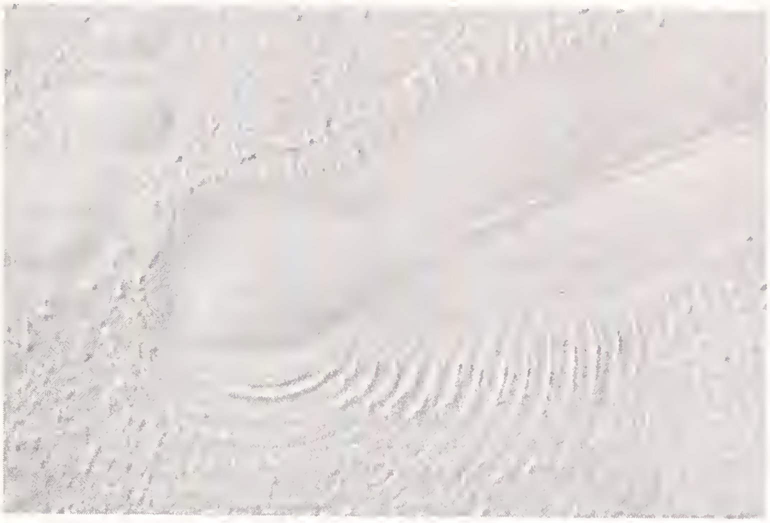

(a) After laser irradiation

(b) After first etching using 5 % HF for 5 minutes

(c) After second etching using 25 % HF for 5 minutes

Figure 11. Nomarski micrograph of a laser damaged site on the polished fused silica [14].

Effect of Surface Finishing on the Damage Threshold of Fused Silica at 1.06μm*

H. Vora

Honeywell Corporate Technology Center
10701 Lyndale Avenue South
Bloomington, Minnesota 55420

and

W.H. Lowdermilk and J.E. Swain

Lawrence Livermore National Laboratory
University of California
P.O. Box 5508, L-470
Livermore, California 94550

In an effort to determine the effect of surface finishing on the damage threshold of fused silica at 1.06 μm, several fused silica samples were polished mechanochemically using $SrCO_3$, MgO and NiO slurry, and colloidal silica as polishing media as well as mechanically using 0.3μm sapphire abrasive. Employment of a hard abrasive, such as sapphire, in polishing of fused silica introduces scratches and subsurface microfractures, which are not observed in mechanochemically polished samples of fused silica because the material removal in mechanochemical polishing occurs through chemical reactions which are activated by application of pressures during polishing. This paper describes various mechanochemical polishing techniques used to prepare fused silica surfaces as well as the results of damage threshold measurements made on mechanochemically and mechanically polished samples of fused silica using 1-ns, 1.06-μm laser pulses.

Key words: Fused silica; mechanochemical polishing; 1-ns, 1.06-μm damage.

1. Introduction

Earlier measurements of the surface damage thresholds for 1-ns, 1.06-μm laser pulses for a series of BK-7 and fused silica samples whose surfaces were prepared principally by polishing on a pitch lap using a slurry of cerium oxide in water have yielded the median value of 16 J/cm^2, which is two to three times lower than the bulk damage thresholds of these materials [1][1].

Recently, it has been shown by Temple, et al. [2] that the damage threshold of mechanically polished fused silica surfaces can be increased to a value comparable to the bulk value by carbon dioxide laser polishing. Two possible explanations were given for the observed increase in the surface damage threshold of fused silica by carbon dioxide laser polishing: vaporization of the absorbing impurities (polishing compounds, etc.) from the mechanically polished surface and healing of surface and subsurface microfractures introduced by conventional grinding and polishing processes.

The objective of this work is to determine if the surface damage threshold of fused silica can be improved by mechanochemical polishing. The material removal in mechanochemical polishing occurs through chemical reactions between the workpiece and the polishing medium and as a result of this, fused silica samples free of scratches and subsurface microfractures are relatively easy to obtain using this technique. If the measured damage threshold values of conventionally polished fused silica surfaces are lower than the bulk due to the presence of surface and subsurface microfractures, then significant improvement in the surface damage threshold of fused silica can be realized by mechanochemical polishing. However, if the damage threshold of bare fused silica surfaces is limited by the presence of absorbing impurities in the polished surface, then mechanochemical polishing may not have a significant effect on the surface damage threshold of fused silica. The reason for this is that, except for the employment of higher pressures in mechanochemical polishing,

---

* Work supported by the Lawrence Livermore National Laboratory under Contract #7298101.

[1] Numbers in brackets indicate the literature references at the end of the paper.

the mechanochemical polishing is performed in a manner very similar to the conventional polishing. In both techniques, the workpiece surface is in intimate contact with the lap surface and the polishing medium during polishing. Because of this, the absorbing impurities (which can be polishing compound itself or some impurities present in the polishing compound and lap) are as likely to imbed in the mechanochemically polished samples as in conventionally polished samples.

2. Results and Discussion

Damage threshold measurements for 1-ns, 1.06-μm laser pulses were made on four sets of fused silica samples; each set consisting of three samples which were polished simultaneously. One set was polished mechanochemically with colloidal silica to completely remove scratches and subsurface microfractures introduced by previous grinding and lapping operations. This was verified by Nomarski microscopic examination of the polished surfaces after etching in a 5% HF acid solution. The remaining three sets were similarly polished with colloidal silica initially. Subsequently, one set was polished with a slurry of NiO and MgO in water, another was dry mechanochemically polished with $SrCO_3$, and the third set was polished with 0.3μm sapphire. Scratches and subsurface microfractures were observed in fused silica samples polished with sapphire, but not in those polished with $SrCO_3$ or the slurry of NiO and MgO in water. The hardnesses on Mohs scale of $SrCO_3$, NiO, MgO and Al_2O_3 are respectively 3.5, 5.5, 5.5 and 9 as compared to Mohs hardness in the range of 5.5-6.5 for fused silica. Nomarski micrographs taken before and after HF etching of mechanochemically polished surfaces of fused silica are shown in figure 1.

All fused silica samples used for damage threshold measurements were polished on a polyurethane impregnated polyester lap, which restricts flatness to 1/2-1 light band per centimeter of the polished surface. Measurements were made of the removal rates obtained by mechanochemically polishing fused silica on this lap using $SrCO_3$, MgO and NiO slurry, and colloidal silica as polishing media and the following parameters: pressure, 1.4×10^4 N/m^2; lap diameter, 25cm; lap rpm, 50; and stroke frequency, 30cpm. The data on material removal rates are shown in figure 2 and figure 3, where it is seen that the measured removal rates are 0.3μm/hr for $SrCO_3$, 6μm/hr for colloidal silica and 8μm/hr for NiO and MgO slurry.

The results of damage threshold measurements are summarized in table 1, where it is noted that the exit surface damage thresholds for 1-ns, 1.06-μm laser pulses for all mechanochemically polished fused silica samples lie in the range of 10-17 J/cm^2, which is only marginally higher than the range of 9-11 J/cm^2 measured for fused silica samples polished with 0.3μm sapphire. These results are comparable to those for surfaces polished with cerium oxide. Thus, the process of simply eliminating surface and subsurface microfractures through mechanochemical polishing is not by itself effective in significantly raising the damage threshold of fused silica.

Table 1. 1-ns, 1.06-μm Exit Surface Damage Thresholds of Various Fused Silica Samples

Set	Polishing Medium: Initial	Polishing Medium: Final	Damage Threshold (J/cm^2)
1	colloidal silica	-	16.8 ± 1.8 11.5 ± 1.2 9.7 ± 1.0
2	colloidal silica	$SrCO_3$	16.8 ± 1.9 14.4 ± 1.5 11.8 ± 1.4
3	colloidal silica	MgO & NiO	13.8 ± 1.8 10.4 ± 1.0 10.2 ± 1.0
4	colloidal silica	0.3μm sapphire	11.0 ± 2.6 9.7 ± 1.0 9.3 ± 1.0

The authors would like to thank Drs. K.D. McHenry and B.G. Koepke of the Honeywell Ceramic Center for suggesting $SrCO_3$ compound for mechanochemical polishing of fused silica.

3. References

[1] Lowdermilk, W.H., Milam, D. and Rainer, F., in Laser Induced Damage in Optical Materials: 1979, (NBS Special Publication 568), Bennett, H.E., Glass, A.J., Guenther, A.H. and Newnam, B.E., Eds., p. 391 (1980).

[2] Temple, P.A., Lowdermilk, W.H. and Milam, D., Appl. Opt. 21, 3249 (1982).

(a) (b)

Figure 1. Normarski micrographs of a mechanochemically polished sample of fused silica taken (a) before and (b) after etching.

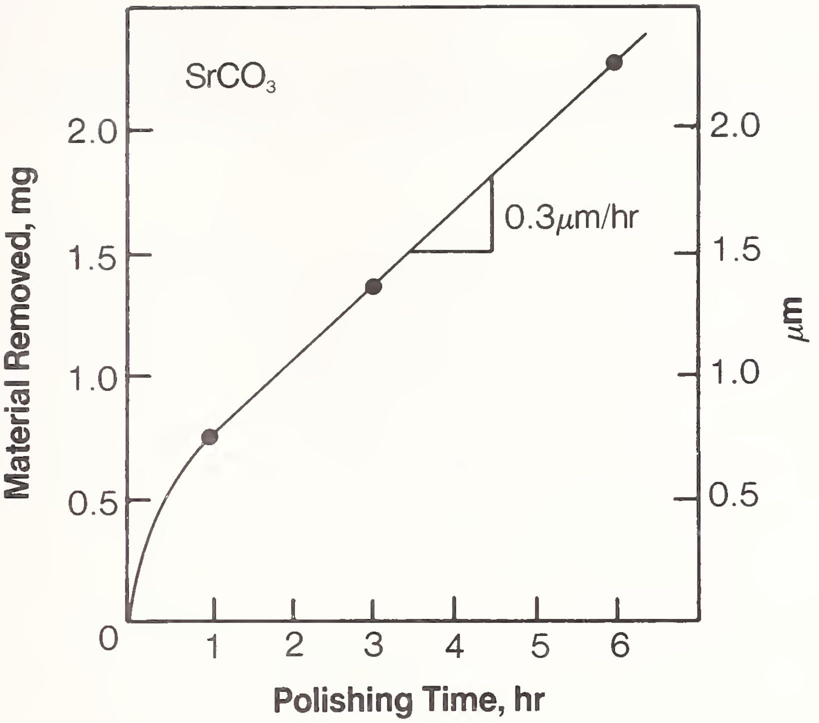

Figure 2. Weight loss of fused silica during dry mechanochemical polishing with $SrCO_3$.

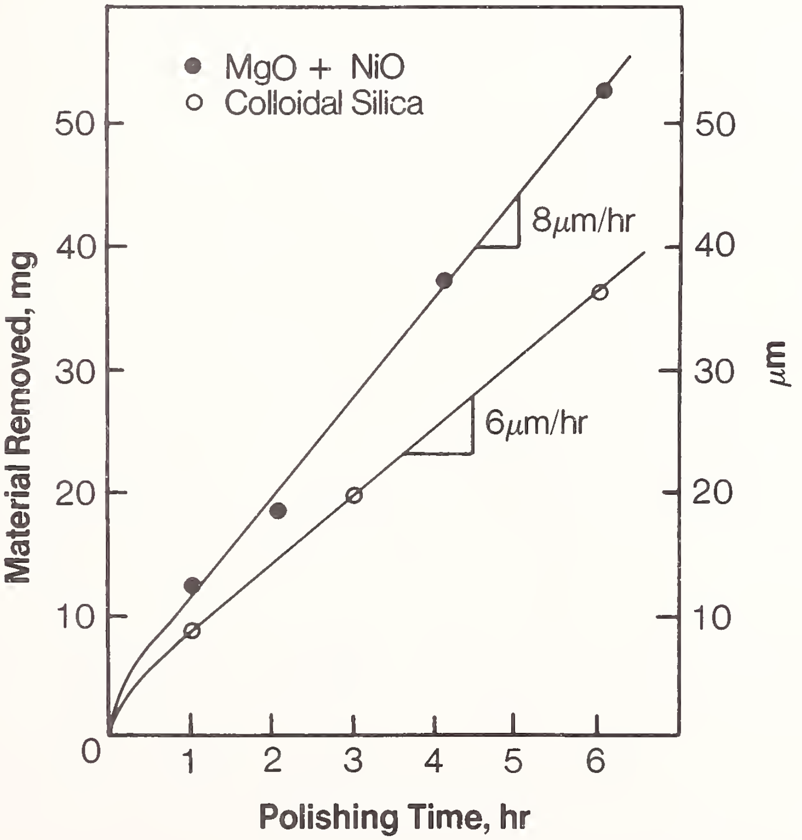

Figure 3. Weight loss of fused silica during mechanochemical polishing with slurries of colloidal silica and NiO and MgO.

The speaker was asked if surface roughness had been measured, and whether the surfaces had been damage tested at $\lambda = 355$ nm. He replied that neither of these measurements was made. In further comments, both by the speaker and from the audience, the beam used in the damage measurements was reported to be 2-3 mm in diameter, and previous tests of CO_2-polished surfaces were cited as evidence that surface damage thresholds could feasibly be as large as 30-50 J/cm^2 for 1-ns, 1064-nm pulses.

SCRATCH STANDARDS SHOULD NOT BE USED TO PREDICT DAMAGE THRESHOLD

Matt Young
Electromagnetic Technology Division, 724.02
National Bureau of Standards
Boulder, Colorado 80303

The scratch and dig standards are the most widely used surface quality standards in the industry. In the proceedings of the 1980 symposium, Harold Bennett showed theoretically that damage ought to be initiated near a defect and related damage threshold to defect size. Evidently because of one or both of these facts, some purchasers may use the scratch standards to specify the surface quality of components intended for high power laser systems. Although damage is often associated with the presence of a defect, this is an inappropriate use of these purely cosmetic standards; the classification of a particular scratch correlates only very loosely with its width or depth. Even if a component is made of glass, little or nothing pertinent to damage threshold may be determined by classifying a scratch according to the cosmetic standards.

Keywords: Laser optics; scratch-dig standards; surface specification.

Laser induced damage to optical surfaces is at least sometimes associated with the presence of a defect on the surface, and Bennett has shown that the threshold for such damage ought to be related to the defect's size and absorption coefficient.[1] In part for this reason, designers of high power laser systems might be tempted to use the scratch and dig standards for specifying optical surface quality.

This would be an improper use of those standards.

The classification of a dig is based on the diameter of the dig; however, the classification of a scratch is based on its visual appearance compared with that of a master standard (Fig. 1). Because of the complexity of the cross section of most scratches, classification, or scratch number, correlates only very loosely with easily measurable quantities such as depth or width. Inasmuch as width is the parameter singled out by Bennett for estimating damage threshold, I anticipate that scratch number will correlate equally loosely, if at all, with damage threshold.

Objective Measurements on Scratch Standards

Because of the difficulty of specifying and procuring standards based on their visual appearance, the National Bureau of Standards has taken on a project to perform objective measurements on sets of standard scratches. The purpose of the project is to enable the contractor to specify the scratches in terms of a more objective criterion than visual appearance. Nevertheless, for the forseeable future, the standard itself will remain a cosmetic one in that optical surfaces in the field will still be compared visually with the standards. Only the standards will be evaluated photoelectrically.

Figure 2 shows the polar scanning apparatus used to examine the scattering patterns of the scratches. The unique aspect of this system (which is described more fully in Ref. 2) is the presence of a pupil, or virtual stop, at the location of the scratch; the pupil is the image of the aperture stop and guarantees uniform illumination in the plane of the scratch.

I also examined the scratches with an optical processor set up for high pass filtering, or edge enhancement. Although the purpose of this experiment was to examine ways of visualizing cosmetic defects, I also placed a fine slit in the image plane and measured the intensity scattered by each of several sets of scratches. This measurement is akin to total integrated scatter (TIS), except that these measurements include only angles between about 0.03° and 4° (an effective F number of about 7).

Finally, the geometrical cross section of the scratch provides depth and width information with which to compare the results of scattering measurements.

Experimental Results

This paper is a by-product of the investigations of the scratch standards; I will report only on experimental measurements germane to the subject at hand.

After examining the polar scans of five sets of certified scratches, my colleague, theorist Eric Johnson, and I restricted our consideration to the range between 5 and 10°. Figures 3a and 3b show on an arbitrary scale the relative intensity scattered by the scratches as a function of scratch number (10, 20, 40, 60, and 80). The open circles represent the average values, and the closed circles represent the highest and lowest values in each set of measurements. Data shown are distilled from angular scans that covered the range from -30° to 30°.

The figures show considerable correlation between scratch number and scattered intensity, but also much overlap, especially at the angle of 10°.

The optical processing experiments show roughly similar results -- rough correlations with a good deal of scatter. For example, Fig. 4 plots relative intensity as a function of scratch number, width and depth.

Depth and width plotted as functions of scratch number (Fig. 5) show more scatter for the numbers 10 and 80 scratches than for the other designations; this is in part because some of the other scratches appear to have been made with the same stylus and are nearly indistinguishable. The two anomalous number 80 scratches also are nearly indistinguishable.

Figure 5b, by the way, shows that the width of a given scratch is not equal to one tenth the scratch number, although you will often hear that claimed.

Conclusions

It would be easy to say that the scratch number has nothing whatsoever to do with any observable property of the scratch and thereby get a good laugh. But the statement has the disadvantage of being untrue. What is true, however, is that all the data show a great deal of scatter, so much that close to half the scratches with a given classification could just as easily have been given the next lower or higher classification. In addition, scratches are made of glass and viewed in transmission; scratches in some other material (which usually has a greater index of refraction) and scratches viewed in reflection usually look far worse. If I were buying parts for a high power laser, I would hate to rely on such a loose standard for avoiding catastrophic damage to my components.

The scratch standards are cosmetic standards and do not pretend to be anything else. Let us leave them to those people who are legitimately concerned with cosmetic defects and find proper performance standards for opticists concerned with damage threshold.

Acknowledgements

Mrs. Shelley Etzel carried out the tedious profilometer measurements admirably. Dr. Eric Johnson was a great help and sometimes a great comfort during most phases of this project. The work was supported in part by Calibration Coordination Group, Department of Defense, and by the U.S. Army Armament Research and Development Command.

References

1. H. E. Bennett, Insensitivity of the Catastrophic Damage Threshold of Laser Optics to Dust and Other Surface Defects, in Laser-Induced Damage in Optical Materials: 1980, National Bureau of Standards (U.S.) Spec. Pub. 620 (1980), 256-263.

2. M. Young, Objective Measurement and Characterization of Scratch Standards, Proc. SPIE, Vol. 362, in press.

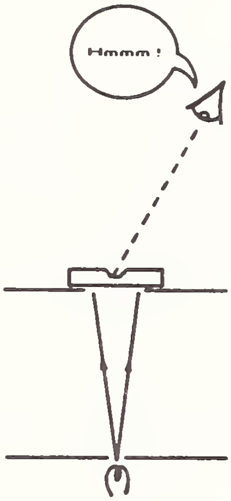

Figure 1. The scratch standards are purely cosmetic.

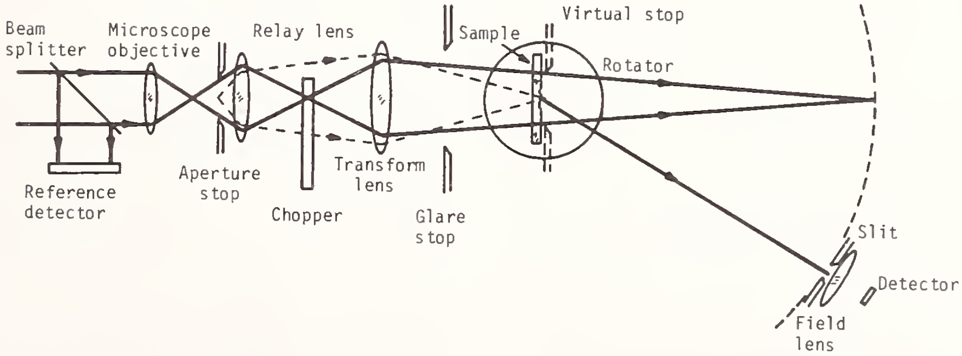

Figure 2. Apparatus used to determine scattering as a function of angle (after Ref. 2).

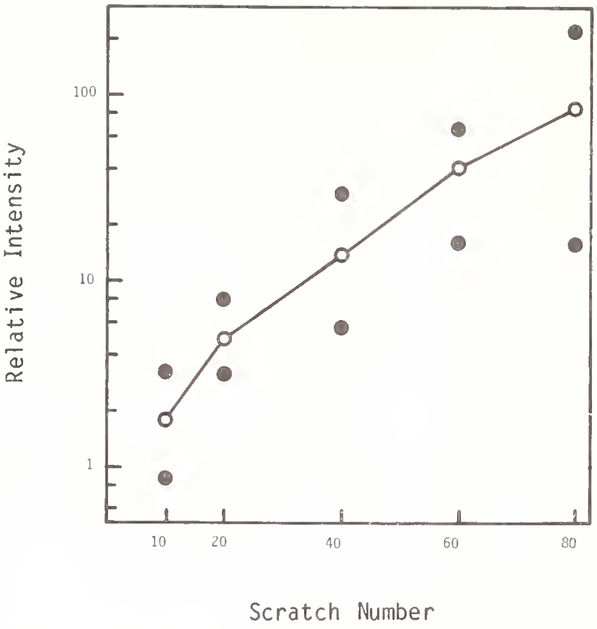

Figure 3a. Intensity scattered at 5° off axis as a function of scratch number. The open circles show the average of five sets of scratches; the closed circles are highest and lowest recorded values.

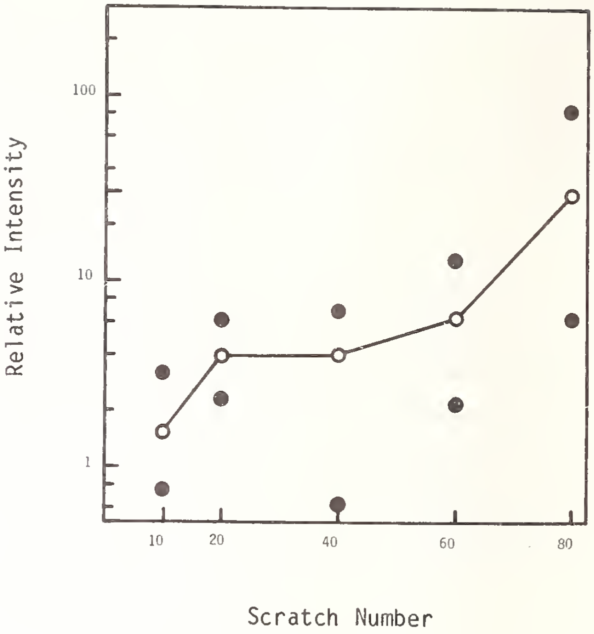

Figure 3b. As Fig. 3a, but data taken at 10° off axis.

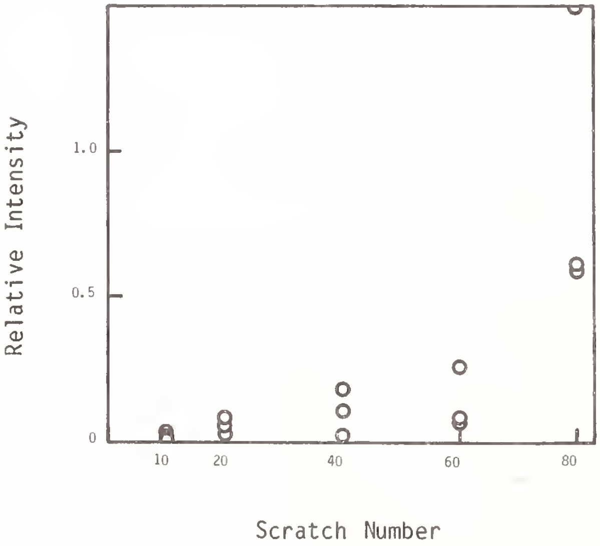

Figure 4a. Intensity scattered into F/7 cone (~4°) as a function of scratch number for three sets of scratches.

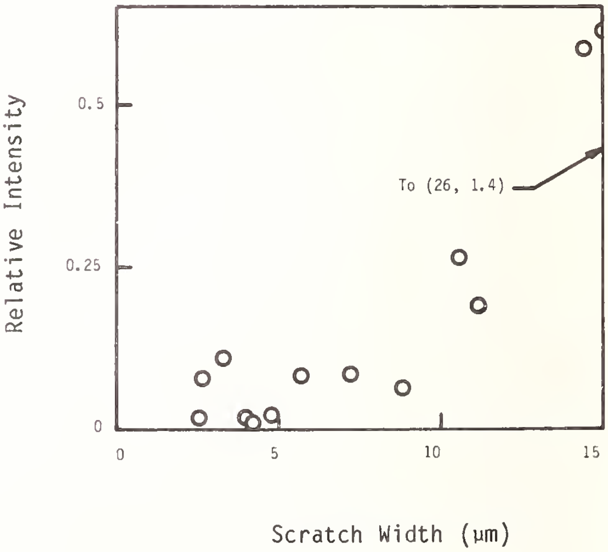

Figure 4b. Data of Fig. 4a as function of measured scratch width. The arrow indicates one extreme point that is not shown on the graph.

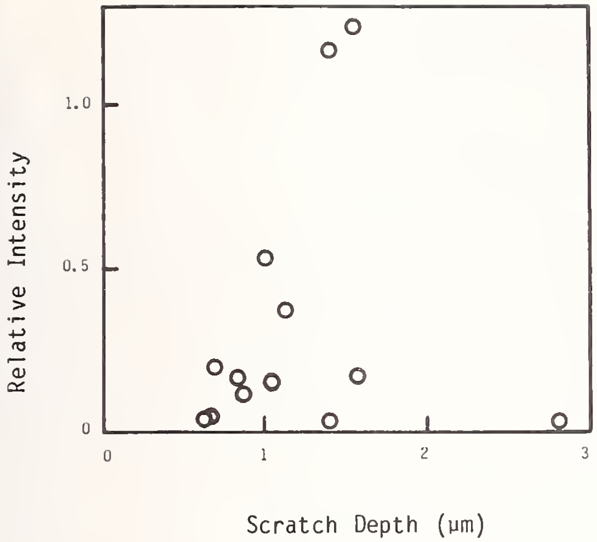

Figure 4c. Data of Fig. 4a as function of measured scratch depth.

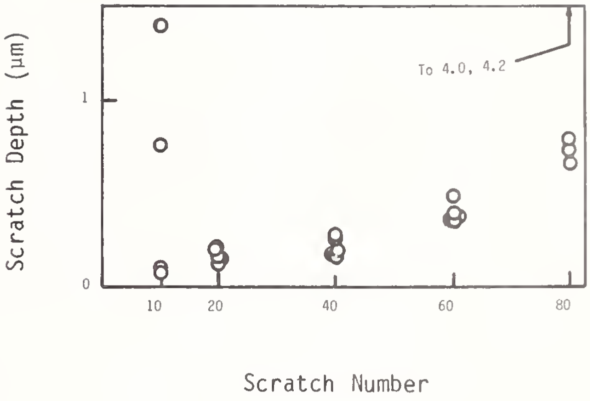

Figure 5a. Measured scratch depth as function of scratch number for five sets of scratches. The arrow indicates two extreme points that are not shown on the graph.

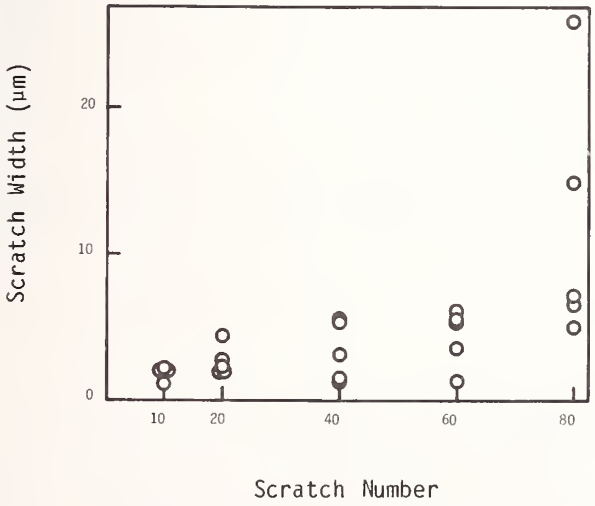

Figure 5b. Measured scratch width as function of scratch number for five sets of scratches.

Those commenting on the paper agreed that scratch-dig specifications were imprecise measures of surface quality, and the speaker suggested that an objective surface roughness standard was needed.

Bulk and Surface Damage Thresholds of Crystals and Glasses at 248 nm*

F. Rainer, W. H. Lowdermilk, and D. Milam

Lawrence Livermore National Laboratory
Livermore, CA 94550

We used 20-ns, 248-nm pulses to study surface and bulk damage in bare, polished samples of UV-transmitting glasses, fluoride crystals and isomorphs of potassium dihydrogen phosphate (KDP). The intent was to test enough samples to establish the safe operating limits for currently available windows and crystals finished by routine techniques for optical fabrication. In fluoride crystals, thresholds for bulk inclusion damage and for rear-surface damage were comparable. The median rear-surface threshold was 16 J/cm^2. The fluence limit in fused silica windows was determined by the threshold for rear-surface damage, which ranged from 5 to 9 J/cm^2. For the isomorphs of KDP, the limiting fluence was the threshold for front-surface damage, which ranged from 3 to 9 J/cm^2.

Key words: damage; fluoride crystals; KDP isomorphs; laser-induced damage; UV glasses.

1. Introduction

Continued interest in the use of short-wavelength lasers as drivers for inertial confinement fusion experiments stimulated us to study the laser damage thresholds of many UV transmitting materials. In this paper we present the results of damage tests conducted on bare, polished surfaces and bulk materials at 248 nm using 20-nsec, p-polarized laser pulses.

2. Experimental Procedure

We used a discharge-pumped KrF laser to irradiate the samples. Typically, the beam diameter (e^{-2} in intensity) at the sample was 1.5 mm, but the beam contained intensity spikes which were as small as 0.1 mm in diameter (at 90% of peak fluence). For each shot, the absolute fluences in the sample plane were computed through analysis of a photographic image of the intensity distribution in the beam.

From 7 to 20 sites were tested on each sample with each site being irradiated only once. The samples were mounted on a two-position rotating stage which allowed the test site to be moved from the irradiation station in the beam line to the field of view of a Nomarski microscope. Test sites were photographed, at magnifications of 100 to 420, before and after each shot. The samples were also visually inspected with a microscope, and with the unaided eye using intense white light illumination.

Laser damage was defined to be a permanent alteration on the surface, or in the bulk, that could be detected by these examinations. Threshold was defined to be the average of the highest nondamaging fluence and the lowest damaging fluence. Details of these techniques are described in detail elsewhere [1], [2].

3. Experimental Results

3.1 UV Glasses

Fused silica (polished with abrasives that consist largely of CeO_2) is routinely used in fabrication of UV-transmitting windows and lenses. Figure 1 gives the thresholds for six samples of fused silica and one sample of a UV-transmitting glass, UVFK54. Sample 4 was tested three times, once as received from the vendor (data set 4A) and twice after it was repolished with high-purity ZrO_2 (data sets 4B and 4C, which are discussed below). Arrows plotted in figure 1 indicate that thresholds were only determined to be greater or less than the plotted value. Bulk damage was a limiting problem only in UVFK54, in which color centers were formed in single shots

---

*Work performed under the auspices of the U.S. Department of Energy by the Lawrence Livermore National Laboratory under contract W-7405-ENG-48.

at fluences as low as 2 J/cm^2. Bulk damage, consisting of self-focusing tracks that emanated from the rear surface, occurred in the UV7940 sample, but only at fluences greater than the threshold for rear surface damage. For all Suprasil samples, the bulk thresholds were greater than either front-surface or rear-surface thresholds.

For conventionally polished samples of fused silica (data sets 1,2,3,4A and 6; Fig. 1), the maximum operating levels were set by the threshold for rear-surface damage, which ranged from 5 to 9 J/cm^2. Since we do not know how 248-nm surface-damage thresholds are influenced either by polishing compounds and procedures or by surface cleanliness, two additional experiments were performed. One surface of sample 4 was repolished with high-purity ZrO_2. This surface was retested twice (data set 4B), once as a front surface and once as a rear surface. Within experimental uncertainty, thresholds were unchanged (or perhaps slightly reduced). However, during these repeat tests, low thresholds (data set 4C) were observed for the surface of sample 4 which had not been repolished. We can only speculate that this resulted from surface contamination. We also tested one surface that had been repolished using a bowl-feed process (front surface of sample 5); its threshold was below the front-surface thresholds of conventionally polished surfaces included in these tests. Although positive results were not obtained in these two attempts to increase surface damage thresholds, we believe thresholds might be improved by additional study because the bulk threshold of fused silica is not a limiting problem.

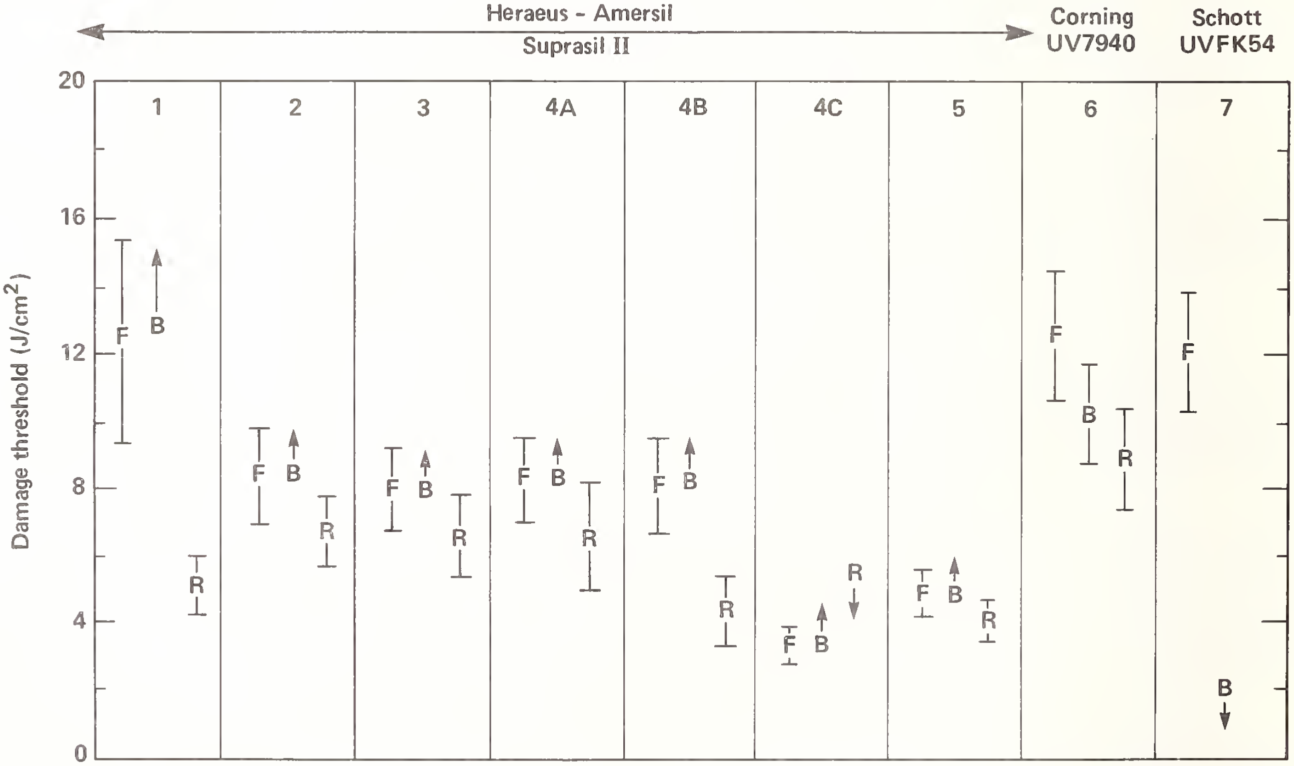

Figure 1. Laser damage thresholds of UV glasses for 248-nm, 20-ns pulses. The letter designations are F for front surfaces, B for bulk material, and R for rear surfaces.

3.2 Fluoride Crystals

Because they have good UV transmission, fluoride crystals are candidate materials for use in 248-nm lasers. We tested 6 single-crystal samples of LiF, and 13 fine-grained polycrystalline LiF samples made by press forging. Both types of samples were cut from 4 different boules to avoid biasing the data to the characteristics of an individual boule. Figure 2 shows damage thresholds for each sample, and the median threshold for each group of samples. We were unable to determine the threshold for rear-surface damage in the single-crystal samples because the surfaces had a high density of residual polishing scratches. The experimental arrangement allows preshot and postshot microscopy of the entrance surface, and minor damage can be detected on even a structured surface. Damage on exit surfaces was detected by independent microscopic examination of the surface following completion of the experiment, and minor damage could not always be distinguished from pre-existent surface structure.

The data in figure 2 indicate that bulk damage is a limiting problem in LiF. The median threshold for bulk damage was only slightly greater than the threshold for rear-surface damage. The bulk damage consisted of starburst-type fractures with 4 orthogonal rays. The number and sizes of these fractures did not always scale with fluence, and in some cases the spacing of the fractures was comparable to the diameter of the laser beam. This suggests that the damages were caused by isolated defects or inclusions, and that use of a larger beam, or testing of more sites, might have located volumes with lower thresholds. However, no one boule yielded crystals with predominantly high or low thresholds, although thresholds of the single-crystal samples were 40% greater than thresholds of forged crystals. Therefore, the data set taken as a whole suggests that the bulk material in randomly selected LiF crystals will be resistant to damage at fluences up to 16 J/cm^2, and that forged crystals will survive 10 J/cm^2. Median bulk thresholds should be higher, 26 J/cm^2 for single crystals and 18 J/cm^2 for forged samples.

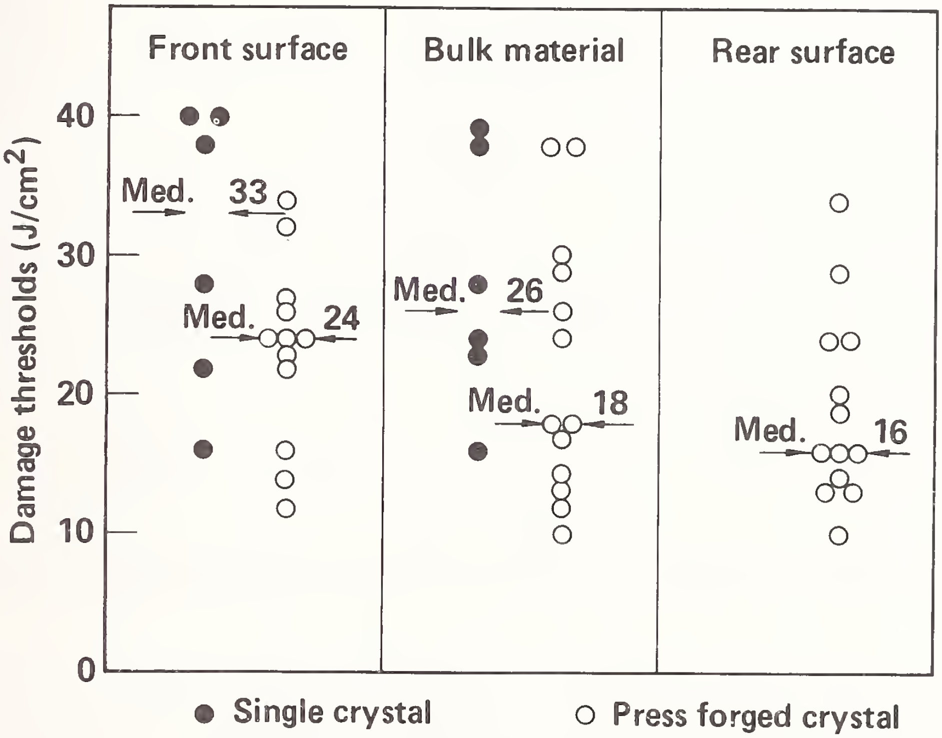

Figure 2. Damage thresholds of 6 single LiF crystals and 13 press-forged LIF crystals for 248-nm, 20-ns pulses.

The surfaces of the single crystals and the forged samples exhibited a common damage morphology. At threshold, damage produced a spatially uniform alteration of the surface. In microscopic examinations with bright field illumination, these damages were visible as areas with different surface luminosity, which suggests that the surface had been locally smoothed or melted. When examined with Nomarski microscopy, the damaged areas were also visible, indicating that surface height as well as surface texture was altered. As the incident fluence was increased, the shape and size of the damage increased proportionally. At fluences well above threshold, surface damage in the forged crystals consisted of a surface array of orthogonal cracks and of isolated surface pits. It is possible that some surface pits resulted from fracture of material around inclusions located near the surface. Further, our studies of surface damage in LiF proved to be somewhat irrelevant because bulk thresholds for these materials were low.

We also tested 3 CaF_2 crystals and one sample each of MgF_2, BaF_2 and NaF. Thresholds for these samples are given in figure 3. To allow easy comparison of thresholds of all fluorides tested, we also give in figure 3 the median threshold and spread of thresholds of the LiF crystals. Only for MgF_2 and NaF did the bulk threshold for damage exceed the threshold for front-surface damage. Except for one CaF_2 crystals, which had an unusually low threshold, and the BaF_2 crystal, rear-surface thresholds of these additional fluorides are comparable to those of LiF crystals.

The threshold surface-damage morphology varied for each sample, but in general consisted of a highlighting of existing surface defects and polishing scratches. A subjective assessment of laser-induced fluorescence, as judged by the naked eye, was made for all samples. No fluorescence was observed in the MgF_2 sample and only a slight amount in the others. This is perhaps relevant since the MgF_2 crystal had good bulk damage resistance. In magnitude of fluorescence the materials, ranked in the order (low to high): MgF_2, LiF_2, NaF, BaF_2 and CaF_2.

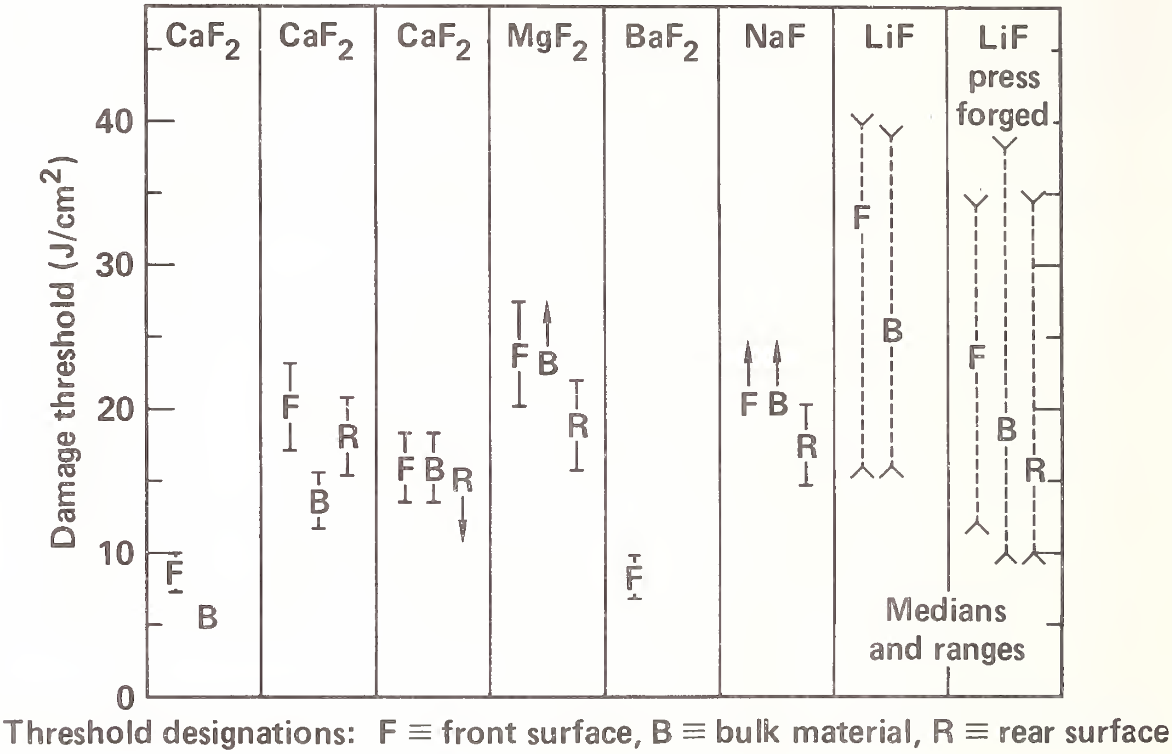

Figure 3. Laser damage thresholds of fluoride crystals for 248-nm, 20-ns pulses.

Three of the samples, one each of MgF_2, BaF_2 and CaF_2, had been tested earlier using 266-nm pulses with durations of 100 and 700 psec [3]. A plot of those thresholds, together with the current 20-ns, 248-nm thresholds is shown in figure 4 as a function of pulsewidth. The slopes of the straight-line fits to these few data points indicate the front-surface thresholds scale as the square root of the pulsewidth.

3.3 Isomorphs of KDP

Damage thresholds of KDP and its isomorphs are of general interest since these crystals are routinely used to produce fourth-harmonic 266-nm radiation from input 1064-nm pulses. Since thresholds at 248 nm and at 266 nm should be approximately equal, we tested four potassium dideuterium phosphate (KD*P) crystals, and one crystal each of KDP and of aluminum dihydrogen phosphate (ADP). Front surface thresholds of these crystals, shown in figure 5, ranged generally from 3 to 5 J/cm^2 although the threshold of the KDP sample was greater than 6 J/cm^2. This can be compared with the surface threshold of a KDP crystal that was measured earlier with 0.7-nm, 266-nm pulses, 6.5 + 1.4 J/cm^2 [3]. Therefore, the available data suggest that UV thresholds of KDP are rather constant over the range of pulse durations from 0.7 ns to 20 ns. If this result is generally true, it will severely limit use of KDP in frequency quadrupling of long duration 1064-nm pulses.

These crystals are mechanically soft and difficult to polish, and all surfaces tested had a high density of polishing scratches that could be observed with a Nomarski microscope. With minor exceptions, all crystals had similar damage morphologies. At fluences slightly above threshold, damage consisted of diffuse alterations of surface texture and depth, somewhat like the uniform surface damage described above for LiF. The surface alteration accentuated the appearance of scratches on KDP and KD*P, but actually masked the scratches on ADP. Damage in KDP and ADP was always accompanied by the faint emission of white light. The KD*P samples did not emit light except at fluences 2-3 times greater than threshold. At approximately 20 J/cm^2, in all crystals, front surface damage sites contained linear cracks, and at higher fluences, jagged pieces of crystal were broken off the surface.

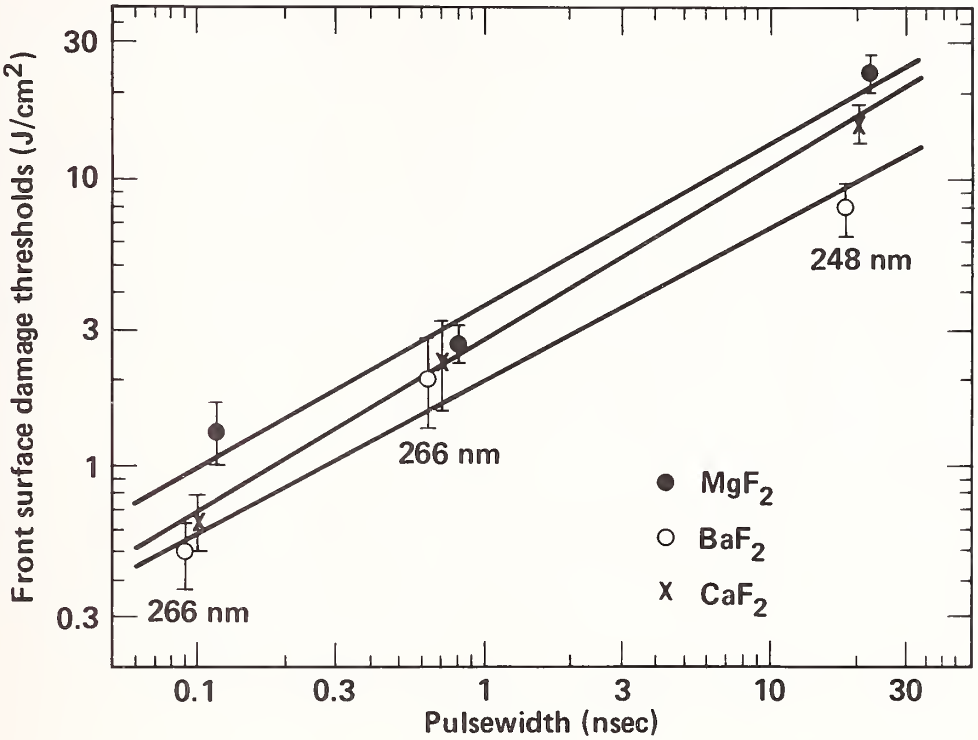

Figure 4. Pulsewidth dependence of front-surface laser damage thresholds of fluoride crystals in the UV.

We presented only front-surface thresholds in figure 5, because we were unable to produce bulk damage or rear-surface damage in these crystals, except at fluences well above the front-surface threshold. This is unusual, since intensity at the rear surface of a transparent window is greater than intensity at the front surface by the ratio $I_{rear}/I_{front} = 4n^2/(n+1)^2$, where n is the refractive index [4]. KDP is mildly birefringent; its 248-nm indices of refraction are approximately 1.52 and 1.56 [5]. Therefore, the intensity ratio was $I_{rear}/I_{front} = 1.47$. Assuming that the rear surfaces were, on the average, as resistant to damage as were the front surfaces, the lack of rear-surface damage implies that the transmission across the sample was $\leq 1/1.47 = 68\%$.

To test this conclusion, we measured transmission in these six crystals as a function of intensity. At very low fluences, the net transmission of KDP and KD*P was approximately 90%, and the loss was primarily due to surface reflectivity. At fluences approximately equal to the damage thresholds (4-10 J/cm^2 delivered in 20 ns), additional intensity dependent losses as large as 20% (averaged across the spatial distribution of the beam) were observed. Since the intensity distribution was highly irregular, this implies that the intensity dependent loss for the intense spikes in the beam was greater than 20%. Transmission of the ADP sample was only 50% even for very low fluences. Nonlinear absorption was not observed in LiF.

The published value of the two-photon absorption coefficients at 266 nm in KDP and ADP are, respectively, $(2.7 \pm 2.0) \times 10^{-10}$ cm/W and $(2.4 \pm 1.8) \times 10^{-10}$cm/W [6]. Using these values, the predicted nonlinear losses in 1-cm thick samples irradiated at intensities ranging from 0.25 to 0.50 GW/cm^2 is 2-20%. Our transmission measurements, supported by the failure to observe rear-surface damage, imply that the 248-nm two-photon absorption coefficients were larger than published 266-nm by a factor of 2-10.

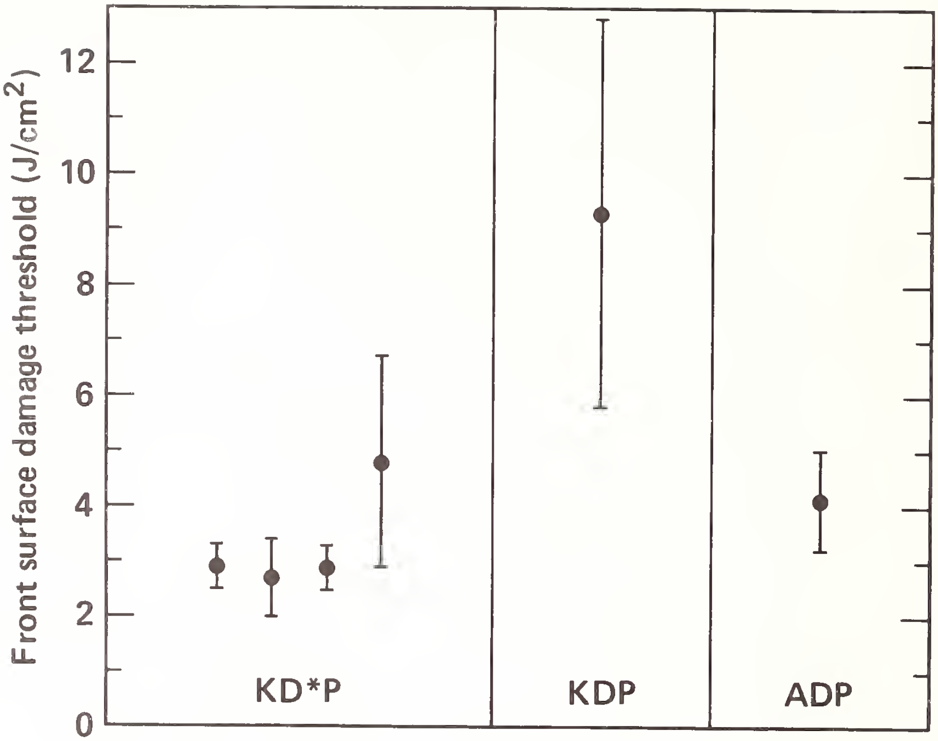

Figure 5. Front surface.laser damage thresholds of KDP isomorphs for 248-nm, 20-nm pulses.

4. Conclusions

We used 20-ns 248-nm pulses to measure laser-damage thresholds of several samples each of UV-transmitting glasses, fluoride crystals and isomorphs of KDP. The safe operating fluence for all fused silica windows that we tested was set by the threshold for rear-surface damage, which ranged from 5 to 9 J/cm^2. These thresholds are comparable to those of the most damage resistant reflective and antireflective 248-nm thin-film coatings [1],[2]. Bulk damage was not a limiting problem in fused silica, but color centers were formed in UVFK54 by single irradiations at less than 2 J/cm^2. Because the bulk of fused silica is damage resistant, improvements in surface damage thresholds are possible, but positive results were not obtained in brief attempts to improve thresholds, either by use of nonabsorbing abrasives or by alteration of the polishing procedure. Further, when one surface of a window was repolished, the threshold of the opposite surface was decreased, presumably due to surface contamination.

In LiF crystals, the threshold for bulk inclusion damage was only slightly greater than the rear-surface threshold. The median rear-surface threshold of forged LiF crystals was 16 J/cm^2; all LiF crystals survived at 10 J/cm^2. Two CaF_2 crystals damaged at comparable levels; the third damaged in the bulk at 6 J/cm. Because the surface thresholds are comparable to bulk thresholds, performance of these crystals cannot be improved by improving the surfaces. In the only samples of MgF_2 and NaF tested, bulk thresholds were greater than surface-damage thresholds which were 17-18 J/cm^2. If these thresholds are representative of the materials, improvements in surface thresholds are possible.

Isomorphs of KDP had entrance-surface thresholds between 3 and 9 J/cm^2, and exhibited nonlinear absorption which prevented damage of the rear surface.

5. References

[1] Rainer, F.; Milam, D.; Lowdermilk, W. H., Laser damage thresholds of thin film optical coatings at 248 nm. Nat. Bur. Stand. (U.S.) Spec. Publ.; (Laser Induced Damage in Optical Materials: 1981) - to be published.

[2] Rainer, F.; et.al., Scandium oxide coatings for high-power UV laser applications. Appl. Opt. 21 (20): 3685-3688; 1982 October 15.

[3] Deaton, T. F.; Smith, W. L., Laser-induced damage measurements with 266 nm pulses. Nat. Bur. Stand. (U.S.) Spec. Publ. 568: 417-424; 1980 July.

[4] Crisp, M.D.; Boling, N. L. ; Dube, G. Importance of fresnel reflections in laser surface damage of transparent dielectrics. Appl. Phys. Lett. 21(8): 364-367; 1972 15 October.

[5] Milek, J. T.; Welles, S. J. Linear electrooptic modulator materials. U.S. Dept. of Comm, Nat. Tech. Info. Service Doc. AD704 556; 1978 January. 177p.

[6] Liu, P.; Smith, W. L.; Lotem, H.; Bechtel, J. H.; Bloembergen, N. Absolute two-photon absorption coefficients at 355 and 266 nm. Phys. Rev. B 17(12): 4620-4632; 1978 June.

PULSED LASER INDUCED OPTICAL SURFACE DAMAGE STUDIES IN DIFFERENT GASES

John Kardach*
Air Force Institute of Technology
Wright Patterson Air Force Base, Ohio 45433

and

Alan F. Stewart and Arthur H. Guenther
Air Force Weapons Laboratory
Kirtland Air Force Base, New Mexico 87117

The pulsed laser induced damage threshold of several optical surfaces has been measured as a function of the pressure and type of ambient gas. Measurements were made in vacuum and various pressures of nitrogen, Freon 14 (CF_4) and SF_6 in an attempt to decrease the growth rate of the avalanche which accompanies pulsed laser induced damage. Test samples included conventional dielectric coatings of ZrO_2, diamond turned copper, bare surfaces of fused silica and ARG-2 glass, and "porous" surface layers of both leached ARG-2 glass and some sol-gel coatings.

From this preliminary study, it is apparent that the ambient gas has no observable effect on 1-on-1 surface damage thresholds (although some improvement in N-on-1 damage levels had been reported). The present finding is in agreement with previous observations that damage sites appear to be initiated on or just below the surface of optical elements. For uncoated surfaces, both conventional and porous, initiation sites seem to be isolated impurities embedded near the surface resulting in the formation of pits. In either case, such damage initiation levels are unmodified by the presence of electronegative gases, and no change in threshold is observed.

Key words: Laser damage; surface; gases; leached surfaces.

Introduction

The present understanding of avalanche breakdown in solids, or more specifically at their surface, has two major deficiencies [1].[1] In the first place, the source for the "seed" or initiating electron is usually not known or specified. Explanations range from cosmic ray induced ionization to easily ionized low-lying impurity states. Secondly, the rate of generation of electrons in a solid phase avalanche process is open to much speculation. Without a deeper understanding of these two facets of the breakdown process, it is impossible to adequately predict when the breakdown process will ensue under a given set of conditions. However, if the concentration of "seed" electrons or the multiplication rate during the avalanche process can be altered by some method, a greater understanding of the total damage process may be revealed or at least parameterized. To this end, we resorted to the potential use of efficient electron scavengers to either modify the seed electron concentration or more probably slow the avalanche growth rate, which leads to the observation of a visible spark. This damage associated spark can efficiently absorb the remaining laser energy, and the ensuing heated plasma reradiate onto the optical surface, producing the catastrophic, irreversible morphologically observed changes in the sample surface.

We have investigated the effect of various electronegative gases on laser induced surface damage thresholds. It is well known that gases such as sulfur hexaflouride can strongly inhibit electrical breakdown in sparkgaps and other discharge devices. Such electronegative gases also exhibit high laser induced breakdown thresholds. If surface damage occurs because of an avalanche process, the close proximity of such an electronegative gas could modify the damage

---

[1] Figures in brackets indicate the literature references at the end of this paper.

*Submitted in partial fulfillment of the Master of Science degree in Physics at the Air Force Institute of Technology, Wright Patterson Air Force Base, Ohio 45433.

process. Although independently suggested, it was discovered during the course of this investigation that an increase in N-on-1 laser damage threshold for porous surfaces immersed in SF_6 had been previously reported in the literature [2]. The objectives of this research effort were to study the effect of electronegative gases on various classes of optical surfaces and carefully parameterize the effect.

Data for this study was obtained using a 1.06μm laser having a 5 nsec FWHM pulse duration. The testing matrix included measurements in vacuum and four or five pressures of three gasses--nitrogen, Freon 14 (CF_4), and SF_6--along with a selection of samples, λ/2 (at 1.06μm) thin films of ZrO_2, diamond turned copper, bare surfaces of fused silica and ARG-2 glass, and "porous" surface layers on leached ARG-2 glass as well as both leached and unleached sol-gel coatings [3].

Experimental

All experiments were conducted with an Nd:YAG laser, beam diagnostics and testing chamber as depicted in fig. 1. The laser and diagnostics are as described in refs. 4 and 5. With good beam quality in a TEM_{ooq} mode, the laser produces a few hundred millijoules in a pulse duration of 5 nsec FWHM. With a magnification of 10X, the spatially resolved beam profile of 175μm ($1/e^2$ radius in intensity) could be reimaged onto a vidicon target for real time measurement. In addition, beam scans were taken throughout the focal volume using a 36μm wide slit and a sensitive pyroelectric detector. The intensity distribution at the sample is obtained from the beam energy, the spatial profile obtained from the vidicon system or beam scans and the temporal profile from a fast biplanar photodiode.

The testing chamber is detailed in fig. 2. The system is cryopumped for operation to 10^{-6} Torr. A gas manifold and accurate capacitance pressure gauges allow for filling the chamber with N_2, CF_4 or SF_6 to pressures up to 2 atmospheres. The sample mount, shown in fig. 2, is designed to provide a full range of motion adjustments by remotely controlled stepper motor drives.

Damage testing was conducted on a variety of sample types. Fused silica surfaces produced by controlled grinding were tested uncoated and with λ/2 thin films of ZrO_2. Commercially available diamond turned copper mirrors and ARG-2 glass were also employed as test specimens. The ARG-2 glass is phase-separable, and half of the samples were acid leached to produce a "porous" antireflective surface layer [6]. The "porous" layer in leached ARG-2 extends several microns or so inside the surface. This is contrasted with a "porous" layer depth of less than a half micron in samples tested with sol-gel coatings. In addition, the sol-gel coatings could be etched to approximately double the average pore diameter, up to 50 Å [7, 8]. These coatings had a measured projected surface area of $10 m^2/gm$ and a composition of $66\ SiO_2 \cdot 18\ B_2O_3 \cdot 7\ Al_2O_3 \cdot 6\ Na_2O \cdot 3\ BaO$ [9]. Pore diameters in leached ARG-2 range up to an order of magnitude larger.

Each sample was dedicated to a particular gas. Experiments began with testing in vacuum at the base pressure of the chamber, typically 5×10^{-6} Torr. Gas pressures used for successive tests were ~ 1, 50, 200, and 600 Torr. The sample surface was allowed to stabilize for about an hour at each new pressure before testing began. Samples were initially cleaned by a standard alcohol-laden lens tissue pull.

Each irradiated site was examined under a Nomarski microscope to determine if damage had occurred. Spark formation was found to be a positive indicator only at fluences well above threshold. At or near threshold, the damage morphology always consisted of a field of one or more small pits in every sample tested.

Because the samples were sealed in an environmentally controlled chamber, it was not efficient to check for damage after each 1-on-1 irradiation. Thus, a set of 30 to 40 ranging exposures were first made, the sample was removed and an initial estimate of the damage threshold was determined. The sample was reinserted, and the remaining exposures were made in the vicinity of the estimated threshold; in all, between 120 and 160 testing events were accomplished for each gas and pressure. Representative examples of the test data are shown in figs. 3 and 4, exhibiting the damage threshold analysis in both J/cm^2 and GW/cm^2.

The definition of damage threshold [5] used in this experiment is given by eq. (1).

$$\frac{E_{\text{threshold}}}{\text{Area}} = \frac{1}{2}\,\frac{E_{\max}\text{ no damage} + E_{\min}\text{ damage}}{\text{Area}} . \qquad (1)$$

This damage threshold represents an average value midway between the defect dominated minimum damage level and the highest nondamaging fluence (presumably approaching the intrinsic value). From figs. 3 and 4, it is very clear that the damage threshold defined in this fashion is an average value. Another figure of merit listed in table 1 is the spread defined by

$$S = \frac{E_{\max}\text{ no damage} - E_{\min}\text{ damage}}{E_{\text{threshold}}} .$$

The spread combined with the damage threshold completely describe data sets such as in figs. 3 and 4.

Results

The data from these experiments representing over 10,000 shots is summarized in table 1. As indicated, the ambient gas had no noticeable effect on surface damage thresholds for the conventional samples tested. From previous observations, it was apparent that damage in single layer thin film coatings seems to be initiated primarily at the substrate-coating interface [5]. Unless the coating is extremely thin or permeable to gases, the surrounding atmosphere would have little effect on threshold pit formation. Similarly, pit formation observed in damage tests on fused silica indicates damage is initiated at the defect or inclusion on or just below the surface. Damage in diamond turned copper also showed pit formation near threshold, even though damage was expected to be purely thermal in origin. Representative near threshold damage sites for each of the seven surfaces tested appear in figs. 5 and 6.

From the data in table 1, it is clear that the ambient gas has no observable effect on surface laser damage thresholds as defined herein. At least this is true for the samples studied and with beam spot sizes of a few hundred microns. The spread in each experiment is larger than any observed charge in threshold. With a larger spot size (≥1mm), it is entirely possible that a sharp threshold with near-zero spread would be observed [10]. Under those circumstances, it might be possible then to measure with confidence a 20 percent increase in damage threshold. However, in these experiments the spread ranges from 0.19 to 1.51--essentially masking any potentially observable effect.

The minimum damaging fluence for a sample is expected to be completely dependent on resident defects. It is important to note, however, that additional defects can be introduced by the measurement technique. Large damage sites can splatter molten material over a wide area. Also, plasma formation in the ambient gas could lead to deposition of contaminants. It was for this reason that SF_6 and CF_4 were chosen as the electronegative gases. The major fraction of SF_6 decomposition is SF_4, a gaseous product. Furthermore, fully flourinated CF_4 leaves no carbon deposits or any observable pressure increase after the passage of an electric arc, while other mixed chlorine or flourine compounds decompose, forming Cl_2 or F_2 [11]. These are important considerations since there is evidence that for certain laser-ambient gas-sample composition (particularly thin films) combinations, there may be chemical reactions, including some in the solid phase, taking place in the presence of optical breakdown [12].

The spacing between sites was 1 mm or larger, which appeared to be adequate to preclude associated damage or other modification of adjacent sites. The sol-gel coatings were not very uniform, and testing at higher pressures involved sites nearest the edge of the substrate (the most troublesome area). The spreads measured in these particular data sets are very large and overlap, precluding any definitive conclusions.

The largest spreads listed in table 1 were measured for the leached surface ARG-2 samples. These surfaces were extremely nonuniform but exhibited definite zones with higher damage thresholds. We can only conclude from this observation that the acid leaching process is not yet sufficiently well controlled. With a large diameter beam of a millimeter or more, this leached surface nonuniformity might average out and become unobservable.

Discussion

The data summarized in table 1 shows that the ambient gas has no observable effect on the surface damage threshold as defined in these experiments. This appears to be in contradiction with data reported by Eron'ko et al. in ref. 2. However, the Russian data dealt with an experiment as contrasted to ours in table 2.

Let's examine table 2 in some detail and discuss the differences between the two experiments and how these differences might affect the results obtained. First, Eron'ko's pulse duration was 70 nsec, while in this work it was 5 nsec FWHM; we would expect that the longer pulse would produce a larger spread in the damage threshold determination as one moves from site to site on the sample. The same increase in spread would be seen from differences in the beam diameter, where the Soviet work was 60μm, while in this work it was 330μm at the $1/e^2$ points. Again, the smaller spot size should lead to a large variability in the damage threshold; however, no comments relative to the spread were given in the cited Soviet reference. The wavelengths were the same in the two cases, but test procedures were different. In the Soviet work the experiment was performed in an N-on-1 mode, while in this work it was 1-on-1. It is certain that preconditioning can play a major role in N-on-1 testing. However, Eron'ko reported that a positive effect was seen from the first irradiation, which means that preconditioning was not a concern and that their results should be similar to this 1-on-1 investigation. The damage threshold definition was also different, but here we feel that the difference is significant. In the Soviet work damage was assessed by the production of a spark and related plasma, while in this work damage was the identification of the formation of pits from Nomarski microscopy. In the Soviet work an improvement in the threshold was noted when surfaces were immersed in an electronegative gas, particularly when those surfaces were porous. No improvement was noticed in this work. These conclusions are not necessarily in disagreement. Furthermore, the affects of variation of the pressure on the damage threshold over the range of 10^{-5} to 600 Torr were also studied. No change in threshold was noticed. The gases were sufficiently similar in the two experiments, with SF_6 being common to both investigations. And finally, samples studied were also sufficiently similar in that in both the controlled grind fused silica, porous coatings, and dielectric thin films were investigated.

The significant difference was in the definition of damage threshold. As was previously stated in this paper, sparks or plasma threshold were only observed at higher radiation levels, well above the threshold for pit formation. One might expect that the sparks produced by an avalanche process to be controlled to some degree by an electronegative gas in which electron generation and loss rates would be affected, and thus it is possible that the Soviets would see a "beneficial" effect. And it might be added that since the catastrophic failure of optical surfaces are primarily produced by the heated plasma accompanying the laser irradiation, one might ameliorate this problem by the use of an electronegative gas. However, on the other hand, if a more meaningful definition of damage is the first observations of an irreversible structural change, then the addition of electronegative gas will not play any major role in modifying a threshold, so defined.

It is unlikely that an N-on-1 experiment can be designed with sensitivity to the formation of individual submicron pits. If we had defined damage threshold in another manner--the occurrence of "uniform" damage, for instance--our data would have overlooked the defect dominated sites with the lowest damaging fluence. This points to an intrinsic problem with N-on-1 testing since most diagnostics (spark formation, probe beam scattering, etc.) are sensitive only to large scale "uniform" or catastrophic damage.

Conclusions

The data from this experiment show that short pulse laser induced damage thresholds of various optical surfaces are defect dominated. Even with porous surfaces such as leached ARG-2 and sol-gel coatings, the low damage threshold of resident defects predominate over any effect which is due to the ambient gas. The large spread observed in our data indicates that further studies in this area require more homogeneous porous surfaces. Better control and uniformity have been reported for neutral solution coatings, and they should be investigated in future work. In addition, it may be necessary to use larger beam diameters to reduce the spread in the data before the effects (if any) of immersion in an electronegative gas can be seen. Spectroscopic observations of laser induced damage to optical surfaces immersed in index matching liquids or other environments only show spectra characteristic of the optical element and not of the ambient media [13], further supporting our contention that the damage initiation process is not appreciably affected by the environment in a gross sense (however, absorbing species adsorbed on the surface can play a role).

The absence of any noticeable effect is further supported by the result that ambient gas type or pressure does not play an observable role in laser induced damage of optical surfaces when that damage is defined as the first permanent observable morphological change.

References

[1] There is an extensive literature on avalanche breakdown. See, for example, the section "Electron Avalanches" in "Index of Papers Laser Induced Damage in Optical Materials Symposia: 1969-1978" published by Air Force Weapons Laboratory, Kirtland AFB, New Mexico 87117.

[2] S. B. Eron'ko, G. T. Petrovskii, A. V. Shatilov, A. K. Yakhkind, and L. V. Aleksandrova, Sov. J. Opt. Technol., 43, 29 (1976).

[3] W. H. Lowdermilk and D. Milam, Appl. Phys. Lett. 36 (11), 891 (1980). L. M. Cook, W. H. Lowdermilk, D. Milam, and J. E. Swain, Appl. Opt., 21, 1482 (1982).

[4] T. W. Walker, A. H. Guenther, and C. G. Fry, NBS Spec. Pub. 568, 405 (1980). T. W. Walker, A. H. Guenther, and P. E. Nielsen, IEEE J. Quant. Elect., QE-17, 2041-2065 (1981).

[5] A. F. Stewart and A. H. Guenther, NBS Spec. Pub., "Proceedings of the Thirteenth Symposium on Optical Materials for High Power Lasers (1981)," to be published.

[6] Y. Asahara and T. Izumitani, J. of Non-Crystalline Solids, 42, 269-280 (1980).

[7] S. P. Mukherjee and W. H. Lowdermilk, Appl. Opt., 21, 293 (1982).

[8] M. J. Minot, J. Opt. Soc. Am., 66, 515 (1976).

[9] Sol-gel coatings were provided by C. J. Brinker, Division 5845, Sandia National Laboratories, Albuquerque, New Mexico 87185.

[10] D. Milam, "Optical Coatings - Applications and Utilization II," SPIE, 140, 52-61 (1978).

[11] J. P. Manion, J. A. Philosophos, and M. B. Roberson, IEEE Transactions Electrical Insulation, E1-2, No. 1, 1-10 (1967).

[12] V. A. Artem'ev, A. M. Bonch-Bruesch, and Y. I. Chernaza, Ivestiya Akademii Nauk SSSR, Seriza Fizidieskaya 44, 2108 (1980).

[13] C. Yamanaka, T. Sasaki, M. Honggo, and Y. Nagao, NBS Spec. Pub. 356, 104 (1971).

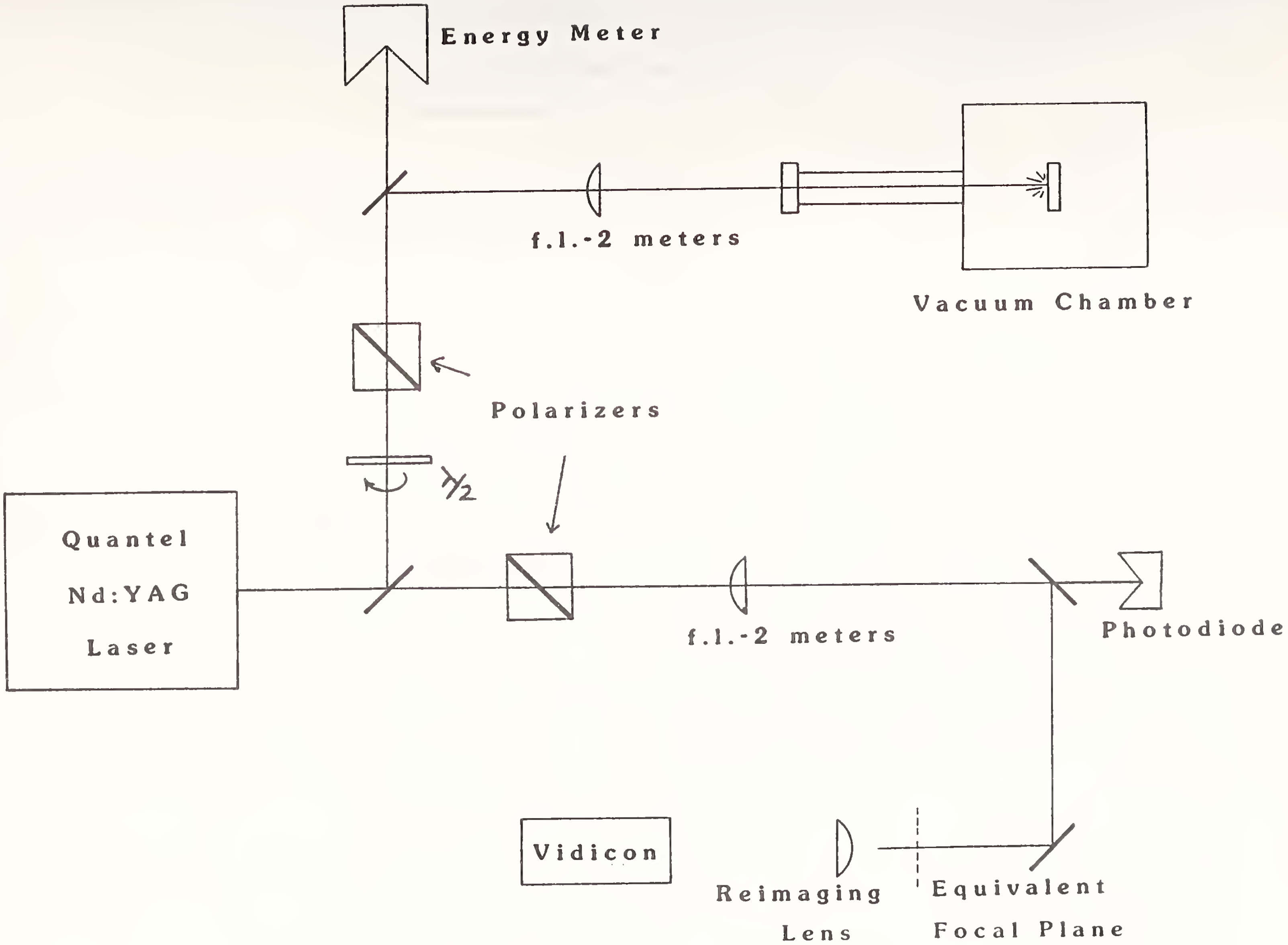

1. Experimental Apparatus for Laser Damage Studies in Different Gases.

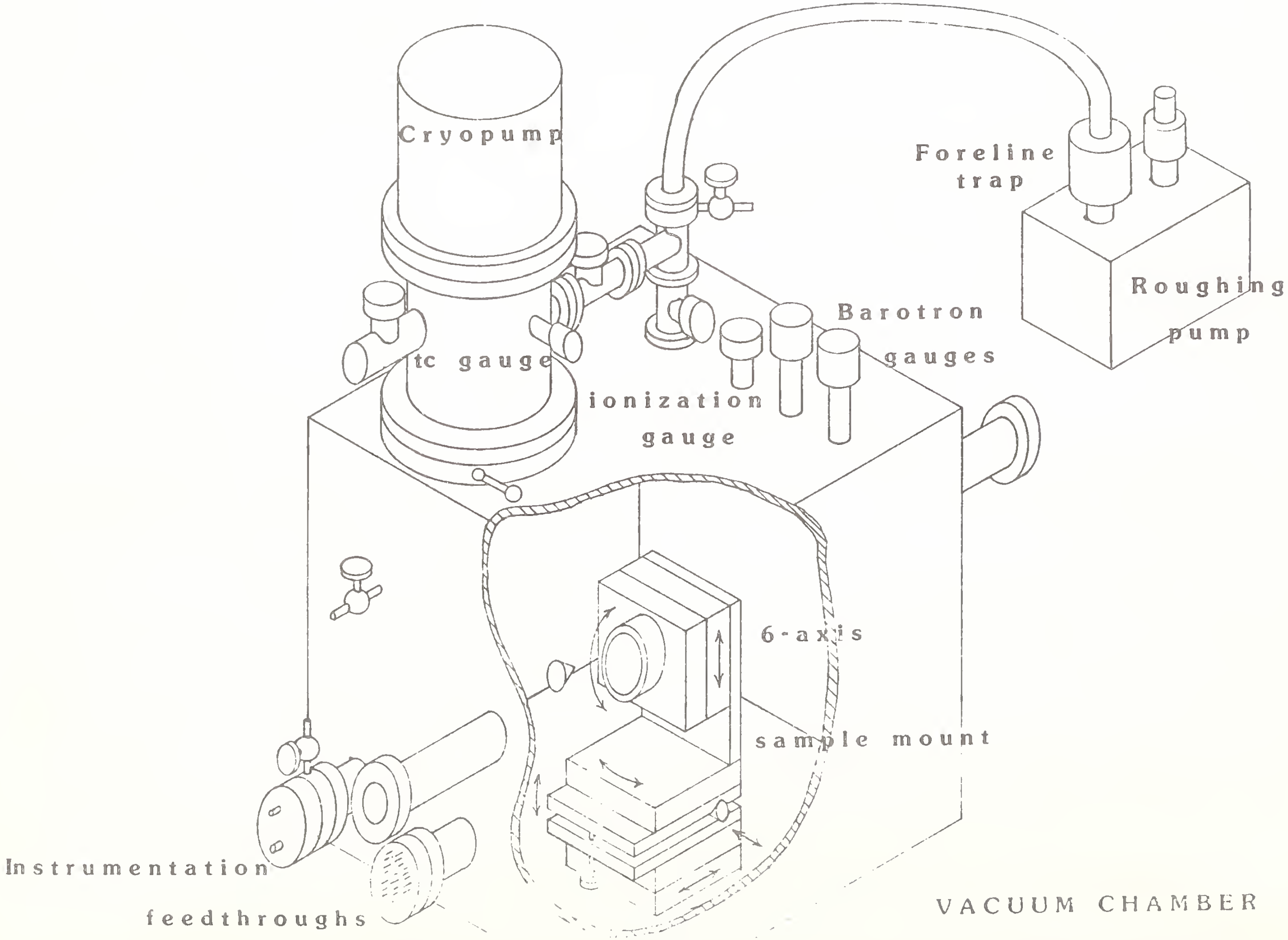

2. Testing Chamber with Detail of Sample Mount.

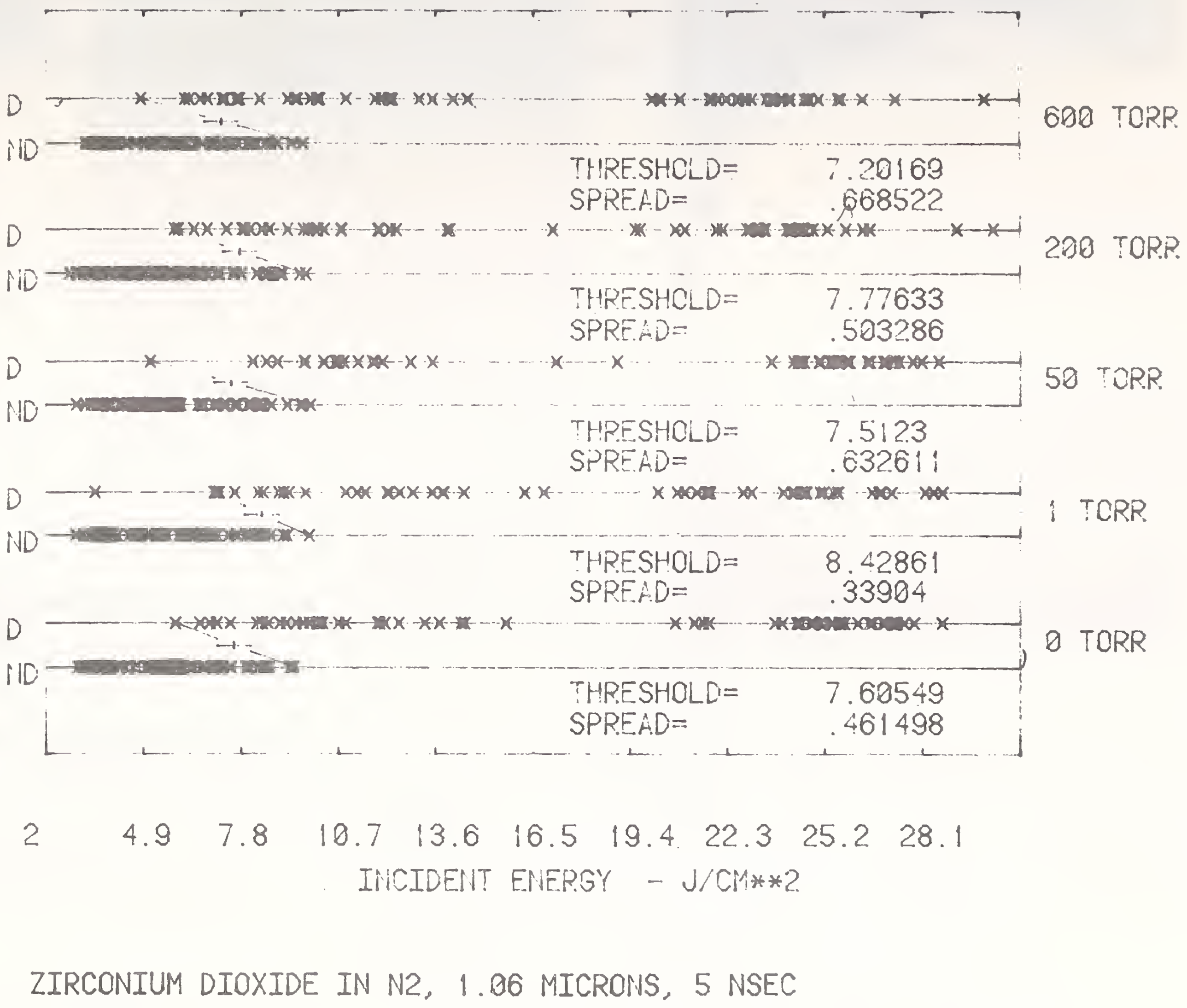

3. Damage Threshold Data (Energy Fluence) Obtained on a ZrO_2 Coating.

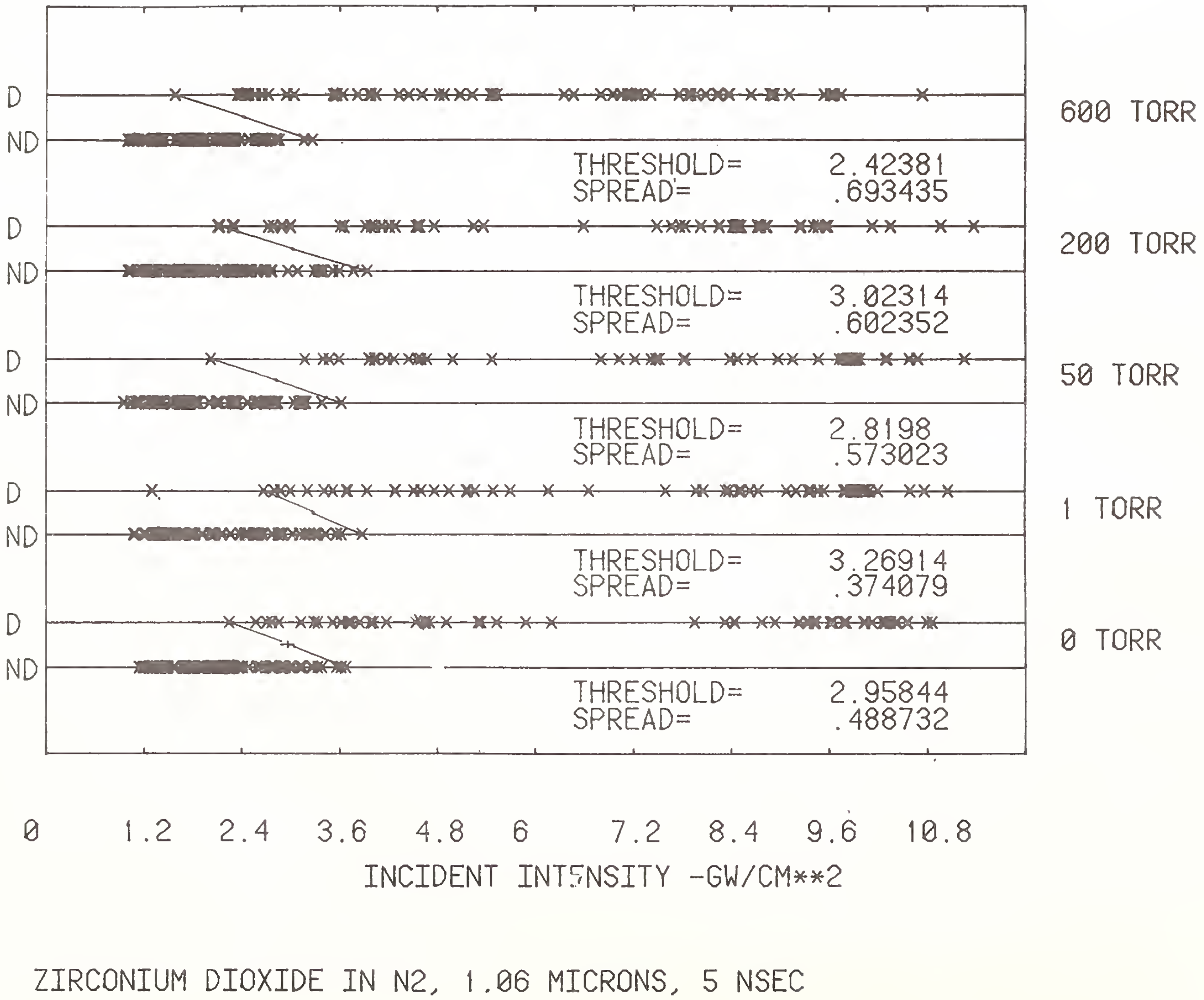

4. **Damage Threshold Data of Fig. 3 Plotted in Terms of Incident Intensity.**

a. ZrO_2 (λ/2 at 1.06μm) on Fused Silica in 1 Torr N_2 (250x).

b. Diamond Turned Copper in 600 Torr SF_6 (250x).

c. Fused Silica in 600 Torr N_2 (100x).

Fig. 5: Damage Morphology Near Threshold

a. Sol-Gel Coating in 50 Torr CF_4 (50x).

b. Leached Sol-Gel Coating in 1 Torr CF_4 (100x).

Fig. 6: Damage Morphology Near Threshold

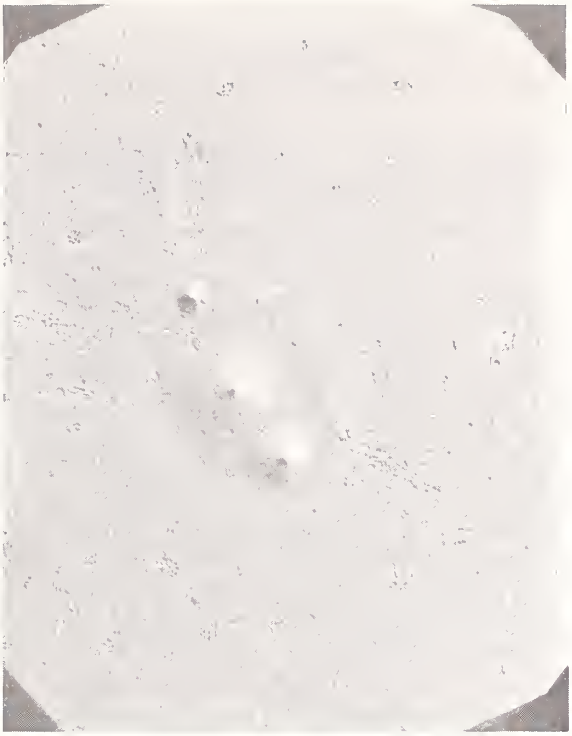

c. ARG-2 in 50 Torr CF_4 (100x).

d. Leached ARG-2 in 600 Torr N_2 (100x).

Fig. 6: Damage Morphology Near Threshold

Table 1
Damage Thresholds and Spreads

SAMPLE	GAS	VACUUM (10^{-5} TORR)	PRESSURES 1 TORR	50 TORR	200 TORR	600 TORR
ZrO_2	N_2	7.6 J/cm^2 (0.46)	8.4 J/cm^2 (0.339)	7.5 J/cm^2 (0.633)	7.8 J/cm^2 (0.503)	7.3 J/cm^2 (0.669)
	CF_4	8.90 J/cm^2 (p.566)	10.0 J/cm^2 (0.628)	11.9 J/cm^2 (0.414)	10.3 J/cm^2 (0.293)	8.7 J/cm^2 (0.474)
	SF_6	9.7 J/cm^2 (0.548)	7.9 J/cm^2 (0.611)	8.7 J/cm^2 (0.608)	9.2 J/cm^2 (0.560)	9.5 J/cm^2 (0.474)
Cu Mirrors	N_2	2.7 J/cm^2 (0.639)	2.8 J/cm^2 (0.554)	3.2 J/cm^2 (0.614)	3.1 J/cm^2 (0.589)	2.9 J/cm^2 (0.647)
	CF_4	2.5 J/cm^2 (0.469)	2.7 J/cm^2 (0.730)	2.8 J/cm^2 (0.933)	3.2 J/cm^2 (0.589)	2.9 J/cm^2 (0.647)
	SF_6	1.9 J/cm^2 (0.818)	1.9 J/cm^2 (0.998)	1.7 J/cm^2 (0.794)	2.1 J/cm^2 (0.823)	1.9 J/cm^2 (0.955)
Fused Silica Substrates (SiO_2)	N_2	57.9 J/cm^2 (0.665)		49.6 J/cm^2 (0.430)		47.2 J/cm^2 (1.170)
	SF_6	60.7 J/cm^2 (0.532)		48.3 J/cm^2 (0.527)		58.7 J/cm^2 (0.972)
Unleached Sol-Gel Derived Coatings	N_2	15.6 J/cm^2 (0.922)	17.9 J/cm^2 (0.057)	17.4 J/cm^2 (0.573)		19.7 J/cm^2 (0.437)
	CF_4	17.7 J/cm^2 (0.531)	20.8 J/cm^2 (0.269)	16.2 J/cm^2 (0.325)		12.3 J/cm^2 (0.630)
	SF_6	18.5 J/cm^2 (0.552)	16.2 J/cm^2 (0.614)	17.0 J/cm^2 (0.518)		14.4 J/cm^2 (0.801)
Leached Sol-Gel Derived Coatings	N_2	14.7 J/cm^2 (0.722)	15.4 J/cm^2 (0.526)	18.7 J/cm^2 (0.443)		14.5 J/cm^2 (0.187)
	CF_4	17.0 J/cm^2 (0.545)	20.2 J/cm^2 (0.711)	20.4 J/cm^2 (0.508)		
	SF_6	16.3 J/cm^2 (0.544)	17.4 J/cm^2 (0.739)	19.7 J/cm^2 (0.608)		18.4 J/cm^2 (0.745)
Unleached ARG-2	N_2	65.6 J/cm^2 (0.566)		64.2 J/cm^2 (0.504)		59.7 J/cm^2 (0.665)
	CF_4	44.0 J/cm^2 (0.939)		38.4 J/cm^2 (0.646)		49.1 J/cm^2 (1.005)
	SF_6	45.9 J/cm^2 (0.369)		43.0 J/cm^2 (0.341)		54.7 J/cm^2 (0.976)
Leached ARG-2	N_2	38.0 J/cm^2 (1.446)		39.8 J/cm^2 (1.426)		50.3 J/cm^2 (1.508)
	SF_6	21.1 J/cm^2 (1.143)		25.7 J/cm^2 (0.661)		23.8 J/cm^2 (1.454)

Table 2
Environmental Effects Comparison

EXPERIMENTAL CONDITION	ERON'KO ET AL.	THIS WORK	REMARKS
Pulse Duration	70 nsec	5 nsec FWHM	Spread Variability
Beam Diameter	60μm (?)	330μm ($1/e^2$)	Spread Variability
Wavelength	1.06μm	1.06μm	Same
Test Procedure	N on 1	1 on 1	Soviet effect seen from first irradiation ~ 1-on-1
Damage Threshold Definition	Spark/Plasma	Pit Formation from Nomarski Microscopy	Different!
Improvement Noted	Yes	No	Not necessarily in disagreement
Pressure Effect	Didn't do	10^{-5} → 600 Torr	No change
Gases	SF_6, air	SF_6, CF_4, N_2, vacuum	Sufficiently similar
Samples	Controlled ground fused silica, SiO_2 coating, porous surfaces	λ/2 ZrO_2 films metal mirrors, controlled ground fused silica, ARG-2 and sol-gel porous surfaces	Sufficiently similar

Pulsed Laser-Induced Damage to Metals at Cryogenic Temperatures*

D. L. Decker, J. B. Franck, W. N. Faith, and J. O. Porteus

Michelson Laboratory, Physics Division
Naval Weapons Center, China Lake, California 93555

Experimental pulsed laser-induced damage thresholds have been determined on diamond-machined metal surfaces at cryogenic temperatures. These multithreshold measurements are in substantial agreement with a simple one-dimensional thermal model previously developed. Differences in damage character do exist, primarily a decreased frequency of localized, imperfection-related damage on cooled surfaces. A detailed intercomparison of experimental and theoretical results is presented with discussion of the practical and fundamental significance of laser mirror operation at cryogenic temperatures.

Key words: cryogenic temperatures; laser damage; optical absorption in metals; surface imperfection.

Introduction

For laser pulse lengths longer than the electron relaxation time ($\sim 10^{-14}$ sec), laser-induced damage in pure metals is thermal in origin. As energy is absorbed from the pulse, the sample surface temperature rises. As the surface temperature rises, the gradient also becomes larger and the thermally induced stress will reach the yield stress of the material; further increase will ultimately result in mechanical slip. As the temperature rises further, melt will be eventually reached. On a well-prepared metal surface, slip will occur at a small fraction of the pulse fluence required to melt the surface [1].[1] For a uniform surface, both slip and melt thresholds are constant at different points on the surface. However, in actual observation, variation does occur due to surface defects, the origin of which has been the subject of much concern and conjecture [1,2]. On metal surfaces, these defects are most often supposed to be absorbing particles of some sort. A statistical description of the defect-related damage can be derived from "small spot" testing a large number of sites, providing a particularly useful way of describing surface uniformity [3].

Thus, although the uniform effects of slip and melt are assumed to be understood, the spatially selective effects are not. It is ordinarily assumed that the intrinsic IR optical absorption can be described by the Drude model with the necessary temperature dependence computed from the temperature dependence of the dc conductivity [4]. If the optical absorption and resulting heat flow can be accurately modeled, a theory of laser-induced melting results. Such a theory has been applied to previous laser damage data, and, for samples initially at room temperature, reasonable agreement has been obtained between theory and experiment [1]. To further examine the validity of these earlier theories and also to explore the consequences of the anomalously low absorption at 2.7 μm wavelength previously reported for silver and copper surfaces at low temperature [4], a series of laser-induced damage studies has been conducted with the sample initially at cryogenic temperature. As will be shown, two primary effects occur which combine to produce a higher threshold fluence for melting when a metal sample is initially at a cryogenic temperature. The optical consequence is to decrease the initial absorption, and the thermal consequence is to increase the total heat required to reach melting.

Theory

The Drude free-electron model provides a convenient theory to describe the IR absorption of a metal. The absorption A is simply related to the plasma frequency ω_p and the relaxation time τ,

---

*Work supported by the Office of Naval Research and Naval Weapons Center Independent Research funding.

[1] Numbers in brackets indicate the literature references at the end of the paper.

$$A \simeq 2/\omega_p \tau \quad . \tag{1}$$

This expression is valid in the limit $(\omega_p\tau)^2 >> (\omega\tau)^2 >> 1$, which applies accurately to silver, copper, and gold at near- and mid-IR wavelengths [4]. Furthermore, τ can be related to the dc conductivity σ by the Lorentz-Sommerfeld relationship which follows from simple transport theory:

$$\tau = 4\pi\sigma/\omega_p^2 \quad \text{(cgs units)} \quad . \tag{2}$$

For temperatures higher than one-third of the Debye temperature (θ_D) for the metal (see Table 1),

$$1/\sigma \simeq \rho_0 + \rho_1 T \quad , \tag{3}$$

where ρ_0 and ρ_1 are constants, independent of temperature [5]. Hence,

$$A \simeq \frac{\omega_p}{2\pi} (\rho_0 + \rho_1 T) \equiv A_0 + A_1 T \quad . \tag{4}$$

This explicit temperature dependence has been verified for silver, copper, and gold in the infrared, although complicated hysteresis and time-dependent "annealing" effects were also seen [4,6]. Laser-induced melting can be simply modeled if a square pulse and one-dimensional heat flow are assumed. The latter approximation is valid for the case in which the irradiated spot size is large compared to the thermal diffusion depth [7]. The one-dimensional heat flow equation and appropriate boundary conditions are

$$K\partial^2 T/\partial x^2 = C\partial T/\partial t \quad , \quad T(x,0) = T_0 \quad , \quad -K(\partial T/dx)_{x=0} = IA \quad , \tag{5}$$

where K is the thermal conductivity, C is the heat capacity of the material, and I is the laser fluence. If A is temperature independent, the surface temperature is

$$T(0,t) = T_0 + [2IA/(\pi KC)^{1/2}]t^{1/2} \quad . \tag{6}$$

If the pulse length is t_p, then setting the final surface temperature to the melt temperature T_M, $T(0,t_p) = T_M$, and solving for It_p, we have the melt threshold fluence θ_M:

$$\theta_M = \frac{(\pi KC)^{1/2}}{2A} (T_M - T_0) t_p^{1/2} \quad . \tag{7}$$

The product KC is only weakly temperature dependent. The temperature dependence of A can be approximately taken into account by replacing A with its average value $[A(T_0) + A(T_M)]/2$.

$$\theta_M \cong \frac{(\pi KC)^{1/2}}{A(T_0) + A(T_M)} (T_M - T_0)\, t_p^{1/2} \tag{8}$$

$$\cong \frac{(\pi KC)^{1/2}}{A_1} \frac{T_M - T_0}{T_M + T_0}\, t_p^{1/2} \quad , \qquad A \cong A_1 T \tag{9}$$

The ratio of the melt threshold fluence for a sample at an initial temperature T_1 to that at T_0 is then

$$\frac{\theta_M(T_1)}{\theta_M(T_0)} = \frac{T_M + T_0}{T_M + T_1} \cdot \frac{T_M - T_1}{T_M - T_0} \tag{10}$$

The first term in this expression accounts for the decrease in absorption for lower initial temperature, and the second for the increase in heat required to reach melting. It is instructive to examine a specific case. For silver,

$$\frac{\theta_M(88°K)}{\theta_M(300°K)} = 1.16 \times 1.23 = 1.43$$

Notice that the two contributions to the increase in melt threshold are nearly equal in magnitude.

If we assume <u>a priori</u> that A is temperature dependent, $A = A_0 + A_1T$, and again adopting a one-dimensional heat flow model, the surface temperature is given by the approximate expression [8]

$$T(0,t) = 2(T_0 + A_0/A_1)e^{\xi^2} - A_0/A_1 \quad , \text{ where } \xi = IA_1(t/KC)^{1/2} \quad , \tag{11}$$

valid for $\xi >> 1$. Setting $T(0,t_p) = T_M$ and solving for IT_p,

$$\theta_M(T_0) \cong \left\{ \ell n \left[\frac{T_M + A_0/A_1}{2(T_0 + A_0/A_1)} \right] \right\}^{1/2} \frac{(t_p KC)^{1/2}}{A_1} \tag{12}$$

The ratio of the melt threshold fluence for a sample at an initial temperature T_1 to that at T_0 is then

$$\frac{\theta_M(T_1)}{\theta_M(T_0)} \cong \left\{ \frac{\ell n[A(T_M)/2A(T_1)]}{\ell n[A(T_M)/2A(T_0)]} \right\}^{1/2} \cong \left\{ \frac{\ell n(T_M/2T_1)}{\ell n(T_M/2T_0)} \right\}^{1/2} \tag{13}$$

Although this expression is based upon a more realistic treatment of the temperature dependence of the absorptance, it does not permit a ready examination of the physical effects as does the earlier expression [eq (10)]. In the analysis section, it will be shown that eqs (10) and (13) yield results of similar magnitude.

Experiment

The experimental laser-induced damage reported in this paper was obtained in a manner similar to that previously reported [1,7]. The laser produced a reproducible Gaussian spatial profile in pulses of 100 nsec duration at 2.7 µm wavelength. Samples were mounted in an ultrahigh vacuum chamber with a base pressure of 10^{-10} Torr. Cooling was accomplished by bringing the samples into contact with a liquid nitrogen reservoir. The samples were then rotated and aligned for damage testing. Once in position for laser irradiation, the samples would begin a long (many-hour) climb in temperature back to ambient. During damage testing, the temperature increase would be no larger than 5°K. The temperatures reported are the average temperatures during a damage sequence. Temperatures were monitored with calibrated thermocouples mounted directly on the samples. Two sample types are reported here: diamond single-point machined, electroplated, high purity gold and OFHC copper. The samples were machined off-center with an interrupted cut and with a round-nosed tool [9]. Figures 1 and 2 show the typical appearance of crater and slip damage to OFHC copper both for an initial temperature at 133°K (a) and at 300°K (b). Figures 3(a) and (b) show the results at cryogenic and ambient temperature for diamond-machined electroplated gold. No differences in damage morphology with initial sample temperature were evident in examining hundreds of damage sites on both copper and gold. Table 2 presents a summary of multithreshold results for both sample types, with fluence values given as well as the ratio of cryogenic and ambient threshold fluences.

In addition to the determination of threshold values for melt, slip, and other damage effects, data were also obtained to determine the onset fluence for pitting. Pitting is a localized melting occurring as a consequence of spatially selective absorption or thermal effects [1-3,7]. Using a power law fit to the pitting frequency data with P = 0.1, the following onset fluences were obtained using the statistical model of Porteus [3] for the OFHC copper sample previously examined,

$$I_0(133°\mathrm{K}) = 176.1\ \mathrm{J/cm^2} \quad ; \quad I_0(300°\mathrm{K}) = 134.9\ \mathrm{J/cm^2}$$

$$\frac{I_0(133°\mathrm{K})}{I_0(300°\mathrm{K})} = 1.31$$

Analysis

The advantage in computing ratios of melt thresholds, as in eqs. (10) and (13), is that only a minimum of material constants are required for an analysis. Using values of the melting temperatures for copper and gold as given in Table 1, the following ratios are obtained using eq. (13) for copper and gold, respectively:

$$\frac{\theta_M(133°\mathrm{K})}{\theta_M(300°\mathrm{K})} = 1.41$$

and

$$\frac{\theta_M(139°\mathrm{K})}{\theta_M(276°\mathrm{K})} = 1.33$$

These values agree well with the measured values given in the previous section for copper and gold, 1.32 and 1.25, respectively. The discrepancy in both cases is about 6% and is well inside that permitted by experimental uncertainty. For a given sample type, except for the flash threshold ratio on electroplated gold, the ratios are remarkably consistent with the melt threshold ratios for the several damage effects reported. This is not unexpected, since in all cases the effects are thermal in origin. It might be argued that slip is a more complicated phenomenon, involving the mechanical properties of the material. However, actual slip occurs at the same temperature (gradient) regardless of the initial conditions. The cryogenic absorption and heat capacity effects determine the details in the rise to this threshold condition, at which temperature (gradient) the mechanical properties are the same in all cases.

Not expected, however, is the discovery of the same threshold ratio for the onset of selective damage, an effect assumed to be defect related. It has been long assumed that the localized laser-induced damage seen on bare metal surfaces is due to small, highly absorbing particles, perhaps submicron in size [1-3]. The temperature and wavelength dependence of the absorption associated with such a particle is obviously unknown, but would not be expected to be the same as the metal itself. The simplest explanation for the effects observed here is that the defect is not an absorbing particle but is rather thermal in origin. A small localized crack could thereby isolate a piece of the surface. In absorption, this particle behaves just as the parent metal, but as laser heat is deposited in it, it increases in temperature very rapidly, reaching melt temperature before the bulk.

There is no evidence for the anomalously low absorption previously observed for diamond-machined copper and silver. The very low absorption reported earlier would result in a further increase in melt threshold values. In fact, the measured values are lower than those computed for both copper and gold [4]. The simple Drude model with a temperature dependence introduced from experimental values of the dc conductivity provides an absorption model in excellent agreement with the measured thresholds for diamond-machined OFHC copper and gold.

Conclusions

No unusual laser-damage morphology is associated with a sample at a cryogenic initial temperature. This statement follows from microscopic examination of hundreds of damage sites on diamond-machined gold and copper. The experimentally determined melt threshold values for copper and gold vary with initial sample temperature in good agreement with simple theory. In this theory, it is assumed that the optical absorption varies linearly with temperature. There is then no evidence for the anomalous near-IR absorption previously reported for diamond-machined and evaporated metal films. The diamond-machined optical surfaces examined in this work behaved in accordance with the simple Drude model.

In a separate series of measurements, the onset fluence for selective damage on diamond-machined copper was determined using the statistical model developed by Porteus. Surprisingly, the selective damage onset fluence varies with initial sample temperature in the same fashion as the melt threshold fluence. The simplest explanation is that the absorption mechanism for selective damage has the same temperature dependence as uniform damage. The lower threshold values and selective nature of this damage must then be due to localized thermal defects. Such a defect results from the inability of a small surface region to conduct heat deposited by the pulse into the interior of the sample. The surface temperature thus reaches a damaging value more readily than it would over uniform material. Such a spatially nonuniform defect could be caused by a crack or void near the surface, and in OFHC copper is often observed in association with grain boundaries.

Defect-related damage, of course, has been detected on a wide variety of sample types including dielectric-coated multilayer mirrors. Much work has been accomplished in an attempt to detect and identify the "absorbing" defects responsible. It seems very likely that in many cases the defects are actually thermal in origin and that no impurity particle is involved. This simple idea accounts for the inability, in most cases, to discover *a priori* a defect by optical means which upon subsequent damage testing will produce local damage.

Although cryogenic laser damage measurements are difficult to perform, unique information about both intrinsic and extrinsic selective damage mechanisms can be obtained. No doubt it would be worthwhile to repeat the experiment described in this paper on dielectric-coated samples. As a practical matter, operating a bare metal diamond-machined silver, copper, or gold mirror at 80°K will result in a decrease in absorption by a factor of about 5 in the IR and an increase in the thermal conductivity of most metals by a factor of about 1.5. As demonstrated in this paper, both intrinsic and extrinsic damage thresholds on bare copper and gold can be increased by a factor of 1.3 to 1.5 over the same temperature range. No one would consider cryogenic laser mirror operation and its additional complexity for ordinary use. However, in some critical applications, the advantages summarized above may well argue for cryogenic operation.

References

[1] Porteus, J. O.; Decker, D. L.; Seitel, S. C.; Soileau, M. J. "Dependence of metal mirror damage thresholds on wavelength, material, pulse length, and preparation method," in Laser Induced Damage in Optical Materials: 1980, Bennett, H. E.; Glass, A. J.; Guenther, A. H.; Newnam, B. E., ed. 1980 September 30-October 1; Boulder, CO. Nat. Bur. Stand. (U.S.) Spec. Publ. 620; 1981 October. Pp. 201-209.

[2] Seitel, S. C.; Porteus, J. O.; Decker, D. L.; Faith, W. N.; Grandjean, D. J. "Effect of surface preparation methods on laser-induced pitting of Cu mirrors at 10.6 μm wavelength," IEEE J. Quantum Electron. QE-17; 2072-2077; 1981.

[3] Porteus, J. O. "Determination of the onset of defect-driven pulsed laser damage in 2.7 μm optical coatings," (U) presented at the High Power Laser Optical Components Topical Meeting, Boulder, CO, 1982 November.

[4] Decker, D. L.; Hodgkin, V. A. "Laser mirror operation at cryogenic temperatures," presented at the 13th Annual Symposium on Optical Materials, Boulder, CO, 1981 November. (Proceedings in process.)

[5] Kittel, C. Introduction to Solid State Physics, 5th ed.; chapter 6. New York; John Wiley & Sons; 1976.

[6] Decker, D. L.; Hodgkin, V. A. "Wavelength and temperature dependence of the absolute reflectance of metals at visible and infrared wavelengths," in Laser Induced Damage in Optical Materials: 1980, Bennett, H. E.; Glass, A. J.; Guenther, A. H.; Newnam, B. E., ed. 1980 September 30-October 1; Boulder, CO. Nat. Bur. Stand. (U.S.) Spec. Publ. 620; 1981 October. Pp. 190-200.

[7] Porteus, J. O.; Decker, D. L.; Faith, W. N.; Grandjean, D. J.; Seitel, S. C.; Soileau, M. J. "Pulsed laser-induced melting of precision diamond-machined Cu, Ag, and Au at IR wavelengths," IEEE J. Quantum Electron. QE-17; 2078-2085; 1981.

[8] Carslaw, H. S.; Jaeger, J. C. Conduction of Heat in Solids. London; Oxford University Press; 1948.

[9] Saito, T. T., ed. Advances in the Precision Machining of Optics, Proceedings of the Society of Photo-Optical Instrumentation Engineers 93; 1976.

Table 1. Values of the melting temperature T_M and the Debye temperature θ_D for silver, copper, and gold

Metal	T_M (°K)	θ_D (°K)
Ag	1259	220
Cu	1356	315
Au	1337	165

Table 2. Measured threshold fluence values for diamond-machined electroplated gold and OFHC copper. Values shown are in J/cm^2 and are for a pulse of 100 nsec duration at 2.7 μm. Additional details given in the text.

	Diamond-machined electroplated gold			Diamond-machined OFHC copper		
	T = 139°K	T = 276°K	Ratio	T = 133°K	T = 300°K	Ratio
Slip	124 ± 28	105 ± 4	1.18	----	90 ± 2	----
Melt	174 ± 11	139 ± 6	1.25	251 ± 13	190 ± 25	1.32
Pit	174 ± 11	139 ± 6	1.25	251 ± 13	190 ± 25	1.32
Crater	174 ± 11	140 ± 6	1.25	274 ± 15	218 ± 23	1.26
Flash	174 ± 11	199 ± 23	0.87	274 ± 15	218 ± 23	1.26

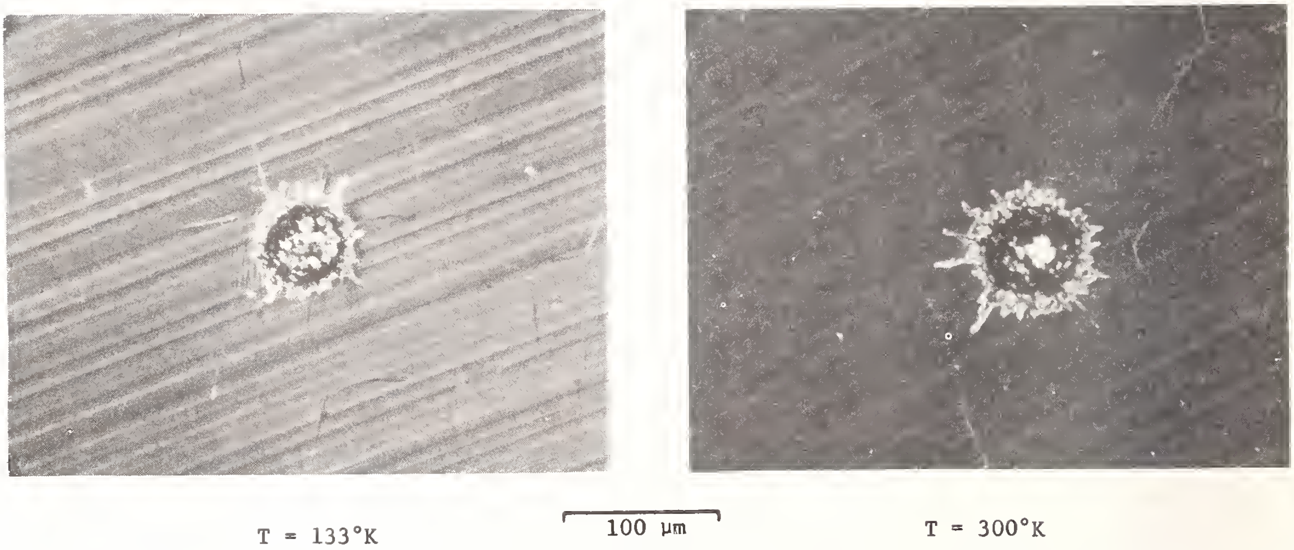

Figure 1. Nomarski micrographs of damage sites showing cratering on a diamond-machined OFHC copper surface with the initial sample temperature at 133°K in (a) and 300°K in (b). No differences in morphology are evident.

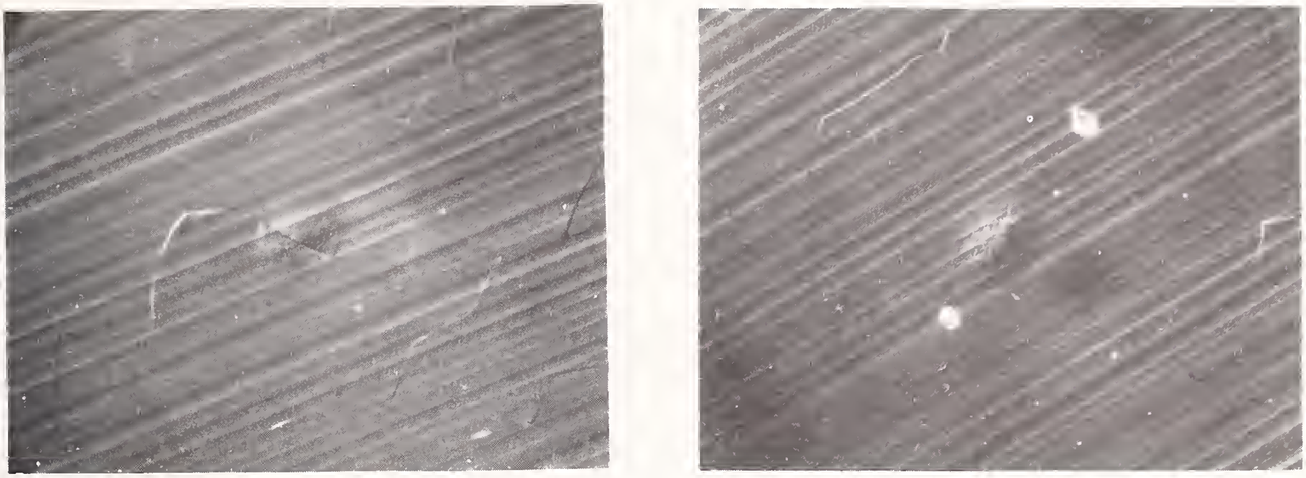

T = 133°K

100 µm

T = 300°K

Figure 2. Nomarski micrographs of damage sites showing slip on a diamond-machined OFHC copper surface with the initial sample temperature at 133°K in (a) and 300°K in (b). No differences in morphology are evident.

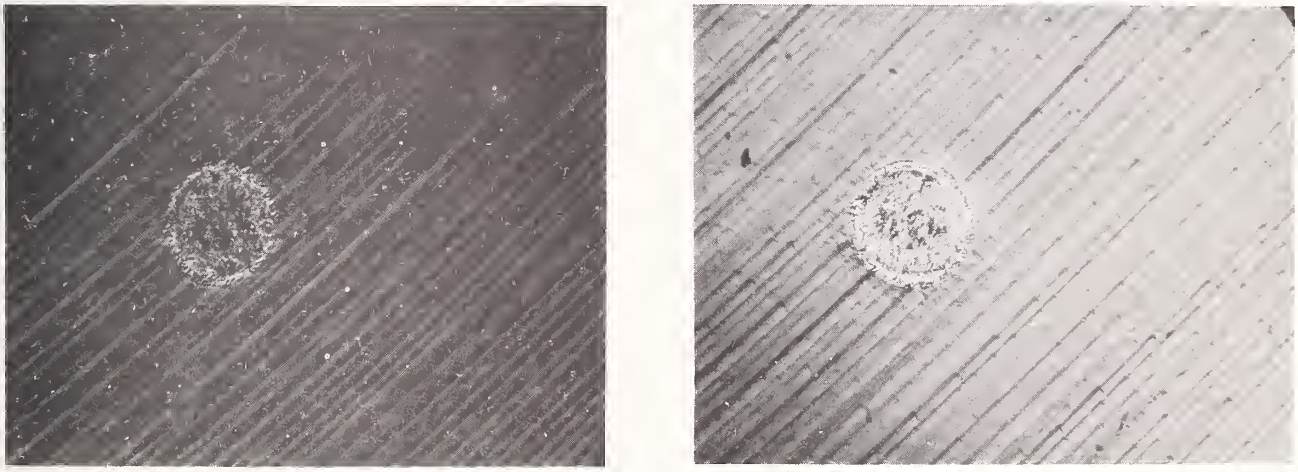

T = 139°K

100 µm

T = 276°K

Figure 3. Nomarski micrographs of damage sites showing cratering on a diamond-machined electroplated gold surface with the initial sample temperature at 139°K in (a) and 276°K in (b). No differences in morphology are evident.

Single and Multiple Pulse Catastrophic Damage in Cu and Ag Diamond Turned Mirrors at 10.6, 1.06 and 0.532 µm

N. Koumvakalis, C. S. Lee, and M. Bass

Center for Laser Studies, University of Southern California
University Park, DRB 17, Los Angeles, CA 90089-1112

The results of single and multiple pulse damage studies at 10.6, 1.06 and 0.532 µm in diamond turned bulk Cu and diamond-turned electrodeposits of Ag on Cu are presented. The single pulse damage threshold decreases or remains constant with increasing spot size as previously reported. On the other hand, the multiple pulse threshold increases with increasing spot size. The difference in their behavior suggests that the two phenomena are the result of different mechanisms. Localized surface defects and impurities appear to be responsible for single pulse damage, while for multiple pulse damage a model is proposed based on the cumulative effect of plastic deformation induced by thermal stresses.

Key words: Copper mirror; damage; defect; diamond-turned; multiple pulse; pulsed calorimetry; silver mirror; single pulse; thermal gradient stress.

1. Introduction

The continuous development of high power pulsed lasers has made the question of radiation induced resistance of the optical components employed an important problem. Copper and silver mirrors because of their high reflectivity and good thermal conductivity are used extensively in laser applications. These mirrors must withstand high-intensity, short-pulse irradiation in multiple as well as in single pulse operation. Last year [1] we presented data for Cu mirrors, where, at 1.06 µm the multiple pulse damage threshold increased with increasing beam size. The effect was attributed to stress developed during the pulse with no further analysis.

The scope of the present work is to analyze the observed behavior of Cu and Ag mirrors under 10.6 µm, 1.06 µm and 0.532 µm multiple and single pulse irradiation and present a model to explain the damage processes. In the case of multiple pulses, we examine the thermomechanical stress degradation of the metal surface under laser irradiation. As a result, we can describe multiple pulse damage in terms of a cumulative process where the damaged medium has a memory of the preceding pulses if the power is more than a certain threshold value. The single pulse damage process is described in terms of a defect triggered breakdown.

2. Experimental

The samples used were OFHC bulk Cu and electrodeposited Ag on Cu substrates diamond turned in the facilities of the NWC in China Lake. We also used OFHC bulk Cu diamond turned by Intop Corp.

The damage test facilities are depicted in figure 1 and are in principle the same as those used in previous damage and calorimetry studies [1,2]. An important addition was the use of a SHG crystal in the Molectron Nd:YAG laser which allowed irradiation with 0.532 µm light.

The repetition rate of both lasers - 10 Hz for the Nd:YAG at both 1.06 and 0.532 µm and 5/8 Hz for the CO_2 laser - set a limit to the maximum number of shots used for the experiment, the limit being 10^4 shots for the Nd:YAG and 1,500 shots for the CO_2 laser.

The quality and reproducibility of the laser beams is of crucial importance in damage experiments. Therefore their temporal as well as spatial profiles were periodically monitored. For the Nd:YAG laser at 1.06 µm and 0.532 µm, we used a fast photodiode to measure the temporal profile and a Reticon diode array to monitor the spatial distribution of the laser beam. For the CO_2 laser, we used a photon drag detector to monitor the temporal waveform while the spatial profile was determined by beam scans.

The sample was positioned in a calorimetric chamber evacuated to ~100 mTorr (see figure 1). A site was then selected on the sample's surface and irradiated with many pulses of constant energy. Damage would occur instantly or after a number of pulses. For the 10.6 µm and 1.06 µm irradiation damage was monitored by using laser calorimetry. As described previously [1,2] upon damage the behavior of the heating curve displayed in real time would change dramatically while at the same time one could observe a flash or spark. Due to the increased absorption of Cu and Ag at 0.532 μm detection of damage with laser calorimetry presented serious technical problems. Therefore, a photomultiplier with appropriate filtering was used which detected the increased scattering which accompanied damage as well as the broad spectrum of wavelengths produced by the intense plasma formed during the catastrophic damage process.

After damage, the number of pulses required to cause failure N, and the corresponding intensity I_N, were recorded. Then a new site was selected and irradiated at a lower intensity, where more pulses were required to produce damage until an intensity was reached showing no evidence of causing failure after 1,500 pulses at 10.6 μm and 10,000 pulses at 1.06 and 0.532 μm.

The same experiment was then repeated for several beam sizes in order to determine the multiple as well as the single pulse damage intensity as a function of the beam size. (In this work beam size is given as the radius of the beam where the intensity is $1/e^2$ of the axis intensity).

3. Results

Figure 2 shows a plot of the log of the number of shots N vs intensity for diamond turned Cu at 10.6 μm, 1.06 μm and 0.532 μm, while figure 3 shows the same plot for diamond turned Ag. One notices that as the intensity is reduced more pulses are required for damage.

Figure 4 shows a plot of the multiple pulse damage intensity for a certain number of shots (open circles) as well as the single pulse damage (solid circles) as a function of beam radius for diamond turned Cu at 10.6, 1.06 and 0.532 μm. Figure 5 shows the same plot for diamond turned Ag. The single pulse damage threshold decreases or remains constant as the beam size increases. In contrast the multiple pulse damage threshold increases with increasing beam size in a linear fashion.

An examination of the damage morphology with a Nomarski microscope reveals that single pulse damage generally occurs at localized defect sizes. On the other hand, in multiple pulse damage, prior to catastrophic failure (i.e. before a flash or spark were observed), the irradiated sites become roughened and the degree of roughness increased with increasing number of pulses. The results for Cu are shown in reference 2. Figure 6 shows the results for Ag at 0.532 μm. In Figure 6a, the site was irradiated for 1,500 pulses, while in Figure 6b, the site was irradiated for 5,000 pulses. Catastrophic failure was not observed in either case. We were able to detect the increased scattering due to surface roughening at 0.532 μm with the photomultiplier before catastrophic failure occurred.

4. Discussion

The observed beam-size dependence for single pulse damage is similar to the one observed for damage to thin films and surfaces of transparent media [3,4,5]. The model suggested in that work, which seems also to be valid for metal mirrors, assumes that the nature and distribution of surface defects determine the beam size dependence. As a result, the probability of the laser beam striking a defect will be greater for larger beam sizes. If the beam size is larger than the mean distance between defects so that the beam area striking the samples encompasses several of them, the damage threshold will be invariant with spot size increase. Apparently the range of beam sizes used in the present experiment (r_{1/e^2} between 50 and 250 μm) satisfies the condition. There is recent evidence [6] that multiple pulse damage in dielectric reflectors follows the same trend in its beam size dependence as the single pulse damage, namely the laser damage intensity decreases or remains constant for increasing beam size. Damage following the above trend can be characterized as extrinsic.

An entirely different description applies to the multiple shot damage we observed in Cu and Ag. The sample morphology before catastrophic damage occurred was indicative of an accumulation process suggested before [7]. To explain the accumulation of deformation leading to catastrophic damage as well as the unexpected spot size dependence of the multiple pulse damage threshold we considered the generation of stress by a local temperature gradient associated with a non-uniform temperature field.

The temperature distribution produced by a Gaussian beam at the end of a square pulse of duration τ_p, assuming that the thermal diffusion length is negligible in comparison to the beam dimension, is given by:

$$T(r) = \frac{AI_0\sqrt{\tau_p}}{\rho C\ \sqrt{\pi\kappa}}\ \exp\left(-r^2/w^2\right) \tag{1}$$

for $w \gg \sqrt{4\kappa\tau_p}$

where:

A = absorptance

I_0 = peak intensity

ρ = material density

C = specific heat

κ = thermal diffusivity

w = spot radius at $1/e^2$

τ_p = pulse duration

The shear stress of a plane metal surface subjected to heating is proportional to the temperature gradient introduced, so that the maximum shear stress (occurring where the temperature gradient is maximum) is given by:

$$\sigma_s^{max} = \frac{AI_0\alpha E\tau_p}{\sqrt{2e}(1-\nu)\rho C}\ \frac{1}{\nu} \tag{2}$$

where the additional parameters are:

E = Young's modulus

α = coefficient of thermal expansion

ν = Poisson's ratio

When the shear stress exceeds the yield stress σ_y of the material, the metal deforms plastically. The onset of plastic deformation is defined when:

$$\sigma_s \geq \sigma_y$$

Substituting σ_s from (2) and solving for the critical now intensity I_y

$$I_y(w) = \frac{\sqrt{2e}\ (1-\nu)\ \rho C\sigma_y}{AE\tau_p}\ w$$

According to Porteus et. al. [3], the most dominant damage mechanism on clean and carefully prepared surfaces, as is our case, is slip bands resulting from thermal stresses and having a threshold significantly lower than the one required for catastrophic damage. The slip bands and the other plastic deformations occurring when the yield strength of the surface is exceeded during each pulse, will manifest themselves as an increase in surface roughness. Repetitive pulse illumination will cause an accumulation of plastic deformation and a continuous increase in surface roughness until catastrophic damage occurs.

5. Conclusion

The single as well as the multiple pulse damage behavior of Cu and Ag diamond turned mirrors at 0.532 µm, 1.06 µm and 10.6 µm as a function of the laser beam size have been examined. For the single shot damage, a probabilistic model can be applied in which the nature and distribution of defects are responsible for the observed behavior. Such a damage process can be characterized as intrinsic. In the case of multiple pulse damage, a cumulative process triggered by thermal stresses leads to the observed spot size dependence and demonstrates that multiple pulse damage is dominated by an intrinsic process.

The authors express their thanks to Dr. D. Decker from the NWC in China Lake and P. Engstrom from INTOP Corporation for kindly supplying the crystals. They also want to thank Dr. L. Merkle for helpful discussions. This work was sponsored by ONR-SRO Research Grant No. N00014-70-C-0896.

6. References

[1] Koumvakalis, N.; Lee, C. S.; and Bass, M., Proceedings of the 13th Symposium on Laser Induced Damage in Optical Materials, Boulder, Colorado, Nov. 1981 and to be published by the National Bureau of Standards.

[2] Lee, C. S.; Koumvakalis, N.; and Bass, M., Appl. Phys. Lett. 41 (7), 1922.

[3] DeShazer, L.G.; Newnam, B. E.; and Leung, K. M., Appl. Phys. Lett. 23, 707 (1973).

[4] Wang, V.; Giuliano, C. R.; and Garcia, B., NBS Special Publication No. 435, 1973, p. 216.

[5] Bettis, J. R.; House II, R. A.; and Guenther, A. H., NBS Special Publication No. 462, 1976, p. 338.

[6] Foltyn, S. R.; Jolin, L. J.; and Newnam, B. E., Proceedings of the 14th Symposium on Laser Induced damage in Optical Materials, Boulder, Colorado, 1982, November and to be published by National Bureau of Standards.

[7] Musal Jr., H. M. NBS Special Publication No. 568, 1979, p. 159.

[8] Porteus, J. O.; Decker, D. L.; Jernigan, J. L.; Faith, W. N.; and Bass, M., IEEE J. Quantum Electr. QE-14, 776 (1978).

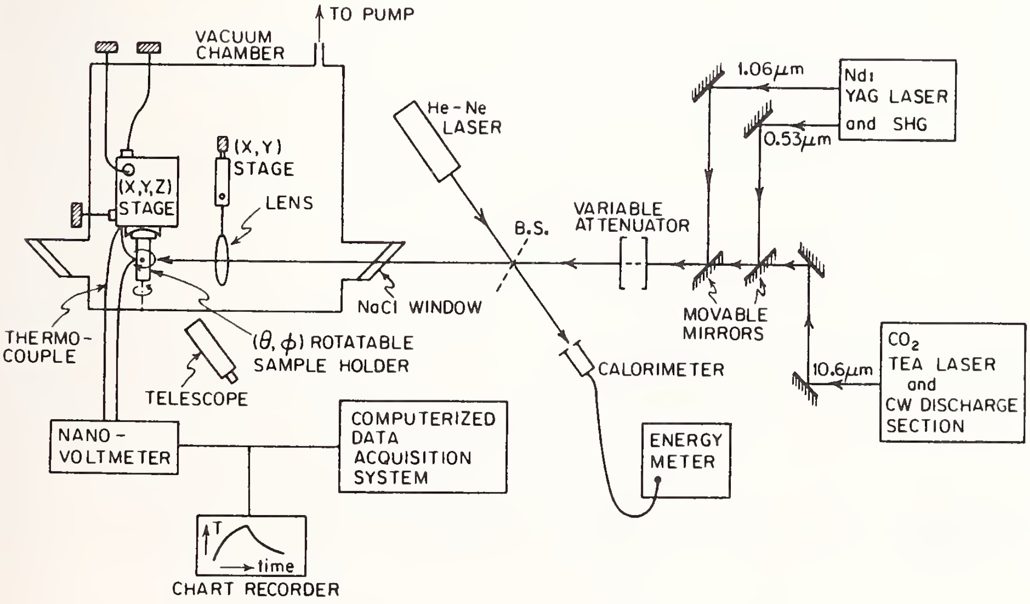

Figure 1. Schematic of experimental apparatus.

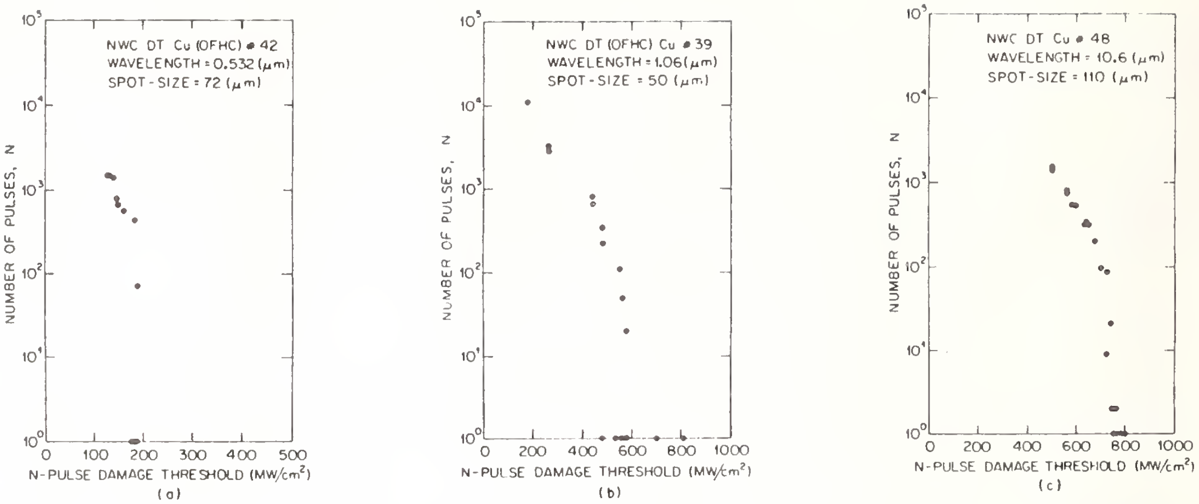

Figure 2. Measured log N vs I_N for diamond-turned OFHC Cu irradiated at a) 0.532 μm b) 1.06 μm c) 10.6 μm.

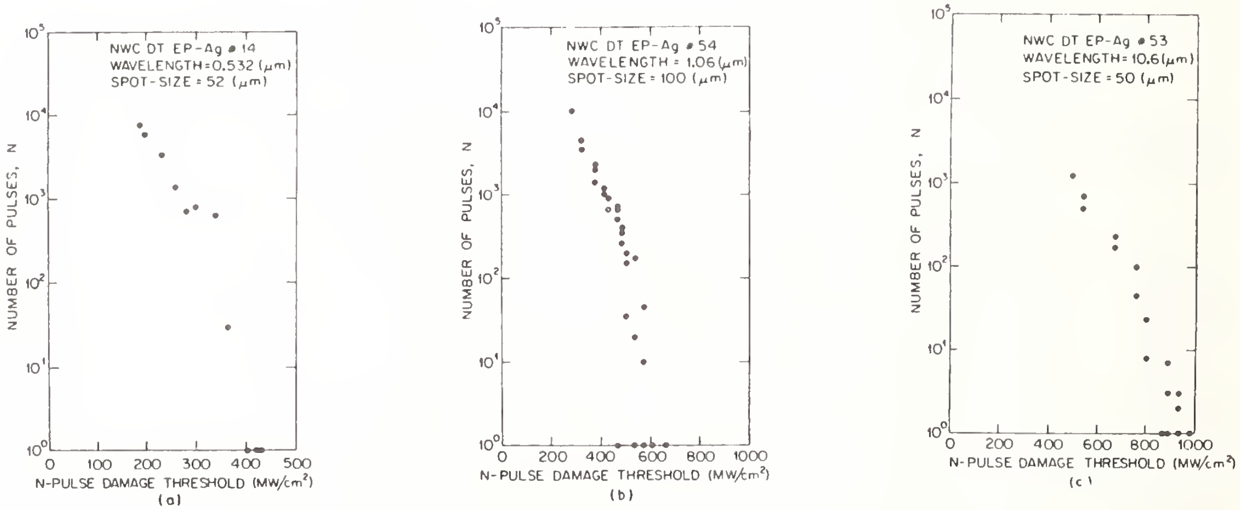

Figure 3. Measured log N vs I_N for diamond-turned electroplated Ag irradiated at a) 0.532 μm b) 1.06 μm c) 10.6 μm.

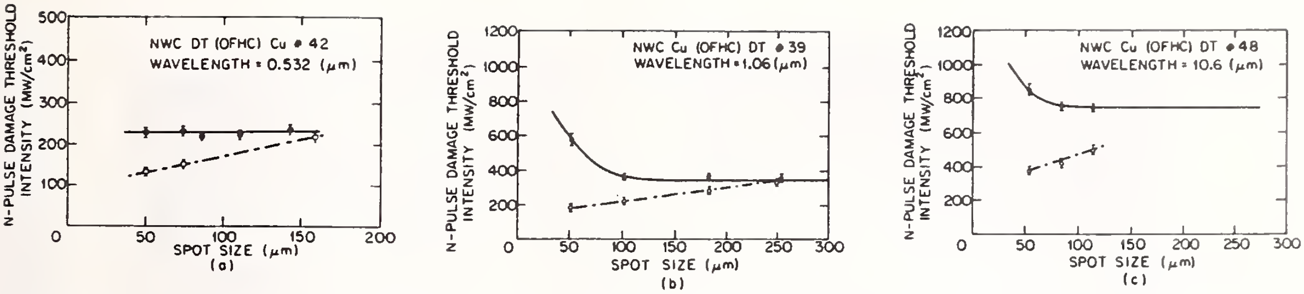

Figure 4. I_N vs W for diamond-turned OFHC Cu irradiated at a) 0.532 μm b) 1.06 μm c) 10.6 μm, N = 10^3 shots.

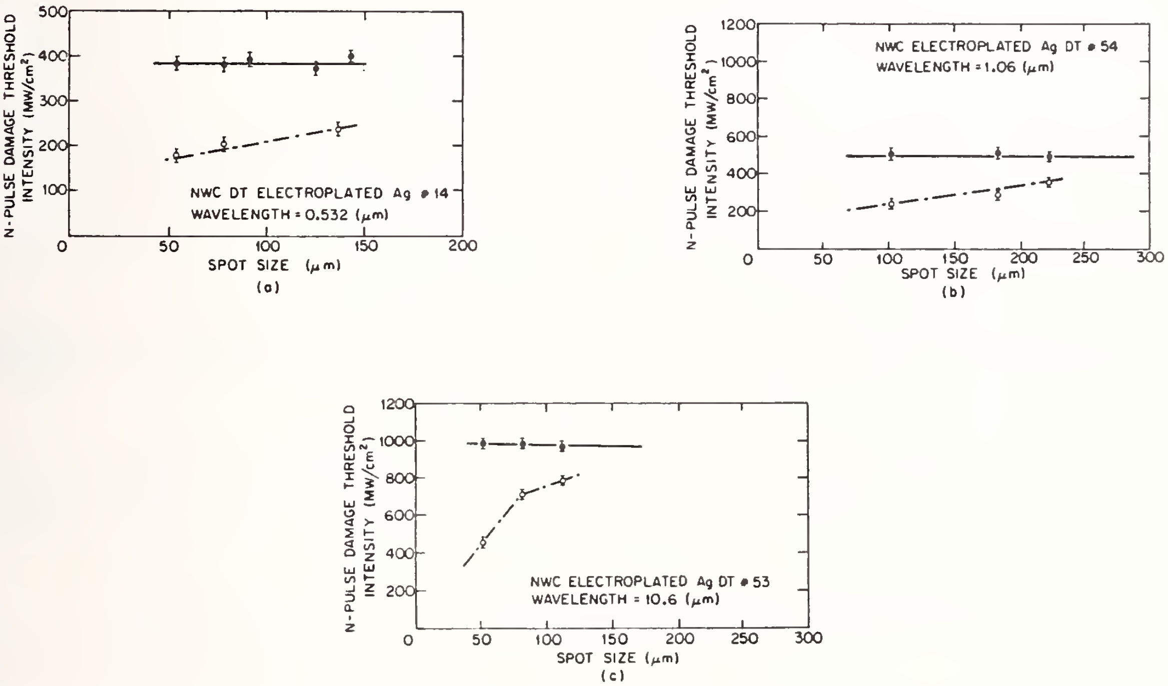

Figure 5. I_N vs w for diamond turned electroplated Ag irradiated at a) 0.532 μm b) 1.06 μm c) 10.6 μm. N = 10^3 shots.

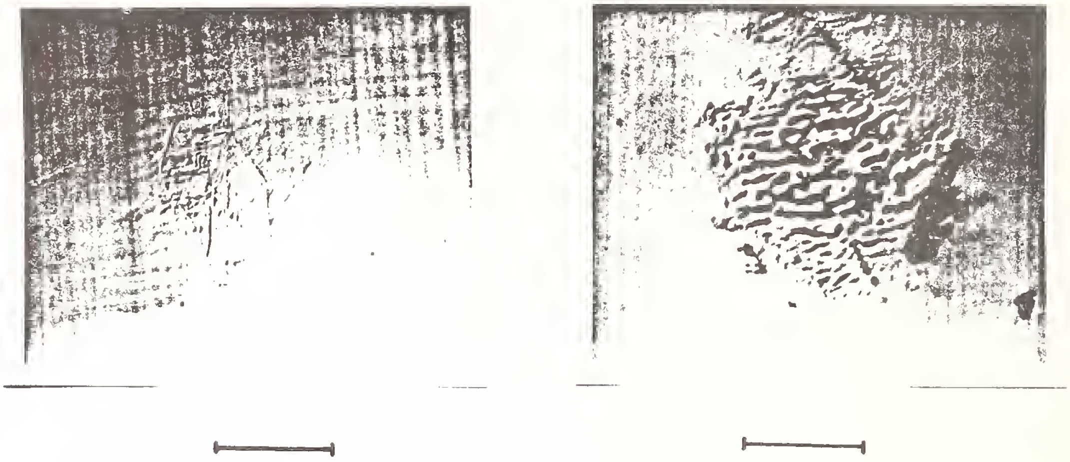

a) b)

Figure 6. Nomarski micrograph of laser-induced surface roughening in diamond-turned electroplated Ag at constant intensity for two different numbers of pulses. a) N = 1,500 b) N = 5,000.

In response to questions, the speaker emphasized that thresholds increased when spot size increased only during multiple-shot tests on metal surfaces. For single-shot tests, thresholds decreased when spot size increased.

"First Order Analytical Technique For Evaluating The Heat Transfer, Coolant Channel Thermal and Pressure Ripple, Bending, Burnout, and Coating Damage on Single and Multilayer Laser Mirror Cooled Heat Exchangers"

James R. Palmer

TRW
One Space Park, Redondo Beach, California 90278

Laser mirror cooled heat exchangers become somewhat complicated to evaluate when the analyst must consider elements other than the heat transfer. This analytical technique is organized to assist in the first order evaluation of a cooled heat exchanger mirror, withoutusing large, complex codes, in order to determine if the mirror heat exchanger is within the boundaries of the problem to be investigated.

The process goes step by step, first evaluating the requirements for single or multiple pass, determining the pressure drop through the mirror and the gradient through the face plate. The temperature gradient for the channel web is determined and the relationship of pressure and thermal ripple are integrated with the channel web distortion to achieve a RMS ripple value. The overall distortion of the mirror, i.e., a focus term, is evaluated as a function of total gradient through the total thickness. The relationship of coating defects, i.e., damage, with respect to location over a web and over a cooling channel, acting in concert with the cooling fluid, is determined. The cooling fluid properties and film coefficients are then related to the coating defect, and defect zone, wherein burnout, nucleate boiling and film boiling may be established as an additional constraint on the design. As a result, the investigator will have a reasonably well rounded - upper bound, view of how the mirror will respond to the particular conditions imposed by the particular laser system.

Key words: coating defects; cooled laser mirrors; defect damage; hot face design; limiting flux density; mirror damage, vapor barrier-induced burnthrough.

Introduction

A technique is suggested for providing a comprehensive analytical technique for evaluating, to the first order, the thermal, structural, and optical properties of an optical element. Primarily, the technique addresses cooled Laser Mirror Heat Exchangers. However, as an aside, many of the structural expressions will apply to uncooled mirrors when combined with expressions presented by the author, last year.

Essentially, the technique describes the process for evaluating the fluid mechanics within the mirror coolant channels. The heat transfer and steady-state gradients are developed in concert with the analytical and graphical solution of burnout, incipient and pool boiling, and saturation temperature of the coolant fluid.

Based on the heat transfer and fluid mechanics, the analytical expression for static deflection are developed for the channels, webs, and overall bending of the optical elements. The last element of the technique is the development of the analytical solutions for determining the maximum defect size that may be tolerated based on limiting temperature condition of coating or sub-cooled boiling at the coolant channel wall. The last element of the technique is the development of analytical solutions for evaluating temperature gradients and bending of transmissive optics.

The objective of this paper is to develop the various analytical expressions in a step wise fashion in order to lead the reader through each process and, then, to show how the various elements fit together in a comprehensive fashion. At the very outset, of course, the flux density that will irradiate the optic must be known. Secondly, one must know the reflectivity of the optical surface. From this information one will find the absorbed flux density. So that, simply:

---

[1] Numbers in brackets indicate the literature references at the end of the paper.

$$Fo = I_o(1 - R) \qquad (1)$$

where:

I_o = Incident Flux Density, BTU/HR-FT^2 (W/CM^2)
R = Reflectivity
Fo = Absorbed Flux Density, BTU/HR-FT^2 (W/CM^2)

Assuming parallel flow and uniform absorption over the surface of the heat exchanger, determine the amount of flux density that will be absorbed over each top channel, see Figure 1.0. The absorbed flux density for each channel will be partioned between the free span over the flowing fluid and the webb that separates one channel from the other. Typically, the webb thickness will be 5.4 times the channel width and will receive 16% of the absorbed energy. The distribution of absorbed energy between the channel span and the channel webb will be:

Q(.84) = Absorbed energy through span, BTU/HR (Watts) (2)

Q(.16) = Absorbed energy through webb, BTU/HR (Watts) (3)

The fluid mechanics of the system are reasonably straight forward. At the outset, the amount of temperature increase in the flowing fluid should be determined, based on system requirements. So that, temperature increase is found from:

$$\Delta_T = Q/C\rho G\ 3600 \qquad (4)$$

where:

Q = Total absorbed energy/channel, BTU/HR (Watts)
C = Specific Heat, BTU/#-°F (kCal/kgm-°C)
ρ = Density, #/FT.^{3} (kg/M^3)
G = Mass Flow Rate, #/Sec., (M^3/sec.)

Having determined the appropriate temperature increase of the cooling fluid for the allowable mass flow rate, the additional values may be determined so that:

$$R_e = \frac{G\rho}{\mu} \text{ or } \frac{VD_H\rho}{\mu} \quad [1] \qquad (5)$$

where:

R_e = Reynolds Number, dimensionless
G = Mass Flow Rate, FT.^{3}/sec (M^3/sec)
V = Velocity, FT./sec (M/sec)
D_H= Hydraulic Diameter, FT. (Meters)

$$D_H = 4\ \frac{\text{AREA}}{\text{DIAMETER}} \quad [2]$$

μ = Viscosity, #/FT.Sec. (kg/m-sec)

A polynomial expression for (μ) has been derived, for english units, to provide a curve fit for water between 32°F and 200°F and atmospheric pressure. This polynomial expression was derived using the Forward Doolittle Technique:

$$\mu \frac{\#}{\text{Ft-Sec.}} = 1.61861\ (10^{-3}) - 1.661365\ (10^{-5})\ (T°F) + 4.8557\ (10^{-8})\ (T°F)^2 \qquad [3] \tag{6}$$

The pressure drop through the channel is found from:

$$\Delta_p\ \ \#/in^2 = \frac{[f\frac{L}{DH} + \Sigma K_L]\ V^2 \rho}{144\ (2g)} \quad [4]\ [5] \tag{7}$$

where:

L = Length of channel flow, Ft. (m)

D_H = Hudraulic Diameter, Ft. (m)

ΣkL = 1.5 for entrance and exit losses, non dimensional

V = Velocity, Ft./Sec. (m/Sec.)

ρ = Density, #/Ft.^{3} (kgm/m^3)

$R_e > 2000$	$f = [1.84 \log_{10}(R_e) - 1.64]^{-2.0}$	Idel'check	[6]
$R_e > 2000$	$f = .184(R_e)^{-2.0}$	Blausis	[7]
$R_e > 2000$	$f = .0056 + .50(R_e)^{-.32}$	Koo	[8]
$R_e > 2000$	$f = \frac{64}{R_e}$	Moody	[9]

For water, the expression,(Eq. 7), reduces to:

$$\Delta_p\ \ \#/in.^2 = \left\{ [(f\frac{L}{D_H} + 1.5]\ V^2 (6.729) 10^{-3} \right\} \tag{8}$$

The steady-state heat transfer and subsequent steady state temperature gradient through the top face plate may be found from the following expressions. For the portion of the abosrbed flux to be removed from the channel span:

The heat transfer coefficient for Laminar flow, i.e., $R_e < 2000$, is found from the Graetz expression:

$$Nu_\alpha = \frac{h_c D_H}{k} = 3.65 + \frac{0.065 (D_H/L)\ R_e P_R}{1+0.04[(D_H/L)\ R_e P_R]^{2/3}} \tag{9}$$

Sieder and Tate have developed an empirical equation for Laminar flow conditions, such that:

$$Nu_\alpha = \frac{h_c D_H}{k} = 1.86 \left[\frac{R_e\ P_R\ D_H}{L}\right]^{1/3} \left(\frac{\mu_B}{\mu_S}\right)^{0.14} \quad [11] \tag{10}$$

Where:

h_c = Film heat transfer coefficient, BTU/HR-Ft.^{2}-°F (w/cm^2-°C)

k = Thermal Conductivity of cooling fluid, BTU/HR-Ft.-°F(W/Cm-°C)

μ_B = Bulk fluid Viscosity, #/Ft. Sec. (gm/cm-sec.)

μ_S = Viscosity of liquid at surface temperature, #/Ft. Sec. (gm/cm-sec.)

P_R = PRANDTL NUMBER = $\frac{C\mu}{k}(3600)$

For water between 32°F and 200°F at atmospheric pressure, the following polynominal may be used for determining the thermal conductivity of water, in english units: [12]

$$k\ \mathrm{BTU/HR\text{-}FT.\text{-}°F} = .290402 + 9.563962(10^{-4})(T°F) - 2.196228(10^{-6})(T°F)^2 \quad (11)$$

Prandtl number for water between 32°F and 200°F at atmospheric pressure may be found from the following polynominal:

$$P_R = 18.8104 - .208228(T°F) + 6.29383(10^{-4})(T°F)^2 \quad (12)$$

For fully developed turbulent flow, i.e., $R_e > 2000$, the film coefficient may be found from any of the following expressions:

Dittus Boelter Expression

$$Nu_T = \frac{h_c D_H}{k} = .023\,[R_e]^{0.8}[P_R]^{(1/3)} \quad [13] \quad (13)$$

Petuhkov Expression

$$Nu_T = \frac{h_c D}{k} = \frac{(f/8) R_e P_R}{1.07 + 12.7(f/8)^{.5}(P_R{}^{.66} - 1.0)} \quad [14] \quad (14)$$

Seider and Tate Expression

$$Nu_T = \frac{h_c D_H}{k} = .023\,[R_e]^{0.8}[P_R]^{1.3}\left[\frac{\mu_B}{\mu_S}\right]^{0.14} \quad [15]\ [16] \quad (15)$$

From the information generated from the above expressions, the termperature gradient across the stagnation boundary and the temperature gradient across the face-plate may be determined. So that;

Inside wall temperature will be found from:

$$\frac{0.84Q}{h_c A} = [T_{wall} - T_{Bulk}] \quad [17] \quad (16)$$

where:

A = Channel Surface Area. Ft.^{2}(cm^2)

A = Channel width x channel length

The steady state surface temperature is found from:

$$0.84Q = -kA\frac{d_T}{d_X} \quad (17)$$

The variables are separated, so that;

$$\frac{0.84Q}{A}\int_0^L dX = -\int_{T_{Hot}}^{T_{Cold}} k\,dt \quad (18)$$

with (k) independent of (T)

$$0.84Q = \frac{kA}{L}(T_{Hot} - T_{Cold}) \quad [18] \quad (19)$$

where:

ℓ = thickness of face-plate, Ft.(M)

T_{Hot} = Reflective Surface Temperature

T_{Cold} = Inside wall temperature = T_{wall}

So, then, from (19).

$$T_{Hot} = \frac{0.84Q(\ell)}{kA} + T_{wall} \qquad (20)$$

The Webb temperature may be determined, for both the reflective surface and the bottom of the Webb that attaches to the face-plate of the second channel, or substrate, if a second set of channels is required. Basically, the Webb may be treated as a rectangular fin with heat transfer at the end. The generalized solution for this case is:

$$\frac{d^2\Theta}{dx^2} - m^2\Theta=0 \qquad (21)$$

$$\Theta=C_1 e^{mx} + C_2 e^{-mx} \qquad (22)$$

For the case of heat flow from the edge of the fin, the boundary conditions are:

$$\text{at } (x)=b, \ \frac{d\Theta}{dx} = -\frac{h_e}{k}\Theta_e \qquad (23)$$

$$\text{at } (x)=0, \ \Theta=\Theta_o \qquad (24)$$

Differentiating (Eq. 22) and substituting (Eq. 23)

$$C_1 m e^{mb} - C_2 m e^{-mb} = -\frac{h_e}{k}[C_1 e^{mb} - C_2 e^{-mb}] \qquad (25)$$

Substituting (Eq. 24) into (Eq. 22) provides:

$$\Theta_o = C_1 + C_2 \qquad (26)$$

Solving (Eq. 25 and Eq. 26) simultaneously gives:

$$\Theta=\Theta_o\left\{\frac{[e^{mb(x/b-2)} + \alpha e^{-mb(x/b)}]}{\alpha - e^{-2mb}}\right\} \qquad (27)$$

where:

$\alpha=\frac{m+h_e/k}{m-h_e/k}$ h_c=Eq. 10, 13, 14, or 15

$m=[\frac{2h_c}{k\,S_o}]^{.5}$ S_o= Webb thickness, Ft.

$\Theta_o=T_o-T_{Hot}$ b = channel + face-plate depth, Ft.

$\Theta=T-T_{Bulk}$

$h_e=k/b$

EQ. 27 May be differentiated for the ideal case, so that;

$$\frac{d\Theta}{dx} = \frac{d}{dx}\left[\frac{\Theta_o(e^{mb(x/b-2)} + \alpha\ e^{-mb(m/b)}}{\alpha + e^{-2mb}}\right] \tag{28}$$

$$\text{at}(x) = 0 \qquad \frac{d\Theta}{dx} = \frac{\Theta_o m(e^{-2mb} - \alpha)}{\alpha + e^{-2mb}} \tag{29}$$

So, then, heat flow through the base of the fin:

$$.16Q = -kS_o\ L_o \left.\frac{d\Theta}{dx}\right|_{x=o} = \frac{kS_oL_oM\Theta_o(\alpha - e^{-2mb})}{\alpha + e^{-2mb}} \tag{30}$$

move conveniently,

$$.16Q = kS_oL_oM\Theta_o\ \frac{[({}^{h}e/mk) + \text{TANH mb}]}{1 + (h_e/mk)\ \text{TANH mb}} \tag{31}$$

Since .16Q is a known value, Eq. 31 may be written to solve for the temperature at the reflective surface of the fin and the tip of the fin. Re-arranging Eq. 31.

$$T_o - T_{Wall} = \frac{.16Q\ [1 + (he/mk)\ \text{TANH mb}]}{k\ S_oL_o\ m\ [(he/mk) + \text{TANH mb}]} \tag{32}$$

where:

L_o = Length of the channel, Ft.

and from Eq. 27, for x = b

$$T_e - T_{Bulk} = -\frac{(T_o - T_{Wall})[e^{mb(1-2)} + \alpha\ e^{-mb}]}{\alpha - e^{-2mb}} \quad [19], [20], [21] \tag{33}$$

Knowing the various temperatures, as determined by the foregoing expressions, it is possible to determine the deflection caused by the various thermal gradients.

For deflection due to thermal gradient across the channel span, which is a fully clamped geometry, is found from the following:

Bending Moment:

$$M = \frac{\alpha(T_{Hot} - T_{Cold})(1 + \mu)D}{L} \tag{34}$$

where:

T_{Hot} = Eq. 20 $\qquad\mu$ = Poisson's Ratio

T_{Cold} = Eq. 16

L = Thickness of face-plate

α = Coefficient of expansion of face-plate material, in/in-^{o}F

D = Modulus of Rigidity

$$D = \frac{Et^3}{12(1-\mu^2)}$$

E = Modulus of Elasticity, #/in^2

The apparent load is found from:

$$\hat{Q} = \frac{M(16)}{(1+\mu)R^2} \tag{35}$$

where:

R = Half-width of channel span

Deflection at the center of a Rectangular Element fully clamped and width of channel to length of channel ratio > 3.0, which is the case for most mirrors:

$$\Delta_1 = \left[\frac{\hat{Q}(2R)^4}{D}\right] 2.6(10^{-3}) \quad [22], [23], [24], [25], \tag{36}$$

In order to be most conservative, the webb will be allowed to grow without restraint, i.e., without Poisson effect, so that:

$$\Delta_2 = \alpha(T_o - T_e)b \quad [26] \tag{37}$$

The channel span deflection resulting from hyrdraulic pressure is found from:

$$\hat{Q}_1 = [P_1 + \Delta_P]2^{-1} \tag{38}$$

where:

P_1 = Entrance pressure, #/in^2

Δ_P = Pressure drop through the heat exchanger, #/in^2
= Eq. 7

For clamped rectangular geometry as indicated by (Eq. 36)

$$\Delta_3 = \left[\frac{\hat{Q}_1(2R)^4}{D}\right](2.6)10^{-3} \quad [27] \tag{39}$$

The ripple for the face-plate as a result of the thermal gradient across the face-plate, the axial gradient along the webb and the deflection from the hydraulic pressure will be found from:

$$\text{RMS}(\Delta) = \left[\frac{\Delta_1 + \Delta_2 + \Delta_3}{2\sqrt{2}}\right] \tag{40}$$

The next area of concern is the overall bending of the optic. The radius of curvature due to temperature difference between the coolant channels and the back surface of the substrate is found for a free geometry:

$$R_o = \frac{t}{\alpha\Delta T} \quad [28] \tag{41}$$

where:

t = Substrate thickness, inches

α = Coefficient of Expansion

Δ_T = T_e - Ambient temperature

T_e = Temperature at the end of the webb

$D = \frac{Et^3}{12(1-\mu^2)}$ R = Radius of the optical element inch

The apparent load due to the bending is found from:

$$\hat{Q}_o = \frac{8\ D(1 + \mu)}{R_o (R)^2} \qquad [29] \qquad (42)$$

For a plate simply supported:

$$\Delta_o = \frac{\hat{Q}_o R^4}{64D} + \frac{\hat{Q}_o R^4}{16D(1+\mu)} \qquad [30], [31]$$

For a circular plate that is supported on the edge at three (3) points, 120° apart, with the load uniformly distributed, the deflection at the center would be:

$$\Delta_o = \frac{.0362\pi\hat{Q}_o R^4}{D} \qquad [32] \qquad (43)$$

The next element of the analysis is to evaluate the possibility of subcooled boiling, i.e., burnout. It should be pointed out that a defect that becomes absorbing will allow the spot (defect) site to increase in temperature in as much as the heat transfer across the stagnation boundary of the fluid is by conduction only. In this problem, only the localized spot is affected. Little heat is carried to the surrounding by diffussion since the differences in thermal diffusivity of the face-plate materials and the cooling fluids are large. Essentially, then, the fluid will be a virtual insulator to the channel wall and will allow the channel wall, at the localized spot, to increase in temperature without producing a significant change in the bulk fluid flowing in the channel. The localized spot (defect) at the wall, then will experience localized boiling. [33].

There are techniques for evaluating the points of boiling as a function of the referenced film coefficient, temperature of the bulk fluid, velocity of the bulk fluid, and the pressure in the system. A graphing technique for evaluating burnout and incipient boiling has been explained by the author in a previous paper [34]. However, the technique is essential to this first order analysis system and may be evaluated using a plot of the following expressions as shown in the graph of figure 6.0.

The heat transfer before boiling if found from:

$$\frac{Q}{A} = h_c\ [(T_W - T_S) + (T_S - T_B)] \qquad [35] \qquad (44)$$

where:

T_W = Inside channel wall temperature

T_S = Saturation temperature of the cooling fluid at average pressure of the mirror

T_B = Bulk average temperature of the cooling fluid

Incipient boiling is found from:

$$\left[\frac{Q}{A}\right]_i = 15.60(\bar{P})^{1.156}\ [T_W - T_S]^{2.30/\bar{P}^{0.0234}} \qquad [36] \qquad (45)$$

where:

$\bar{P}$ = Average absolute pressure, PSIA

Fully developed boiling is found from:

$$\left[\frac{Q}{A}\right]_B = \left[\frac{(T_W - T_S)\ \mathrm{EXP}\ (\bar{P}/900)}{60}\right]^4 (10^6) \qquad [37] \qquad (46)$$

Burnout, based on velocity, is found from the McAdams correlation:

$$\left[\frac{Q}{A}\right]_{B.O} = 4(10^5)V^{1/3} + 4.8(10^3)(T_S - T_B)V^{1/3} \quad [38] \qquad (47)$$

By plotting equations 45 through 47, as shown in figure 6.0, the maximum temperature increase at a defect site on the channel wall may be determined. As pointed out previously by the author, the maximum temperature for reflective coating should not exceed 200°C(392°F). This value is some what conservative; however, transcending this temperature invites catastrophic damage, based on experience. This temperature may be achieved either on the coating surface or through burn-back from incipient boiling at the channel surface, resulting from an absorbing defect of the appropriate size. [39]

The maximum defect size for 100% absorbing defect may be evaluated from the Palmer-Bennett model. [40]

$$\Delta_T = \frac{F_o\sqrt{\alpha\tau}}{K}\left\{1.1284 - 2\text{ierfc}\ \frac{R}{2\sqrt{\alpha\tau}}\right\} \text{ For Reflective Surface} \qquad (48)$$

$$\Delta_T = \frac{F_o\sqrt{\alpha\tau}}{K}\left\{2\text{ierfc}\ \frac{Z}{2\sqrt{\alpha\tau}} - 2\text{ierfc}\ \frac{(Z^2 + R^2)^{.5}}{2\sqrt{\alpha\tau}}\right\} \text{For channel wall} \qquad (49)$$

where:

Δ_T = Maximum temperature increase over steady-state. This value will depend on which element is controlling -- viz., maximum coating temperature or incipient boiling at channel wall.

Z = Thickness of face-plate, FT.

F_o = Absorbed Flux Density, BTU/HR-Ft.^{2}

K = Thermal Conductivity of face plate material, BTU/HR-FT.-°F

α = Thermal diffusivity of face-plate material, FT.^{2}/HR

τ = Run time, HRS.

$$\text{ierfc}\ (x) = \int_x^\infty [1-\text{erf}(\xi)]\, d\xi$$

$$\text{erf}\ (x) = \frac{2}{\pi}\int_0^\infty e^{-\xi^2}\, d\xi$$

$\alpha^o = \alpha(6\sqrt{\alpha\tau})/Z$ For $6\sqrt{\alpha\tau} > Z$

R = Defect radius, FT.

Knowing the value of Δ_T, the maximum defect radius may be found from:

$$2\text{ierfc}\left(\frac{R}{2\sqrt{\alpha\tau}}\right) = 1.1284 - \frac{K(\Delta_T)}{F_o\sqrt{\alpha\tau}} \qquad (50)$$

A value of anti -[2ierfc(x)] has been developed through a set of polynominals derived from using the forward Doolittle Matrix Technique; so that:

$$\text{For } (x) = \left\{2\text{ierfc}\ \left(\frac{Z}{2\sqrt{\alpha\tau}}\right) - \frac{K(\Delta T)}{F_o\sqrt{\alpha\tau}}\right\} \text{ OR } \left\{1.1284 - \frac{K(\Delta T)}{F_o\sqrt{\alpha\tau}}\right\}$$

$(x) = o \text{ to } 1(10^{-4}) \quad R = 2\sqrt{\alpha\tau}(2.6)$

$(x) =$ .0001 to .002 $\quad R = 2\sqrt{\alpha\tau}[2.576486 - 656.947(x) + 1.87357(10^5)(x)2]$

$(x) =$ .002 to .0253 $\quad R = 2\sqrt{\alpha\tau}[2.062964 - 52.9737(x) + 1.07615(10^3)(x)^2]$

$(x) =$ .0254 to .1364 $\quad R = 2\sqrt{\alpha\tau}[1.58956 - 8.663(x) + 26.882(x)^2]$

$(x) =$ .1365 to .3119 $\quad R = 2\sqrt{\alpha\tau}[1.2648 - 3.121(x) + 3.1847(x)^2]$

$(x) =$ .3120 to .6284 $\quad R = 2\sqrt{\alpha\tau}[1.04463 - 1.671(x) + .7755(x)^2]$

$(x) =$ .6285 to 1.1284 $\quad R = 2\sqrt{\alpha\tau}[.8424 - 1.0125(x) + .23617(x)^2]$

Conversly

The polynominal for 2ierfc (x) for intervals of (x) will be: [41]

x Interval	2ierfc (x)
0 - 0.299	$1.1284 - 1.998(x) + 1.11(x)^2$
0.30-0.5499	$1.1150743 - 1.90863(x) + 0.9543(x)^2$
0.55 - 0.9999	$1.012 - 1.5524(x) + .64346(x)^2$
1.0 - 1.599	$.6271 - 0.76914(x) + 0.241964(x)^2$
1.6 - 2.0	$.21573 - 0.21165(x) + 0.0525(x)^2$
2.1 - 2.5	$.05124 - .041425(x) + .0083939(x)^2$

In order to illustrate the techniques, a working example will be given to take the reader through the use of each expression. Additionally, an output of the Doc Jim Code, which calculates the values, will be shown at the end of this portion.

Problem:

A cooled laser mirror, with three channel passages, as shown in figure 3.0, will absorb 10^3 BTU/HR-Channel. The face-plates of the heat exchanger will be 0.020" thick. The channel geometry will be 0.081" wide, 0.020" high with a webb thickness of 0.015". The channel will be 6.0" long. The cooling medium will be water, which will enter the mirror at 70°F and 150 PSIG entrance pressure. The face-plates will be made of Moly. The velocity of the water will be 35 FT./Sec. at fully developed profile. Run time is 15 seconds.

From Eq. (2), (3) we know that the portion of energy for the channel span and webb will be:

$$\text{Span} = .84(10^3) = 840 \text{ BTU/HR}$$
$$\text{Webb} = .16(10^3) = 160 \text{ BTU/HR}$$

The hyrdraulic diameter of the cooling passages will be:

$$D_H = \left[4\frac{(.081 \times .020)}{(2 \times .081 + 2 \times .020)}\right] 12^{-1}$$

$$D_H = 2.67(10^{-3})\text{FT.}$$

The temperature rise of the water for each channel will be, from Eq. 4:

$$\Delta_T = \frac{10^3 \text{ BTU/HR}}{1.0 \frac{\text{BTU}}{\#\text{-}°\text{F}} \; 62.35 \frac{\#}{\text{FT.}^3} \; 35 \frac{\text{FT.}}{\text{Sec.}} \; \left(\frac{.081 \times .020}{144}\right) 3600 \frac{\text{Sec.}}{\text{Hr.}}}$$

$$\Delta_T = 11.315°\text{F}$$

The first cut viscosity will be based on the end point temperature of the water, i.e., 70 + 11.315 = 81.385°F.

$$\mu = 1.61861(10^{-3})-1.661365(10^{-5})(81.315)+4.8557(10^{-8})(81.315)^2$$

$$\mu = 5.887(10^{-4})\frac{\#m}{FT.\text{-}Sec.}$$

From Eq. 5

$$R_e = \frac{35\ FT./Sec.\ (2.67)10^{-3}\ FT.\ 62.35\ \#/FT.^3}{5.887(10^{-4})\frac{\#}{FT.\text{-}Sec.}} \qquad R_e = 9896.8$$

Friction from Eq. 7

$$f = [1.84\ \log_{10}(R_e)-1.64]^{-2.0}$$

$$f = 3.065(10^{-2})$$

Pressure Drop from Eq. 8

$$\Delta_p = \left\{[.03065\ \frac{.5}{2.67(10^{-3})}]+1.5\right\}\ 35^2(6.729)10^{-3}$$

$$\Delta_p = 59.677\ \#/in.^2$$

Since $R_e > 2000$, the film coefficient will be found from Eq. 13. The Prandtl and thermal conductivity will be found from Eq. 12 and Eq. 11 respectively:

$$P_R = 18.8104 - .208228(81.315)+6.29383(10^{-4})(81.315)^2$$

$$P_R = 6.04$$

$$k = .290402 + 9.56396(10^{-4})81.315-2.196228(10^{-6})81.315^2$$

$$k = .3536\ BTU/HR\text{-}FT.\text{-}°F$$

The heat transfer film coefficient is found from Eq. 13:

$$h_c = \frac{.3536}{2.67(10^{-3})}(.023)(9896.8)^{.8}(6.04)^{1/3}$$

$$h_c = 8719\ BTU/HR\text{-}FT.^2\text{-}°F$$

The heat transfer area over the span is:

$$A = (.081 \times 6)144^{-1}$$

$$A = 3.375(10^{-3})FT.^2$$

Recheck Viscosity, Prandtl and Conductivity based on

$$\overline{T} = (104.2 + 70)\ 2^{-1}$$

$$T = 87.1°F$$

$$\mu = 5.399(10^{-4})\quad PR = 5.448\quad k = .3908$$

/new/ $R_e = 10792 \qquad f = .0299\quad \Delta_p = 58.55\ \#/in.^2$

$$h_c = 10002\ BTU/HR\text{-}FT.^2\text{-}°F$$

$$T_{Wall} = 104°F$$

The reflective surface of the mirror will be from Eq. 19: $T_{Hot} = \dfrac{840\ \frac{BTU}{HR}\ (\frac{.020}{12})}{84\ \frac{BTU}{HR\text{-}FT.\text{-}°F}\ (3.375)10^{-3}Ft^2} + 104°F$

$T_{Hot} = 109°F$

Temperature balance along the webb will be evaluated from Eq. 32 and Eq. 33.

$$M = \left[\frac{10002 \times 2}{84(\frac{.015}{12})}\right]^{.5}$$

$M = 436.5/FT.$ $\qquad\qquad L_o = 6" \text{ OR } 0.5 \text{ FT.}$

$b = 3.33(10^{-3})FT.$

$h_e = 84/3.33(10^{-3})$

$h_e = 25202 \text{ BTU/HR-FT.}^2\text{-°F}$

$$\alpha = \frac{m + he/k}{m - he/k}$$

$\alpha = 5.3956$

$TANH(mb) = .8966$

$$T_o = \frac{160\frac{BTU}{HR}\left[1+(\frac{.6874}{FT.^2} \times .8966)\right]}{84\ \frac{BTU}{HR\text{-}FT.\text{-}°F}\ \left(\frac{.015}{12}\right)FT.\ \ (.5\ FT.)\left[\frac{.6874}{FT.^2} + .8966\right]\ (\frac{436.5}{FT.})} + 104°F$$

$$T_o = \frac{258.605 \quad \frac{BTU}{HR\text{-}FT.^2}}{34.6695 \quad \frac{BTU}{HR\text{-}FT.^2\text{-}°F}} + 104°F$$

T_o=111.5°F Reflective Surface temperature over the webb

From Eq. 33

$$T_e = \frac{[112-87.1][EXP(-1.45485)+5.3956 \times EXP(-1.45485)]}{5.3956 - EXP\ (-2 \times 1.45485)} + 87.1°F$$

$$T_e = \frac{36.43}{5.341} + 87.1°F$$

$T_e = 93.92°F$

The span bending moment will be found from Eq. 34.

$$M = \frac{2.77(10^{-6})/°F(109-104)(1.3)D}{.02"}$$

$$D = \frac{46(10^6)(.02)^3}{12(1-.3^2)}$$

$D = 33.7$

$M = .03033$ #-in./in.

$$Q = \frac{.03033(16)}{(1 + \mu)(.08112)^2} = 227.58 \text{ \#/in.}^2$$

$$\Delta = \left[\frac{227.58(.081)^4}{33.7}\right]2.6(10^{-3})(.0254)10^6$$

$\Delta_1 = \ 1.9198(10^{-2})\mu$

$$\Delta_2 = 2.77(10^{-6})(111.5 - 93.92)\ 3.33(10^{-3}) \times 12 \times .0254 \times 10^6$$

$$\Delta_2 = 4.947(10^{-2})\mu$$

$$\Delta_3 = \left[\frac{104(.081)^4}{33.7}\right]\ 2.6(10^{-3}) \times .0254 \times 10^6$$

$$\Delta_3 = 3.4766(10^{-3})\mu$$

$$\text{RMS}\ (\Delta) = [1.9198(10^{-2}) + 4.947(10^{-2}) + 3.4766(10^{-3})](2\times\sqrt{2})^{-1}$$

$$\text{RMS}\ (\Delta) = 2.5507(10^{-2})\mu$$

The overall bending of the optic which is 12.0" in diameter with a 2.0" thick substrate is found from Eq. 41 through Eq. 44.

$$R_o = \frac{2.0}{(93.92 - 70)\ 2.77\ (10^{-6})}$$

$$R_o = 30185 \text{ inches}$$

$$D = \frac{46(10^6)\ 2^3}{12\ (1-.3^2)}$$

$$D = 33.6996(10^6)$$

$$\hat{Q}_o = \frac{8(33.6996)10^6(1.3)}{30185\ (6)^2}$$

$$\hat{Q}_o = 322.5\ \#/\text{in.}^2$$

Bending for a simply supported plate:

$$\Delta_o = \frac{322.5(6)^4}{64(33.6996)(10^6)} + \frac{322.5(6)^4}{16(33.6996)10^6(1.3)}$$

$$\Delta_o = 7.9(10^{-4}) \text{ inches}$$

Δ_o = 20.1μ if there were only one (1) flow channel

Bending for an optic support at three places 120° apart:

From Eq. 44

$$\Delta_o = \frac{.0362(\pi)\ 322.\ }{33.6996(10\ )}\frac{(6)^4}{}\ (.0254)10^6$$

Δ_o = 35.826μ if there was only one (1) flow channel

The boiling and burnout characteristics of this particular problem can now be evaluated for graphical analysis.

From Eq. 45

$$\left[\frac{Q}{A}\right] = h_c\ [(T_W - T_S) + (T_S - T_B)]$$

$$h_c = 10004\ \text{BTU/HR-FT.}^2\text{-°F}$$

$\bar{P}$ = 118.7 PSIA so that T_S = 340°F [42]

$$T_B = 87.1\text{°F}$$

$$T_S = 340\text{°F}$$

For $(T_W - T_S) = 10, 20, 30$

$$\left[\frac{Q}{A}\right] = 2.63\,(10^6),\ 2.73(10^6),\ 2.83(10^6)$$

For incipient boiling:

$$\left[\frac{Q}{A}\right]_i = 15.60(\bar{P})^{1.156}\ [T_W - T_S]^{2.30/\bar{P}^{\,0.234}}$$

For $(T_W - T_S) = 10, 20, 30$

$$\left[\frac{Q}{A}\right]_i = 4.46(10^5),\ 1.85(10^6),\ 4.26(10^6)$$

For fully developed boiling:

$$\left[\frac{Q}{A}\right]_B = \left[\frac{(T_W - T_S)\text{EXP}(\bar{P}/900)}{60}\right]^4 (10^6)$$

For $(T_W - T_S) = 10, 20, 30$

$$\left[\frac{Q}{A}\right]_B = 1308,\ 20923,\ 1.06(10^5)$$

Burnout is found from:

$$\left[\frac{Q}{A}\right]_{B.O} = (4(10^5)(35)^{1/3} + 4.8(10^3)(340-87.1)35^{1/3}$$

$$\left[\frac{Q}{A}\right]_{B.O} = 5.28(10^6)$$

From figure 6.0,which is a graphical plot of the previous expression, it becomes apparent that the wall temperature may be substantially above 391°F, which is the limit of the coating. Consequently, the maximum temperature rise for a defect will be:

Allowable $\Delta_T = 391 - 111.5$

$$\Delta_T = 279.5°\text{F}$$

$$F_o = 1(10^3)\ \text{BTU/HR}/(.081 \times 6 \times 144^{-1})$$

$$F_o = 2.963(10^5)\ \text{BTU/HR-FT.}^2$$

So that, from Eq. 49;

$$\frac{R}{2\sqrt{\alpha\tau}} = 1.1284 - \frac{279.5°\text{F}\left(84\ \frac{\text{BTU}}{\text{HR-FT.-°F}}\right)}{2.963(10^5)\ \frac{\text{BTU}}{\text{HR-FT.}^2}\left[2\ \frac{\text{FT.}^2}{\text{HR}}\ (4.16)10^{-3}\text{HR}\right]^{.5}}$$

$$2\text{ierfc}\frac{R}{2\sqrt{\alpha\tau}} = .2604$$

The polynominal for solving the anti-2 ierfc(.2604)

$$R = 2\left[2\ \frac{\text{FT.}^2}{\text{HR}}\ (4.16)10^{-3}\text{HR}\right]^{0.5}\left[1.2648 - 3.121(.2604) + 3.1847(.2604)^2\right]$$

R = .122 FT. DIAMETER = 2.9 inches which is much larger than a single channel. The following pages show the results of the Doc Jim Code which solves each of the elements which have been shown in the example.

The last area to be visited with analytical evaluation is the problem one encounters with transmissive optics. The major mechanism for damage in a CW Laser System is the surface absorptions, vis-a-vis, bulk absorption, self-focusing, photon absorption, et al.

In most cases, the beam foot-print covers only a central portion of the transmissive element. Consequentially, there are both axial and radial gradients which set up bi-axial stresses. Additionally, bubbles and striae become notch points or stress risers in the material. In the case of thermal loading, bubbles and striae become absorbing defects, much like what has been discussed in the foregoing. The following, then, is a technique for evaluating the temperature rise on the first and second surface of transmissive optics and the resulting stress and deflection that will result. The temperature rise on the front surface of a transmissive optic with a substantial dimension is found from:

$$\Delta T_{°F} = \frac{F_{o_1} (\alpha\tau)^{0.5}}{K} (1.1284) \qquad (51)$$

When: $R/2(\alpha\tau)^{0.5} \geq 3.0$

The temperature rise on the back surface of a transmissive optic for this set of conditions is found from:

$$\Delta T_{°F} = \frac{\left[F_{o_2} + I_o \left(1 - e^{-\beta t}\right)\right]}{K} (\alpha\tau)^{0.5}\ 1.1284 \qquad [42] \qquad (52)$$

Where:

$Fo = I_o(1-R)$, BTU/HR-Ft.^{2}, Absorbed flux density

I_o = Incident Flux density, BTU/HR-Ft.^{2}

β = Attentuation coefficient, cm.$^{-1}$

τ = Thickness of the optic, cm.

For a transmissive optic that is irradiated by a spot, i.e.,

Where: $R/2(\alpha\tau)^{0.5} < 3.0$

The temperature rise on the surface is found from:

$$\Delta T_{°F} = \frac{F_{o_1} (\alpha\tau)^{0.5}}{K} \left\{ 1.1284 - 2\,\text{ierfc} \frac{R}{2(\alpha\tau)^{0.5}} \right\} \qquad (53)$$

and for the back surface, for the same conditions:

$$\Delta T_{°F} = \frac{\left[F_{o_2} + I_o\left(1-e^{-\beta t}\right)\right] (\alpha\tau)^{0.5}}{K} \left\{ 1.1284 - 2\,\text{ierfc} \frac{R}{2(\alpha\tau)^{0.5}} \right\} \qquad (54)$$

Thermal shock becomes the major problem with these damage mechanisms. Once the coating becomes debilitated, the thermal stresses will begin to build quite rapidly.

Kreidl and Wood propose a model that suggest that an axial gradient sufficient to produce a tensile stress of 1000 PSI between the two surfaces should be a limit of the design. So that,

$$(\Delta_T)_{1000} = \frac{2(10^3)(1-\mu)}{E\gamma} \quad [43] \tag{55}$$

Where:

μ = Poisson's Ratio

E = Young's Modulus, (#/in.^{2})

γ = Coefficient of thermal expansion, (in./in-$^\circ F_{\Delta_T}$)

Fundamentally, then, the damage due to thermal gradient for a transmissive optic:

When: $R/2(\alpha\tau)^{0.5} \geq 3.0$

$$2000 > \left\{\left[\frac{F_{o_1}(\alpha\tau)^{0.5}}{K}(1.1284)\right] - \left[\frac{F_{o_2} + I_o(1-e^{-\beta t})}{K}(1.1284)\right]\right\} \times E\gamma(1-\mu)^{-1.0} \tag{56}$$

and for: $R/2(\alpha\tau)^{0.5} < 3.0$

$$2000 > \left\{\left[\frac{F_{o_1}(\alpha\tau)^{0.5}}{K}\left(1.1284 - 2\text{ierfc}\frac{R}{2(\alpha\tau)^{0.5}}\right)\right] - \left[\frac{F_{o_2} + I_o(1-e^{-\beta t})}{K}\left(1.1284 - 2\text{ierfc}\frac{R}{2(\alpha\tau)^{0.5}}\right)\right]\right\} \times E\gamma(1-\mu)^{-1.0} \tag{57}$$

As the equations indicate, the value on the right hand side will be a negative value. The sign convention only indicates the tensile or compressive condition. The front surface will be in compression and the second surface will be in tension.

The bending of the transmissive optics may be found, as previously, from EQ. 41. For most conditions, the optic may be treated as simply supported around the peripheral edge.

Then, for a round window:

$$R_o = \frac{t}{\alpha\Delta T} \tag{58}$$

$$\hat{Q}_o = \frac{8D(1+\mu)}{R_o(R)^2} \tag{59}$$

and:

$$\Delta_o = \frac{\hat{Q}_o R^4}{64D} + \frac{\hat{Q}_o R^4}{16D(1+\mu)} \quad [44] \tag{60}$$

For a rectangular window that is simply supported:

$$R_o = \frac{t}{\alpha\Delta T} \tag{61}$$

$$\hat{Q}_o = \frac{8D(1+\mu)}{R_o(R)^2} \quad \text{where: } R=.5 \times \text{short side dimension, inches} \tag{62}$$

$$\Delta_o = \frac{Q_o(2R)^4}{D}(\lambda) \qquad [45] \tag{63}$$

For a ratio of the sides, i.e., the long side divide by the short side:

$$\frac{S\ (\text{long})}{S\ (\text{short})} = Z$$

For interval (Z):

1.0 to 2.0	$-6.9953(10^{-3})+1.34996(10^{-2})(Z)-2.4674(10^{-3})(Z)^2$
2.0 to 5.0	$3.6464(10^{-3})+1.20792(10^{-2})(l\ Z)-3.9140(10^{-3})(LnZ)^2$ [46]
5.0 to ∞	.01302

There are additional conditions where transmissive optical elements are used, e.g., a second surface reflecting beam splitter, or a simple second surface reflector.

For: $R/2(\alpha\tau)^{0.5} \geq 3.0$

$$\Delta T_{°F} = \frac{\left[2\ F_{o_1} + I_o(1-e^{-2\beta t})\right] 1.1284\ (\alpha\tau)^{0.5}}{K} \tag{64}$$

The second surface temperature rise is found from:

$$\Delta T_{°F} = \frac{\left[F_{o_2} + I_o(1-e^{-\beta t})\right] 1.1284(\alpha\tau)^{0.5}}{K} \tag{65}$$

For: $R/2(\alpha\tau)^{0.5} < 3.0$ The front surface temperature rise:

$$\Delta T_{°F} = \frac{\left[2\ F_{o_1} + I_o(1-e^{-\beta tz})\right]}{K}(\alpha\tau)^{0.5}\left\{1.1284 - 2\text{ierfc}\ \frac{R}{2(\alpha\tau)^{0.5}}\right\} \tag{66}$$

For the second surface temperature rise:

$$\Delta T_{°F} = \frac{\left[F_{o_2} + I_o(1-e^{-\beta t})\right](\alpha\tau)^{0.5}}{K}\left\{1.1284 - 2\text{ierfc}\ \frac{R}{2(\alpha\tau)^{0.5}}\right\} \tag{67}$$

Typical Thermal-Mechanical Properties
of Commonly Used Optical Materials

Table 1.0 (46)

Optical Material	Young's Modulus (E) #/in^2	Thermal Diffusivity (α) Ft^2/HR	Thermal Conductivity (K) BTU/HR-FT-°F	Linear Coefficient of Expansion in/in-°F
Moly	$46(10^6)$	2.05	84	$2.77(10^{-6})$
Copper	$17(10^6)$	4.42	224	$9.28(10^{-6})$
Silicon Carbide	$55(10^6)$	.3525	40	$1.94(10^{-6})$
Berylco-10	$17(10^6)$	2.356	121	$9.80(10^{-6})$
Electroless Nickel	$21(10^6)$	$7.4(10^{-4})$	2.9	$7.64(10^{-6})$
Fused Silica	$10.6(10^6)$	0.033	0.8	$3.11(10^{-7})$
ULE	$9.8(10^6)$	0.03	0.76	$1.67(10^{-8})$
Zerodur	$13.3(10^6)$	0.03	0.948	$6.67(10^{-8})$

REFERENCES

1. Schlichting, Hermann, Boundary - Layer Theory. 6th ed., New York; McGraw-Hill; 1968; pp 744.
2. Denn, Morton, Process Fluid Mechanics. Englewood, New Jersey; Prentice-Hall; 1980; pp 383.
3. Stanby, L.T. Practical Statistics For Petroleum Engineers. Tulsa, Okla.; Petroleum Publishing; 1973; pp 139.
4. Kreith, Frank, Principles of Heat Transfer, 2nd ed., Scranton, PA; International Textbook Co.; 1966; pp 620.
5. Olson, R.M., Engineering Fluid Mecahnics, 2nd ed., Scranton, PA; International Textbook Co.; 1967; pp 392.
6. Idel'Chik, I.E., Handbook of Hydraulic Resistance, Jerusalem, Israel; Israeli Program for Scientific Translations; 1960; pp 560.
7. Denn, Op. Cit.
8. Olson, Op. Cit.
9. Ibid.
10. Edwards, D.K.; Denny, J.E.; Mills, A.F., Transfer Process. 2nd ed., New York, N.Y.; McGraw-Hill Book Co.; 1973; pp 421.
11. Sieder, E.N.; Tate, C.E., Heat Transfer and Pressure Drop in Tubes. Ind. Eng. Chem. 28; 1429; 1936.
12. Stanley; Op Cit.
13. Dittus, F.W.; Boelter, L.M., Heat Transfer in Automobile Radiators of the Tubular Type, Vol 2. Berkley, CA; University of California Berkley Publ. Eng; 1930. pp 443-461.
14. Petukhov, B.S.,"Heat Transfer and Friction in Turbulent Pipe Flow with Variable Properties" in Advances in Heat Transfer, Vol. 6, James P. Hartnett and Thomas F. Irvine, ed. New York, N.Y.; Academic Press; 1970; pp 503-564.
15. Sieder and Tate; Op. Cit.
16. Kreith; Op. Cit.
17. Ibid.
18. Ibid.
19. Kern, D.Q.; Kraus, A.D., Extended Surface Heat Transfer. New York, N.Y.; McGraw Hill Book Co.; 1972. pp 805.
20. Harper, D.R.; Brown, W.B., Mathematical Equations for Heat Conduction in the Fins of Air Cooled Engines; N.A.C.A. Rept. 158, 1922.
21. Berger, Arthur,"Principles of Heat Transfer Augmentation 1: Single-Phase Heat Transfer", in Heat Exchangers, S. Kakac; A.E. Bergles; F. Mayiuger, ed. New York, N.Y.; McGraw-Hill Book Co.; 1959; pp 580.
22. Timoshenko, S.; Woinowsky-Kreiger, S., Theory of Plates and Shells. New York, N.Y.; McGraw-Hill Book Co.; 1959; pp 580.
23. Roark, Raymond, Formulas For Stress and Strain. 4th ed., New York, N.Y.; McGraww-Hill Book Co.; 1965; pp 432.

24. Harvey, John, Pressure Component Construction. New York, N.Y.; Van Nostrand Reinhold Co.; 1980; pp 479.

25. Sneddon, I.N.; Berry, D.S.,"The Classical Theory of Elasticity," in Elasticity and Plasticity, Vol. VI. S. Flugge, ed. Berlin, Germany; Springer-Verlag; 1958; V-126.

26. Timoshenko; Op. Cit.

27. Ibid.

28. Harvey; Op. Cit.

29. Ibid.

30. Ibid.

31. Roark; Op. Cit.

32. Timoshenko; Op. Cit.

33. Palmer, J.R.; Bennett, H.E., "Relationship Between Coating Defects and The Limiting Flux Density a Cooled Laser Mirror Can Withstand," in Proceedings of 13th Annual Symposium on Optical Materials for High Power Lasers, Bennett, H.E.; Glass, A.J.; Guenther, A.H.; Neuman, B.E., ed. 1981 Nov. 17-18.

34. Ibid.

35. Rohsenow, W.M.,"Boiling", Chapter 13 in Handbook of Heat Transfer, W.M. Rohsenow; J.P. Hartnett, ed. New York, N.Y.; McGraw-Hill Book Co.; 1973; 13.1-13.75.

36. Long, L.S., Boiling Heat Transfer and Two Phase Flow. Huntington, N.Y.; Robert E. Kreiger Publishing Co.; 1975; pp 242.

37. Van Stralen, S.; Cole, R., Boiling Phenomena, Vol. I. New York, N.Y.; McGraw-Hill Book Co.; 1979; pp 443.

38. McAdams, W.H., Heat Transmission, 3rd ed. New York, N.Y.; McGraw-Hill Book Co.; 1954; pp 392.

39. Bennett, H.E.,"Insensitivity of the Catastrophic Damage Threshold of Laser Optics to Dust and Other Surface Defects," in Proceedings of 12th Annual Symposium on Optical Materials for High Power Lasers, Bennett, H.E.; Glass, A.J.; Guenther, A.H.; Newman, B.E., ed. 1980 September 30 - October 1; Nat. Bur. Stand. (U.S.) Spec. Publ. 620; 1981 October; 256-263.

40. Palmer and Bennett; Op. Cit.

41. Ibid.

41. Schneider, P.J., "Conduction," Chaper 3 in Handbook of Heat Transfer, W.M. Rohsenow, ed., New York, N.Y.; McGraw-Hill Book Co.; 1973; 3.1 - 3.134.

43. Kreidl, N.J.; Rood, J.L., "Optical Materials," Chapter 5, Vol. I, in Applied Optics and Optical Engineering, R. Kingslake, ed., New York, N.Y., Academic Press; 1965;Pg. 74.

44. Harvey, op. cit.

45. Timoshenko and Woinowsky-Kreiger, op. cit.

46. Barnes, W.P., "Optical Materials-Reflective," Chapter 4, Vol. VII , in Applied Optics and Optical Engineering, R. Shannon and J. Wyant, ed., New York, N.Y.;Academic Press; 1979; Pg. 102.

```
********************************

 DOCJIM LASER MIRROR PROGRAM

 THERMAL DISRIBUTION FOR THE FIR
ST AND SECOND MIRROR CHANNEL

********************************
EVALUATION OF, MOLY
 WITH THE FOLLOWING PROPERTIES

CONDUCTIVITY= 84 BTU/HR-FT-ΔF
COEFF OF EXPANSION,(α)=
 2.77777777778E-6 IN/IN-ΔF
MODULUS OF ELASTICITY,(E)=
 46000000 #/IN^2
INLET PRESSURE OF,  150 #/IN^2

OPTICAL ELEMENT RADIUS OF 6
INCHES

OPTICAL ELEMENT THICKNES OF 2
INCHES

********************************
      REYNOLDS NO.=VDρ/μ

Re= 10853 6185192

********************************
      FRICTION FACTOR

    Φ=(1.84*LGT(Re)-1.64)^-2

ƒ= 2.98761501345E-2

********************************
       PRESSURE DROP

ΔP=((F*L/D)+ΣK)*V^2*ρ*(144*2*g)^
-1

ΔP= 58.4337026147 PSI

********************************
     DITTUS-BOELTER FILM

h=.023*(Re)^.8*(Pr)^.333*(k/D)

h= 10004.0377948 BTU/HR-FT^2-ΔF

********************************
   PETUKHOV FILM COEFFICIENT

h=(Φ/8)*Re*Pr/1.07+12.7(Φ/8)^.5*
(Pr^.66-1))*K/D

h= 11967.4755972 BTU/HR-FT^2-ΔF

********************************
      VELOCITY OF FLUID=

 35 FEET/SECOND

********************************
       VISCOSITY-μ=

 5.36835479311E-4 #/FT-SEC

********************************
      DIAMETER OF DUCT=

  00267 FEET
```

```
********************************
       LENGTH OF DUCT=

 .5 FEET

********************************
       PRANDTL NUMBER=

 5.41398744428 DIMENSIONLESS
********************************
       DENSITY OF FLUID=
 62.35 #/FT^3

********************************
     CONDUCTIVITY OF FLUID

  390834918999 BTU/HR-FT-ΔF

********************************
  TEMPERATURE AT INSIDE SURFACE
OVER THE CHANNEL

SURFACE TEMP= 104.901215027
DEG F

********************************
  TEMPERATURE AT END OF THE WEBB

SURFACE TEMP= 94.4540664032
DEG F

********************************
TEMP. OF THE RECEIVING SURFACE O
VER THE CHANNEL

SURFACE TEMP= 109.839486632
DEG F

********************************
TEMP. OF THE RECEIVING SURFACE O
VER THE WEBB

SURFACE TEMP= 112.510977152
DEG F

********************************
THE AVG WATER TEMPERATURE IS

 87.4506075135 DEG F

********************************
TEMPERATURE INCREASE OF THE FLOW
ING WATER, NECESSARY TO UNLOAD
 1000 BTU/HR-CHANNEL

ΔT= 11.3146330735 DEG F

********************************
THERMAL BEND'G FOR THE CHANNEL

ΔS= 1.50748721696E-2 (μ)METERS

********************************
THERMAL BENDING FOR THE WEBB

ΔS= 5.09606147801E-2 (μ)METERS

********************************
PRESSURE BEND'G FOR THE CHANNEL

ΔS= 8.79143779499E-3 (μ)METERS

THE AVERAGE PRESSURE=
 104.216851308 #/IN^2.
```

```
****)                   ********
   RMS RIPPLE OF THE CHANNEL

RMS ΔS= 2.64553129512E-2
(μ)METERS

********************************
THE BENDING MOMENT PER UNIT OF C
LAMPED EDGE (M)=α*ΔT*(1+ν)*D/t

M= 1487.94583935 #-IN/IN

APPARENT LOAD (q)=8*D*1+ν)/R^2*P
o

q= 330.654630968 #/IN^2

********************************
THE CHANGE IN RADIUS OF CURVATUR
E Ro=1/(α*ΔT)

Δ= 29442.9559537 IN

********************************
THE CHANGE IN CURVATURE FOR A FR
EE EDGE Δ=q*R^4/(16*D*(1+ν))+q*R
^4/(64*D)

Δ= 15.5285308554 (μ)METERS

SUM(ΣΔ)= 15.5285308554
(μ)METERS FOR A FREE EDGE GEOMET
RY

********************************
THE CHANGE IN CURVATURE FOR A TH
REE POINT SUPPORT-Δ=.0362*π*q*R^
4/D

Δ= 36.7321704267 (μ)METERS

********************************
```

```
********************************

     DOCJIM ROHSENOW-BERGLES
PROGRAM FOR BURNOUT AND BOILING
BURNOUT-INCIPIENT-POOL BOILING

********************************

    FORCED CONVECTION

(Q/A)=Hc*((Tw-Ts)+(Ts-Tbulk))

Tw-Ts=10 DEG ΔFTwall= 351 DEG F
Q/A)= 2640055.6 BTU/HR-FT^2

Tw-Ts=20 DEG ΔFTwall= 361 DEG F
Q/A)= 2740095.6 BTU/HR-FT^2

Tw-Ts=30 DEG ΔFTwall= 371 DEG F
Q/A)= 2840135.6 BTU/HR-FT^2

Tw-Ts=40 DEG ΔFTwall= 381 DEG F
Q/A)= 2940175.6 BTU/HR-FT^2
```

```
********************************

  INCIPIENT NUCLEATE BOILING

(Q/A)=15.6*(P)^1.156*(Tw-Ts)^2.3
0/P^.0234

Tw-Ts=10 DEG ΔFTwall= 351 DEG F
Q/A)= 444589.744656 BTU/HR-FT^2

Tw-Ts=20 DEG ΔFTwall= 361 DEG F
Q/A)= 1849732.16233 BTU/HR-FT^2

Tw-Ts=30 DEG ΔFTwall= 371 DEG F
Q/A)= 4258807.72915 BTU/HR-FT^2

Tw-Ts=40 DEG ΔFTwall= 381 DEG F
Q/A)= 7695879.43378 BTU/HR-FT^2

********************************

       POOL BOILING

(Q/A)=((Tw-Ts)*EXP(P/900))^4*1E6

Tw-Ts=10 DEG ΔFTwall= 351 DEG F
Q/A)= 1307.70403911 BTU/HR-FT^2

Tw-Ts=20 DEG ΔFTwall= 361 DEG F
Q/A)= 20923.2646256 BTU/HR-FT^2

Tw-Ts=30 DEG ΔFTwall= 371 DEG F
Q/A)= 105924.027167 BTU/HR-FT^2

Tw-Ts=40 DEG ΔFTwall= 381 DEG F
Q/A)= 334772.234011 BTU/HR-FT^2

********************************
BURNOUT AS A FUNCTION OF VELOCIT
Y

(Q/A)=4E5*V^(1/3)+4.8E3*(Ts-Tbul
k)*V^(1/3)

VELOCITY= 35 FT/SEC

(Q/A)= 5294940.45761 BTU/HR-FT^2

********************************

   PROPERTIES OF EVALUATION

SATURATION TEMP= 341 DEG F

ABSOLUTE SATURATION PRESSURE=
 118.7 PSIA

FILM COEFFICIENT= 10004
BTU/HR-FT^2-ΔF

AVERAGE BULK TEMP= 87.1 DEG F

VELOCITY OF COOLANT= 35 FT/SEC

COOLANT MATERIAL=WATER

********************************
```

```
********************************

DOCJIM MAXIMUM DEFECT ANALYSIS

********************************

 THE MAXIMUM DEFECT SIZE FOR A T
EMP RISE OF- 279.5 -WILL BE-
 .243929127034 -FT. IN DIA.
 D= 74357.3013364 (μ) METERS

********************************

2ierfc(Z/2*(α*τ)^.5).

2ierfc= 1 1284

********************************

2ierfc((z^2+r^2)^.5/(2*(α*τ)^.5)
)

2ierfc= .260399311165

RECIPROCAL FUNCTION OF THE 2ierf
c

RECIPROCAL= .668027426545


********************************

THE ANALYSIS HAS BEEN BASED ON-
MOLY
-WITH THE FOLLOWING PROPERTIES

α= 2 FT^2/HR

τ= 4.16666666667E-3 -HOURS,i.e.,
 15 -SECONDS

K= 84 BTU/HR-FT-F

T= 1.66666666667E-3
FEET OF THICKNESS- .02 -INCHES

ΔT= 279.5
ALLOWABLE INCREASE IN TEMPERATUR
E-DEG F

Q= 296300
MAX ABSORBED LOAD-BTU/HR-FT^2

********************************


********************************
* DOCJIM COOL LASER MIR  GRAD.*
*    FOR-MOLY-HOT FACE MAT   *
*********************************
    SURFACE TEMP INCREASE
********************************

ΔT= 278.96907438 DEG F

ΔT= 154.9828191 DEG C

SURFACE TEMPERATURE 111.5 +
 278.96907438 = 390.46907438
DEG F
```

```
*********************************
********************************
        RADIUS OF DEFECT

R=  122 FEET

R= 37189.4528273 (μ)METERS

********************************
      TEMPERATURE INCREASE
********************************

ΔT= 278.96907438 DEG F
ΔT= 154.9828191 DEG C

 BACK SURFACE TEMPERATURE 104 +
 278.96907438 = 382.96907438
DEG F

********************************
     FOR IRRADIANCE TIME

τ= 4.16666666667E-3 HOURS

*********************************
   THE THERMAL LOAD IS

Fo= 296300 BTU/HR-FT^2

*********************************
     2ierfc-X/(2*(α*τ)^.5)

2ierfc= 1.12834 FRONT SURFACE

*********************************
   2ierfc-(T^2+R^2)/(2*(α*τ)^.5


2ierfc= .261944953747
BACK SURFACE

*********************************
 MATERIAL PROPERTIES OFMOLY
THERMAL CONDUCTIVITY= 84
BTU/HR-FT-ΔF

THERMAL DIFFUSIVITY= 2 FT^2/HR

TOTAL THICKNESS OF THE ELEMENT=
 1.66666666667E-3 FT

T= .02 INCHES

********************************
```

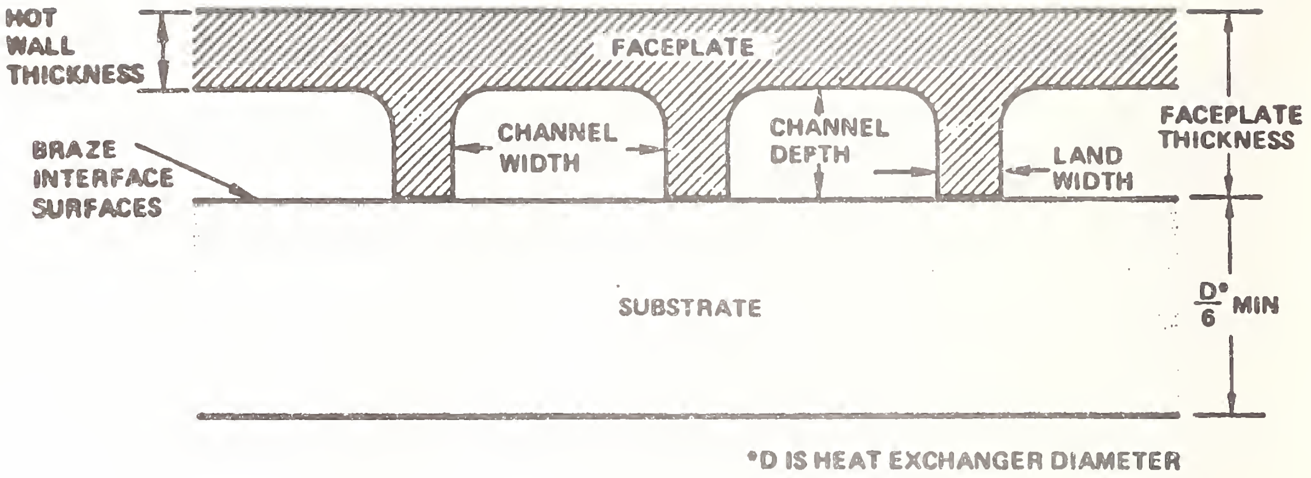

Figure 1.0

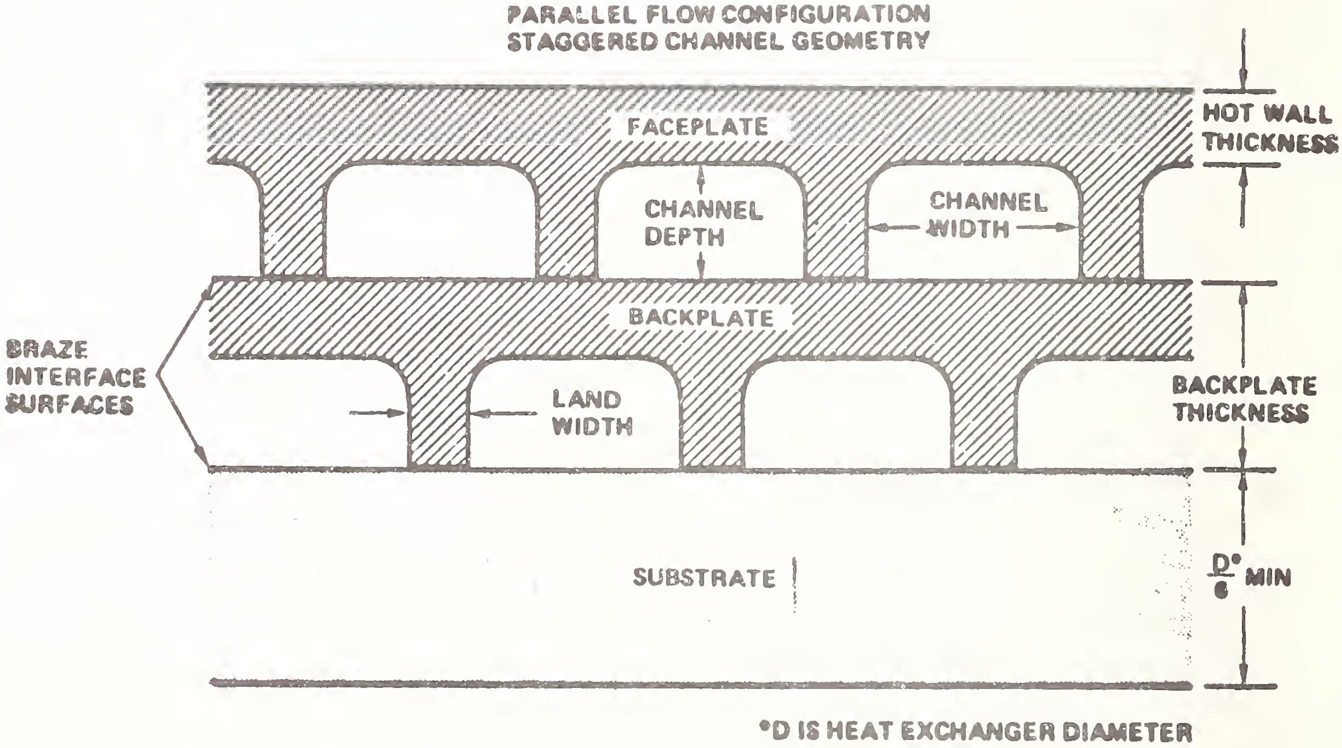

Figure 2.0

PARALLEL FLOW CONFIGURATION
STAGGERED CHANNEL GEOMETRY

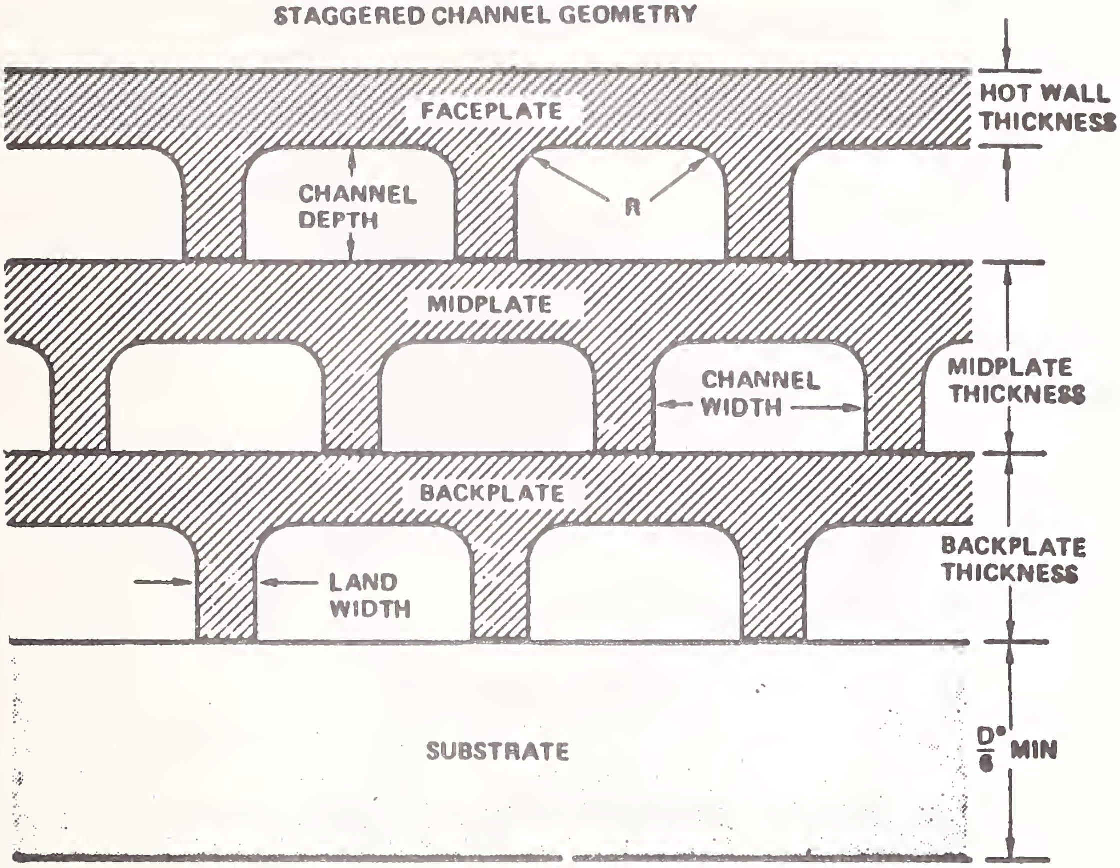

*D IS HEAT EXCHANGER DIAMETER

Figure 3.0

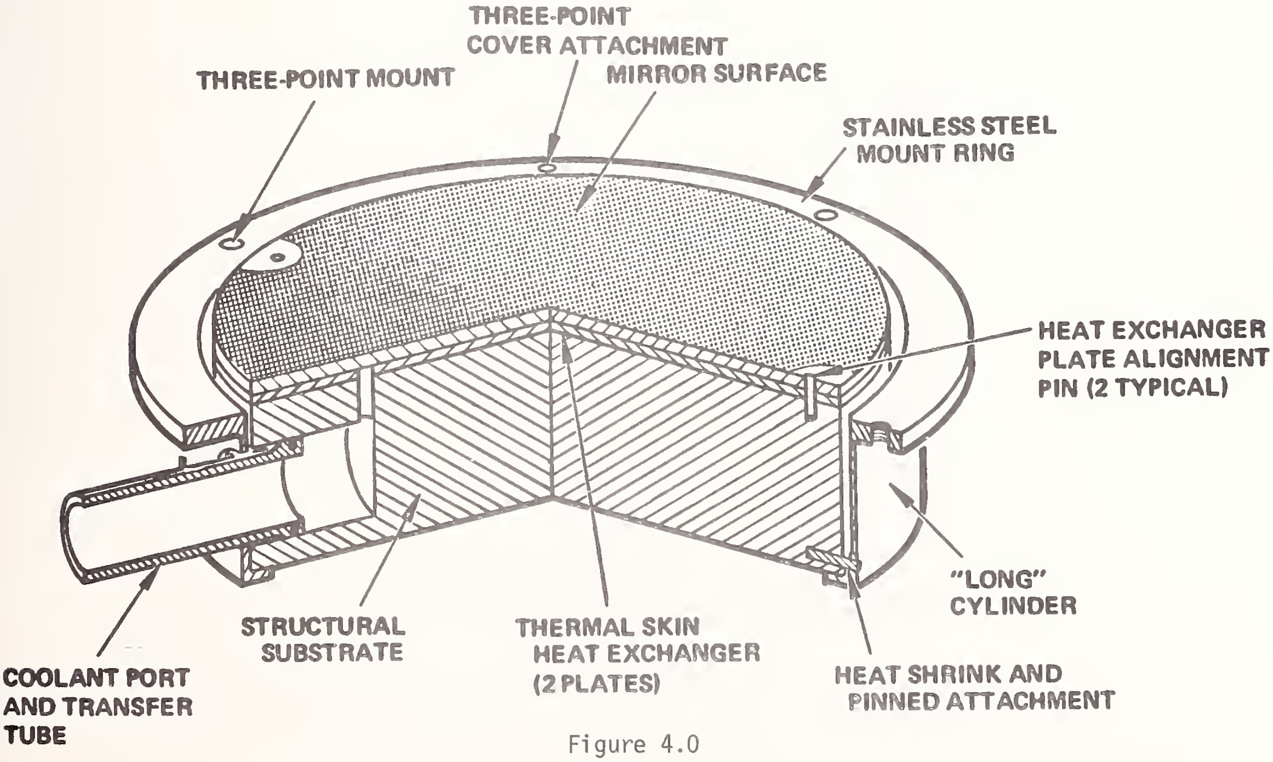

Figure 4.0

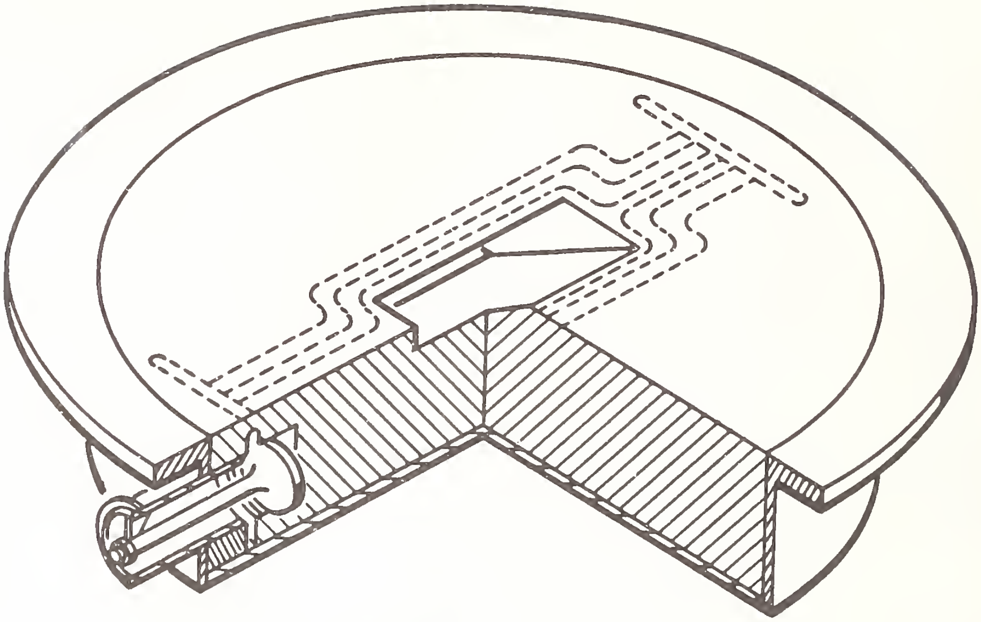

VERTICAL FLOW CONCEPT

Figure 5.0

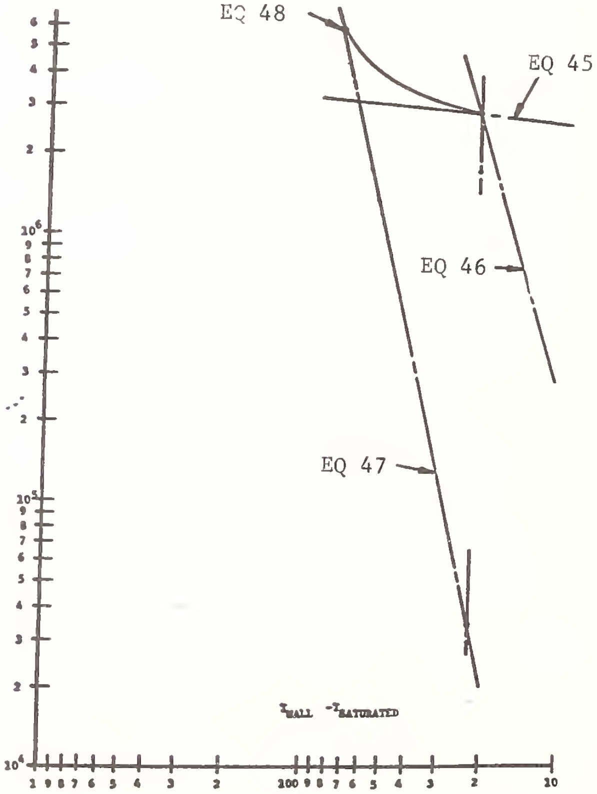

Figure 6.0

The speaker was asked whether he thought it feasible to generate a family of curves that would allow a typical user of cooled mirrors to determine whether he would be operating at a safe power level: the speaker believed such curves were feasible. He said, however, that it was not possible to specify an optimum pressure drop across an arbitrary set of channels, or to predict the effect of nonuniform, non reproducible beam shapes.

ADAPTIVE FORCE OPTICAL ELEMENTS BASED ON OPEN PORE STRUCTURES

V.V.Apollonov, S.A.Chyetkin, V.Yu.Khomich, A.M.Prokhorov

P.N.Lebedev Physical Institute of the USSR Academy of
Sciences, Leninsky prospect, 53, Moscow, USSR

Formation and transmission of high evarage power laser radiation flows with a divergence close to diffraction limit is one of the actual problem in high intensity laser optics.

This paper presents the results of investigations of the phase correctors for laser system optical tracts basing on cooled force optics elements /I/. A reflecting surface shape is controlled by deformation of the porous heatexchanger.

The phase correctors' application, made on the base of force optics elements is not restricted by the adaptive optics. For example, the use of adaptive reflectors in the optical location laser systems will allow to extend the possibilities of latters due to beam formation with the required optical properties of the wave front (WF). A possibility to control the shape of reflecting surface of the cooled force optics elements, executed on the base of open porosity structures is considered within the following model assumptions: porous heatexchanger with the radius R and thickness H($H \ll R$) is tightly fixed over the base and lateral surface into an absolutely rigid material (as compared to porous structure (PS))body over the whole surface except those parts, which are connected with the actuator system (as the absolutely rigid material cylinders with radius $a \ll R$), capable to produce given transfers or amplifications. The layer deviding radiation and heatcarrier prepared on free PS heatexchanger surface is a base for reflecting coating.

An assumption of the absolute rigidity of the force optics elements' and actuators' body allows not to consider the deformation of latters while forming a given shape of the reflecting surface $W_{ref}(r, \varphi)$. $W_{ref}(r,\varphi)$ is determined by the following way: for the incident beam with WF $\Phi_1(r,\varphi)$ and initial reflecting surface shape $\Phi_2(r,\varphi)$, conjugated $W_{ref.}$ is determined by connection:

$$W_{ref}(r,\varphi) = 1/2\left[\Phi_2(r,\varphi) - \Phi_1(r,\varphi) + N\lambda\right]$$

where N - is the laser radiation wavelength, N - is the integer.

To the main types of Φ_1 we refered the wave front tilt, defocusing, spherical abberation /2-3/, and as a function of the given reflecting beam WF form - surface, i.e. $\Phi_2(r,\varphi) = 0$.

For given Φ_1 and Φ_2 it is impossible an accurate formation of the reflecting force optics element surface shape W_{ref} by the control system with a finite number of actuators. Therefore, one should find the optimal way to design the moving structure of actuators, namely, their number and mutual location in order to provide a required accuracy of conjugation of the reflecting adaptive force optics element surface shape with the main types of WF laser radiation abberations.

Before solving the above problem let us consider the deformation transmission characteristics of the separate actuators of the adaptive force optics element.

Within the approximate linear theory of elastic porous heatexchanger deformation of the cooled force optics elements the problem of definition of the reflecting surface shape W_{ref} (resulted from the action of actuator, placing on the unreflected side of PS at distance b out of mirror axis) reduces to the equation /4/:

$$\Delta_{\perp} W + \frac{2(1-\nu)}{1-2\nu}\frac{\partial^2 W}{\partial z^2} = 0$$

$$W\big|_{z=0} = u_0\,\theta\left(a^2 - (b-x)^2 - y^2\right);\ \frac{\partial W}{\partial z}\Big|_{z=H} = 0;\ W\big|_{r=R} = 0$$

where ν - is the Poisson coefficient, θ - is the Kheviside function, u_0 - is the value of actuator shifting, whose solution for $W_{ref.} = W(z=H)$ is the following:

$$W_{ref} = \frac{8 u_0 a}{R} \sum_{K=0}^{\infty} \sum_{j=1}^{\infty} A_{Kj} \frac{\mathcal{J}_K(\mu_j^{(K)} r/R) \cos K\varphi}{\mu_j^{(K)} \, ch\, \mathcal{D}_{jK} \, (1+\delta_{K,0})}$$

where $A_{Kj} = \mathcal{J}_K(\mu_j^{(K)} b/R)\, \mathcal{J}_1(\mu_j^{(K)} a/R) / \mathcal{J}^2_{K+1}(\mu_j^{(K)})$, $\mathcal{J}_K(\;)$ - is the Bessel function of the order of K, $\mu_j^{(K)}$ - is the j-th equation root: $\mathcal{J}_K(\mu_j^{(K)}) = 0$; $\mathcal{D}_{jK} = \mu_j^{(K)} \sqrt{\frac{1-2\nu}{2(1-\nu)}}\, H/R$ and the effort to be applied to actuator is defined as:

$$P = \iint\limits_{S':(x-b)^2+y^2 \leqslant a^2} \sigma_{zz}\big|_{z=0}\, ds' = -8\pi u_0 R E \sqrt{\frac{2(1-\nu)}{1-2\nu}}\, \frac{1}{1+\nu} \left(\frac{a}{R}\right)^2 \sum_{K=0}^{\infty} \sum_{j=1}^{\infty} A^2_{Kj} \frac{th\, \mathcal{D}_{jK}}{\mu_j^{(K)} (1+\delta_{K,0})}$$

where E - is the Junge module of PS heatexchanger.

From the analysis of above dependences it is seen, that a transmission deformation function (i.e. response function of reflecting surface to actuator action) is of smooth Gaussian, which width is measurable with the actuator radius (Fig. 1 A). Dependence of the maximum response function on parameters HR and AR is represented in Figs. 1 B and 1 C, and dependence of the response function width Δ , defined over level I/2 - in Figs. 1 D and 1 E. Dependence of dimensionless specific pressure $\sigma = \sqrt{\frac{1-2\nu}{2(1-\nu)}}\, \frac{P(1+\nu)R}{8\pi u_0\, a^2}$; $AR = \frac{a}{R}$ $HR = \frac{H}{R}$ where G - is the module pf PS shifting out of HR and AR parameters is represented in Figs. 1 F and 1 G.

From the above dependences it follows, that in case of wide response function with $\Delta > 1$, its maximum value $W_0/u_0 < 1$ whereas in case of narrow response function (Δ = I) W_0/u_0 reaches its maximum value equal to I, and value σ tends to minimum. According to relationships, represented in Figs. 1 B and 1 C the maximum of W_0/u_0 reaches at AR, such that AR $\geqslant$ I5HR.

In KOAT systems, operating in real time, the reflecting mirror surface should change according to a change of phase distortions along laser beam propagation trasse, whose times of "cooled" existence is only 0.I - I μsec. Therefore a frequancy range width of actuator system effects should be I - IO KHz and in deformated PS no resonance effects should be exhibited.

We define a spectrum of the relative PS vibrations using the approximate dynamical elasticity equation:

$$\frac{1}{c^2} \frac{\partial^2 W}{\partial t^2} = \Delta_\perp W + \frac{2(1-\nu)}{1-2\nu} \frac{\partial^2 W}{\partial z^2}$$

on the base of which the frequency spectrum of the adaptive force optics element is defined as:

$$\omega_{mj\ell} = \frac{c}{R}\left[\mu_j^{(m)2} + \frac{\pi^2}{4}(1+2\ell)^2 (R/H)^2 (2(1-\nu)/(1-2\nu))\right]^{1/2} > \pi \frac{c}{H}$$

where C - is the sound velocity in PS material.

The nodes' position over unreflecting PS side is defined by the following expressions:

$$\mathcal{J}_m(\mu_j^{(m)} r^{(nod.)}_{mj\ell}/R) = 0 \;; \quad m\, \varphi^{(mj\ell)}_{nod.} = \pi(1+2\ell)/2$$

The crests' position over unreflecting PS side is defined as:

$$\mathcal{J}'_m(\mu_j^{(m)} r^{(cr)}_{mj\ell}/R) = 0 \;; \quad m\, \varphi^{(mj\ell)}_{cr.} = \pi \ell$$

Thus, if the actuators' frequency spectrum do not reaches $\pi C/H$, no resonance effects, affected upon the stability of operation of the adaptive force optics element control system, should be observed. If the operation frequencies are over $\pi C/H$ then one of the method to avoid the resonance effects is to choise the actuator position in the bundles of porous layer vibrations.

The analysis of the PS stressed state shows, that the reflecting surface shape is the Fourier series over a full (on circular R radius aperture) system of functions of $\{J_K(\mu_j^{(K)} r/R)\cos K\varphi\}$. That is any phase distortion represented by function $F(r,\varphi)$ such, that one exists an integral $\iint F^2(r,\varphi)\,ds$ can be corrected with any accuracy ε , having used accordingly a projected system of actuators; ε is defined here by a number of used actuators and their mutual position.

In the process of correction one manufactures the reflection surface shape W_{ref}.

$$W_{ref} = \sum_{n=1}^{N} U_n \Psi_n(b_n, \varphi_n, r, \varphi)$$

where $\{b_n, \varphi_n\}$ - are the center coordinates of n-th actuator over the unreflecting porous layer side, (r,φ) - are the coordinates of the reflecting surface point, Ψ_n - is the response function of reflecting surface to n-th actuator action. A problem of conjugation of the reflecting force optics element surface shape and laser radiation flow with the disturbed wave front $F(r,\varphi)$ reduces to definition of $U_n;\{b_n,\varphi_n\}$ at which an error of conjugation ε is determined as:

$$\varepsilon = \frac{1}{S}\iint_S \Big[F(r,\varphi) - \sum_{n=1}^{N} U_n\Psi_n\Big]^2 W_1(r,\varphi)\,ds$$

where N - is the actuator number, $W_1(r,\varphi)$ - is the aperture function, giving a range to the reflecting mirror surface for which the adaptive equation is carried out should be minimum.

According to a method of the most little squares, mimimum of ε achieves over a large number of values $\{U_n\}$ if the condition $\partial\varepsilon/\partial U_n = 0$ is satisfied for any $1 \leqslant n \leqslant N$.

Vector $\{U_n\}$, minimizing the functional ε is solution of the linear equations' system

$$\sum_{K=1}^{N} A^*_{Kn} U_K = B_n$$

where the matrix elements A^*_{Kn} of dimensions $N \times N$ are defined as

$$A^*_{Kn} = \frac{1}{S}\iint_S W_1(r,\varphi)\Psi_K\Psi_n\,ds$$

i.e. are the characteristic of number and mutual positions of the force optics element actuators' system. The elements B_n of the vector $\vec{B}$ of dimension N:

$$B_n = \frac{1}{S}\iint_S W_1(r,\varphi)F(r,\varphi)\Psi_n\,ds$$

are defined not only by a force optics elements construction, but the function type, describing WF disturbance of laser beam.

A compensation error ε is defined as:

$$\varepsilon = |F|^2 - \sum_{n=1}^{N} U_n B_n$$

where $|F|^2 = \frac{1}{S}\iint_S W_1(r,\varphi)F^2(r,\varphi)\,ds$

We determined a type of elements A^*_{kn}, B_n, $|F|^2$ for the basic abberation forms.

In the case, if the aperture function $W_1(r,\varphi) = \Theta(R_1 - r)$ where R_1 - is the radius of "active" subaperture and $R_1 < R$, the elements of the transmission matrix of mirror are the following:

$$A^*_{nm} = \sum_{K=0}^{\infty} \sum_{\substack{i,j=1 \\ i \neq j}}^{\infty} \frac{A_{Kj}(b = b_m) A_{Ki}(b = b_n) \cos K(\varphi_n - \varphi_m)}{\mu_i^{(K)} \mu_j^{(K)} \operatorname{ch} \mathcal{D}_{iK} \operatorname{ch} \mathcal{D}_{jK}} \times$$

$$\times \frac{\mu_i^{(K)} J_K(\mu_j^{(K)}\gamma) J_{K-1}(\mu_i^{(K)}\gamma) - \mu_j^{(K)} J_K(\mu_i^{(K)}\gamma) J_{K-1}(\mu_j^{(K)}\gamma)}{\mu_j^{(K)2} - \mu_i^{(K)2}} + \frac{1}{2}\gamma \sum_{K=0}^{\infty} \sum_{j=1}^{\infty} \frac{A_{jK}(b = b_n)}{\mu_j^{(K)2}} \times$$

$$\times \frac{A_{jK}(b = b_m) \cos K(\varphi_n - \varphi_m)}{\operatorname{ch}^2 \mathcal{D}_{jK} (1 + \delta_{K,0})} \left(J_K^2(\mu_j^{(K)}\gamma) - J_{K+1}(\mu_j^{(K)}\gamma) J_{K-1}(\mu_j^{(K)}\gamma) \right)$$

where $\gamma = R_1/R$

If $\gamma \to 1$, i.e. control is carried out along the whole aperture of adaptive force optics element:

$$A^*_{nm} = \sum_{K=0}^{\infty} \sum_{j=1}^{\infty} A_{jK}(b = b_m) \frac{J_K(\mu_j^{(K)} b_n / R)(\delta_{K,0} + \cos K(\varphi_n - \varphi_m))}{\mu_j^{(K)2} (1 + \delta_{K,0})^2 \operatorname{ch} \mathcal{D}_{jK}}$$

With correction of WF tilt, described by expression

$$F(r,\varphi) = r \operatorname{tg}\alpha \sin\varphi \, \Theta(R_1 - r)$$

where α - is the tilt angle of WF surface, the vector element B_n is the following:

$$B_n = -\operatorname{tg}\alpha \frac{R R_1}{8a} \sum_{j=1}^{\infty} A_{j1}(b = b_n) \frac{J_2(\mu_j^{(1)}\gamma) \sin\varphi_n}{\mu_j^{(1)2} \operatorname{ch} \mathcal{D}_{j1}}$$

and expression for $|F|^2$:

$$|F|^2 = \frac{1}{4} \operatorname{tg}^2\alpha \, R^2 \gamma^4$$

With correction of cylindrical bend of flat WF, described by function at the same subaperture $R_1 < R$

$$F(r,\varphi) = \pm (r^2 \sin^2\varphi - R_1^2) \Theta(R_1 - r) / 2R_2$$

where R_2 - is the cylindrical surface radius, the components B_n are defined as follows:

$$B_n = \frac{\gamma R^3}{32 R_2 a} \left\{ \sum_{j=1}^{\infty} \frac{A_{j0}(b = b_n)}{\mu_j^{(0)3} \operatorname{ch}(\mathcal{D}_{j0})} \left[\frac{4 J_1(\mu_j^{(0)}\gamma)}{\mu_j^{(0)2}} - 2\gamma \frac{J_0(\mu_j^{(0)}\gamma)}{\mu_j^{(0)}} \right] + \right.$$

$$\left. + \frac{\gamma^2 \cos 2\varphi_n}{2} \sum_{j=1}^{\infty} \frac{A_{j2}(b = b_n)}{\mu_j^{(2)3} \operatorname{ch} \mathcal{D}_{j2}} J_3(\mu_j^{(2)}\gamma) \right\}$$

and

$$|F|^2 = \frac{5 R_1^6}{32 R^2 R_2^2}$$

At correction of defocusing $F(r,\varphi) \pm (R^2 - r^2)/2R_2$ where R_2 - is the spherical surface radius, the components B_n are equal:

$$B_n = \frac{z_{max}}{(a/R)} \sum_{j=1}^{\infty} \frac{J_0(\mu_j^{(0)} b_n/R)\, J_1(\mu_j^{(0)} a/R)}{\mu_j^{(0)4}\, J_1(\mu_j^{(0)})\, ch\, \mathcal{D}_{jo}}$$

where $z_{max} = R^2/(2R_2)$ and $|F|^2 = R^4/(12 R_2^2)$.
Spherical abberation is determined as $F(r,\varphi) = \pm 0.25 B (r^4/R^4 - 1)$ so component B_n is equal

$$B_n = \mp \frac{4 z_{max}}{a/R} \sum_{j=1}^{\infty} \frac{J_0(\mu_j^{(0)} b_n/R)\, J_1(\mu_j^{(0)} a/R)\, (\mu_j^{(0)2} - 4)}{\mu_j^{(0)6}\, J_1(\mu_j^{(0)})\, ch\, \mathcal{D}_{jo}}$$

and $z_{max} = B/4$ and $|F|^2 = 8 z_{max}^2 / 15$.
In case of small-scale distortion for approximation of which we use the gaussian function: $F(r,\varphi) = U_1 \exp(-K_0 r^2)$ where $K_0 = 2/a_1^2$, a_1 -is the cross-section size, determined over level $1/e^2$, such that $a_1 \gtrsim a$, $|F|^2 = U_1 a_1^2/4R$ and the corrected vector B_n is defined as:

$$B_n = \frac{U_1 a_1^2}{16 a R} \sum_{j=1}^{\infty} \frac{A_{jo}(b = b_n)}{\mu_j^{(0)}\, ch\, \mathcal{D}_{jo}} \exp\left(- \frac{\mu_j^{(0)2} a_1^2}{8 R^2}\right)$$

Thus, we have design a model of the adaptive force optics elements executed on the base of structure with open porosity. A problem of conjugation of the reflecting surface shape with the basic abberation types is solved. The main expressions, describing an algorithm of optimal phase-conjugation are obtained.

References.

I. V.V.Apollonov, P.I.Bystrov, V.F.Goncharov, A.M.Prokhorov, V.Yu.Khomich, Kvantovaya electronika, 6, No I2, I979, p.2533.

2. Avisonis P.V. Overview of adaptive optics technology.-Physics of Quantum Electronics, I978, v.6, p.I-54.

3. Hogge C.B. Adaptive optics in high energy laser system. - Physics of Quantum Electronics, I978, v.6, p.55-I20.

4. V.V.Apollonov, A.M.Prokhorov, V.Yu.Khomich, S.A.Chyetkin. Pis'ma v ZhTF, 7, 22, I982, p.I388.

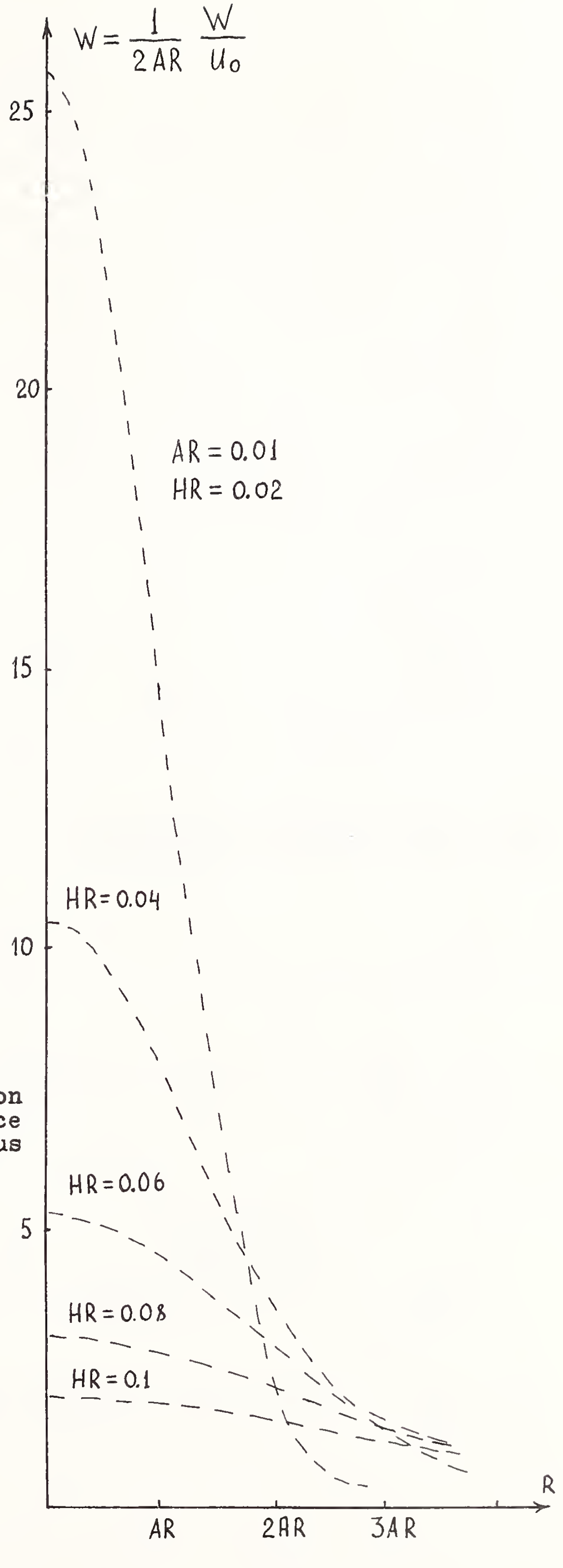

Fig.I A. Response function of AFOE reflecting surface made on the base of porous structure due to parameters AR and HR.

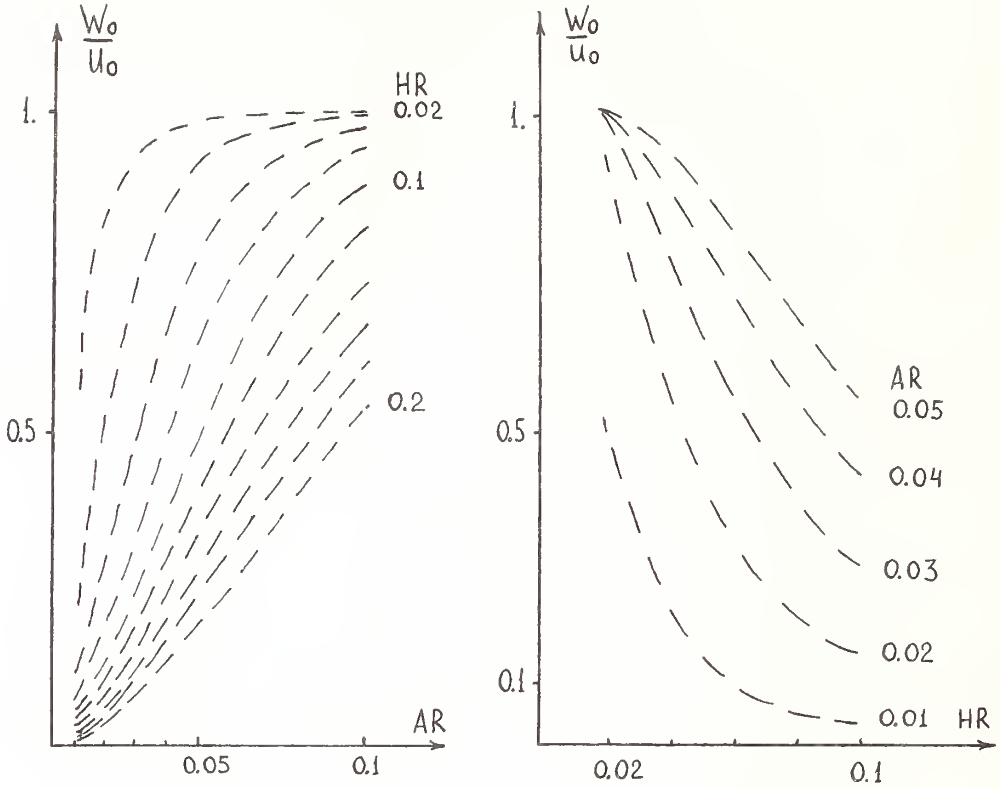

Fig. I B.

Fig.I C.

Dependence of maximum response function of AFOE reflecting surface on parameters AR and HR.

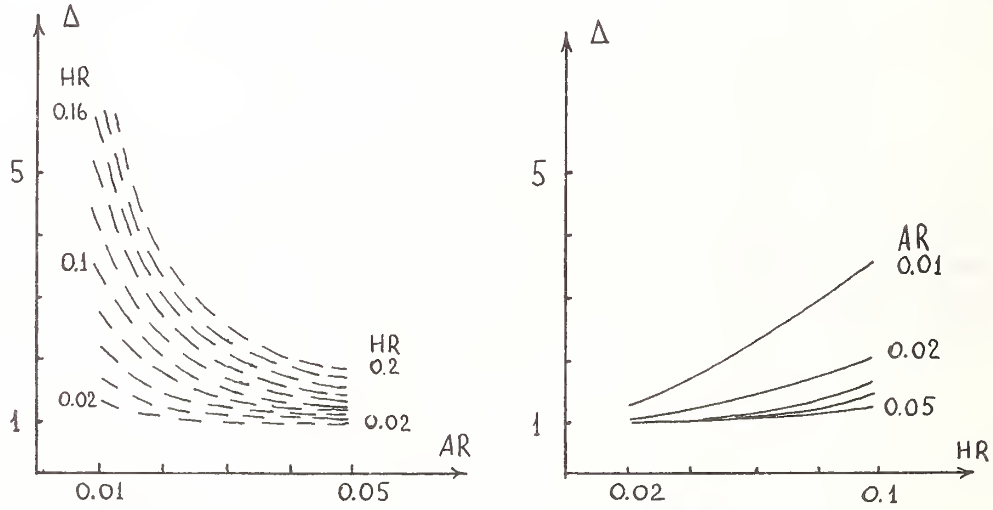

Fig.I D.

Fig.I E.

Dependence of AFOE response function width on parameters AR and HR.

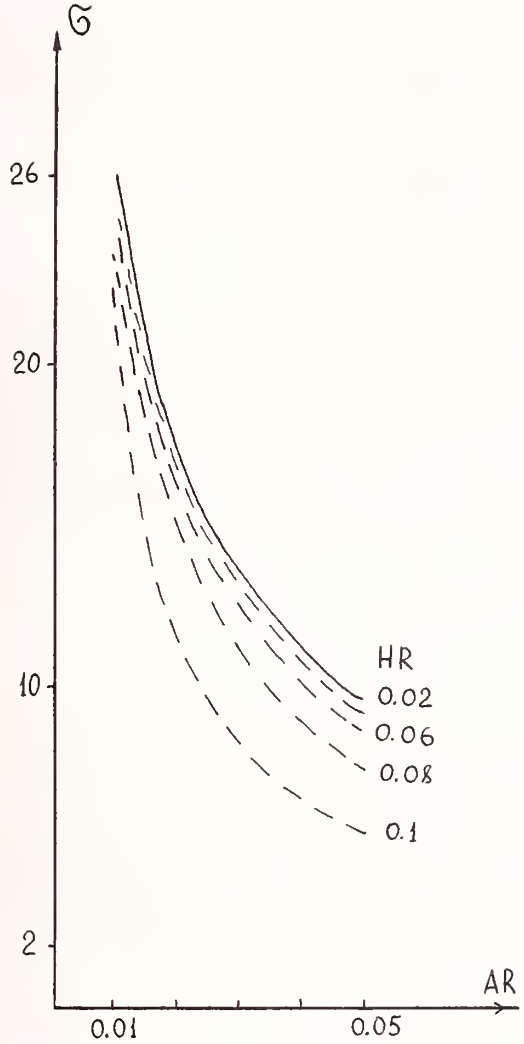

Fig.I F.

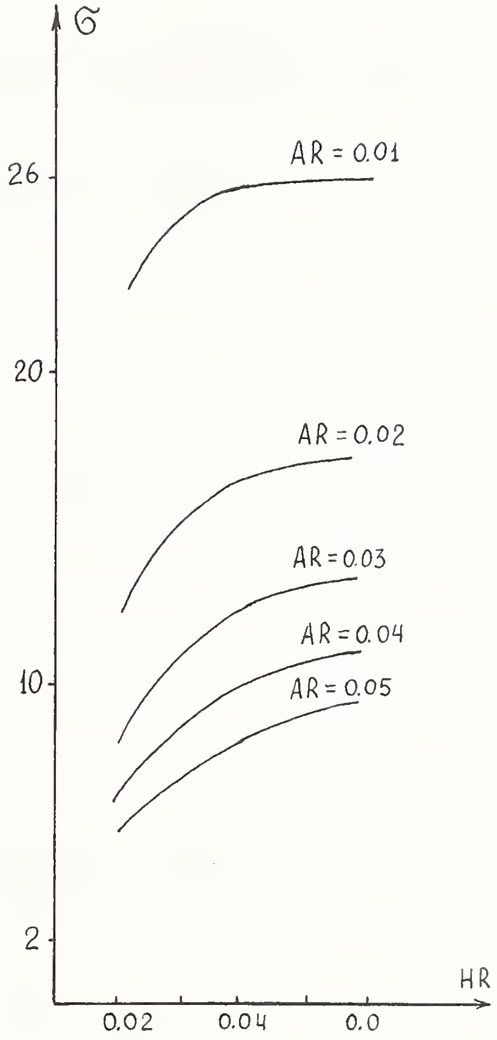

Fig.I G.

Dependence of specific pressure value $\sigma = \sqrt{\frac{1-2\nu}{2-2\nu}}\,\frac{P(1+\nu)R}{8\pi u_0 E a^2}$ in the place of actuator and porous heatexchanger connection on parameters AR and HR.

Optical Figure Requirements for Laser Mirrors Used at Oblique Incidence[*]

H. E. Bennett

Michelson Laboratory, Physics Division
Naval Weapons Center, China Lake, California 93555

In order to achieve near diffraction-limited power densities in a focused laser beam, the wave front distortion introduced by the relay optics must be closely controlled. The figure tolerances for the individual components required to achieve this control are usually derived from normal incidence arguments. However, turning flats are usually used at nonnormal incidence, typically 45 degrees. It is shown that the rms figure irregularities are less important at nonnormal incidence than at normal incidence, but that sphericity, which introduces astigmatism, is much more important at nonnormal incidence. If a focal shift can be tolerated, however, the wave front error at nonnormal incidence caused by a turning flat containing sphericity will be less than that at normal incidence from a flat having an equal peak-to-valley random figure error.

Key words: laser mirrors; optical error budget; optical figure; optical flats; spherical power; turning mirrors.

Introduction

The ability of a laser system to focus energy is greatly influenced by the optical train through which the light is focused. The Maréchal criterion is often used for superior imaging optics [1].[1] To meet this criterion, the cumulative rms wave front distortion for wavelength λ must not exceed λ/14, which is approximately equivalent to the well-known Rayleigh quarter-wave criterion. The optical resolution achievable using an optical train meeting the Maréchal or Rayleigh criterion is equal to that of a perfect optical system. The on-axis focused power density, however, is only 80% of that for a perfect system [1], leading to the conclusion that it is more difficult to achieve the highest quality power handling optics than it is to achieve diffraction-limited imaging optics.

The ratio of the axial intensity I (for an aberrated signal) to I_o (for an aberration-free system) is given by the Strehl relation [2]:

$$\frac{I}{I_o} = 1 - \left(\frac{2\pi\sigma}{\lambda}\right)^2 \quad , \qquad (1)$$

where λ is the wavelength and σ is the rms deviation of the wave front from its ideal value. Equation (1) has been shown [3] to be a valid indicator of optical image quality in the range $0.6 \leqslant I/I_o \leqslant 1.0$. In designing an optical train, figure tolerances must be assigned to the various components [4] so that the resultant wave front error, after passing through the system, does not exceed the desired value of σ.

Usually lenses and mirrors containing power are used at nearly normal incidence. However, plane mirrors are frequently used at nonnormal incidence. Only a slight sphericity is then required to produce significant astigmatism. The sphericity tolerance is the subject of this paper.

Wave Front Analysis

When mirrors are used at normal incidence, the optical path difference caused by a surface irregularity of height h_i exceeds it by a factor of 2. The rms wave front error σ_i is thus twice the rms figure error δ_i of the mirror surface. If the mirror is used at nonnormal incidence, the contribution of an irregularity of height h_i to the wave front error will be $2h_i\cos\theta$, where θ is the angle of incidence. It follows that

---

[*] Work supported in part by Navy Independent Research Funding.

[1] Figures in brackets indicate the literature references at the end of the paper.

$$\sigma_i = 2\delta_i\cos\theta \quad (2)$$

and surface irregularities relative to the best-fit sphere are less important at oblique incidence than they are at normal incidence. At nonnormal incidence, however, a spherical surface having a sagittal depth h gives an astigmatic contribution to σ. If a quasi-plane mirror containing a slight amount of spherical power is used at 45 degrees, for example, the path difference between the beams reflected from the edge of the mirror and from its center is $2h\cos45° = \sqrt{2}h$, as shown in figure 1.

A circular beam incident on a nearly plane mirror will produce an elliptical footprint with semimajor axis b_a and semiminor axis b, where 2b is the diameter of the incident beam. This footprint is shown on a circular mirror in figure 2(a). The semimajor axis of the ellipse is b_a, where

$$b_a\cos\theta = b \quad . \quad (3)$$

The sagittal depth of a plane wave front after reflection from a spherical mirror of radius of curvature R at angle θ is $(b_a^2/2R)2\cos\theta$ along the p-direction; along the s-direction, $(b^2/2R)2\cos\theta$. Here p and s are directions parallel and perpendicular, respectively, to the plane of incidence. After reflection, the beam is still circular in cross section but the wave front is toroidal, as shown in figure 2(b), and astigmatism caused by the difference in sagittal depth of the wave front in the p- and s-directions will be present at focus, as illustrated in figure 2(b). The maximum difference is

$$\frac{1}{R}(b_a^2 - b^2)\cos\theta \quad .$$

Substituting from eq (3), it becomes

$$\frac{b^2}{R}\frac{\sin^2\theta}{\cos\theta} \quad .$$

The best-fit sphere will bisect the astigmatic wave front, as illustrated in figure 2(c). The maximum deviation of the wave front from a best-fit sphere will then be half the deviation of the wave fronts from each other.

At 45 degrees to the s- or p-directions, the aberrated wave front coincides with the best-fit spherical wave. The difference between the aberrated and best-fit spherical wave fronts as a function of azimuthal angle ϕ and distance from the optic axis r is then

$$\frac{r^2}{2R}\frac{\sin^2\theta}{\cos\theta}\sin\phi \quad ,$$

where $0 \leqslant r < b$ and $\phi = 0$ at 45 degrees to the s-direction. The rms deviation of the astigmatic wave front from a best-fit spherical wave front is then σ_a, where

$$\sigma_a^2 = \frac{\int_0^{2\pi}\int_0^{b}\left(\frac{r^2}{2R}\frac{\sin^2\theta}{\cos\theta}\sin\phi\right)^2 r\,dr\,d\phi}{\pi b^2} \quad (4)$$

so that

$$\sigma_a = \frac{b^2}{4\sqrt{3}R}\tan\theta\sin\theta \quad . \quad (5)$$

Spherical Wave Front Error

In addition to the astigmatic wave front error, there is also a spherical wave front error (the best-sphere). Since the two errors are correlated, the resultant wave front error is their sum. In many applications, however, the spherical wave front error can be neglected since it only displaces the focal point of the system, as illustrated in figure 3. In the original focal plane, the on-axis intensity is decreased from I_o to I, where [5]

$$\frac{I}{I_0} \cong 1 - \frac{1}{3}\left(\frac{\pi a_1}{\lambda}\right)^2 \tag{6}$$

and a_1 is the maximum difference in sagittal depth, as illustrated in the figure. A focal shift by an amount Δf, where f is the original focal length and

$$\Delta f = 2a_1(f/b)^2 \quad , \tag{7}$$

restores the on-axis focal intensity to its initial value.

Comparison of Normal and Oblique Incidence Wave Front Errors

The decrease in on-axis intensity caused by astigmatism introduced by using a slightly spherical mirror at nonnormal incidence, cannot be corrected by a focal plane shift. If we neglect the spherical wave front contribution, a comparison of the effect of random and spherical figure error in mirrors can be summarized as follows. From eq (1) the decrease in on-axis intensity caused by figure error [2] is $1 - (2\pi\sigma/\lambda)^2$. At normal incidence, $\sigma = 2\delta$ where δ is the random rms deviation of the mirror from a best-fit sphere. At a nonzero angle of incidence θ, astigmatism is also present; thus, from eqs (2) and (5),

$$\sigma^2 = (2\delta\cos\theta)^2 + (b^2/4\sqrt{3}R)^2\tan^2\theta\sin^2\theta \quad , \tag{8}$$

where the sum of the squares is taken because the contributions of random figure errors and astigmatism are assumed to be uncorrelated.

If the flat is filled by the beam at angle θ, the sagittal depth of the sphericity h is

$$h = \frac{1}{2R}\left(\frac{b}{\cos\theta}\right)^2 \quad . \tag{9}$$

Substituting eq (9) into eq (8), the rms wave front error σ is given by

$$\sigma = (4\delta^2 + \frac{h^2}{12}\sin^4\theta)^{1/2}\cos\theta \quad . \tag{10}$$

Usually, optical figure specifications are made in terms of the peak-to-valley deviations from a reference plane. Since random figure errors on a well-polished part are vaguely sinusoidal, they may be related approximately to the peak-to-valley random figure error p_v by

$$p_v = 2\sqrt{2}\delta \quad . \tag{11}$$

An optician can readily perform the measurement of peak-to-valley figure error by placing a reference flat on the part being made and observing the interference fringes formed. Thus a quarter-wave surface, assuming no sphericity were present, would be one for which $p_v = \lambda/4$, where λ, the wavelength of light, is typically either 6328 Å (if a HeNe laser is used to make the measurement) or 5461 Å (if a mercury light is used). If sphericity were present but no random irregularities, a quarter-wave surface would be one for which $h = \lambda/4$. Figure 4 gives a plot of peak-to-valley figure error and sagittal depth versus wave front error.

Conclusion

It is clear from eq (10) that the tolerance on sagittal depth can be significantly looser than that on random figure irregularities if a slight focal shift can be tolerated. If the figure error of the mirror is specified in terms of the magnitude of peak random irregularities allowed at normal incidence (i.e., p_v) and only spherical power is present, its sagittal depth can be 3.4 times the p_v value at an angle of incidence of 45 degrees and 3.3 times it at 60 degrees. At grazing incidence, the wave front error caused by either random irregularities or spherical power approaches zero. We may conclude that an optical flat which meets a given peak-to-valley figure specification for random surface figure errors will always introduce less wave front error when used at nonnormal incidence than it will at normal incidence. In addition, if a small focal shift can be tolerated, the wave front error introduced by sphericity which meets the peak-to-valley figure specification will be less than that introduced by random figure errors.

With modern computerized interferometric equipment, it is posssible to separate random errors about a best-fit sphere from the sagittal depth of the sphere and determine both δ and h. With such equipment, a good idea of the actual performance of a turning flat may be obtained from eq (10).

References

[1] Born, M.; Wolf, E. Principles of Optics, 3rd ed. New York; Pergamon Press; 1965. Pp. 468-469.

[2] Strehl, K. "Atmospheric irregularities and zonal aberration of objectives," Z. Instrum. 22; 213-217; 1902.

[3] King, W. B. "Dependence of the Strehl ratio on the magnitude of the variance of the wave aberration," J. Opt. Soc. Am. 58; 655-661; 1968.

[4] Bennett, H. E. "Thermal distortion thresholds for optical trains handling high pulse powers," in Laser Induced Damage in Optical Materials: 1976, Glass, A. J.; Guenther, A. H., ed. 1976 July 13-15; Boulder, CO. Nat. Bur. Stand. (U.S.) Spec. Publ. 462; 1976 December. Pp. 11-24.

[5] Lowenthal, D. D. "Maréchal intensity criteria modified for Gaussian beams," Appl. Opt. 13; 2126-2133, Errata, 2774; 1974.

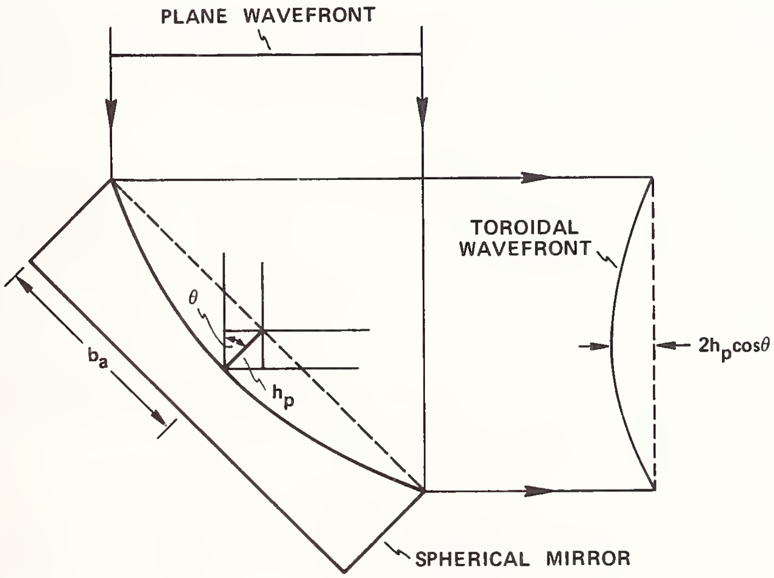

Figure 1. Astigmatism produced by oblique reflection from a spherical mirror.

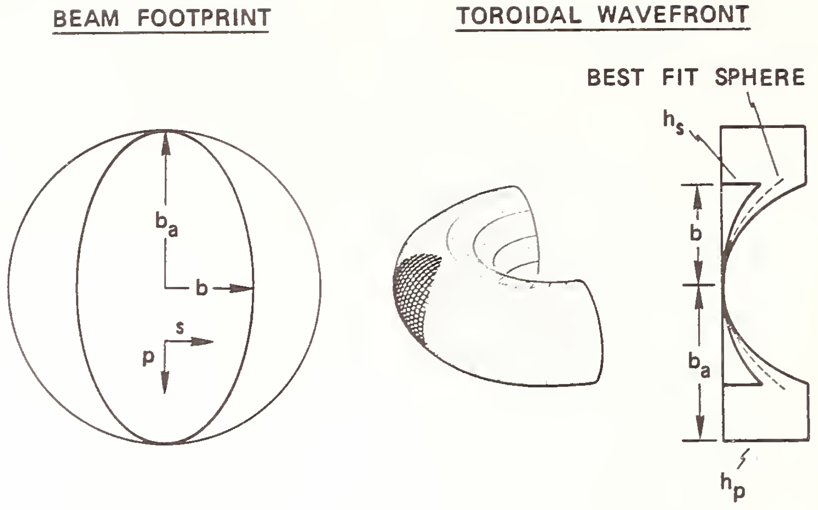

(a)

(b)

Figure 2. Origin of toroidal wave front caused by oblique reflection from a nearly flat spherical mirror. The ellipse in (a) shows the area of the circular mirror illuminated at a 45-degree angle of incidence by a round beam. After reflection, the wave front in the s-direction has a different curvature from that in the p-direction as seen in (b). The best-fit sphere averages between them.

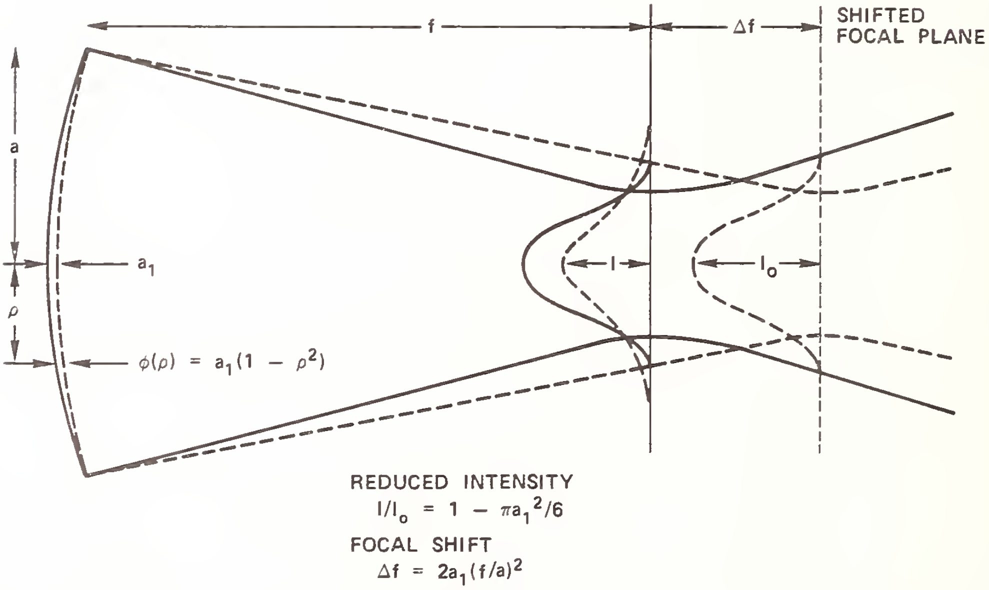

Figure 3. Drop in on-axis intensity I caused by spherical wave front error restored to I_0 by shifting focal plane to right.

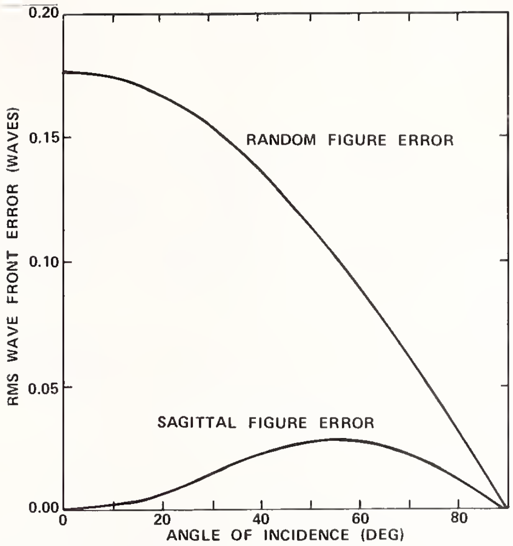

Figure 4. Root mean square wave front caused by random peak-to-valley and sagittal quarter-wave figure errors.

The speaker was asked about the validity of having treated lack of sphericity and random height fluctuations as independent quantities, and replied that while he did not believe there was necessarily any correlation between the two types of error, the basic effect of dropping the assumption would be the requirement of slightly tighter surface specifications.

Molecular Beam Epitaxy

Mehmet Rona and Philip W. Sullivan

Arthur D. Little, Inc.
Cambridge, MA 02140

MBE is a technique for the deposition of single crystal films in ultra high vacuum. The technique has been developed within the last five to ten years predominantly by the semiconductor industry.

In vacua of approximately 10^{-10} Torr, materials are thermally evaporated from boron nitride crucibles onto a substrate, the temperature of which is precisely regulated. Single crystal films up to 5 cm OD have been grown that demonstrate surface roughness no worse than one atomic layer locally (approximately 3-5Å) and global film thickness variations less than one percent. Multiple films of different chemical compositions but similar lattice structures have been deposited on one another with precisely defined chemical boundaries and no interlayer diffusion.

Multilayer dielectric coatings for high energy laser systems have consistently failed to provide performances expected on the basis of bulk materials properties. Instead, the observed effects support the following simplified model of the behavior of dielectric materials in the presence of intense electric fields.

The substitution of polycrystalline films by single crystal films should offer improvement on two counts: (a) reduced absorption of energy by electrons in low energy surface states, and (b) longer mean free paths of electrons in the conduction band, with reduced possibility of electron avalanche breakdown and massive energy transfer to the lattice.

Keywords: Laser coating; molecular beam epitary; optical thin film; single crystal films.

1. Introduction

The rapid development of semiconductor technology over the last thirty years has imposed increasingly stringent design requirements on the materials technologist. The late 1970's and early 1980's have seen a huge increase in interest in devices which require highly precise control of physical dimensions and semiconductor composition. Although silicon still dominates the semiconductor device market there is much interest in very high speed and optical devices fabricated mainly from compound semiconductors whose constituents can be found in groups III and V of the periodic table, e.g., GaAs, InP and alloys GaAlAs, GaInP, GaInAsP, etc. Such materials have the same crystal structure as Si but have electronic properties which make them more attractive for use at high frequencies and in active and passive optical components. Such components are, by nature, smaller and characteristically more dependent on surface and interface roughness. Moreover dopant homogeneity and incorporation level must, of necessity, be accurately controlled. For these reasons, many modern devices are fabricated in thin, single crystal (or epitaxial) layers which are grown onto a bulk crystal slice. Several techniques are used to grow epitaxial layers; these will be discussed in the next section. All of the techniques, however, are characterized by the following:

A) Crystal growth rates are slow compared to bulk crystal growth rates and thus allow precise control of layer thicknesses and therefore device size, at least in the dimension parallel to the growth direction.

B) Dopant incorporation and alloy composition is well controlled. N- and P-type levels may be set with some precision and resolution.

2. Epitaxial Growth Techniques: VPE, LPE and MBE

The three major growth techniques used for growing epitaxial layers are vapor phase epitaxy (VPE), liquid phase epitaxy (LPE) and molecular beam epitaxy (MBE). A comparison is given in Table 1 of the three techniques for the growth of GaAs.

Table 1. A Comparison Of Growth And Material Parameters For GaAs Grown By LPE, VPE and MBE

	LPE	VPE		MBE
		CVD	MO-CVD	
Growth Rate (μm/min)	$\sim$1	$\sim$0.1	$\sim$0.1	$\sim$0.01[4]
Growth Temp. (°C)	850	750	750	550
Thickness Control (Å)	500	250	100(50)[1]	5
Interface Width (Å)	>50	$\sim$65	<20(16)[3]	<15(9)[2]
Dopant Range (cc^{-1})	$10^{13}-10^{19}$	$10^{13}-10^{19}$	$10^{14}-10^{19}$	$10^{14}-10^{19}$
Mobility, 77°K (cm^2/Vs)	150,000 - 200,000	150,000 - 200,000	120,000	105,000

(1) Reported but unpublished to date (R.D. Dupuis, Appl. Phys, Lett., 35 (1979), 331)

(2) Minimum sputter auger measured width with broadening correction (C.M. Garner, et al., Appl. Phys. Lett., 34 (1979, 610)

(3) Minimum sputter auger measured width with broadening correction (R.D. Dupuis et al., in *Gallium Arsenide and Related Compounds*, Inst. of Physics, London (1970), p.1)

(4) This growth rate has recently been increased by little more than one factor of ten.

SOURCE: Reference 1 (4th footnote has been added).

In VPE, a heated stream of compounds or elements is passed over the substrate slice. Chemical interactions of the gases with the substrate cause the layer to form and grow. The apparatus normally consists of a quartz furnace in which the substrate is held and through which the reactants pass, at or near atmospheric pressure.

LPE involves cooling a solution which is saturated with the components required to grow the crystalline layer. The solution is maintained in intimate contact with the substrate.

Molecular Beam Epitaxy[1, 2] can be defined as the growth, under ultra high vacuum conditions, of single crystal layers of electronic materials, from thermally generated beams of the constituent elements. For example, to grow gallium arsenide (GaAs) separate crucibles containing the elements gallium and arsenic are heated in an evacuated chamber. The resulting vapor products Ga and As$_4$ are directed towards the surface of a suitable single crystal slice, often called the substrate. If the substrate is clean and presents a plane crystal surface to the arriving molecules and the lattice size is similar or identical to that of GaAs then the substrate crystal structure seeds the growth of a single crystal GaAs layer. Such a layer will then be called epitaxial (Greek roots, epi meaning "close to" taxis meaning "arrangement") because it has nearly the same crystal structure as the substrate. If the substrate is GaAs then the layer is said to be homo-epitaxial, otherwise, the layer is heteroepitaxial.

Although the MBE technique is basically vacuum evaporation, it differs in critical features from conventional vacuum deposition methods. Indeed interest in MBE technology evolved from the difficulties encountered by workers, in the late 1950's and 1960's, in the preparation of single crystal layers by vacuum evaporation. In 1958 Gunther[3] reported the use of the so-called "three temperature method" to grow compound semiconductors. To grow InSb separate crucibles containing the elements were heated to different temperatures T_1 and T_2 in order to regulate the stoichiometry of the layer grown onto the substrate (held at temperature T_3). All of the films were polycrystalline. In the following decade many groups grew compound semiconductors of poor crystalline quality using vacuum evaporation. In 1968 Davey and Pankey[4] succeeded in growing GaAs onto a heated GaAs substrate by using an impinging beam of gallium atoms along with a sufficiently high background pressure of arsenic. In the same year, Arthur[5] reported the growth of GaAs from thermally generated molecular beams in an all metal vacuum system. Arthur used liquid nitrogen panels to collimate the beam sources and studied the interaction of As molecules with the GaAs substrate surface. Soon after, Joyce and coworkers[6] performed a definitive set of experiments which determined the surface reaction kinetics of Ga, As_4 and As_2 species on a clean GaAs surface. These experiments led to what is now referred to as Molecular Beam Epitaxy (MBE). Cho and coworkers[2,7] developed the technique to its present level by studying the growth and characteristics of GaAs and AlGaAs layers. Their pioneering work on the fabrication by MBE of a large number of important devices kindled an interest which has spread to more than 100 groups throughout the world.

An important distinction that must be drawn between vacuum evaporation and MBE, is found in the ultimate pressures and relative cleanliness of the techniques. Vacuum evaporation is normally associated with metal contact preparation in diffusion and ion pumped glass bell-jar vacuum systems with ultimate background vacuum pressures in the range 10^{-7} to 10^{-6} Torr, while the ultimate background pressures in MBE are usually in the range 10^{-11} to 10^{-10} Torr, an improvement by four orders of magnitude. To put this comparison into perspective it is instructive to convert pressures into number densities of molecules. As the background pressure drops in the vacuum system, that is, as the number of gas molecules per cm^3 decreases, it takes longer for background or contaminant gases to completely cover a freshly clean substrate with a single atomic layer. At background pressures of 10^{-6} Torr such a layer forms in one second. The much lower pressures available in the MBE vacuum system guarantee that once the crystal surface is clean it remains so for a period which is very long compared to a typical layer growth run. This is crucially important since the quality of the epitaxial layer is sensitive to impurities, both on the substrate surface and incorporated during the growth.

In summary, the properties of thin metal, semiconductor and dielectric films grown by conventional vacuum deposition are limited by cleanliness. The layers are invariably of extremely poor crystalline quality. At best the films are composed of polycrystals or randomly oriented microcrystalline areas whose lateral dimensions are similar to the film thickness. In addition, impurities, which migrate to the polycrystal grain boundaries, often have a deleterious effect on the electronic properties of the layer. Polycrystalline layers are often rough on a microscopic scale, and difficulties encountered in accurately defining sharp geometrical device shapes can be a severe hindrance in optical components. On the other hand, layers grown by MBE are epitaxial, that is, they are single crystals. Edges which have been etched in device fabrication steps are characteristically exceptionally smooth and film surfaces are smooth on an atomic scale. Consequently the interface roughness between two layers grown consecutively in an MBE system can be less than a few atomic steps. Such characteristics make MBE layers eminently suitable for use in optical devices. Furthermore, the growth of dielectric multilayers by molecular beam epitaxy does not replicate surface topography from layer to layer.

3. Equipment for Molecular Beam Epitaxy

Figure 1 shows a commercially available MBE machine of the type installed in the Arthur D. Little, Inc., MBE laboratory. A schematic drawing is shown in Figure 2. In the design of MBE equipment close attention is paid to the elimination of sources of impurities. Essentially an MBE system system consists of a stainless steel ultra high vacuum chamber with thermal effusion sources containing suitable elements to grow the compound crystal of interest. The cells are constructed of refractory materials such as pyrolitic boron nitride. Additional ovens may be used to generate beams of impurity elements to dope the material, n- and p- type. Each oven has an aperture positioned so that the vaporization products are directed towards the substrate which is mounted on a heated block of molybdenum. A small molybdenum plate or shutter can be interposed between each cell aperture and the substrate to facilitate abrupt changes in doping density and/or structure. For example, by opening and closing the aluminum oven shutter during simultaneous gallium, arsenic and aluminum evaporation the growth of superlattices of AlGaAs/GaAs can be achieved. Similarly, the repeated actuation of shutters in front of cells containing n- and p- type doping materials during gallium arsenide growth has led to the development of a new type of doping superlattice. Most MBE systems have extensive internal cryopanels which are double skinned stainless steel containers through which liquid nitrogen is passed, thereby reducing the temperature to 77K. The cryopanels reduce background

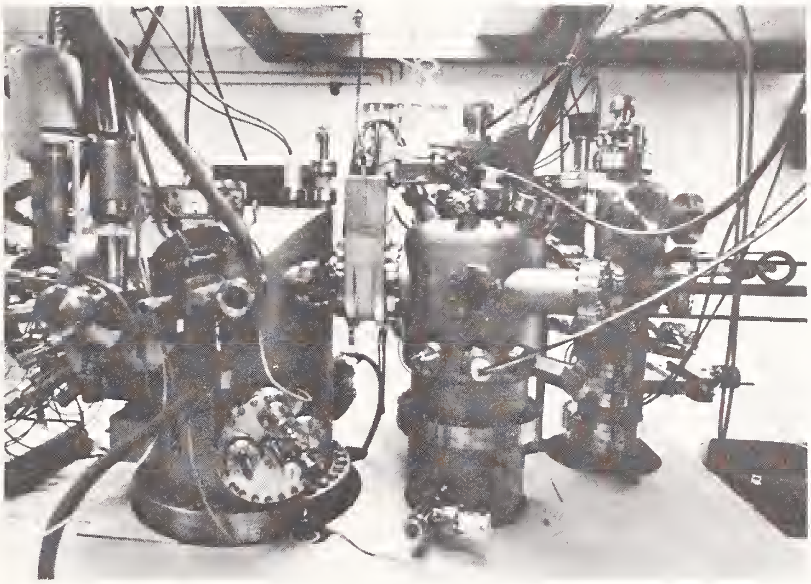

Figure 1. Photograph of Arthur D. Little MBE Installation

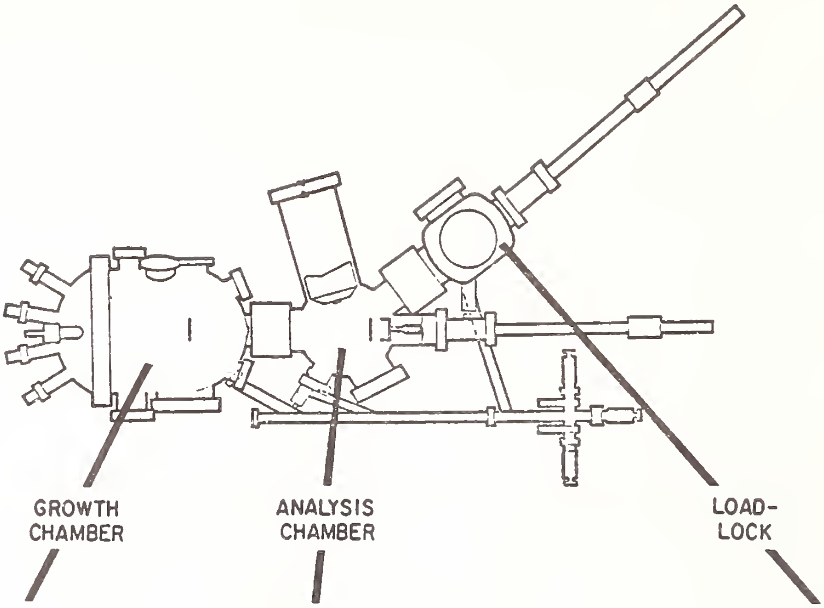

Components

8 Thermal sources

2 e gun sources

Microcomputer controls

Cryoshields

Rotating and heated substrate holder

Cryopump

400 l/sec ion pump

Ti sublimation pump

2 Nude ion gauges (1 flux meter)

Diagnostics

Reflection Electron Diffraction (RED)

Residual Gas Analyzer (QMA)

Components

Ar ion gun (etch profiling)

850°C Sample heating capability

Substrate holder

Nude ion gauge

Cryoshield

200 l/sec ion pump

Ti sublimation pump

Diagnostics

Scanning Auger Microprobe (SAM)

Secondary Electron Emission Microscope (SEEM)

Components

Ar ion gun (cleaning)

250°C substrate holder

Nude ion guage

Cryopump

Figure 2. Schematic of Arthur D. Little MBE System

pressures by removing condensible gas species and inhibiting the scatter of effusing species from the stainless steel walls of the vacuum chamber.

4. Diagnostic Facilities

One of the advantages of MBE over other growth techniques is that the ultra high vacuum environment permits the use of in-situ diagnostic techniques. The technique which is routinely used in MBE is reflection electron diffraction (RED) in which an electron beam of energy 5 to 15 keV impinges on the substrate surface at a glancing angle. The electron beam is diffracted by the ordered array of surface and near surface atoms in the crystal in much the same way as x-rays are diffracted by a crystal, or light is diffracted by a periodic grating. The diffraction pattern generated by the crystal surface/electron beam interaction is conveniently displayed on a fluorescent screen situated within a vacuum viewing port diametrically opposite the electron beam gun. Surface roughness on a microscopic scale gives rise to a spotty pattern due to transmission of the electron beam through the 3 dimensional surface projections while an atomically smooth surface is characterized by a streaked pattern. For example, the pattern obtained from a clean polished (100) surface of a cubic semiconductor crystal slice is usually "spotty". The spots signify that the surface, although mirror smooth to the naked eye, is microscopically rough. On exposing such a surface to epitaxial growth in an MBE system, it has been shown in many cases, that after only 150 Angstroms of growth the spots in the diffraction pattern become elongated indicating a significant improvement in surface smoothness. The reason for this is that the surface morphology of the layer is determined by the crystal structure and not by the topography of the underlying substrate. Thus single crystal layers grown by MBE are characteristically smooth and are well suited to devices in which surface or interface morphology is a crucial factor, for example, integrated optical components and devices which make use of the 2-dimensional effects associated with semiconductor interfaces.

Other important diagnostic techniques are Auger electron spectroscopy (AES)* and quadrupole mass spectrometry. The former is used to study the chemical species present on the surface of material. As shown in Figure 2, the SAM unit is situated in a chamber which can be isolated from the growth environment. Substrates may be introduced into the analysis chamber without disturbing the vacuum conditions in the growth chamber. The substrates may then be cleaned and inspected by SAM to insure the complete removal of contamination from the crystal surface. Quadrupole mass spectrometry is used to identify and estimate the partial pressure of background species in the vacuum system. It is often used on a routine basis to decide whether the vacuum environment is suitable for growth of an epitaxial layer.

5. Materials, Devices and Structures Grown by MBE

Although GaAs has been used as an example in much of the preceding description it should be realized that many materials have been grown by MBE. The list of materials given in Table 2 is not intended to be complete but serves to illustrate the point.

---

*Sometimes referred to as a Scanning Auger Microprobe (SAM)

Table 2. Crystalline Films Grown With Molecular Beam Epitaxy

IV:	Ge
	GeSi
	Si
I-VII:	KCl
II-VI:	CdS
	CdSe
	CdTe
	ZnS
	ZnSe
	ZnTe
	Zn(SeTe)
	HgTe
	HgCdTe
II-VII:	$\mathrm{BaF_2}$
	$\mathrm{CaF_2}$
	$\mathrm{(BaCa)F_2}$
	$\mathrm{SrF_2}$
IV-VI:	(PbGe)Te
	PbS
	PbSe
	PbTe
	(PbSe)Te
	(PbSn)Se
	(PbSn)Te
	SnTe
	PbEu
	PbYbTe
	PbMnTe
III-V:	AlAs
	(AlGa)As
	AlP
	GaAs
	Ga(AsP)
	Ga(AsSb)
	(GaIn)As
	(GaIn)(AsP)
	(GaIn) P
	GaP
	GaSb
	GaN
	(AlGa)N
	InAs
	(InAl)As
	InP
	InGaAlP
	InSb
Metals:	Al
	Ag
	Au
	Fe
	Sn

Progress in devices and structures fabricated using MBE material is also proceeding apace. A very successful program aimed at developing solid state double heterostructure lasers has been undertaken by Tsang[11] at Bell Labs.

Similarly the growth of superlattices has received considerable attention along with the development of the modulation doped heterojunction. In this device an n-doped layer of AlGaAs is grown onto an MBE-grown undoped GaAs layer. Since there is a higher electron affinity in GaAs than in AlGaAs excess electrons spill over from the AlGaAs into a thin surface region of the GaAs close to the interface. The electrons which find themselves in this region are spatially separate from their parent donor ions and thus are free to move without impedance from ionized impurity scattering centers. The electron mobility is therefore high. This is the basis of the high electron mobility transistor (HEMT) - a device made possible by MBE technology.

Many other new applications are possible. For example, the possibility arises of vertically stacking devices; of "writing" devices into epitaxial layers by steering ionized dopant beams; of growing consecutive layers of metals, insulators, semimetals and semiconductors. Applications in new areas of physics are also currently under investigation, e.g., ultrasmall electronic devices, quantum interference effects, metallic superlattices and metastable phases.

MBE technology is being developed in a number of ways. Increases in substrate size have already been accommodated from dimensions less than 1" diameter up to 3" diameter. It is expected that MBE systems can be scaled up further. Furthermore, the development of "beam processing systems" has already been predicted. In these systems, thermal effusion sources would be only one of several techniques to transport energetic elements and molecules to the substrate. Other ways may involve low energy ionization and electron beam evaporation. Substrates could also be processed in a number of ways within the vacuum system, e.g., by laser, electron beam or thermal annealing.

6. Characteristics of Multilayer Dielectric Optical Coatings

Simple multilayer dielectric (MLD) coatings consist of thin films of alternating regions of high and low indices of refraction, each having very low optical absorption. Although the design of such film stacks are relatively straightforward, in practical cases, serious problems are encountered. They fall into two somewhat, but not completely, independent areas; problems related to the absorption characteristics of the films and their damage thresholds.

A vexing aspect of optical performance of thin films is that although the optical absorption can be made small, it is still, in general, orders of magnitude higher than would be predicted from the absorption coefficients of the bulk material used in making the film. Furthermore, the damage thresholds of material surfaces are always somewhat lower than that of the bulk.

While the excess optical absorption of films can be attributed to impurities and high surface-to-volume ratio of the polycrystals, the relationship between the film's structural properties and its resistance to damage manifests itself in a complicated manner. For example, the effects of surface topography may enter the problem both in defining thermal paths and in the formation of high field regions. Furthermore, the existence of interface electronic states contributes to the absorption characteristics of the interface and the increased scattering caused by surface roughness plays a role in determining the damage threshold. However, in all of these matters, as well as the gross surface properties of a film, the grain size of microcrystals forming the film plays a central role.

In addition to these two general problem areas, a third and equally important problem area concerns the optical requirement that the optical phase-shifts should be constant within one percent and independent of position across the area of the film.

7. Application of Molecular Beam Epitaxy to the Fabrication of Optical Coatings

The majority of current processes for manufacturing MLD mirrors involve conventional vacuum deposition techniques such as evaporation and sputtering. These methods produce amorphous or microcrystalline films; we argue that they cannot improve upon the performance limitations already set by optical absorption and damage thresholds, and described in the preceding paragraphs.

As described earlier, molecular beam epitaxy (MBE) is an ultra high vacuum technique which has recently reached a degree of near-commercial maturity in the semiconductor device fabrication industry. Layered structures called "Superlattices" containing extremely well defined and almost atomically smooth interfaces can be grown with an unequalled morphology and high or precisely controlled purity single crystal films. The technique has a demonstrated performance in semiconductor physics and technology which makes it a plausible process candidate to satisfy the materials, morphological and thickness uniformity requirements of MLD mirror manufacture. We justify this conclusion with the following observations.

Single crystal films or films with large crystal grain sizes and thus small surface-to-volume ratios are expected to have fewer numbers of localized states in the energy gap and less optical absorption. Further, an electron in the conduction band is less likely to be the instigator of laser-induced breakdown in a crystal where the momentum relaxation time is longer. Single crystal films with low density of defects and smooth interfaces would directly contribute to a longer momentum relaxation time. These constitute the microscopic basis for the expectation that epitaxial films will have superior performance as MLD components in comparison with polycrystal films.

An equally important additional microscopic advantage of epitaxial growth is that grown layers do not replicate the surface roughness of the substrate, but instead tend to be atomically smooth. The reason for this phenomenon is that the surface morphology is determined by the crystal structure and not by that of the underlying surface topography. Long-range order of the crystal insures that the free energy of an epitaxially placed atom in a valley on a rough surface is less than that of one which is placed epitaxially on a peak. For amorphous films, the free energy is independent of position on the (rough) surface since there is no long-range order.

As a production process, the existence of a load lock and facilities to clean by heating and ion bombardment of substrates in-situ in UHV environment make MBE a unique method to minimize the existence of "extrinsic" damage centers in the finished product.

From a materials point of view MBE has already been demonstrated on many very important optical materials such as ZnS, ZnSe, CaF_2, etc. Table 2 contains a list of materials which have been successfully deposited epitaxially with the MBE process. Although the list is not exhaustive, it suggests that it is now possible to examine experimentally, the behavior of MBE grown MLD reflector stacks in intense laser beams.

9. References

[1*] M.B. Panish, Science, Vol 208, pp 916-922, (May 1980).

[2*] A.Y. Cho and J.R. Arthur, Prog. Solid State Chem., 10, 157 (1975).

[3] K.G. Gunther, Naturwissenschafte, 45, 415 (1958).

[4] J.E. Davey and T. Pankey, J. Appl. Phys., 39, 1941 (1968).

[5] J.R. Arthur, J. Appl. Phys., 39, 4032 (1968).

[6] C.T. Foxon, and B.A. Joyce, Surf Sci. 64, 293, 1977.

[7] A.Y. Cho, J. Vac. Sci Technol, 16, 275 (1979).

[8] P.W. Sullivan, RFC Farrow and G.R.Jones, submitted to J. Cryst. Growth Nov. (1981)

[9] P.W. Sullivan, T.I.Cox, RFC Farrow, G.R. Jones, D.B.Gasson, C.S.Smith, 28th American Vacuum Society Meeting, USA Nov. (1981).

[10] M. Faurie, Presented at MBE Workshop, Santa Barbara, Sept. 1981.

[11] W.T. Tsang, Appl. Phys. Lett. 34, 473 (1979).

*Authoritative review articles

Ion Beam Sputter Deposition of Optical Coatings

J. R. Sites, P. Gilstrap, and R. Rujkorakarn

Department of Physics, Colorado State University
Fort Collins, Colorado 80523

A beam of 500-1200 eV argon and oxygen ions, neutralized with an equal number of electrons, strikes a target, and the sputtered particles from a deposited layer of SiO_2, Ta_2O_5, or TiO_2. A second beam at lower energy is aimed at the substrate and used for stress modification and pre-deposition sputter cleaning. Deposited films are mechanically stable, nearly amorphous, and extremely adherent; internal stress is compressive. The primary contaminant is carbon, which is less than one percent. Refractive indices near 1 µm are 1.47 for SiO_2, 2.03 for Ta_2O_5, and 2.27 for TiO_2. Optical absorptance of half wavelength films at 1.06 µm is near 10^{-4} for SiO_2 and Ta_2O_5 and near 4×10^{-4} for TiO_2. Damage tests with a 114 µm radius, 1.06 µm wavelength laser beam show an onset energy flux for visible damage in the 15 to 40 J/cm^2 range for single layer films, slightly less for a three layer structure.

Key words: optical coatings; ion beam; SiO_2; Ta_2O_5; TiO_2; absorptance; laser damage.

1. Introduction

Ion beam sputter deposition has proven to be a useful technique for producing thin films for applications including solar cells [1], optical recording media [2], insulators on semiconductors [3], silicides [4], and diamondlike films [5]. The broad beam Kaufman-type ion source developed for space propulsion [6] is nearly ideal for this purpose. A discharge chamber with magnetic confinement of electrons produces a relatively uniform plasma from essentially any gas or mixture of gasses. A grid system extracts positive ions and a neutralizing filament adds an equal number of electrons to the beam. The neutral beam does not diverge appreciably and can be used with insulating targets and substrates.

In the work described here a Kaufman-type ion source is used to fabricate oxide films of both high and low refractive indices for reflectance enhancement. Results to date are very encouraging in that both the mechanical and optical properties of the films are approaching those desired for coating mirrors subjected to large optical power densities.

2. Experimental Procedure

The ion beam sputter deposition apparatus is shown in figure 1. The primary ion source produces a beam of monoenergetic positive ions, in the present case either argon or an argon/oxygen mixture. The ion energy is controlled by the potential difference between the source and ground and is typically 500 to 1200 eV. The ion current density is controlled by the gas input to the source and the discharge potential; it is typically 1.0 to 1.5 ma/cm^2.

The primary ion beam strikes a target that is either metallic or the oxide being deposited. In either case some additional oxygen is necessary and is mixed with the argon in the source. Oxide targets require about 10% oxygen in the beam; metallic targets, 30 or 40%. The system configuration allows a change of targets *in situ*, a change which can be made either quickly or gradually.

A second ion beam is aimed directly at the substrate. It is generally run at a lower energy (∿300 eV) and is used to sputter clean the substrate prior to deposition. This step seems to be important in producing films with very high adherence. The second beam is also used during deposition in an effort to modify stress in the deposited layers.

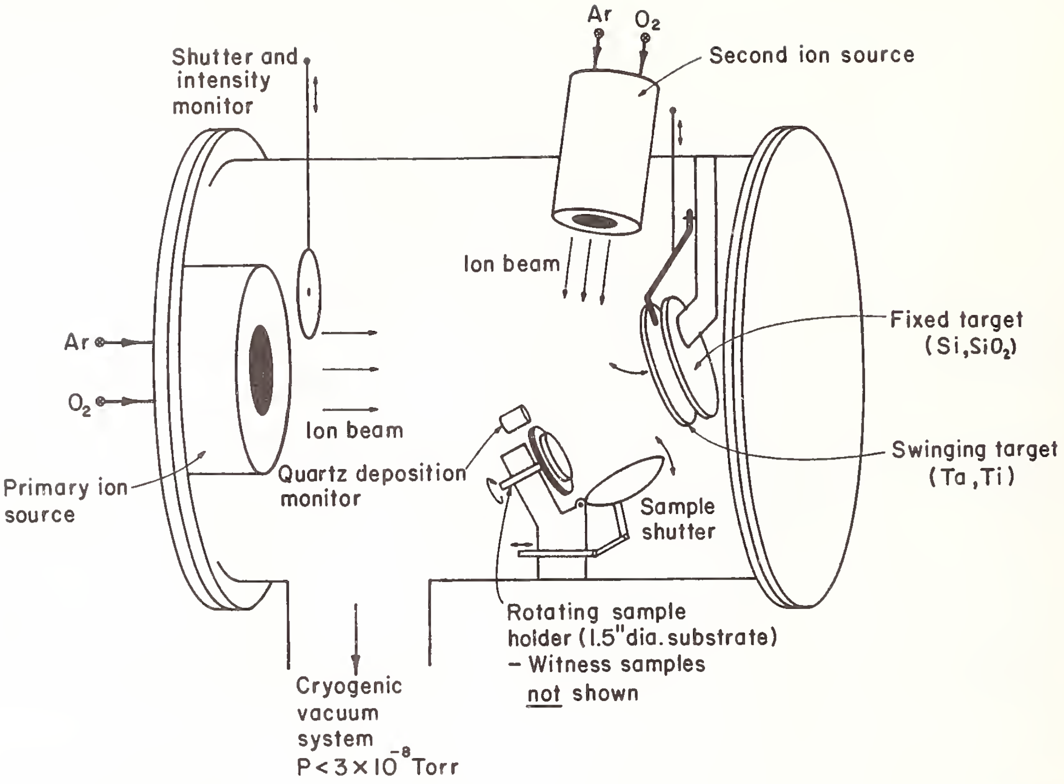

Figure 1. Ion beam sputter deposition apparatus.

3. Results

Three oxides have been deposited by the ion beam technique: SiO_2, Ta_2O_5, and TiO_2. Both quartz and silicon targets were used to produce SiO_2, with similar results either way. Only metallic targets have been used for the other two oxides.

The refractive indices of the three oxides were deduced from the reflectivity spectrum of single layer films and are illustrated in figure 2. The SiO_2 index is essentially that expected; The TiO_2 value is fairly high for a nearly amorphous film, implying that it is quite dense; the Ta_2O_5 refractive index is slightly lower than anticipated, but there is relatively little reported work for comparison.

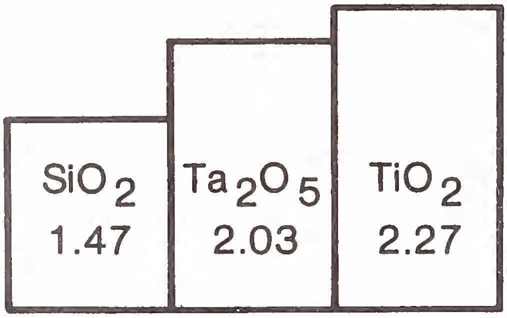

Figure 2. Refractive indices of deposited films.

In addition to the single layer films, three layer coatings of high-low-high index films on quartz have been fabricated. Both Ta_2O_5 and TiO_2 have been used for the high index material, SiO_2

for the low index. Figure 3 shows the reflectivity spectrum of quarter wave Ta_2O_5-SiO_2-Ta_2O_5

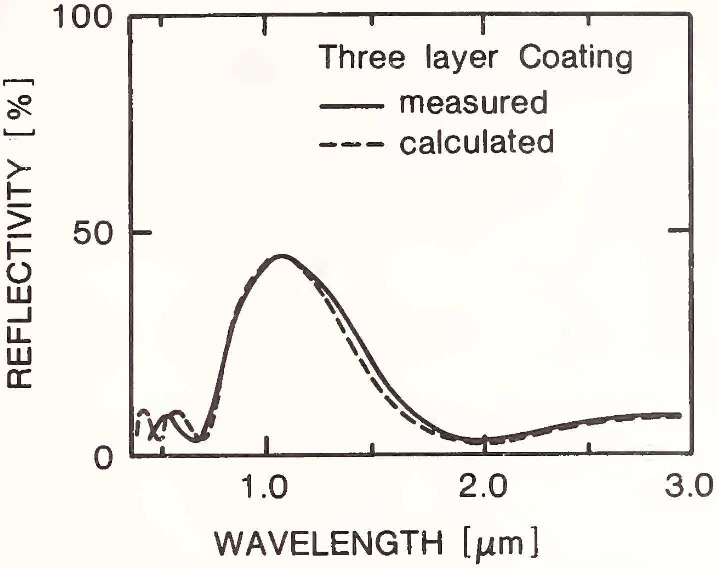

Figure 3. Comparison of calculated and measured reflectivities for quarter wave Ta_2O_5-SiO_2-Ta_2O_5 coating.

layers coating quartz with the thicknesses selected for a peak reflectivity at 1.06 μm. The agreement with the spectrum anticipated from calculation using the matrix technique [7] is quite good.

Compositional analysis of the ion beam sputter deposited films utilized ESCA techniques. In all the samples there was carbon impurity on the surface, but it almost completely disappeared under a light sputter etch. The residual carbon was just at the limit of experimental resolution, about one percent. All other impurities were below the resolution of the instrument (see fig. 4). In

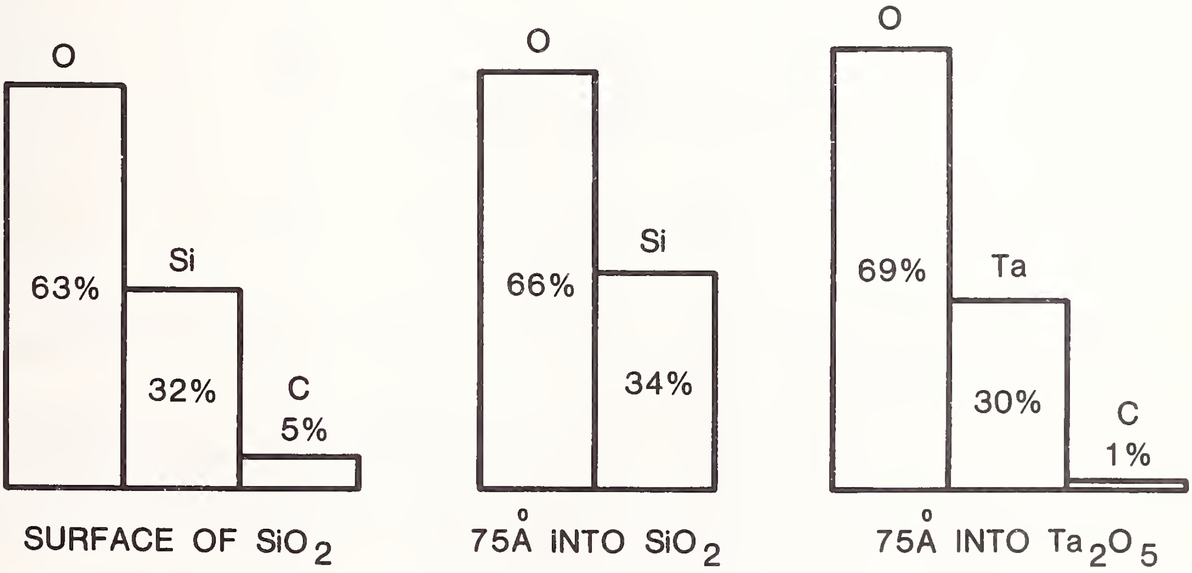

Figure 4. Composition of nominal SiO_2 and Ta_2O_5 films.

general the ESCA measurements suggested that the films contained slightly less oxygen than the nominal SiO_2 and Ta_2O_5 labels. (TiO_2 films have not yet been analyzed.) At low oxygen concentrations in the sputter beam, the oxygen content of the films not surprisingly dropped to lower values.

The adherence of the oxide coatings has been very good as is typical of ion beam sputter deposited films in general. Apparently the relatively high energies of the sputtered particles (∼20 eV) create both dense films and ones that adhere well to a substrate. Both the single layer and three layer coatings exceeded the limit of our adherence tester (10,000 psi or 6×10^7 N/m^2). In this technique a metal piece is epoxied to the coating then pulled until the coating comes off or until 10,000 psi is reached. When we forcibly removed the metal piece by twisting with a pair of pliers, the substrate generally cracked before the coating failed.

Stress in our single layer films was always compressive. It was determined by measuring the radius of curvature of a thin substrate before and after deposition [8]. We found the SiO_2 films to have a larger internal stress than either the Ta_2O_5 or the TiO_2. Attempts to modify the stress using the second ion beam were only partially successful (see fig. 5). The effect of the second ion beam was to lower the SiO_2 stress somewhat and leave that of the Ta_2O_5 essentially unchanged. The difference in stress between the two materials, however, is decreased considerably. Measurements of TiO_2 stress modification have not been completed.

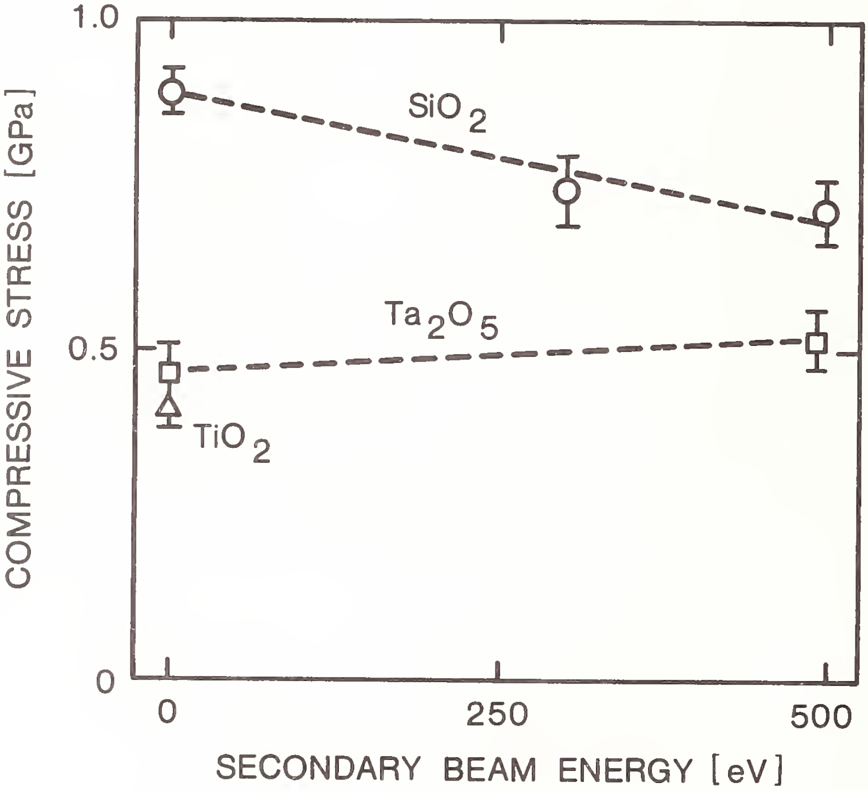

Figure 5. Stress in single layer films showing the effect of substrate bombardment with a second ion beam.

Optical absorptance of half-wave, single layer films was measured at OCLI using absorptance calorimetry with 1.06 μm radiation. As seen in figure 6, the absorptance of both SiO_2 layers and Ta_2O_5 layers was near 10^{-4}. That of TiO_2 was somewhat higher. Also shown in figure 6 is a half wavelength SiO_x film deposited by sputtering SiO_2 without any oxygen in the beam. The much larger absorptance clearly illustrates the need to add extra oxygen.

Laser damage tests at AFWL showed that both single layer and three layer films have a reasonable ability to withstand damage from high intensity radiation. When damage did occur, it was most pronounced at small, micron sized scattering centers in the films. We believe these defects are caused by residual particles not removed by our cleaning processes. Generally the damage threshold was higher when the laser failed to hit any defects, lower when it struck one or more, as illustrated by the dashed boxes in figure 7. Less intensive tests were made on the three layer coating and as with some of the other measurements, we have not yet tested the TiO_2 films.

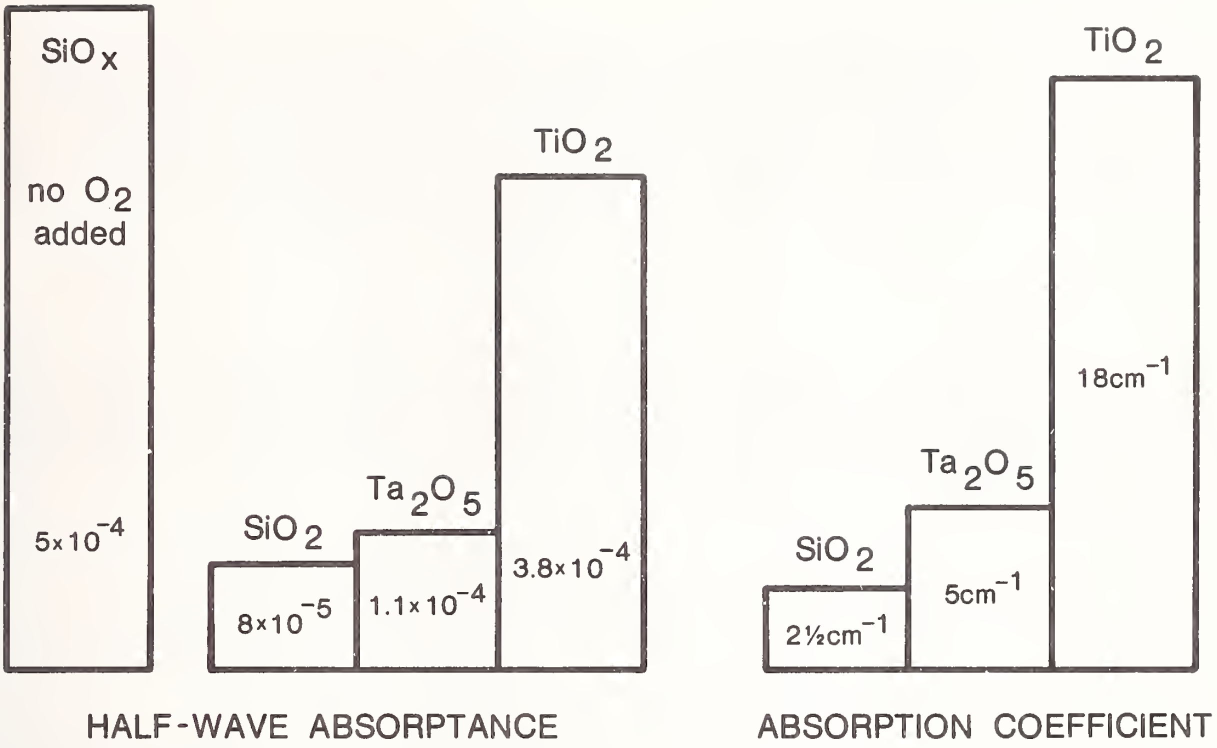

Figure 6. Optical absorption of single layer films.

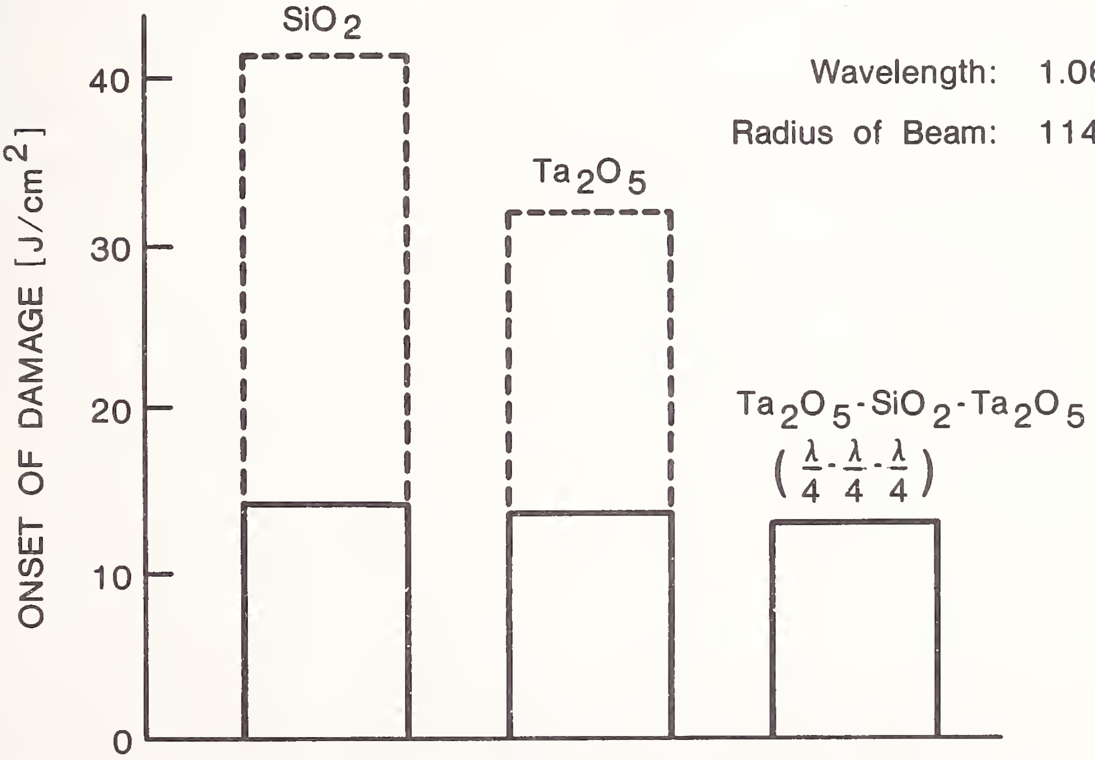

Figure 7. Laser energy density necessary to visibly damage coatings. Dashed boxes enclose region where damage sometimes occurred and sometimes did not.

4. Conclusions

We find that ion beam sputtering is an attractive technique for the deposition of optical coating layers. The films are very sound mechanically; they have excellent adhesion, they are relatively dense, and as far as we can tell, they are stable. Internal stress is compressive and can be modified somewhat with a second beam aimed at the substrate. Optical absorption in single layers is relatively low, and the energy density necessary for laser damage is relatively high. For multilayer films, it is straightforward to change from one composition to the other, and we see no major difficulties in scaling the technique to more layers and larger sized surfaces.

We would like to thank Kent Geib of our University for the ESCA measurements, Tom Allen and Jerry Dodds of Optical Coatings Labs for the absorption calorimetry, and Alan Stewart and Ed Miesak of AFWL for the laser damage tests. The work reported here is supported by the Air Force Weapons Laboratory under Contract F29601-82-K-0009.

5. References

[1] Burk, D. E.; DuBow, J. B.; Sites, J. R. Fabrication of OSOS cells by neutral ion beam sputtering. Proc. 12th IEEE Photovoltaics Specialists Conf. 971-974; 1976.

[2] Rossnagel, S. M.; Robinson, R. S.; Kaufman, H. R. Ion beam sputter deposition of high density optical recording media. Unpublished report, CSU Physics Department, 1982.

[3] Meiners, L. G.; Pan, R.; Sites, J. R. Oxide barriers on GaAs by neutralized ion-beam sputtering. J. Vac. Sci. Technol. 14(4): 961-963; 1977 July/Aug.

[4] Weinmeister, R. E.; Mahan, J. E. Electronic transport and microstructure in molybdenum silicide thin films. Appl. Phys. Lett. 39(12): 347-351; 1981 December.

[5] Banks, B. A.; Rutledge, S. K. Ion beam sputter-deposited diamondlike films. J. Vac. Sci. Technol. 21(3): 807-814; 1982 Sept./Oct.

[6] Kaufman, H. R. Technology of electron bombardment ion thrusters, in Advances in electronics and electron physics, Vol. 36, L. Merton, ed. New York: Academic Press; 1974. 265-373.

[7] Abelès, F. Sur la propagation des ondes electromagnétiques dans les milieux stratifiés. Ann. Phys. 5: 504-520; 1950.

[8] Rossnagel, S. M.; Gilstrap, P.; Rujkorakarn, R. Stress measurement in thin films by geometrical optics. J. Vac. Sci. Technol. in press.

In response to questions, the speaker stated (1) that the packing fraction for the films had not been measured, and (2) that oxygen had only been introduced into the chamber through the ion beam itself since it was thought that molecular oxygen wasn't sufficiently reactive. When asked to clarify his assertions that the films were noncrystalline and very adherent, the author conceded that his data indicated absence of crystallites greater than 100 Å in size, and that sputter deposited oxide films on glass usually had good adherence.

Optical Characterization of Plasma Deposited Hard Carbon Coatings

B. Dischler, A. Bubenzer, P. Koidl, G. Brandt, O.F. Schirmer

Fraunhofer-Institute for Applied Solid State Physics (IAF)
Eckerstr. 4, D-7800 Freiburg i. Br., West-Germany

Hydrogenated amorphous carbon films (a-C:H) have been deposited on Ge, Si and glass substrates in a RF excited glow discharge from benzene vapour. These films are hard, chemically inert and IR-transparent and therefore very promising for protective and antireflective coatings for IR-optical components. We report on the optical properties of a-C:H and their quantitative dependence on deposition parameters. Absorption spectra of a-C:H coatings in the wavelength range 0.2 - 20 µm have been extracted from transmission and reflection measurements. In addition CO_2 laser damage thresholds are reported. For a-C:H with refractive index n = 1.93 the following absorption coefficients have been measured: 250, 25, 15, 200 and 780 cm^{-1} at wavelengths of 10.6, 3.8, 2.8, 1.3 and 1.06 µm respectively. The increased short wavelength absorption and its possible dependence on dangling bond density - as determined by electron spin resonance - is discussed.

Key words: absorption; amorphous hydrogenated carbon; hard coating; infrared; laser damage; optical properties; plasma deposition; thin film.

1. Introduction

Amorphous hydrogenated carbon (a-C:H) offers the potential of extreme hardness, resistance against chemical attack and optical transparency over a wide spectral range. Consequently this material has found increasing interest as a protective coating for optical components. Although hard carbon coatings are offered commercially, this material is physically not well understood. In particular there is insufficient quantitative information on the optical properties and their dependence on the conditions of preparation.

We shall report on the optical absorption of a-C:H showing that at HF and DF laser wavelengths the absorption of our films is an order of magnitude below the best values quoted previously. In addition CO_2 laser damage data will be reported.

2. Preparation and Film Properties

Hard carbon coatings have been prepared by rf [1-4] and dc [5,6] plasma deposition, ion beam [7-10] and sputtering techniques [11-12]. We used the first method since it offers the possibility to grow homogeneous large area coatings on insulating substrates with relatively high deposition rates.

a-C:H has been deposited onto negatively biased Ge, Si or glass substrates in a 2.3 MHz-excited RF glow discharge sustained by benzene vapour. The apparatus as described previously [13] has been implemented by an optical pyrometer for the measurement of the film temperature during growth.

The deposition process and the film properties can be controlled precisely and reproducibly by the two parameters: negative bias voltage, V_B, and hydrocarbon pressure, P. As an example, figure 1 shows the dependence of the refractive index on V_B and P. The inner rectangle defines the parameter range used for the deposition of a-C:H. The solid lines are curves of equal refractive index. As shown by the dotted lines there is a wide parameter range within which n is determined by a single parameter, namely V_B/P.

The tunability of the refractive index is important for the design of optical coatings. By adjusting the refractive index exactly to n = 2.0, single layer AR coatings on Ge have been realized with a residual reflection below 0.2% [13].

Table 1 summarizes important deposition parameters, thin film properties and their dependence on V_B and P. A detailed study and a discussion of the range of validity of the given relationships will be published separately [14].

3. Optical Characterization

Transmission and reflection measurements in the wavelength range 0.2 - 20 µm have been performed on two double beam spectrometers, each equipped with an on-line computer (Perkin Elmer 330 + 3500 data station and Perkin Elmer 580B + 3600 data station). All transmission (T) and reflection (R) spectra are stored electronically and the loss spectrum (A) is computed according A = 1-R-T. Surface losses can be ruled out because A scales exactly with film thickness (in units of half wave layers). Comparison with calorimetrically determined absorption shows that scattering can be neglected. Thus

Table 1: Deposition parameters, a-C:H thin film properties and their interdependence

Property	Value/Range	Linear Function of
Deposition parameters		
bias voltage, V_B	0.4 - 1.8 kV	
gas pressure, P	10 - 60 μbar	
growth rate	100 - 2500 Å/min	$V_B P$
film temperature	40 - 140° C	$V_B^2 P^{1/2}$
a-C:H Properties		
density	1.5 - 1.8 g/cm³	$V_B P^{-1/2}$
refractive index	1.8 - 2.2	$V_B P^{-1}$
hydrogen content	~ 30 at%	V_B, weak P-dependence
optical gap	0.8 - 1.8 eV	V_B, weak P-dependence
Knoop hardness	1250 - 1650 kp/mm²	to be determined
electr. resistivity	~ 10^{12} Ωcm	to be determined

the loss spectrum represents essentially the absorption of the a-C:H thin film. After correcting for standing wave effects [15], the absorption coefficient is calculated. Figure 2 shows the absorption coefficient between 2.5 and 14 μm. The strong absorption at 3.4 μm results from C-H stretching vibrations. The absorption beyond 6 μm is due to C-H deformation and C-C bond stretching vibrations. At 10.6 μm the method described yields an absorption coefficient between 250 and 300 cm^{-1}. This value has been confirmed by laser calorimetry.

Figure 3 shows the absorption from the CH-stretch band towards higher energy. Spectra of three different carbon films with refractive indices of 1.85, 1.93 and 2.16 are shown. The absorption minimum occurs around 2.8 μm. The spectral dependence is quite different from an Urbach type absorption edge as observed e.g. in diamond (fig. 3a). There is a subexponential increase of the absorption towards higher energy. Replotting the curves in figure 3b shows that - except for the lowest tail - the absorption in a-C:H follows the relation

$$(\alpha E)^{1/2} = G\ (E - E_{opt}).$$

This relation also holds for the absorption edge of a-Si:H [16,17]. Extrapolation of the straight lines to the abscissa yields the optical gap, E_{opt}. The gradient G was found to be constant. Thus, the differences in optical absorption for $E > E_{opt}$ are fully characterized by E_{opt}.

The optical gap can be influenced by means of V_B and P (see table 1). It is important to note that the sub gap absorption tails shift with the optical gap itself. Thus E_{opt} also determines the near infrared absorption of a-C:H.

In table 2 we list the measured absorption of different a-C:H coatings at important laser wavelengths. Very low absorption is found at 2.8 and 3.8 μm especially for the low index films. These absorption coefficients are an order of magnitude below the best values reported before [18]. The near IR absorption of the n = 2.0 sample has been confirmed by low temperature calorimetric spectroscopy [19,20].

4. CO_2 Laser Damage

Most applications of hard carbon coatings concentrated so far in the 8 - 12 μm region. Therefore CO_2 laser damage measurements are of importance.

Germanium windows coated on either side with a quarter wave AR film of a-C:H (n = 2, thickness = 1.3 μm) have been used for damage measurements.

AT GEC, Hurst Research Centre, single shot CO_2 laser damage thresholds have been measured using the experimental setup as described in this volume [23]. 1/1-damage thresholds ranging between 110 and 280 MW/cm² have been observed.

Multiple pulse measurements have been performed at Eltro GmbH., Heidelberg. A CO_2-TE laser emitting pulses of 50 ns width with a TEM_{00} transverse mode profile has been focussed to a 1.5 mm diameter spot. At a continuous irradiation at 1 Hz prf a N/1-damage threshold of 50 MW/cm^2 corresponding to 5J/cm^2 has been measured. This lower value as compared to the single shot damage threshold indicates an accumulation or memory effect.

Table 2: Optical absorption coefficients (cm^{-1}) in a-C:H

E_{opt} (eV)	Refr. Index	Wavelength (µm)				
		10.6	3.8	2.8	1.3	1.06
1.76	1.85	250	15	< 10	52	150
1.28	1.93	250	25	15	200	780
1.10	2.00	250	40	26	550	1900
0.96	2.16	250	110	60	2800	6000
			a) 121	a) 429	a) 446	

a) from ref. [18]

5. Discussion

It has been shown that besides the already established usefulness of a-C:H in the 10 µm region, this material has a window of very low absorption at HF and DF laser frequencies. The residual absorption as well as the increase towards higher energy reflects the onset of electronic absorption and is characterized by the optical gap.

It has been found that E_{opt} and the content of bonded hydrogen depend in much the same way on the deposition parameters (see table 1 and [14]),suggesting a correlation between these two quantities. In fact there is a linear dependence of E_{opt} on the hydrogen content, as shown in figure 4. A similar behaviour has been observed in a-Si:H and a model by Cody et al. [17] suggests that hydrogen relaxes structural disorder by saturating dangling bonds thus leading to an increased optical gap.

Although the microstructure of a-C:H is more complex than in tetrahedrally coordinated a-Si:H [15], the similarity of the absorption edge and its dependence on hydrogen content suggest that the same physical model holds for both materials. In fact, electron spin resonance experiments, as described below, indicate that dangling bonds are present in high concentration in our a-C:H thin films.

ESR experiments have been performed at room temperature on a 9.7 GHz (X-band) spectrometer. A signal with a g-factor of 2.0027 and a typical linewidth of 2 Gauss, previously attributed to dangling bonds in a-C:H [21,22], has been observed. Using an a-C:H sample prepared with V_B = 1.5 kV and P = 33 µbar, a spin density of 9 x 10^{19} cm^{-3} has been determined. Work to establish a correlation between dangling bond density and hydrogen content is under way.

6. Summary

The optical properties of plasma deposited hard a-C:H coatings were investigated. For the first time complete optical absorption spectra between 0.2 and 20 µm have been measured. Laser damage thresholds at 10.6 µm are reported, showing that a-C:H is suited for medium power CO_2 laser applications. The absorption in the visible and near infrared is determined by the optical gap, which depends linearly on hydrogen content and can be varied between 0.8 and 1.8 eV. Very low absorption is achievable in the 2 to 6 µm region. This result together with the chemical resistance makes a-C:H very interesting as a coating material for HF and DF laser components.

We are indebted to R.M. Wood (GEC, Wembley), J. Ruger and F. Prein (Eltro, Heidelberg) for providing the laser damage data and to S. Hunklinger (MPI, Stuttgart) for communicating the low temperature calorimetry results.

7. References

[1] L. Holland and S.M. Ojha, Thin Solid Films *38*, L17 (1976)

[2] D.A. Anderson, Phil. Mag. *35*, 17 (1977)

[3] S. Berg and L.P. Anderson, Thin Solid Films *58*, 117 (1979)

[4] K. Enke, H. Dimigen and H. Hübsch, Appl. Phys. Letters *36*, 291 (1980)

[5] D.S. Whitmell and R. Williamson, Thin Solid Films *35*, 255 (1976)

[6] B. Meyerson and F.W. Smith, J. Non-Cryst. Solids *35-36*, 435 (1980)

[7] S. Aisenberg and R. Chabot, J. Appl. Phys. *42*, 2953 (1971)

[8] C. Weissmantel, Thin Solid Films *92*, 55 (1982), and references therein

[9] E.G. Spencer, P.H. Schmidt, D.C. Joy and F.J. Sansalone, Appl. Phys. Letters *29*, 118 (1976)

[10] J.C. Angus, M.J. Mirtich and E.G. Wintucky, in *Metastable Materials Formation by Ion Implantation*, S.T. Picraux and W.J. Choyke, Eds., p. 433, Elsevier, N.Y. (1982)

[11] B.A. Banks and S.K. Rudledge, J. Vac. Sci. Technol. *21*, 807 (1982)

[12] D.R. McKenzie, R.C. McPhedran, L.C. Botten, N. Savvides, and R.P. Netterfield, Appl. Optics *21*, 3615 (1982)

[13] A. Bubenzer, B. Dischler, A. Nyaiesh in *Laser Induced Damage in Optical Materials: 1981*, eds. H.E. Bennett, A.H. Guenther, D. Milam, B.E. Newnam (NBS Spec. Publ.)

[14] A. Bubenzer, B. Dischler, G. Brandt and P. Koidl, submitted to J. Appl. Phys.

[15] B. Dischler, A. Bubenzer and P. Koidl, Appl. Phys. Lett. (in press)

[16] E.C. Freeman and W. Paul, Phys. Rev. *20*, 716 (1979)

[17] G.D. Cody, T. Tiedje, B. Abeles, B. Brooks, and Y. Goldstein, Phys. Rev. Letters *47*, 1480 (1981)

[18] T.J. Moravec, in *Summary of the Workshop on Diamond-Like Carbon Coatings*, Albuquerque, N.M., April 1982, p. 7 (B. Bendow, Ed.)

[19] A. Bubenzer, S. Hunklinger and K. Dransfeld, J. Non-Cryst. Solids *40*, 605 (1980)

[20] S. Hunklinger, private communication

[21] R.J. Gambino and J.A. Thompson, Solid State Commun. *34*, 15 (1980)

[22] T. Shimizu, M. Kumeda and Y. Kiriyama, Solid State Commun. *37*, 699 (1981)

[23] R.M. Wood, S.K. Sharma and P. Waite, "Variation of Laser Induced Damage Threshold of Germanium with Laser Pulse Repetition Frequency" in *Laser Induced Damage in Optical Materials: 1982*, eds. H.E. Bennett, A.H. Guenther, D. Milam, B.E. Newnam; (NBS Spec. Publ., this volume)

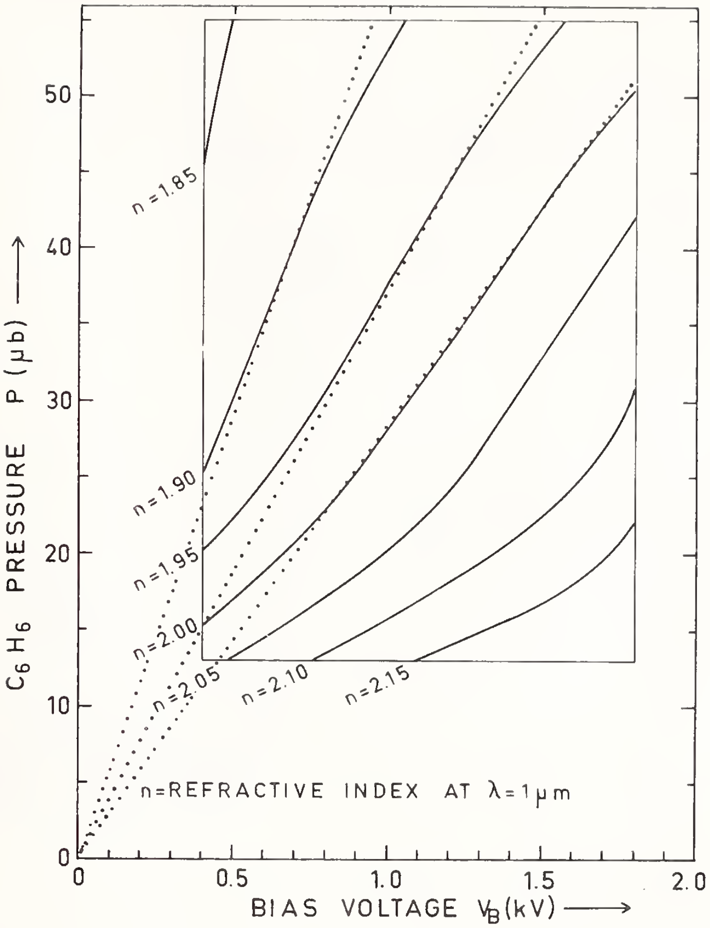

Figure 1: Curves of equal refractive index (solid lines) as a function of bias voltage and benzene vapour pressure.

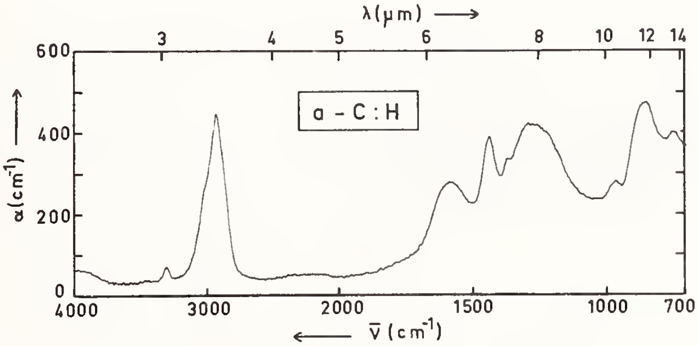

Figure 2: Infrared absorption coefficient of a-C:H.

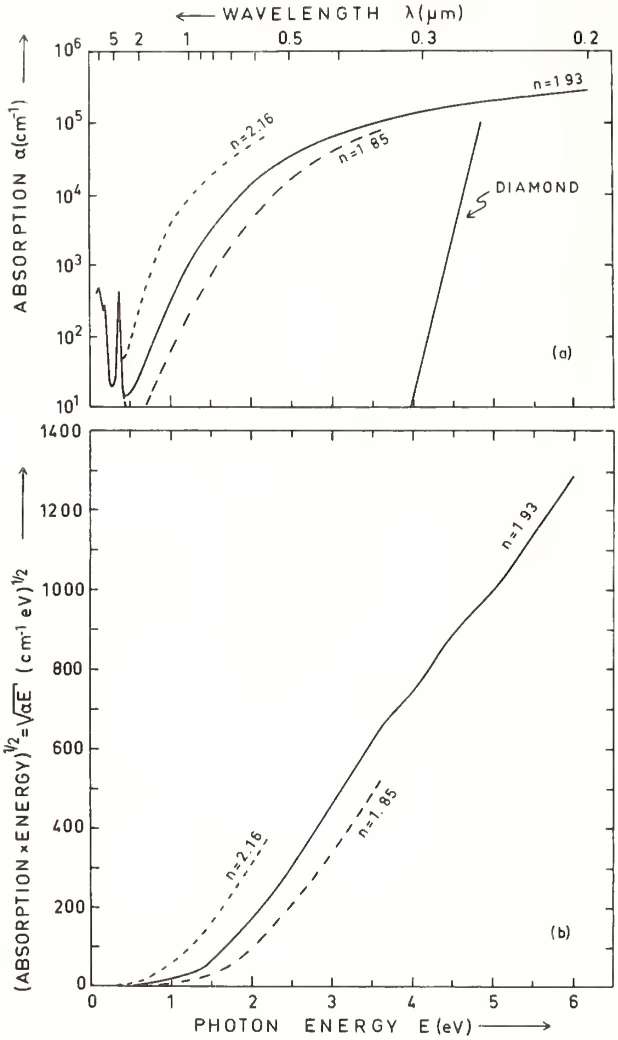

Figure 3: (a) Absorption edge of three a-C:H films with different refractive index. (b) Results for the same three samples, replotted to demonstrate optical gap behaviour.

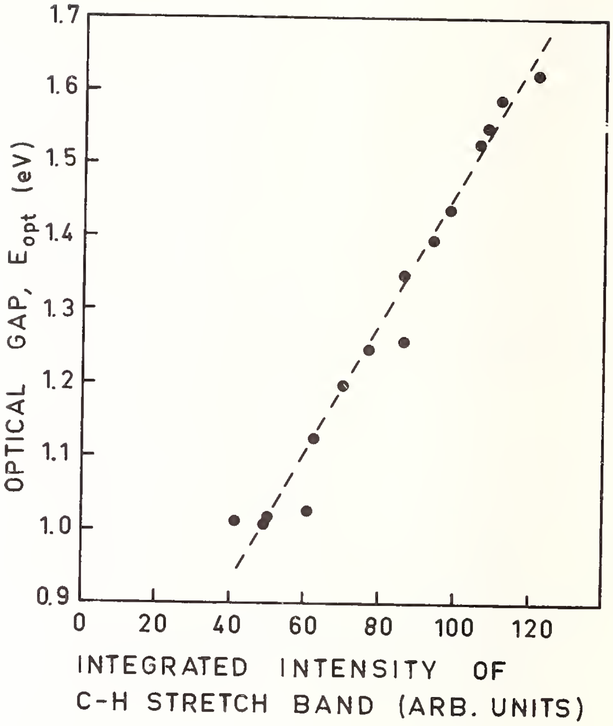

Fig. 4: Optical gap as a function of relative concentration of bonded hydrogen.

Scaling Up the Neutral Solution Anti-Reflection Process

G. Richard Wirtenson and Norman J. Brown

Lawrence Livermore National Laboratory
University of California
Livermore, California 94550
and
Lee M. Cook
Schott Optical Glass Inc.
400 York Ave.
Duryea, Pennsylvania 18642

ABSTRACT

The Neutral Solution Process[1,2] for chemically producing anti-reflection coatings has been scaled up and used successfully to treat components as large as 90-cm diameter. Since the process is primarily determined by diffusion through the surface, it has proven to be relatively insensitive to fluid flow effects which influence the chemical concentration build-up at the surface. Large parts visually appear more uniform than small parts processed in model tanks. The major problems encountered have been associated with using plastic support components beyond their normal temperature limits and in handling parts to the required cleanliness outside of a clean room environment.

Key words: Anti-Reflection; Coating; Laser Damage Resistant Neutral Solution; Surface Leaching; Thin Film.

1. Introduction

About a year ago, the Schott Glass Co., developed a chemical back-etch process for producing low reflectance surfaces on certain glasses[1,2,3]. This process produced such promisingly useful properties as regards reflectance and laser damage, that the Lawrence Livermore National Laboratory purchased the right to use it for the Laser Fusion Program and immediately began scale-up operations for the Novette Laser. Pending patent clarification, chemical details cannot be disclosed at this time. However, this restriction does not impede discussion of the process in sufficient detail for the laser damage community to have meaningful discussions on practicality and economic feasibility.

The process is not completely understood at this time, but usable surfaces to 90-cm diameter have been produced that show excellent low reflectance characteristics, good damage threshold, and considerable promise for improvement in the reflectance levels. Reflectance minima have been produced at 530 nm and 1060 nm both singly and almost simultaneously, and the process can be controlled to yield minima anywhere from about 400 nm to at least 2500 nm. Figure 1 shows a two surface transmission scan obtained from a 5-cm diameter BK-7 witness piece processed with an 80-cm Novette focusing lens. An unprocessed piece would transmit about 92%. This scan was made on a Cary 17 spectro- photometer and verified on a Perkin-Elmer 330 which yielded identical results. At the same time, it is a rather extreme result, more typical results showing 0.5 to 0.8% losses through two surfaces in the peak transmission regions.

2. Operational Process Sequence

The process sequence begins in the clean-room where pneumatically expanding rings grip the part on its edge to lift it into the ring seats of plastic holders. From this point on, points within the clear aperture are never contacted by solids.

Work performed under the auspices of the U.S. Department of Energy by LLNL under Contract No. W-7405-Eng-48.

Just before being immersed in the clean deionized water in an electropolished stainless steel tank, the optics are given a final rinse with alcohol to remove a layer of hydrocarbons that quickly forms on glass surfaces in almost any environment. Failure to do this can result in a blotchy surface. Immersed in the covered tank, the part and fixture are moved from the clean room to the processing area. Here they are quickly loaded into polypropylene plastic tanks (fig. 2) filled with deionized water. The water is filtered to 1 micron when it enters the processing area and again as it comes from area holding tanks; however, airborne particulates most likely contaminate the processing tanks.

The deionized bath is brought to temperature on a programmed linear ramp. Chemicals are then introduced for a minimum one hour etch. This solution can be flushed with four throughputs of deionized water from tanks at the same temperature or the etch can be allowed to remain in the tank since it is compatible with the process. Chemicals are then added to the tank and the processing is allowed to progress for two to four days depending on the wavelength of interest. 40 to 70 hours of processing time, allows an hour or two latitude in timing. By means of witness pieces, progress is monitored at about two thirds of the estimated period and at least twice more towards the end of the period using spectrophotometer measured transmission maxima and a linear extrapolation. Processing is quenched by a flush with deionized water at processing temperature using the four times throughput. Again a linear programmed ramp is used to cool the tanks to room temperature. Slow cooldown is precluded by a slight erasure of the process in protracted exposure to hot deionized water. Throughout the process, the tanks have been enclosed in portable clean hoods. These are now removed and the part in its holder is quickly removed to the stainless steel, water filled transport tank. Surfaces are manually sprayed with water during this transfer to prevent drying. Some particulates are undoubtably transferred and others acquired during this transfer, but immersed in a bipolar fluid, they do not appear to fix onto the surface. Their concentration in the clean tank fluid is decreased a hundredfold during the sloshing transport to the clean room. Because the processed surfaces are extremely sensitive to water spotting, Freon, immiscible with water, is introduced into the tank and water is skimmed from the surface. The liquid Freon is continuously cycled through a filter and water trap. The chilling effect of Freon evaporation precludes removal of the part into the direct atmosphere since this could result in severe thermal stress or condensation of water vapor. A second stage with plastic windows is attached to the portable tank and brought to saturation with Freon vapor. The optic is raised into this vapor for drying. It is first scanned visually for traces of water droplets which are readily distinguishable on the surface as the Freon sheets off. If any are present, the lens is repeatedly dunked until none appear. It is then allowed to dry in the freon atmosphere with little chilling and is subsequently removed (fig. 3) into the clean room atmosphere. This process is shown schematically in figure 4.

A number of elements are processed on one side only. These are protected on one side by a double Viton "O"-ring and a cover. When the part is immersed in the processing tank, the cavity fills with deionized water. The cavity is vented to the atmosphere through tubes rising above the maximum fluid level to permit outgassing and accommodate expansion.

This equalizes pressure and prevents serious ingress of chemical into the back cavity in the event of "O"-ring failure of which there have been several. This failure mode has been eliminated by the use of heat-sealed vulcanized "O"-rings. This cavity is wedged open prior to post processing immersion in Freon.

3. Damage Threshold

The Neutral Solution processed parts show damage thresholds (fig. 5) at least two to three times that of vapor deposited layers producing the same optical results. We can postulate a number of possible reasons for this.

a. The process involves chemical etching. We may be etching away chemical contamination and traces of physical disruption produced by the polishing process.
b. The interface between bulk and leached layers is not only less contaminated but both structurally and chemically continuous.
c. The altered layer has a density gradient which could possibly absorb dynamic shock or impede electromagnetic effects. Electron microscopy indicates the pores are on the order of 40-60 angstroms as shown in figure 6.

4. Surface Characteristics

The Neutral Solution processed surfaces show slightly nonlinear effects when compared to the linear progression of a vapor deposited coating. This is because there exist in the former both density and chemical gradients in the leached layers.

The surfaces are extremely fragile and cannot stand much physical contact. We have successfully drag wiped several 5-cm specimens without noticeable effect on damage threshold, but drag wiping on some others has shown visible scratching so this has been avoided with all parts. We have also seen surface damage when spraying these parts with Freon at 80 psig.

The surfaces are prone to hydrocarbon adsorption which can increase surface reflectivity to non-processed levels. This adsorption is obviously a function of the environment. Some specimens at Schott have been exposed to the atmosphere for almost a year with changes of only a couple of tenths of a percent in reflectivity. Others at both Schott and LLNL have shown almost complete but reversible regression in two months. The effects have been erratic and appear as a reflective film growing inward from the edges. FTIR (Fourier Transform Infrared Spectrscopy) and GCMS (Gas Chromatography/Mass Spectrometry) have identified this film as predominately the hydrocarbon, dioctyl phthalate. It should be noted that dioctyl phthalate molecules are of a size that will fit within the pores and have an index near 1.5, virtually identical to BK-7. Simple flushing with ethyl alcohol quickly restores the surfaces to their immediately post process state as far as reflectivity is concerned. Figure 7 shows the reduced transmittance due to contamination of the processed surface by dioctyl phthalate and the restored transmittance after ethyl alcohol washing. Some surfaces exposed to vacuum on one side only have shown almost total regression to preprocessed reflectance levels in a few weeks while the side exposed to atmosphere showed little effect. Other surfaces have regressed at a slower rate. Similar recovery effects were observed with hydrocarbon solvents. Deliberate exposure of surfaces to high molecular weight hydrocarbons such as index-matching oils produce significantly less changes in the reflectance again in agreement with the electon microscopy data on surface porosity.

Since the process is in part an etching process, it tends to uncover subsurface damage and traces of incomplete polishing. Several pieces have been covered with fine scratches and sleeks after processing. The evidence that these are due to polishing is that they may be restricted to a single surface when both have received identical processing. These surfaces had all been carefully inspected prior to processing and in a number of cases, carefully documented, these surfaces had not contacted anything solid from the time of their arrival at LLNL. It is not clear whether these sleeks, etc., contribute to lowering the damage threshold since the etching tends to open up and round the crack apex.

5. Design Considerations

The chemistry is quite delicate and very sensitive to contamination, particularly metallic contamination. Common plasticizers also have an effect. A small rubber "O"-ring was sufficient to disturb a reaction in about one cubic foot of solution. To-date we have limited contact of the processing fluids to the glass, Viton, Teflon, and natural polypropylene.

The process takes place at a temperature near the boiling point of water. This is considerably above a practical use limit of the polypropylene selected for lens holding fixtures, etc. As a result we have been plagued with plastic shrinkage. This tends to be a function of plastic thickness with thicker parts, presumably less completely cured, showing a greater shrinkage. The shrinkage is also non-isotropic. Pieces shrink differently in length and width and from side to side. This amounts to 2-3%, a significant amount in 48 inch holders. The problem has been ameliorated but not eliminated by a precook or preshrinking operation between rough and finish machining operations, but slow shrinkage is still being observed through over a dozen cycles of several days duration each.

During processing the fluid temperature is maintained within a fraction of a degree. The size of the parts and the strong thermal coupling between part and fluid make thermal stress a dominant consideration during heating and cooldown cycles. These are linearly programmed and are of 2 to 6 hours duration each depending on part thickness. These long-times preclude visual observations of the part during processing, so small witness samples are periodically removed (fig. 8) for this purpose.

If the witness samples are of nearly identical composition and processing, their processing rate may be dominated by the processing rate of the large part. However, the rate is strongly dependent on annealing rate and glass composition, and virtually identical glasses from different melts have been found to vary somewhat in processing rates.

We are working on a laser reflectometer to detect changes in reflectivity through the fluid, but it is not yet clear how effective this will be.

For work at a specific laser frequency, the uncertainty in location of the part minimum is not as intolerable as it sounds. The minima are quite broad and the differences between the part and the witness samples have been on the order of 10% or less in peak wavelength position.

Bubbles are almost always present in flowing solutions of these chemicals at these temperatures. The possibility that these may be trapped and collect on an underside dictated processing in a vertical position.

Considerable effort was expended on achieving uniform flow. This has not been a problem. One advantage of the process is that in retrospect rates seem to be determined more by diffusion processes inside the surface than by chemical concentration at the surface. Thus moderate attention to flow uniformity is sufficient. We have been pleasantly surprised to find that larger pieces process more uniformly than smaller pieces because it is easier to maintain uniform flow in a larger setting.

To summarize to this point, the process produces surfaces with some features desirable and others less than desirable. We trying to determine these and how or whether we can live with them. We have found the process is scalable and relatively inexpensive, demonstrating this on parts as large as 90-cm diameter. Figure 9 shows the largest aperture processed in both the development (24-cm diameter) and scale-up (90-cm diameter) phases. Figure 10 shows processed 80-cm diameter f/20 spatial filter lens. The diameter and quantity of parts scaled-up during FY-82 is shown in figure 11. We are ignorant of many details and the crash nature of the program has precluded optimization, but there is considerable promise for future growth.

6. Surface/Subsurface Chemistry

While working on this process, the authors, two chemists and an engineer with diverse backgrounds in glass chemistry, vacuum coating, and optical polishing have been forced to share their ignorance. The process has raised questions for which we have, as yet, no answers, but questions that may be of interest to the laser damage community.

These questions have to do with the contamination of surfaces and the depth of contamination as influenced by pre-leaching processing parameters. Before beginning this process we knew that there was a surface layer a fraction of a micron deep that somehow differed from the substrate bulk. The outer quarter to half micron of fused silica etches much more rapidly than the bulk in HF for example. Underlying this layer are a pattern of abrasive particle tracks and a roughness greater than that of the polished surface. Some material has obviously been transported over the surface at least to a depth of a few tens of angstroms, the typical track depth on finely polished surfaces. The remaining thousand or more angstroms may be similarly regeled material or material changed by diffusion of species into or out of the layer, or just structurally disturbed.

Early in the process development, we needed some large pieces of glass for dummy runs. We had some acceptable stock of vacuum coated elements unusable for other purposes due to laser damage. We etched off the coatings with hydrofluoric acid. In this process, we have seen rubbing streaks etch into the substrates below the coatings, streaks representing stroking of a type we had not used. We are certain these are residuals from a cleaning process occurring between polishing and coating. Yet these pieces had received near state-of-the-art cleaning just prior to coating. Next we found that a brief polish was insufficient to remove chemical traces introduced in the stripping process resulting in a different processing rate. A second lengthy polish still did not result in a normal processing rate. Similar effects have been seen on witness samples. Desiring a quick turnaround we simply repolished some witness pieces removing slightly over one micron of surface. They processed differently. Next we polished off about five microns. These came closer to a normal processing but there were perceptible differences.

We do have witness samples successfully reprocessed to virgin material response by passing through a grind sequence. However, it is not clear whether it is the quantity of material removed or the suddeness of the removal preventing recontamination that produces the result. Figure 12 shows this effect.

We have seen differences in processing rates for parts polished in different shops, differences in parts from the same shop, and differences in rates between two surfaces of the same part. These have been small with little effect on the result, but they have been perceptible. At the same time we have not observed rate differences on differing parts of a single surface even in highly figured aspheric surfaces of large diameters. Thus surface figure is not perceptibly changed during processing[3]. Thus, for this type of leaching process, the chemical state-of-the-surface has an important rate-determining effect. A relatively consistent surface may be prepared, especially for plano-plano parts, using state-of-the-art finishing techniques. However, the grinding and polishing process does not necessarily guarantee a well defined surface chemistry. It appears that one cannot simply give mechanical guidelines for the finishing process. At the same time one cannot logically hope to chemically characterize each glass surface before treatment.

It seems difficult to conceive of a diffusion process permitting significant contamination into or leaching out of microns of material, thousands of atom layers, but we are seeing results of contamination persisting through at least a few microns of polishing removal, and we are not the only ones. A recent Soviet paper[4] investigating the effects of prepolishing treatment on polishing rates inferred for at least one glass a perceptible effect persisting through 25 microns of polishing removal. One possibility is that prepolishing contamination persists through appreciable polishing because some contaminants reinfect the fresh surface as layers are removed. There is a growing body of evidence about ion absorption and re-sorption on glass surfaces during the leaching process. Tait and Jensen[5] have reported effects of solution and glass additives on leaching characteristics of nuclear waste glasses. Zinc, in particular, produced markedly lower leaching rates and the effect is the same whether the ions are introduced into the glass or into the leaching solution. More importantly surface analysis shows strong enrichment of this ion within the leached surface layer. Similar surface enrichment effects and changes in leach rates have been recently reported by Buckwalter and Pederson[6] for leaching in lead and aluminum metal containers. One of the authors has observed environment effects when leaching flat glass samples. In this case, tin found before treatment on a single glass surface as a contaminant from manufacturing is observed on both surfaces after leaching in apparent high localized concentrations. What is important about these findings is that the absorbing ions remain on the leached layer for very long leaching times, i.e., they are continually adsorbing and resorbing onto the moving leaching boundary as the corrosion process works it way into the glass. As many of these elements are commonly encountered as structural materials, as additives to many plastics, and because the chemical nature of the polishing process is largely the same as aqueous corrosion of glass, it is suspected that surface enrichment of polished glass surfaces by metal ions may be more wide spread than has been thought.

7. Summary

The neutral solution process adds an important class of high laser damage threshold surfaces to the anti-reflection treatment repertoir. The ease with which the process can be scaled to large size optics is also attractive. Both glass chemistry and the present delicacy of the surfaces require special design consideration. Observations made during the processing raise questions on the control of near surface chemistry during glass polishing operations, questions that may be important for laser damage work.

References

[1] Schroeder H., "Thin Film Formation on Glass Surfaces in Chemical Coating Processes", Proc. Tenth Int. Cong. on Glass, Kyoto 8-118 (1974).

[2] Cook, Lee M., and Mader, Karl-Heinz, "Intergral AR Coated Glasses for High Energy Laser Applications", Proceedings Electro-Optic/Laser 1981, Anaheim, CA, Nov. 17-19, 1981.

[3] Cook, Lee M., Ciolek, Sally, and Mader, Karl-Heinz, "Intergral Antireflective Surface Production on Optical Glass", Journal of the American Ceramic Society, Vol. 65, No. 9, September 1982.

[4] Kudryavtseva, N.L., Yakovleva, T.P., and Khodakov., G.S., "The Effect of Polisher Suspension on the Micro-Hardness of Optical Glass", Soviet Journal of Optical Technology", Vol. 48, No. 12, December 1981.

[5] Tait, J.C., and Jensen, C.D., "The Effect of Zn (II) Ion Adsorption on the Durability of Sodium Borosilicate Glasses", Journal of Non-Crystalline Solids, Vol. 49, 1982 Special Issue.

[6] Buckwalter, C.Q., and Pederson, L.R., "Inhibition of Nuclear Waste Glass Leaching by Chemisorption", Journal of the American Ceramic Society, Vol. 65, No. 9, September 1982.

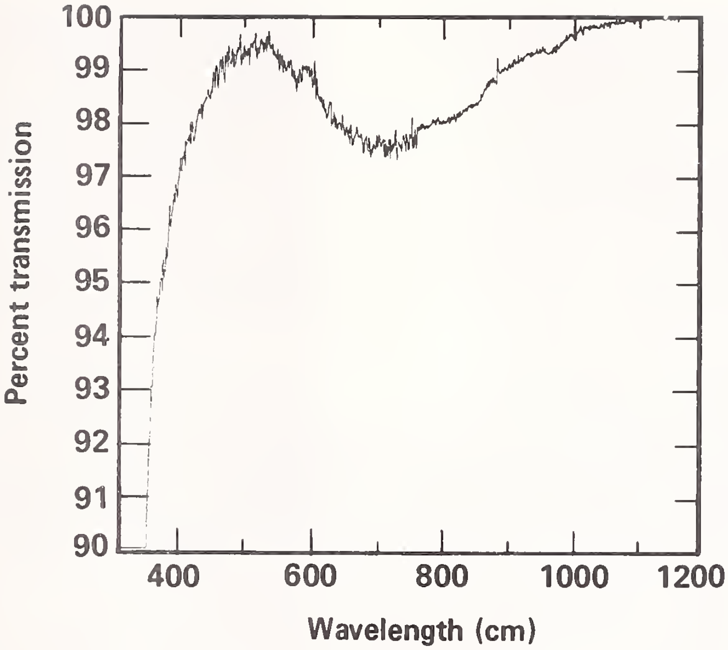

Figure 1. Spectrophotometer transmission through two surfaces of 1 cm thick BK-7 witness piece.

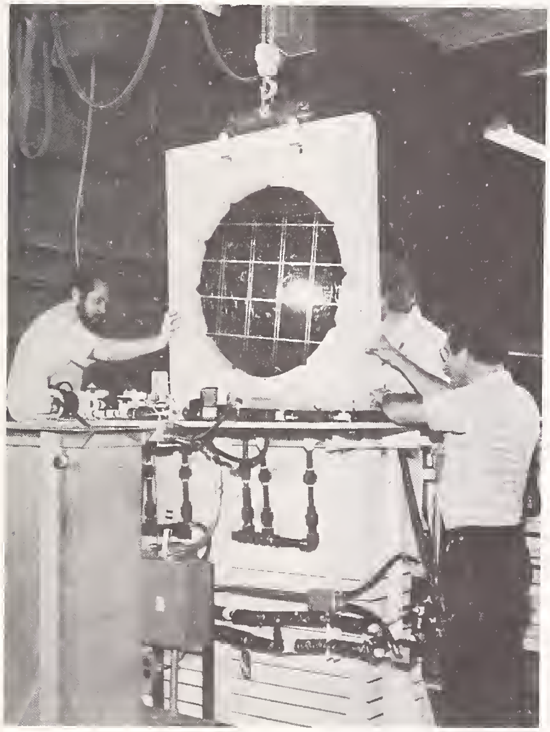

Figure 2. Loading an 80-cm diameter crystal array apodizer

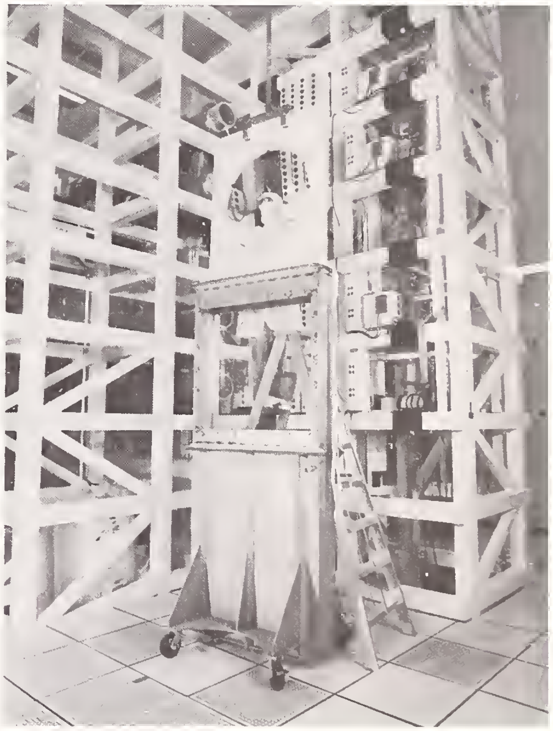

Figure 3. Removal of an 80-cm diameter f/20 spatial filter lens from the freon cleaning stage.

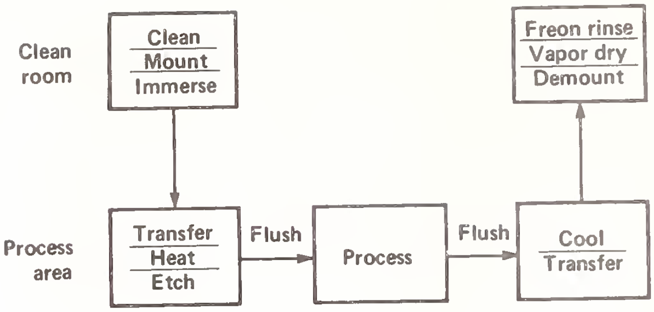

Figure 4. Operating sequence of scaled up Neutrol Solution Process.

Witness pieces processed in developmental phase	
NSP surface (average for 15 samples)	12.5
Laser annealed NSP surface	23.3
Witness pieces processed in operational phase	
NSP surface	12.2
Laser annealed NSP surface	25.0
46-cm aperture lens NSP surface	15.0

Note: 532 nm damage threshold values are similar to 1064 nm thresholds

Figure 5. Damage threshold at 1064 nm, 1 nsec (J/cm^2)

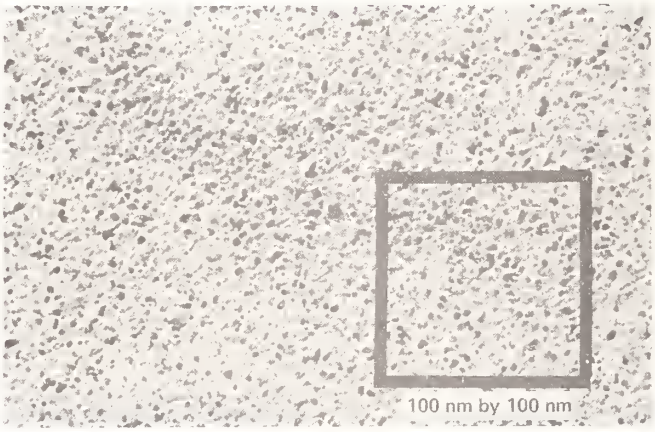

Figure 6. Transmission electron micrograph of replica of neutral solution processed surface.

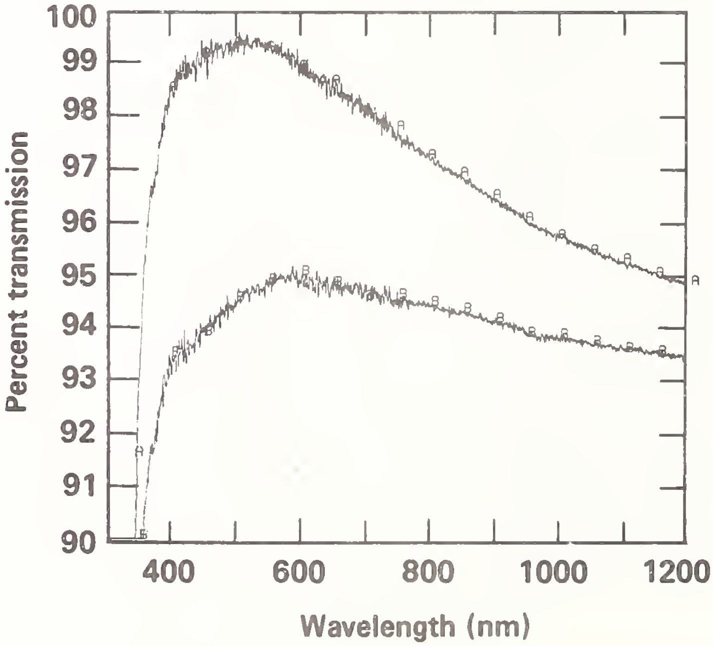

Figure 7. Two surface transmission of 1-cm thick primary green part contaminated with doctylphthalate during 2 months storage (B) and after ethyl alcohol rinse (A).

Figure 8. Removing a witness during processing of a large optic.

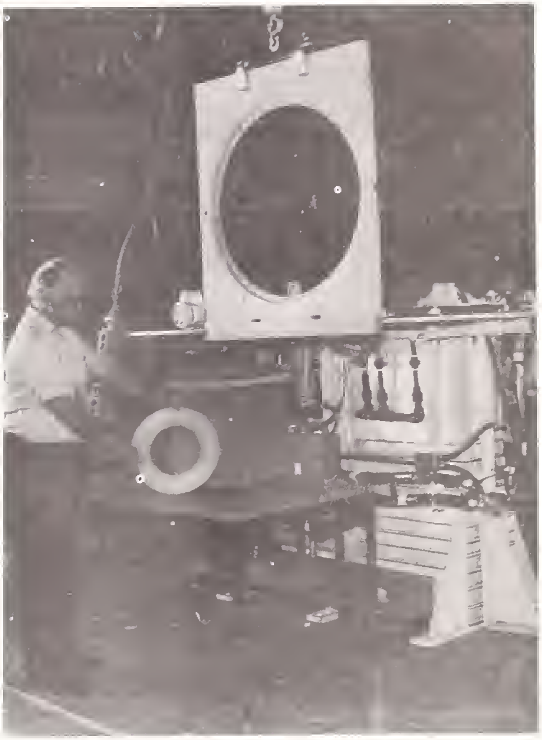

Figure 9. Largest aperture processed during development (24-cm diameter) and operation (90-cm diameter).

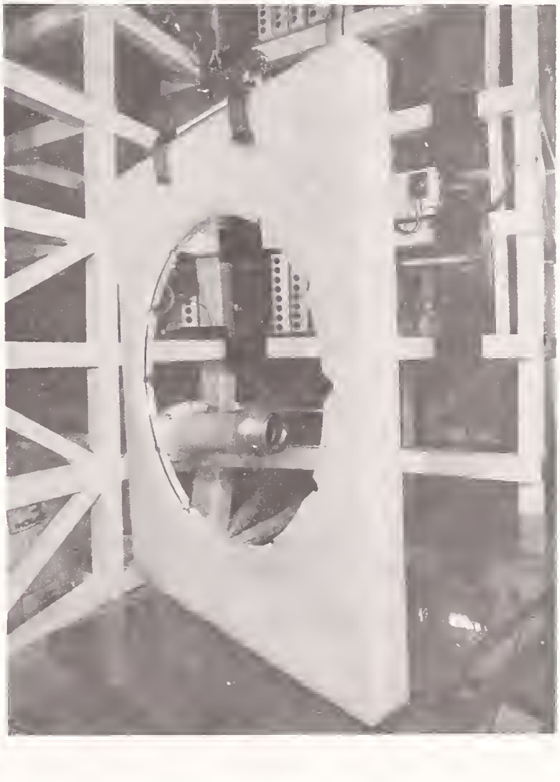

Figure 10. Processed 80-cm diameter f/20 spatial filter lens.

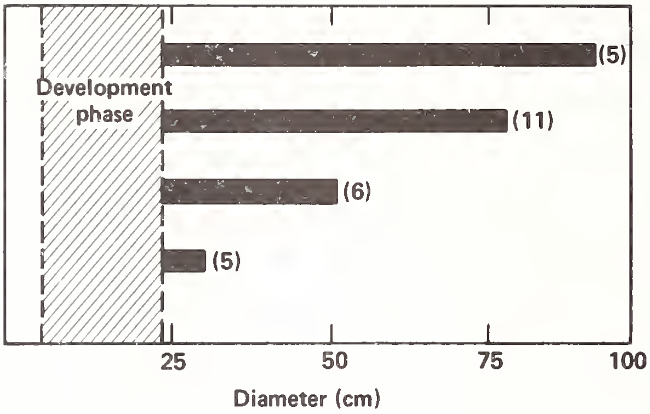

Figure 11. Diameter and quantity of parts treated to-date in neutral solution scale-up operation .

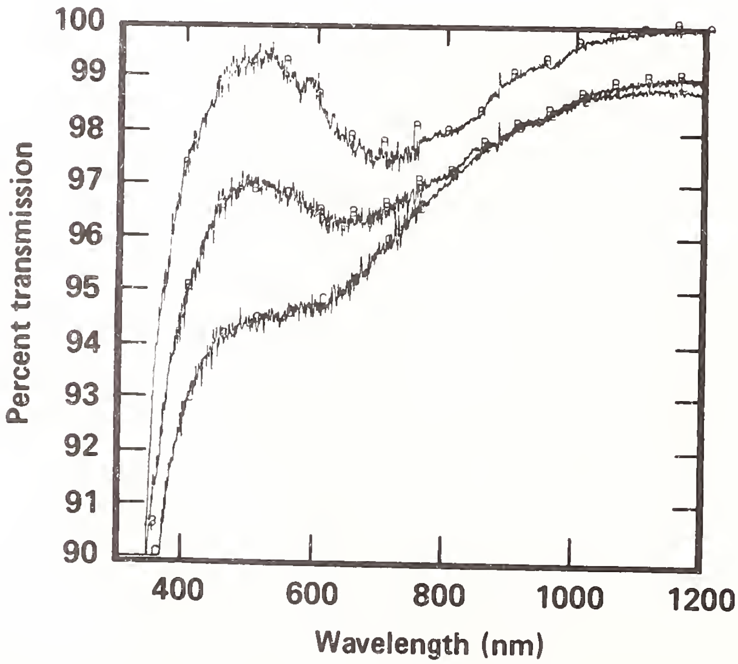

Figure 12. Two surface transmission through 1-cm virgin material (A) material repolished without regrind (B) and material repolished and etched (C).

When asked whether aging of neutral-solution-processed surfaces would be a serious system problem, the speaker replied that rinsing aged surfaces with ethanol had been effective in restoring high transmission. The speaker was asked whether the rate of processing depended on the preparation of the substrate surface, and replied that sample-to-sample variations in processing rate were observed, but site-to-site variations in processing rate of the surface of a particular large optical element had not been observed.

Progress in Ultraviolet Damage Testing at Los Alamos

S. R. Foltyn, L. J. Jolin, and B. E. Newnam

University of California, Los Alamos National Laboratory,
Chemistry Division, Los Alamos, New Mexico 87545

A laser damage test facility is described which employs in-line beam diagnostics and a real-time video monitoring system. Testing at three excimer laser wavelengths is accomplished at 35 pps with a nominal 10-ns pulsewidth. The test spotsize ($1/e^2$ diameter) is typically 0.6 mm. Samples have consisted primarily of multilayer dielectric reflectors composed of a variety of materials. In particular, the best results - $\cong 3$ J/cm^2 at 248 nm, $\cong 5$ J/cm^2 at 308 nm, and $\cong 8$ J/cm^2 at 351 nm - have been obtained consistently for coatings utilizing ThF_4, Al_2O_3, or Sc_2O_3 as the high-index component. Significant improvement has resulted from the use of non-quarterwave designs at 248 and 308 nm. Also presented are preliminary 248 nm test results for LiF -- both single crystal and press-forged -- and KD*P.

Key words: dielectric reflectors; excimer laser; KD*P; LiF; non-quarterwave designs; video monitoring.

1. Introduction

Although the basic principles behind, and operation of the Los Alamos uv damage test facility [1] have remained unchanged over the past three years, we describe here some experimental improvements which provide capabilities for (1) remote video monitoring; (2) high throughput testing; and (3) real-time beam diagnostics. A summary of test results for multilayer dielectric reflectors at 248, 308, and 351 nm is presented along with test results for LiF (press-forged and single crystal) and KD*P.

2. Apparatus

The experimental layout is shown in figure 1. Propagating at about 300X the diffraction limit, the beam is relayed from the laser room with a 2-m lens and is reflected twice at small angles before being focused into the test plane at left center. A few parts per thousand are transmitted through the dielectric turning mirrors and are used to power a fast vacuum photodiode and a silicon photodiode array for temporal and spatial profiling, respectively. A 5° uncoated Suprasil wedge provides somewhat larger beam fractions to a calorimeter which monitors average power and to a pinhole/pyroelectric detector combination used to monitor peak fluence. Hardware descriptions are given in [2]. While these diagnostics provide the capablity to observe and correct changes in beam quality during testing, the documented beam characterization is always performed in the actual test plane. For alignment purposes, a He-Ne beam is split into two paths, one being collinear with the uv beam and the other off-axis. The location of the ultraviolet focal volume is pinpointed in space by the intersection of these two beams.

Damage is observed in real-time with a long working-distance microscope [3] at about 100X. Magnifications from 45X to 1000X are available. Because of the long working distance and the use of transparent substrates, the microscope can be placed behind the sample and can thus be used at normal incidence. An alternative scheme is being devised for use with opaque substrates. A high resolution video system [4] attached to the microscope provides not only for operator safety but allows the use of a video cassette recorder for preserving visual images of damage onset and growth during irradiation. One application of this system is described elsewhere in these proceedings [5]. In the future, it may be desirable to sync the video framing rate (30 Hz) to the laser so that an individual video frame can be recorded for each laser shot. Figure 2 is a photograph of the test section showing, right to left, sample holder mounted on an X-Y stepper assembly, microscope modified for horizontal optical axis, and video camera.

3. Test Results

3.1. LiF

Test results for six LiF samples (three press forged, three single crystal) are shown in figure 3. Probability of damage is determined experimentally by testing ten sites at each of several fluence levels and plotting the number of damaging sites versus peak test fluence. The zero-percent intercept of a linear regression fit is defined as the laser damage threshold. This is in contrast to conventional notation in which threshold is approximately the fluence at which damage probability is 50%. The slope of a probability curve is determined by the relationship between beam size and the density of defects which are responsible for damage. A steep slope correlates with high defect density and vice versa. A more detailed discussion of this relationship and the threshold definition is contained in [5].

The bands in figure 3 represent the observed variations in each type of sample. The crosshatched area is for single crystals while the clear area was obtained for press-forged samples. From the analysis above, it can be concluded that press forging does not alter the defects themselves since thresholds are no different than for single crystal samples, but that the average density of defects has been increased by forging.

Damage in all samples was observed primarily in the bulk material. In that the test beam was focused on the front surface, beam divergence in the sample resulted in a fluence uncertainty of up to 25%. However, a change in the opposite direction results if self focusing is present. An initial analysis indicates that the two effects cancel one another and that the beam is effectively collimated in the volume of interest.

3.2. Multilayer Dielectric Reflectors

Table 1 is a summary of test results for a variety of reflector designs at three wavelengths. Peak fluence thresholds are as defined in the previous subsection and represent average values over no fewer than three samples. Wavelength scaling is evident; however, the data base is not sufficient to allow quantification of trends.

Table 1. Test Results for 99% Reflectors

HR Coating	Threshold at 248 nm (J/cm^2)	Threshold at 308 nm (J/cm^2)	Threshold at 351 nm (J/cm^2)
ThF_4/Na_3AlF_6	3.3	2.8	--
Al_2O_3/SiO_2	3.0	5.2	8.5
Sc_2O_3/SiO_2, MgF_2	2.9	5.4	--
Same as above, non-qw	4.2	6.8	--

Figure 4 illustrates the ability to improve 308-nm damage resistance by shifting the standing-wave field peak out of the high-index/low-index interface region [6,7]. This is accomplished by the use of outermost layers of nonquarterwave optical thickness. The results shown are for three layer-thickness variations plus a standard quarterwave design for comparison: The use of in-chamber shutter masking allowed all four designs to be deposited [8] in a single run. Thresholds are summarized in table 2.

Table 2. 308 nm Thresholds for non-QW Reflector Designs

Design	Threshold
1 - Field suppressed in MgF_2	5.2 J/cm^2
2 - All quarterwave	5.4 J/cm^2
3 - Field suppressed in Sc_2O_3 (one pair)	6.6 J/cm^2
4 - Field suppressed in Sc_2O_3 (two pair)	6.8 J/cm^2

For a detailed analysis of a similar test at 248 nm, see [9].

3.3. KD*P

A somewhat different damage behavior was observed during testing of four KD*P crystals (fig. 5). Depending upon fluence level, damage was delayed by a variable amount: Several thousand shots were required at a few J/cm^2 while, at 8-9 J/cm^2, damage was produced in only a few hundred shots. From a physical point of view, threshold is the asymptotic value of the solid curve; however, in a practical sense, a system operating at a very low pulse rate could run at much higher levels for an extended period without experiencing damage problems.

4. Conclusions

We have described some recent improvements to an existing ultraviolet laser damage test facility which center around a video monitoring system and in-line beam diagnostics. Test results for state-of-the-art reflectors are presented as well as preliminary results for LiF and KD*P.

5. References

[1] Foltyn, S. R.; Newnam, B. E.; Jolin, L. J. Laser damage results and analyses for uv reflectors under multiple-shot irradiation. Proceedings of the 13th Boulder Damage Symposium, November, 1981 (to be published).

[2] ITT 4014 vacuum photodiode; Reticon 256G silicon photodiode array (25 μm resolution); Scientech 36-0001 surface absorbing calorimeter; Molectron J3-05 pyroelectric detector behind a 50 μm diameter pinhole.

[3] Bausch & Lomb "MicroZoom" microscope.

[4] RCA TC1005/01 camera; Conrac SNA-14C monitor.

[5] Foltyn, S. R. Spotsize effects in laser damage testing. Elsewhere in these proceedings.

[6] Gill, D. H.; Newnam, B. E.; McLeod, J. Use of nonquarterwave designs to increase the damage resistance of reflectors at 532 and 1064 nanometers. Nat. Bur. Stand. (U.S.) Spec. Publ. 509; 1977 December. p. 260.

[7] Apfel, J. H. Optical coating design with reduced electric field intensity. App. Opt. 16(7) 1880-1885; 1977.

[8] These reflectors were designed and deposited by Optical Coating Laboratories, Inc., Santa Rosa, CA.

[9] Newnam, B. E.; Foltyn, S. R.; Jolin, L. J.; Carniglia, C. K. Multiple-shot ultraviolet laser damage resistance of nonquarterwave reflector designs for 248 nm. Proceedings of the 13th Boulder Damage Symposium, November, 1981 (to be published).

MULTIPLE-SHOT LASER DAMAGE TEST FACILITY

REAL-TIME VIDEO MONITORING

- HIGH RESOLUTION CAMERA AND MONITOR
- VIDEO CASSETTE RECORDER
- 1/100 th SECOND CLOCK

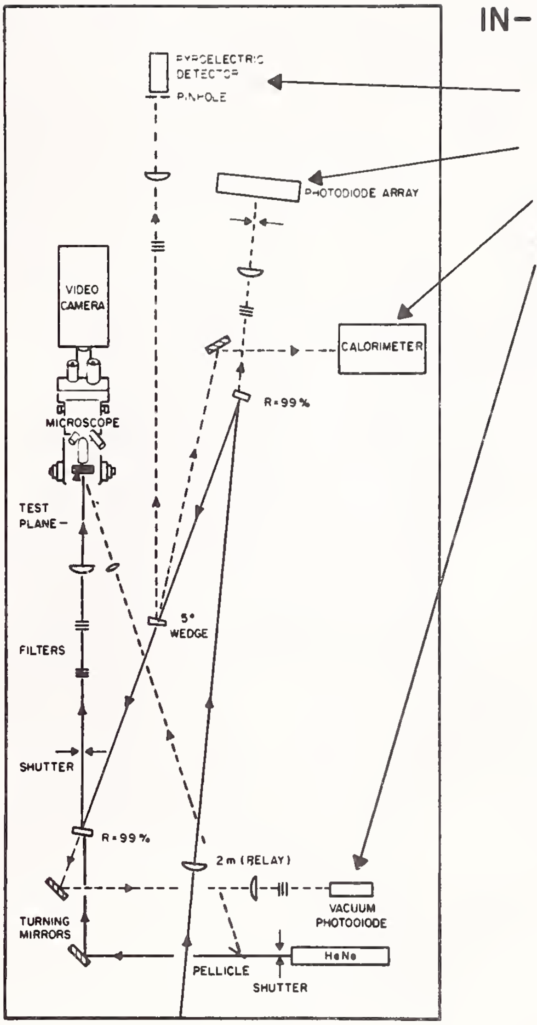

IN-LINE DIAGNOSTICS

- PEAK FLUENCE
- SPATIAL PROFILE
- AVERAGE POWER
- PULSEWIDTH

Figure 1. Line drawing of the Los Alamos laser damage test facility.

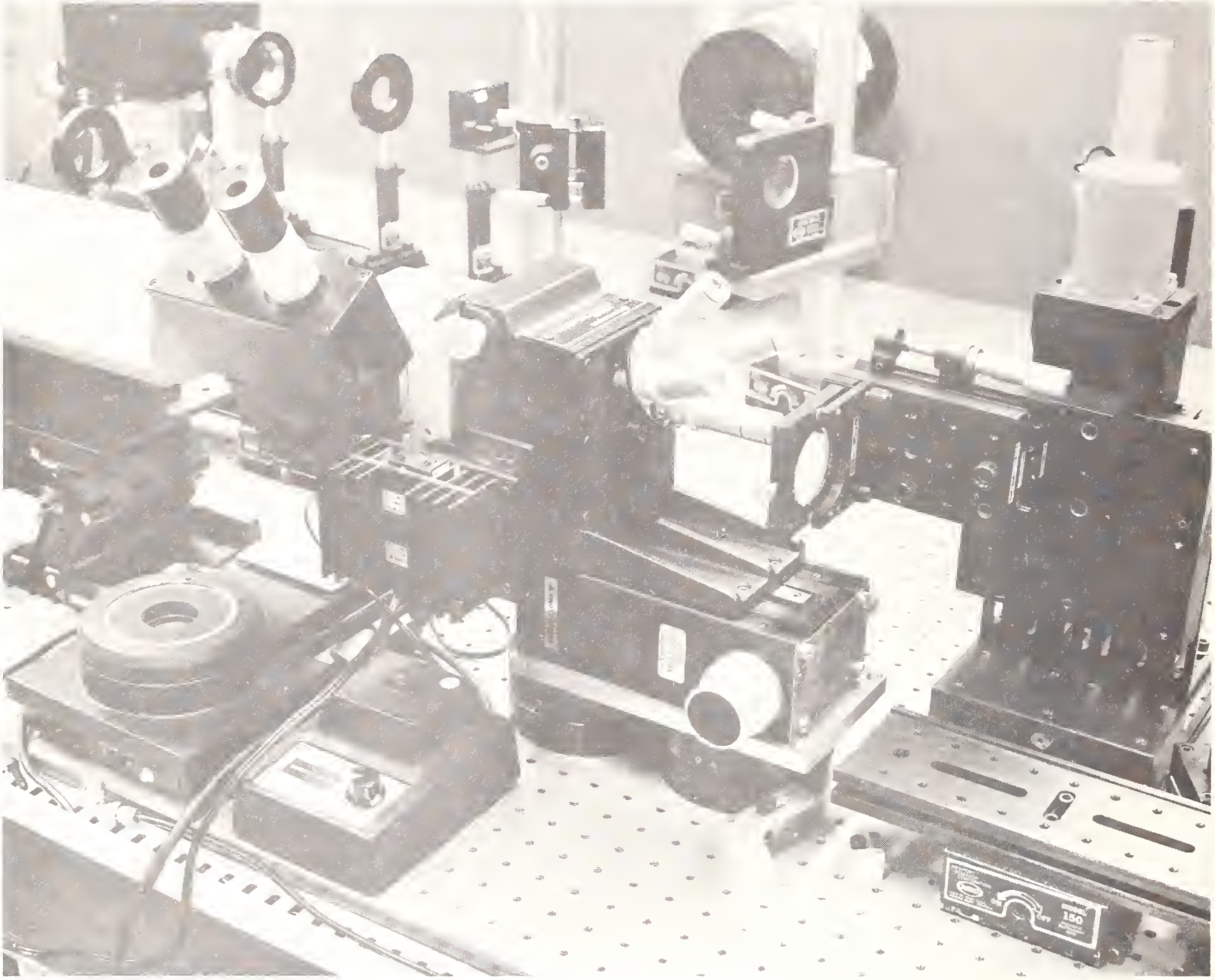

Figure 2. Photograph of test section. Sample holder on X-Y steppers is located a few cm from objective of microscope (center). Beam enters from right.

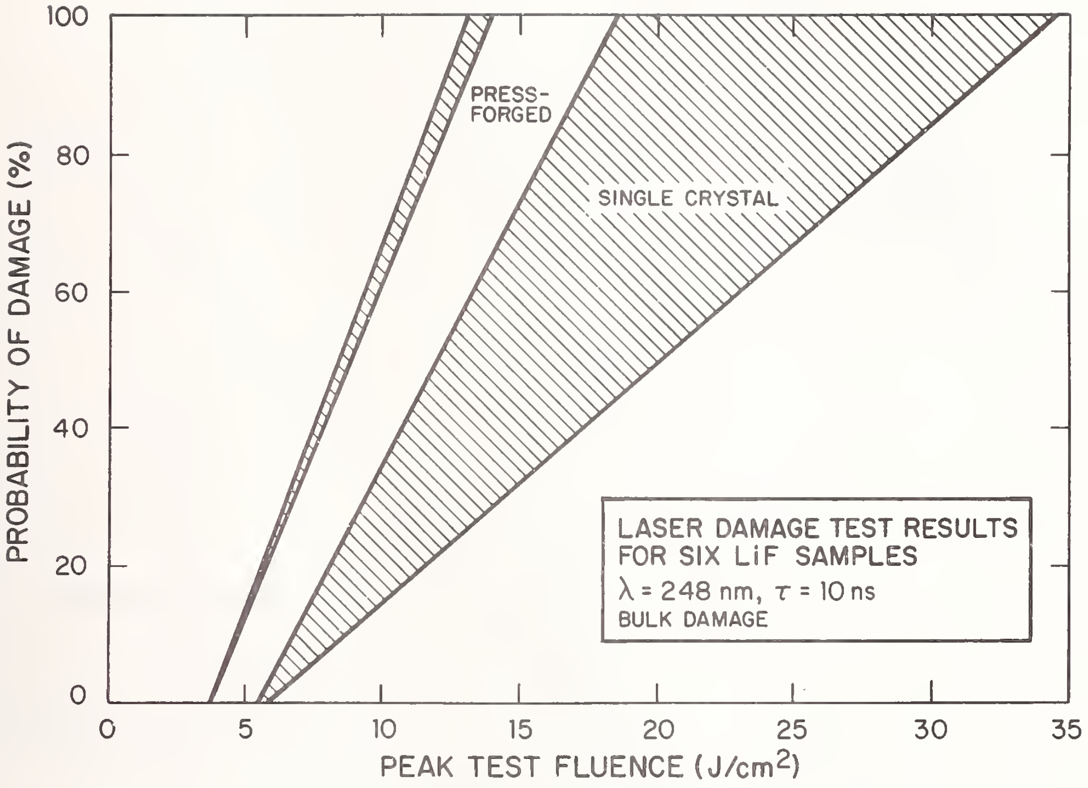

Figure 3. Test results for LiF. The cross-hatched region is for single crystal samples while press-forged material gave results represented by the clear area. Slopes of probability curves indicate a higher average defect density for the press-forged samples.

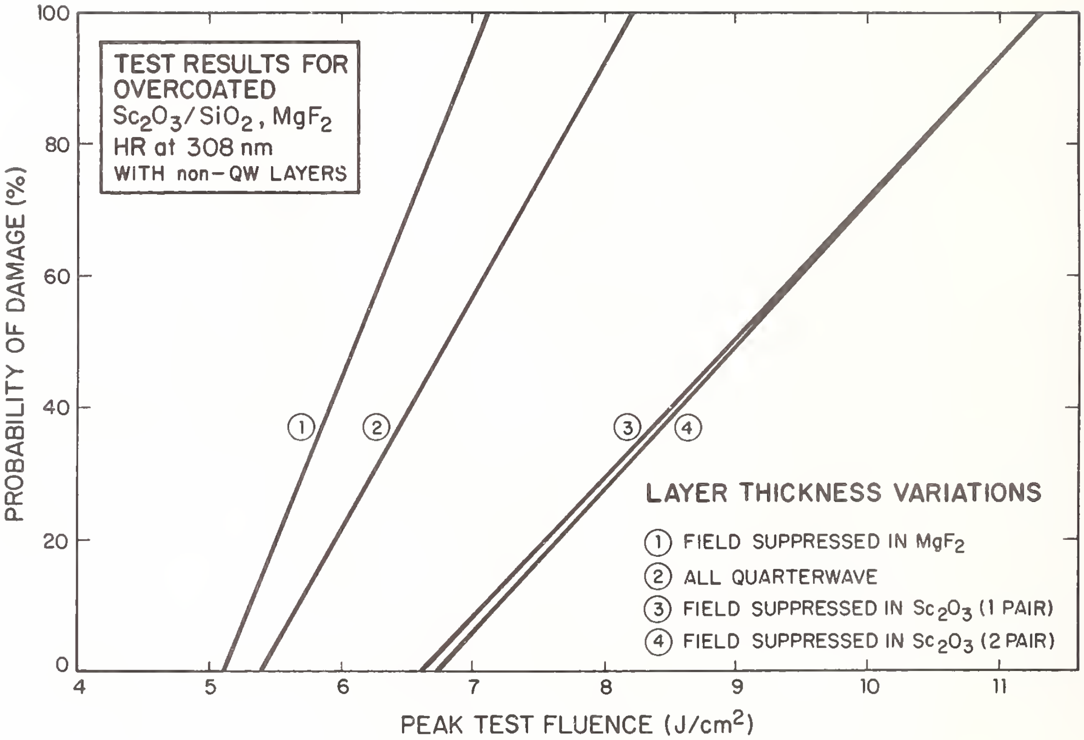

Figure 4. Probability curves for 380 nm reflectors which are identical except for the thickness of the outer four layers. A 25% improvement was realized by suppressing the peak SW field in the high index material.

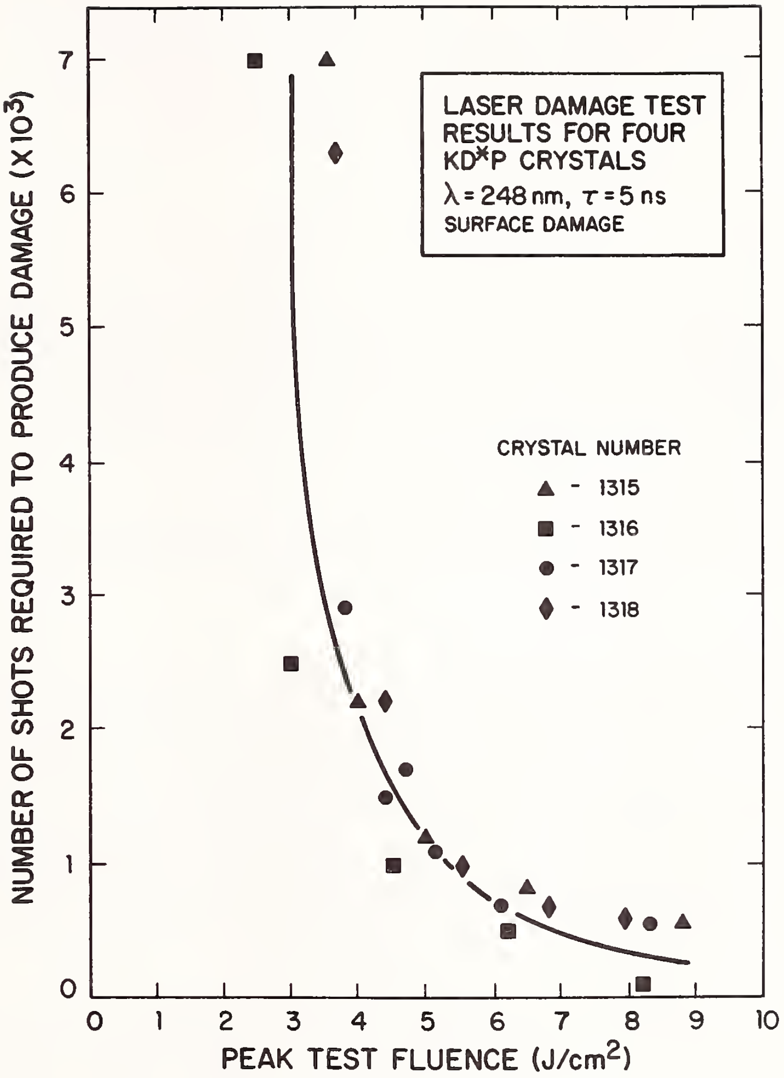

Figure 5. Delayed damage in KD*P crystals.

Damage Thresholds of Thin Film Materials and High Reflectors at 248 nm*

F. Rainer, W. H. Lowdermilk, and D. Milam

Lawrence Livermore National Laboratory
Livermore, CA 94550

C. K. Carniglia, T. Tuttle Hart, and T. L. Lichtenstein

Optical Coating Laboratory, Inc.
Santa Rosa, CA 95403

Twenty-ns, 248-nm KrF laser pulses were used to measure laser damage thresholds for halfwave-thick layers of 15 oxide and fluoride coating materials, and for high reflectance coatings made with 13 combinations of these materials. The damage thresholds of the reflectors and single-layer films were compared to measurements of several properties of the halfwave-thick films to determine whether measurements of these properties of single-layer films were useful for identifying materials for fabrication of damage resistant coatings.

Keywords: absorption; environmental stability; index of refraction; halfwave-thick layers; laser-induced damage; reflectors; stress; UV coating material.

1. Introduction

Because UV lasers are potentially useful for the investigation of inertial confinement fusion, we have continued development of thin-film coatings for KrF lasers. In previous experiments we tested a large number of coatings made from a limited set of thin-film coating materials, principally SiO_2, MgF_2 and Sc_2O_3, which were selected primarily because they are highly transmissive at 248 nm [1], [2]. Lengthy studies of a few materials allow optimization of the deposition parameters for these materials, and provide a sensibly large data base for evaluation of coatings made from the materials. However, since time and expense limit the number of such studies that can be performed, there is the possibility that potentially superior materials will remain unidentified. It would, therefore, be advantageous to discover relationships between damage thresholds of coatings and the physical properties of the coating materials which could be used to guide material selection. In this paper we describe a material survey whose aim was to establish such relationships.

There are two general formats for survey studies of thin-film materials. An evaluation of a large number thin-film materials can be made by studying either single-layer films of the materials or by studying properties of multilayer coatings made from the materials. Testing of halfwave-thick single layers is attractive because, in principle, the materials can be individually evaluated and because internal electric fields experienced by halfwave films during laser damage testing do not depend strongly on the refractive index of the material. The physical properties of single-layer films may, however, be affected by contact of the film with both the substrate and the atmosphere. Testing highly reflective multilayer coatings made of the materials to be evaluated eliminates the influence of the substrate, and provides direct information about a useful coating design. Also, environmental degradation or contamination of a given film layer could be prevented by overcoating the reflector with a film of a more stable material. The disadvantages of using multilayer reflectors are that the materials are tested in combinations, rather than individually, and that given a number of materials, there are many potentially interesting material combinations.

It is also important to note that a survey study of thin film materials cannot be expected to provide an unambiguous ranking of the relative worth of many coating materials. A survey, by necessity, includes only a few films of each material, but characteristics of thin films are reproducible only for those materials for which deposition has been optimized, which is the task one seeks to avoid by conducting a survey. A survey may reveal general relationships between laser damage thresholds and measured physical properties of films, and these relationships would, in turn, indicate which materials should be studied more carefully.

---

*Work performed under the auspices of the U.S. Department of Energy by the Lawrence Livermore National Laboratory under contract W-7405-ENG-48.

We decided to evaluate the effectiveness of material surveys by testing both halfwave-thick layers of 15 oxide and fluoride materials, and highly reflective quarterwave stack reflectors made from 13 combinations of the same materials. The coatings were made at Optical Coating Laboratory, Inc. (OCLI) by electron-beam evaporation of the materials onto fused silica substrates that had been bowl-feed polished at OCLI. For single-layer films, measurements of the refractive index, absorption, stress, environmental stability and the position of the UV band edge were made. For both films and high reflector (HR) coatings, the threshold for damage by 20-ns, 248-nm KrF laser pulses was measured at Lawrence Livermore National Laboratories (LLNL). Results of these measurements and a discussion of possible correlations between the thresholds of the reflective coatings and physical parameters of the materials are presented.

2. Experimental Procedure

Damage thresholds were measured at LLNL with 20-ns, 248-nm pulses generated by a discharge-pumped KrF laser. At the surface of the sample, the beam was 1.5 mm in diameter at the e^{-2} intensity level, but the intensity distribution was nonuniform. The highest fluences in the beam occurred at isolated maxima, where fluence was uniform to within + 5% over areas not less than 0.1 mm in diameter. For each shot, the beam was photographed with Kodak 1-Z spectroscopic plates, and the intensity distribution was determined by densitometry. Peak fluence for each shot was computed by numerically integrating the intensity distribution and normalizing the integral to agree with the measured pulse energy.

The samples were mounted on a rotating stage which allowed the irradiated test site to be moved into the field of view of a Nomarski microscope. Test sites were photographed before and after irradiation at a magnification of 420. The test sites were also inspected visually using either Nomarski or bright-field microscopy, and under intense white light illumination using the unaided eye. Damage was defined to be a permanent surface alteration that was detectable by any of these inspection techniques.

Each test site was irradiated once. The average number of sites tested per sample was seven. Damage was defined as the average of the lowest fluence that caused damage and the highest fluence which did not cause damage. A detailed description of the laser system used in these tests and of our experimental procedure has been previously presented [1].

Other parameters of the coatings were measured at OCLI. Transmittance and reflectance were measured with a Cary 17-DX spectrophotometer. Index of refraction for the individual coating materials was calculated from the measured reflectance and transmittance of thick single-layer films. The absorption coefficient of a film material was measured by coating a halfwave-thick layer of the material on a high reflector and measuring the decrease in reflectance. Film stress was determined by interferometric measurements of the stress-induced flexure of coated substrates 0.38 mm in thickness. The absorption edge was defined to be the wavelength at which the transmission of a coating with a 1.5-µm optical thickness was 50%. Since tranmission measurements could not be made at wavelengths below 200 nm, the band edge could not be measured in some films. These materials were separated into two groups: those with some measurable absorption at 200 nm (absorption edge less than 200 nm) and those with no detectable absorption at 200 nm (band edge much less than 200 nm).

3. Single-Layer Films

Halfwave-thick layers of 15 oxide and fluoride films were fabricated by OCLI using electron-beam evaporation of the materials onto fused silica substrates that had been bowl-feed polished by OCLI. The films of most of these materials had generally good cosmetic appearance, and contained only isolated defects with typical dimensions of 1 µm. There were, however, some exceptions. Films of YF_3 were mosaic arrays of 10-µm-sized areas presumably caused by local stress fracture. Some areas on Na_3AlF_6 films were clean, but other areas had a streaked appearance. Films of both ZrO_2 and NaF had a hazy, fogged appearance.

We measured laser damage threshold for two halfwave-thick layers of each material. The damage thresholds are given in figure 1. The morphology of damage in each film was also recorded. Three general types of damage were observed, and the nature of the damage correlated with the measured damage threshold. In low-threshold films, damage appeared as micropits which were aligned in either straight or curved rows that resembled polishing sleeks. In medium-threshold films, damage usually was seen as a spatially uniform area (shaped like the incident laser beam) which was visible by either bright-field or Nomarski microscopy. This implies alteration of both surface texture, which effects white-light visibility, and surface height, the parameter observed in Nomarski microscopy. The altered areas also contained a few pits, which were typically 1 µm in diameter. High-threshold films, such as SiO_2 and ThF_4, had damage morphologies much like the damage that is observed on front surfaces of bare polished fused silica: pits 1 µm in diameter which are surrounded by halos at high fluences.

The damage thresholds ranged from less than 1 J/cm^2 in ZrO_2, which is comparable to the damage fluence for some metallic films, to 25 J/cm^2 in ThF_4, which is about twice the front-surface threshold of bare polished fused silica [3]. The latter is an unusual result for which we have no satisfactory explanation; thresholds of coated surfaces rarely exceed those of bare surfaces. However, the experimental observation we are reporting is straightforward. When we use the test procedure described above, we find 1) thresholds ranging from 9 to 15 J/cm^2 for front surfaces of bare polished silica substrates [3], 2) thresholds exceeding 20 J/cm^2 for some silica surfaces coated with low-index films, and 3) the same morphology of damage for both types of surfaces. It is also interesting to note that substrate structure appeared to influence damage morphology on low-threshold films, but not on moderate- or high-threshold films. Absorption by impurities trapped in polishing scratches could have caused this damage, but all substrates were similarly polished, so scratches on substrates irradiated at higher fluences should also have damaged. The implication is, therefore, that in low-threshold films, the film material itself had been influenced by the presence of the polishing sleek.

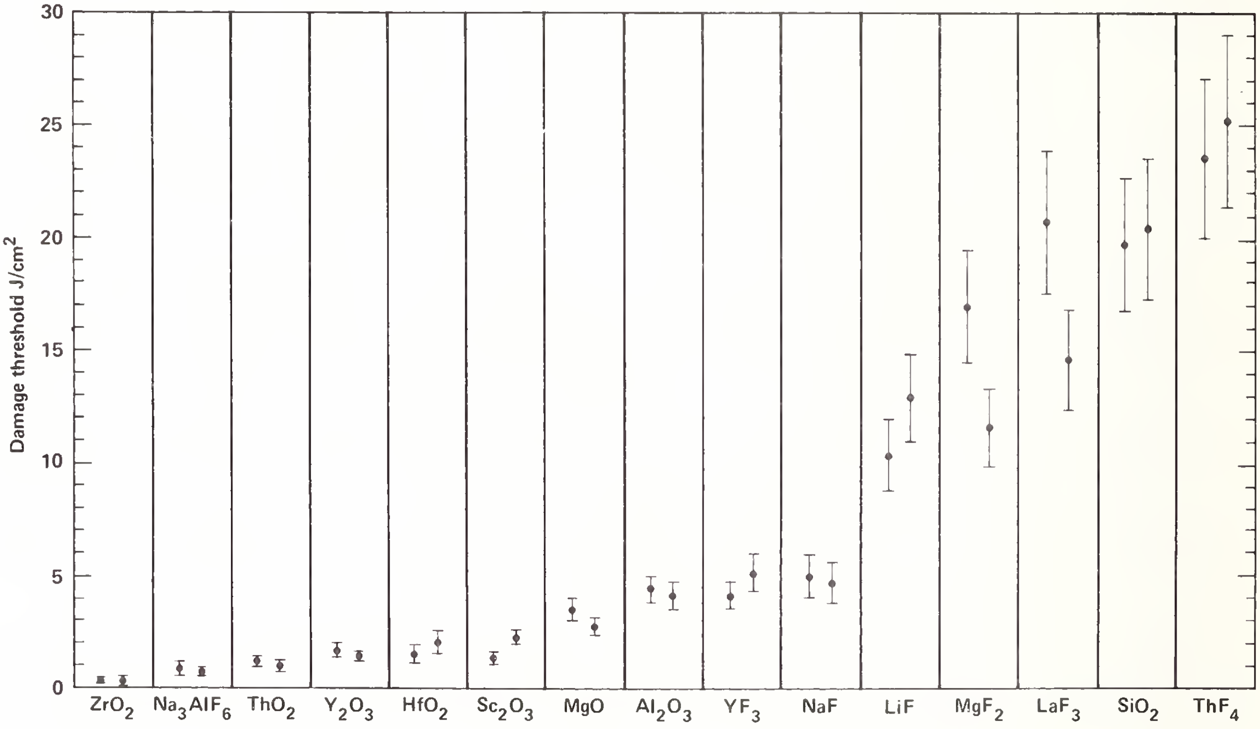

Figure 1. Laser damage thresholds (20 ns, 248 nm) of halfwave-thick films.

Next, consider the comparison of the film thresholds to physical properties of the films. In figure 2, four properties of the films are plotted as a function of the average threshold for each material. Thresholds were largest in the films with low refractive index, which (excepting SiO_2) were all fluorides. The high-index films (which were all oxides), and the films of Na_3AlF_6 (which had poor physical properties), had low thresholds. Our results are generally similar to those of Newnam and Gill who used 22-ns, 266-nm pulses to test single layers of six oxide materials and three fluoride materials [4], and those of Walker, et.al., who tested films of six oxides and three fluorides with 15-ns, 266-nm pulses [5]. Among these three studies, both the threshold ranking of individual film materials, and the absolute values of thresholds reported for a given film material, vary considerably, suggesting that it is difficult to establish true comparisons of materials in thin-film form. However, the general correlation between high thresholds and low refractive indices is present in all three studies. This correlation was first observed by Turner [6], and later developed as a threshold scaling law by Bettis, et. al. [7]. The scaling law predicts some of the results of the three UV damage studies. However, the scaling rule is based on the assumptions that damage is caused by electron avalanche and that thresholds should scale according to the strength of the local electric field. The law would not be applicable if linear absorption were the dominant mechanism for damage in UV film materials.

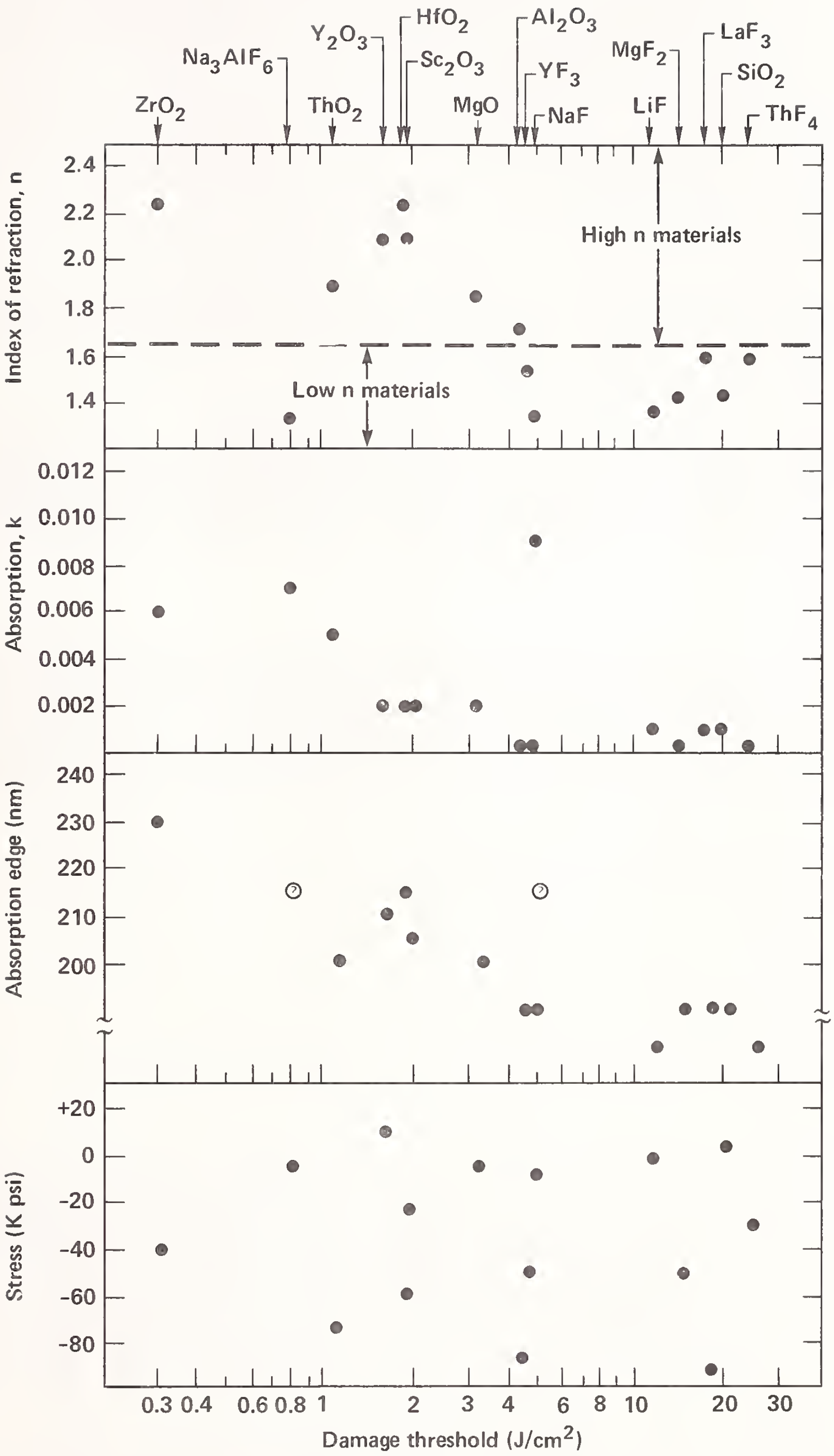

Figure 2. Index of refraction, absorption, position of the UV band edge and film stress for 15 UV coating materials plotted as a function of the average of the damage thresholds measured on two halfwave-thick samples of each material.

We also found that thresholds varied systematically with film absorption and with the spectral position of the UV band edge. Highly absorbing films had low thresholds. All low-absorption films had UV band edges below 200 nm, so absorption and position of the band edge were closely related. In fact, since the oxides were the materials which had band edges in the near UV, high absorption, and also high refractive index, it is possible that the apparent correlation between UV damage thresholds and index is accidental. Again, there were exceptions. NaF was very absorptive, but had a moderately large threshold, and scattering losses in both Na_3AlF_6 and NaF were so large that we could not measure the positions of the band edge.

The only previous study of the correlation between UV thresholds and film absorption concluded that linear absorption was responsible for damage induced by 266-nm 22-ns pulses in ZrO_2 [4].

Finally, we found no correlation between film stress and damage threshold, and a possible correlation between cosmetic appearance and threshold. The ZrO_2 and NaF films had a foggy appearance, and the film of Na_3AlF_6 exhibited streaked areas. The threshold of the ZrO_2 film was less than that of any other film tested, and these two fluoride films had thresholds less those of other materials with comparable properties.

Although the material characteristic responsible for damage in a given material is not known, trends in the entire set of data identify the characteristics that are associated with good resistance to damage by 248-nm irradiation. The film material should have low refractive index, low absorption, band edge located at a wavelength well below 248-nm, good cosmetic quality, and good environmental stability when exposed to high humidity. For single-layer films stress did not influence thresholds.

4. High Reflectors

Reflectors for use at 248 nm were fabricated by OCLI from 13 high-index/low-index combinations of the materials that were studied as single-layer films. Four reflectors of each type were made, two in each of two coating runs. Each reflector had a minimum of 15 quarterwave-thick layers and was overcoated with a halfwave-thick layer of the low-index material used in the reflector stack. The coatings were deposited onto conventionally polished substrates of BK-7.

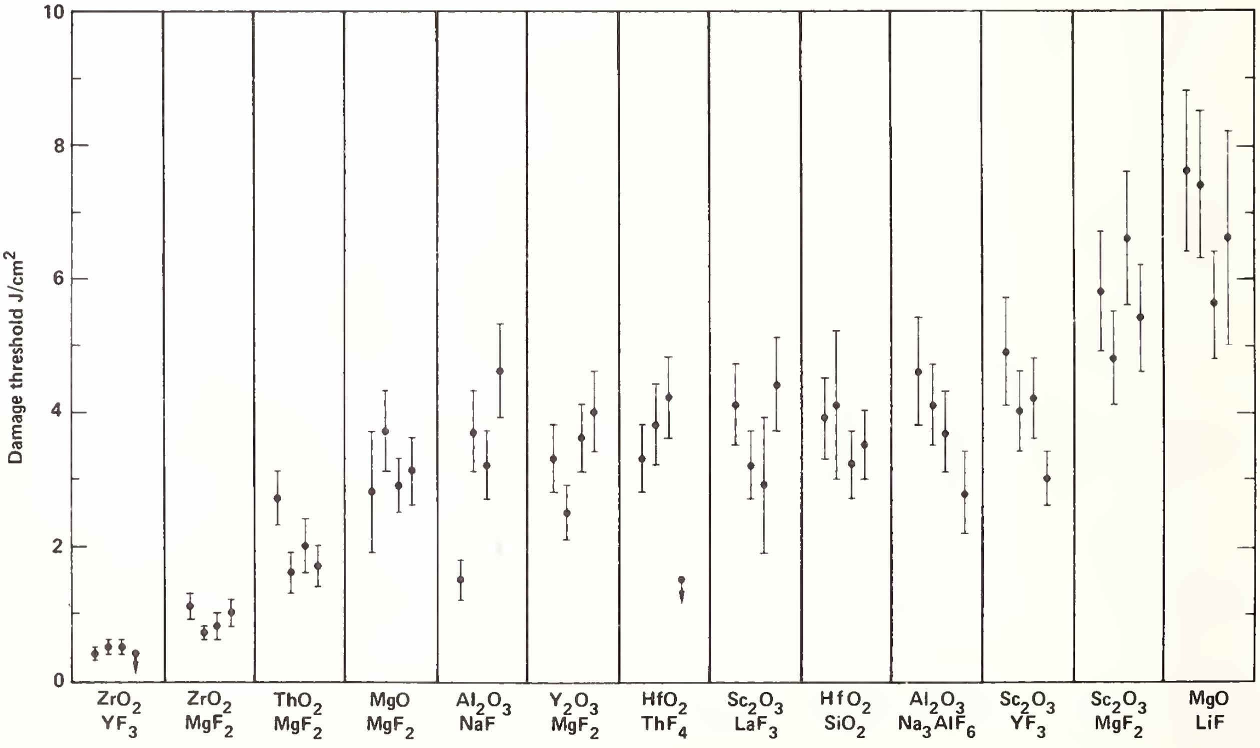

Figure 3. Laser damage thresholds (20 ns, 248 nm) of quarterwave-stack multilayer highly reflecting coatings made from 13 combinations of high-index and low-index materials.

The cosmetic appearance of most reflectors was usually like that of halfwave-thick films of its constituent materials, but the surface density of defects was slightly higher in reflectors. All reflectors with ZrO_2 and NaF had a foggy granular appearance, and reflectors with YF_3 had stress fractures. Other unusual reflectors included the following: those with HfO_2 had many cosmetic defects and sections of missing coating; those with Na_3AlF_6 were densely fogged, and had large circular voids; the ThO_2/MgF_2 reflectors appeared scuffed and nonuniform.

Damage thresholds of these reflectors, shown in figure 3, fell into three groups: below 3 J/cm^2, between 3 and 5 J/cm^2, and greater than 5 J/cm^2. Reflectors with the lowest thresholds were fabricated with high-index materials that had low thresholds when tested as single layers, ZrO_2 and ThO_2. In contrast, the low-index material Na_3AlF_6 had a low threshold when tested as a single layer, but when combined with Al_2O_3, produced a reflector with moderate threshold. Reflectors of Sc_2O_3/MgF_2 and MgO/LiF had the highest thresholds, the median values being 5.6 and 7.0 J/cm^2, respectively. It is interesting that these largest reflector thresholds were considerably greater than the thresholds of single layers of the high-index materials, and considerably less than the highest thresholds observed in single layers of the low-index materials.

Rank	High-n material	Low-n material	Index n	Abs. k	Abs. edge	Stress	Thresh-old	Cos-metic	Environ-mental	
1	MgO	LiF	●	○	●	●	○	?	○	Low-n materials
2	"	MgF_2								
1	Sc_2O_3	MgF_2	●	●	?	○	X	X	?	
2	"	YF_3								
3	"	LaF_3								
1	Al_2O_3	Na_3AlF_6	?	●	?	●	X	●	?	
2	"	NaF								
1	HfO_2	SiO_2	●	○	○	●	○	?	?	
2	"	ThF_4								
1	ZrO_2	MgF_2	●	?	?	○	●	●	?	
2	"	YF_3								
1	Sc_2O_3	MgF_2	X	●	○	X	○	●	X	High-n materials
2	Y_2O_3	"								
3	MgO	"								
4	ThO_2	"								
5	ZrO_2	"								
1	Sc_2O_3	YF_3	●	●	●	●	●	●	?	
2	ZrO_2	"								

Figure 4. Comparison of threshold ranking (high to low) of reflectors to ranking of coating materials with respect to increasing refractive index, absorption, position of band edge, and stress, and with respect to decreasing threshold of halfwave-thick films, cosmetic appearance and environmental stability. Reflectors are grouped into subsets containing a common material, and within each subset, are ranked by decreasing threshold. For each subset, we indicate whether each possible ranking of the varied materials agreed (●) or disagreed (X) with the threshold ranking. In some instances there were either minor disagreements (O) or the material ranking could not be established (?).

A major purpose of this study was to determine whether the threshold ranking of reflectors could have been predicted from either the threshold ranking of single layers of the constituent materials, or the ranking of the constituent materials in terms of their physical properties. A comparison between these rankings is shown in figure 4. The lefthand columns of Fig. 4 list the pairs of materials from which reflectors were made. The list is organized so that all reflectors containing a given material appear as a group. Groups of reflectors with a common high-index material are at the top of the figure; groups with a common low-index material are at the bottom. Inside a given group, the reflectors are ranked in order of decreasing threshold. In the righthand part of the figure, we use four symbols to indicate whether the ranking of thresholds in a group of reflectors agreed (●) or disagreed (X) with a particular ranking for the materials that were varied in that group. The open circle indicates an insignificant inconsistency between threshold rankings of reflectors and a material ranking based on only a slight difference in physical parameters or reflector thresholds. The symbol (?) indicates no material ranking was possible because material parameters were equal or unknown.

As an example, consider the set of three reflectors that contained Sc_2O_3 as the high-index material and either MgF_2, YF_3 or LaF_3 as the low-index material. Threshold ranking (high to low) for these reflectors agreed with material rankings based on increasing refractive index ($n = 1.43$ for MgF_2, $n = 1.54$ for YF_3, $n = 1.59$ for LaF_3) and increasing absorption ($k < .001$ for MgF_2, $k < .001$ for YF_3, $k = .001$ for LaF_3); disagreed only slightly with the ranking based on increasing magnitude of film stress (-50 Kpsi for MgF_2, -49 Kpsi for YF_3, -91 Kpsi for LaF_3); and strongly disagreed with the rankings based on decreasing damage thresholds of the film (14.4 J/cm^2 for MgF_2, 4.6 J/cm^2 for YF_3, 17.7 J/cm^2 for LaF_3) and decreasing cosmetic quality (the YF_3 films had stress fractures). Films of MgF_2, YF_3 and LaF_3 had comparable environmental stability and comparable positions for their UV band edges, so rankings could not be established on the basis of these properties.

The entire set of data in figure 4 shows two general trends. First, when various low-index films were used with a given high-index film (top half of figure), the highest reflector thresholds were correlated with use of the low-index material with lowest refractive index. Absorption, position of the UV band edge, and stress were reasonably good indicators of the merit of the low-index materials, whereas thresholds of single-layer films and cosmetic appearance were sometimes poor selection criteria. Attempts to correlate environmental stability with reflector thresholds were inconclusive. Second, when various high-index materials were used with a given low-index material, optimum reflector thresholds were correlated with minimal absorption and best cosmetic appearance in the high-index film. Of these, we suspect that absorption is the strongest parameter. There was also reasonable correlation between reflector thresholds and either position of the UV band edge or threshold of single-layer films of high-index materials. The refractive index, stress and environmental stability in high-index materials did not correlate with reflector thresholds.

5. Summary

We measured laser damage thresholds for halfwave-thick layers of 15 oxide and fluoride materials, and for HR coatings made from 13 combinations of these materials. Several physical properties of the single-layer films were also measured.

Of the HR coatings tested, those made of Sc_2O_3/MgF_2 and of MgO/LiF had the highest median thresholds, which were, respectively, 5.6 and 7.0 J/cm^2. The thresholds of single-layer films ranged from less than 1 J/cm^2 for ZrO_2 to more than 20 J/cm^2 for SiO_2 and ThF_4. Thresholds were greatest in films of materials for which refractive index and absorption were small, and the position of the UV edge was well below 248 nm. Thresholds of single-layers did not correlate with film stress.

Measurements of thresholds for halfwave-thick single layer films did not identify the materials from which the reflectors with greatest threshold were fabricated. The survey was moderately successful in identifying material characteristics which effect thresholds of reflectors, and identified a promising material combination, MgO/LiF, which we had not previously studied.

In reflectors made of pairs of materials having a common high-index material, and various low index materials, the largest thresholds for the reflectors correlated with use of the low-index material with lowest refractive index. In reflectors with a common low-index material, thresholds correlated with use of the high-index material with the lowest absorption.

6. Acknowledgements

We appreciate the assistance of Steven Brown, Julius Goldhar, John Lutz and Ross Rapoport in maintaining the damage facility, and of Diane Kelly in preparation of the manuscript.

7. References

[1] Rainer, F; Lowdermilk, W. H.; Milam, D.; Hart, T. T.; Lichtenstein, T. L.; and Carniglia, C. K., Scandium oxide coatings for high-power UV laser applications. Applied Optics 21(20): 3685-3688; 1982 October 15.

[2] Hart, T. T.; Lichtenstein, T. L.; Carniglia, C. K.; and Rainer, F., Effects of undercoats and overcoats on damage thresholds of 248 nm coatings, to be published in the report of the 1981 Boulder Conference.

[3] Rainer, F.; Lowdermilk, W. H.; and Milam, D., Bulk and surface damage thresholds of crystals and glasses at 248 nm. Elsewhere in these proceedings.

[4] Newnam, B. E.; and Gill, D. H., Ultraviolet damage resistance of laser coatings. Nat. Bur. Stand. (U.S.) Spec. Publ. 541: 190-201; 1978 December.

[5] Walker, T. W.; Guenther, A. H.; Fray, C. G.; and Nielson, P., Pulsed damage thresholds of fluoride and oxide thin films from 0.26 μm to 1.06 μm. Nat. Bur. Stand. (U.S.) Spec. Publ. 568: 405-416; 1980 July.

[6] Turner, A. F., Ruby laser damage thresholds in evaporated thin films and multilayer coatings. Nat. Bur. Stand. (U.S.) Spec. Publ. 356: 119-123; 1971 November.

[7] Bettis, J. R.; Guenther, A. H.; and Glass, A. J., The refractive index dependence of pulsed laser induced damage. Nat. Bur. Stand. (U.S.) Spec. Publ. 414: 214-218; 1974 December.

LASER DAMAGE THRESHOLDS OF OPTICAL COATINGS AT 351 nm

J. A. Abate and R. Roides

B.P. Oil, Inc.
Laboratory for Laser Energetics
University of Rochester
250 East River Road
Rochester, New York 14623

S. D. Jacobs, W. Piskorowski, and T. Chipp

Laboratory for Laser Energetics
University of Rochester
250 East River Road
Rochester, New York 14623

The damage thresholds of several optical coatings to 351 nm laser radiation will be presented along with a discussion of the optical sytem used to make these measurements.

We have investigated the influence of substrate type, substrate polish - standard commercial vs. superpolished, post coating baking, and the effect of overcoats and undercoats on the observed damage threshold. The coating materials investigated include Ta_2O_5/SiO_2, Sc_2O_3/SiO_2, Al_2O_3/MgF_2, and Y_2O_3/SiO_2. We report measurements on both AR and HR dichroic coatings designed to operate at 1.054 µm and 351 nm.

Keywords: Coatings; laser damage; multilayer dielectric coating.

As the laser fusion community proceeds to frequency convert their Nd:glass lasers to shorter wavelengths, the importance of the performance of optical coatings at these wavelengths becomes of great interest. Of particular interest to the University of Rochester's Laboratory for Laser Energetics (LLE) is the performance of these coatings at the tripled frequency of Nd:glass, 351 nm. The fluence level at which the optical coatings can transport the UV beam will have a major impact on the size, cost, and energy-on-target in any UV upgrade to the 24-beam laser at LLE, known as OMEGA.

Over the last several years a major effort has gone into measuring and attempting to improve the damage thresholds of optical coatings at 1.06 µm. Until recently, very little has been done at shorter wavelengths. What has been done (1) has shown that the damage thresholds are considerably lower than those at 1.06 µm. State-of-the-art coatings for 1.06 µm have damage thresholds (2) for 1 nsec pulses of 6 to 10 J/cm^2, for high reflectors (HR) and 4 to 7 J/cm^2 for anti-reflectors (AR). The results reported here and elsewhere (3), show damage thresholds with 351 nm light, for 1 nsec and 400 psec pulses rarely over 2.5 J/cm^2 for standard optical thin films.

A diagram of the apparatus used to measure the damage thresholds is shown in figure 1. Damage testing is done by irradiating a given sample and characterizing the incident light pulse's energy, spatial intensity distribution, and pulse width. These parameters change from shot to shot, so it is imperative that they be accurately determined for each and every shot.

The LLE UV damage tester uses the output of the Glass Development Laser (GDL) after the 40 mm rod amplifier. This gives typically an output of 1.6 J of 1.06 µm light and the laser system can be fired every 10 minutes. This output is directed to a set of KDP cyrstals, operated in a similar manner to Seka, et al. (4), to produce 351 nm light. The efficiency of conversion is 50%. The residual 1.06 µm and 0.53 µm light from the tripling process is removed by a dichroic mirror and the 0.35 µm light is then focused onto the coating sample. A half-wave plate and a set of two dielectric polarizers are used to throttle the amount of energy that is delivered onto the sample. This keeps the loading on the KDP crystals the same for all intensities on the sample and, as a result, keeps the beam profile and pulse width relatively constant during the tests. The beam is 5 mm in diameter

---

[1] Numbers within parentheses indicate the literature references at the end of this paper.

when it strikes the sample.

An uncoated wedge picks off a portion of the beam and directs it to a set of diagnostics to measure the energy, pulse width, and intensity profile of the beam for each shot. The intensity profile is recorded both on film and solid state TV camera. The TV image is recorded in a mini-computer with the aid of a high-speed video digitizer. Figure 2 shows a block diagram of a data collection system. The maxiumum energy density is determined from this spatial distribution and the total energy on the sample. This analysis takes approximately 5 minutes. The determination of coating damage is done by taking photo-micrographs of the portion of the sample that is irradiated, both before and after the shot.

We have investigated the effect of a number of different parameters on the performance of several optical coatings to 351 nm laser irradiation. In figures 3 through 7, the results of tests on some 82 samples are presented. In each of these figures we have indicated the coating vendor; the pulse width the tests were performed at; the coating type and operative angle of incidence; the substrate type (P - Pyrex, F - fused silica, or BK - BK-7) and any substrate vendor information, if available; the method of polishing used on the substrate whether standard commercial polish or in several samples in figure 6, a super-polish performed by OCLI; the post-coating baking conditions, if any; and the coating materials and design, (the coating design is indicated schematically in terms of quarter-wave layers of the individual materials. For example, in figure 3,]9 (TS)T2S indicates that on the substrate, "] ", there are 9 alternating quarter waves layers of Ta_2O_5, "T", and SiO_2, "S" followed by a quarter wave of Ta_2O_5 and a half wave layer of SiO_2 at the surface). The accuracy to which the damage threshold was determined for each sample is indicated by the width of the box representing that sample. The mean threshold for similar groups of samples is both plotted as a dashed line and indicated at the right-hand side of the figure.

Several trends become apparent on analysis of the data. The highest damage threshold that we have measured has been an AR-treatment to BK-10 glass developed by Schott Glass. In this process, known as the "Neutral Solution Process," (5) the surface of the glass is etched to a quarter wave depth by a weak acid, leaving a surface with a reflectivity of less than 0.5%. Previous surface treatments (6) to produce AR properties have not been very durable and could not be cleaned without damage to the surface. The Neutral Solution Process is cleanable and appears fairly durable. This plus a damage threshold of 9 J/cm^2 would make this coating look very promising for future UV systems, except that all the glasses it can be applied to presently have been shown to be solarized at 351 nm (7). It can be seen from figures 4 and 6 that thicker AR coatings tend to have a lower threshold than thinner AR's. There is also evidence in figure 6 that the addition of a barrier layer between the substrate and the coating shows some improvement in the damage threshold, even though the number of samples tested is small. In terms of the materials used in the AR coatings tested, Sc_2O_3 consistently showed higher thresholds than those containing Y_2O_3. Also the Sc_2O_3 film produced by OCLI showed a 30% improvement when deposited on "super-polished" substrates rather than on substrates with a standard commercial polish. No significant improvement was seen in those coatings that underwent a post coating bake.

The results in figures 4 and 5 show that coatings deposited on fused silica substrates tend to have lower thresholds than coatings deposted on BK-7 or Pyrex. We did not see any noticable improvement in the HR coatings tested when an half-wave overcoat was added to the coating design. We did, however, see an overall improvement when the order of the layers was reversed in the design, for a group of dichroic HR coatings shown in figure 5 (ID 827 and 829).

In figure 8 we show phase contrast photo-micrographs at both 50X and 1280X representatives of the damage morphology seen in the coatings we have tested. In general, the size of the characteristic HR damage is somewhat smaller and usually more dense in nature than the AR damage at threshold. For both types of coatings near threshold the damage takes the form of small individual pits or craters in the coatings.

What is striking about the data presented in figure 3-7 and data presented by other authors is that thresholds are consistently between 2-3 J/cm^2 and that the methods that seem to markedly effect the damage thresholds of optical coatings at 1.06 µm seen to have little or no effect at 351 nm.

References

(1) Douton, T. F.; Smith, W. L. 1979 Symposium on materials for high power lasers. Nat. Bur. Stand. (U.S.) Spec. Publ. 568; 1979.

Newnam, B. E.; Gill, D. H. 1978 Symposium on materials for high power lasers. Nat. Bur. Stand. (U.S.) Spec. Publ. 541; 1978.

(2) Walker, T. W.; Guenther, A. H.; Nielsen, P. IEEE J. Q. E. QE-17 10: 2041-2065, 1981 October.

Loudermilk, W. H.; Milam, D.; Rainer, F. 1979 Symposium on materials for high power lasers. Nat. Bur. Stand. (U.S.) Spec. Publ. 568; 1979.

(3) Rainer, F.; Deaton, T. F. Tech. Digest CLEO '81 - WH-2, Washington, DC, June 10-12, 1981.

Abate, J. A. Tech. Digest CLEO'81, THB-10, Washington, DC, June 10-12, 1981.

(4) Seka, W.; Jacobs, S. D.; Rizzo, J. E.; Boni, R.; Craxton, S. Opt. Comm. 34: 469; 1980.

(5) Cook, L. M.;Lowdermilk, W. H.; Milam, D.; Surain, J. E. App. Opts. 21(8): 1482; 1982 April 15.

(6) Minot, M. J. J. Opt. Soc. Am. 66: 515; 1975.

(7) Jacobs, S. D.; Abate, J. A. Tech. Digest CLEO'81, THB-11, Washington, DC, June 10-12, 1981.

Acknowledgement

This work was partially supported by the U.S. Department of Energy Inertial Fusion Project under contract DE-AC08-80DP40124 and by the Laser Fusion Feasibility Project at the Laboratory for Laser Energetics which has the following sponsors: Empire State Electric Energy Research Corporation, General Electric Company, New York State Energy Research and Development Authority, Northeast Utilities, The Standard Oil Company (Ohio), and the University of Rochester. Such support does not imply endorsement of the content by any of the above parties.

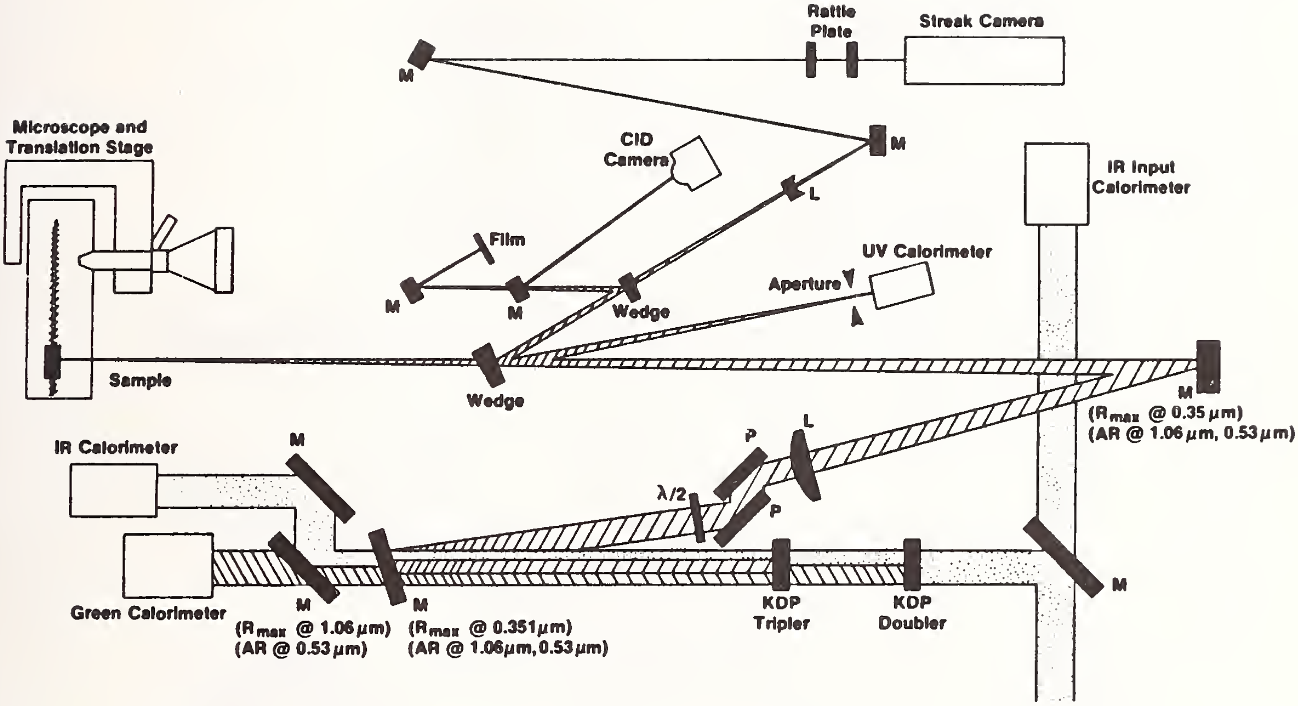

Figure 1. UV Damage Tester.

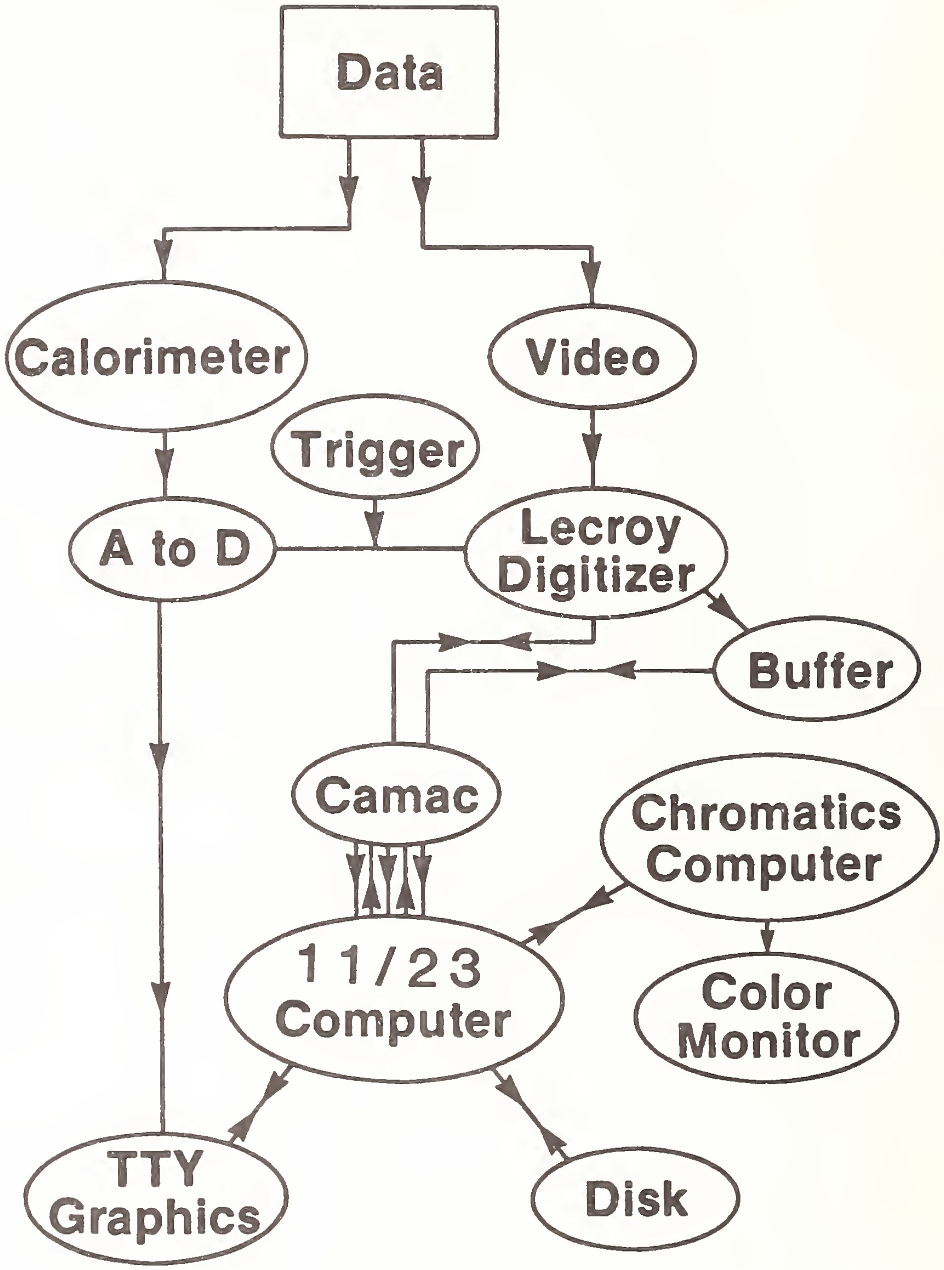

Figure 2. Block diagram of data collection system.

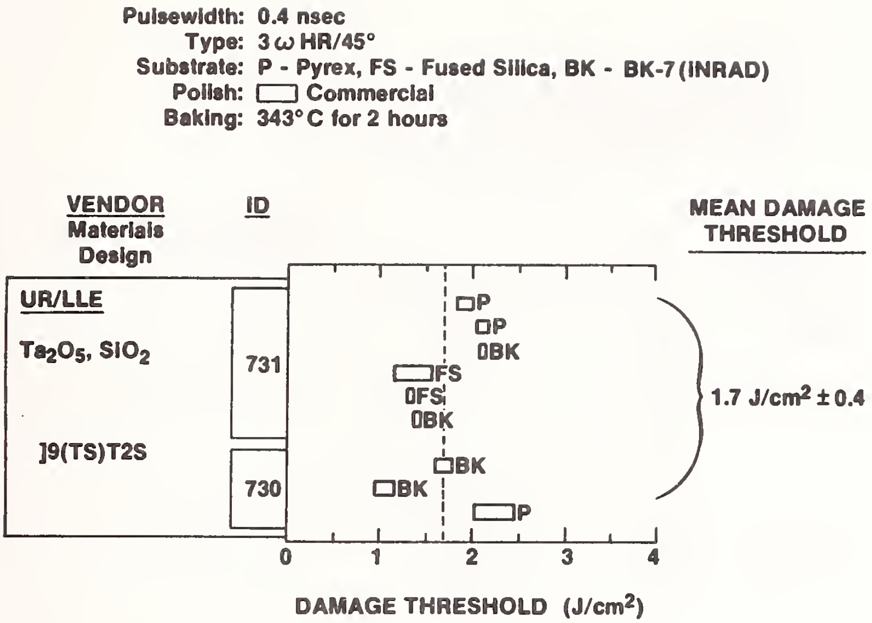

Figure 3. 351 nm damage tests on highly reflecting coatings at 0.4 nsec.

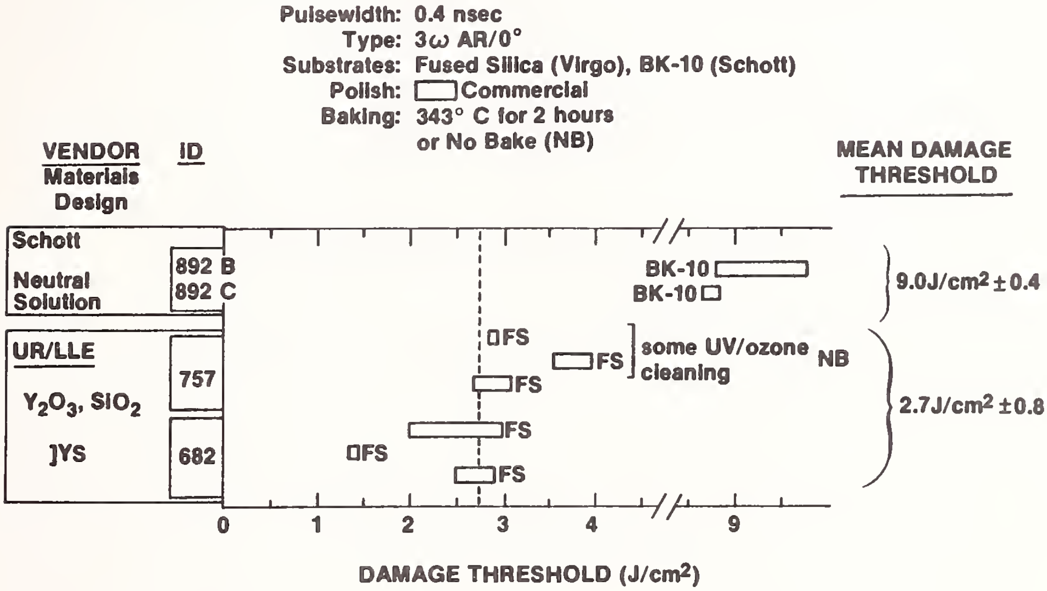

Figure 4. 351 nm damage tests on antireflecting coatings at 0.4 nsec.

Pulsewidth: 1.0 nsec
Type: 1ω - 3ω HR/45° and 57°
Substrate: P - Pyrex (ESCO), FS - Fused Silica, BK - BK-7 (Virgo)
Polish: ▭ Commercial
Baking: 343° C for 2 hours

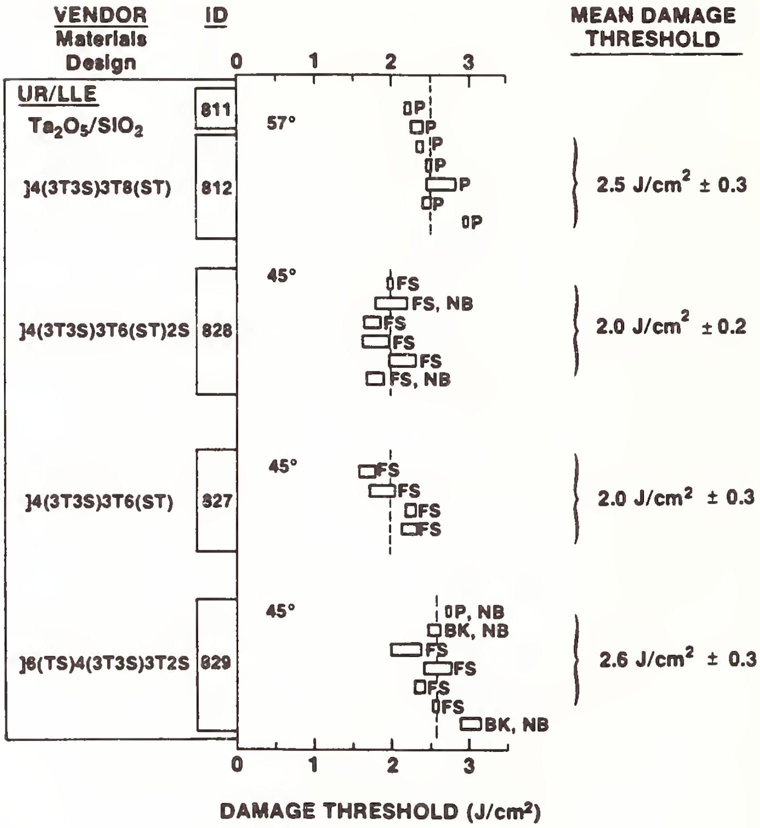

Figure 5. 351 nm damage tests on highly reflecting coatings at 1.0 nsec.

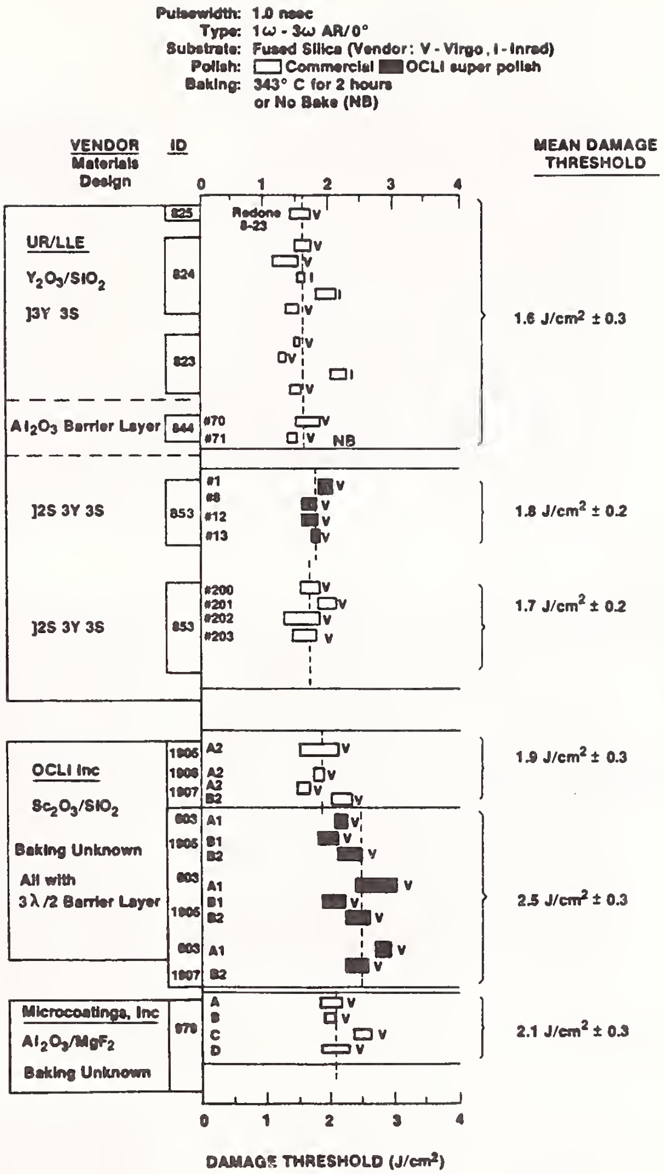

Figure 6. 351 nm damage tests on antireflecting coatings at 1.0 nsec.

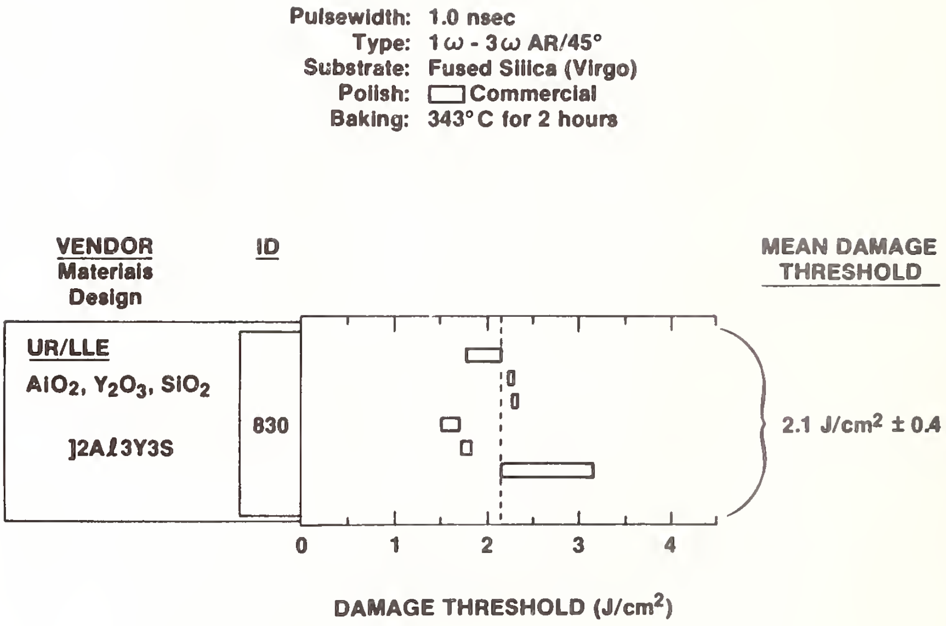

Figure 7. 351 nm damage tests on antireflecting coatings at 1.0 nsec.

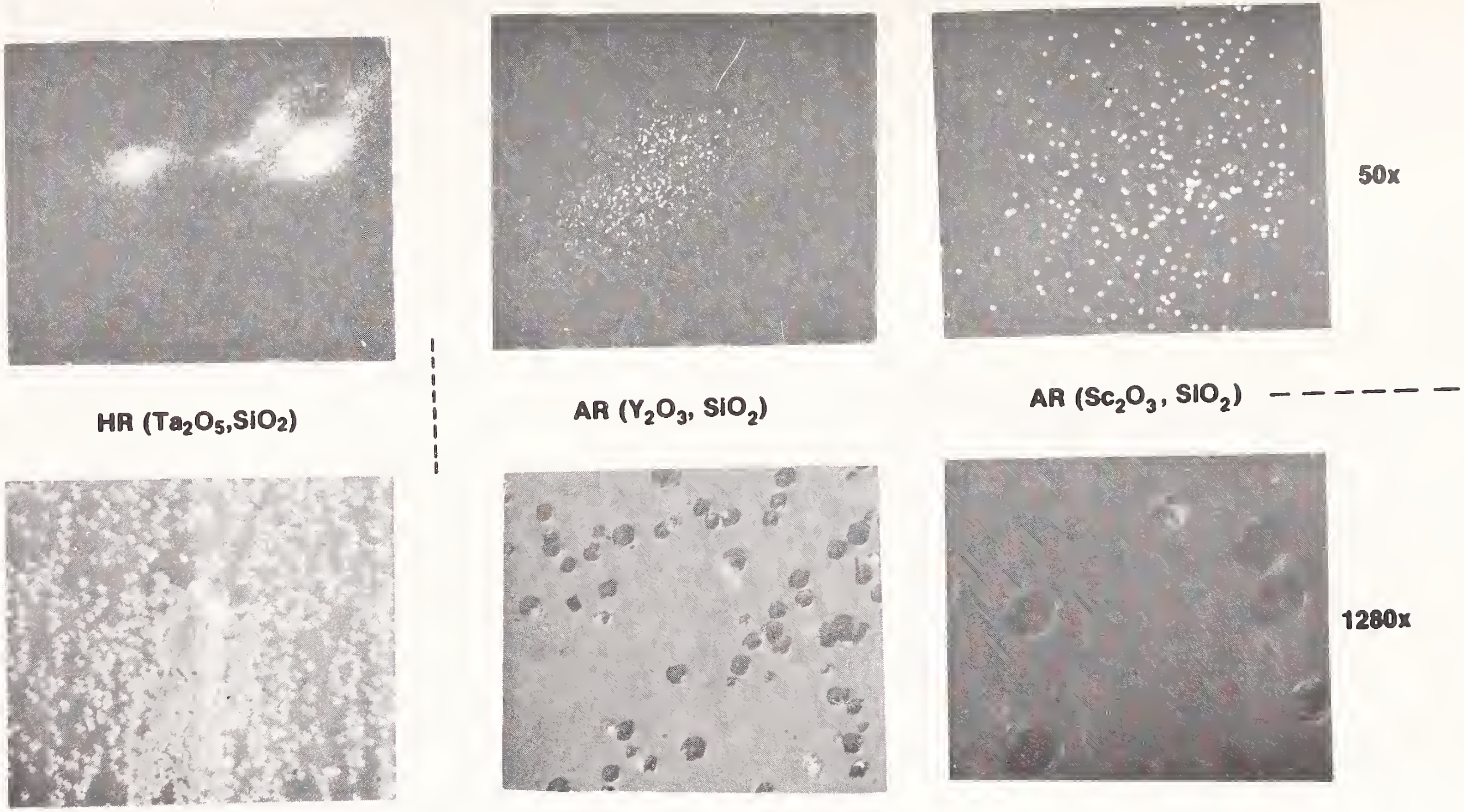

Figure 8. Phase contrast photomicrographs of representative 351 nm laser damage.

Raising the Surface Damage Threshold of Neutral Solution Processed BK-7 by Pulse Laser Irradiation*

J. E. Swain, W. H. Lowdermilk and D. Milam

Lawrence Livermore National Laboratory
Livermore, CA 94550

Gradient-index antireflecting surfaces can be produced by neutral solution processing of bare polished surfaces on borosilicate glasses. These processed surfaces have a median surface damage threshold of 12 J/cm^2 for 1-ns, 1064-nm pulses. The surface damage thresholds can be increased to fluences as large as 25 J/cm^2 by irradiating the surface with 1064-nm wavelength pulses at fluences below the initial threshold of 12 J/cm^2. For surfaces in their initial state, or surfaces subjected to repetitive laser irradiation, surface damage thresholds increased as the square root of pulse duration over the range of pulse durations from 1-20 ns.

Key words: neutral solution processing, laser damage, laser conditioning, antireflection films.

Schott Optical Glass Inc. recently developed a process for producing gradient-index anti-reflecting (AR) surfaces on borosilicate glass by leaching the glass in a nearly neutral solution of Na_2HAsO_4 in water [1]. This "neutral solution process" (NSP) was used to produce AR surfaces on BK-7 borosilicate crown glass, which is widely used for optical components of visible and near-infrared lasers. These NSP AR surfaces exhibited a median damage threshold of 12 J/cm^2 for 1-ns, 1064-nm pulses, which is more than twice the 5 J/cm^2 median threshold of silica-titania multilayer AR coatings [2]. Figure 1 compares these data. Recently we found that the damage threshold of NSP AR surfaces could be increased by as much as a factor of two by irradiating the surface with laser pulses at fluence levels slightly below the initial 12 J/cm^2 threshold.

Our experimental procedure for measuring laser damage thresholds has been described [3]. The procedure consists of irradiating a site on the surface of a sample with a pulsed Nd-glass laser beam approximately 2.5 mm in diameter. We examine the irradiated site, both before and after the laser shot, using a Nomarski microscope with magnification of 100. The sample is moved after each shot so that each site is irradiated only once. The fluence of the laser pulse is increased with each shot until damage occurs. The occurrence of damage is identified by a permanent change in the surface morphology observed using the Nomarski microscope. This measurement technique, in which each site on the surface is irradiated only once, is commonly called a "1-on-1" measurement.

The occurrence of damage in 1-on-1 tests of NSP AR surfaces was always accompanied by laser-induced emission of light. This light is probably recombination radiation from the plasma generated at the surface by the intense laser irradiation. Light emission from NSP AR surfaces was also frequently observed in the 1-on-1 tests at fluence levels slightly below those required to produce damage visible by microscopic examination. If, rather than moving the sample after each shot, we continued to irradiate the same surface area at fluence levels below the 1-on-1 threshold, light emission ceased after a small number of shots. The required number of shots was typically 1-8 and depended on the laser pulse duration. We found that after such treatment, the laser fluence could be raised to a level well above the 1-on-1 threshold before light emission or damage occurred. The threshold for damage determined by this procedure is called the "n-on-1" damage threshold.

We have measured 1-on-1 and n-on-1 thresholds for NSP AR surfaces using 1064-nm pulses at five pulse durations: 1,3,6,9 and 20 ns. Thresholds for a particular sample are shown in figure 2. Thresholds, either n-on-1 or 1-on-1 were defined to be the average of the least fluence that caused damage and the greatest fluence that caused no damage. The uncertainty depended on the separation of the two fluences which defined threshold, and on the uncertainty in fluence measurements themselves, ± 5%. In 1-on-1 measurements, front and rear surface damage thresholds were the same, as expected for a substrate with AR films on both surfaces. In the n-on-1 measurements with 6,9 and 20-ns pulses, rear-surface thresholds were less than front-surface thresholds, an observation for which we currently have no satifactory explanation. The

---

*Work performed under the auspices of the U.S. Department of Energy by the Lawrence Livermore National Laboratory under contract W-7405-ENG-48.

two straight lines drawn through the data have slope one-half. Therefore, over the range of pulse durations from 1 to 20 ns, thresholds of NSP surfaces scale in proportion to the square-root of pulse duration.

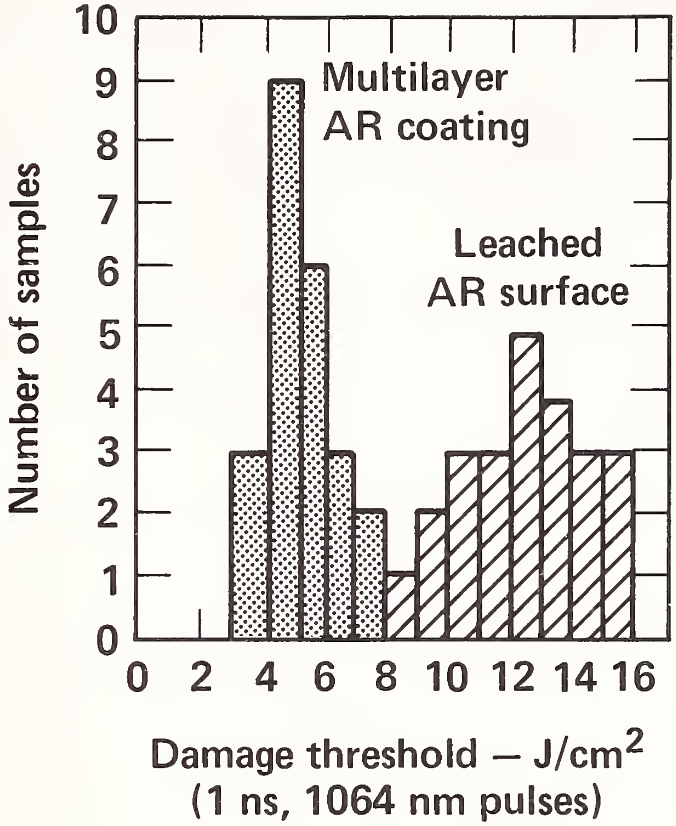

Figure 1. The median one-on-one surface damage threshold of neutral solution processed BK-7 is a factor of two higher than that of electron beam deposited dielectric AR coatings.

A possible mechanism for the increase in damage threshold measured in the n-on-1 tests is the removal of absorbing impurities from the surface by subthreshold irradiation. We believe absorption of energy from the laser pulse by particulate impurities is a common cause of damage to optical surfaces of transparent dielectric materials irradiated by laser pulses with near-ir or shorter wavelengths [4]. When irradiated initially at high fluence, as in the 1-on-1 tests, these particulates absorb laser energy and can reach temperatures above 1000°K, which is sufficient to induce surface damage by stress fracture or melting. When irradiated at lower fluence, the particles reach lower temperatures, which may be sufficient to promote desorption, but insufficient to produce damage. In some photographs of NSP AR surfaces taken with a scanning electron microscope, particles are visible in areas that were not subjected to n-on-1 irradiation, but absent from irradiated areas.

Another possible mechanism for removing particulates by low fluence irradiation is the emission of electrons or ions from the surface [5]. The quantity of charge emitted may be sufficient to substantially alter the static electric forces which normally bind particulate impurities to the surface.

The heating and desorption mechanism is, however, more consistent with our observation that "laser cleaning" is more easily accomplished using pulses of longer duration. When surfaces were irradiated with 20-ns pulses at subthreshold fluence, light emission usually ceased after one shot. Using pulses of shorter duration, more shots were required to "clean" the surface sufficiently that light emission ceased. At the shortest pulse duration used (1-ns), 6-8 shots were usually required. The maximum fluence at which the "cleaning" can be performed is that just below the 1-on-1 damage threshold, which, as shown in figure 1, increases as the square root of the pulse duration. Consequently, these results indicate that the total fluence accumulated over all the shots required to "clean" the surface and affect an increase in threshold is roughly constant.

In conclusion, we have found that the damage threshold of gradient-index AR surfaces of neutral-solution-processed BK-7 glass can be increased by as much as a factor of two by pulsed laser irradiation at fluence levels just below the 1-on-1 damage threshold. Damage thresholds of these AR surfaces increase with the square root of the laser pulse for pulse durations in the range from 1 to 20 ns, and the improvement in threshold due to "laser cleaning" occurs over this entire range of pulse duration.

We are grateful for technical assistance by S. E. Peluso and for assistance by Treva Janssen and Diane Kelly in preparing the manuscript.

References

[1] Cook, L. M.; Mader, K. H.; and Schnabel, R. "Integral antireflecting surfaces on silicate glass", U.S. Patent Application, Ser. No. 309,149, October 6, 1982.
[2] Cook, L. M.; Lowdermilk, W. H.; Milam, D. and Swain, J. E.; Applied Optics 21, 1482 (1982).
[3] Milam, D. SPIE, Vol. 140, 52-61 (1978).
[4] Lowdermilk, W. H. and Milam, D. IEEE J. Quant. Elect. QE-17, 1881 (1981).
[5] Logothetis, E. M. and Hartman, P. L. Phys. Rev. 187, 460 (1969).

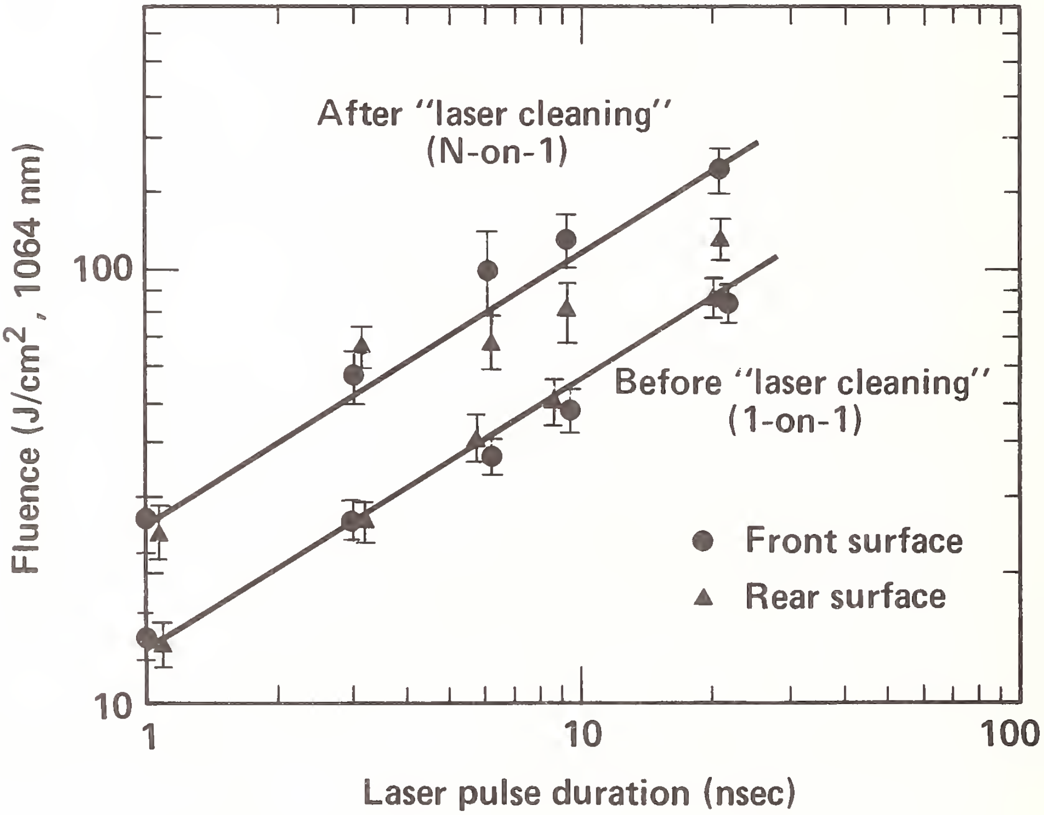

Figure 2. Pulse duration dependence of damage thresholds measured with 1064-nm laser pulses on the front surface and rear surface of a window with NSP AR surfaces. The straight lines are square-root functions. "Laser cleaning" produced n-on-1 thresholds that were nearly twice as large as 1-on-1 thresholds.

In response to several questions, the speaker stated: (1) the minimum reflectance obtained at a tuned frequency is about 0.1%, but reflectance less than 0.5% at both 532 nm and 1064 nm can be obtained by tuning the minimum to a frequency between these wavelengths, (2) the surface reflectance is highly uniform even on 90-cm parts, (3) the ratio of front surface to rear surface laser-conditioned thresholds was greatest at 20-ns, where the ratio was about equal to the factor of 1.4 expected for the bare glass, (4) the term "laser cleaning" was being used as a generic term, and the threshold increase could be due to a variety of effects such as burning away of sharp points, evaporation of absorbing residue from the pores, or melting and collapsing the pore structure, (5) stress-related damage mechanisms have not been considered, (6) the surfaces made by this process are stronger than those etched into phase-separated glass, but weaker than hard e-beam deposited oxide films, (7) the process works on any borosilicate glass but no such glasses usable in intense 355-nm beams are presently known, and (8) Livermore is producing the films for their own use under license from Schott.

DAMAGE THRESHOLD MEASUREMENTS AT 1.06 µm AT CENTRE D'ETUDES DE LIMEIL

D. Friart, M. Novaro, F. Garaude

Commissariat à l'Energie Atomique, Centre d'Etudes de Limeil
B.P. n° 27, 94190 Villeneuve-Saint-Georges, France

B. Geenen, A. Malherbes, J. Guerain

Société MATRA, 93 avenue Victor Hugo
92502, Rueil-Malmaison, France

J.J. Romé, M.T. Buffenoir, P. Perbal

M.T.O. S.A., 11 rue Ampère
B.P. n° 6, Massy Cedex, France

M. Soulie

CILAS, Route de Nozay
91460 Marcoussis, France

We have measured the damage threshold of a serie of different optical components at 1,06 µm, 3 ns. These optics were coated with anti-reflective, high reflectivity and polarizing films. Damage thresholds for A.R. and H.R. were around 5 J/cm^2.

Key words : laser induced damage, damage threshold, anti-reflective coatings, high reflectivity coatings.

1. Introduction

The Octal laser facility is an eight beam neodymium glass laser recently reconditionned and upgraded. It is now in operation at the Centre d'Etudes de Limeil, France. Its realization required the development of new multidielectric coatings with high level damage thresholds.

Consequently during 1981 we developped a damage test facility at 1.06 µm wavelength. During 1981 and early 1982 we have tested almost 500 samples and 200 components manufactured by french companies (MATRA, MTO and CILAS).

The damage threshold of A.R. and H.R. coatings were of the order of 5 to 6 J/cm^2 on these samples.

2. Damage threshold determination

The damage tests at 1.06 µm were carried out with the laser facility described below and shown in figure 1. First, a QUANTEL oscillator generated a 3 ns, 3 mJ laser pulse. A 20 ps time resolution streak camera was used to record 50 shots ; its appeared that there was no modulation in the pulse.

Second, the pulse was amplified trough a 6 mm followed by a 9 mm diameter road amplifiers with small signal gain around 100.

Attenuation of the beam was realized with a half wave plate inserted between two polarizers. At this level the beam fluence was around 0.5 J/cm^2. We increased the fluence with a 2.5 m focal length lens. Sample were positionned at 2 m from the lens in order to obtain a sufficiently large irradiated area. At this point the beam diameter was 1.8 mm.

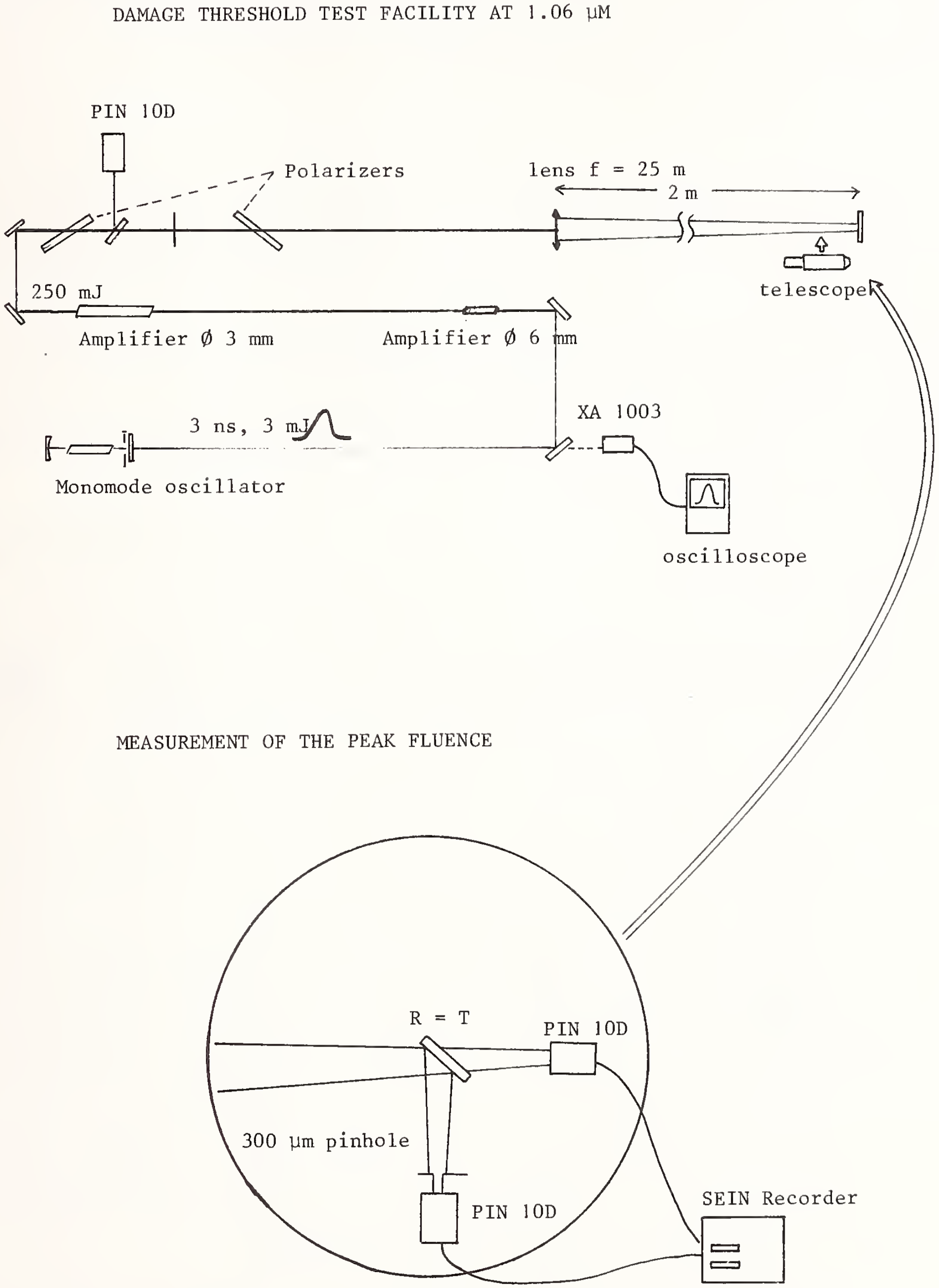

DAMAGE THRESHOLD TEST FACILITY AT 1.06 μM

MEASUREMENT OF THE PEAK FLUENCE

FIGURE 1

Energy was measured with a PIN 10 D detector calibrated with a SCIENTECH calorimeter inserted in the test beam.

We used a combination of pinhole and detectors described schematically in figure 1 to measure the peak fluence (J/cm^2). The pinhole had a 300 µm diameter and we assumed a constant fluence over this surface which is small compared to the spot size of the beam (1.8 mm).

The samples were controled by using a one hundred times magnification telescope.

3. Results

ZrO_2 and TiO_2 were used as high index materials for A.R. and H.R. coatings. Results obtained on testing samples are presented in table 2, results on Octal components are presented in table 1.

Better testing reproductibility and high damage thresholds were obtained on samples coated with TiO_2/SiO_2.

A.R. coatings with a monolayer of MgF_2 showed a strong dependance of damage threshold with substrate material and polishing on both samples and components.

For H.R. coatings we noticed lower results for large components than for small samples (3.7 J/cm^2 compared to 6 J/cm^2). No satisfactory explanation has been found yet, but very few large components have been coated with TiO_2/SiO_2.

TABLE 1 - DAMAGE THRESHOLD OF COMPONENTS

Coating	Supplier	Dimension of compcnents (mm) and substrate material	Number of coatings tested	Median Damage Threshold J/cm^2
A R Monolayer R ≈ 1%	MTO	140 FR4	18	5,3
		172 BK7	24	5,8
		90 Silicate Rod	24	5,1
		130 BK7	16	4
	MATRA	200 BK7	9	4
		200 BK7	9	5,4
A R ZrO_2/SiO_2 Multilayers R ≈ 0,2%	MTO	130 BK7	27	3,1
	MATRA	200 BK7	9	3,7
		120 Silicate Rod	24	5
	CILAS	64 Silicate Rod	30	3,8
Polarizers ZrO_2/SiO_2	MATRA	130 x 286 BK7	30	4,9
		70 x 150 BK7	5	4,5
H R TiO_2/SiO_2	MATRA	200	15	3,7
		200	7	2,6
		200	7	3,8
		200	9	3,7
		200	9	4

TABLE 2 - DAMAGE THRESHOLD OF SAMPLES

Supplier	Coating	Number of Sample	Median Damage Threshold J/cm^2	Standard Deviation
MATRA	H R ZrO_2/SiO_2	6	4,9	2,5
		6	3,3	1,2
	H R TiO_2/SiO_2	4	3,2	1,2
		16	6,7	1,9
		5	6	2
	A R ZiO_2/SiO_2	18	4,2	1,2
		26	3	1
	A R TiO_2/SiO_2	4	4,6	0,6
		10	5	1,1
MTO	A R 2 Layers	20	3,2	0,6
	A R MgF_2	10	4	0,7
	A R MgF_2	13	5,4	0,6
	A R MgF_2	20	5,3	0,6

In response to a question regarding the computation of fluence by measuring the energy transmitted through an aperture, the speaker replied that measurements had been made with apertures of various sizes, and the results were consistent, so he believed that his test beam was uniform over the aperture used in fluence measurements. The speaker also stated that visual inspections by microscopy were made before and after each shot to determine whether damage had occurred, and that the damage threshold was defined to be the average of the lowest fluence causing damage and the greatest fluence that caused no damage.

Impurities in ThF_4 Optical Coatings*

Galen J. Hansen, Daines Lund, Alfred T. D'Agostino,
and Wilford N. Hansen

Utah State University
Logan, UT 84322

Impurities in ThF_4 films simulating HEL optical coatings were studied using multi-internal reflection IR spectroscopy. Water was the main impurity found. D_2O as vapor and liquid was used to examine the lability of the water impurity. Films were also heated in vacuum while simultaneously observing their IR spectra to see at what temperature the water was driven off, and whether the water would then be reabsorbed. Results indicate the following: 1) the water was tightly bound within the films, and was not free to come and go; 2) some films were more porous than others; 3) CeF_3 and other caps on top of films in this study did not help eliminate moisture contaminaton; 4) films with no water or which lost their water did not absorb any additional water; 5) films showed no moisture degradation over time. The general conclusion was that water impurity in ThF_4 films originated with the ThF_4 starting material and did not enter the films during or after film preparation.

Key words: deuterium oxide; HEL optical coatings; impurities; optical coatings; reflection spectroscopy in thin films; thorium fluoride; water contamination.

1. Introduction

Impurities can be a significant problem in high energy laser optical coatings. They can directly absorb the radiation to promote laser damage, and they can cause degredation of the coating otherwise. In the case of thorium fluoride films, moisture is especially troublesome because it absorbs at desired laser operational wavelengths. To date it shows a stubborn tendency to be there, sometimes in large amounts.

In this work, a number of thorium fluoride films were examined for impurity content. Water was the main impurity found. The amount and behavior of the unwanted moisture was studied in varous films. It was hoped to determine the origin and nature of the impurities, and whether pure durable ThF_4 films can be made.

Multiple internal reflection IR spectroscopy is a very sensitive method for in-situ non-destructive observation of individual molecular species. Using this technique, monolayer amounts of impurity molecules can be identified and quantified [1]. This spectroscopy was the main technique used in this investigation. A typical set-up is that shown in figure 1. Sensitivity is directly proportional to the number of reflections (N) at the sample, i.e. absorbance $\propto N$, and is also proportional to the electromagnetic field squared, i.e. $\langle E^2 \rangle$, at the site of the impurity. By arranging to have both N and $\langle E^2 \rangle$ large, sensitivity is maximized. (A geometric factor of $1/\cos\theta$ is also important, but assumed constant here.) The large fields obtainable by using internal reflection is illustrated by figure 2. By adjusting polarization and angle, the large $\langle E^2 \rangle$ values can be placed to maximize the impurity spectra [1,2].

While figure 2 is for a two-phase system, the $\langle E^2 \rangle$ values at the interface are changed little by the presence of a small amount of impurity, and the picture is still valid. For three or more phases, the situation is more complicated but still tractable. Thus, the large $\langle E^2 \rangle$ values can be placed where desired in a system of thin films. Palik and Holm have also made impurity studies of thick

---

* This work was sponsored by DARPA, and monitored by AFWL, Air Force Systems Command, United States Air Force, Kirtland Air Force Base, New Mexico.

films using internal reflection spectroscopy [3]. They tended to emphasize absorptance calculations rather than $\langle E^2 \rangle$ field manipulation.

In this work we used D_2O to help determine the nature of the water in the ThF_4 films. The infrared spectra of D_2O are shifted with respect to H_2O, so that any exchange was readily detected.

The purpose of this study was to determine in a general way the nature and long term behavior of impurities in various ThF_4 films. For this purpose ThF_4 films were deposited on infrared transparent internal reflection plates. The films were prepared in various ways. Variations included starting material purity, heating of substrate, capping with cerium fluoride and other materials, and detailed deposition procedures. All films were furnished by the Air Force Weapons Lab. A table of representative films is found below. Results showed that the nature of optical films depends critically on preparation procedures.

Table 1. Thorium Fluoride Film Description

Film	Substrate, thickness, internal incidence angle	# of internal reflections	ThF Film Thickness	Preparation Conditions	Additional Overlayer or underlayer	Comments
#1(1)	ZnSe-4mm =30°	22	5000 Å	Preheated to 150°C before and during deposition	- - -	Coated both sides
#2(1)	ZnSe-2mm =45°	25	5000 Å	- - -	100 Å SiO Overlayer	Coated both sides
#3(2)	ZnSe-2mm =60°	14	4000 Å	- - -	- - -	Coated both sides
#4(2)	ZnSe-2mm =45°	25	3000 Å	- - -	1000 Å CeF_3 Overlayer	Coated both sides
#5(3)	Ge-2mm =30°	22	2.5μ	- - -	- - -	Coated one side only

(1). Group 1 - Some samples originally contained large amounts of water. Such films are assigned to group 1, and Films #1 and #2 are representative of group 1 samples.

(2). Group 2 - Some samples originally contained moderate amounts of water. Films #3 and #4 are representative of the group 2 samples.

(3). Group 3 - Some samples originally contained very little water. Film #5 is one such film.

2. Experimental

2.1 Samples

The samples examined in this study consisted of thin ThF_4 films varying in thickness from 3000Å to 2.5μ, deposited on ZnSe or Ge substrates. Some of the films had an additional overlayer of CeF_3 or underlayer of SiO. The substrates were 50mm x 20mm on the side, with ends cut at 30°, 45°, or 60° for internal reflection. All substrates were 2mm thick, except for the 30° ZnSe substrates which were 4mm thick. The number of reflections within a sample was determined by the length and thickness of the substrate, and by the internal angle-of-incidence, which was usually the same as the angle of the substrate end. Samples were used for both internal reflection and transmission IR spectroscopy.

The samples examined could be divided into three groups based on water content and the date of preparation. Five samples (samples #1-#5) are herein described, along with the results of their experimental treatments. However, they are only representative of a larger number of samples which were studied. Group one was represented by samples #1 and #2, while group 2 included samples #3 and #4, and sample #5 represented group 3.

Sample #1 consisted of 5000Å ThF_4 evaporated on a 30° ZnSe substrate which was preheated to 150°C before and during deposition. For sample #2, a 100Å SiO layer was evaporated on a 45° ZnSe substrate, with 5000Å ThF_4 coated on top. Also included in group 1 are ThF_4 films capped with ZnSe. Sample #3 consisted of 4000Å ThF_4 deposited on a 60° ZnSe substrate, while for sample #4, a 3000Å ThF_4 film was deposited on a 60° ZnSe substrate, with a final overlayer of 1000Å CeF_3. Sample #5 comprised 2.5μ ThF_4 on a 30° Ge substrate. Sample #5 was coated only on one side, while samples #1 through #4 were coated on both sides equally. Internal IR spectra were taken of all samples upon being received and again at the start of this study.

2.2 Treatments

The following is a chronological breakdown of the various treatments to which the samples were subjected (also see table 2).

Samples of group 1 and 2 were first soaked in D_2O vapor for 7 days; then heated in D_2O vapor to over 90°C for 2 hours; then heated in H_2O vapor at 70°C for 24 hours; then finally heated in vacuum at 70°C for 24 hours. Each of these treatments was performed by placing the samples in a vacuum desiccator and the air evacuated. When subjected to H_2O or D_2O vapor, a small amount of the liquid was placed in a beaker in the desiccator, and heated by placing the desiccator in an oven. Internal reflection IR spectra of each sample were taken before and after each of these treatments.

Later, samples from group 1 were individually placed in a 10^{-6} torr vacuum and heated at intervals up to 400°C while simultaneously taking their IR transmission spectra. The vacuum chamber was specially designed to fit into the sample compartment of a Cary White 90 IR Spectrophotometer. It consisted of a glass cylinder with KBr windows on the ends and a standard taper cap on the top to which was connected the sample holder. The sample holder comprised a rectangular shaped aluminum tube which was wrapped with stainless steel sheathed heating coils. Samples were fitted upright inside the tube. The temperature was controlled automatically and monitored per a thermo-couple placed near the sample. Heating the sample did not interfer with the IR spectrum because the sample and reference beams were chopped before the sample compartment. After heating, D_2O vapor was allowed into the vacuum chamber. Then the samples were removed and placed in D_2O vapor for two weeks at room temperature. We were then so bold as to submerge sample #2 in liquid D_2O for 6 days. Some samples from group 3 were also placed in liquid D_2O for 18 hours. However, these samples contained very little water originally, and were not heated or treated in any other way beforehand.

3. Results

A. The broad IR absorption bands of the moisture found in the ThF_4 films were nearly identical to those of pure water [4].

B. The amount of water impurity originally found in the ThF_4 films as received varied greatly from one group of films to the next. The films of group 1, represented by samples #1 and #2, originally contained large amounts of water, which can be seen as the large H_2O absorption bands in figures 3 and 4. Some of the films in this group had ZnSe caps. Those samples of group 1 whose substrates were heated during film preparation, and those capped with ZnSe did not vary significantly in water content from the other samples in the group. The films of group 2, including samples #3 and #4, contained moderate amounts of water as seen by the H_2O absorption bands in figures 5 and 6, which are much smaller than the H_2O bands in figures 3 and 4. Note that the spectra of sample #3 were taken internally at a 60° angle-of-incidence which allowed only 14 reflections and made the sensitivity smaller than for 45° samples. The films of group 3 represented by sample #5 contained almost no water (fig. 7). In figure 7, the H_2O bands are indeed very small. The hydrocarbon seen in figure 7 is due to the uncoated side of sample #5.

C. When left in D_2O vapor at room temperature, what was at first thought to be D_2O-H_2O exchange took place readily in samples #1 and #2 (figs. 8,9) and not at all in samples #3 and #4. However, there is also present a rather large band at 1440 cm^{-1} due to HDO (figs. 8,9). There must have been some D-H exchange taking place. The samples were then heated in D_2O to see what percentage of the H_2O absorption bands could be displaced by D_2O and HDO bands. Figures 8 through 12 show that the H_2O absorption bands were largely replaced by D_2O and H_2O bands in samples #1 and #2, somewhat in sample #4, and not at all in samples #3, even at temperatures greater than 90°C. Note also that the HDO band in sample #2 was rather small after heating. This is because the amount of HDO is related to the remaining amount of H_2O. Part of the remaining band at 1440 cm^{-1} was probably due to hydrated ZnSe.

D. When heated in H_2O vapor, the D_2O and HDO bands were replaced by H_2O bands once again (figs. 13-15). However, two additional bands could be seen at 1430 cm^{-1} and 1540 cm^{-1}. These bands were originally present in sample #1 which was preheated to 150°C when first made (fig. 3), and in sample #4 which was capped with CeF_3 (fig. 6). These two bands seem to be hydrated ZnSe. After being heated at 70°C in a vacuum, the water bands remained unchanged. Very little water was driven off any of the samples at this temperature.

E. Sample #2 was placed in vacuum (fig. 16) and heated, while simultaneously observing its IR spectrum. The water did not begin to leave appreciably until the sample was heated above 200°C. Most of the water was driven off when heated at 300°C for several hours (fig. 17). The same was true for other samples which contained water, even some which had not been subjected to the previously mentioned treatments of samples #1-#4. However, in all cases there remained a small amount of residual moisture, even when heated to 400°C.

F. Once gone, water impurity did not re-enter the films. This seems to disagree with the results of Palik, et.al. [5]. This result was true both for films which originally contained very little water, and for films whose water was driven off at elevated temperatures. After being submerged in liquid D_2O for almost a week, sample #2 (water was drived off) showed no evidence of D_2O impurity (fig. 18). Sample #5 and other films which originally contained very little water, but were treated in no other way, showed no D_2O contamination, even after being soaked in liquid D_2O for a day.

A summary of sample treatment and results is found below in table 2.

Table 2

Film	Treatment	Original Amt H_2O	Amt of D-H exchange room temp	Amt of D-H exchange heated >90°	Amt of Water after heated in H_2O 70°C	Amount of Porosity
#1	A	Large	Large	Large	Returned to original amt	Large
#2	A,B,C	Large	Large	Large	Returned to original amt	Large
#3	A	Moderate	None	Very little	Returned to original amt	None
#4	A	Moderate	Very Little	Moderate	Returned to original amt	None
#5	D	Very Little				

A - Soaked in D_2O vapor for 7 days; then heated in D_2O vapor to >90°C for 2 hours; then heated in H_2O vapor at 70°C for 24 hrs; then heated in vacuum to 70°C for 24 hrs.

B - Placed in 10^{-6} torr vacuum, and heated in intervals up to 400°C.

C - Removed from vacuum, and placed in D_2O vapor at room temp for 2 weeks; then submerged in D_2O liquid for 6 days.

D - Placed in liquid D_2O for 18 hours.

4. Discussion

A number of important conclusions regarding the preparation and integrity of good pure durable thorium fluoride films can be drawn from the preceeding results. Some conclusions are certain while others are probable.

A. To begin with, some thorium fluoride films contained a great deal of moisture, perhaps five percent by volume, within the film [6]. The broad, intensely absorbing spectral regions of this moisture, at 2.6µ - 3.8µ, 5.8µ - 8µ, and >10µ, would surely affect the optical performance of the films. The fact that this moisture impurity had the same spectral signature as liquid water indicated that it was present mainly as bound water and not as something else such as hydroxide or hydrolyzed fluoride, although some of these may have also been present.

B. None of the films dealt with in this study showed signs of degradation under moderate conditions over a period of 1-4 years. A small increase in the moisture content of some of the films over time or in humid atmosphere was noted, but this never amounted to more than a one or two percent increase. Cracks in the film or spots of moisture degradation were seen only when heated in steam. (We made no attempt to study film damage due to heating in water vapor.) Even when submerged, none of the films were altered. A study which dealt more with ThF_4 film degradation is found in reference 7.

C. Evidently the water was tightly bound within the ThF_4 film. The water did not leave freely under vacuum, but was driven off only at temperatures greater than 200°C. So, what was thought to be H_2O - D_2O exchange in result B must actually have been H-D exchange. D_2O absorption bands due to H-D exchange are indistinguishable from those from D_2O - H_2O exchange. However, the HDO band at 1440 cm^{-1} in figures 8, 9, and 12 is also evidence of H-D exchange. Also, the water was evidently bound within the ThF_4 structure by the O, leaving the H's free. This is evidenced by, 1) The vibrational bands of the tightly-held water which are the same as those of liquid H_2O, and 2) the relatively free H-D exchange in samples #1 and #2.

D. The H-D exchange also indicated that some films were more porous than others. In order for the D of D_2O to exchange with the H of H_2O freely, (a good deal of H-D exchange was evident in samples #1 and #2 after sitting in D_2O vapor at room temperature for less than 12 hours), the D_2O evidently was able to penetrate the film and approach the H_2O. Sample #3 did not allow any D-H exchange, most likely because it was not porous and did not allow D_2O penetration. The H-D exchange also suggested that the water is not trapped within impenetrable little cells inside the ThF_4 films. Heating the samples up to 400°C would surely have ruined the films if the water had been trapped inside. Heating the substrate during film deposition did not seem to improve film porosity, at least up to 150°C. Palik et. al. claimed that heating the substrate to 200°C was "adequate" for making good films [5]. However, he did not mention how this applies to ThF_4 films containing water.

E. Evidently the CeF_3 cap and other caps do not reduce the moisture content of samples. In this study, all capped samples contained as much moisture as similar samples without caps. In fact, the CeF_3 itself may contain moisture and be more porous than the underlying ThF_4, as evidenced by comparing the H-D exchange of samples #3 and #4 (fig. 5 and 6, 11 and 12, 14 and 15). In a study done by Donovan and Temple, it was found that a ZnSe cap on the ThF_4 film did reduce the H content of the ThF_4 film by an order of magnitude [8].

F. It is an important point that for those films prepared with very little water impurity, and for the dehydrated films, there was no additional water absorption. Even in humid atmosphere, and even submerged in liquid for days the films did not acquire moisture, but remained anhydrous. At first it was assumed by nearly everyone that the wet films acquired their moisture after being taken out of the preparation chambers. This is now quite doubtful. Also, there was far too much moisture in most of the films to have come from the residual gas of a 10^{-6} vacuum chamber. Heating the substrate to 150°C during deposition or adding a CeF_3 or ZnSe cap did not help eliminate moisture by more than a few percent. Therefore, the moisture in the ThF_4 films most likely originated with the ThF_4 source material.

G. The evanescent wave of the totally reflected (internal) IR radiation is strongest at the film-substrate interface. Its penetration depth at 45° is on the order of 0.2µ. So the $\langle E^2 \rangle$ field will not be very big at the air-film interface of sample #2, and virtually zero for sample #5. Transmitted IR radiation "sees" the air-film interface. Therefore, if the hydrocarbon bands of sample #2 at 2930 cm^{-1} and 2850 cm^{-1} are larger for transmission than for internal reflection (figs. 13 and 16), most of the hydrocarbon must be located on the outer surface of the film. The same reasoning can be used to determine the location of the moisture within the films. This has been done in reference 9. Profiling the water content within some ThF_4 films has also been done by Donovan and Temple using nuclear resonance [8].

5. Conclusion

The key to preparing pure durable thorium fluoride films is evidently to start with pure dry feed stock. Surely this is possible if careful inorganic preparation techniques are used. Some salts are impossible to dry if you start with the hydrated form. ($CrCl_3 \cdot 6H_2O$ is an example.) However, if they are made anhydrous to begin with, they have no affinity for water. Perhaps this is true of thorium fluoride films.

The fact that the results of this study do not agree with some results of other studies merely points out the necessity of cooperation between the various research groups, and the need for more detailed information concerning method of film preparation, origin and nature of starting materials, as well as treatment of films immediately after preparation.

References

[1] Hansen, Wilford N. Reflection Spectroscopy of Optical Coatings. J. Opt. Soc. Am. 69(2): 264-272; 1979 February.

[2] Hansen, Wilford N. J. Opt. Soc. Am. 58(3): 380-390; 1968 March.

[3] Palik, E.D.; Holm, R.T. Internal Reflection-Spectroscopy Studies of Thin Films and Surfaces. Opt. Eng. 17(5): 512-524; 1978 September-October.

[4] Rusk, Alvin N; Williams, Dudley; Querry, Marvin R. Optical Constants of Water in the Infrared. J. Opt. Soc. Am. 61(7): 895-903; 1971 July.

[5] Palik, E.D.; Gibson, J.W.; Holm, R.T.; Hass, M.; Braunstein, M.; and Garcia, B. Infrared Characterization of Surfaces and Coatings by Internal-Reflection Spectroscopy. Appl. Opt. 17(11): 1776-1785; 1978 June.

[6] Anderson, Wayne J.; Hansen, Wilford N. Reflection Spectroscopy Analysis of Surfaces and Thin Films. Proceedings of SPIE Conference, April 1981.

[7] Humpherys, T.W.; Lusk, R.L.; Jungling, K.C. Charactarization of Thin Films for Laser Systems Using Surface Analytical Techniques. J. Vac. Technol. 18(2) 296-300, 1981.

[8] Donovan, T.M.; Temple, P.A. The Relative Importance of Interface and Volume Absorption by Water in Evaporated Films. NBS Spec. Publ. 568:237-246, 1979.

[9] Hansen, Wilford N. Spectroscopic Study of Small Absorptions in Optical Coatings. AFWL-TR-81-139; 1982 April. 57 p.

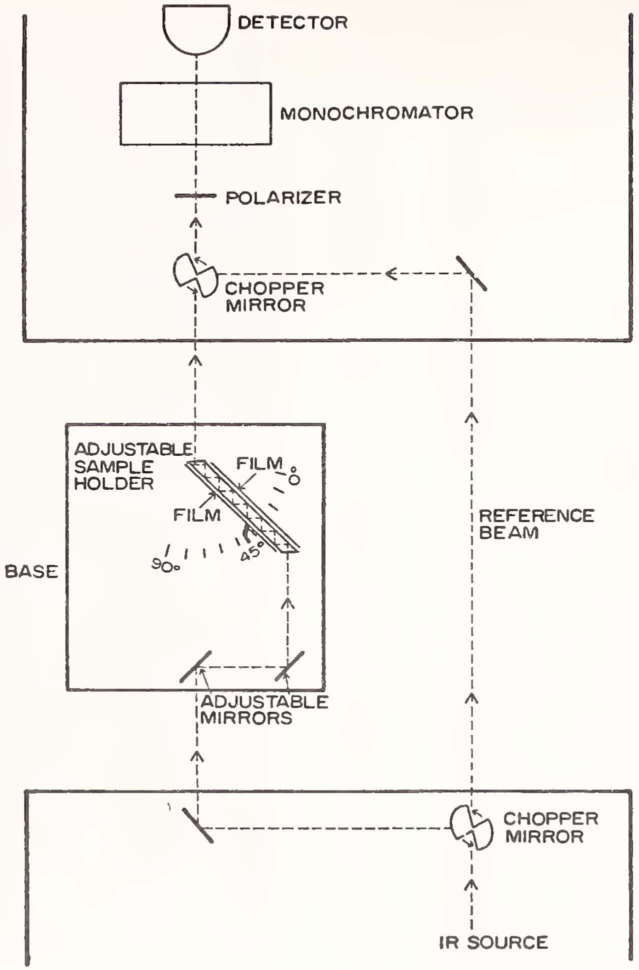

Figure 1. Internal reflection setup inside a PE 180 IR Spectrophotometer. Film is deposited on both sides of an IR-transparent substrate.

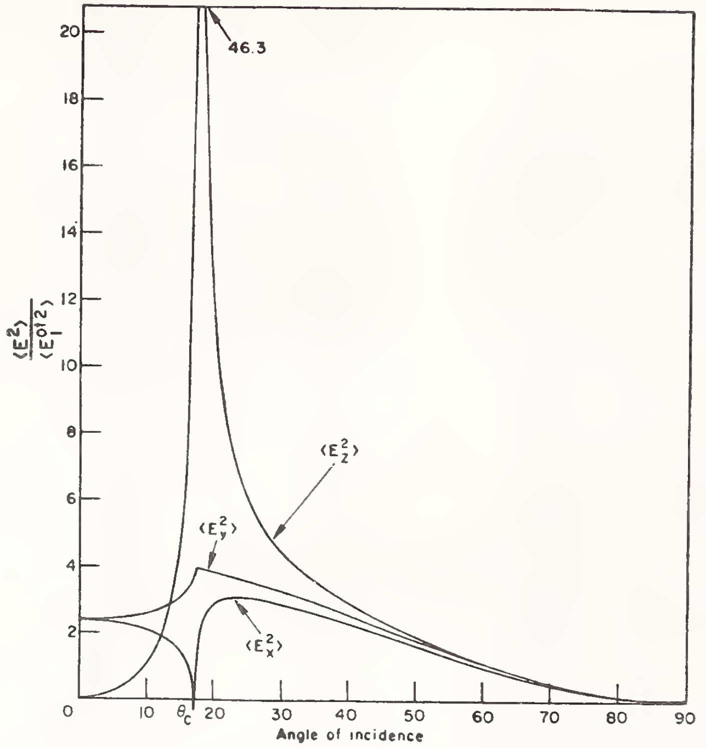

Figure 2. The $\langle E^2\rangle$ field strength at a substrate-film interface, as a function of angle-of- incidence. Internal reflection ($n_2/n_1 \approx .33$). $\langle E^2\rangle \propto$ sensitivity: θ_c=critical angle.

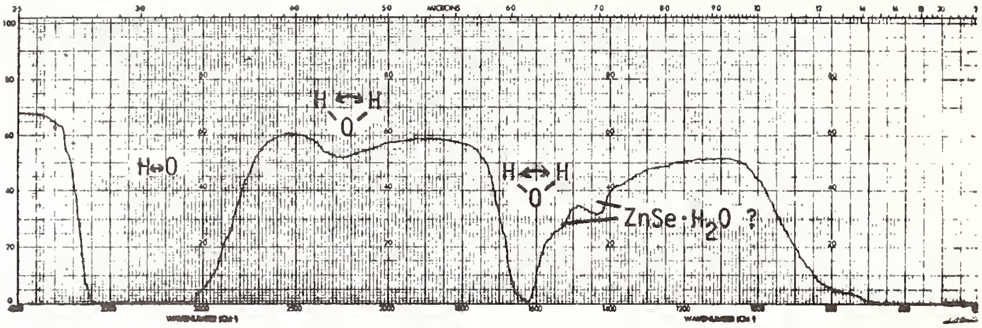

Figure 3. Sample #1 Internal reflection
5000Å ThF_4 on ZnSe
θ=30° 22 reflections
As received

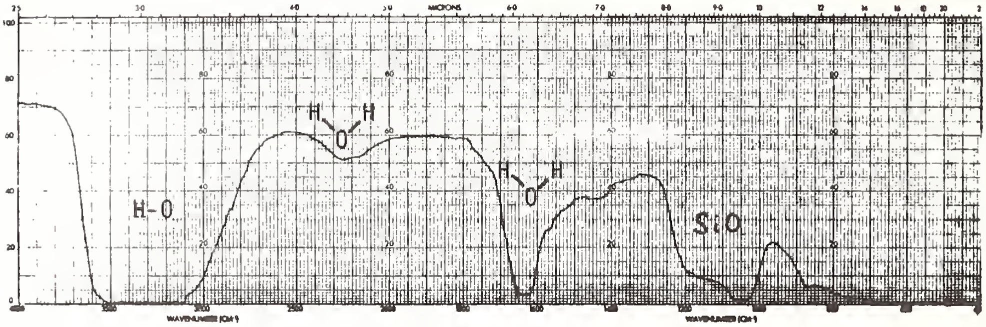

Figure 4. Sample #2 Internal reflection
100Å SiO, 5000Å ThF_4 on ZnSe
θ=45° 25 reflections
As received

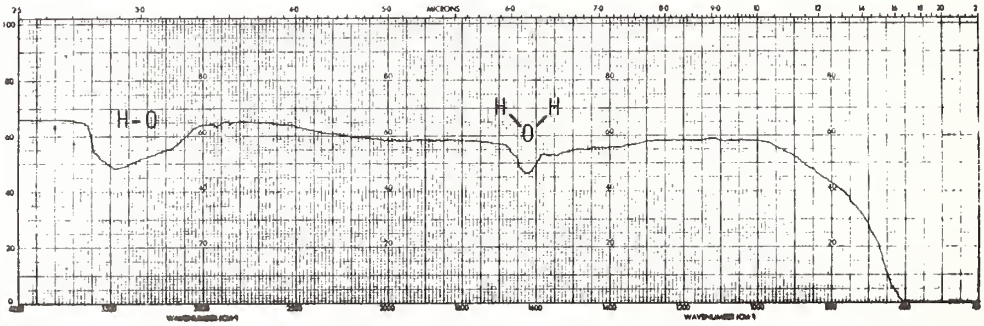

Figure 5. Sample #3 Internal reflection
4000Å ThF_4 on ZnSe
θ=60° 14 reflections
As received

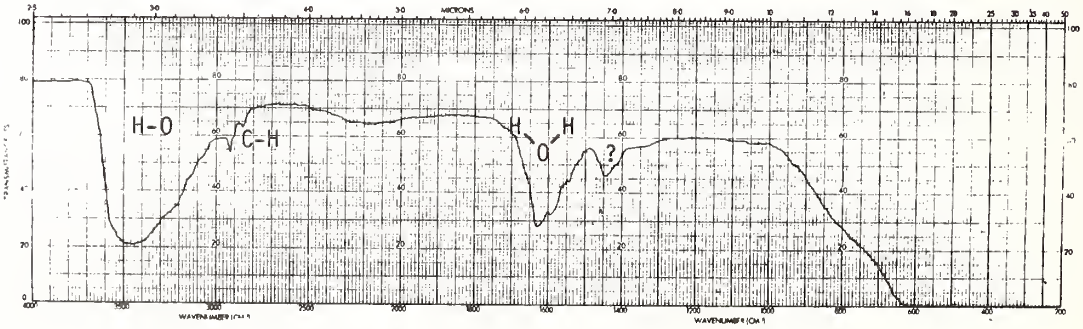

Figure 6. Sample #4 Internal reflection
3000Å ThF_4, 1000Å CeF_3 on ZnSe
θ=45° 25 reflections
As received

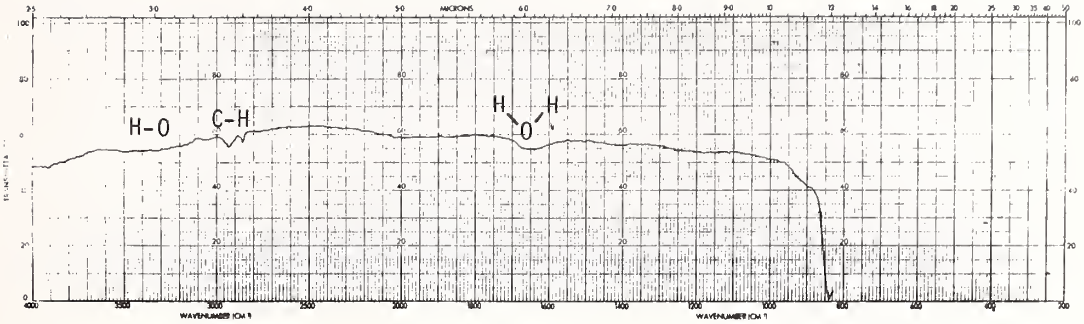

Figure 7. Sample #5 Internal reflection
2.5μ ThF_4 on Ge (one side)
θ=30° 22 reflections
As received

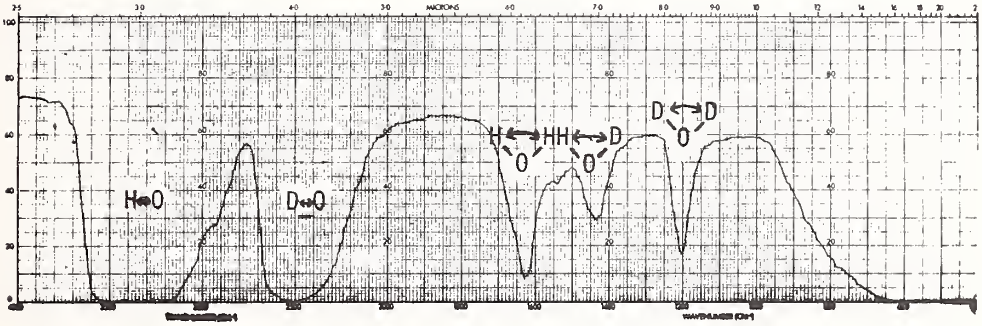

Figure 8. Sample #1 Internal reflection
5000Å ThF_4 on ZnSe
θ=30° 22 reflections
Soaked in D_2O vapor 7 days rm. temp.

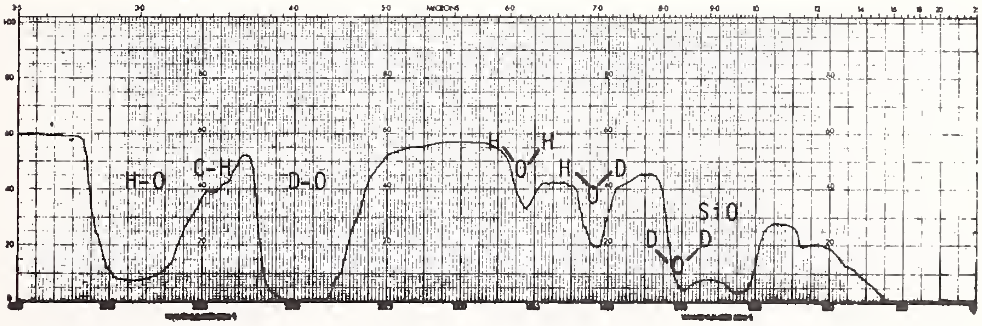

Figure 9. Sample #2 Internal reflection
100Å SiO, 5000Å ThF_4 on ZnSe
θ=45° 25 reflections
Soaked in D_2O vapor 7 days rm. temp.

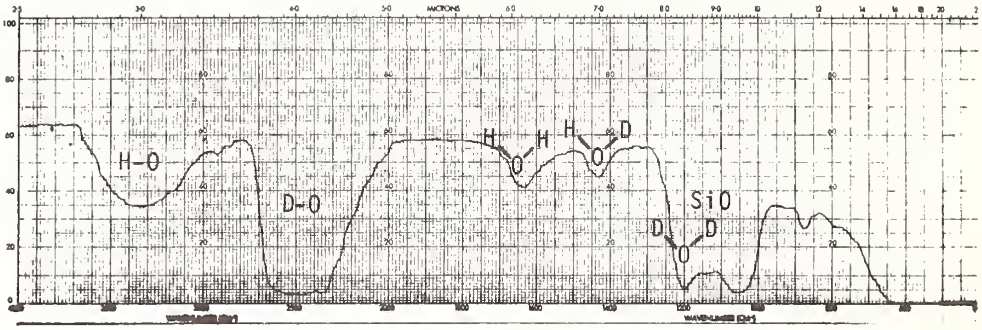

Figure 10. Sample #2 Internal reflection
100Å SiO, 5000Å ThF_4 on ZnSe
θ=45° 25 reflections
Heated >90°C 2 hrs. in D_2O vapor

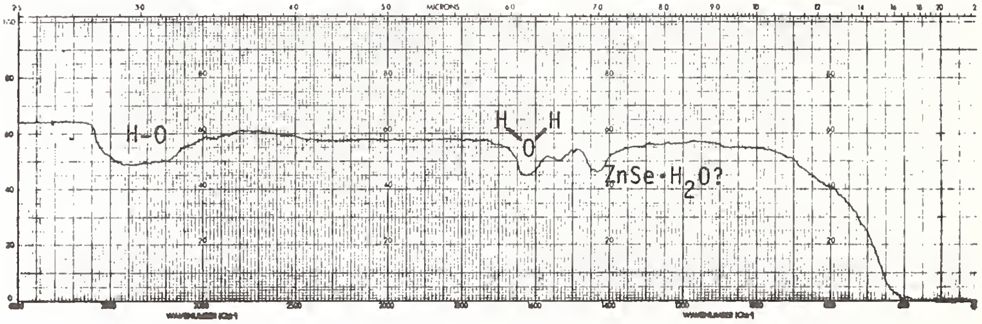

Figure 11. Sample #3 Internal reflection
4000Å ThF_4 on ZnSe
θ=60° 14 reflections
Heated >90°C in D_2O 2 hrs.

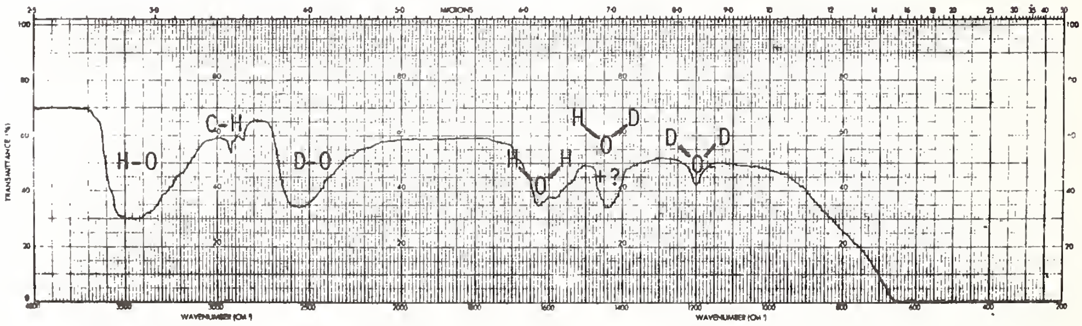

Figure 12. Sample #4 Internal reflection
3000Å ThF_4, 1000Å CeF_3 on ZnSe
θ=45° 25 reflections
Heated >90°C in D_2O vapor 2 hrs.

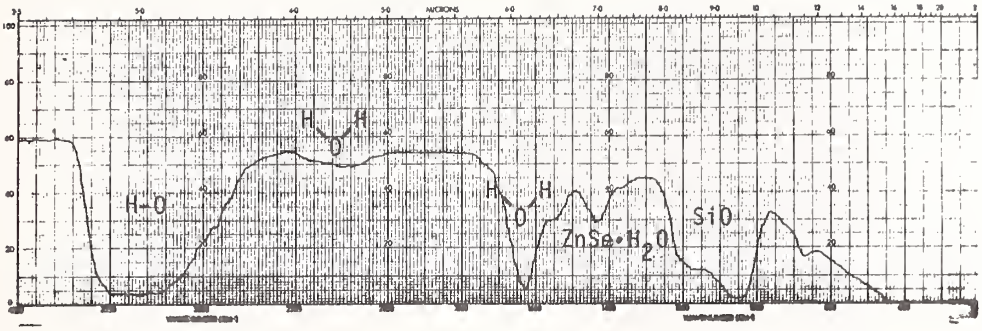

Figure 13. Sample #2 Internal reflection
100Å SiO, 5000Å ThF_4 on ZnSe
θ=45° 25 reflections
Heated in H_2O vapor 24 hrs. 70°C, then
in vacuum at 70°C 24 hrs.

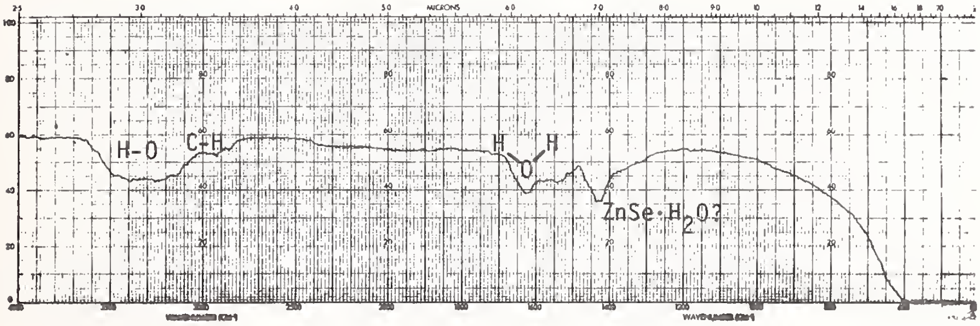

Figure 14. Sample #3 Internal reflection
4000Å ThF_4 on ZnSe
θ=60° 14 reflections
Heated in H_2O vapor at 70°C 24hrs., then
in vacuum at 70°C 24 hrs.

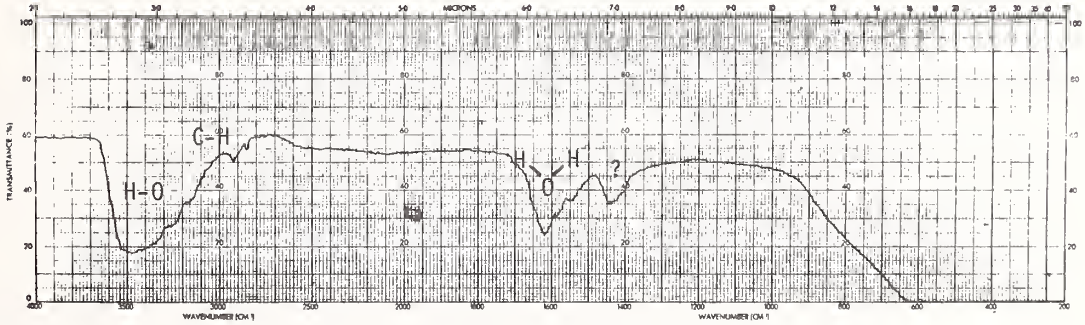

Figure 15. Sample #4 Internal reflection
3000Å ThF_4, 1000A CeF_3 on ZnSe
θ=45° 25 reflections
Heated in H_2O vapor at 70°C 24 hrs., then
in vacuum at 70°C 25 hrs.

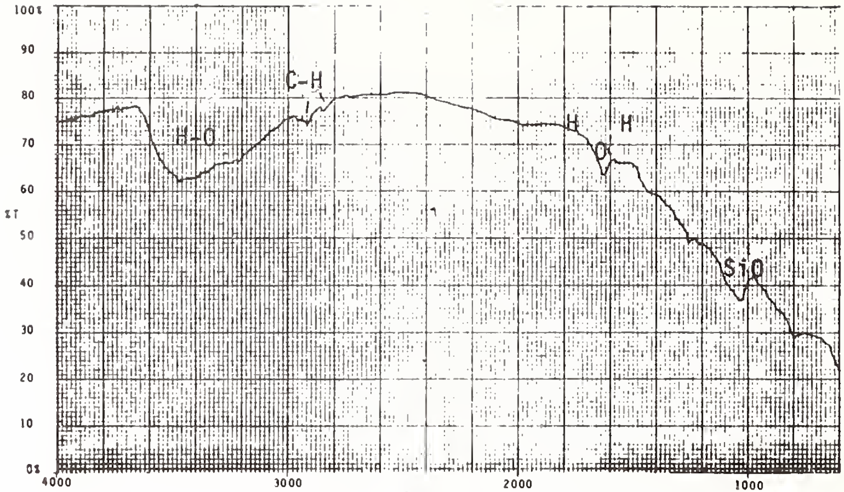

Figure 16 Sample #2 Transmission through both sides
100Å SiO, 5000A ThF_4 on ZnSe
Same as fig.13

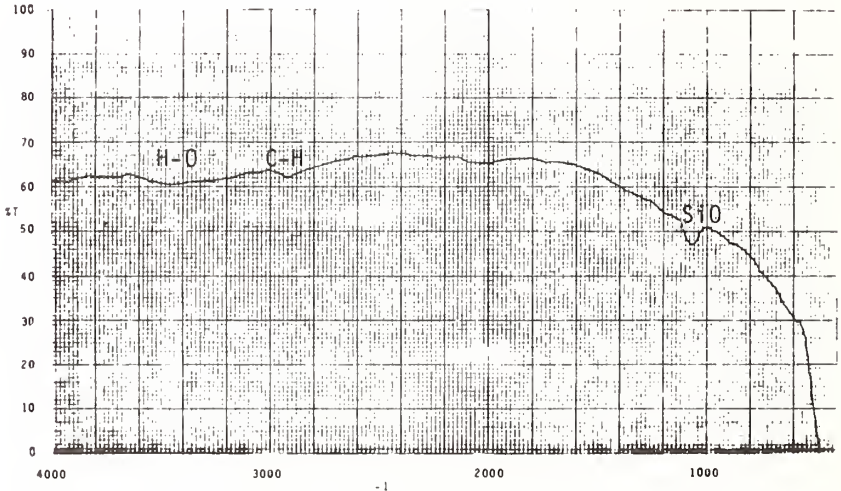

Figure 17. Sample #2 Transmission through both sides
100Å SiO, 5000A ThF_4 on ZnSe
Heated at 300°C for several hrs. in vacuum, then at 400°C for ½hr.

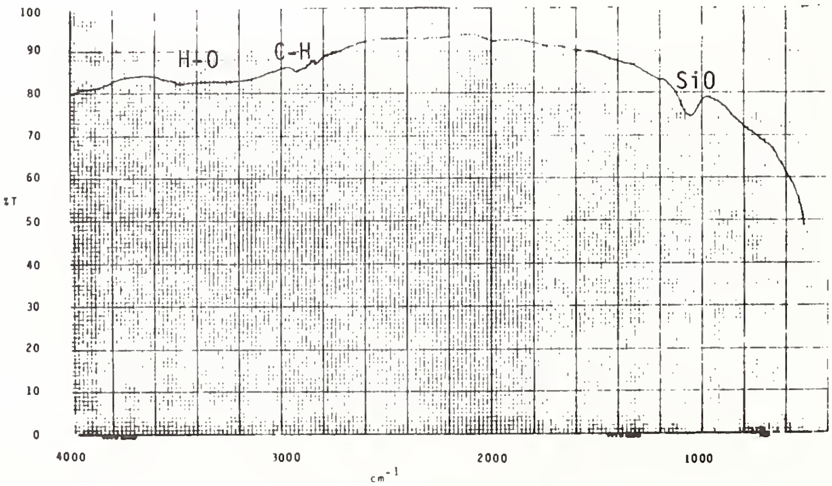

Figure 18 Sample #2 Transmission through both sides
100Å SiO, 5000A ThF_4 on ZnSe
Soaked in liquid D_2O for 6 days (submersed)

Reflectance Spectrum of Non-Optimum Multilayer Coatings

R. Rujkorakarn, R. W. Hannum, and J. R. Sites

Physics Department, Colorado State University
Fort Collins, Colorado 80523

The reflectance spectrum of light normally incident on arbitrary multilayer coatings is calculated by the matrix technique. The purpose is to use the details of the measured spectrum from a reflection enhancing coating to identify an individual layer and the specific parameter (thickness, refractive index, or absorptance) that are responsible for less than optimum peak reflectance. As previously discussed by Bennett and co-workers, the secondary features of the spectrum, particularly the adjacent minima, are more sensitive than the peak to thickness errors; the peak is more sensitive to problems with the index or with absorption. For concreteness, we have defined optimum conditions as those producing the maximum possible reflection at 1.06 μm. We display results for variations in a three layer coating, which is a useful starting point for exploratory experimental work, and for a fifteen layer coating which is nearing the infinite limit for practical coatings.

Key words: absorption; equivalent substrate; extinction coefficient; multilayer coatings; peak reflectance; quarter-wave thickness; refractive index deviation; secondary features; thickness errors; transparent substrate.

1. Introduction

The reflectance spectrum of a multilayer optical coating can be accurately calculated, and often is, by multiplying the 2 × 2 matrices associated with the layers of the coating [1]. Less common, however, is the calculation of reflectance spectra variations with systematic deviations from optimum conditions in one or more layers of a multilayer coating.

In the current work we have mathematically varied the thickness, refractive index or absorption of one of the outer layers of an otherwise ideal reflection enhancing multilayer coating. We have then examined the primary maxima and minima of the resulting spectrum to determine which are most sensitive to these deviations from ideality. For concreteness, we considered coatings with low index of refraction layers at or near 1.48 and with high index at 2.03. Thicknesses were chosen to yield maximum reflection at a wavelength of 1.06 μm, and the substrate was taken to be transparent. We show here results for three layers (high-low-high indices), which is the simplest effective multilayer case, and for fifteen layers. Clearly, however, the general trends shown in the graphs to follow can be applied to other coating parameters.

2. Reflectance Calculation

Following Abelès [1], the reflectance of a system of layers between an incidence medium (index n_o) and transparent substrate (index n_s), shown in figure 1, can be calculated from the characteristic (M) of the coating.

$$(M) = \begin{pmatrix} M_{11} & M_{12} \\ M_{21} & M_{22} \end{pmatrix} = (C_1)(C_2)\ldots(C_j)\ldots(C_s) \qquad (1)$$

The fundamental period matrix (C_j) is related to the Fresnel reflection coefficient r_j and the phase retardation δ_j of each layer such that

$$(C_{j+1}) = \begin{pmatrix} e^{i\delta_j} & r_{j+1}e^{i\delta_j} \\ r_{j+1}e^{-i\delta_j} & e^{-i\delta_j} \end{pmatrix} \qquad (2)$$

For normal incidence, the Fresnel reflection coefficient is defined as

$$r_j = \frac{n_{j-1}-n_j}{n_{j-1}+n_j} \tag{3}$$

The outermost layer is j = 1, that next to the substrate, j = m, and the substrate j = s. $\delta_j = 2\pi n_j d_j/\lambda$ where n_j is the refractive index, and λ is the wavelength of radiation.

Several closed form expressions can be calculated by approximating the matrix calculation [2, 3, 4]. The reflectance of a coated substrate is given by [5]

$$R = \frac{M_{21}M_{21}^*}{M_{11}M_{11}^*} \tag{4}$$

The reflectance can be maximized through the constructive interference of alternating high-low refractive index layers, each one-quarter wavelength thick [6]. That of a glass or quartz substrate (∿4%) can be enhanced to something in excess of 99% for a specific wavelength.

3. Thickness Errors

The calculated reflectance of a three-layer coating is shown in figure 2. The solid line in each case is for three layers, each at exactly one-quarter wavelength for 1.06 µm radiation. The dashed line indicates a layer that is too thick, and the dotted line, one that is too thin. The maximum reflection does not change much (<1%) even with the artificially high 20% deviations shown. As previously noted [7], the minima on either side of the major peak (R_{max}) show large changes in amplitude, especially when one of the high index layers is altered. When the outer layer thickness is too large (fig. 2a), the adjacent low wavelength minimum (L_{min}) decreases nearly to zero, and the high wavelength minimum (H_{min}) increases. With the inner layer (fig. 2c) the opposite is true. For thickness deviations in the middle layer (fig. 2b) the minimum reflectance is nearly unchanged, but the adjacent low wavelength maximum (L_{max}) varies strongly with thickness.

The trends of figure 2 are perhaps better illustrated in figure 3 where the secondary features of the reflectance are plotted as a function of thickness deviation. Since the features are qualitatively different in each case, it should be possible to use the calculated spectrum to identify which layer differs from its ideal thickness.

Fifteen layers (fig. 4) present a more difficult situation for identifying thickness problems, but the general trends persist. The reflectance variations when the outermost layer is varied (fig. 4a) are qualitatively similar to the three layer case. The largest reflectance peak (∿99%) is much narrower. In figure 4b, we see a secondary peak reflectance near 0.5 µm. This peak occurs when the thickness of alternate layers is increased or decreased relative to one another by a total of 20%. This peak is analogous to the enhanced feature of L_{max} at 0.85 µm in figure 4a and becomes more pronounced as the number of thickness altered layers is increased. Moreover, the high envelope at the left-hand side of the secondary peak indicates that all high index layers are too thick. On the contrary, when all the low index layers are too thick, the high envelope appears on the right.

4. Variations in Index

Returning to three layer coatings, variations of the calculated reflectance spectra with refractive index are shown in figure 5. Here the large variations shown are even less likely than 20% thickness variations, but are again depicted to show the trends in the spectra. R_{max} is lowered or raised as the ratio of high to low indices is decreased or increased. Again, however, the behavior of the secondary features differs considerably depending on which layer is affected. For the middle, low index layer (fig. 5b) neither L_{min} nor H_{min} changes significantly with index changes, but L_{max} is enhanced with a smaller high to low index ratio. The coating yields a larger L_{max} with a refractive index increased for any high index layer, but the effect on the minima depends on which layer is altered. When the outer layer index is increased both minima increase, with the inner layer both decrease.

For fifteen layers, the trends of the secondary features are basically the same as for the three layer coating when the outermost layer index is varied. There is relatively little variation in R_{max} and the minima despite the same large variation in refractive index. However, index errors show up significantly at L_{max}. The increase of L_{max} due to index change is about three times of that in the three layer case.

5. Absorption

Absorption in a multilayer coating consists of the effects due to film volume, layer interface, scattering and surface plasmons. For simplicity we assume an ideally smooth surface, which allows us to neglect contributions for the scattering and surface plasmons. Overall absorption can be characterized by the extinction coefficient k which is the imaginary part of the complex refractive index $\bar{n} = n-ik$. k can be defined in terms of the absorption coefficient β by the equation $k = \beta\lambda/4\pi$. Here the calculated reflectance spectra for a three layer coating with and without absorption are displayed in figure 6. As k increases in figure 6, R_{max} and L_{max} decrease while the adjacent minima become more shallow. Such trends also persist for the case of a fifteen layer coating, with larger effects due to the higher number of layers. In contrast to the results of multilayer coatings on metallic substrates [7], we see that R_{max} is more sensitive to absorption variations than L_{min} and H_{min}. The discrepancy can be explained in terms of an equivalent substrate of refractive index $n_s^{\pm}$ [4]. $n_s^{\pm}$ is a dielectric equivalent of the metal substrate and its innermost film layer. This layer differs from quarter-wave thickness to achieve phase compensation between the metallic substrate and other layers of the coating. In general $n_s^{\pm} << n_s$ where n_s is the refractive index of a normal substrate. While the absorption remains comparable at the minima for coatings on both kinds of substrate, $n_s^{\pm}$ gives rise to a smaller amount of absorption at R_{max} than n_s. Eventually, R_{max} becomes less sensitive than the minima to the change in k as appeared in the results of Bennett and Burge [7].

6. Conclusion

In the calculated reflectance spectrum of light normally incident on a multilayer coating, we find that in addition to the primary peak R_{max}, secondary features such as L_{min}, H_{min} and L_{max} can be very informative for determining the ideality of the coating.

For a three layer coating consisting of alternating high and low index dielectrics on a transparent substrate, the reflectances and wavelength locations of the secondary features are good indicators of thickness errors in any individual layer. Uniform refractive index variations in the outer or inner layer gives rise to indistinguishable R_{max} and such cases can only be differentiated on the basis of their secondary features. Furthermore, R_{max} is considerably more sensitive to the index change than to the thickness change. If absorption takes place equally in all layers, and interfacial scattering is neglected, the influence it has on the minima is less than that on R_{max}. Thus, the increase (decrease) of reflectances at the minima (maxima) can indicate the amount of absorption.

Calculated reflectance spectra for fifteen layer coatings reveal trends qualitatively similar to a three layer case when only coating errors in the outermost layers are considered. Due to the large number of layers, little difference appears in the characteristics of the secondary features for errors among the three outer layers. R_{max} is narrow and its magnitude is close to one. Absorption raises the minima and lowers the maxima. The secondary maximum is enhanced to form a distinctive peak, if the high and low index layers are alternately too thick and too thin.

Acknowledgement

This work was supported under the grant from Air Force Weapons Laboratory Contract F-29601-82-K-0009.

References

[1] Abelès, F. Sur la propagation des ondes electromagnétiques dans les milieux stratifiés. Ann. Phys. 5, 505 (1950).

[2] Giacomo, P. Propriétés chromatiques des couches réfléchissantes multi-diélectriques. J. Phys. Rad. 19, 307 (1958).

[3] Sparks, M. A simple method for calculating the optical properties of multilayer-dielectric reflectors. J. Opt. Soc. Am. 67, 1590 (1977).

[4] Bennett, H. E.; Burge, D. K. Simple expressions for predicting the effect of volume and interface absorption of scattering in high-reflectance or antireflectance multilayer coatings. J. Opt. Soc. Am. 70, 268 (1980).

[5] Heavens, O. S. Optical Properties of Thin Solid Films. London; Butterworth; 1950. 72 p.

[6] Macleod, H. A. Thin Film Optical Filters. New York; Elsevier; 1969. 4 p.

[7] Bennett, H. E.; Burge, D. K. Limits to the validity of evaluating a quarter-wave, high reflectance multilayer through analysis of its secondary structure. 13th symp. on optical materials for high power lasers; Boulder, 1981.

[8] Pulker, H. K. Optical losses in dielectric films. Thin Solid Films 34, 343 (1976).

[9] Loomis, J. S. Absorption in coated laser windows. Appl. Opt. 12, 877 (1973).

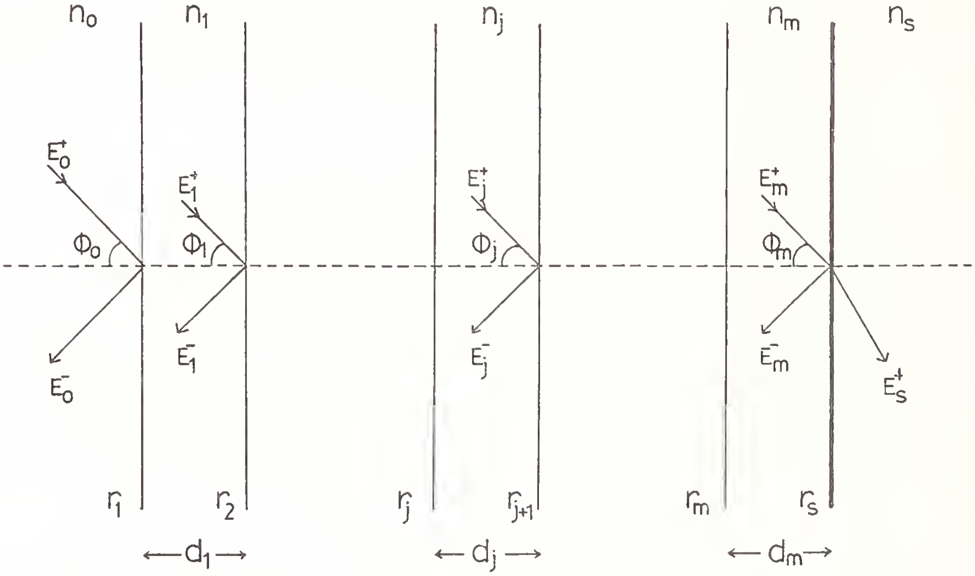

Figure 1. Structure of a multilayer coating.

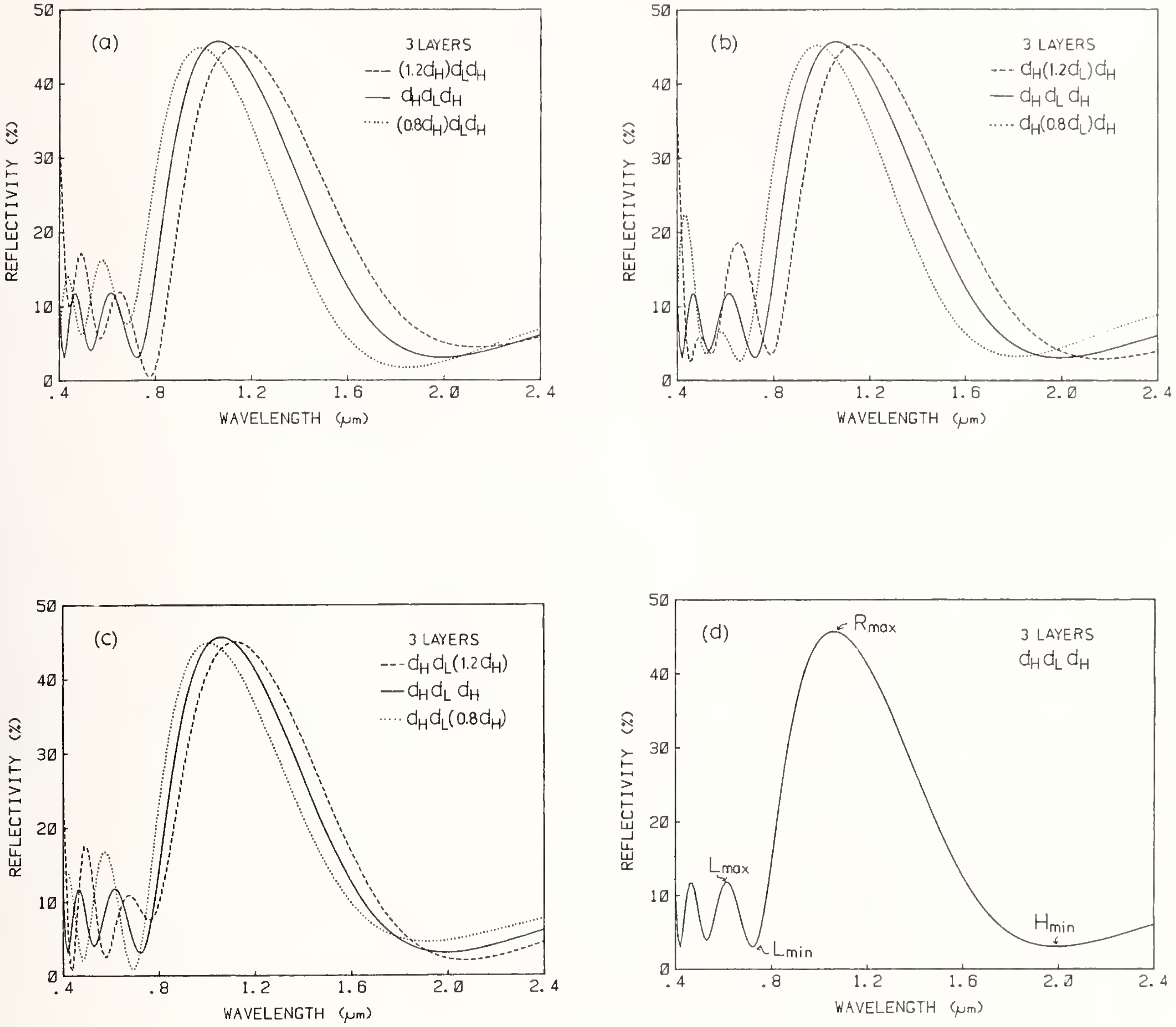

Figure 2. Calculated reflectance spectra for thickness variations of: (a) the outer layer, (b) the middle layer, (c) the inner layer, and (d) with no variations. d_H = 1.06 μm/4n_H, d_L = 1.06 μm/4n_L where n_H = 2.03, n_L = 1.48.

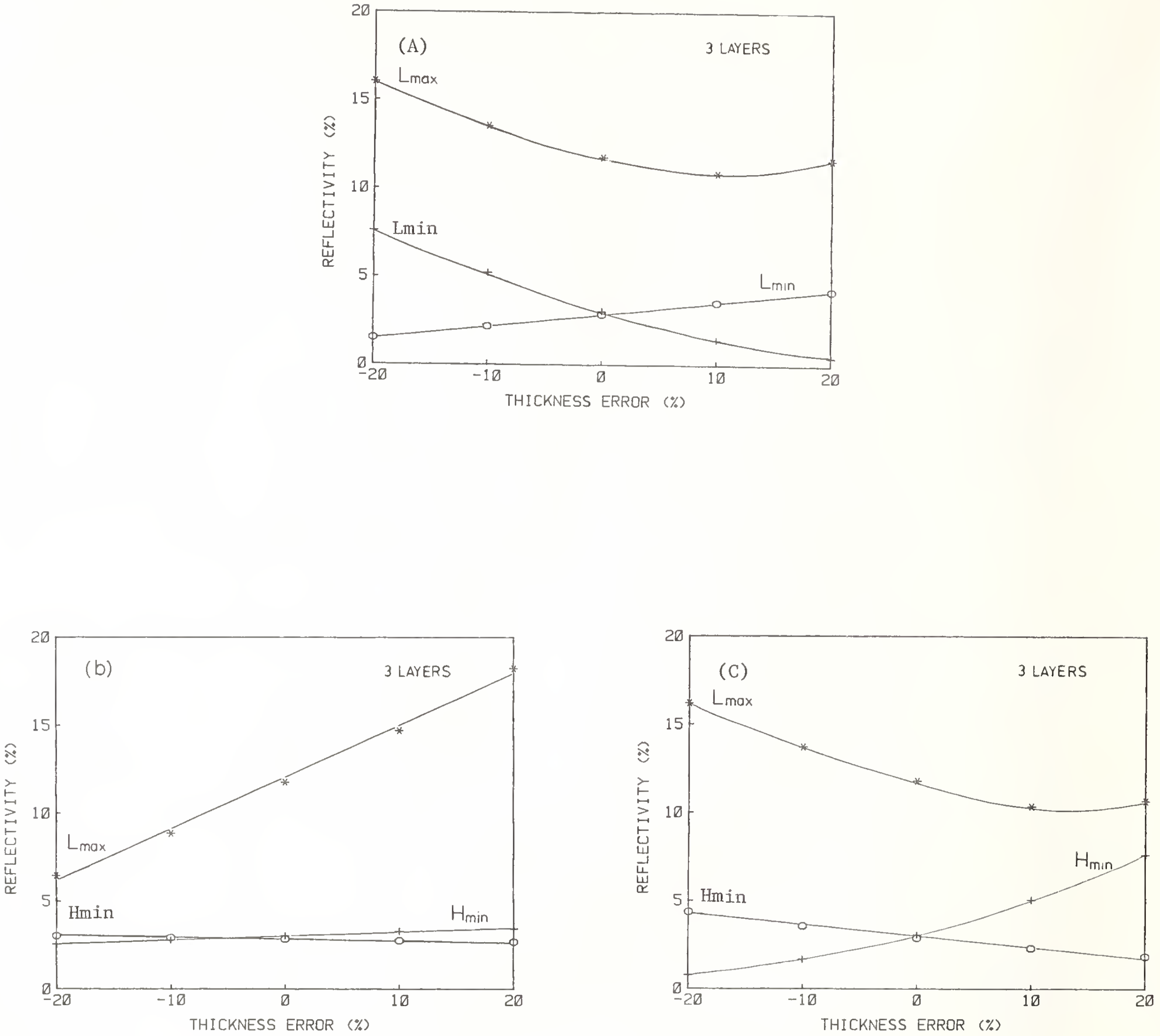

Figure 3. Reflectances of the secondary features vs. thickness deviation of: (a) the outer layer, (b) the middle layer, and (c) the inner layer.

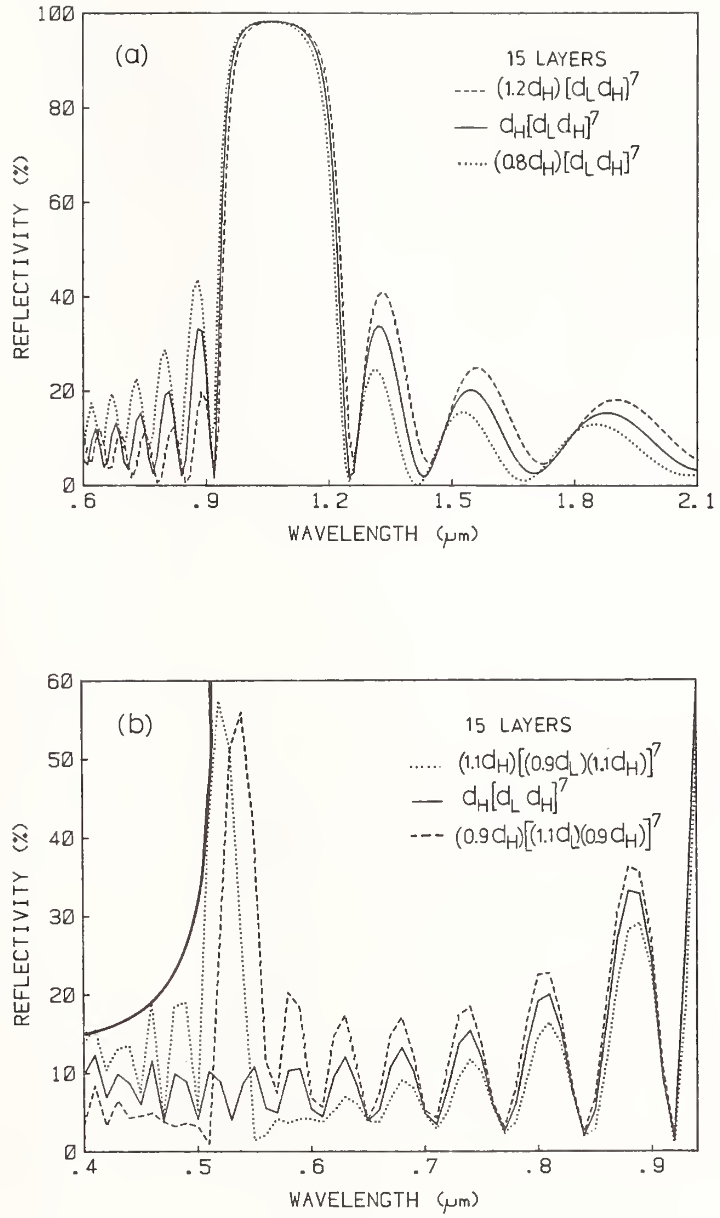

Figure 4. Calculated reflectance spectra of a fifteen layer coating when (a) only the outer layer thickness is altered (by 20%), and (b) all the layer thicknesses are altered (each by 10%).

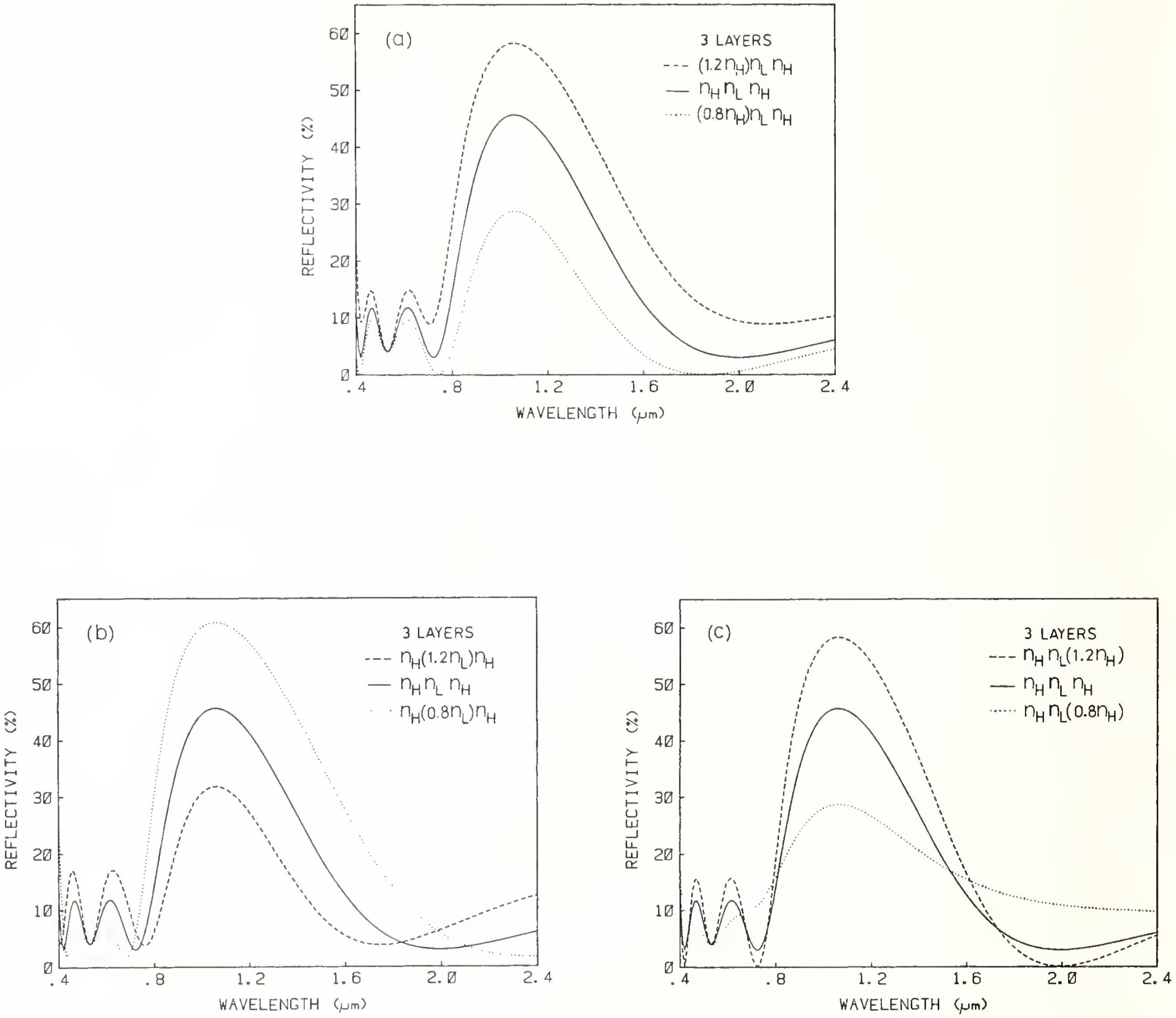

Figure 5. Calculated reflectance spectra for refractive index variations of: (a) the outer layer, (b) the middle layer, and (c) the inner layer. n_H = 2.03 and n_L = 1.48.

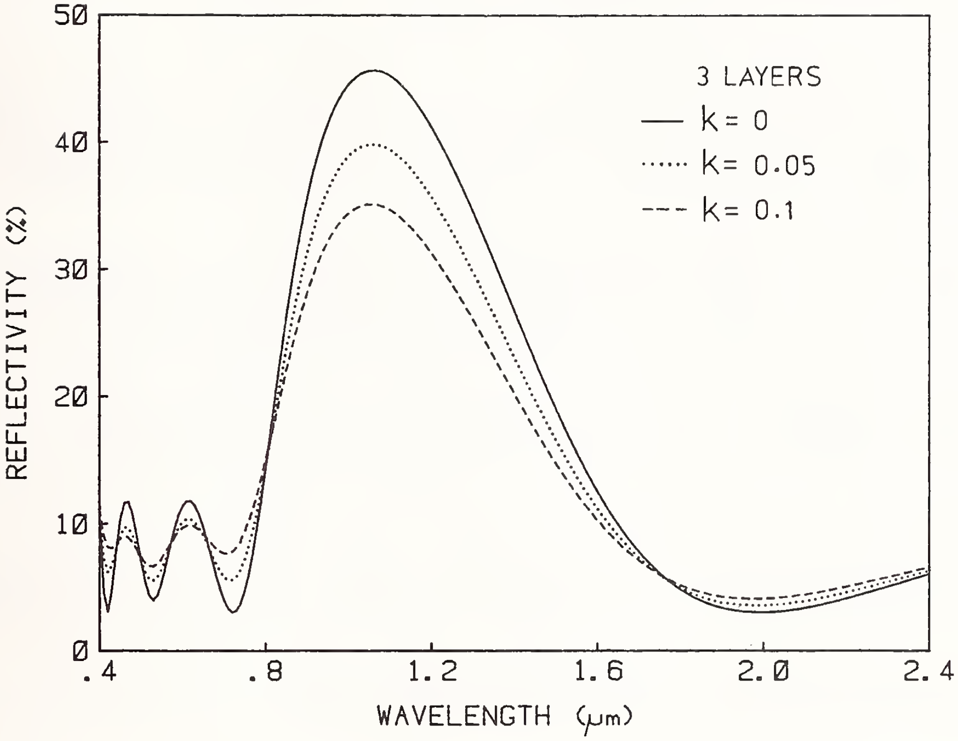

Figure 6. Calculated reflectance spectra of a three layer coating without absorption and with absorption for two different values of extinction coefficient.

Environmental Study of Single and Multilayer Dielectric Films for 2.8 (μ) Subjected to Humidity, Ethanol, HF, and H_2S

James R. Palmer

TRW
One Space Park, Redondo Beach, California 90277

This study was conducted in order to evaluate the response of various coatings on various first layer metals when subjected to 95% relative humidity at 35°C, 95% saturated ethanol vapor at 35°C, 10% by volume of HF and H_2S.

The study is conducted in two phases. In the first phase, four (4) sample single layer dielectric coatings on a silver base layer, deposited on a molybdenum substrate, were evaluated The coatings consisted of SiO with a thickness < 283 Å and ZnS with coating thickness values of 314Å and 5244Å, and 5473Å. The samples were subjected to Humidity, liquid water, HF, and H_2S in series. Reflectance and scatter measurements were made on the samples before and after each environment.

In the second phase, forty-eight combinations of single layer films on metals and six multilayer dielectrics on a silver alloy was evaluated using a double blind test. One matrix of the twenty four configurations were subjected to the environments in series. One matrix was subjected to each environment independently.

Each coating sample was examined under the microscope and a photograph made at 5x and 400x. After each run, the sample was again examined and photographed. Additionally, another matrix was subjected to mechanical tests of eraser rub, cheese cloth, tape, and a spectrophotometric scan to determine any H_2O or OH absorption.

Photographs from the first phase of the study and optical changes as a function of environment are shown graphically in the paper. The details of the coating chemistries and test plan for evaluation are discussed and the results and conclusions are presented.

Key Words: coating chemistry; coating damage; defect damage; HF, NH_3, H_2S environments; mirror damage; single layer , multilayer dielectric coatings.

Introduction

A large number of single and multilayer dielectric coatings were produced on one inch diameter float glass substrates. A very small selection of samples were produced on one and a half inch diameter molybdenum substrates. The coatings and mechanical testing were provided by OCLI. The Molybdenum substrates were tested and measured at Naval Weapons Center China Lake. The float glass coated samples were tested and evaluated at TRW. Additional testing was performed on samples including NH_3, air conditioned air, and outside air environments. The results of the tests performed on the float glass are shown in figures 1.0, 2.0, and 3.0, in tabular form. The results of the tests and measurements performed at the Naval Weapons Center are shown in figures 4.0 and 5.0.

The results of the environmental tests at the Naval Weapons Center show that reflectivity and scatter change in moderate fashion for all the tests through HF. However, there is a demonstrable change in both reflectivity and scatter when the samples were subjected to wet H_2S. There has been some criticism of the wet H_2S environment as being too severe. However, the test does provide a substantial bound to the types of conditions that the coatings and substrate metals may be able to withstand.

Essentially, the single layer dielectric coatings on the float glass did not withstand the various environments very well. Except for Al_2O_3 and SiO all of the oxide coatings failed the OCLI spectrophotometric absorption measurement, i.e., the oxide coatings manifested an absorption greater than 5%. Single layer Al_2O_3 and ZnS on Au, Cu, and Al proved superior in their resistance to chemical response to the various environments. With the exception of $Ag/(ThF_4/Zn\ Se)^5$, the multilayer dielectric coatings demonstrated substantial resistance to the effects of the various environments.

For the most part, coatings that were subjected to the outside air indicated substantial chemical activity after one week of exposure. Some of the effects were very dramatic. Because of the chemical makeup of the air, however, this environment is much too stringent and is not regarded as a real application environment that one would encounter in most normal operating conditions.

The NH_3 environment had a substantial effect on MgF_2/Cu, bare Cu, Si/Ag alloy and $ZrO_2Y_2O_3$/Ag alloy. The remainder of the samples indicated no changes after two hours in the environment.

Continued experiments with samples that are maintained in an air conditioned environment indicate that there will be chemical activity early on; or, there will be no activity at all. Each week, the samples are cleaned, i.e., ethanol is allowed to stay on the coated surface for two minutes. The surfaces are cleaned using a cotton swab. The surfaces are blown clean with dry nitrogen. After the first two weeks, minor changes were noticed at pre-existing defect areas on Al_2O_3/Au and ZnS/Au. No other areas of the coating appeared to be affected. MgF_2/Cu, bare Cu, and most all of the Ag alloy based single layer dielectric coatings manifested substantial changes in the Al_2O_3 and ZnS. Additionally, there have been no changes in any of the other coatings which were unaffected from the outset.

There were two phases to this study. The first phase involved ZnS/Ag/Mo, SiO/Ag/Mo and Ag/Mo. The SiO/Ag coating was on the order of 283°A of thickness. There were three (3) coating thickness values for the ZnS/Ag/Mo: 314 A, 5244 A°, and 5473 A°.

This first set of samples were placed in storage for one month after first undergoing characterization for reflectivity and total integrated scatter. After the samples were removed from storage they were again characterized for reflectivity and scatter. Each sample was subjected to each of the environments in series. The first environment was humidity. The test required 95% saturated vapor at 35°C. The samples were allowed to stay in the environment for half an hour. At the end of the half hour, the samples were measured for reflectivity and scatter. If there was a change of less than 0.1% the sample was re-introduced for one hour. If there was a change $> 0.1\% < 0.15\%$ the samples were re-introduced for one-half hour. If there was a change $> 0.15\%$ the sample was no longer subjected to this test and was prepared for the next environment.

The second environment consisted of placing de-mineralized water on the surface for one-half hour. After the half-hour was complete, the surface was blown dry with dry nitrogen and evaluated for reflectivity and scatter. According to the criteria indicated above, the samples were, or were not re-introduced to the environment. The thin ZnS demonstrated substantial staining at the end of the first half hour.

The third environment was a mixture of 10% by volume of HF in nitrogen. Ten seconds were allowed for the mixture to be introduced and completely diffuse in the bomb. The samples were allowed to continue in the environment for twenty seconds of residence time. Ten seconds were allowed for purging the HF-nitrogen mixture from the bomb. This environment was continued for two cycles. Reflectivity and scatter measurements were made at sixteen hour and forty hour intervals.

The last environment, and perhaps the most severe, was a 10% by volume of H_2S in nitrogen with a relative humidity of 95% at 35°C. The samples were subjected to the same cycle duration as the HF. The same criteria for evaluation was employed. The samples were only introduced into this environment for two cycles. The results of this phase of the experiment are shown in figures 4.0 and 5.0.

The second phase of this experiment used float glass samples with a multiplicity of coating and metal chemistries. The material combinations that were selected for this experiment are:_

SLDC

Au/AL_2O_3, Au/Si, Au/ZnS, Au/MgF_2, Au/CeO_2, Au/ZrO_2, Au/Y_2O_3

Cu/AL_2O_3, Cu/MgF_2

AL/AL_2O_3, AL/MgF_2, AL/ZrO_2

Ag/Si, Ag/MgF_2

Ag ALLOY/MgF_2, Si, CeO_2, ZrO_2, ZnS, $ZrO_2Y_2O_3$, AL_2O_3

MLDC

$Au/(AL_2O_3/ZnS)^5$, $Au/(SiO/Si)^5$
$Cu/(AL_2O_3/ZnS)^5$, $Cu/(SiO/Si)^5$
$AL/(SiO/Si)^5$, $AL/(AL_2O_3/ZnS)^5$
$Ag/(ThF_4/ZnSe)^5$, Ag ALLOY$(SiO/Si)^5$, Ag ALLOY$(AL_2O_3/ZnS)^5$

The selection criteria used by OCLI for determining which coating and metal combinations would be most suitable, were:_

DIELECTRICS	METALS
INDEX OF REFRACTION	CHEMICAL REACTIVITY
ABSORPTION (OH)	REFLECTIVITY AT 2.8 μm - R > 95%
PACKING DENSITY	ADHERENCE
STRESS	HARDNESS
CHEMICAL REACTIVITY	

Unlike the first phase of this experiment, the second phase was undertaken to evaluate a large selection of metals and coating combinations on the basis of chemical activity, rather than optical changes. There were a total of twenty-four different metal-coating combinations. There were twenty-four sets of these samples produced for this experiment.

This set of experiments was set up as a double blind test. One set of samples was introduced to each set of environments in series. Another set of samples were introduced to each environment independently. In this manner, any chemical activity would be distinguished as being a function of the individual environment or a cumulative effect of one environment to another. The result of this technique produced an interesting outcome in that those chemistries that were deemed to have failed did so on both the serial and independent sample simultaneously. None of the failed chemistries did so independent of the other like chemistry for any given environment. A schematic of the double blind test is shown in figure 6.0.

The test set-up is shown in figures 7.0 and 8.0. The samples were placed on stacked sheets of wire mesh on a central rod. The forty-eight specimens were placed on the screens and the complete set was inserted into special bell jar with a stopper at the mouth. The gas lines were inserted through the stopper. The bell jar was then suspended in a water bath to maintain a constant temperature commensurate with the gas temperature to preclude condensation on the samples or bell jar walls. The respective gas environment was passed through a heat transfer coil which was immersed in the water bath to insure the proper temperature of 35°C.

At the outset, all of the samples were examined with a microscope and photographed at 5x and 400x. The surfaces were scanned to find any outstanding defects in the coating. The position of such defects were marked on an X-Y coordinate system so that any chemistry that resulted in these areas would be disregarded after the samples had been submitted to the environments. All 576 samples were characterized and photographed in this manner and the photographs were placed in lab books.

The serial and independent samples were subjected to the humidity test, first Four (4) one-half hour tests were conducted. After each half hour test, the samples were examined under the microscope and scanned at 5x. Any areas that became suspect were then examined at 400x. Following the test, the independent samples were vacuum bagged with desiccant and stored.

The ethanol was introduced with nitrogen to a 95% saturation level at 35°C. This technique is less severe than placing liquid water on the surface; however, it was felt that subjection of the samples to two hours of saturated vapor at 35°C would be more consonant with actual operational procedures. The same procedure for evaluation was used to determine pass or fail.

For the HF test, pre-mixed bottled gas was used. The HF was 10% by volume in nitrogen. The samples were subjected to four twenty second cycles. Again, the temperature was maintained at 35°C. This test was utilized to reproduce an upset condition in a device which would spray HF gas onto operating optics. The same procedure for evaluation of the coatings was used.

The H_2S test also used 10% by volume in nitrogen pre-mixed bottle gas. The samples were subjected to four cycles of twenty seconds each. The temperature was maintained at 35°C. Unlike the previous phase of this experiment, the H_2S in nitrogen was maintained in the dry condition. The dry condition was regarded as more representative of the actual conditions that may be expected. Again, the same conditions for evaluation and discriminating were used.

The results of the OCLI mechanical, and spectrophotometric tests, along with the TRW environmental results, are shown in tabulated form in figures 1.0, 2.0, and 3.0.

Additional tests were performed on the sample sets. One set of twenty four samples were placed in a cage, on screens, and placed on the roof of a TRW building in El Segundo, Ca. The samples were protected from sunlight so that a photochemical process would not be introduced into the problem. A startling result confronted the investigators after the first week. Almost all of the samples manifested substantial deleterious effects. The experiment continued for two additional weeks and the deterioation of the coatings continued for this period of time. After reviewing the average chemistry of the air at the locality, which contained substantial PPM of ozone, this test was determined to be much too stringent for the actual conditions that the coatings would be expected to experience.

One set of samples was subjected to 99% saturated NH_3 in 1% wet nitrogen for thirty minutes, at 35°C. MgF_2/Cu, bare Cu, Si/Ag ALLOY and $ZrO_2Y_2O_3$/Ag ALLOY indicated substantial change after the first half-hour run. Three additional half-hour runs were made and none of the other samples indicated any changes. One may conclude from these results that, for the most part, the coatings are resistant to slightly moist NH_3.

The last portion of this phase of the experiment, which is still ongoing and may ultimately be the most important, is the air conditioned environment. One set of samples were placed on screens in an isolated air conditioned room. The room temperature is maintained at 68°F ± 5°. The humidity is maintained at 40% ± 5%. No one goes into the room except once a week when the samples are removed for examination and photographing and returned to the room. The samples are microscopically examined at 5x and 400x.

After the first two weeks, minor changes were noticed at pre-existing defect areas on AL_2O_3/Au and ZnS/Au. No other areas of the coating appeared to be affected. MgF_2/Cu, bare Cu, and most all of the Ag ALLOY based single layer dielectric coatings indicated substantial changes. However, in the eight weeks since the first examination, there has been no additional deterioation of the Al_2O_3/Au or ZnS/Au. Additionally, outside of the coatings that initially failed, there has been no change in the remaining samples.

In recent weeks, the experiment has been expanded in that each sample is subjected to reagent grade ethanol placed on the coating surface for two minutes. After the two minute internal, the coating surface is cleaned with a cotton swab. The ethanol is blown from the surface with dry nitrogen and the surface is examined under the microscope. The only sample that has suffered deleterious effects is the evaporated bare gold. After the first series of ethanol rub, the gold coating manifested severe scratch lines.

At the end of this paper there are a number of photographs of the various coatings that have failed under various environments that have been discussed. The result of these experiments has been to narrow the field of suitable metal and coating candidates that may be used in this particular application. A very important result of these various situations relates to the care that must be taken with optics, that have similar coatings, when used in laser optical systems.

Acknowledgements

This work was supported by DARPA. The author would like to give special recognition to Michael Kenney for his efforts in preparing and photographing the test specimens.

RUN #	CHEMISTRY DIELECTRIC THICKNESS	50 RUB CHEESECLOTH	20 RUB ERASER	TAPE TEST	TAPE 50 TEST RUB	HUMIDITY	TAPE 50 TEST RUB	BAKE	% A65 028	CONSECTUTIVE	TRW HUMIDITY	TRW ETHANOL	TRW HF	TRW H_2S	TRW ENVIRONMENT		
1016 693-1	Cr/Au/ZnS THIN	F	F	P	PF	F			1%		P	P	P	P	F		
693-2	Cr/Au/ZnS THICK	P	F	P	PP	P	PP		1%		F	F	F	P	F		
693-3	Cr/Au/Al_2O_3 THIN	P	P	P	PP	P	PF		1%		P	P	P	P	F		
693-4	Cr/Au/Al_2O_3 THICK	P	P	P	PP	P	PP		1%		P	P	P	P	F		
694-1	Cr/Au/CeO_2 THIN	F	F	P	PF	P	P		>5%		P	P	P	P	F		
694-2	Cr/Au/CeO_2 THICK	P	F	P	PF	P	P		>5%		P	P	P	P	P		
694-3	Cr/Au/Si THICK	P	F	P	PP	P	PP		1%		P	P	P	P	F		
694-4	Cr/Au/Si THIN	P	F	P	PP	P	PP		1%		P	P	P	P	F		
695-1	Cr/Au/MgF_2 THIN	P	F	P	PP	P	PP		5%		P	P	P	P	F		
695-3	Cr/Cu/MgF_2 THIN	F	F	P	PP	F			5%		P	P	P	F	F		
695-4	Cr/Cu/MgF_2 THICK	P	F	P	PP	F			5%		P	P	P	F	F		
696-1	Cr/Au/ZrO_2 THIN	F	F	F	F				>5%		P	P	P	P	F		
696-2	Cr/Au/ZrO_2 THICK	P	F	P	PP	P	PP		>5%		P	P	P	P	P		
696-3	Cr/Au/Y_2O_3 THIN	P	F	P	PP	P	PP		>5%		P	P	P	P	F		
696-4	Cr/Au/Y_2O_3 ZrO_2 THICK	P	P	P	PP	P	PP		>5%		P	P	P	P	F		
697-1	Al/MgF_2 THIN	P	F	P	PP	P	PP		5%		P	P	P	P	F		
697-2	Al/MgF_2 THICK	P	P	P	PP	P	PP		5%		P	P	P	P	F		
697-3	Al/ZrO_2 THIN	P	F	P	PF	P	P				P	P	P	P	F		
697-4	Al/ZrO_2 THICK	P	P	P	PP	P	PP				P	P	P	P	P		

Figure 1.0

RUN #'	CHEMISTRY DIELECTRIC THICKNESS	50 RUB CHEESECLOTH	20 RUB ERASER	TAPE TEST	TAPE 50 TEST RUB	HUMIDITY	TAPE 50 TEST RUB	BAKE	% AbS 028	CONSECUTIVE	TRW HUMIDITY	TRW ETHANOL	TRW HF	TRW H_2S	TRW ENVIRONMENT		
1016 698-1	Cr/Cu/Al_2O_3 THIN	F	F	P	PF	P	PP		1%		P	P	P	P	F		
698-2	Cr/Cu/Al_2O_3 THICK	P	F	P	PP	P	PP		1%		P	P	P	P	P		
698-3	Al/Al_2O_3 THIN	P	F	P	PP	P	PP		1%		P	P	P	P	P		
698-4	Al/A_2O_3 THICK	P	P	P	PP	P	PP		1%		P	P	P	P	P		
699-1	Cr/Au/$(Al_2O_3/ZnS)^5$	P	F	F	PP	P	F	P	1%	T2	P	P	P	P	F		
699-2	Cr/Au/(SiO/Si) 5	P	P	P	PP	P	PP	P	1%	P	P	P	P	P	F		
699-3	Cr/Au	F	F	P	PP	P	P	P		C1	P	P	P	P	F		
700-1	Cr/Cu/$Al_2O_3/ZnS)^5$	P	F	P	PP	P	FF	P	1%	T2	P	P	P	P	P		
700-2	Cr/Cu/$(SiO/Si)^5$	P	P	P	F	P		P	1%	T2	P	P	P	P	F		
700-3	Cr/Cu	F	P	P	PF			F		C1	P	P	P	F	F		
701-1	Al/$(Al_2O_3/ZnS)^5$	P	F	P	PP	P	F	P	1%	T2	P	P	P	P	P		
701-2	Al$(SiO/Si)^5$	P	P	P	PP	P	PP	P	1%	P	P	P	P	P	F		
701-3	AL	F	P	P	PP	P	P	P		C1	P	P	P	P	F		
712-1	Ag/$(ThF_4/ZnSr)$ 5 ·	F	F			P		P	1%	T1	P	F	P	P	F		
712-2	Ag/Si .26	P	F			P		P	1%	T1	P	P	P	P	F		
712-3	A_S/Si .05	F	F			P		P	1%	T1	P	P	P	P	F		
712-4	Ag/MgF_2 .11	P	F			P		P	4%	T1	P	P	P	P	F		

Figure 2.0

RUN #	CHEMISTRY DIELECTRIC THICKNESS	50 RUB CHEESECLOTH	20 RUB ERASER	TAPE TEST	TAPE 50 TEST RUB	HUMIDITY	TAPE 50 TEST RUB	BAKE	% AG5 028	CONSECTUTIV	TRW HUMIDITY	TRW ETHANOL	TRW HF	TRW H_2S	TRW ENVIRONMEN		
1001 -	ALL CHEMS BELOW + Ag/Alloy																
2125	MgF_2 .126	F	F			P		P	>5%	T1	P	P	P	P	F		
2126	MgF_2 .63	P	F			F		P	>5%	T1	F	F	F	F	F		
2127	Si .049	F	F			F		P	1%	T1	F	F	F	F	F		
2128	Si .245	P	F			P		P	1%	T1	P	P	P	P	F		
2129	CeO_2 .085	F	F			F		P	4%	T1	P	P	P	F	F		
2130	CeO_2 .43	F	F			F		F	4%	T1	P	P	P	F	F		
2131	ZrO_{25} .087	F	F			P		P	>5%	T1	P	P	P	P	F		
2132	ZrO_2 .44	P	F			P		P	>5%	T1	P	P	P	P	F		
2133	ZnS L073	F	F			P		P	4%	T1	P	P	P	P	F		
2134	ZnS .37	P	F			P		P	4%	T1	P	P	P	P	F		
2135	$ZrO_2Y_2O_3$ .096	F	F			P		P	>5%	T1	P	P	P	P	F		
2136	$ZrO_2Y_2O_3$ .48	P	F			P		P	>5%	T1	P	P	P	P	F		
2137	Al_2O_3 .10	P	F			P		P	5%	P	P	P	P	P	F		
2138	Al_2O_3 .51	P	F			F		F	5%	T1	P	P	P	P	F		
2139	$(SiO/Si)^5$	P	P			P		P	4	T2	P	P	P	F	F		
2140	$(Ag_2O_3/ZnS)^5$	P	F			P		P	4	P	P	P	P	P	F		

Figure 3.0

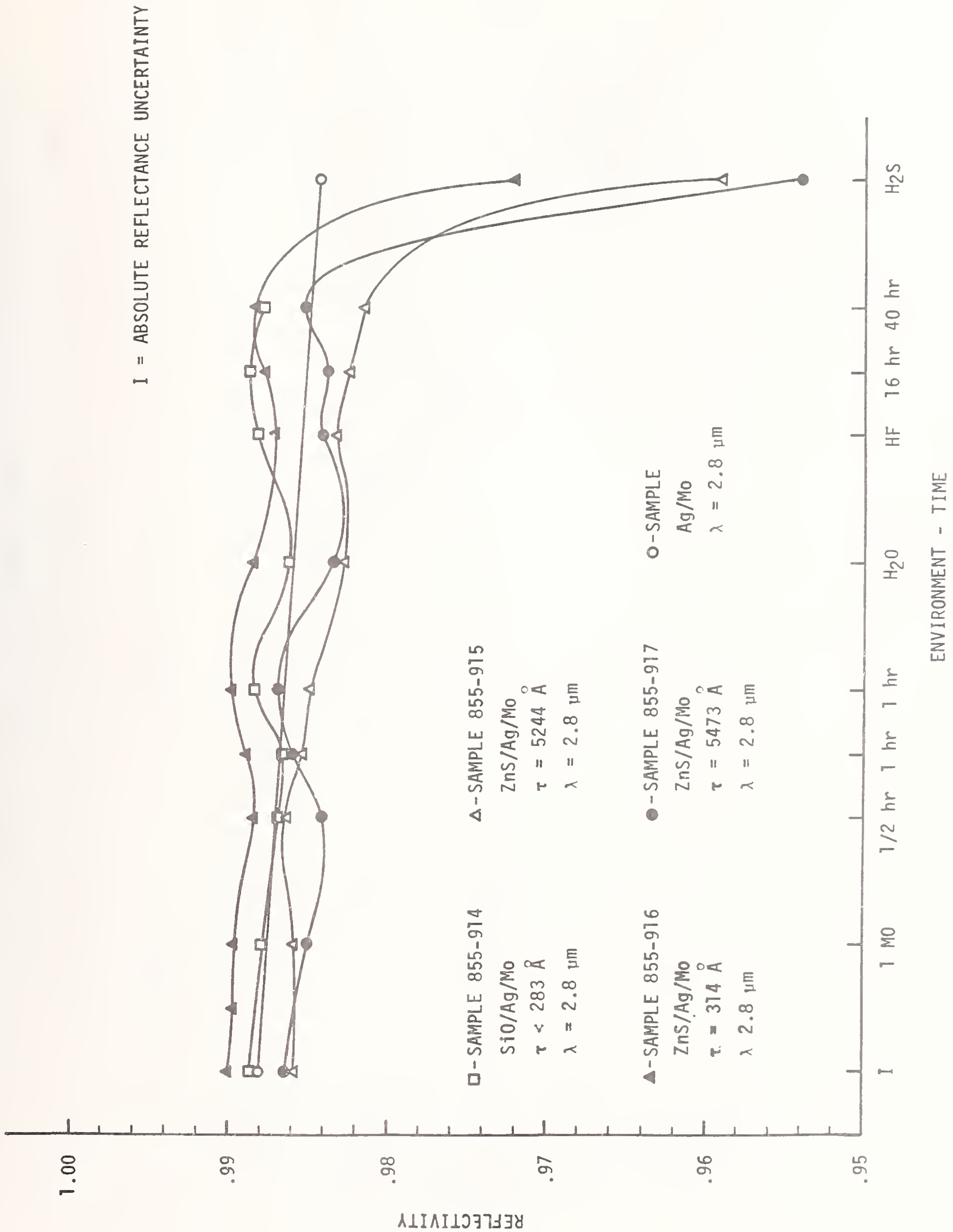
I = ABSOLUTE REFLECTANCE UNCERTAINTY
REFLECTIVITY
1.00
.99
.98
.97
.96
.95
I
1 MO
1/2 hr
1 hr
1 hr
H_2O
HF
16 hr
40 hr
H_2S
ENVIRONMENT - TIME
□-SAMPLE 855-914
SiO/Ag/Mo
τ < 283 Å
λ = 2.8 μm
△-SAMPLE 855-915
ZnS/Ag/Mo
τ = 5244 Å
λ = 2.8 μm
▲-SAMPLE 855-916
ZnS/Ag/Mo
τ = 314 Å
λ 2.8 μm
●-SAMPLE 855-917
ZnS/Ag/Mo
τ = 5473 Å
λ = 2.8 μm
○-SAMPLE
Ag/Mo
λ = 2.8 μm

Figure 4.0

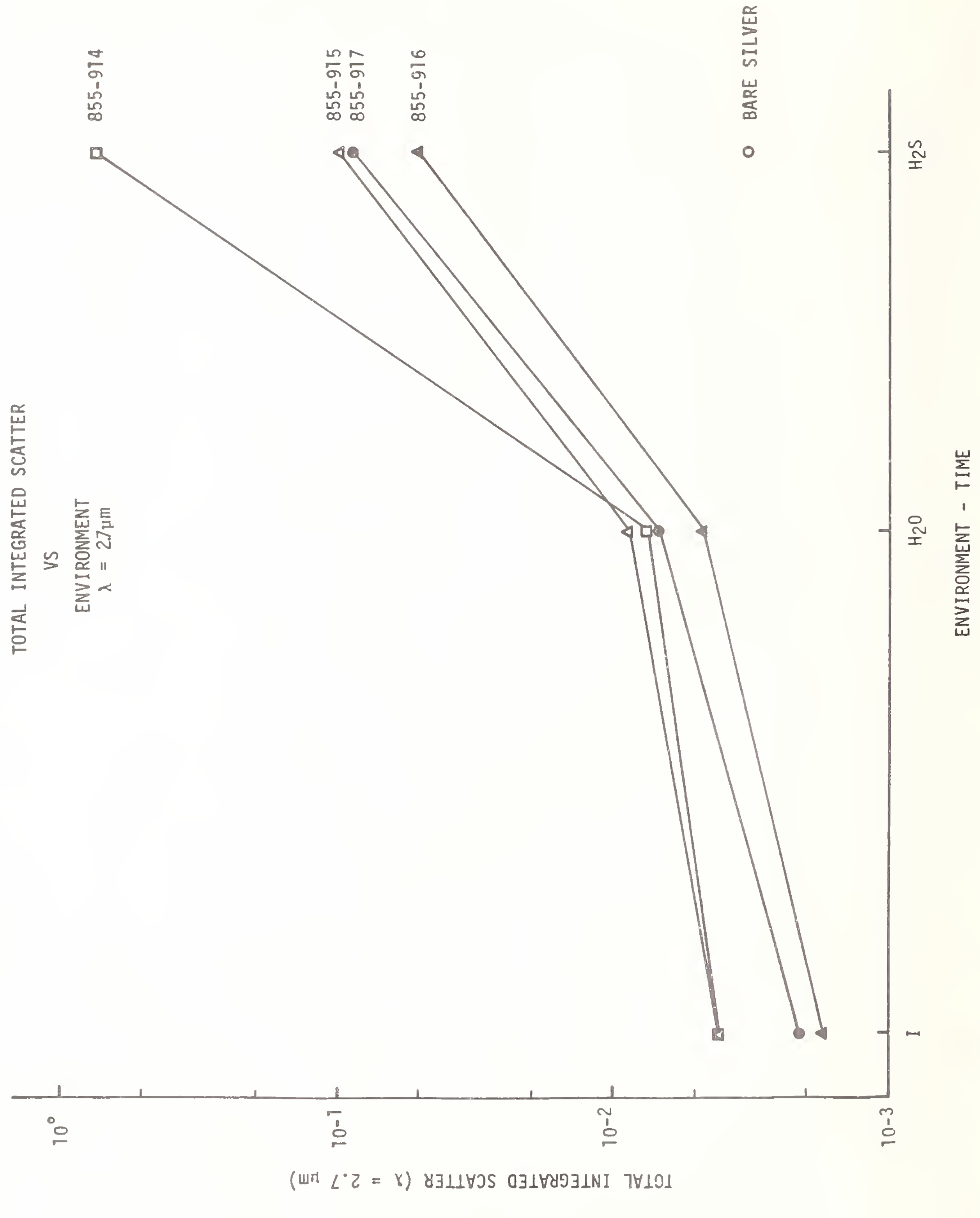
TOTAL INTEGRATED SCATTER
VS
ENVIRONMENT
λ = 2.7μm
855-914
855-915
855-917
855-916
○ BARE SILVER
10^0
10^{-1}
10^{-2}
10^{-3}
TOTAL INTEGRATED SCATTER (λ = 2.7 μm)
I
H_2O
H_2S
ENVIRONMENT - TIME

Figure 5.0

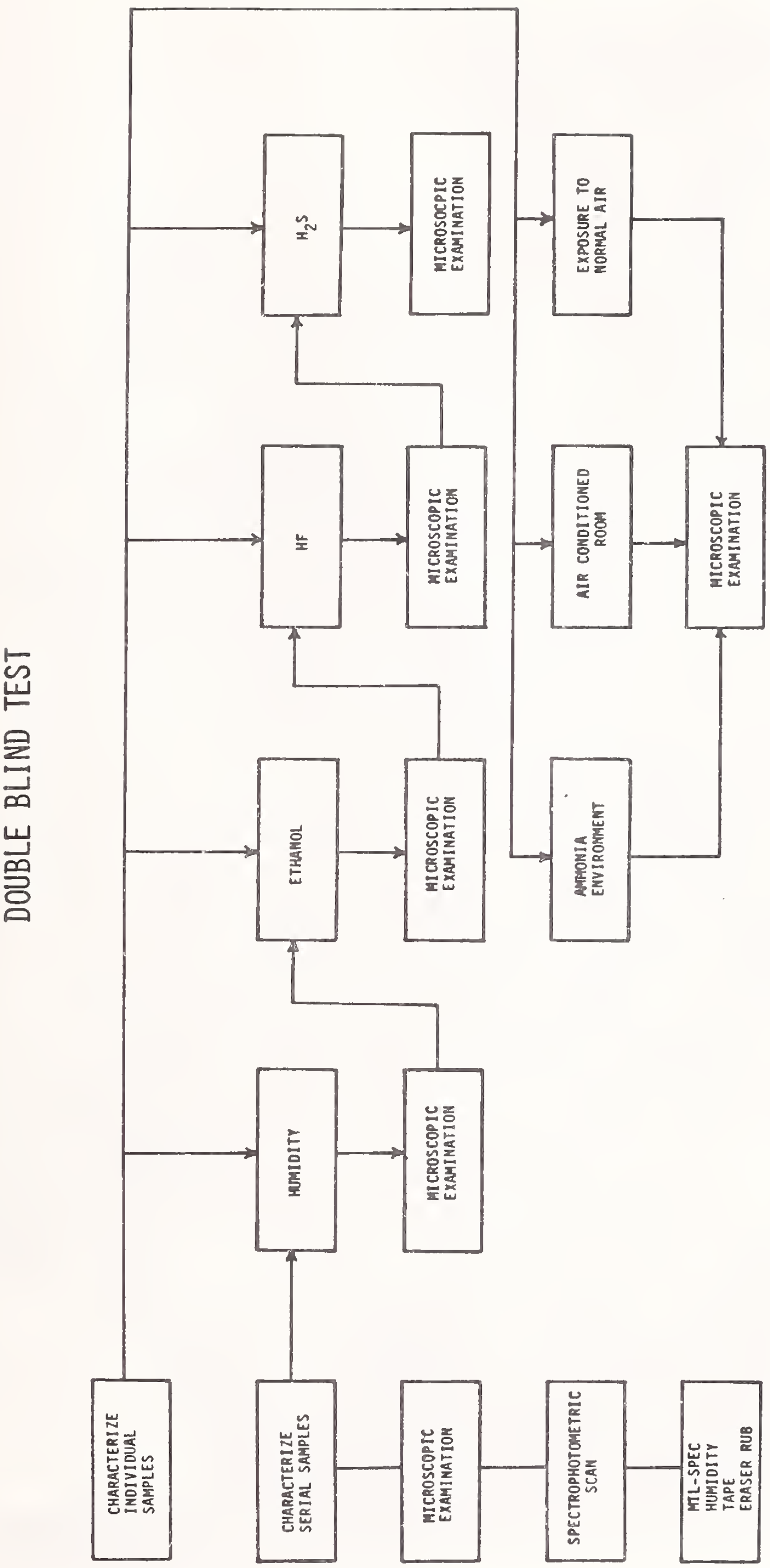
DOUBLE BLIND TEST
CHARACTERIZE INDIVIDUAL SAMPLES
CHARACTERIZE SERIAL SAMPLES
MICROSCOPIC EXAMINATION
SPECTROPHOTOMETRIC SCAN
MIL-SPEC HUMIDITY TAPE ERASER RUB
HUMIDITY
MICROSCOPIC EXAMINATION
ETHANOL
MICROSCOPIC EXAMINATION
AMMONIA ENVIRONMENT
HF
MICROSCOPIC EXAMINATION
AIR CONDITIONED ROOM
MICROSCOPIC EXAMINATION
H_2S
MICROSOCPIC EXAMINATION
EXPOSURE TO NORMAL AIR

Figure 6.0

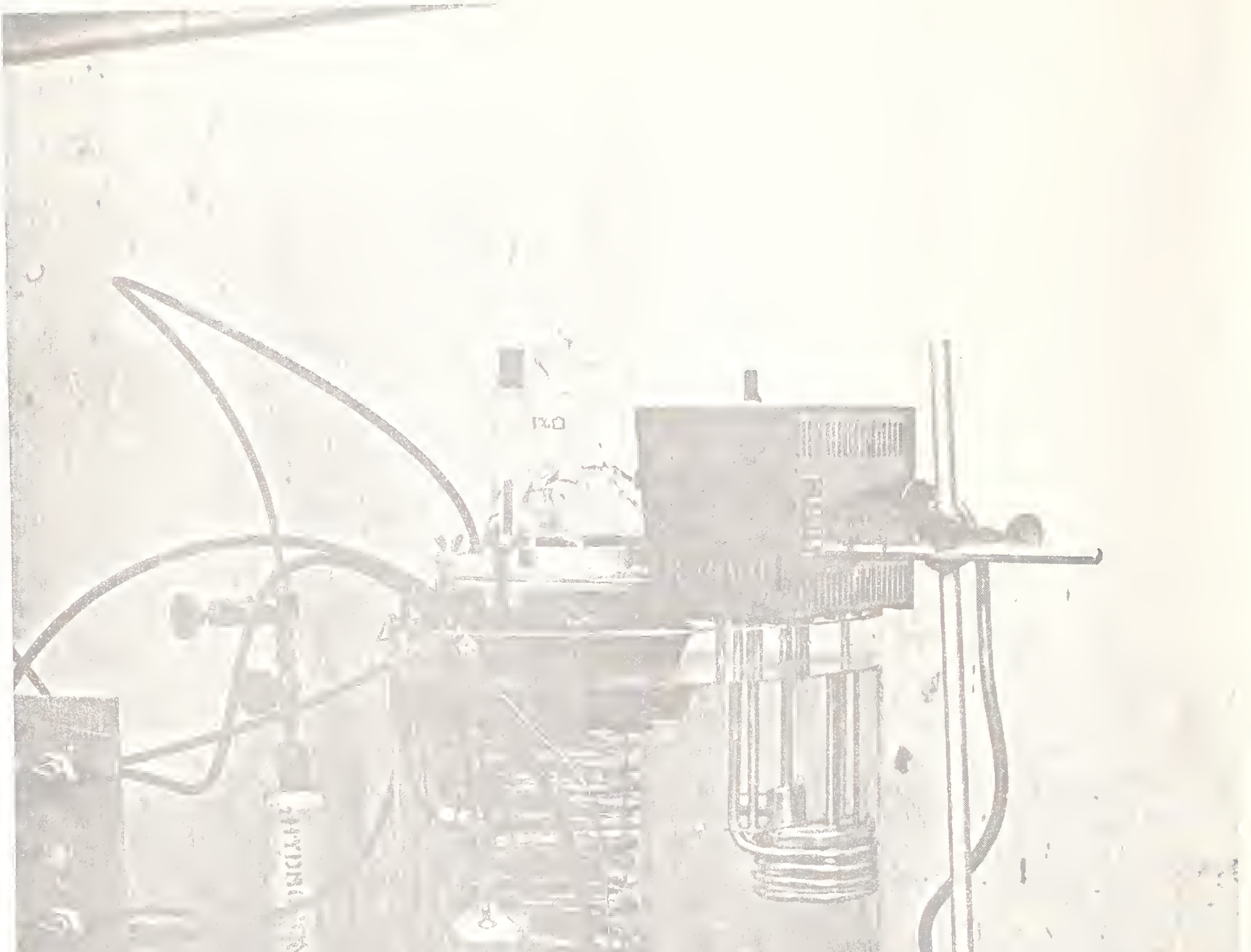

Figure 7.0

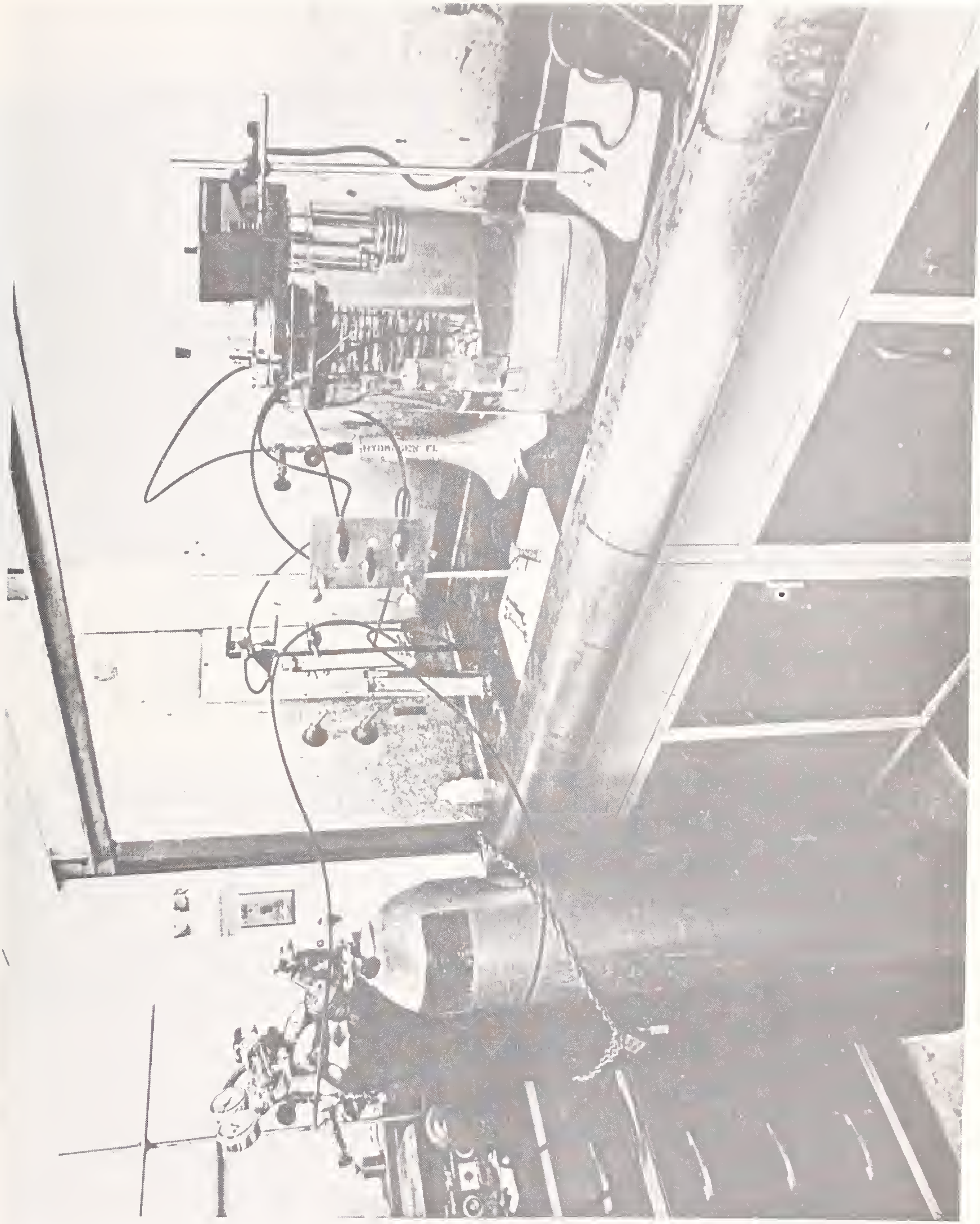

Figure 8.0

693-2-10
Cr/Au/ZnS Thick

693-2-6
Cr/Au/ZnS Thick

2126-9
Ti/AgAlloy+MgF_2

2126-6
Ti/AgAlloy+Si Thin

2127-9
Ag/Ag Alloy/Si Thin

2127-6
Ti/Ag Alloy + Si Thin

ETHANOL ONLY

693-2-9
Cr/Au/ZnS Thick

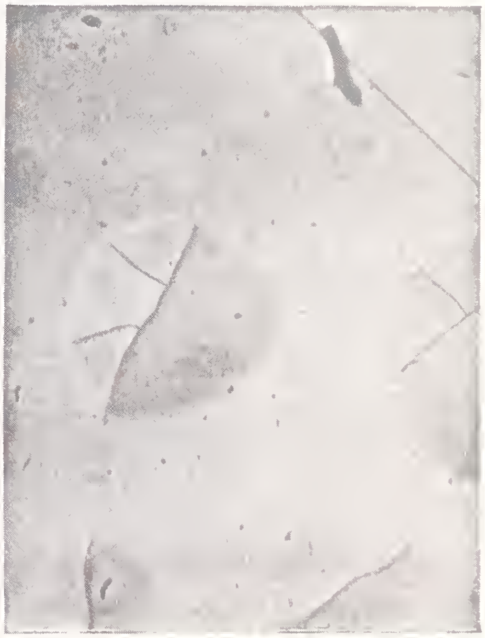

2126-10
Ti/Ag Alloy + MgF_2

ETHANOL ONLY CONT'D.

2127-10

Ag/Ag Alloy + Si Thin

712-1-10

Ag/(ThF4/ZnS)^5

ETHENOL + HUMIDITY

712-9-1

Ag/(ThF4/ZnSe)^5

693-2-11

Cr/Au/Zns Thick

2126-11

Ti/Ag Alloy + MgF_2

2127-11

Ag/Alloy MgF_2 Thin

H_2S

695-3-12
Cr/Cu/MgF_2 Thin

695-4-12
Cr/Cu/MgF_2 Thick

700-3-12
Cr/Cu/MgF_2 Thin

2126-12
Ti/Ag Alloy + MgF_2 Thick

2127-12
Ti/Ag Alloy + Si Thin

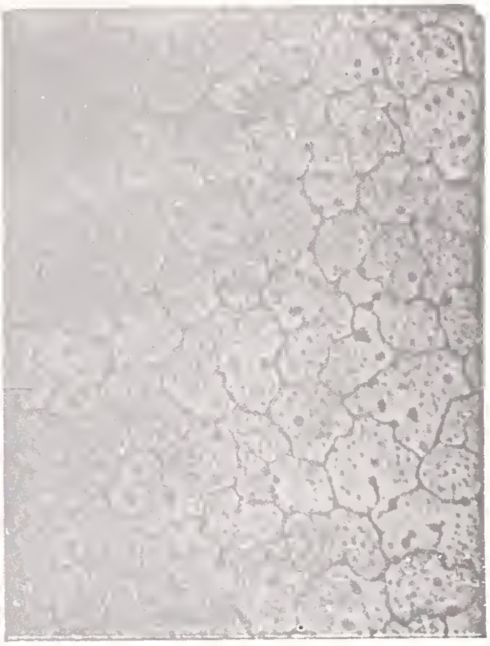

2129-12
Ti/Ag Alloy + CeO_2 Thin

2130-12
Ti/Ag Alloy + CeO_2 Thick

2138-12
Ti/Ag Alloy+Al_2O_3 Thick

H_2S + HF + ETHANOL + HUMIDITY

695-3-9

$Cr/Cu/MgF_2$ Thin

695-4-9

$Cr/Cu/MgF_2$ Thick

700-3-7

Cr/Cu

2129-9

Ti/Ag Alloy + CeO_2

H_2S + HF + ETHANOL + HUMIDITY CONT'D.

2130-9
Ti/AgAlloy+CeO_2 Thick

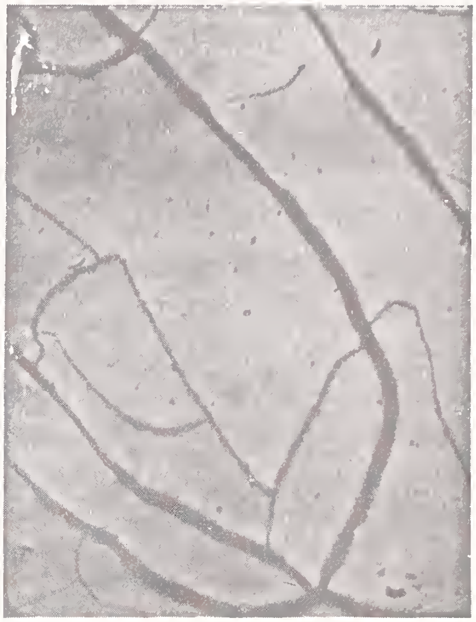

2138-9
Ti/AgAlloy+Al_2O_3 Thick

A.C. ENVIRONMENT PASS

2137-7
Ti/Ag Alloy/Al_2O_3 Thin

60x Before

2137-7
Ti/Ag Alloy/Al_2O_3 Thin

400x After

A. C. ENVIRONMENT PASSED

693-4-7 60x Before
Cr/Au 5Qw Al_2O_3 @ 751nm

693-4-7 400x After
Cr/Au 5Qw Al_2O_3 @ 751nm

700-1-6 60x Before
Cr/Cu $(Al_2O_3/ZnS)^5$ @ 1.54nm

700-1-6 400x After
Cr/Cu $(Al_2O_3/ZnS)^5$ @ 1.54nm

A.C. ENVIRONMENT FAILURES

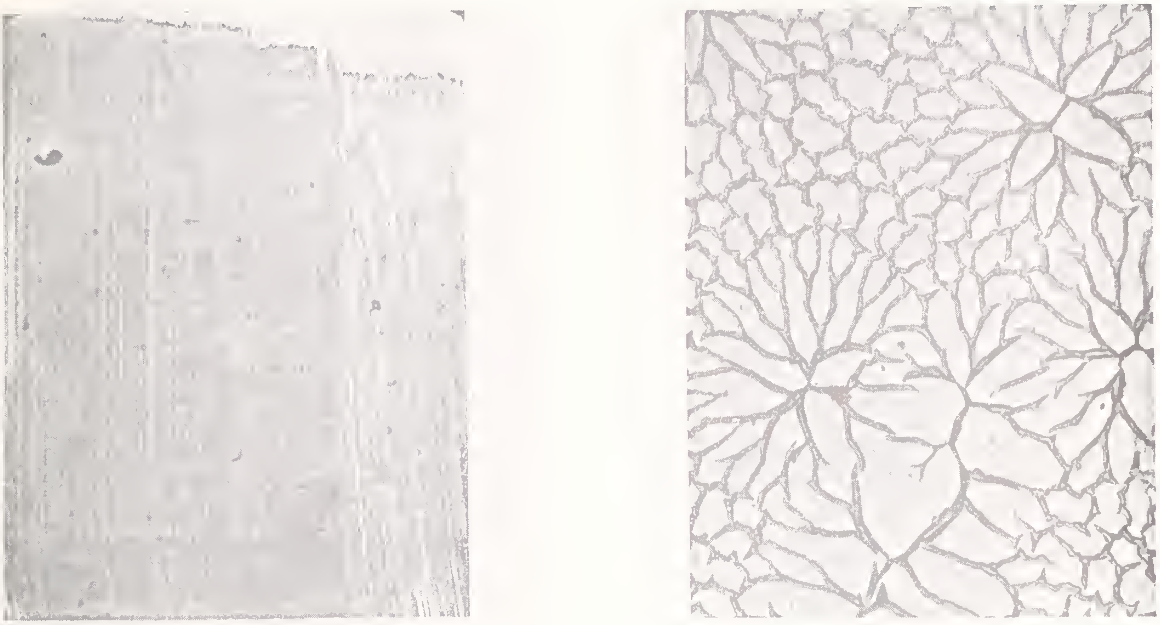

2127-7 60x Before 2127-7 400x After

Ag Alloy/Si Thin

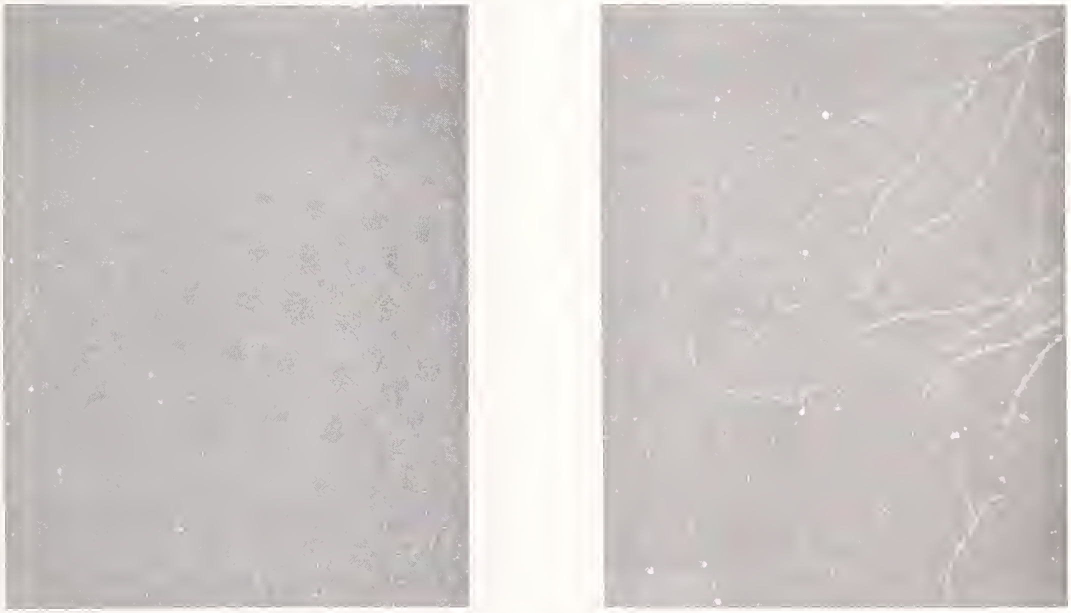

695-4-8 60x Before 400x After

Cr/Cu 5 QW MgF_2 @ 725nm

A.C. ENVIRONMENT FAILURES

695-3-8 60x Before

400x After

Cr/Cu 1 Qw MgF_2 @ 725nm

2128-7 60x Before

2128-7 400x After

Ag Alloy/Si Thick

A.C. ENVIRONMENT FAILURES

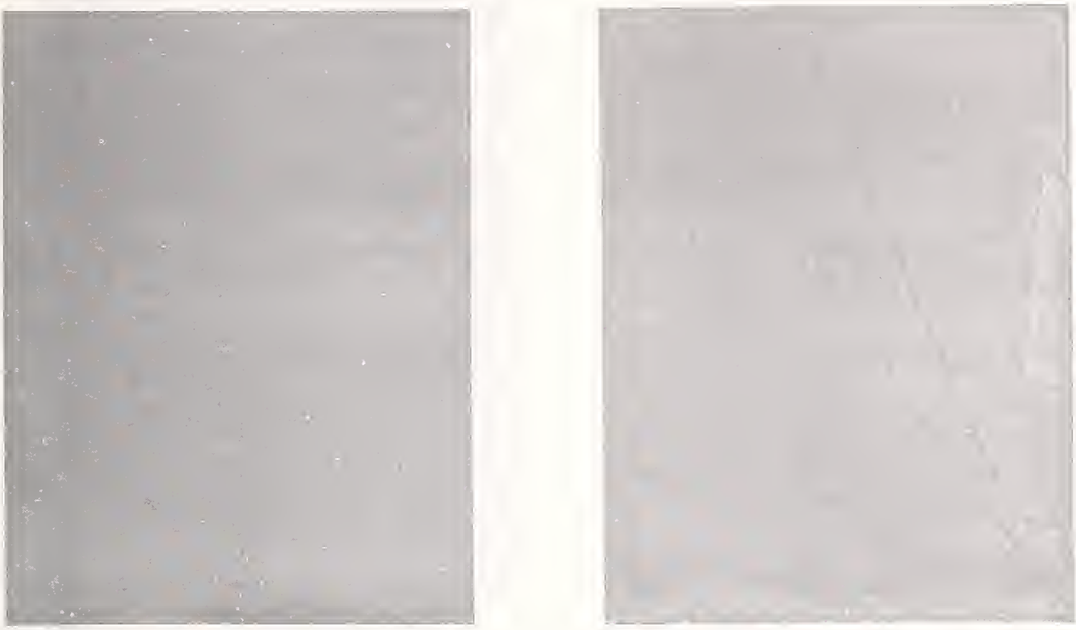

Before

After

GOLD SCRATCH TEST

NH_3 REJECTS

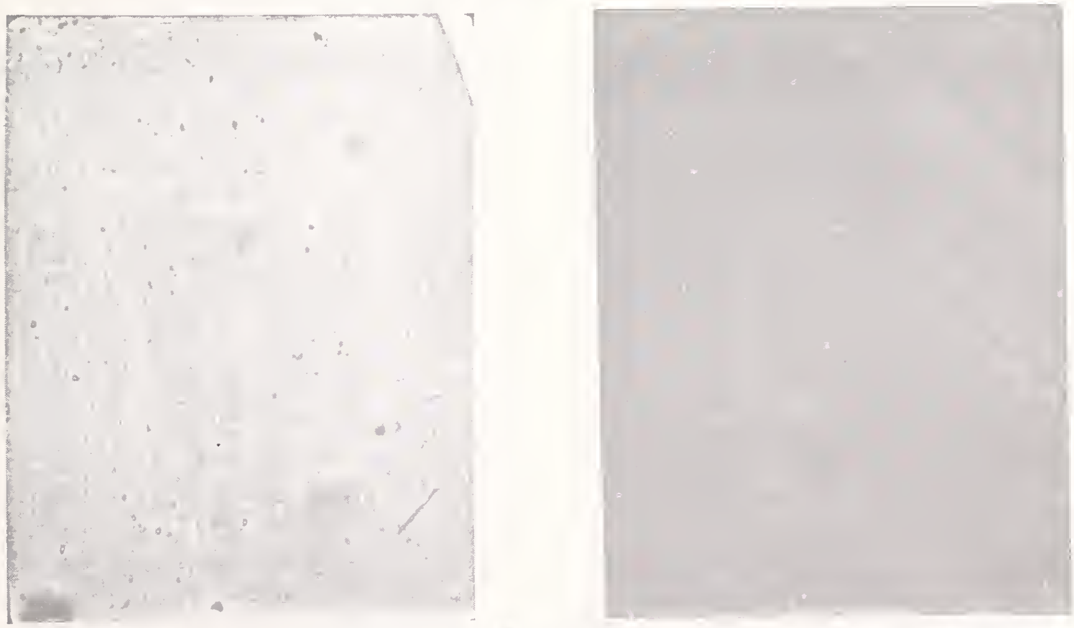

60x Before 695-3-13

400x After

Cr/Cu 1 Qw MgF_2 @ 725nm

NH_3 REJECTS

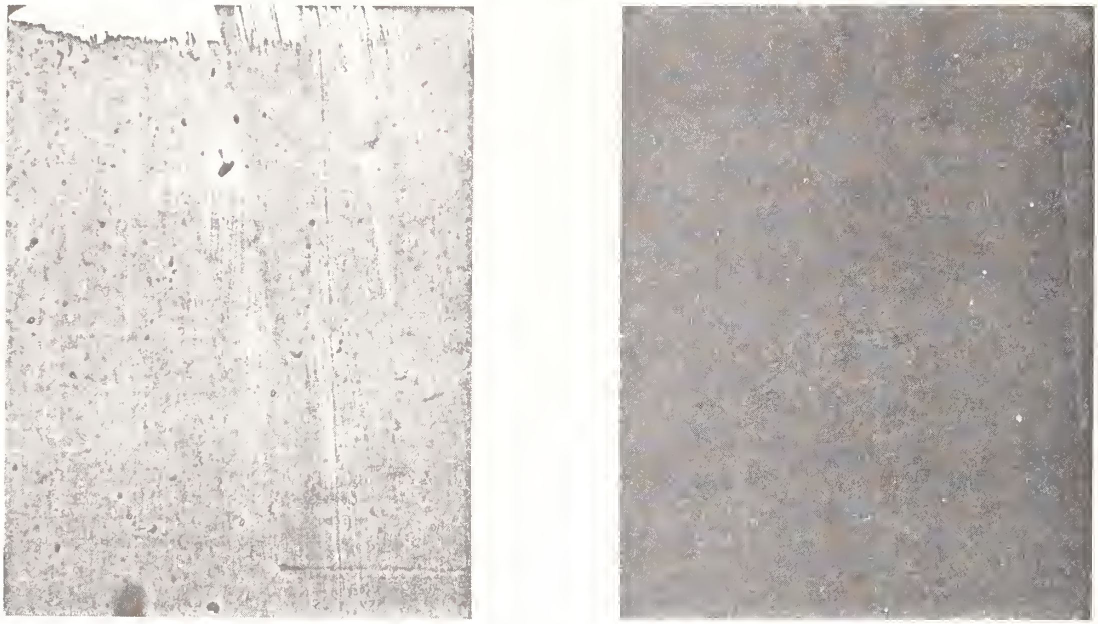

60x Before

400x After

695-4-13

Cr/Cu 5Qw MgF_2 @725nm

60x Before

400x After

2136-12

Ag Alloy/$ZrO_2Y_2O_3$ Thick

NH_3 REJECTS

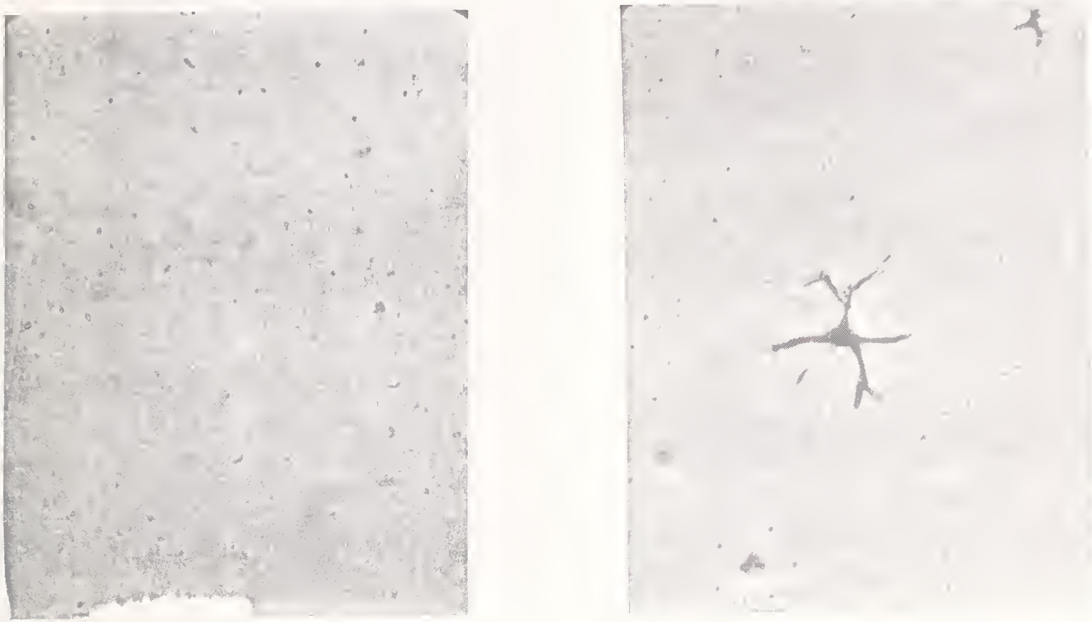

60x Before

400x After

2127-8

Ag Alloy/Si Thin

ON ROOF FOR 1 WEEK

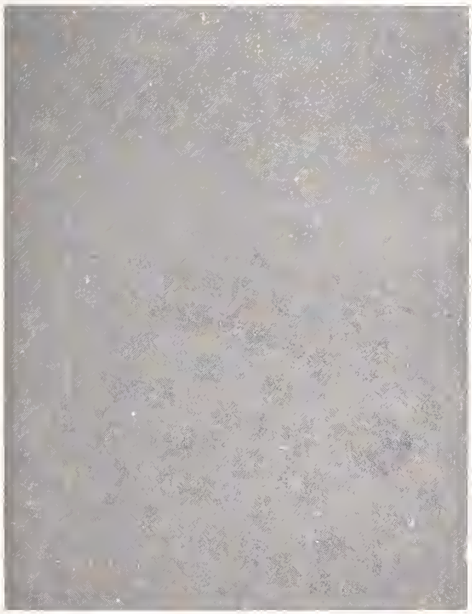

700-2-14 Cr/Cu/(SiO/Si)^5

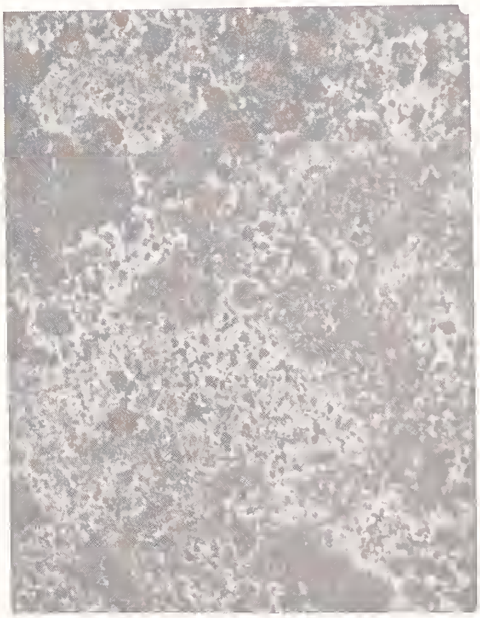

700-3-14 Cr/Cu

ON ROOF FOR 1 WEEK

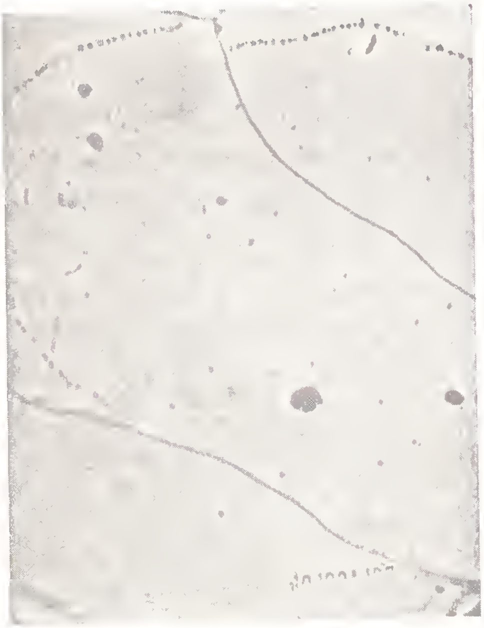

2138-14
Ag Alloy + Al_2O_3 Thick

2139-14
Ag Allov (SiO/Si)^5

2131-14
Ti/Ag Alloy + ZrO_2 Thin

2130-14
Ti/Ag Alloy + CeO_2 Thick

Photothermal Deflection Microscopy of Thin Film Optical Coatings

W.C. Mundy, R.S. Hughes
Department of Physics and Computer Science
Pacific Union College
Angwin, CA 94508

C.K. Carniliga
Optical Coating Laboratory, Inc.
2789 North Point Parkway
Santa Rosa, CA 95401

A system has been developed which employs the photothermal deflection effect to map the absorption characteristics of thin film optical coatings used in high energy laser applications. The high spatial resolution, low-level absorption data provided by this system may reveal flaws which could become damage sites when exposed to high energy laser radiation.

The system, in which an argon ion laser (514.5nm) is used for the pump source and a He-Ne laser is used as the probe source, has been used to study a halfwave optical thickness ZrO_2 coating on a super-polished fused silica substrate. The sample was mounted on an x-y translation stage which was driven by stepper motors in increments of 4µm in either direction. Qualitative data are presented of mappings of areas of the coating in which defects were found which were not observed with Nomarski microscopy. Measurements are in progress to ascertain correlations between the absorption and laser induced damage sites.

Key words: dielectric thin films; microscopy; optical absorption; photothermal deflection microscopy.

When electromagnetic radiation is absorbed by a medium, some of the radiant energy is converted to thermal energy, which causes local changes in the index of refraction of the absorbing medium and of a thin layer of the atmosphere adjacent to the sample surface [1]. This variation in the index of refraction, and hence the amount of absorption of the incident pump beam by the sample, is measured by the deflection of a probe light beam which intersects the pump beam near the sample surface. If the wavelength of the pump beam is varied, an absorption spectrum of the surface at the location of the intersecting beams can be generated. This phenomenon has been utilized in the recent development of photothermal deflection spectroscopy [2-5]. If, for a given pump wavelength, the sample is translated in both directions parallel to the sample surface, a map of the absorption characteristics of the surface can be obtained. This technique has been referred to as photothermal deflection microscopy [6].

This paper reports preliminary work demonstrating the feasibility of using photothermal deflection microscopy (PDM) to provide high spatial resolution maps of the absorption characteristics of thin film optical coatings. A small area of a coating has been mapped as part of the development of the technique, but the limiting characteristics and parameters of this technique are yet to be explored.

The experimental arrangement is shown schematically in figure 1. The 514.5nm line (approximately 350mW cw) from an argon ion laser was used as a pump source. This beam was directed so that it was normal to the sample surface and it was focused on the surface with a 120mm focal length lens. The probe beam from a two milliwatt He-Ne laser was focused with a 75mm focal length lens at the sample surface adjacent to the pump beam. Its angle of incidence was approximately 35 degrees with respect to the normal. The relative positions of the pump and probe beams were adjusted to maximize the deflection of the probe beam. The sample was mounted on an x-y translation stage which was driven by stepper motors in increments of 4µm in either direction. An EG & G FND-100 photodiode was positioned to receive the probe beam that was reflected from the front surface of the sample. A 632.8nm pass filter with 10nm half-band-width was placed in front of the detector. When the detector was translated across this reflected beam, a Gaussian curve was obtained for the intensity distribution of the beam in a plane perpendicular to the beam at the detector. The detector was then located on the edge of the beam where the derivative of the Gaussian distribution was a maximum so that small angular deflections of the beam would result in a maximum variation of the detected beam intensity. The signal from the detector was amplified with a lock-in amplifier synchronized with a chopper, which modulated the pump laser beam at a frequency of 37Hz.

The signal from the amplifier was routed to a voltage-to-resistance converter and then to one of the eight paddle ports of an Atari 800 computer. (An Atari computer was selected because it has analogue inputs and programmable I/O lines.) The value of resistance was digitized by the computer and the signal was then available for processing and display. The response of the computer was linear with the output of the lock-in amplifier to within 0.5%.

The output register of the Atari can be loaded with desired bit patterns which can be made available at any of the joy stick ports. This capability was used to generate a signal which was decoded by a "one of sixteen" decoder chip to drive operational amplifiers that controlled the stepper motors on the translation stages on which the sample was mounted. Figure 2 shows a block diagram of the signal electronics.

The computer was programmed to repeatedly translate the sample a predetermined distance and measure the absorption level until the desired horizontal scan was obtained. Then predetermined vertical displacements were executed, each followed by another horizontal scan, until the desired area was covered. The color of each pixel of a color monitor was determined by the magnitude of the absorption signal. This generated a four-color (a limitation of the Atari) contour map of the absorption characteristics of the sample. Absorption magnitude detail for a given contour can be enhanced by manipulating the stored data. For example, enhancement was obtained by varying the absorption signal levels at which the colors were changed and by stepping through the same four colors more than once. All absorption data were relative as the PDM system has not been calibrated.

This system was used to map the absorption characteristics of single-layer thin film optical coatings made from materials used in high energy laser applications. Preliminary scans demonstrated that the high spatial resolution, low-level absorption data provided by this system may reveal flaws which could become damage sites when exposed to high energy laser radiation. Figure 3 shows an absorption contour map of a 250μm x 550μm area of an evaporated ZrO_2 coating on a super-polished fused silica substrate. The ZrO_2 film had an optical thickness equal to half of the 514.5nm pump wavelength. Each square pixel provides information about the absorption for a given sample position. The sample was translated 4μm between each data point or pixel. The four shades represent 4 different ranges of absorption levels. These are 0 to 15, representing the background level of absorption, 15 to 40, 40 to 70, and 70 and greater representing the highest level observed. These data were repeatable as observed in several scans made over a period of a week.

Figure 3 shows several small absorption sites and one fairly large one. An enlargement of this major absorbing site was obtained by rescanning the sample and displaying each element using a four times larger pixel (an option of the Atari graphics). Figure 4 shows a 75μm by 150μm enlargement of the primary absorbing site made in this manner. This does not correspond to an increase in resolution, since adjacent pixels still correspond to sample sites separated by 4μm, but it allows the details of the absorbing site to be more easily observed.

The area of the sample shown in Figures 3 and 4 was inspected using Nomarski microscopy. No features were observed corresponding to the major absorption site detected by photothermal deflection microscopy. This indicates that photothermal deflection microscopy can detect sites which might not otherwise be seen and which might be precursors to laser damage.

Areas that should be pursued using PDM include studying the correlation between absorption and laser induced damage sites, performing high resolution elemental analysis of absorption sites, calibrating the system so that absolute absorption data are available, developing submicron spatial resolution, and carrying out wavelength-dependent absorption studies.

References

[1] Smith, D.C. "Thermal defocusing of CO_2 laser radiation in gases," IEEE J. Quantum Electron. QE-5, 600 (1969).

[2] Boccara, A.C.; Fournier, D.; Badoz, J. "Thermo-optical spectroscopy: Detection by the mirage effect," Appl. Phys. Lett. 36, 130 (1980).

[3] Boccara, A.C.; Fournier, D.; Jackson, W.; Amer, N.M. "Sensitive photothermal deflection technique for measuring absorption in optically thin media," Opt. Lett. 5, 377 (1980).

[4] Murphy, J.C.; Aamodt, L.C. "Photothermal spectroscopy using optical beam probing: Mirage effect," J. Appl. Phys. 51, 4580 (1980).

[5] Jackson, W.B.; Amer, N.M.; Boccara, A.C.; Fournier, D. "Photothermal deflection spectroscopy and detection," Appl. Opt. 20, 1333 (1981).

[6] Murphy, J.C.; Aamodt, L.C. "Optically detected photothermal imaging," Appl. Phys. Lett. 38, 196 (1981).

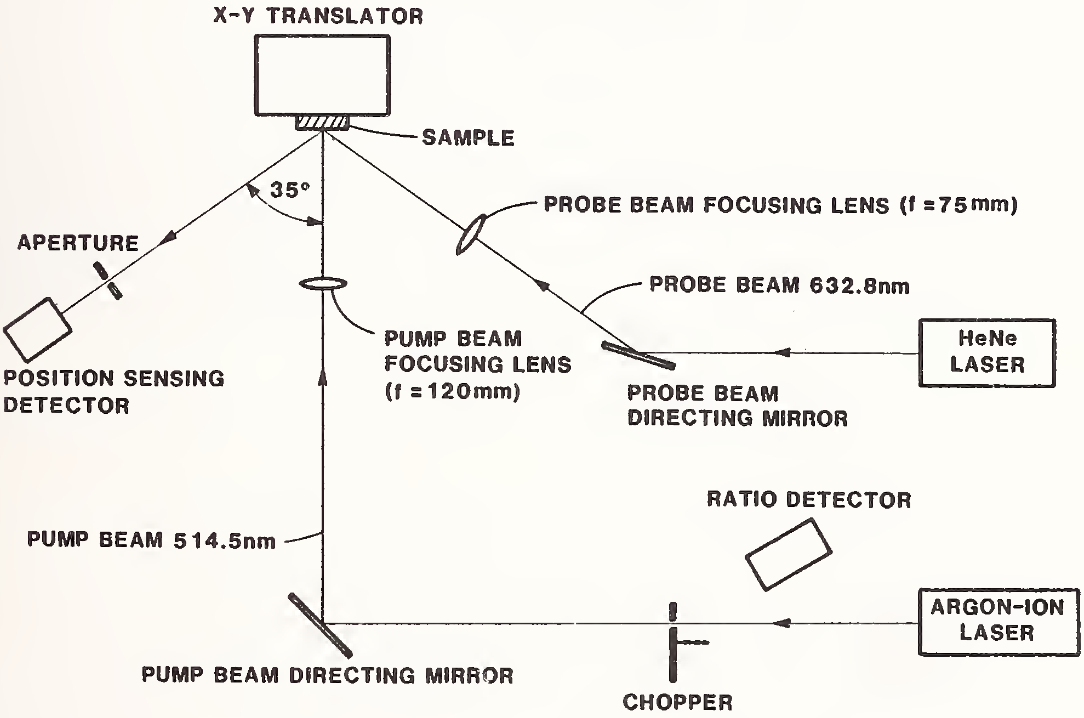

Figure 1. Photothermal deflection microscopy experimental arrangement.

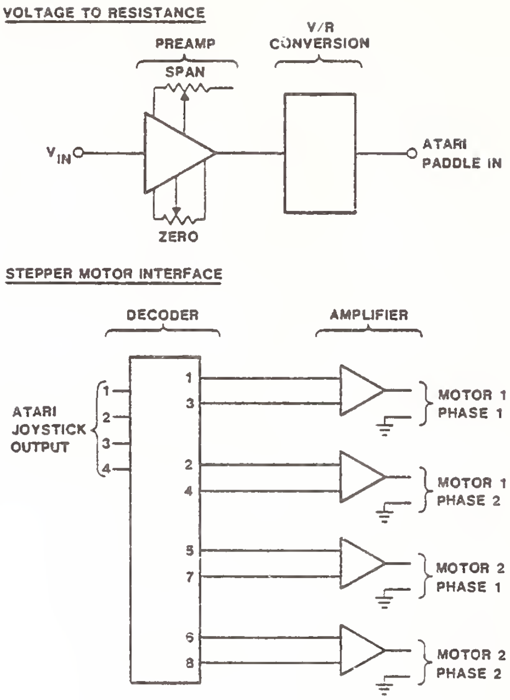

Figure 2. Block diagram of the signal electronics

Figure 3. Photograph of PDM contour video display of $\lambda/2$ optical thickness of ZrO_2 on a superpolished fused silica substrate. Contour covers a 250μm x 550μm area.

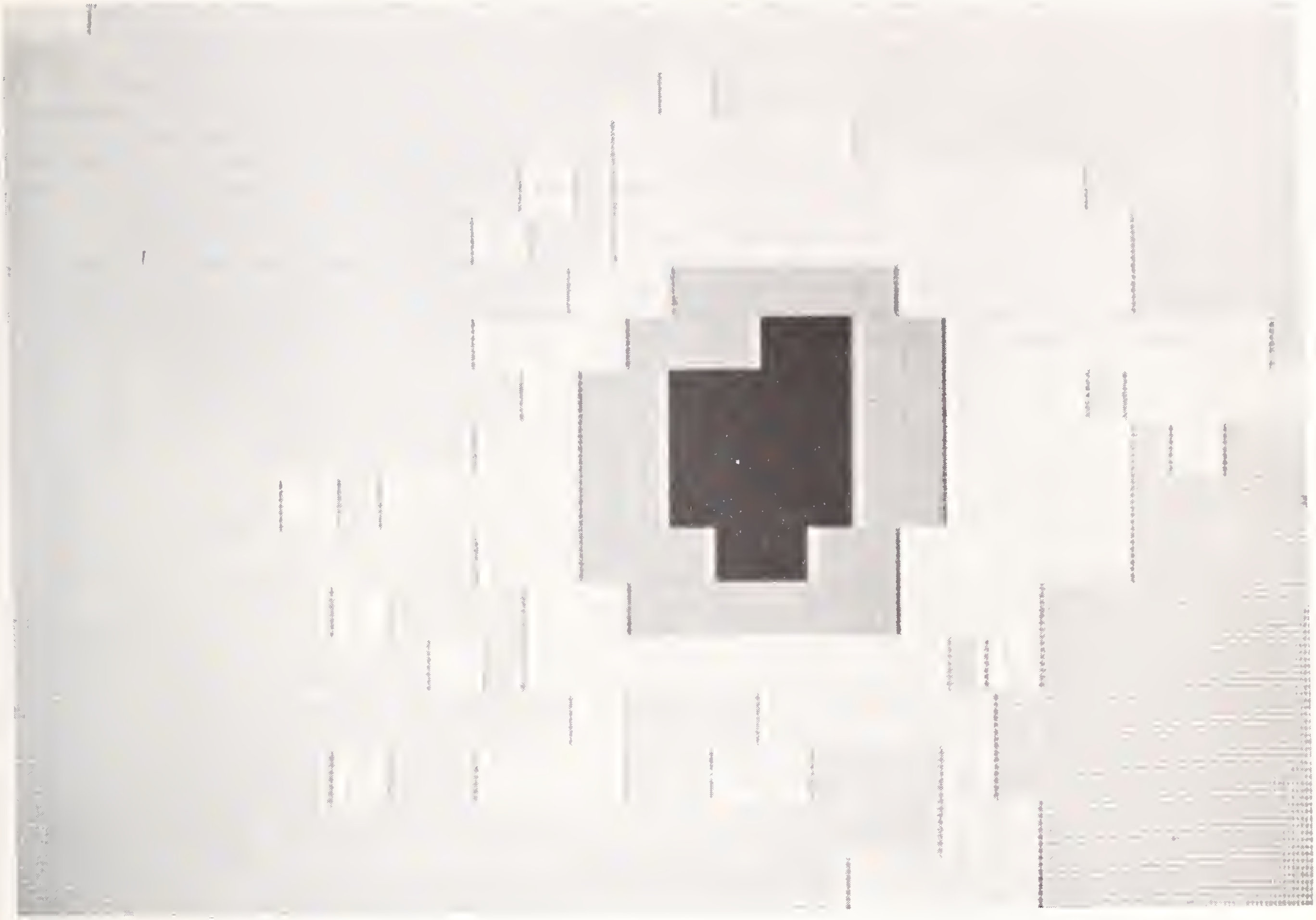

Figure 4. 75µm x 150µm contour of primary absorbing site in figure 3.

Several in the audience questioned whether a study of thin films of materials gave a true measure of the relative merit of the materials. The speaker replied that the data had good internal consistency; with few exceptions, films of a given material had similar thresholds even though they were made in two or more coating runs, but conceded that the results might be biased by the relative experience of the coater in depositing various materials. In response to other questions, the authors clarified that (1) coating stress was inferred from interferometric measurements of stress-induced flexure of thin substrates that were coated simultaneously with damage-test samples, (2) that he had no explanation why substrate polishing seemed to effect low-threshold films but not high-threshold films since all substrates were similarly polished, and (3) that Al_2O_3 *had not been included in the list of most promising materials because the half-wave layers of* Al_2O_3 *were highly stressed. A strong criticism was made of the fact that the data were presented as linear plots of thresholds as a function of variables such as refractive index and stress, instead of through functional forms developed during previous studies of the scaling of damage thresholds with physical parameters of the coating.*

Interaction Mechanisms of Laser Radiation With Ocular Tissues*

David H. Sliney

US Army Environmental Hygiene Agency
Aberdeen Proving Ground, Maryland 21010, USA

Many investigations of laser injury to the eye have been conducted over the past 20 years for the purpose of setting standards for safe exposure of the human eye. Such studies have also played an important role in the developments of laser applications in medicine and surgery. A review of this extensive body of experimental data suggests that there are at least three dominant mechanisms of injury which are well accepted. However, other effects cannot be ruled out, and several studies suggest that the time-course of injury and repair as well as the physical aspects of the interaction of biological tissue with optical radiation must be considered. The scaling relations of spot-size, and pulse-duration dependence of threshold differ from those applicable to material damage.

KEY WORDS: Eye; laser damage; optical breakdown repetitive pulses; retinal injury; spot-size dependence; thermal injury; thermoacoustic injury.

1. Introduction

In the course of development of laser biomedical applications and safety standards for human exposure, it is necessary to critically examine not only the thresholds of injury in biological tissue, but also the mechanisms of laser interaction with the tissue and the mechanisms of biological damage and repair. It would be unwise to simply determine acute injury thresholds and then to set exposure limits below these thresholds. Knowledge of the mechanisms of interaction and damage are important because of our limited ability to predict the delayed onset of adverse biological effects. The delayed appearance of lenticular cataract only years after ocular exposure to a radiation insult is but one example of such delayed effects. Through knowledge of the mechanisms of interaction of laser radiation with biological tissue and from the extensive experience with the effects of heat and conventional optical radiation exposure on man, it is possible to provide the best judgement of what levels should not be hazardous to health. Depending upon the nature of the injury mechanism, one is better able to predict the likelihood for delayed effects at levels below acute injury thresholds. The presently accepted ocular exposure limits attempt to take these considerations into full account [1].

Unfortunately, there are at least three types of exposure where the cycle of injury and repair are not well understood: ultrafast (sub-nanosecond) pulsed exposure, the spot-sized dependence of retinal injury for q-switched exposure durations, and the additive effects of multiple-pulse exposures. We shall examine each of these problem areas and one more, and suggest some possible explanations for some of the biological effects that have been reported. It is, of course, impossible in this brief paper to review all of the many studies of laser biological effects; however, several representative references will be provided on each major point. The absence of references to many specific reports that were considered in this presentation should not be interpreted as suggesting that the referenced papers are the only relevant ones. Many others have been reviewed [2]. Furthermore, a major purpose for presenting this review at the Boulder Damage Symposium is to encourage physical scientists and engineers to take a greater interest in this subject. Hopefully this can lead to a wider critique of biomedical studies and to suggestions for further, meaningful investigations.

---

* The opinions or assertions contained herein are the private views of the author and are not to be construed as official or as reflecting the views of the Department of the Army or Department of Defense.

2. Principal Damage Mechanisms

It is widely accepted today in the biomedical community that there are at least three dominant mechanisms of injury involved in laser damage to the cornea, lens and retina of the eye. These three dominant mechanisms of injury are initiated by: a photochemical event, a thermal event, or an interaction dependent upon the electric field strength of the incident optical wave. The latter mechanism (or mechanisms) apply to ultra-fast exposures. The thermal effects are clearly dominant in the infrared and for almost all pulsed exposures between 1 ms and 1-5 seconds. The photochemical events are generally limited to wavelengths less than 550-650 nm, and then are clearly evident only for lengthy exposures of 10 s to several hours. There are clearly cases where two or more injury mechanisms jointly play a role. Sometimes it has been necessary to choose extreme parameters of exposure to study the mechanism, e.g., very large retinal images or very long exposure durations that may be unrealistic in our normal environment. Varying the wavelength has also led to interesting findings.

A common error that is often made when interpreting the biological effects of laser radiation is to consider only the physical interaction of the optical radiation with matter and the dissipation of the absorbed energy away from the site of exposure (e.g., by heat conduction). We must remember that a biological system is dynamic, and that immediately following an insult to tissue some biological actions can be expected. Several repair processes can start to work almost immediately. Also, several adverse reactions can be initiated by the initial insult and become apparent only long after exposure. Delayed onset of the appearance of tissue injury is particularly common with photochemically initiated events. Examples of photochemical effects are: retinal injury from lengthy exposures (10-1000 s) to short-wavelength light or skin or corneal injury following UV exposure. Retinal lesions from 441.6-nm (He-Cd) laser radiation at injury threshold typically do not appear for 48 hours [3] and erythema and photokeratitis typically do not appear for several hours following exposure to 300-nm UV radiation [1].

Although erythema (sunburn of the skin) and keratoconjuctivitis (welder's flash) following UV irradiation of the skin and eye have been studied extensively from the beginning of the century, the exact chain of events following exposure, and even the site of the initial photochemical event and the chromophores are not really known. Several therories exist, but no theory attempts to explain all aspects of the delayed reaction. Since reciprocity of UV irradiance and exposure duration exists for exposures of microseconds to 1000 s or more, and since the action spectrum for each of these effects has a sharp cutoff in the 305-315-nm band (where individual photons have insufficient energy to cause the reaction), no one doubts that the injury mechanism is initiated by a photochemical event. Photosensitizers permit less energetic near-UV (UV-A) photons to elicit the same result as 300-nm photons.

Photochemical retinal injury from laser exposures lasting greater than 10 s has only recently been studied extensively [3-6] and is today still not well understood. Figure 1 shows the approximate action spectrum measured outside of the eye for this effect. Thresholds for UV retinal damage, if measured at the retina, are lower than at 440 nm, but fortunately the intact crystalline lens filters out the UV and protects the retina. The thresholds at the retina for this effect vary from about 20-30 J/cm^2 at 442 nm to 3000 J/cm^2 at 632 nm as shown in Figure 2 [2,3]. Ham and his colleagues have studied many histological cross-sections of photochemically damaged retinae of rhesus monkeys and argue that damage is always seen first in the retinal pigmented epithelium (RPE), [3] but others claim that photochemical injuries show damage throughout all layers of the retina [5-6]. Figure 3 shows the retinal layers. There are probably several chromophores in the retina that are sensitive to blue light and ultraviolet (UV-A) radiation. In fact, the appearance of UV-A retinal lesions and 441.6-nm lesions are different [3,4]. The time course of appearance also varies with wavelength, just as does the time course of appearance of UV erythema varies between 254-nm and 300-nm radiation. Clearly the melanin pigment in the RPE plays a major role, but as Ham has pointed out, melanin could act as both a source and sink for free radicals, because of its unusual characteristic of containing stable free radicals, possessing semiconductor properties, surface metal ions, and its characteristic of both scavenging for free oxygen and producing free radicals, depending upon the light environment [3]. Others report that the melanin in the RPE changes with age, [7] that it loses its photoprotective ability with increased light exposure, that acute retinal lesions from blue-light exposures contain melanin granules resembling senile melanin, [3] and that senile macular degeneration (a major cause of blindness in old age) is caused to some extent by short-wavelength light [8]. Since melanin is the major concentrated absorbtion site of laser radiation in the retina, it plays the key role in retinal thermal injury, photochemical injury, and probably also in ultra-fast injury events. As more basic research is performed on melanin, more understanding of laser injury mechanisms will follow. Possible blue-light chromophores for retinal injury include flavoproteins, glutathione peroxidase and other light-activated enzymes, and cytochrome-C [1,2].

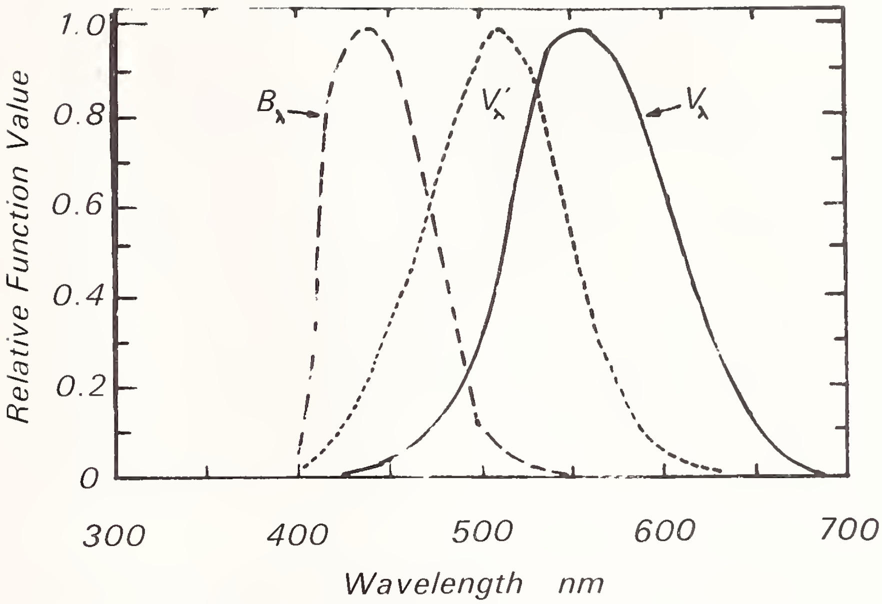

Figure 1. Spectral Weighting Functions. The spectral weighting function now used for the analysis of retinal injury from blue-light [2](B_λ) is compared with the night vision, or scotopic (V'_λ), and the photopic (V_λ) daylight spectral response of the human eye. The peak of the "blue-light hazard" function is at 435-440 nm.

3. Determining Injury Thresholds

Thresholds of biological injury may be determined by direct observation, by microscopic study (histology) or by measuring a functional change. In any case, a probit plot is frequently made (Figure 4) to provide some statistical insight into the quality of the data and the injury mechanism. As shown in Figure 4, the true-statistical variation in injury threshold from different exposure sites or different individual animals may be distorted by poor focusing at the retina or by other experimental errors. While some errors will shift the probit line to the right, other errors (such as focusing) will reduce the slope of the line.

4. Retinal Thermal Injury

Retinal thermal injury has been studied extensively, [9-14] and many mathematical models of heat flow and temperature rise in the retina have been developed [9-13]. If the average temperature rise in the RPE is calculated, it is shown that the temperature rise required for an experimentally determined retinal lesion increases for shorter and shorter exposure times from 10 s down to about 7 ms. But then, unexpectedly this temperature rise decreases for pulse durations less than approximately one ms [1,2,11]. Figure 5 illustrates that the peak temperature rise calculated for the average density RPE is greatest for 1-ms exposures; there is little difference in this trend other than peak values, whether one calculates this temperature dependence at the center of a minimal, 16-µm diameter image or at a point just outside the image. The same threshold injury dependence applies to large image size lesions [11]. Hayes and Wolbarsht argued that for pulse durations less than 1 ms, one must consider the melanin granule temperature rise and its cool-down [14]. At threshold irradiances for 20-ns exposures the melanin granules are raised to incandescence. Marshall notes that vacuoles in mitochondria are seen following q-switched exposures, but not in retinal injury from 1-s exposures [15]. Several differences in the onset-time of the visible lesion and in the histological appearance of the lesion resulting from sub-microsecond exposures have led most of us to argue that injury mechanisms for q-switched exposures are not limited to the simple thermal coagulation of proteins.

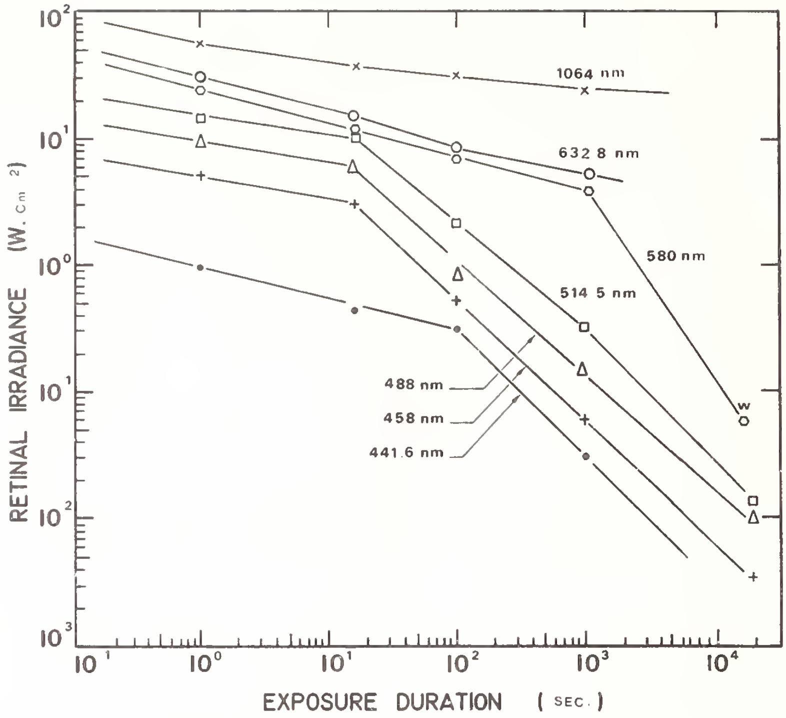

Figure 2. Photochemical and Thermal Retinal Injury Thresholds. Threshold retinal injury from a photochemical retinal injury mechanism appear only for exposure durations exceeding 10 s; the appearance of injury is delayed; the effect is limited to short wavelengths (higher photon energies) and reciprocity of irradiance and exposure duration is observed. The thresholds for the 1064-nm wavelength are clearly those of a thermal damage mechanism. Data points are from reference 3 (exposures less than 10^4 s) and 6 (longer durations) [2].

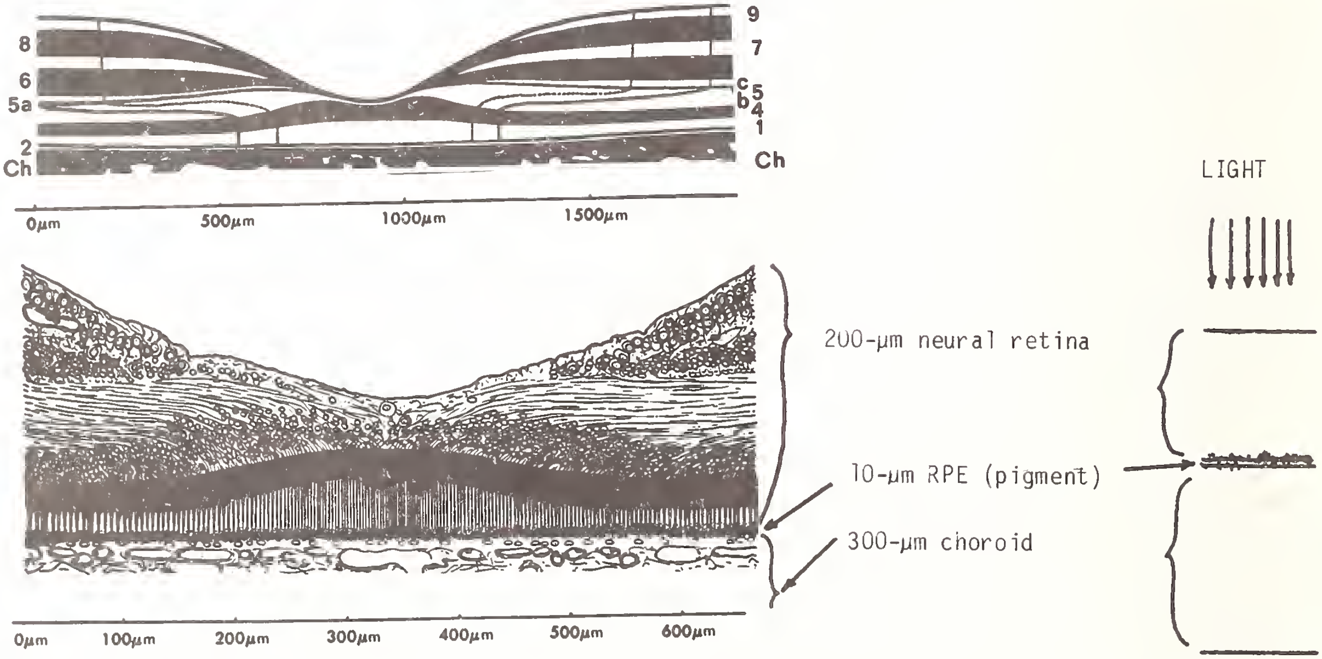

Figure 3. Retinal Structure. This drawing shows the different layers of the retina and adjoining choroid. The neural retina layers are nearly transparent. Most light is absorbed in the 3 to 10 µm thick RPE and the choriod capilaries. Left panel shows variation of layers in central retina at the fovea where neural layers are pulled back. Adapted from Polyak [in 2].

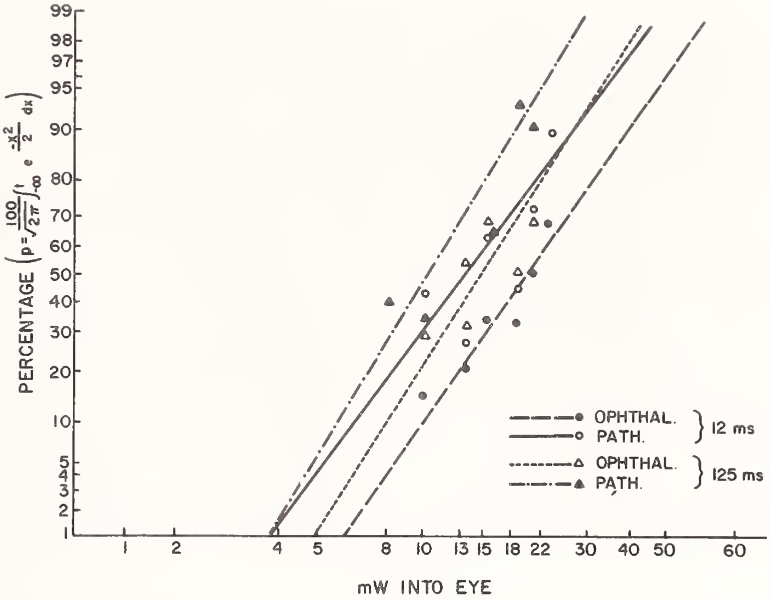

Figure 4. Probit Plots. The use of probit analysis to determine a slatistical "threshold" (the ED-50) is particularly important when dealing with the structural and pigment variation common in biological systems. The steepness of the curve gives a clue to injury mechanism, but also shows the care of the experimental procedure. When attempting to achieve a minimal (nearly diffraction- limited) focal spot on the retina, a slight refractive error or corneal scattering will lead to a higher "threshold" (ED-50) and a less steep slope of the probit curve.[2,25].

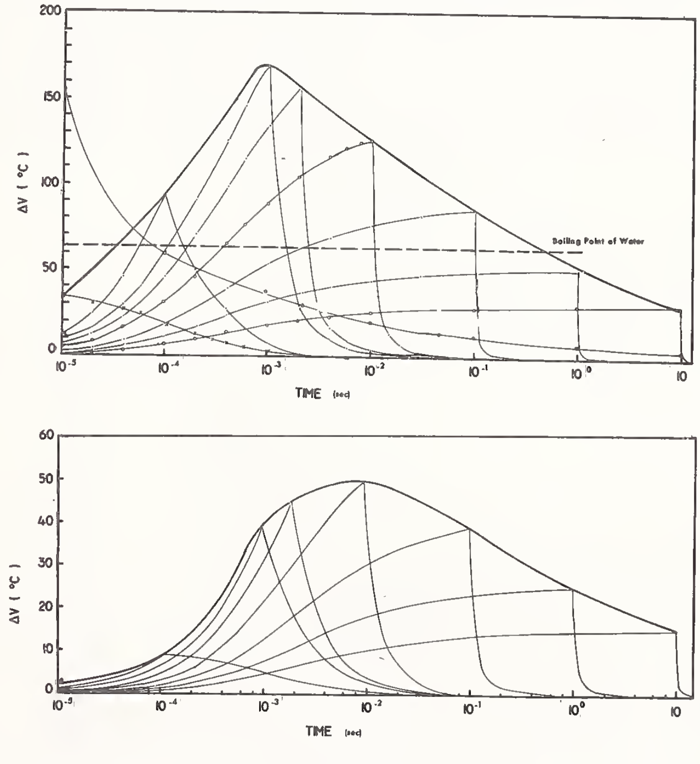

Figure 5. Time-Temperature Histories for Injury Thresholds as Calculated by a Thermal Model [2]. The upper curves are calculated for 0.01-ms to 10-s exposure for minimal image size lesions in the rhesus monkey. Temperature rises are at the center of a 10-μm thick RPE at the center of a 16-μm image. The upper bold curve is an envelope of the peak temperatures reached for each time-temperature history. The lower curves are for the same minimal threshold irradiance data in the rhesus monkey, but this time the point of temperature calculation was moved to a point at the center of the 10-μm thick RPE, but 20 μm radially from the center of the image. The latter points would indicate the time-temperature history of cells just adjacent to the imaged retinal area. Note that the peak of the temperature elevation for the 10-μs pulse does not occur until 0.1 ms, and the boiling point of water is never reached by any of the latter curves.

There are two curious results that are not really explained by any of the mathematical models for thermal injury. All of the thermal models would predict that for exposures less than approximately 100 μs the temperature rise would be so great prior to any significant heat flow that there should be no difference in injury thresholds for exposure durations less than 0.1-1.0 ms, and there should also be no variation of threshold with image size. The melanin-granule models suggest some decrease in damage threshold for the RPE cells themselves for the shorter exposure durations, since the incandescent granules could destroy adjacent structures in the cell, but certainly no image size dependence of injury could be explained. Heat flow from large images during 1-s exposures is insufficient to cool the center of the image for the same irradiance that causes no injury in a smaller image. This leads to the image-size dependence predicted for exposure durations exceeding 1 ms. The rate-constants for thermal coagulation of proteins are such that thermal models that include a rate-process dependent term predict that injury from a 20-ns exposure should occur before heat flow becomes significant (i.e., in less than 100 μs) [16]. The temperature rise in the outer receptor layer where irreversible damage occurs is 10 times less for a 20-ns pulse than for a 1 ms pulse, but the time-temperature history in this layer should be the same for either pulse, since heating occurs in this layer only from conduction of heat from the adjacent RPE. The rate-process models do predict one scaling relation: the decrease in threshold radiant exposure (J/cm^2) as a function of the pulse duration t raised to the 3/4 power for exposure durations ranging form 20 μs to 10 s (Figure 6) [9]. Another scaling relation is seen in Figure 7: the retinal injury threshold for <u>all</u> exposure durations, from 30 ps to 10 s varies approximately as the reciprocal of the image <u>diameter</u> for image sizes of 20 μm to at least 1 mm.

Another anomaly not explained by the thermal models is the fact that the thresholds for 10-20 ns exposures are greater than the thresholds for 500-ns to 10-us exposures for the same image size and same wavelength [2]. This curious phenomenon is shown in Figure 6, and many more data points between 10 ns and 1 μs that are not shown offer solid evidence that this temporal dependence of threshold for such short exposures is real and not an experimental artifact. What is the explanation? Two possibilities appear reasonable to me. As the pulse duration decreases, more energy could go into a noninjurious dissipative mechanism such as an accoustic transient at threshold. Of course this very mechanism is known to be the principal cause of severe, almost explosive damage in the retina for suprathreshold exposure levels. An alternate, and perhaps more appealing explanation is that melanin may be a saturable absorber like some other organic molecules, and as the irradiance increases for shorter exposure durations, the amount of energy absorbed in the granules becomes less. I have tried to detect such behavior by irradiating a vial of melanin in a water suspension with a q-switched pulsed laser beam, but was unable to achieve a clear result because I could not prepare a sufficiently dense and uniform suspension of melanin granules.

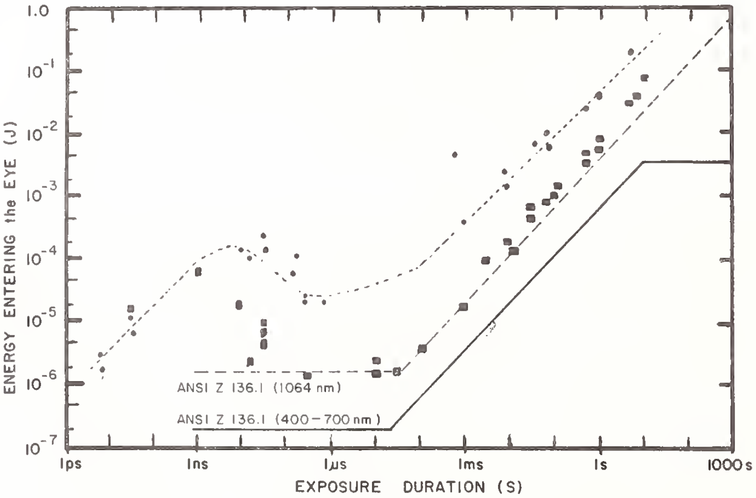

Figure 6. The Dependence of Retinal Injury Threshold Upon Pulse Duration. The injury thresholds in the rhesus monkey are plotted as a function of total laser energy entering the eye vs exposure duration. The dashed line shows the laser safety limits (ANSI Z-136.1). Note the anomalous increase in thresholds for both 1064-nm [●] and visible light [■] at 10 and 20 ns when compared to thresholds at 10-20 μs. Safety limits do not exist for mode-locked pulse durations. Adapted from refs 2 and 18.

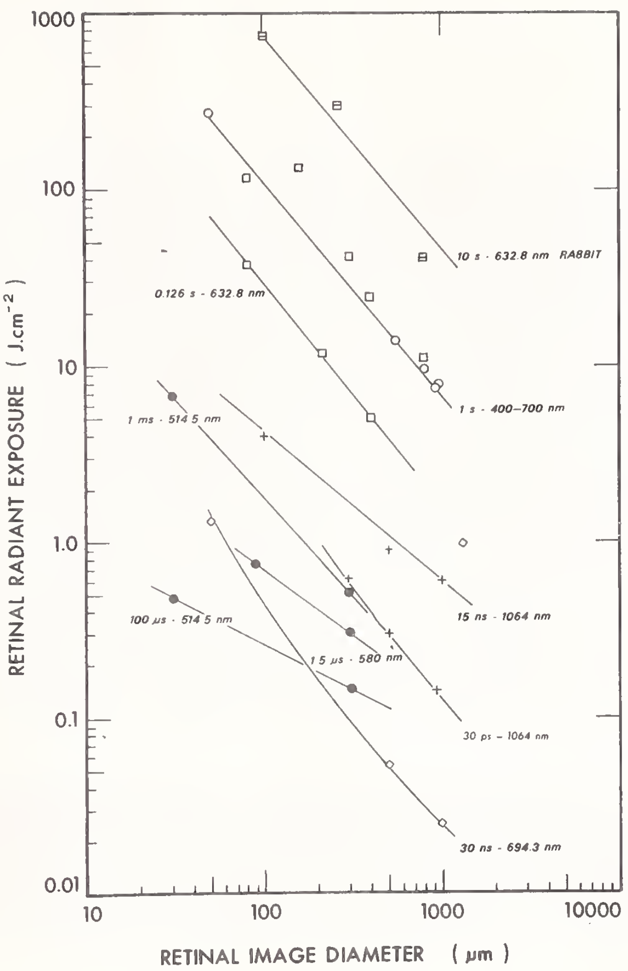

Figure 7. Scaling Relation for Retinal Injury Threshold with Spot Size [2]. While the reduced exposure threshold for large spot sizes (d_r) is expected for longer exposure durations (due to heat conduction), the same dependence of approximately $1/d_r$ is surprising for 15-ns and 30-ps pulses.

Perhaps the most curious contradiction of the thermal model is the collection of experimental threshold data that clearly show that pulsed exposures separated by durations adequate for almost complete cooling of small image sizes (e.g., 100 ms) show an additivity of exposure. Minimal image sizes should cool within 1-10 ms and the thermal model predicts that no reduction in injury threshold should result from exposure to a train of pulses separated by that duration, even if the pulsed exposures are superimposed over the same retinal area. A large collection of data now suggests that one can empirically predict that the threshold exposure of a single-pulse in a train is decreased proportionally to $N^{-1/4}$ where N is the number of pulses in the train [17]. This relation holds for 10-ns pulses, 10-µs pulses, and 10-ms pulses over a wide range of pulse separations and exposure durations for small image sizes. According to one study it appears not to occur for large image sizes [18]. But then another study with large image sizes does tend to show the additive effect [20]. One phenomenon -- biological repair -- may explain these and the other anomalies.

5. A Rapid Repair Mechanism

Mathematical models of heat flow suggest that the elevated temperature in a 20-um diameter irradiated area will return to normal within a few milliseconds [13]. However, all of the repetitive-pulse injury thresholds show an additivity for pulses separated by several milliseconds and even 100 ms. One possible explanation for this apparent contradiction would be the presence of a rapid repair mechanism for retinal thermal injury following short-pulse exposure. I would suggest one hypothesis: the existance of a repair mechanism that precludes the appearance of a thermally induced lesion for small spot sizes at levels near a threshold for immediate injury. It would be consistent with present threshold data to hypothesize that if exposures are delivered during the period of primary activity of this repair mechanism (1 ms to 10 s), any further exposures may inhibit the repair process. In fact, one could even expect that the area already exposed could be more vunerable to further injury if exposed during this repair period. Furthermore, if we hypothesize that this repair mechanism is most effective for small image sizes, we can explain most of the experimental data. It certainly would be plausible that closure of a damaged hole in a ruptured membrane would be more rapid and more effective for the smaller lesion. If the repair mechanism involves the activity of surrounding, unexposed (or uninjured) cells, or the movement of enzymes, then the rapid repair of a few cells would be quickest and most effective for the smaller image areas. It is true that I am being very speculative, since the evidence for such a repair mechanism at present is still quite limited. In my judgement, the study of retinal pigment epithelium (RPE) cells in vitro (i.e., in a dish) by King and Geeraets [19] lends support to this hypothesis. In their study the thresholds of injury for 20-μm and 135-μm diameter spots in their cell culture exposed to 30-ns ruby (694.3-nm) laser radiation were the same; i.e., there was no variation of threshold with spot size.

It was once argued that the spot-size dependence for short-pulse exposures was due to the inability to see very small retinal lesions through the slightly scattering ocular media with the ophthalmoscope, but later studies showed that this contrast problem played only a minor role and then only for image diameters below 50 μm. Since there would be no external limiting membrane and no underlying Bruch's membrane and choriocapillaris (structures on either side of the RPE), a repair process from adjacent cells above and below (or damage of the absent structures) would not be possible in the cell culture.

Since the retinal irradiance threshold reduction for a train of very many pulses and for very large spot sizes (~1 mm) are similar, these lowered thresholds may be the lower asymptote for retinal injury thresholds. The higher thresholds for the appearance of a single, small-image exposure or intermediate exposures may be the result of a rapid repair process. Further threshold studies of very large retinal image sizes and very long trains of pulses appears to be justified. A study by Greiss, et al., shows that thresholds for repeated exposures of the retina at 1064 nm (nonphotochemical process of injury) for 0.9-mm image diameters in the rhesus monkey retina were not reduced from a single-pulse threshold as shown in Figure 8 [18]. We would therefore expect that lesions from different pulse conditions would appear somewhat like those shown in Figure 9, which to some extent agrees with the descriptions of experimental thresholds. Regrettably, there is another earlier study which contradicts this. Walkenbach found a reduction in the threshold with additional pulsed exposures for image sizes of 200 μm to 800 μm diameter [20].

The large volume of studies of laser damage to nonbiological materials is useful to consult when considering biological injury thresholds from pulsed lasers. A spot-size dependence and repetitive-pulse additivity of damage thresholds in coatings and bulk solids have sometimes been reported, but the direct comparison to retinal tissue is often not possible. For example, the spot-size dependence for damage in "transparent" materials is argued to be due to the probablistic character of exposing a small area of the material which also contains a microscopic imperfection or absorption site. The same argument has been made for optical coatings [21]. Such a spot-size dependence is for focal diameters of less than 400 μm in these low absorption materials and damage threshold exposures are at least 100 times greater than for the RPE. A more realistic comparison can be made with damage thresholds of absorptive layers, such as photographic print films or carbon paper [22,23]. Bergqvist, et al., [22] did not find significant additivity for trains of 1064-nm pulses focused to a 20-μm spot on a dark x-ray film. Studies of 694.3-nm damage thresholds for 20-ns exposures in my laboratory some years ago did not reveal a spot-size dependence for focal spot diameters greater than 100 μm [2]. From all of these observations, I favor a working hypothesis that a retinal repair process is influencing the observed thresholds for an opthalmoscopically visible lesion for q-switched laser exposures [1].

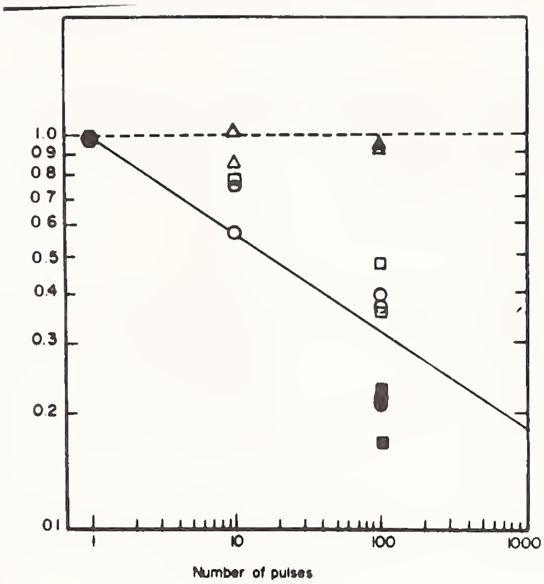

Figure 8. Ratio of Retinal Injury Thresholds for Different Pulse Trains. The empirical relation $N^{-1/4}$ is plotted as a solid line. Relative threshold exposure per pulse is shown for 0.9-mm image size △; for 30-μm spot size macular exposure O; and for 30-μm paramacular exposures □; open symbols are 1064 nm; dark symbols, 532 nm. From Greiss, et al., (1980) [18].

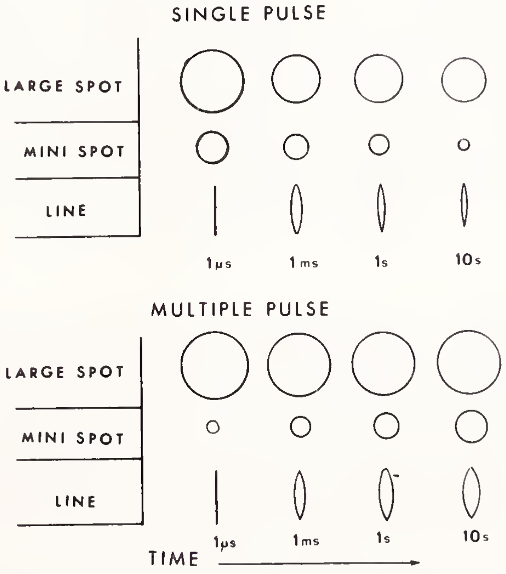

Figure 9. The Hypothesized time Course of the Appearance of a Threshold Retinal Lesion. Note that the repetitive pulsed exposure during the time depicted here would prevent repair of the irradiated area.

An alternative hypothesis for this spot-size dependence could also be related to the method of detecting a visible lesion. When the investigator observes a damage site during and after the pulsed exposure, he often reports the appearance of a brief enhancement of retinal reflection at the exposure site [25]. This could be the result of a rapidly formed gas bubble at the junction between the RPE and the retina. The gas bubble is reabsorbed into the adjacent tissue more readily for the smaller lesion. The longer the bubble lasts could be the greater the adverse effect upon adjacent tissue.

Still another (but related) alternative hypothesis would be the release of a biochemically toxic agent following membrane rupture [26]. When released in a sufficiently great quantity (as with a large image), the toxic dose is sufficient to result in permanent injury. Whatever factors play a significant role await further research.

6. Retinal Effects From Semiconductor Diode Laser Exposures

A puzzling change in the appearance of the retina has been reported by Beatrice, et al., following exposure of the rhesus monkey retina to trains of Ga-As (904-nm) laser pulses with average power levels entering the eye of only 22 μW to 260 μW [27]. This effect, which sometimes fades, and has not been detectable by histology, is not always seen and it is difficult to relate to pulse repetition frequency. Attempts to duplicate the finding have not always been successful, although a retinal change appearing as a darkening was observed at 300 uW by Ham and Mueller for a high-frequency pulse train. Since some emissions of blue light at 452 nm were noted as a result of frequency doubling in those specific diodes that caused some of the "changes," it appeared reasonable to speculate that the alteration at such low levels (well below thermal injury thresholds) could have been due to the self-oscillation found in most semiconductor diode lasers. The self-oscillation typically occurs at frequencies of 250-500 MHz, and individual pulses are less than 100 ps [28]. This behavior of diode lasers and self-mode-locking of most He-Ne lasers may point to an explanation of two curious experimental findings for lowered thresholds for trains of exposures lasting several seconds. Besides the GaAs laser thresholds for 10-1000 s, the threshold reported for 1000-s He-Ne exposures may be slightly lower due to this effect. Since most future human exposure to laser radiation may occur through the use of Ga-As lasers employed in fiber-optic communication systems and from He-Ne lasers, the study of these new phenomena as they affect retinal injury is clearly important. I should like to emphasize, however, that the presence of a visible change does not necessarily mean damage, any more than the detectable bleaching of visual pigments upon exposure to intense light. It may well be that these changes at 850-905 nm may be due to the photoactivation of enzymes [29,30]. Biscar reports that bovine a-chymotrypsin was activated at a very narrow band of wavelengths between 853 nm and 857 nm. This demonstrated that such effects could be produced in the near-infrared, and at a very select wavelength band [30]. Such observations force one to consider selective laser chemistry as a potential mechanism for laser injury in biological systems at irradiance levels believed only recently not to be of concern [31-32]. To my knowledge, such phenomena have yet to be shown to be plausible as injury mechanisms, but such possiblities cannot be overlooked. The effects of resonant interaction of a mode-locked train of pulses with a crystal lattice, although improbable in the retina, cannot be completely ruled out either, when one considers the regular organization of some retinal structures [33]. Lund has recently reported an apparent wavelength dependence of retinal injury thresholds between 700 nm and 950 nm that does not follow the absorption spectrum of melanin [34]. However, there were pulse width variations with the dye laser used. These could have lead to some of the differences. We must await the results of further studies to find the answer to this new puzzle.

7. Conclusions

Although much of the biological threshold data for laser injury of the eye can be understood as following the prediction of either a photochemical or thermal model, some remaining data require more complex models -- such as the incorporation of biological repair or biological amplification of the initial effect. Work continues in this area. Other areas of needed research include the further understanding of picosecond-pulsed injury of the retina, although most evidence suggests that it depends on the peak power in the pulse for pulse durations between 5 ps and 100 ps. Competing damage processes resulting from multi-photon absorption and electron avalanche effects as occur in solids, [35] probably explain the higher threshold for 532 nm when compared to 1064 nm at the same pulse duration (30 ps) as the data of Goldman show [36].

Interest in Nd:YAG mode-locked and q-switched laser injury of the retina has recently been elevated by the introduction of these types of lasers to cut membranes by producing microplasmas in the clear media of the eye [37,38].

Still further research is also necessary to understand the effects of speckle upon retinal function at very low, chronic exposure durations as reported by Zwick [39]. It may well be that if we force ourselves to stare at a large area diffuse laser reflection, the speckle which produces a myraid of areas of very high contrast borders at the retina may affect those neural mechanisms that detect borders in our normal world. Fortunately, most of us find it uncomfortable to stare at speckle for long periods, and this effect is hopefullly just a laboratory curiosity. Clearly there is still much to learn vis-a-vis laser irradiation of the eye.

I would like to thank Dr. M. L. Wolbarsht of Duke University for helpful criticism during the development of this paper, and Dr. J. Taboada of the USAF School of Aerospace Medicine who pointed out the existence of references 30 and 33 (Biscar, and Ratjska & Piekara).

8. References

[1] D. H. Sliney, Interaction mechanisms of laser radiation with ocular tissues: Implications for human exposure limits, Kvant Elektron., 7(10):2271-2281 (1980) and Soviet J. Quant. Electr., 10(10):1278-1284 in translation.

[2] D. H. Sliney and M. L. Wolbarsht, Safety with Lasers and Other Optical Sources, New York, Plenum Publishing Corp. (1980).

[3] W. T. Ham, Jr., J. J. Ruffolo, Jr., H. A. Mueller, and D. Guerry, III, The nature of retinal radiation damage: dependence on wavelength, power level, and exposure time, Vision Res., 20(12): 1105-1111, (1980).

[4] W. T. Ham, Jr. H. A. Mueller, J. J. Ruffolo, Jr., D. Guerry III, and R. K. Guerry, Action spectrum for retinal injury from near-ultraviolet radiation in the aphakic monkey, Am. J. Ophthal., 93(3):299-306, 1982.

[5] T. B. Williams and B. N. Baker, (Eds.), The Effects of Constant Light on the Visual Process, Plenum Publishing Corp., New York (1980).

[6] T. Lawwill, S. Crocket, and G. Currier, Retinal damage secondary to chronic light exposure, Doc. Opthal., 44(2):379-402 (1977).

[7] L. Feeny-Burns, The pigments of the retinal pigment epithemlium, in Current Topics in Eye Reasearch, Vol. 2, Academic Press, New York, pp. 119-179, (1980).

[8] R. W. Young, A theory of central retinal disease, in Future directions in Ophthalmological Research (M. L. Sears, Ed.), Yale University Press, New Haven, (1981).

[9] R. G. Allen, Retinal thermal injury, in (M. L. Walbarsht and D. H. Sliney, eds.) Ocular effects of non-ionizing radiation, Proc. Soc. Photo-Opt. Eng., 229:80-86 (1980).

[10] J. J. Vos, A theory of retinal burns, Bull. Math. Biophys., 24:115-128 (1962).

[11] A. M. Clarke, W. Geeraets, and W. T. Ham, Jr., An equilibrium thermal model for retinal injury, Appl. Opt., 8:1051-1054 (1969).

[12] A. Vassiliadis, Ocular damage from laser radiation, in (M. L. Wolbarsht, Ed.) Laser Applications in Medicine and Biology, Vol. 1, Plenum Press, New York (1971), pp. 125-162.

[13] M. A. Mainster, T. J. White, J. H. Tips, and P. W. Wilson, Retinal-temperature increases produced by intense light sources, J. Opt, Soc. Am., 60:264-270 (1970).

[14] J. R. Hayes and M. L. Wolbarsht, Thermal model for retinal damage induced by pulsed lasers, Aerospace Med., 39:474-480 (1968).

[15] J. Marshall, A. M. Hamiliton, and A. C. Bird, Histopathology of ruby and argon laser lesions in monkey and human retina, a comparative study, Br. J. Opthal., 59(1):610-630 (1975).

[16] C. Hu and F. S. Barnes, The thermal-chemical damage in biological material under laser irradiation, IEE Trans Biomed Eng, BME-17:220-229, 1970.

[17] B. E. Stuck, D. J. Lund, and E. S. Beatrice, "Repetitive Pulse Laser Data and Permissible Exposure Limits," Report No. 58, Letterman Army Institute of Research, Presdio of San Francisco, San Francisco, CA, (1978).

[18] G. A. Greiss, M. F. Blankenstein and G. G. Williford, Ocular damage from mutiple-pulse laser exposures, *Health Physics*, 39(6):921-927 (1980).

[19] R. G. King and W. J. Geeraets, The effect of Q-switched ruby laser on retinal pigment epithelium in vitro, *Acta Opthalmologica*, 46:617-632 (1968).

[20]. Walkenbach, J. E., Determination of retinal lesion threshold energies of pulse repetition Nd^{+3}:YAG laser in the rhesus monkey, Masters Thesis, Medical College of Virginia, Richmond, VA, June 1972.

[21] R. H. Picard, D. Milam, and R. A. Bradbury, Statistical analysis of defect-caused laser damage in thin films, *Appl. Opt.*, 16:1563-1571 (1977).

[22] T. Bergqvist, B. Hartmann, and B. Kleman, Imaging properties of the eye and interaction of laser radiation with matter, *in* (Tengroth and Epstein, eds.) *Current Concepts in Ergrophthalmology*, pp. 55-71, Ergophthalmologica Internationalis, Department of Opthalmology, Karolinska Institute, Stockholm (1978).

[23] J. E. Sollid, S. J. Thomas, and C. R. Phipps, Jr., Damage threshold variation with spot size at 10.6 um for Kalvar and Polaroid films, *Appl. Opt.*, 18(4):424 (1979).

[24] D. J. Lund, E. S. Beatrice, and S. T. Schuschereba, Bioeffects concerning the safe use of GaAs laser training devices, pp. 15-29 in (Beatrice, E. S., ed.), "Combat Ocular Problems," Letterman Army Inst. Res., 1982.

[25] E. S. Beatrice, Letterman Army Institute of Research, private communication.

[26] M. L. Wolbarsht, Duke University, private communication.

[27] E. S. Beatrice, D. J. Lund, M. Carter, and D. M. Talsma, "Retinal Alterations Produced by Low Level Gallium Arsenide Laser Exposure," Report No. 38, Letterman Army Institute of Research, Presidio of San Franscisco, San Franscisco, CA (1977).

[28] R. W. Dixon, Current directions in GaAs laser device developmemt, *Bell System Tech. J.,* 59(5):669-722 (1980).

[29] D. H. Hug, P. S. O'Donnel, and J. K. Hunter, Light activation of enzymes, *Photochem. and Photobiol.,* 32:841-848 (1980).

[30] J. P. Biscar, Photon enzyme activation, *Bull. Math. Biol.,* 38:29-38 (1976).

[31] E. Theile, M. F. Goodman, and J. Stone, "Can lasers be used to break chemical bonds selectively, *Optical Engineering*, 19(1):10-20 (1980).

[32] A. N. Oraevskii and P. G. Pleshanov, Selective phochemical mechanisms in the biological action of laser radiation, *Sov. J. Quantum electron.*, 8(10):1263-1268 (1978), originally *Kvantovaya Electron.*, 5:2243-2251 (1978).

[33] B. Ratajska and A. H. Piekara, Role of relaxation in the resonant interaction of light pulses with matter, *Appl. Opt.*, 17(23):3815-3817 (1978).

[34] D. J. Lund, E. S. Beatrice, and S. T. Schuschereba, Bioeffects concerning the safe use of GaAs laser training devices, pp. 15-29 in (Beatrice, E. S., ed.), "Combat Ocular Problems," Letterman Army Inst. Res., (1982).

[35] H. E. Bennet, A. J. Glass, A. H. Guenther, and B. E. Newman (Eds.), Laser Induced Damage in Optical Materials, "NBS Special Publication 568, US Department of Comerce, National Bureau of Standards, Boulder, CO, (1980).

[36] A. I. Goldman, W. T. Ham, Jr., and H. A. Mueller, Ocular damage thresholds and mechanisms for ultrashort pulses of both visible and infrared laser radiation in the rhesus monkey, *Exp. Eye Res.*, 24(1):45-56 (1977).

[37] D. H. Sliney, YAG Laser Safety, Chap 5, in (S. L. Trokel, ed.) YAG Laser Ophthalmic Microsurgery, Appleton-Centry-Crofts, East Norwalk (1983).

[38] M. A. Mainster, D. H. Sliney, C. Davis Belcher, III, and S. M. Buzney, Laser photodisrupters: damage mechanisms, instrument design and safety, scheduled for publication in Ophthalmology, 1983.

[39] Zwick, H. and Jenkins, D. L., Coherency Effects on Retinal Neural Processes of Pseudemys, Technical Note No. 81-20 TN/Dec, 82, Division of Ocular Hazards, LAIR, San Francisco (1982).

Spotsize Effects in Laser Damage Testing

S. R. Foltyn

University of California, Los Alamos National Laboratory
P. O. Box 1663, Los Alamos, NM 87545

For the past three years a program of testing and evaluation of HR coatings at excimer laser wavelengths has been in progress. During this period, an unconventional method has been employed to plot damage data: Ten sites are irradiated at each test fluence and the fraction of damaging sites is plotted as a function of peak fluence. The resulting curves slope from a fluence at which no damage was produced to a higher fluence at which all ten sites damaged. Attempts to explain wide slope variations among a variety of tested samples have led to a simple model which correlates slope, defect density, and Gaussian spotsize of the test beam. Specifically, the model predicts steep slopes if the beam is large compared to the mean defect spacing. In contrast to conventional notation, threshold is defined as the highest fluence at which the sample could not be damaged. Implicit in the model is that threshold thus defined is independent of spotsize while conventional thresholds have a calculable dependence. In the limit of large spotsize, the two thresholds are identical. Test results for various spotsizes are reported and analyses of previously published experimental data are presented in support of this model.

Key words: coating defects; damage probability; damage statistics; defect density; laser damage; size effects; spotsize; spotsize effects.

1. Introduction

One of the more interesting and certainly one of the most frustrating aspects of measuring laser damage thresholds is that the results of such measurements are influenced to varying degrees by an enormous range of parameters. Variables are introduced throughout the life cycle of a test sample; during fabrication (materials, polishing, cleaning, coating design or deposition parameters), during testing (wavelength, pulselength, spotsize, statistical variations), and in-between (storage, handling, cleaning) [1]. As a consequence, individual test results become meaningless without extensive characterization and documentation; valid intercomparisons between test facilities become virtually impossible.

In this work, the effect of one of these variable parameters - spotsize - is analyzed. It is shown that spotsize effects can arise from an improper, although traditional, definition of threshold and that a more realistic method of defining threshold leads to test results which are independent of spotsize.

2. Spotsize Effects

The first reported observations of spotsize effects - the apparent increase in damage threshold with decreasing test spotsize - appeard in the literature nearly ten years ago [2,3]. A physical model was described in which the samples under test contained a distribution of damage-prone defects that were more likely to be irradiated (hence damaged) by large laser spots than small ones. Similar observations have been described and analyzed in succeeding years [4-11], but despite considerable attention, there remains an aura of skepticism surrounding thresholds measured with small spots and a corresponding drive to do very expensive large-spot (>1 cm) testing with high-energy lasers. Interestingly, the beastly nature of such lasers (i.e., poor beam quality and repeatability) can itself introduce large uncertainties in the test results.

3. Threshold Definition

The Los Alamos excimer laser damage test facility has been in operation for the past three years [12,13], during which time an unconventional method has been employed for plotting test results and defining damage threshold. This is illustrated in figure 1. Here, a 308 nm reflector of Sc_2O_3/MgF_2 design was irradiated at nine different peak fluence levels. Ten discreet sites on the coated surface were tested at each fluence and the fraction of sites that damaged (i.e., the probability of damage) was plotted as a function of peak test fluence. Damage threshold is defined as the zero-percent crossing of a linear regression fit - 6.2 J/cm^2 in this case. (Note that in figure 1, a logarithmic fit is used; the difference in threshold is insignificant).

Figure 2, in contrast, shows the same data replotted in the conventional manner. For each site tested, a closed circle was placed at the "damage" level, or an open circle was used to indicate no damage. Traditionally, threshold is defined as the average of the highest nondamaging and the lowest damaging levels, corresponding roughly to the fluence at which half of the test sites damaged - 8.6 J/cm^2.

The zero-percent, or onset, definition is more satisfying for several reasons:

- * Damage probability curves demonstrate threshold-saturation behavior - the zero-percent definition of threshold is consistent with accepted notation (e.g., laser gain curves).
- * The onset fluence constitutes a maximum "safe" operating level. The reflector characterized in figure 2 will damage at levels well below the conventionally defined threshold fluence.
- * As will be shown, the slope of a probability curve, and accordingly, the 50% damage probability, depends upon the test spotsize. The conventional threshold definition is, therefore, a convolution of the actual defect threshold and the focusing geometry used for testing.

4. Influence of Spotsize on Probability Curves

4.1. A simple Model

In order to demonstrate the effect of spotsize on the slope of a damage probability curve, a simple model is presented which begins with the familiar Gaussian intensity distribution

$$\phi_{(r)} = \phi_o \exp\,(-2r^2/\omega_o^2) \qquad (1)$$

where the temporal integral has been performed and $\phi_{(r)}$ is the fluence at radial distance r, ϕ_o is the peak fluence at the beam center, and ω_o is the beam radius at the 1/e^2 amplitude (spotsize). Consider a test surface that is populated with a random distribution of identical defects, each of which has the property that, when immersed in a fluence exceeding some defect threshold fluence ϕ_{th}, damage occurs. Referring to figure 3, eq (1) can be rewritten to express the area A_D within which damage can occur in terms of the peak test fluence and spotsize:

$$A_D = \frac{\pi\,\omega_o^2}{2}\,\ell n\left(\frac{\phi_o}{\phi_{th}}\right) \qquad (2)$$

From Poisson statistics, the probability P_D that A_D contains one or more defects (i.e., the probability of damage is

$$P_D = 1 - \exp\,(-\lambda A_D) \qquad (3)$$

where λ is the surface density of defects. Combining eqs (2) and (3) yields

$$P_D = 1 - \left(\frac{\phi_{th}}{\phi_o}\right)^{\frac{\pi\,\omega_o^2\lambda}{2}} \qquad (4)$$

which, as required, is the probability of damage as a function of peak test fluence with spotsize and defect density as parameters.

Thus far, the model is two-dimensional but easily converted to the 3-D case that is applicable to damage in bulk materials. However, for a multilayer dielectric reflector - particularly with a low index ratio as is typical for uv materials - it is useful to sum 2-D damage probabilities over each of the high-index/low-index coating interfaces where the standing-wave fields are peaked. At the ith interface, the peak fluence is reduced by a factor η_i given by

$$\eta_i = \left(\frac{n_L}{n_H}\right)^{2(i-1)} \qquad (5)$$

where n_L and n_H are the low- and high-indices, respectively. Summing over all interfaces for $\eta_i \phi_o \geq$ ϕth (precludes negative contributions to the damage probability) gives the total damage probability for a multilayer reflector:

$$P_D = \sum_i 1 - \left(\frac{\phi_{th}}{\eta_i \phi_o}\right)^{\frac{\pi \omega_o^2 \lambda}{2}} \qquad (6)$$

A numerical evaluation yields the curves of figure 4. At a fixed beam size and index ratio (the chosen values are similar to those encountered experimentally), the only adjustable parameter is defect density. In figure 4, where a relatively low density of 2.5 mm^{-2} was used, contributions from the first and successive interfaces are plotted separately. It should be noted that for a n_H of 2.0 or larger and a similar defect density, the first-interface probability rises steeply and little damage occurs in deeper layers.

Examination of eq (4) reveals that as the exponent of the fraction (ϕ_{th}/ϕ_o) is increased, the damage probability increases, giving rise to a steeper slope. It is this relationship that leads to a decrease in conventional threshold for large spots or high defect density.

4.2. Experimental Support

In that the previous model was developed assuming a spatially Gaussian intensity distribution, measurements were conducted to demonstrate the applicability of the 248 nm spot used in these tests. While a TEM$_{oo}$ beam is not necessary, it is required that A_D increase logarithmically with peak fluence. As shown in figure 5, this condition is met experimentally. Other pertinent test conditions include pulse repetition rate (35 pps) and pulselength (15 ns).

Mean spot diameters of 0.31, 0.58, and 1.46 nm were used to irradiate eight samples from a single run of Al_2O_3/SiO_2 reflectors. A complete data set for the three samples tested with $2\omega_o$ = 0.58 mm is shown in figure 6. The solid line is the result of a least-squares fit and serves as a reasonable approximation to the hypothetical probability curve of figure 4. The dashed lines form a band which is ± one standard deviation from the best fit. Similar bands in figure 7 illustrate the observed variations in slope with spotsize. Note that, in the conventional sense, threshold increases from about 2 J/cm^2 for the large spot to almost 7 J/cm^2 for the 0.31 mm spot, while the zero-probability intercepts remain unchanged. It should be pointed out that even though the best fit for each spotsize gave an onset fluence of 1.8 J/cm^2, the onset uncertainty, as indicated by the width of the bands in figure 7, increases for smaller spots.

An attempt was made to correlate the results of figure 7 with those predicted by eq (6). Plots were generated for the appropriate spotsizes using the defect density as an adjustable parameter. Solid lines within the shaded bands of figure 8 illustrate that a quite reasonable fit is obtained for λ = 3.5 mm^{-2}.

To check this result, an independent measurement of defect density was carried out by damaging and counting the defects in a relatively large coated area. Fluence was adjusted to produce damage in the outer HL interface only. Defects in each of fifty-five 1 mm^2 samples areas were counted resulting in the histogram of figure 9, which is a fair approximation of the Poisson distribution function. The average measured defect density was 3.2 mm^{-2} which is in agreement with the fitted value of 3.5.

5. Quantitative Spotsize Dependence of Conventional Thresholds

In order to quantify the spotsize dependence inherent in the conventional threshold definition, Eq. (4) can be rewritten in terms of d_o, the mean defect spacing:

$$P_D = 1 - \left(\frac{\phi_{th}}{\phi_o}\right)^{\frac{\pi w_o^2}{8d_o^2}} \qquad (7)$$

This expression is valid for damage in a single layer coating, on a surface, or, as indicated earlier, for a multilayer reflector with a high index ratio. Now, considering that the conventionally defined threshold ϕ_{conv} is the peak fluence for which P_D = 50%, eq (7) can be manipulated to express the functional relationship between conventional threshold, defect threshold, spotsize, and mean defect spacing:

$$\log\left(\frac{\phi_{conv}}{\phi_{th}}\right) = \frac{2.4}{\pi}\left(\frac{d_o}{w_o}\right)^2 \qquad (8)$$

The significance of this expression becomes apparent in figure 10. Here, the conventional threshold (normalized to the defect threshold) is plotted versus spotsize (normalized to the mean defect spacing). Conventional threshold exceeds the defect threshold by 10% for spotsizes as large as four times the distance between defects. In figure 11, 694 nm thresholds obtained by DeShazer, et al. in 1973 are shown to correlate with this predicted behavior.

6. Other Models

The statistical model of Section 4.1 is a very simple one. More sophisticated models exist [14,15] which propose that, instead of being singular, defect thresholds are distributed. This feature is perhaps more physically satisfying, but is not necessary to explain the results presented in section 4.2. In addition, it is not intended that the work here preclude the applicability of thermal models or the possibility of a spotsize effect resulting from self-focusing or other processes.

7. Conclusions

It is shown that spotsize effects can arise as a consequence of dependence of the conventionally defined threshold upon the slope of a damage probability curve. A model is developed and experimental evidence presented suggesting that the zero-probability intercept, or damage onset, is spotsize independent. It is proposed for this reason, and others, that the laser damage threshold be redefined accordingly.

The author wishes to acknowledge both the work of L. J. Jolin, who performed the damage testing, and the help and support of Brian Newnam.

8. References

[1] The most comprehensive source of information regarding parametric studies of laser damage can be found in the proceedings of the first thirteen Boulder Damage Symposia.

[2] DeShazer, L. G.; Newnam, B. E.; Leung, K. M. The Role of Coating Defects in Laser-Induced Damage to Thin Films. Nat. Bur. Stand. (US) Spec. Publ. 387; 1973, 114p.

[3] Aleshin, I. V.; Bonch-Bruevich, A. M.; Zinchenko, V. I.; Imas, Ya. A.; Komolov, V. L. Effect of Absorbing Inhomogeneities on Optical Breakdown of Transparent Dielectrics. Sov. Phys. Tech. Phys. 18: 1648; 1974.

[4] Wang, V.; Guiliano, C. R.; Garcia, B. Single and Multilongitudinal Mode Damage in Multilayer Reflectors at 10.6 μm as a Function of Spot Size and Pulse Duration. Nat. Bur. Stand. (US) Spec. Publ. 435; 1975, 216 p.

[5] Bettis, J. R.; House, R. A.; Guenther, A. H. Spot Size and Pulse Duration Dependence of Laser-Induced Damage. Nat. Bur. Stand. (US) Spec. Publ. 462; 1976, 338 p.

[6] Tang, C. C.; Leung, K. M.; Bass, M. Re-examination of Laser Induced Breakdown in the Alkali Halides at 10.6 μm. Nat. Bur. Stand. (US) Spec. Publ. 462; 1976. 346 p.

[7] Van Stryland, E. W.; Soileau, M. J.; Swirl, A. L.; Williams, W. E. Pulse-Width and Focal-Volume Dependence of Laser-Induced Breakdown. Nat. Bur. Stand. (US) Spec. Publ. 620; 1980. 375 p.

[8] Sioleau, M. J.; Franck, J. B.; Veatch, T. C. On Self-Focusing and Spot-Size Dependence of Laser-Induced Breakdown. Nat. Bur. Stand. (US) Spec. Pub). 620; 1980. 385 p.

[9] Gorshkov, B. G.; Danieleiko, Yu. K.; Manenkov, A. A.; Prokhorov, A. M.; Sidorin, A. V. Size Effect and Statistics of Laser Damage to Alkali-Halide Crystals at the 10.6 μm Wavelength. Sov. J. Quantum Electron. 11(1): 81-84; 1981 January.

[10] Bessonova, T. S.; Danileiko, Yu. K.; Nikolaev, V. N.; Sidorin, A. V. Optical Strength of LiF Crystals. Sov. J. Quantum Electron. 11(10): 1383-1384; 1981 October.

[11]· Stewart, A. F.; Guenther, A. H. Preliminary Experimental Results of Spot Size Scaling in Laser-Induced Damage to Optical Coatings. Presented at Thirteenth Annual Symposium on Optical Materials for High Power Lasers, November, 1981 (to be published).

[12] Foltyn, S. R.; Newnam, B. E. Multiple-Shot Laser Damage Thresholds of Ultraviolet Reflectors at 248 and 308 nanometers. Nat. Bur. Stand. (US) Spec. Publ. 620; 1980. 265 p.

[13] Foltyn, S. R.; Newnam, B. E.; Jolin, L. J. Laser Damage Results and Analyses for uv Reflectors Under Multiple-Shot Irradiation. Presented at the Thirteenth Annual Symposium on Optical Materials for High Power Lasers, November, 1981 (to be published).

[14] Danileiko, Yu. K.; Minaev, Yu. P.; Nikolaev, V. N.; Sidorin, A. V. Determination of the Characteristics of Microdefects from Statistical Relationships Governing Laser Damage to Solid Transparent Materials. Sov. J. Quantum Electron. 11 (11): 1445-1449; 1981 November.

[15] Porteus, J. O. Determination of the Onset of Defect-Driven Pulsed Laser Damage in 2.7 μm Optical Coatings. Presented at Topical Meeting for High Power Laser Optical Components, November, 1982.

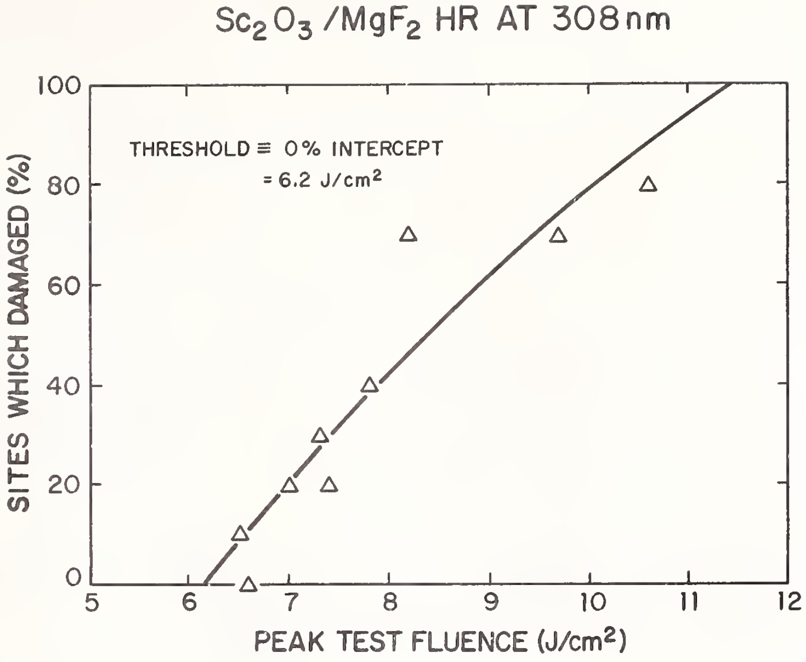

Figure 1. Results of a standard test at 308 nm of a Sc_2O_3/MgF_2 reflector. Each triangle represents the fraction of ten test sites which damaged at a particular test fluence. Damage threshold is the zero-probability intercept - 6.2 J/cm².

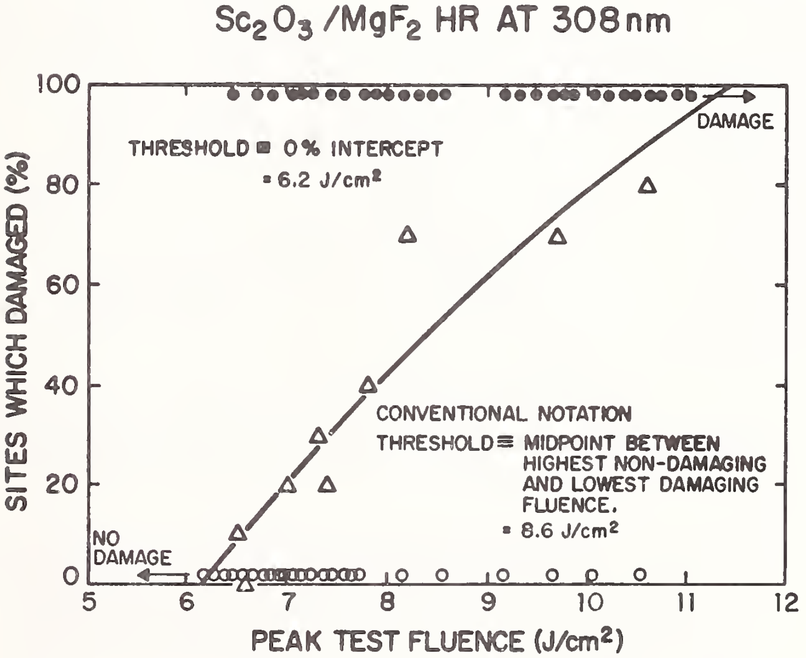

Figure 2. The data of figure 1 are replotted in the conventional manner (open and closed circles). As defined conventionally, threshold is 8.6 J/cm².

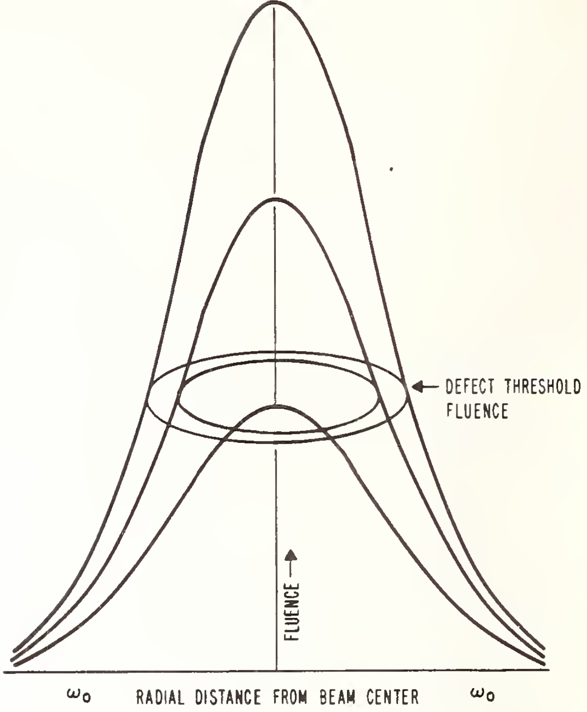

Figure 3. For a given defect threshold fluence, the area within which damage can occur increases logarithmically with peak fluence.

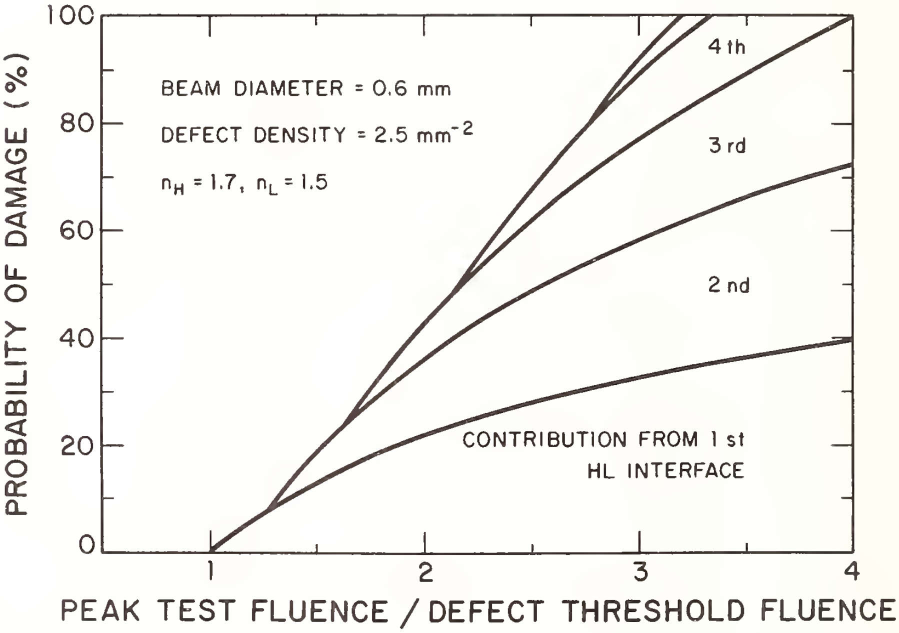

Figure 4. Calculated damage probabilities for a multilayer reflector with a low index ratio. For the case shown, damage can occur in the five outermost HL interfaces. The net damage probability is, to a good approximation, a straight line.

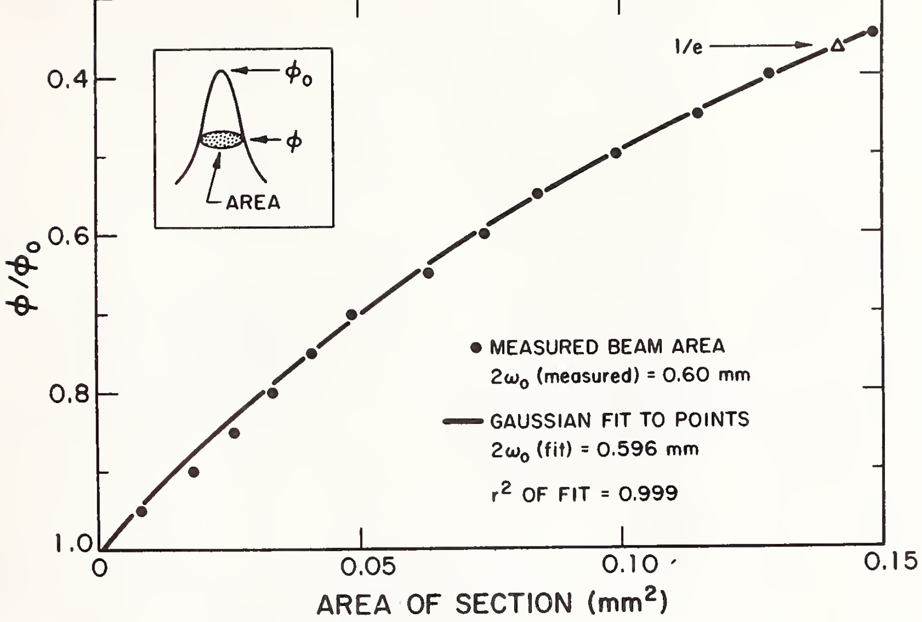

Figure 5. Spatial comparison of test beam to an ideal Gaussian. A good fit assures the validity of a comparison between theory and experiment.

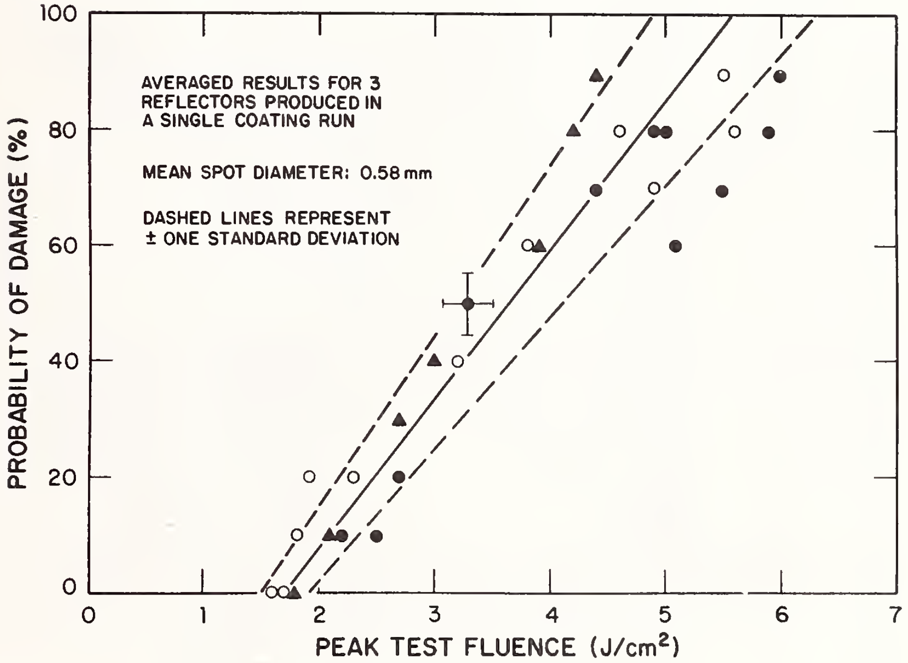

Figure 6. Results of testing three reflectors with a spot diameter of 0.58 mm. The dashed lines extend ± one standard deviation from the best fit. The error bars indicate a ± 5% uncertainty in measurement of both fluence and probability.

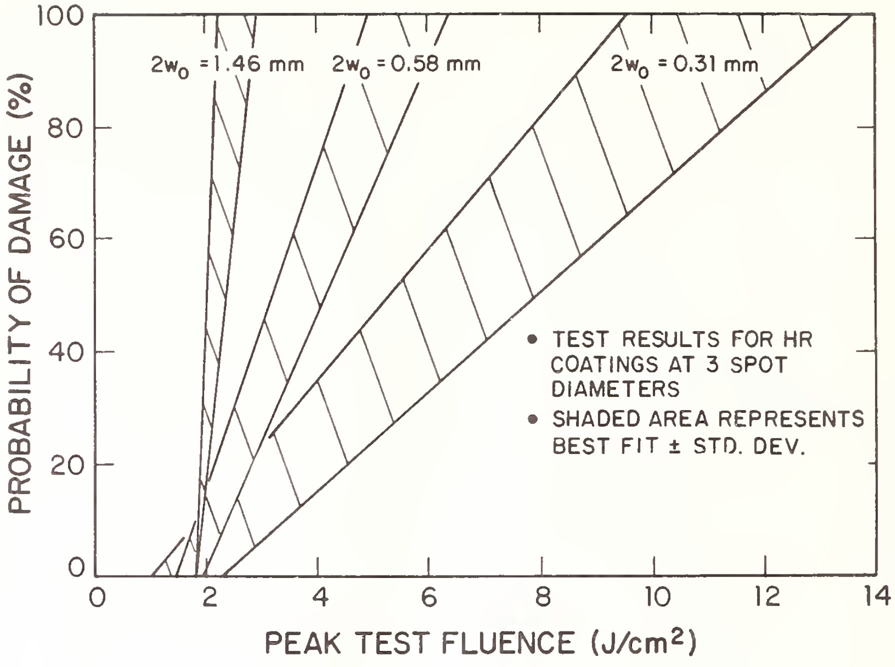

Figure 7. Results of testing identical reflectors at three different spotsizes.

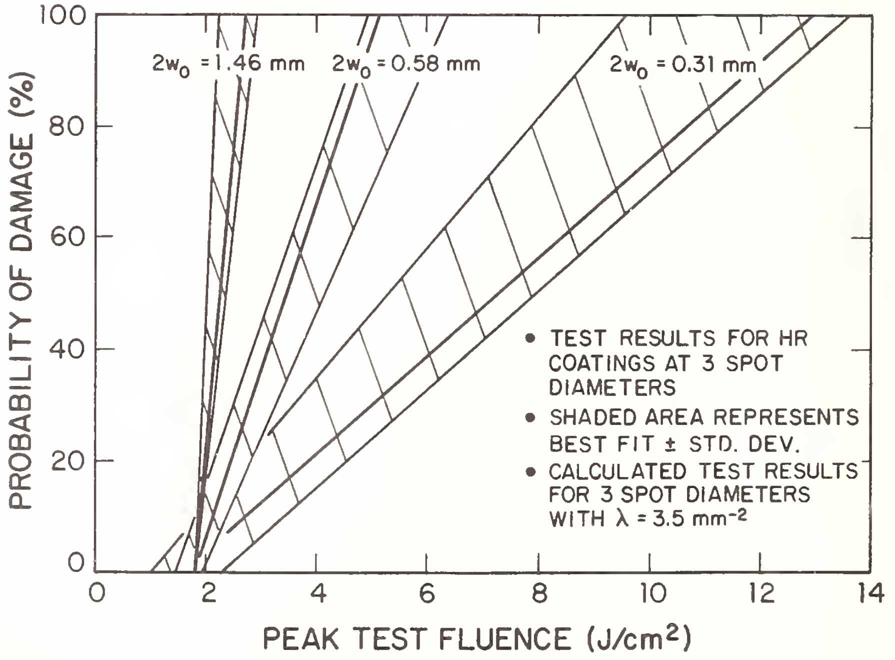

Figure 8. The solid lines within the shaded areas are calculated curves obtained from eq (6) by using the appropriate spotsize values and treating defect density as a fitted parameter. The best fit is obtained for a defect density of 3.5 mm^{-2}.

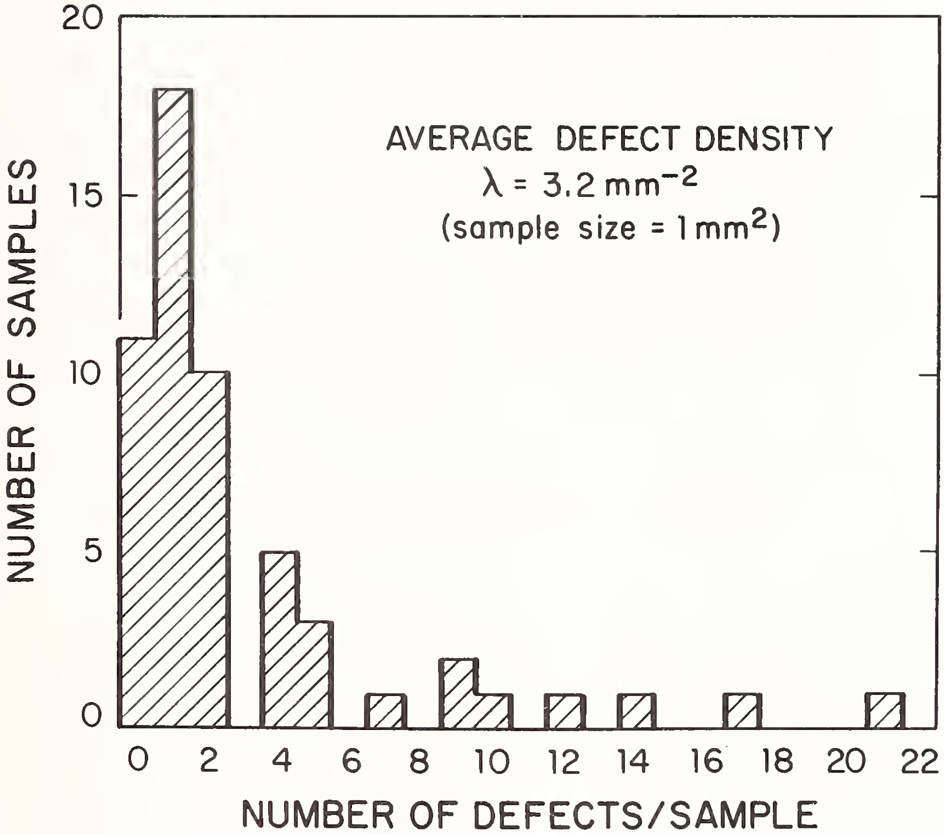

Figure 9. A defect counting experiment was performed to verify the fitted value of defect density. Fifty-five 1 mm^2 samples were damaged yielding an average defect density of 3.2 mm^{-2}. The histogram is a fair approximation of the Poisson distribution function.

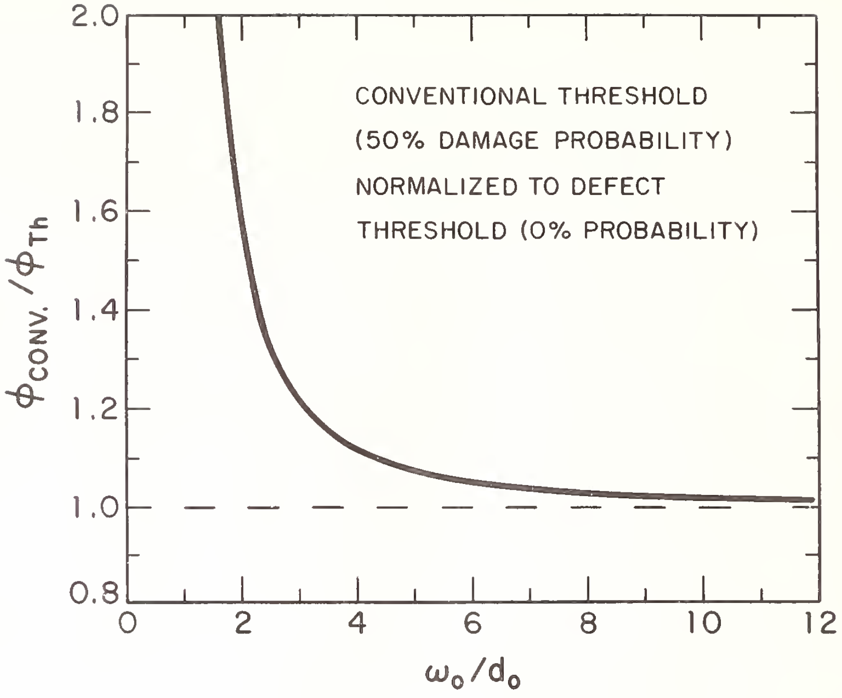

Figure 10. Quantitative behavior of the conventional threshold as a function of spotsize.

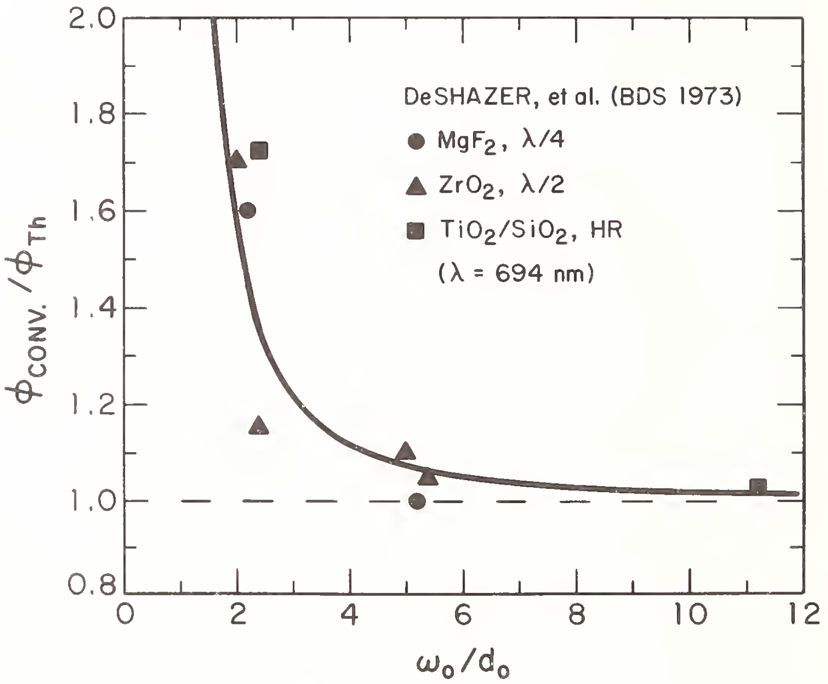

Figure 11. Test results from reference 2 plotted on the curve of figure 10. Good agreement demonstrates the applicability of a simple model to the explanation of spotsize effects.

The speaker was asked if he had considered more than a single type of defect in his analysis, and replied that the fit of his data to the "single-defect" model was adequate. In response to a second question, he said the "effective density of defects" was determined by counting defects in large-area damage sites irradiated at a few percent over threshold fluence.

PULSED LASER INDUCED DAMAGE OF AN OPTICAL MATERIAL WITH A SPHERICAL INCLUSION: INFLUENCE OF THE THERMAL PROPERTIES OF THE MATERIALS

M. R. Lange and J. K. McIver
Institute for Modern Optics
University of New Mexico
Albuquerque, New Mexico 87131

and

A. H. Guenther and T. W. Walker
Air Force Weapons Laboratory
Kirtland Air Force Base, New Mexico 87117

In a recent set of papers, a model was developed to describe the role of spherical inclusions (impurities) in the pulsed laser induced damage of optical thin films (dielectrics). The numerically generated relation of the damage threshold in J/cm^2 as a function of the radius of the inclusion had a minimum, whose value varied as the square root of the incident laser pulse length. This prediction agrees with the frequently observed trend that longer laser pulses yield higher damage thresholds.

In this paper it is shown analytically that the damage threshold as a function of radius of the spherical inclusion does indeed have a minimum that varies as the square root of the laser pulse length. Furthermore, this minimum is shown to be relatively insensitive to the thermal properties of the impurity for a wide range of typical optical materials. However, the effect of the thermal properties of the host on this minimum is more complicated. One is able to show that for many host/impurity combinations, the minimum damage threshold varies as the square root of the thermal conductivity of the host, thus indicating that the thermal properties of the host material may be a useful indicator of pulsed laser induced damage sensitivity.

Key words: Laser damage; damage threshold; spherical inclusion; thermal properties; impurity.

Introduction

One possible reason for the low damage threshold of optical thin films is the increased absorption, relative to the material in bulk form, of the incident radiation by the ever present impurities within the film. For the particular case of dielectric films, a previous study[1,2] [1] concentrated on developing an understanding of the variation of the damage threshold of a thin film as a function of the radius of a spherical inclusion embedded in the material. That study predicted that the damage threshold should vary as the square root of the laser pulse length t. Numerous experimental investigations have provided evidence for this assertion (see, for example, the work of Milam [3,4]).

In the work herein, the results of a further study of laser damage due to a spherical inclusion embedded in a host are presented. In particular, the sensitivity of the damage threshold to the thermal properties of the host and inclusion are investigated. One finds that for many cases of interest, the damage threshold is relatively insensitive to the thermal properties of the impurity but varies measurably with the thermal properties of the host. From this study, the point of damage is found to scale linearly with a material dependent temperature and as the square root of the products of the thermal conductivity and specific

---

[1] Figures in brackets indicate the literature references at the end of this paper.

heat of the host material. This variation of the damage threshold with the thermal properties is in addition to the $\sqrt{t}$ dependence mentioned previously.

Model

As is the case with previous investigations [1,2,5] of impurity initiated damage, the present model has a spherical absorbing particle with radius "a" embedded in a host material. The inclusion absorbs radiation from the incident laser field and rises in temperature. Once the temperature of the impurity or host reaches some critical temperature (e.g., melting point), the system is assumed to damage. From this simple description, it is patently clear that the rate at which the heat is conducted away from the inclusion can play a crucial role in determining the damage threshold.

As has been discussed in previous work [2], the well known approximate solution of Hopper and Uhlmann [6] for this problem is not valid (nor was it meant to be) when the coefficient of thermal diffusivity in the impurity is small. This restriction excludes the possibility of using their solution when the impurity is a dielectric. For this, the case of prime interest, it is necessary to turn to an exact solution of the heat diffusion equation for the temperature, such as given by Goldenberg and Tranter [7].

$$T = \frac{3QI}{4\pi K_i a} \left\{ \frac{1}{3} \frac{K_i}{K_h} - \frac{2b}{\pi} \int_0^\infty \exp\left(\frac{-y^2 t}{\gamma}\right) F(y) dy \right\}$$

$$F(y) = \frac{(\sin y - y \cos y) \sin y}{y^2 [(c \sin y - y \cos y)^2 + b^2 y^2 \sin^2 y]}, \qquad (1)$$

$$\gamma = a^2/D_i, \quad b = \frac{K_i}{K_h} \frac{\sqrt{D_h}}{\sqrt{D_i}}, \quad c = 1 - \frac{K_h}{K_i},$$

K is the thermal conductivity in J/s-cm-°K, and D is the thermal diffusivity in cm^2/s. The subscripts refer to the host h or the impurity i. It should be noted that the above equation is not in its most general form. It has been rearranged to give the temperature at the surface of an impurity of radius a in cm. The quantities Q and I that occur in eq. (1) are the absorption cross section in cm^2 and the intensity of the incident laser pulse in $watts/cm^2$.

A rigorous treatment of the absorption of radiation by the impurity requires that the Mie cross section be used for Q. In that case, the absorption would be frequency dependent. This topic will be the subject of a later paper. Since in this study one is interested in the effects of the thermal properties, the small wavelength limit of the Mie cross section will be used; i.e., $Q = \pi a^2$.

In keeping with common practice, the temperature at which damage occurs is assumed to be known. The dependent variable in eq. (1) is then the intensity for a given pulse length necessary to achieve this temperature. To conform to the damage threshold usually measured in experiments, the energy per unit area (J/cm^2) is defined as

$$E = It \qquad (2)$$

Results

In a previous study [2] employing eq. (1), the damage threshold E was investigated as a function of the radius of the impurity. This work showed that the function E(a) had a minimum (see fig. 1), and that this minimum damage threshold varied as $\sqrt{t}$. This scaling has been verified experimentally [1,3,4].

Since a sample that contains inclusions will most likely have a distribution of sizes [8], the damage threshold of the system will be determined by the minimum of E(a), if it occurs at a radius a that is within the thickness of the film. As can be seen from fig. 1, minimums do exist within the film for common pulse lengths and thin film material and geometrical parameters. For this reason, the term damage threshold will for the remainder of this discussion refer to the minimum of E(a).

Because the determination of the thermal properties of the inclusions and host is a difficult experimental problem, a theoretical study of the sensitivity of the damage threshold to these quantities is a worthwhile endeavor. It is, of course, a relatively simple procedure to vary the thermal constants and determine the damage threshold numerically. In fact, this has been done, and the results are presented for the case of platinum in glass (fig. 2) and ThO_2 in ThF_4 (figs. 3-4). These two examples cover the most interesting regions of parameter space; i.e., impurities with both good and poor thermal conductivity embedded in a poor thermal conductor (see table 1). It is important to note that if the heat capacity C_p in J/g-°K and the density ρ in g/cm^3 of the material is assumed to be held fixed, then D and K vary at the same rate since $K = \rho C_p D$.

Unfortunately, numerical treatments, besides being time consuming, do not readily lend themselves to determining functional dependencies. For this reason, an approximate method of evaluating the integral in eq. (1) has been developed. The key to this method is the realization that as long as $D_i t/a^2 > 1$, the integral is dominated by the exponential. This means that the remaining portion of the integrand can be replaced by a power series in y^2. The zeroth order approximation consists of retaining terms of order one in the power series. The radius at which damage first occurs is then given by

$$a_0 = \frac{\sqrt{\pi D_h t}}{2}\ , \tag{3}$$

while the damage threshold is given by

$$E_0 = 16T\frac{\sqrt{\rho_h C_{ph} K_h t}}{\pi}\ . \tag{4}$$

Equation (4) is particularly interesting because it not only verifies the $\sqrt{t}$ dependence previously suggested but also predicts that the damage threshold scales linearly as the temperature at which damage occurs and as the square root of the product of the specific heat and conductivity of the host. In this reasonable approximation, the damage threshold is independent of the properties of the impurity.

In order to visualize the effect of the properties of the impurity on the damage threshold, it is necessary to keep terms of order y^2 in the expansion in the integral. In this case, the damage threshold is given by

$$E_1 = 16T\frac{\sqrt{\rho_h C_{ph} K_h t}}{\pi}\ \frac{1}{1 + \frac{\pi \rho_i C_{pi}}{120 \rho_h C_{ph}}\left[15\frac{\rho_h C_{ph}}{\rho_i C_{pi}} - 10 - \frac{K_h}{K_i}\right]} \tag{5}$$

Note that this expression also scales as $T\sqrt{t}$. , however, the dependence on the thermal properties is more complicated. For dielectric materials, the second term in the denominator is $\lesssim 0.1$, thus making it a relatively unimportant contribution to the final answer. The first order correction, therefore, does not substantially influence the scaling predictions of eq. (4).

A comparison of eq. (5) with the numerical integration of the exact solution shows suprisingly good agreement (see figs. 2-4). This reinforces the conclusion that for impurity-dominated damage, the threshold scales as $T\sqrt{\rho_h C_{ph} K_h t}$ and is relatively insensitive to the thermal properties of the inclusion.

Discussion

Although this model provides some new scaling laws for damage thresholds, it is not capable of making quantitative predictions. It also ignores several potentially important phenomena. One of these is the frequency dependence of the absorption cross section. Another is the finite thickness of the film and the effect of the substrate. The list of neglected factors and phenomena can become lengthy. On the other hand, if absorption of radiation occurs primarily in the inclusion, then at what rate the temperature rises in any part of the impurity still depends on how fast the surrounding material can remove the heat from the source. It is, therefore, not unreasonable to assume that further refinements of this basic model will not substantially change the conclusions presented in this paper.

References

[1] T. W. Walker, A. H. Guenther, and P. Nielsen, Pulsed Laser-Induced Damage to Thin-Film Optical Coatings - Part I: Experimental," IEEE J. Quantum Electron., QE-17, 2041 (1981).

[2] T. W. Walker, A. H. Guenther, and P. Nielsen, "Pulsed Laser-Induced Damage to Thin-Film Optical Coatings - Part II: Theory," IEEE J. Quantum Electron., QE-17, 2053 (1981).

[3] D. Milam and R. A. Bradbury, "Laser Damage Threshold for Dielectric Coatings as Determined by Inclusions," Appl. Phys. Lett., 23, 654 (1973).

[4] D. Milam, "1064NM Laser Damage Threshold of Polished Glass Surfaces as a Function of the Pulse Duration and Surface Roughness," Laser Induced Damage in Optical Materials: 1978, A. J. Glass and A. H. Guenther Eds., NBS Spec. Pub. 541, 164, Washington DC: U.S. Gov't Printing Office (1978).

[5] C. J. Duthler and M. J. Sparks, "Extrinsic Absorption in Laser Window Materials," Laser Induced Damage in Optical Materials, A. J. Glass and A. H. Guenther Eds., NBS Spec. Pub. 414, 219, Washington DC: U.S. Gov't Printing Office (1974).

[6] R. W. Hopper and D. R. Uhlmann, "Mechanism of Inclusion Damage in Laser Glass," J. Appl. Phys., 41, 4023 (1970).

[7] H. Goldenberg and J. C. Tranter, "Heat Flow in an Infinite Medium Heated by a Sphere," Brit. J. Appl. Phys., 3, 296 (1952).

[8] V. V. Artem'ev, A. M. Bonch-Bruevich, I. E. Morichev, I. E. Ivanov, and A. G. Vinogradskii, "Statistics of Microscopic Inhomogeneities and Optical Breakdown of Transparent Media," Sov. Phys. Tech. Phys., 22, 106 (1977).

[9] M. Sparks and C. J.Duthler, Theoretical Studies of High-Power Ultra-Violet and Infrared Materials, Eighth Tech. Rep., 11 (1976).

[10] Handbook of Thermophysical Properties of Solid Materials, Rev. Ed., A. Goldsmith, T. E. Watemman, and H. J. Hirschhorn, New York: MacMillan Company (1961).

[11] Thermophysical Properties of Matter, Y. S. Touloukian, Dir., New York: Plenum Press (1970).

Table 1

Quantities Employed in the Analysis of an Impurity Embedded in a Host

Thermal Properties for ThF_4 (Host) and ThO_2 (Impurity)

K_h = 0.1 (J/cm-s-°K) (9)
K_i = 0.142 (J/cm-s-°K) (11)
D_h = 0.05 (cm^2/s) (9)
D_i = 0.0594 (cm^2/s) (11)

Thermal Properties for Glass (Host) and Platinum (Impurity)

K_h = 0.013 (J/cm-s-°K) (6)
K_i = 0.67 (J/cm-s-°K) (6)
D_h = 0.003 (cm^2/s) (6)
D_i = 0.24 (cm^2/s) (6)

Damage Condition

T_c = 2000 °K

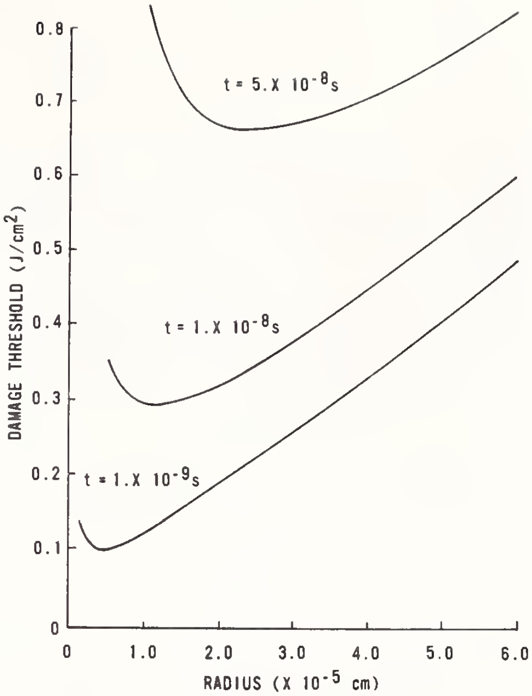

Fig. 1 Damage Threshold as a Function of Impurity Radius for Various Pulse Lengths, the Host is Glass While the Inclusion is Platinum

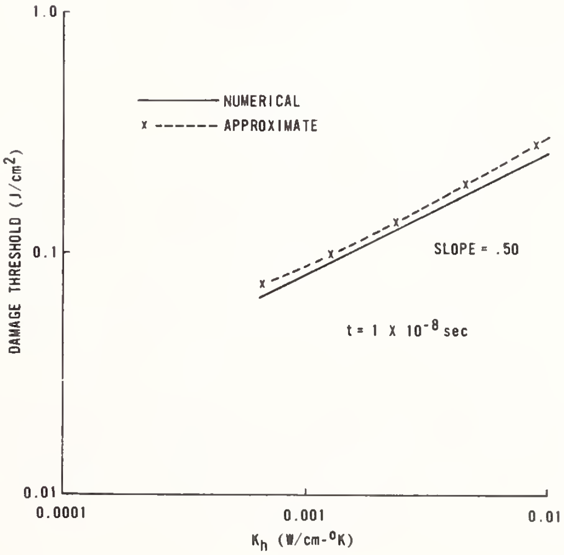

Fig. 2 Damage Threshold as a Function of Host Conductivity: Platinum - Impurity

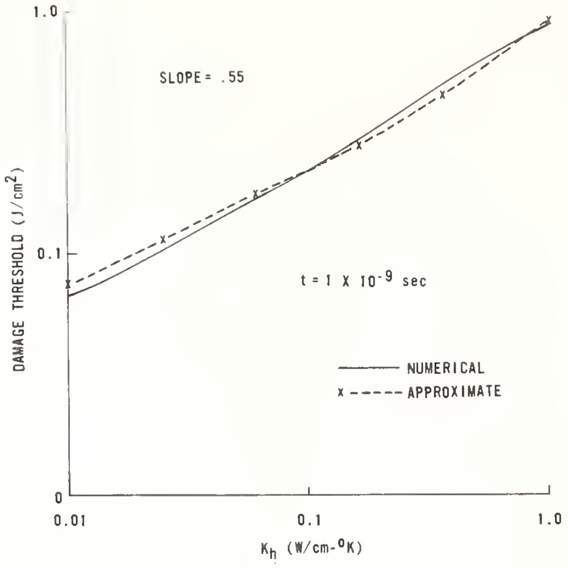

Fig. 3 Damage Threshold as a Function of Host Conductivity: ThO_2 - Impurity

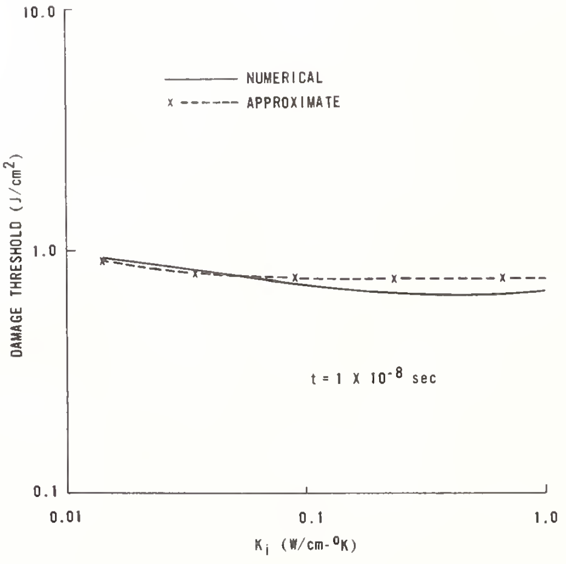

Fig. 4 Damage Threshold as a Function of Impurity Conductivity: ThF_4 - Host

Temporal Dependence of Laser-Induced Breakdown in NaCl and SiO_2

M. J. Soileau, William E. Williams, Eric W. Van Stryland,
Thomas F. Boggess, and Arthur L. Smirl

Department of Physics
Center for Applied Quantum Electronics
North Texas State University
P. O. Box 5368
Denton, Texas 76203

The laser-induced damage (LID) thresholds of fused silica and single crystal NaCl were studied at wavelengths of 0.5 and 1 µm for pulses as short as 4 psec for a variety of focal spot sizes. The problem of sample-to-sample variation was minimized by performing parametric studies on a single sample at a time. Beam distortion measurements and polarization dependence studies of the LID thresholds demonstrate that the contribution of self-focusing to the LID measurements in this work was negligible. The damage threshold field, E_B, was found to increase as the pulsewidth was decreased in both materials at both wavelengths. The strongest pulsewidth dependence observed was approximately an inverse square root proportionality observed in NaCl at 1 µm for pulses shorter than 10 psec. For conditions of equal pulsewidth and the same focal spot size, E_B was less at 0.5 µm than at 1 µm for both materials.

Key Words: Laser Damage, Picosecond Pulses, Fused Silica, NaCl, Avalanche Breakdown, 1.06 µm, 0.53 µm, 1.05 µm.

1. Introduction

The problem of bulk laser-induced damage (LID) in nominally transparent materials has been the subject of extensive investigation [1]. However, after more than 15 years of study, bulk laser-induced damage is still not well understood. A major obstacle to developing models for such damage in highly transparent materials is the lack of a consistent data base for the dependence of LID on such basic parameters as laser wavelength and pulsewidth. The problems of sample to sample variations and the complex interdependence of the damage thresholds on laser frequency, pulsewidth, and focal conditions [2] make the interpretation of isolated data points difficult.

We have tried to minimize these problems by studying LID as a function of wavelength and pulsewidth for a variety of focal conditions on a given sample. In Ref. 2 the LID-thresholds of a sample of fused SiO_2 and a single cyrstal NaCl sample were studied at 1.06 µm as a function of pulsewidth for pulses ranging from 40 psec to 31 nsec using a variety of focal conditions. In that work we found that the laser-induced breakdown threshold field, E_B, (i.e., the r.m.s. field corresponding to the LID threshold peak-on-axis irradiance) was only weakly dependent on the laser pulsewidth. We found that, for the range of parameters used, we could fit all the data in Ref. 2 to the following empirical relationship

$$E_B = A/[t_p^{1/4}\ \omega_o^4] + B \tag{1}$$

where A and B are constants for a given sample, t_p is the laser pulsewidth and ω_0 is the laser focal spot radius. In the present work, we find that this relationship breaks down for pulses shorter than 10 psec.

Here we extend the pulsewidth dependence studies at a wavelength of 1 µm to pulses as short as 4 psec, and we study the LID characteristics of fused SiO_2 and single crystal NaCl at 0.53 µm for pulsewidths in the 20 to 200 psec range. We find that the empirical relationship given by eq. 1 no longer holds for laser pulses shorter than 10 psec. For the shortest pulses (4 - 10 psec at 1.05 µm), E_B varied as approximately the inverse fourth root of the pulsewidth in SiO_2 and as approximately the inverse square root in NaCl for all the focal conditions studied.

For conditions of equal pulsewidth and the same focal spot size, E_B was less at 0.53 µm than at 1.06 µm for both materials for pulses in the 40 to 200 psec range. This result is contrary to the predictions of a simple avalanche breakdown model. Also, the observed dependence, while in the right direction, is much too weak for a strictly multiphoton process. A multiphoton initiated avalanche breakdown process [2] could possibly account for the observed wavelength dependence.

In addition, by carefully studying the polarization dependence of LID and by measuring the distortion of the transmitted beams, we show that the contribution of self-focusing to LID in our experiments is much less than has been assumed by other workers. In fact, for certain focal conditions we demonstrate that the effects of self-focusing are negligible.

2. Experiment

The lasers used in this study were a mode-locked Nd:YAG oscillator-amplifier system and a mode-locked Nd:Glass oscillator system which have been described elsewhere [2,3]. The YAG laser was operated at 1.06 µm and the glass at 1.05 µm. In each case a single pulse of measured Gaussian spatial profile was switched out of the mode-locked train and amplified. The pulsewidth of the Nd:YAG laser was varied from 40-200 psec by selecting various etalons as the output coupler of the oscillator. The glass laser pulsewidth varied from 4 to 10 psec. The pulsewidth and energy of each pulse were monitored. The width of each pulse was determined by monitoring the ratio of the energy in the second harmonic produced in a nonlinear crystal to the square of the energy in the fundamental. A more detailed description of energy and pulsewidth measurement are given in Ref. 2.

A temperature tuned CD*A crystal was used with the Nd:YAG laser to produce pulses at 0.53 µm. Care was taken to filter any residual 1.06 µm radiation from the 0.53 µm beam. The energy in the fundamental pulses at 1.06 µm was kept below a value which would produce saturation effects in the spatial profile of the second harmonic. Two-dimensional scans of the 0.53 µm beam with an optical multichannel analyzer (OMA) verified the absence of saturation effects and the Gaussian spatial profile of the 0.53 µm beam. Such vidicon scans of the spatial beam profile showed that the shot-to-shot variation in the beam width was less than our detection resolution limit of approximately 1%. Light-by-light scattering measurements in a $LiIO_3$ crystal [4] indicated that the 0.53 µm pulses had a Gaussian temporal shape. The results of these measurements confirmed that the 0.53 µm pulsewidth scaled as the 1.06 µm pulsewidth divided by $\sqrt{2}$. This scale factor was used to compute the 0.53 µm pulsewidths from the measured 1.06 µm pulsewidths.

The laser beam was focused into the bulk of the sample using single element, "best form", lenses designed for minimum spherical aberrations. Three lenses of focal lengths 37 mm, 75 mm, and 150 mm were used at various distances from the beam waist to produce the focal spot radii for these experiments. The lowest f-number condition used in these experiments was f/10.3. In each case, the beam diameter was kept below maximum values necessary to ensure diffraction limited performance. Aberrations caused by focusing through the planar surfaces of the samples were calculated to cause an error in the field of less than 0.1% for the worst case. The output energy of the CD*A crystal was monitored continually using a sensitive photodiode peak-and-hold detector, absolutely calibrated with respect to a pyroelectric energy detector. Transmission through the sample was monitored by another peak-and-hold detectors.

In some cases, the transmission detector was replaced by a vidicon tube used in conjunction with an optical multichannel analyzer to scan the transmitted beam profile. Such scans were made at the damage threshold irradiance and for irradiance levels ten times below the damage threshold. In this way, a total time integrated beam distortion at the beam waist of the order of λ/5 could be detected.

The short pulsewidth data (4-9 psec) were taken on the same samples using a microprocessor-controlled Nd:Glass oscillator system operating at a laser wavelength of 1.05 μm [3]. This system produced single pulses of measured Gaussian spatial profile. Shot-to-shot energy fluctuations were determined to be ~20%. The same focusing lenses were used as with the 0.53 μm measurements. Beam scans as a function of distance from the laser were employed (as was also done using the 1.06 μm laser) to determine the beam divergence (0.4 mrad.) and the position and size of the output beam waist. This information and the lens focal length were then used to calculated the beam waist at the lens focus. Energy on target was varied using a calibrated Glan polarizer. The procedures for measuring and continuously monitoring both pulsewidth and energy are identical to those described previously with the Nd:YAG laser system [2].

The breakdown threshold for a given pulsewidth was taken to be that irradiance which produced damage 50% of the time. Each site was irradiated only once. Damage was defined as the appearance of a visible flash in the bulk of the sample or by the observation of forward scattered light from a coaxial HeNe laser as viewed through a ten-power long-working distance microscope. The microscope also was used to verify that damage had occured at the beam focus and was not due to inclusions. For 0.53 μm damage, the appearance of 0.53 μm scattered radiation and HeNe scattered light occurred simultaneously for both SiO_2 and NaCl. In the cases of the 4-9 psec 1 μm data, for both SiO_2 and NaCl, there was a small range of incident energies where damage had occured as determined from scattered HeNe radiation, but no flash was observed. N-on-1 experiments (multiple shot irradiation at the same sample site) conducted at both wavelengths, indicate no change in the breakdown threshold when compared to the 1-on-1 experiments (only one irradiation per sample site).

3. Self-Focusing Considerations

In order to produce laser-induced damage in the bulk of a highly transparent material one must tightly focus the light into the material. Since the beam propagates through the material, one must consider the effects of self-focusing on the results of bulk damage measurements, particularly when the power required to induce damage is of the order of the predicted critical power for self-focusing. Marburger [5] has derived an approximate solution to the nonlinear wave equation for a focused Gaussian beam in a nonlinear medium. This solution (called the constant shape approximation) assumes that, in the presence of self-focusing, the focused beam waist is given by

$$a = (1 - P/P_1)^{1/2} a_o \qquad (2)$$

where P_1 is the critical power for self-focusing

a_0 is the focal radius in the absence of self-focusing, and

P is the input power.

Some workers have assumed that the damage threshold irradiance for highly transparent materials (such as those used in this study) is an intrinsic property [6] of the material and that any apparent dependence of the breakdown irradiance on a_0 is due to self-focusing [7,8,9] The breakdown power then was measured for various values of a_0 and the results fit to the equation

$$1/P_B = 2/I_B \pi a_0^2 + 1/P_1 \tag{3}$$

where P_B is the power required for breakdown and

I_B is the intrinsic damage threshold.

A number of authors have used this technique to extract values for I_B and P_1 for nanosecond [7,8] and picosecond pulses [10,11] In some cases P_1 was calculated [11] in accordance with the relation [5]

$$P_1 = c\lambda^2/32\pi n_2 \tag{4}$$

where λ is the wavelength, and n_2 is the nonlinear refractive index. A new focal radius was calculated using eq. (1). The n_2 values used in these calculations were taken from nanosecond measurements.

There are serious problems associated with using the above mentioned procedure. Subsequent work has shown that I_B is not an intrinsic property of a transparent material as evidenced by large sample to sample variations observed in a given material [2,12]. A second problem is that other self-action effects such as a saturation of the self-focusing or free carrier defocusing may become important at the extremely high irradiance levels required for damage. The presence of these "free" electrons creates a negative change in the index of refraction which can limit the self-focus collapse, [5,13,15] defeat self-focusing entirely, [15] and in some cases lead to self-defocusing of the beam. [16,17] Therefore, before any analysis of damage data can begin, one needs to devise tests which will verify the presence, or absence of self-focusing effects.

One such test arises directly from self-focusing theory which predicts that the critical power for self-focusing is lower for linearly polarized light compared to that for circularly polarized light [18-21]. Experimental measurements in liquids, such as CS_2, conducted by ourselves [22] and others [20,23] have confirmed that this is indeed the case. In solids, Feldman et al. [19] measured ratios of circular polarization thresholds to linear polarization thresholds on the order of 1.1 to 1.3 for fused quartz. These measurements were conducted using nanosecond pulses at 1.06 μm where both electrostrictive and electronic contributions to n_2 are believed to be important. For picosecond pulses the dominant contribution to n_2 is believed to be electronic self-focusing, which is polarization dependent. Thus, if self-focusing effects are important in our measurements, then the breakdown thresholds should be different for different polarization configurations.

In figure 1 we present the results of polarization dependent studies for a sample of fused quartz at a laser wavelength of 0.53 μm and 1.06 μm. The breakdown thresholds are given in terms of the r.m.s. electric field, in MV/cm, corresponding to the peak-on-axis irradiance producing damage. In both cases we used the shortest pulses available to us, which corresponded to the highest input power for the given focal spot radius of 5 μm (HW $1/e^2$ M). As can be seen the breakdown field for linear polarization equals that for circular polarization. In both materials no polarization dependence was observed for pulses between 4-9 psec (FWHM) at 1.05 μm even for the largest spot size used in this study. Similar results were obtained in measurements on a NaCl sample at a 0.53 μm laser wavelength for 30 psec pulses. Thus, for the focal conditions used, we observed no polarization dependence of the breakdown thresholds for either fused quartz or NaCl.

Another, independent test for the presence of self-focusing is to examine the beam spatial profile after transmission through the sample for irradiance levels far below and near the damage threshold. In figure 2 we show two vidicon traces taken in the far field through the center of the 0.53 μm beam after transmission through the fused quartz sample. The focal spot radius (HW $1/e^2$ M) at the beam waist for this configuration, in the absence of self-focusing, in approximately 7 μm. The solid trace was taken near the damage threshold. The dashed trace was taken at an irradiance level approximately 10 times below the damage threshold. Filters were placed in front of the vidicon to adjust the irradiance at the vidicon surface to the same value in both traces in order to minimize any problems in detector nonlinearity. Inspection of figure 2 shows no detectable beam distortion for input powers approximately equal to the damage threshold power. Scans conducted for a focal spot size of 3.4 μm at the 0.53 μm laser wavelength also show no distortions.

The authors are aware that the technique just described monitors the time-integrated beam spatial profile; however, this technique is sensitive to a λ/5 distortion in the total time integrated profile and has proven to be a sensitive technique for monitoring the onset of self-defocusing in solids [16]. These measurements, when taken together with the polarization experiments described above, indicate that self-focusing effects were not important for the geometries used in these experiments. However, the reader should be aware that in other experimental geometries (i.e., less tightly focused beams) self-focusing effects can be important. In fact, preliminary measurements in SiO_2 at 0.53 μm indicate that for a 14 μm focal spot radius the far field beam radii for irradiance at the damage threshold differs from that at low irradiance levels by approximately 28% (indicating that self-focusing has taken place). For that same focal geometry the ratio of the LIB threshold for circularly polarized light to that for linearly polarized light is approximately 1.4. These self-focusing studies are not yet complete and will be reported in detail at a later date. We emphasize that no data are included in this paper for which either the polarization test or the beam distortion test indicate the presence of self-focusing.

4. Experimental Results and Discussions

Tables I-VIII summarize the results of measurements of the laser-induced breakdown thresholds for two different samples of single crystal NaCl and fused silica [24]. The NaCl sample labeled 78-NC-6 is the same sample used in previous picosecond damage studies [2] and in studies at longer pulsewidths and wavelengths [15,25]. Both SiO_2 samples have been used in nanosecond studies at 1.06 μm [26] and the sample labeled 79-FQ-125-1 was used in previous picosecond studies [2]. The uncertainties listed in the tables of data are the relative errors obtained by the method of Porteus et al. [27]. The absolute errors, which include the relative errors and absolute errors in energy, pulsewidth and focal spot radius, are estimated to be ±20% in the breakdown electric fields.

Tables I-IV summarize the results of our measurements at 0.53 μm for laser pulsewidths in the 25 to 200 psec (FWHM) range. These results will be compared here with the results of our earlier studies at 1.06 μm for these same materials over a similar range of pulsewidths. Tables V-VIII contain the results of measurements on these same samples at 1.05 μm for pulses in the 4 - 10 psec range. In addition, Tables VI and VIII contain LID thresholds at 1 µm in the pulsewidth range of 40 to 200 psec for a 7.2 µm focal spot radius. These thresholds are taken from our previous work (Ref. 2) and were interpolated from measurements made at focal spot size of 6.1 and 10.3 µm.

In the paragraphs that follow, we examine the pulsewidth dependence of the threshold breakdown field, E_B, for a given sample at a given wavelength and focal spot radius. We then examine the wavelength dependence of E_B for a given pulsewidth and spot size.

The dependence of E_B on pulsewidth (t_p) is more clearly seen by plotting E_B versus the inverse pulsewidth on a log-log plot. Figures 3 and 4 are such plots for a NaCl sample (82-NC-1) and a SiO_2 sample (79-FQ-7940-1) at 1.05 µm. Note that for a given spot size and for pulses shorter than 10 psec the data for each sample can be fit with a straight line. Over this limited pulsewidth range

$$E_B \propto t_p^{-x} \tag{5}$$

where $x \doteq 0.3$ for the SiO_2 sample and $x \doteq 0.5$ for the NaCl sample. The displacement of each set of data points corresponding to different focal spot sizes indicates a relatively strong spot size dependence in these samples at this wavelength.

Figures 5 and 6 are similar plots for the same two samples (79-FQ-7940-1 and 82-NC-1) at 0.53 µm for pulsewidths in the 25-200 psec range. Again one can fit the data with a linear dependence. However, in this case $x \lesssim 0.1$ for the SiO_2 sample and $x \doteq 0.3$ for the NaCl sample. Similar trends are seen in the data for the other SiO_2 and NaCl samples given in tables II, IV, VI, and VIII.

At 0.53 µm and 1.06 µm the pulsewidth dependence of E_B observed for both materials is in good agreement with the predictions of various avalanche breakdown models [28,29,30]. For example the model proposed by Sparks <u>et al</u>. [28] predicts very little pulsewidth dependence for relatively long pulses (nsec) and a dependence of E_B on pulsewidth which approaches an inverse square root dependence for relatively short pulses, i.e., ten's of picoseconds. The inverse square root of pulsewidth dependence implies that the breakdown fluence is constant (as can be seen in tables VII and VIII for the NaCl samples). We find that for NaCl in the long pulsewidth limit (t_p > 1 nsec) the breakdown <u>field</u> is nearly constant, whereas in the short pulsewidth limit (t_p < 10 psec) the breakdown <u>fluence</u> is nearly constant. The trend in the t_p dependence of E_B for SiO_2 is similar to that seen in NaCl, however, the strongest dependence of E_B on t_p observed was $E_B \propto t_p^{-0.3}$ for pulses shorter than 10 psec at 1.05 µm. It is important to note that the strongest pulsewidth dependence of E_B observed in these measurements was the approximate inverse square root of pulsewidth dependence observed for NaCl for $t_p \lesssim 10$ psec at 1.05 µm. In an avalanche breakdown model this dependence implies an ionization rate (β) which is proportional to the input irradiance. Then the buildup of carriers is given by [28]

$$N = N_o e^{\beta t} = N_o e^{AE^2 t} \tag{6}$$

where N is the carrier density

N_o is the initial carrier density or carrier density produced by multiphoton ionization.
A is constant.

It is commonly assumed that damage occurs when the carrier density reaches a critical value, N_c. Thus eq. 2 gives the following relationship for E_B

$$E_B = (1/\sqrt{t_p})\, \ell n\, [(N_c/N_o)/A]^{1/2} \tag{7}$$

and the [] term is constant for a given sample and laser frequency. The breakdown fluence, ε_B, is proportional to E_B^2 times the laser pulsewidth. Therefore eq. 6 implies that ε_B is a constant for β proportional to E^2.

In the Sparks avalanche breakdown model the ionization rate β is proportional to E^2 in the high electric field limit. This limit corresponds to the situation in which the increase in energy of the electrons in the conduction band is simply proportional to the input irradiance and that all losses are negligible. This simply says that the ionization rate is limited by the rate at which the input light beam can supply energy to the conduction band electrons. For the low field limit, i.e. longer pulses, β is exponentially dependent on E and the resulting pulsewidth dependence is relatively weak. In figure 7, we have reproduced the theoretical curves derived by Sparks et al. [28] showing the predicted dependence of the breakdown electric field, E_B, on pulsewidth and have extended the pulsewidth scale to longer and shorter pulsewidths. These curves were obtained by numerical integration of the Fokker Planck diffusion equation with appropriate boundary conditions reflecting energy loss by electrons to phonons. The solid curve was obtained using a value for σ_{Cl}, the electron-chlorine ion scattering cross section, taken from atomic physics literature. The dotted curve labled "σ_{Cl} adjusted" was obtained using a value for this parameter adjusted so as to give a better fit to experimental LID data available at the time. This cross section appears in the equations used to calculate the electron-phonon relaxation frequencies. The experimental points shown were obtained in this work at 1.05 μm for the NaCl sample labeled 78-NC-6 (Table VIII) and in our previous picosecond study at 1.06 μm [2]. Note the excellent agreement between the Sparks avalanche model and the data obtained here and in Ref. 2 for the 5 μm spot size. Data obtained in the same sample for a larger spot size (7.2 μm) show a similar trend in the functional dependence of E_B on pulsewidth but the values of E_B are lower than those given by this model. The agreement between the absolute values predicted by theory and experiment for 5 μm spot size may be fortuitous since the Sparks model describes intrinsic avalanche breakdown, i.e., the starter electrons necessary to create the avalanche are assumed to be already present. Such a model predicts no spot size dependence of the breakdown field. The relatively strong spot size dependence observed in NaCl at 1.06 μm indicates that damage in this material is probably initiated by some extrensic process; for example, multiphoton ionization of material defects.

Other workers have used an approximate inverse pulsewidth dependence (i.e., x = 1 in eq. 3) to scale breakdown data for various materials [11]. This is a much stronger dependence than is observed in this work. Their strong pulsewidth dependence was determined by combining the 1.06 μm, 30 psec data in Ref. 9 and 1.06 μm, 15 psec data in Ref. 31. These two data points were taken with different focal spot sizes. That is, the 30 psec data point in Ref. 9 was taken with relatively small focal radii (4.7 to 5.9 μm $1/e^2$ radius) and was reduced with the assumption that self-focusing was dominating the observed damage. The 15 psec data point in Ref. 31 was taken with a relatively large focal radius (12.4 μm HW $1/e^2$ M) and thus higher input power. In the latter work the authors assumed that self-focusing was not present in their experiment. The relatively large pulsewidth dependence deduced from these two isolated data points is probably due to differences in experimental conditions used in these two measurements and the different methods of data reduction.

We now examine the wavelength dependence of the breakdown thresholds for laser pulsewidths in the 25 - 200 psec range. In figure 8 we have plotted, in bar graph form, the breakdown electric fields for SiO_2 (sample 79-FQ-125-1) and NaCl (sample 78-NC-6) for 1.06 µm and 0.53 µm for various pulsewidths at a fixed focal spot radius (7.2 µm). The 1.06 µm LID thresholds at the 7.2 µm focal radius are taken from Ref. 2 and are interpolated from measurements at spot sizes of 6.1 and 10.3 µm. In two cases where the pulsewidths did not exactly overlap for the two wavelengths we interpolated the 0.53 µm data between two pulsewidths for which data was available. This procedure was made necessary by the fact that only a limited number of pulsewidths were available at each wavelength studied. The errors due to interpolation are estimated to be within the error bars shown in figure 8.

Note that for each pulsewidth range plotted in figure 8 the breakdown field is less at 0.53 µm than at 1.06 µm for both the SiO_2 and the NaCl sample. Avalanche breakdown theory predicts an increase in E_B with decreasing wavelength, which is clearly inconsistent with the results shown in figure 8. The observed decrease in breakdown field with wavelength, while in the right direction, is much too weak for a strictly multiphoton process. One could possibly account for these results by a multiphoton initiated avalanche breakdown model which has been previously suggested.

Smith *et al.* [11] observed an increase in the breakdown threshold with decreasing wavelength for picosecond pulses. However, the data presented in that work was scaled for the presumed effects of self-focusing using eq. (2) for 1.06 µm and eq. (1) for 0.53 µm over a range of pulsewidths and spot sizes in which we observe no such effects. In addition it is unclear whether the same samples were used in the wavelength comparison. Manenkov [12] observed an initial increase in the damage threshold for a sample of NaCl from 1.06 µm, to 0.69 µm, then a decrease in the damage threshold at 0.53 µm for pulses ranging from 15 to 8 nsec. The data presented in that work was not scaled for self-focusing.

5. Summary

Laser-induced breakdown was studied as a function of pulsewidth and wavelength for a variety of focal conditions in fused SiO_2 and single crystal NaCl. Beam quality measurements and polarization dependence studies indicated the absence of self-focusing effects in these experiments such that no self-focusing corrections need be used.

For the two materials studied the breakdown field (E_B) increases with decreasing pulsewidth. The observed pulsewidth dependence for a given spot size and wavelength is consistent with the pulsewidth dependence predicted by various electron avalanche breakdown models. However, the spot size dependence observed in this study is not predicted by any avalanche theory and is probably due to the extrinsic nature of the observed damage. The strongest pulsewidth dependence observed was in NaCl at 1.05 µm for pulses shorter than 10 psec. For these short pulses E_B increases as the inverse square root of the pulsewidth, indicating that the breakdown fluence is constant.

For conditions of equal pulsewidth and the same focal spot size, i.e., pulsewidths from 45 to 175 psec and a focal spot size of 7.2 µm, E_B is less at 0.53 µm than at 1.06 µm for both materials. Avalanche breakdown theories predict an increase in E_B for shorter wavelengths. The observed decrease in breakdown field with wavelength, while in the right direction, is much too weak for a strictly multiphoton process. A multiphoton-initiated avalanche breakdown process might account for these results. In such a process electrons are excited to the conduction band by multiphoton excitation of impurities or defect states within the material bandgap (i.e., extrinsic effects). After a few electrons are present in the conduction band, avalanche ionization takes over and dominates the damage process. Thus, the frequency dependence observed may be partly due to the multiphoton initiation process and the pulsewidth dependence indicative of an avalanche ionization process.

The authors acknowledge the support of the Office of Naval Research, the National Science Foundation, The Robert A. Welch Foundation, and the North Texas State University Faculty Research Fund.

References

[1] A central depository of work in this area are the proceedings of the symposium on "Laser-Induced Damage in Optical Materials", National Bureau of Standards Special Publications, #341 (1970), #356 (1971), #372 (1972), #387 (1973), #414 (1974), #435 (1975), #462 (1976), #509 (1977), #541 (1978), #568 (1979), #620 (1980). These may be obtained from the Superintendent of Documents, U.S. Government Printing Office Washington, D.C. 20402. Papers in these proceedings contain further reference to materials in this field.

[2] E. W. Van Stryland, M. J. Soileau, Arthur L. Smirl, and William E. Williams, Phys. Rev. B 23, 2144 (1981).

[3] A. L. Smirl, T. F. Boggess, B. S. Wherrett, G. P. Perryman, and A. Miller, IEEE J. Quantum Electron. (to be published).

[4] E. W. Van Stryland, W. E. Williams, M. J. Soileau, and A. L. Smirl, to be published in the Proceedings of the 1981 Conference on Laser-Induced Damage in Optical Materials, Boulder, Colorado.

[5] J. Marburger, in Progress in Quantum Electronics edited by J. H. Sanders and S. Stenhold (Pergamon, Oxford, 1975), Vol. 4, Part 1, and references therein.

[6] Nicolass Bloembergen, IEEE J. Quantum. Electron. QE-10, 375 (1974).

[7] G. M. Zverev and V. A. Pashkov, Sov. Phys. JETP, Vol. 30, 616 (1970).

[8] D. W. Fradin, IEEE J. Quantum Electron. QE-9, 954 (1972).

[9] W. Lee Smith, J. H. Bechtel, and N. Bloembergen, Phys. Rev. B 12, 706 (1975).

[10] W. Lee Smith and J. H. Bechtel, Appl. Phys. Lett. 28, 606 (1976).

[11] W. L. Smith, J. H. Bechtel, and N. Bloembergen, Phys. Rev. B 15, 4039 (1977).

[12] A. A. Manenkov, Natl. Bur. Stand. (U.S.) Spec. Publ. 509, 455 (1977).

[13] R. W. Hellworth, Natl. Bur. Stand. (U.S.) Spec. Publ. 341, 67 (1970).

[14] E. Yablonovitch and N. Bloembergen, Phys. Rev. Lett. 29, 907 (1972).

[15] M. J. Soileau, Ph.D. Thesis, University of Southern California, 1979, unpublished.

[16] E. W. Van Stryland, A. L. Smirl, T. F. Boggess, and F. A. Hopf, in Picosecond Phenomena III (Springer-Verlag, New York, 1982), p. 368.

[17] P. Kelly, A. Schmid, and P. Braunlich, Phys. Rev. B 20, 815 (1979).

[18] Y. R. Shen, Phys. Rev. Lett. 20, 378 (1966).

[19] A. Feldman, D. Horowitz, and R. Waxler, Natl. Bur. Stand. Spec. Publ. 372, 92 (1972).

[20] C. C. Wang, Phys. Rev. 152, 149 (1966).

[21] R. W. Hellworth, Progress in Quantum Electronics, Vol. 5, pp. 1-68, Pergamon Press, N.Y., 1977.

[22] M. J. Soileau, W. E. Williams, E. W. Van Stryland, and S. F. Brown, Proceedings of the Conference on Laser Induced Damage to Optical Materials, 1981, to be published by Natl. Bur. Stand. Spec.

[23] D. H. Close, C. R. Giuliano, R. W. Hellworth, L. D. Hess, F. J. McClung, and W. G. Wagner, IEEE J. Quant. Electron. QE-2, 553 (1966).

[24] The fused silica samples were acquired from Mark Optics, 1510 East St. Gertrude Road, Santa Ana, CA 92705. The SiO_2 designated 78-FQ-125-1 was a General Electric #125, high purity water free sample and the sample designated 78-FQ-7940-1 was a Corning #7940 sample which contained substantial water, but is otherwise a high purity material. Both NaCl samples were single crystal "laser grade" material from the Harshaw Chemical Co., 6801 Cochran Road, Solon, Ohio 44139.

[25] M. J. Soileau, M. Bass, and P. H. Klein, NBS Special Publ. 568, p. 497 (1979).

[26] M. J. Soileau and M. Bass, IEEE Journal of Quantum Electronics QE-16, 814 (1980).

[27] J. O. Porteus, J. L. Jernigan, W. N. Faith, NBS Spec. Pub. 509, 507 (1977).

[28] M. Sparks, T. Holstein, R. Warren, D. L. Mills, A. A. Maradudin, L. J. Shan, E. Loh Jr., and F. King, NBS Spec. Publ. 568, 467 (1979).

[29] S. Brawer, Phys. Rev. B 20, 3422 (1979).

[30] A. S. Epifanov, IEEE Journal of Quantum Electron. QE-17, 2018 (1981).

[31] D. W. Fradin, N. Bloembergen, and J. P. Lettlier, Appl. Phys. Lett. 22, 635 (1973).

Table I. LID data for sample 79-FQ-7940-1 (SiO$_2$) at 0.53 μm. The error values listed are the relative uncertainties in the threshold for damage determined by the method used in Ref. 27. The absolute accuracy of this data and the data presented in the other tables is estimated to be ±20% in the breakdown field. In this table and those that follow W = focal spot radius (HW 1/e^2 M) in microns, t_p = laser pulsewidth (FWHM) in psec, I_B = breakdown irradiance, E_B = breakdown field, P_B = breakdown power and ε_B = breakdown fluence.

W (μm)	t_p (psec)	I_B (TW/cm^2)	E_B (MV/cm)	P_B (MW)	ε_B (J/cm^2)
7.2	25 ± 4	1.32 ± 0.13	18.3 ± 0.9	1.07 ± 0.11	35.0 ± 3.5
	53 ± 5	0.78 ± 0.08	14.1 ± 0.7	0.64 ± 0.06	44.0 ± 4.4
	110 ±10	0.78 ± 0.08	14.1 ± 0.7	0.64 ± 0.06	91 ± 9
5.0	37 ± 5	1.40 ± 0.14	18.9 ± 0.9	0.55 ± 0.06	55 ± 6
	105 ±15	1.20 ± 0.12	17.5 ± 0.8	0.47 ± 0.05	134 ± 13
	140 ±15	1.14 ± 0.11	17.0 ± 0.8	0.45 ± 0.05	169 ± 17
	180 ±20	1.10 ± 0.11	16.7 ± 0.7	0.43 ± 0.04	210 ± 21
3.4	30 ± 5	1.68 ± 0.17	20.7 ± 1.0	0.31 ± 0.03	53 ± 5
	72 ±10	1.34 ± 0.13	18.5 ± 0.8	0.24 ± 0.02	102 ± 10
	105 ±15	1.07 ± 0.11	16.5 ± 0.8	0.19 ± 0.02	83 ± 8

Table II. LID data for sample 79-FQ-125-1 (SiO$_2$) at 0.53 μm. See Table 1 for explanation of symbols and error bars.

W (μm)	t_p (psec)	I_B (TW/cm^2)	E_B (MV/cm)	P_B (MW)	ε_B (J/cm^2)
7.2	25 ± 4	0.96 ± 0.10	15.7 ± 0.8	0.79 ± 0.08	25.5 ± 3.0
	105 ± 15	0.48 ± 0.05	11.0 ± 0.5	0.39 ± 0.04	53 ± 5
	150 ± 15	0.39 ± 0.06	9.9 ± 0.8	0.32 ± 0.04	62 ± 6
5.0	34 ± 4	1.02 ± 0.10	16.1 ± 0.8	0.40 ± 0.04	37 ± 4
	120 ± 15	0.86 ± 0.09	14.8 ± 0.7	0.34 ± 0.03	109 ± 11
	180 ± 20	0.80 ± 0.15	14.3 ± 1.0	0.32 ± 0.03	153 ± 25
3.4	32 ± 4	1.16 ± 0.15	17.2 ± 1.0	0.21 ± 0.02	39 ± 4
	120 ± 15	0.91 ± 0.09	15.2 ± 0.5	0.16 ± 0.02	115 ± 12
	180 ± 20	0.75 ± 0.12	13.8 ± 1.0	0.14 ± 0.01	143 ± 14

Table III. LID data for sample 82-NC-1 (NaCl) at 0.53 μm.

W (μm)	t_p (psec)	I_B (GW/cm^2)	E_B (MV/cm)	P_B (KW)	ε_B (J/cm^2)
14.0	35 ± 4	57 ± 6	3.80 ± 0.25	174 ± 17	2.10 ± 0.20
	80 ± 8	35 ± 4	2.98 ± 0.15	107 ± 10	2.96 ± 0.30
	110 ± 15	32 ± 3	2.87 ± 0.15	100 ± 10	3.77 ± 0.38
7.2	41 ± 9	91 ± 9	4.80 ± 0.35	120 ± 12	3.95 ± 0.40
	82 ± 7	64 ± 6	4.03 ± 0.19	40 ± 4	5.50 ± 0.60
	120 ± 15	47 ± 5	3.45 ± 0.19	29 ± 3	6.00 ± 0.60
3.4	26 ± 4	139 ± 14	5.95 ± 0.48	26.0 ± 0.3	3.83 ± 0.38
	37 ± 3	115 ± 12	5.41 ± 0.33	21.0 ± 0.2	4.50 ± 0.50
	57 ± 3	85 ± 9	4.64 ± 0.30	15.0 ± 0.2	5.10 ± 0.50
	73 ± 4	71 ± 7	4.24 ± 0.52	12.8 ± 0.12	5.50 ± 0.60
	90 ± 10	64 ± 6	4.04 ± 0.18	12.0 ± 0.12	6.10 ± 0.60
	115 ± 15	35 ± 4	3.00 ± 0.31	6.4 ± 0.64	4.30 ± 0.40

Table IV. LID data for sample 78-NC-6 (NaCl) at 0.53 μm.

W (μm)	t_p (psec)	I_B (GW/cm^2)	E_B (MV/cm)	P_B (KW)	ε_B (J/cm^2)
14.0	25 ± 5	120 ± 12	5.53 ± 0.33	370 ± 40	3.19 ± 0.32
	105 ± 15	48 ± 5	3.50 ± 0.20	148 ± 15	5.37 ± 0.54
	170 ± 20	34 ± 6	2.95 ± 0.30	105 ± 10	6.18 ± 0.62
7.2	30 ± 5	148 ± 15	6.14 ± 0.30	120 ± 12	4.72 ± 0.47
	105 ± 15	50 ± 5	3.55 ± 0.20	40 ± 4	5.53 ± 0.56
	150 ± 15	36 ± 4	3.03 ± 0.16	29 ± 3	5.74 ± 0.57
3.4	28 ± 4	184 ± 18	6.86 ± 0.31	33.0 ± 3.3	5.48 ± 0.55
	85 ± 5	82 ± 8	4.56 ± 0.23	15.0 ± 1.5	7.39 ± 0.74
	100 ± 10	66 ± 7	4.10 ± 0.21	12.0 ± 1.2	7.02 ± 0.70
	120 ± 10	55 ± 8	3.75 ± 0.30	10.0 ± 1.0	7.05 ± 0.71
	140 ± 10	44 ± 7	3.35 ± 0.30	8.0 ± 0.8	6.57 ± 0.66
	170 ± 20	34 ± 5	2.95 ± 0.21	6.0 ± 0.6	6.17 ± 0.62

Table V. LID data for sample 79-FQ-7940-1 (SiO_2) at 1.05 μm.

W (μm)	t_p (psec)	I_B (TW/cm^2)	E_B (MV/cm)	P_B (MW)	ε_B (J/cm^2)
14.0	7.9 ± 0.6	1.12 ± 0.11	16.8 ± 0.8	3.44 ± 0.34	9.4 ± 0.9
	6.3 ± 0.3	1.25 ± 0.13	17.7 ± 1.0	3.84 ± 0.38	8.4 ± 0.8
	5.2 ± 0.3	1.42 ± 0.14	18.9 ± 1.0	4.37 ± 0.44	6.9 ± 0.6
	3.6 ± 0.3	1.75 ± 0.18	21.0 ± 1.1	5.39 ± 0.54	6.7 ± 0.7
7.2	8.5 ± 0.5	2.27 ± 0.23	24.1 ± 1.1	1.85 ± 0.19	20.5 ± 2.0
	7.5 ± 0.5	2.20 ± 0.22	23.7 ± 1.1	1.79 ± 0.18	17.5 ± 1.8
	6.5 ± 0.5	2.60 ± 0.26	25.7 ± 1.3	2.12 ± 0.21	18.0 ± 1.8
	5.5 ± 0.5	2.75 ± 0.28	26.5 ± 1.2	2.24 ± 0.22	16.1 ± 1.6
	4.5 ± 0.5	3.14 ± 0.31	28.3 ± 1.3	2.56 ± 0.26	15.0 ± 1.5
	3.6 ± 0.4	3.65 ± 0.37	30.5 ± 1.5	2.97 ± 0.30	14.0 ± 1.4
5.0	8.5 ± 0.5	3.04 ± 0.30	27.8 ± 1.4	1.19 ± 0.12	27.6 ± 2.8
	7.5 ± 0.5	3.24 ± 0.32	28.7 ± 1.3	1.27 ± 0.13	25.9 ± 2.6
	6.5 ± 0.5	3.56 ± 0.37	30.1 ± 1.5	1.40 ± 0.14	24.6 ± 2.5
	5.5 ± 0.5	3.94 ± 0.39	31.7 ± 1.5	1.55 ± 0.16	23.1 ± 2.3
	3.6 ± 0.3	5.00 ± 0.60	35.7 ± 2.0	1.96 ± 0.20	19.2 ± 1.9

Table VI. LID data for sample 79-FQ-125-1 (SiO_2) at 1.05 μm. The data for 7.2 μm size and t_p = 47 to 175 psec is taken from Ref. 2 and is interpolated from measurements made at spot sizes of 6.1 and 10.3 μm and a laser wavelength of 1.06 μm.

W (μm)	t_p (psec)	I_B (TW/cm^2)	E_B (MV/cm)	P_B (MW)	ε_B (J/cm^2)
14.0	9.5 ± 0.5	0.88 ± 0.09	15.0 ± 0.7	2.71 ± 0.27	5.01 ± 0.50
	8.5 ± 0.5	0.90 ± 0.09	15.1 ± 0.7	2.77 ± 0.28	8.14 ± 0.82
	6.5 ± 0.5	1.06 ± 0.11	16.4 ± 0.9	3.26 ± 0.33	7.32 ± 0.73
	4.0 ± 0.5	1.8 ± 0.20	21.4 ± 1.2	5.54 ± 0.56	7.66 ± 0.77
7.2	175 ± 15	0.88 ± 0.12	15.0 ± 1.2	0.72 ± 0.09	163 ± 20
	92 ± 15	0.92 ± 0.13	15.3 ± 1.1	0.75 ± 0.10	90 ± 12
	47 ± 6	0.96 ± 0.14	15.6 ± 1.0	0.78 ± 0.10	48 ± 7
	9.5 ± 0.5	1.93 ± 0.19	22.1 ± 1.1	1.57 ± 0.16	19.5 ± 2.0
	7.5 ± 0.5	2.05 ± 0.21	22.8 ± 1.2	1.67 ± 0.17	16.3 ± 1.6
	6.5 ± 0.5	2.15 ± 0.22	23.4 ± 1.2	1.75 ± 0.18	14.9 ± 1.5
	5.5 ± 0.5	2.30 ± 0.23	24.2 ± 1.2	1.87 ± 0.19	13.5 ± 1.4
	4.5 ± 0.5	2.89 ± 0.29	27.1 ± 1.4	2.35 ± 0.24	13.8 ± 1.4
	3.5 ± 0.5	3.31 ± 0.33	29.0 ± 1.4	2.69 ± 0.27	12.3 ± 1.2
5.0	9.4 ± 0.5	2.60 ± 0.26	25.7 ± 1.3	1.02 ± 0.10	26.0 ± 0.3
	7.5 ± 0.5	3.26 ± 0.33	28.8 ± 1.4	1.28 ± 0.13	26.0 ± 0.3
	6.5 ± 0.5	3.77 ± 0.38	31.0 ± 1.5	1.45 ± 0.15	26.1 ± 0.3
	5.5 ± 0.5	3.98 ± 0.40	31.8 ± 1.6	1.56 ± 0.16	23.2 ± 0.2
	4.5 ± 0.5	4.49 ± 0.45	33.8 ± 1.6	1.76 ± 0.18	21.5 ± 0.2

Table VII. LID data for sample 82-NC-1 (NaCl) at 1.05 μm.

W (μm)	t_p (psec)	I_B (TW/cm^2)	E_B (MV/cm)	P_B (MW)	ε_B (J/cm^2)
	9.5 ± 0.5	0.25 ± 0.03	8.00 ± 0.44	0.77 ± 0.08	2.55 ± 0.26
	8.5 ± 0.5	0.26 ± 0.03	8.18 ± 0.41	0.81 ± 0.08	2.38 ± 0.24
14.0	7.5 ± 0.5	0.29 ± 0.03	8.60 ± 0.43	0.89 ± 0.09	2.31 ± 0.23
	6.5 ± 0.5	0.37 ± 0.04	9.64 ± 0.57	1.12 ± 0.11	2.55 ± 0.26
	5.5 ± 0.5	0.40 ± 0.04	10.10 ± 0.48	1.23 ± 0.12	2.38 ± 0.24
	4.5 ± 0.5	0.45 ± 0.05	10.70 ± 0.58	1.37 ± 0.14	2.12 ± 0.21
	7.5 ± 0.5	0.66 ± 0.07	12.9 ± 0.73	0.53 ± 0.05	5.22 ± 0.52
	6.5 ± 0.5	0.75 ± 0.08	13.8 ± 0.73	0.61 ± 0.06	5.15 ± 0.52
7.2	5.5 ± 0.5	0.88 ± 0.09	14.9 ± 0.81	0.71 ± 0.07	5.12 ± 0.52
	4.5 ± 0.5	0.97 ± 0.10	15.7 ± 0.80	0.79 ± 0.08	4.65 ± 0.47
	3.6 ± 0.3	1.38 ± 0.14	18.8 ± 0.87	1.12 ± 0.09	5.28 ± 0.53
	7.5 ± 0.5	0.74 ± 0.07	13.7 ± 0.65	0.29 ± 0.03	5.86 ± 0.59
5.0	6.5 ± 0.5	1.00 ± 0.10	15.9 ± 0.83	0.39 ± 0.04	6.91 ± 0.69
	5.5 ± 0.5	1.14 ± 0.11	17.0 ± 0.83	0.45 ± 0.05	6.66 ± 0.67
	4.5 ± 0.5	1.29 ± 0.13	18.1 ± 0.91	0.51 ± 0.05	6.20 ± 0.62

Table VIII. LID data for sample 78-NC-1 (NaCl) at 1.05 μm. The data for the 7.2 μm spot size and t_p = 45 to 167 psec is taken from Ref. 2 and is interpulated from measurements made at spot size of 6.1 and 10.3 μm and a laser wavelength of 1.06 μm.

W (μm)	t_p (psec)	I_B (TW/cm^2)	E_B (MV/cm)	P_B (MW)	ε_B (J/cm^2)
	7.5 ± 0.5	0.26 ± 0.03	8.06 ± 0.54	0.79 ± 0.08	2.03 ± 0.20
4.0	6.5 ± 0.5	0.28 ± 0.03	8.44 ± 0.44	0.86 ± 0.09	1.95 ± 0.20
	5.5 ± 0.5	0.32 ± 0.03	9.03 ± 0.44	0.99 ± 0.10	1.87 ± 0.19
	4.5 ± 0.5	0.38 ± 0.04	9.80 ± 0.53	1.17 ± 0.12	1.82 ± 0.18
	167 ± 16	0.083 ± 0.011	4.6 ± 0.3	0.068 ± 0.008	14 ± 1.5
	100 ± 10	0.110 ± 0.008	5.1 ± 0.4	0.090 ± 0.006	11.7 ± 1.2
	45 ± 3	0.118 ± 0.018	5.5 ± 0.4	0.096 ± 0.010	5.56 ± 0.60
7.2	6.5 ± 0.5	0.58 ± 0.06	12.2 ± 0.6	0.43 ± 0.04	4.00 ± 0.40
	5.5 ± 0.5	0.66 ± 0.07	12.9 ± 0.73	0.53 ± 0.05	3.83 ± 0.38
	4.5 ± 0.5	0.80 ± 0.08	14.3 ± 0.63	0.65 ± 0.07	3.83 ± 0.38
	3.5 ± 0.5	0.95 ± 0.10	15.6 ± 0.64	0.77 ± 0.08	3.56 ± 0.36
	7.5 ± 0.5	0.92 ± 0.09	15.3 ± 0.73	0.36 ± 0.04	7.30 ± 0.73
	6.5 ± 0.5	0.94 ± 0.09	15.5 ± 0.69	0.37 ± 0.04	6.53 ± 0.65
5.0	5.5 ± 0.5	1.13 ± 0.11	17.0 ± 0.76	0.44 ± 0.04	6.62 ± 0.66
	4.5 ± 0.5	1.20 ± 0.12	17.5 ± 0.83	0.47 ± 0.05	5.78 ± 0.58
	3.4 ± 0.1	1.60 ± 0.16	20.2 ± 0.94	0.63 ± 0.06	5.78 ± 0.58

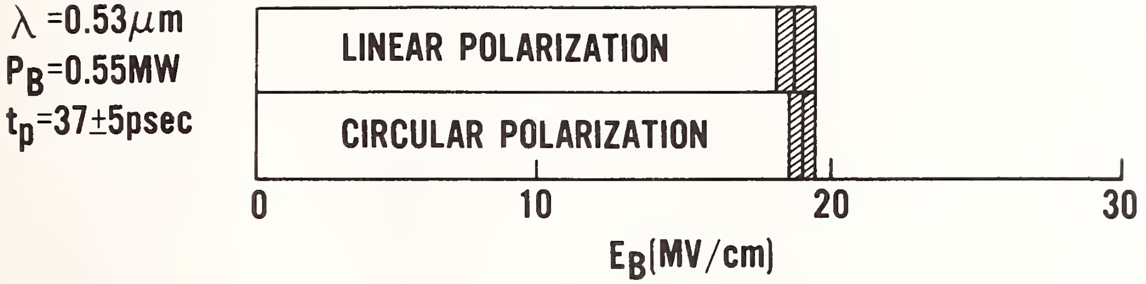

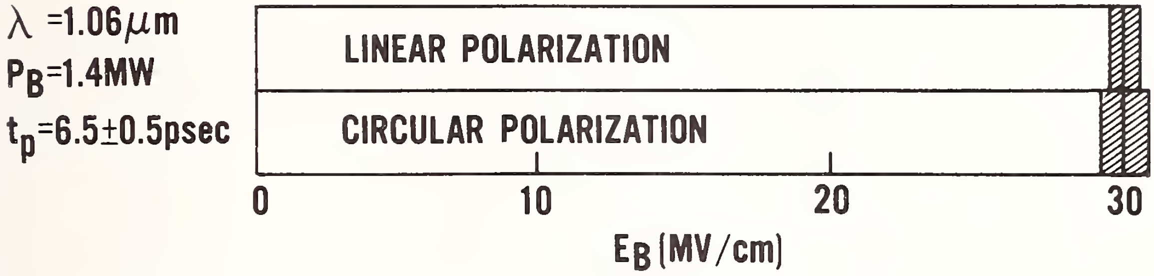

Figure 1. Polarization dependence of E_B for SiO_2. The horizontal axis is E_B, the r.m.s. breakdown field corresponding to the peak on-axis irradiance at damage. P_B is the breakdown threshold power. Note the lack of polarization dependence for both wavelengths. The cross-hatched portions shown above are the relative uncertainties of the thresholds using the procedures given in Ref. 16.

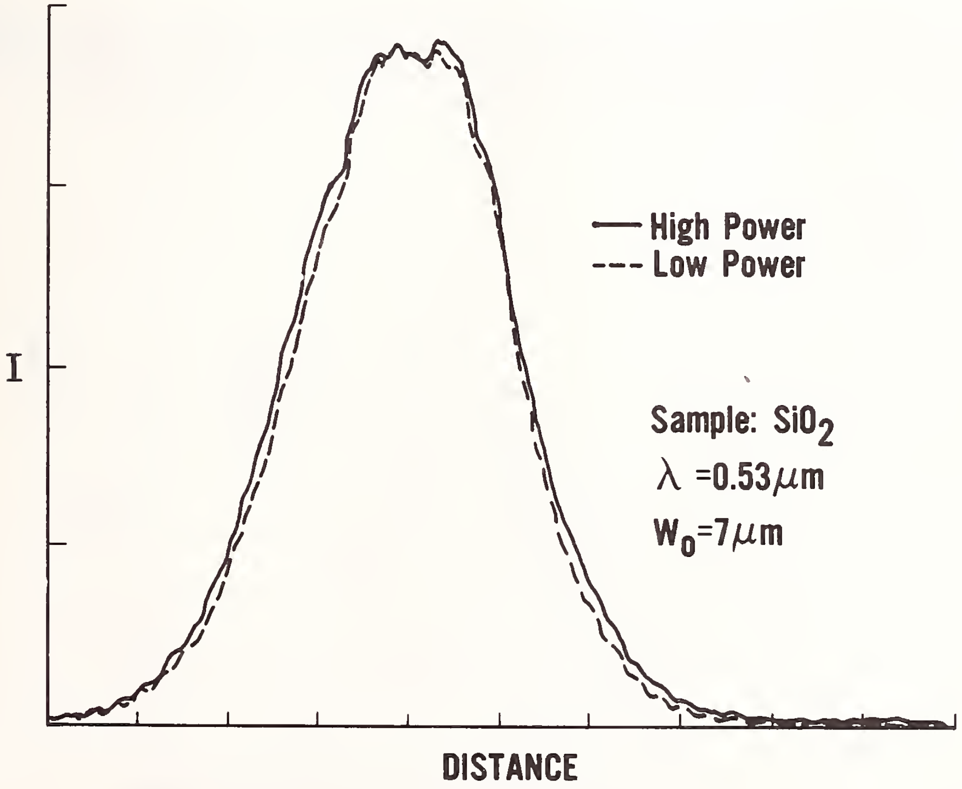

Figure 2. Beam distortion measurements. This is a plot of the far field beam profile of the 0.53 μm beam after propagation through the SiO_2 sample. The quantity ω_0 = 7 μm is the focal spot radius inside the sample calculated using linear Gaussian optics. The curve labeled high power was taken with the input power at the damage threshold level and the one labeled low power was for input power approximately equal to one-tenth the damage threshold power.

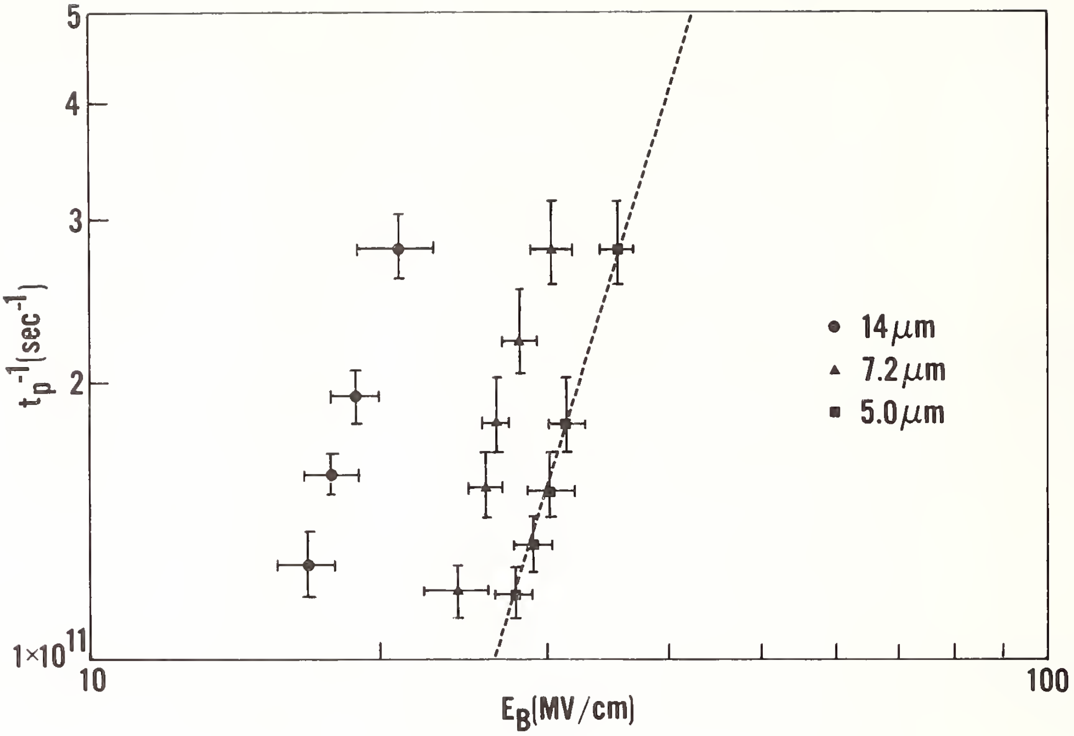

Figure 3. Pulsewidth dependence of E_B for SiO_2 at 1.05 μm. The three sets of points correspond to different focal spot radii and the relatively large displacement of the three sets of points is indicative of a large spot size dependence in the damage threshold. The slope of the least square fit for each set of points is approximately 0.3 for this pulsewidth range (t_p < 10 psec).

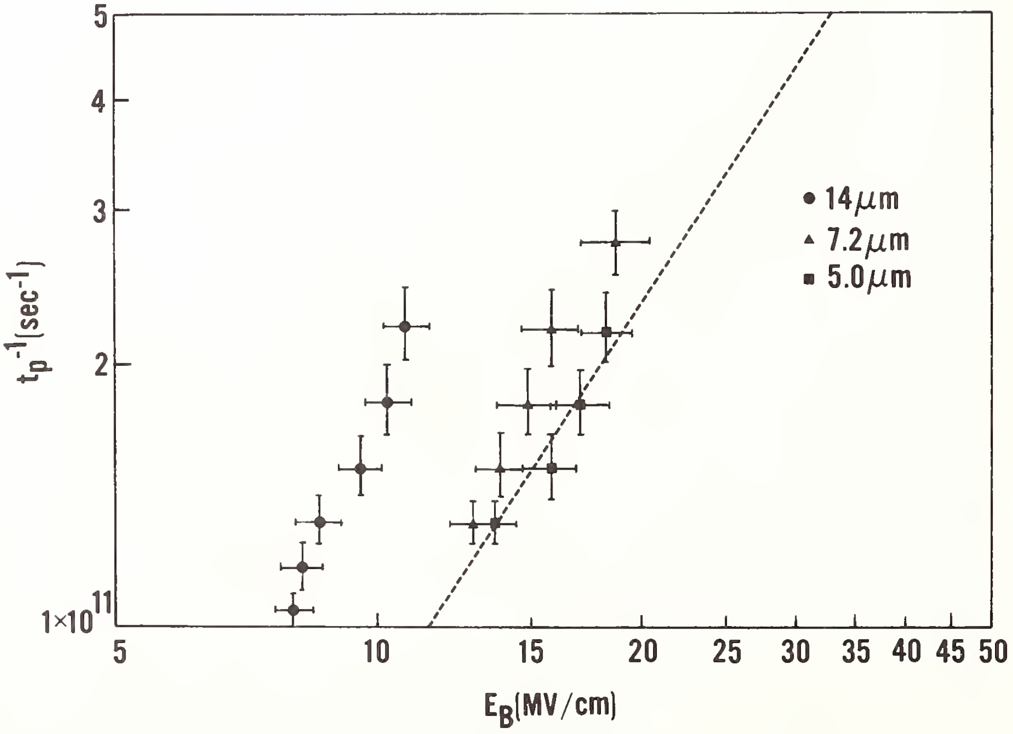

Figure 4. Pulsewidth dependence of E_B in NaCl at 1.05 μm. The slope of the least square linear fit to each of the three sets of points is approximately 0.5. This indicates an inverse square root of pulsewidth dependence of E_B for this pulsewidth range (t_p < 10 psec).

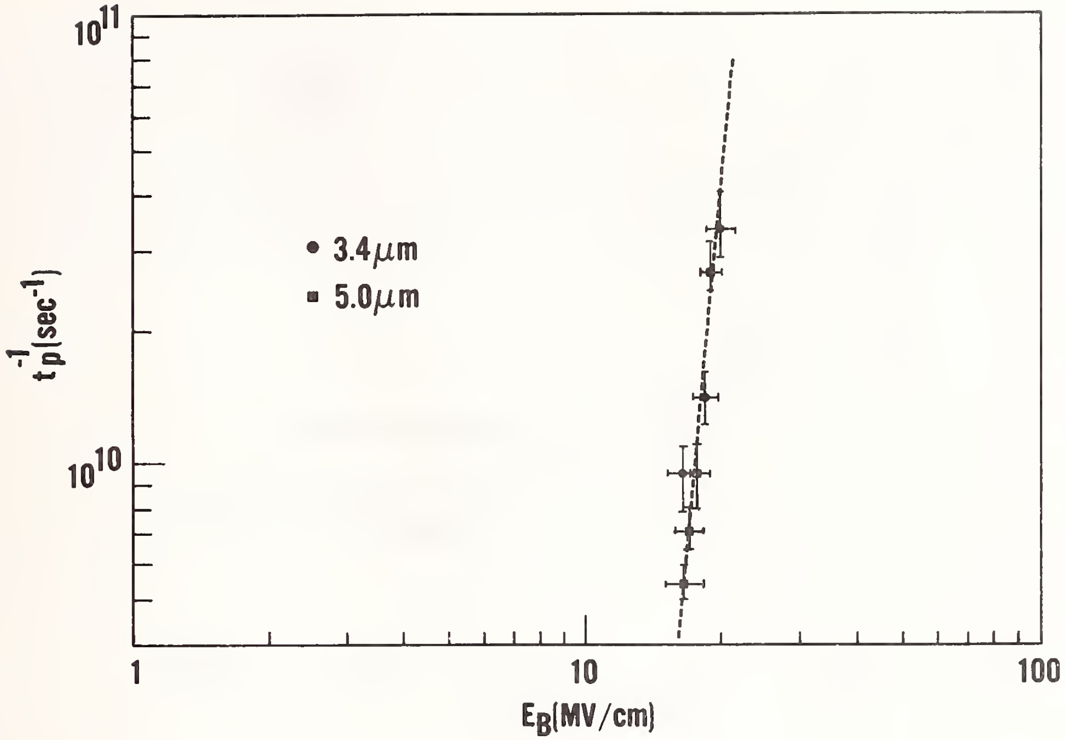

Figure 5. Pulsewidth dependence of E_B in SiO_2 at 0.53 µm. Note E_B is nearly independent of t_p in this pulsewidth range (20 to 300 psec) and that there is little spot size dependence in E_B for the two spot sizes shown (3.4 and 5.0 µm).

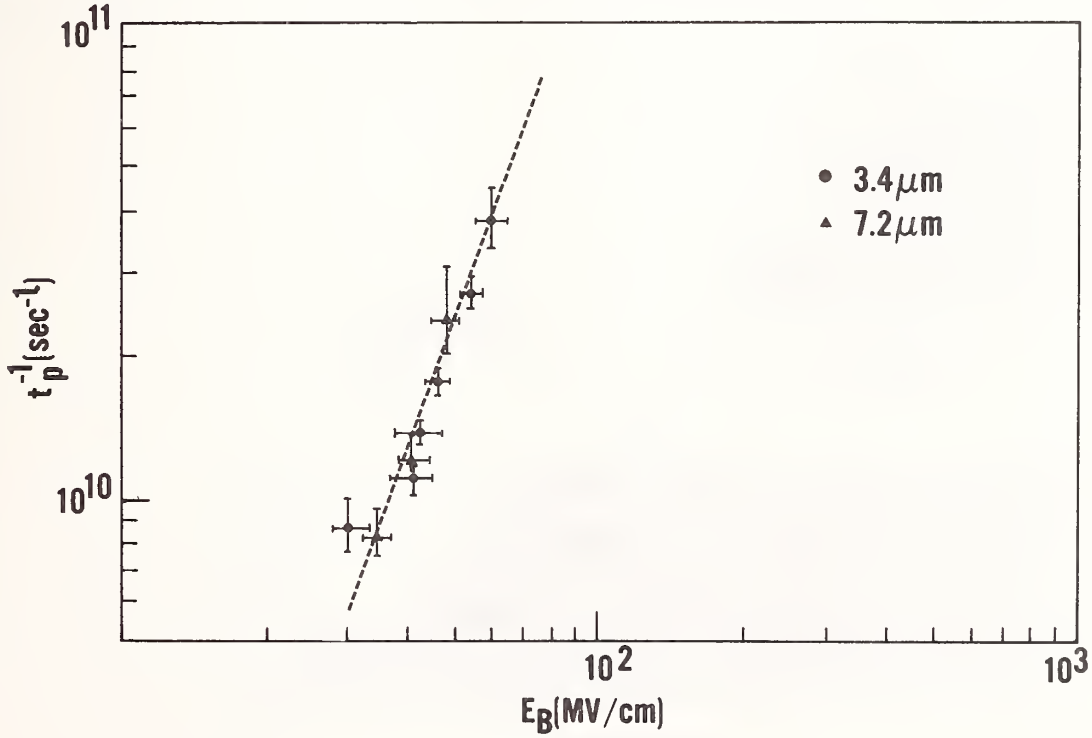

Figure 6. Pulsewidth dependence of E_B in NaCl at 0.53 µm. Note that there is little spot size dependence in E_B for the two spot sizes shown (3.4 and 7.2 µm). The least squares linear fit of these data give a slope of 0.3, or nearly an inverse fourth root dependence of E_B on t_p for pulsewidths in this range (20 to 200 psec).

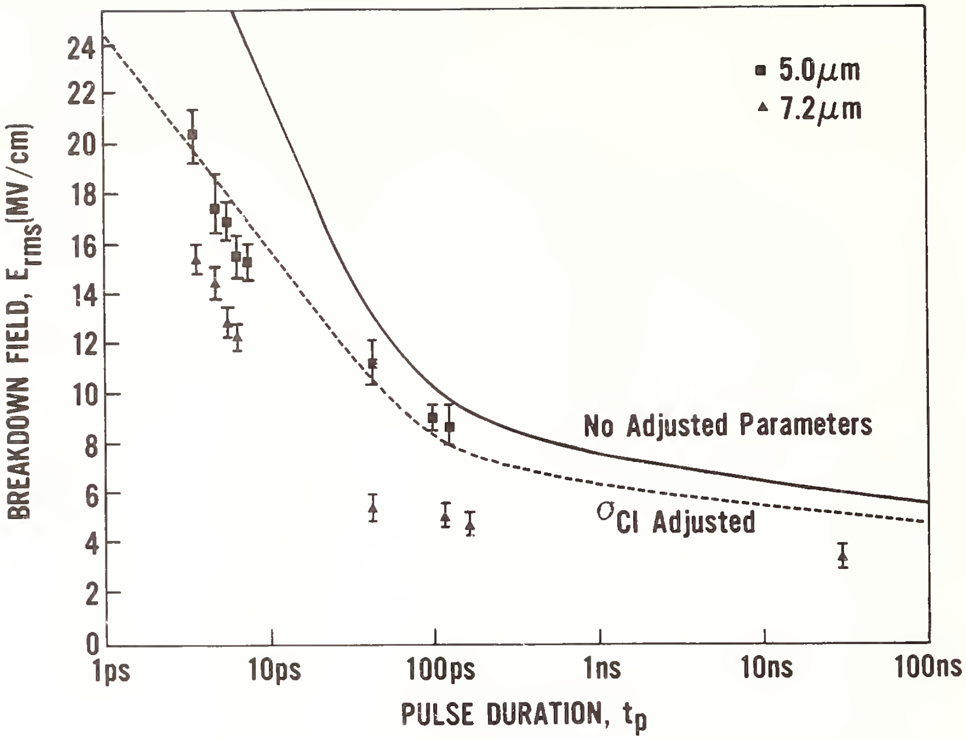

Figure 7. The RMS breakdown field data for NaCl (78-NC-6) at 1.06 μm are plotted as a function of pulse duration, t_p. The solid line and dotted line were obtained from the theory developed by Sparks et al. [28] for NaCl at room temperature. The dotted line uses a different value for the absorption cross section for Cl ions in the theory than the solid line.

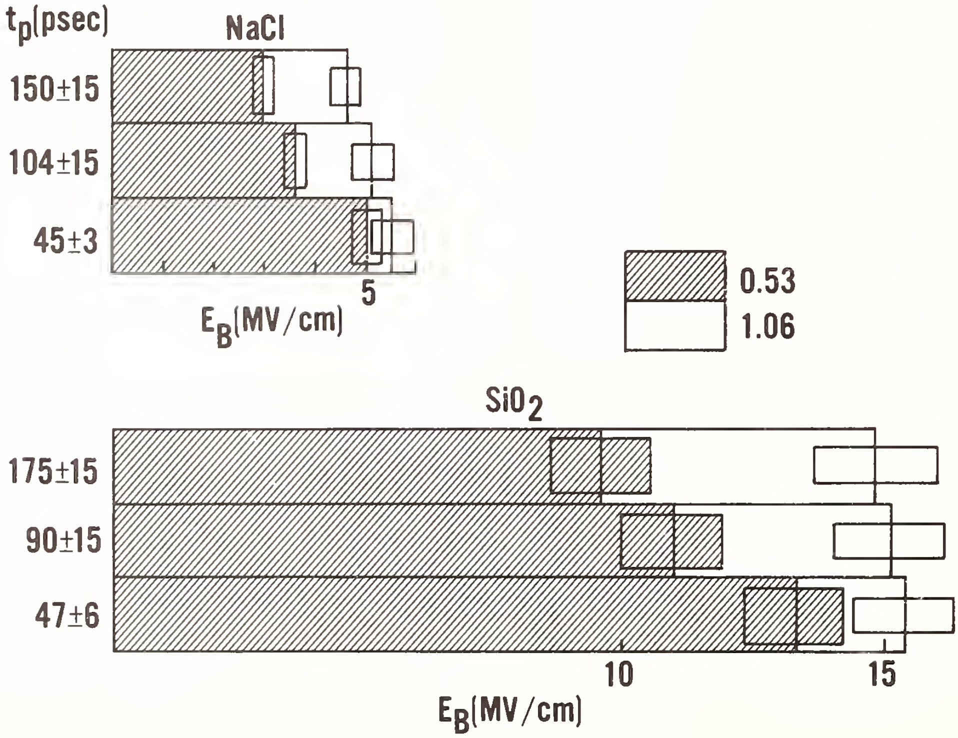

Figure 8. Wavelength dependence of the breakdown field E_B for NaCl and SiO_2 for a variety of laser pulsewidths. All the above data was taken on the same sample of NaCl and the same sample of SiO_2. The 1.06 μm thresholds are taken from Ref. 2 and are interpolated from measurements made at spot size 6.1 and 10.3 μm.

There were several questions regarding the damage mechanism. The author stated that he did not believe electron avalanche was the only mechanism observed in his experiments, because thresholds at 532 nm were less than those at 1064 nm. He speculated that the low 532-nm thresholds might be attributed to avalanche breakdown assisted by multiphoton ionization, and also agreed with the audience that the volume density of damageable defects probably increased as wavelength decreased. The author believed surface thresholds should also scale with laser parameters, but declined to speculate on the exact parametric dependences. The fused silica used in the experiment was water-free material from General Electric Corporation.

Ripple Structures and Enhanced Absorption Associated With Ordered Surface Defects

M. J. Soileau and Eric W. Van Stryland

Center for Applied Quantum Electronics
Department of Physics
North Texas State University
Denton, Texas 76203

Laser-induced ripple structures on material surfaces have been observed by a number of workers for various materials including metals, semiconductors and dielectrics. A model has been proposed [1] which correctly accounts for the spacing and polarization dependence of the ripples, and the association of the ripples with material defects. In this model the ripples are associated with the interference of the incident field with the nonradiative field induced by the interaction of the incident field with the material defects. The association of these features with defects is often difficult to see since real optical surfaces have many defects having a range of sizes and orientations. In this paper experimental results which unambiguously show the association of these features with defects are presented. Quantitative measurements of laser-induced damage thresholds and photoacoustic absorption measurements show a reduction of damage thresholds and increased optical absorption for surfaces with controlled, linear defects aligned orthogonal to the incident laser field (as predicted in ref. 1).

Key Words: Laser-generated ripples; surface damage; surface defects; NaCl; ZnS; ZnSe; CdTe; 1.06 μm; 10.6 μm.

1. Introduction

Laser-generated ripple patterns (LGRP) have been observed in laser-induced damage (LID) to surfaces of various wide bandgaps dielectrics [1-14], semiconductors [14-26], and metals [1,2,14,25,26,28-36]. These features have also been observed in dielectric films used as anti-reflection coatings [6-9]. Careful examination of micrographs in a number of earlier LID papers reveal LGRP on surfaces which were initially unnoticed or were wrongly interpreted as features which were caused by multiple reflections within the sample [37-41]. Recent work has shown these features to be common artifacts of laser annealing experiments, while other experiments have revealed LGRP associated with laser-assisted thin film deposition [36]. The observation of LGRP over such a large range of wavelengths (0.17 to 10.6 μm) and such a wide range of materials has prompted Van Driel to speculate that LGRP are a universal phenomenon common to all laser-surface interactions [42].

Most of the LID experiments referenced above were conducted using optically polished surfaces. Such surfaces, particularly those on exotic materials such as the alkali-halides, contain a high density of defects, e.g., scratches, digs and residual polishing material. LGRP are found to be directly associated with these pre-existing surface defects. Figure 1 shows LGRP running parallel to scratches which are orthogonal to the impressed laser electric field, whereas no LGRP are produced by the same type defect parallel to the field. Similar features have been observed for point defects and grain boundaries in polycrystalline materials.

The observations above lead to a model by Temple and Soileau [1,2] for the formation of LGRP that assumes that these features are initiated by the interaction of the impressed field with pre-existing surface defects. A similar, much more rigorous, model has been proposed by Sipe et al [43]. In that work, the authors show that ripple formation may be initiated by the components of the surface sub-microscopic roughness which are oriented for optimum coupling with the impressed field. Other models [12,36,44] have been recently proposed and these all have the common feature that LGRP result from some sort of scattered wave launched by surface roughness (i.e., submicroscopic surface defects) which then constructively interferes with the impressed field to produce ripples.

The recent models have the common feature that they predict that LGRP are initiated by surface roughness [12,36,43,44]. The model proposed by Temple and Soileau [1,2] predicts that defects of specific sizes and orientation with respect to the incident field should have maximum efficiency for creating LGRP (the model by Sipe et al [43] has a similar provision which they refer to as the "efficacy factor"). Reference 1 predicts that LGRP are easiest to form for scratches of width equal to the laser wavelength and oriented orthogonal to the electric field of a linearly polarized beam. The effects of scratch orientation on LGRP generation on dielectric surfaces have been reported in measurements of the LID thresholds of diamond-turned optical surfaces [10] and more recently in specially prepared Si surfaces [23].

In this paper we report the results of measurements of the thresholds for LGRP formation on NaCl surfaces. We attempted to make the defects nearly "resonant" with the impressed laser field by grinding the NaCl surface with particles of average diameter approximately equal to the laser wavelength (10.6 μm). In addition, we made the observation of LGRP in ZnS, ZnSe, CdTe and other materials.

2. Experimental

A single crystal NaCl specimen was first etched to remove most residual, randomly oriented scratches, due to polishing by the crystal vendor. The sample was then ground on the edge of a polishing wheel using 10 μm alumina grit so as to produce a high density of parallel scratches. A linearly polarized CO_2 TEA laser operated in the TEMoo spatial mode at 10.6 μm was used to irradiate this specially prepared sample. The laser was gain-switched with a partially mode locked temporal profile. The laser was operated without N_2, and the temporal width of the gain-switched envelope was approximately 100 nsec (FWHM). The laser was focused onto the exit surface of the sample. The fluence was varied using a set of Brewster angle polarizers arranged so as to keep the orientation of the laser electric field vector constant at the sample surface. The threshold fluence for the onset of LGRP formation was then measured for the cases where the surface scratches were oriented parallel to and orthogonal to the laser electric field.

This same laser system was used to produce LGRP on the exit surfaces of optically polished ZnSe and ZnS. In addition, a Nd:YAG laser was used to produce LGRP on various materials. The Nd:YAG laser was linearly polarized and operated at 1.06 μm in the TEMoo spatial mode (this laser is more completely described in ref. 45).

The CO_2 laser system described above was also used as the source for orientation dependent absorption measurement for an aluminum diffraction grating. The grating spacing was 9 μm. The absorbed energy was monitored using a photoacoustic technique. The laser-induced acoustic signal was detected by a piezoelectric tranducer pressure contacted with vacuum grease to the rear surface of the metal grating. The absorption, as determined by the piezoelectric peak voltage output, was measured for the cases where the grating grooves were parallel to and orthogonal to the laser electric field.

3. Results and Discussion

Figure 2 is a Nomarski micrograph of LGRP on the specially prepared NaCl surface. The micrograph on the right corresponds to the situation for which the parallel scratches are orthogonal to the incident field vector. Note that as a scratch enters into the high field region it seems to "grow" until its width is approximately equal to the wavelength of the light in the material. A well coordinated ripple pattern results since adjacent ripples are optimumly spaced for maximizing the induced surface field. The micrograph on the right is a picture of a damage sight for the situation where the scratches are parallel to the incident field. The only ripples seen in this micrograph are associated with a scratch (probably left over from the original polishing) which is nearly normal to the impressed field.

We measured the threshold fluence for the onset of LGRP with the laser field parallel to and orthogonal to the parallel scratches. The results of these measurements are shown in figure 3. Note that the threshold for ripple formation is 40% higher for the case where the scratches are oriented parallel to the impressed electric field.

The above result is consistent with the model presented in reference 1 and can be understood in terms of the well known phenomenon of the orientation dependence of absorption of a diffraction grating [46]. Figure 3 is a plot of the 10.6 μm absorption of an aluminum grating with 9 μm grating spacing. The absorption was measured for the cases where the grooves are parallel to and normal to the laser electric field for linearly polarized light. As can be seen in figure 4, the absorption is 4.6 times larger for the case where the grating lines are ortogonal to the impressed field compared to the case where the grating lines are parallel to the incident laser field. So, for this specimen the surface absorption is 4.6 times greater for the case where the defects (i.e., the grating lines) are normal to the incident field. By comparing the results shown in figure 4 with those shown in figure 3 we see that the threshold for initiating LGRP is lowest for the same orientation of the surface defects (scratches) which lead to maximum surface absorption. As the ripples form, coupling of light into the surface increases, and this in turn enhances the formation of more ripples. In fact, an exponential growth of LGRP has been observed [12].

LGRP observed in dielectrics, semiconductors, and metals are very similar in that they run normal to the impressed field and are associated with surface defects. They differ in one important way: the ripple spacing is the free space wavelength (λo) for semiconductors and metals, whereas their spacing is λo/n, (n is the index of refraction), in the wide bandgap dielectrics. Table 1 summarizes the materials for which LGRP have been observed in our lab and the observed ripple pattern spacings. One may speculate about the reason for the difference. One possibility is that the semiconductors undergo a semiconductor to metal phase transition prior to ripple formation. The model given in reference 43 predicts that a transition from λo is λo/n spacing occurs for index of refraction between 4 and 1.5. We attempted to observe the occurance of LGRP with both spacings by examining materials of intermediate index. CdTe and ZnSe were examined at 1.06 µm, and ZnSe and ZnS were examined at 10.6 µm. In addition ZnSe has been studied at 3.8 µm. In all cases the LGRP observed had spacings of λo for these materials.

4. Summary

We have studied LGRP on surfaces with oriented defects (parallel scratches). The threshold for initiation of LGRP was 40% lower for the case where the defects are normal to the impressed laser electric field. Scratches normal to the field produce well coordinated ripple patterns which are clearly associated with the scratches. Photoacoustic measurements of absorption at 10.6 µm of an aluminum grating with 9 µm spacing show that surface absorption is 4.6 times larger for the grating lines normal to the field vector. Thus, we see that LGRP formation is easiest for defect orientation for which surface absorption is maximum.

Ripple patterns were produced on surfaces of CdTe and ZnSe at 1.06 µm and on surfaces of ZnSe and ZnS at 10.6 µm. In all cases the ripple spacing was λo, the free space wavelength. Ripples observed on metals and semiconductors all have a spacing of λo, whereas those observed on wide bandgap dielectrics are spaced at λo/n.

This work was supported by the Office of Naval Research, the National Science Foundation, The Robert E. Welch Foundation and North Texas State University Faculty Research funds.

5. References

[1] P. A. Temple and M. J. Soileau, "Resonant Defect Enhancement of the Laser Electric Field," NBS #462, pp. 371-378 (1976).

[2] P. A. Temple and M. J. Soileau, "Polarization Charge Model for Laser-Induced Ripple Pattern in Dielectric Materials," IEEE Journal of Quantum Electronics, QE-17, 2067-2072 (1981).

[3] M. J. Soileau, H. E. Bennett, J. Porteur, P. Temple, and M. Bass, "Laser Damage to HEL Window Materials as Related to Surface Damage," in Proceedings of the Fifth Annual Conference on Infrared Laser Window Materials, published by the Defense Advanced Research Projects Agency, Arlington, Virginia, pp. 391-417 (1976).

[4] M. J. Soileau, J. M. Bennett, J. O. Porteur, W. Faith, J. Jernigan, and T. T. Saito, "10.6 µm Pulses Laser Damage Studies of Diamond Turned KCl Window Surfaces," NBS #462, pp. 149-157 (1976).

[5] M. Bass, K. M. Leung, C. Tang, and M. J. Soileau, "Pulses Laser Induced Damage at the DF Laser Wavelength," NBS #462, pp. 136-144 (1976).

[6] M. J. Soileau, A. D. Baer, J. O. Porteur, J. L. Jernigan, W. N. Faith, T. M. Donovan, and A. K. Green, "Laser Damage Studies of Low Index Coating Materials at 10.6 µm," NBS # 462, pp. 264-270 (1976).

[7] C. C. Tang, M. Bass, M. J. Soileau, E. W. Van Stryland, "10.6 µm Laser Damage in Coatings Containing As_2S_3 and As_2Se_3," NBS #509, pp. 316-324 (1977).

[8] T. M. Donovan, A. D. Baer, J. H. Dancy, and J. O. Porteur, "Defects and Impurities in As_2S_3, As_2Se_3 and NaF Coatings," NBS #509, pp. 342-351 (1977).

[9] J. O. Porteur, J. L. Jernigan, and W. W. Faith, "Multithreshold Measurements and Analysis of Pulsed Laser Damage on Optical Surfaces," NBS #509, pp. 507-516 (1977).

[10] M. J. Soileau, J. O. Porteur, and D. L. Decker, "Laser-Induced Breakdown of Diamond-Machined Window Surfaces," Appl. Opt. 19, pp. 3043-3044 (1980).

[11] M. J. Soileau and Eric W. Van Stryland, "Laser-Generated Ripple Patterns Associated with Surface Defects," JOSA, 72, p. 1756 (1982).

[12] F. Keilmann and Y. H. Bai, "Periodic Surface Structures Frozen into CO_2 Laser-Melted Quartz," Appl. Phys. A 28, pp. 1-10, (1982).

[13] C. T. Walters, "Surface Scattering at LSD-Wave Initiation Sites on Nonmetallic Materials," Appl. Phys. Lett. 25, pp. 696-698 (1974).

[14] M. Siegrist, G. Kaech, and F. K. Kneubuhl, "Formation of a Periodic Wave Structure on the Dry Surface of a Solid by TEA-CO_2-Laser Pulses," App. Phys. 2, 45-45, 1973.

[15] M. Birnbaum, "Semiconductor Surface Damage Produced by Ruby Lasers," J. Appl. Phys. 36, 3688-3689 (1965).

[16] D. C. Emmony, R. P. Hawson, and L. J. Willis, "Laser Mirror Damage in Germanium at 10.6 µm," Appl. Phy. Lett. 23, 598-600 (1973).

[17] G. N. Maracus, G. L. Harris, C. A. Lo, and R. A. McFarlane, "On the Origin of Periodic Surface Structures of Laser-Annealed Semiconductors," Appl. Phy. Lett. 33, 453-455 (1978).

[18] H. J. Leamy, G. A. Rozzonyi, T. T. Sheng, and G. K. Celler, "Periodic Regrowth Phenomena produced by Laser Annealing of Ion-Implanted Silicon," Appl. Phys. Lett. 32, 535-537 (1978).

[19] M. Oron and G. Sorensen, "New Experimental Evidence of the Periodic Surface Structure in Laser Annealing," App. Phy. Lett. 35, 782-784 (1979).

[20] R. M. Walser, M. F. Becker, J. G. Ambrose, and D. Y. Sheng, "Heterogeneous Nucleation of Spatially Damaged Structures in Crystalline Silicon with Picosecond 1.06 µm and 0.53 µm Laser Pulses," in Laser and Electron-Beam Solid Interaction and Materials Processing, edited by Gibbons, Hess and Sigman (Elsevier, North Holland, 1981), pp. 177-184.

[21] M. F. Becker, R. M. Walser, Y. K. Thee, and D. Y. Sheng, "Picosecond Laser Damage Mechanisms at Semiconductor Surfaces," in Picosecond Lasers and Applications, SPIE vol. 322 (SPIE, Bellingham, Washington, 1982), pp. 93-98.

[22] P. M. Fauchet and A. E. Siegman, "Surface Ripples on Silicon and Gallium Arsenide Under Picosecond Laser Illumination," Appl. Phy. Lett. 40, 824-826 (1982).

[23] J. F. Young, J. E. Sipe, J. S. Preston, and H. M. van Driel, "Laser-Induced Periodic Surface Damage and Radiation Remnants," Appl. Phy. Lett. 41, 261-264 (1981).

[24] P. M. Fouchet and A. E. Siegman, "Surface Ripples on Silicon and Gallium Arsenide Under GaAs Picosecond Laser Illumination," Appl. Phy. Lett 40, 824-826 (1982).

[25] J. F. Figueira and S. J. Thomas, "Generation of Surface Microstructure in Metals and Semiconductors by Short Pulse Co_2 Lasers," Appl. Phys. B 28, 267 (1982).

[26] J. F. Young, J. S. Preston, H. M. van Driel, and J. E. Sipe, "Laser Induced Periodic Surface Structure: II. Experiments on Ge, Si, Al and Brass," Phy. Rev. B 27, 1155-1172 (1983).

[27] Noriaki Tsukada, Sumio Sugata, and Yoh Mita, "New Experimental Evidence of Surface Ripples on Gallium Arsenide in Laser Annealing," Appl. Phys. Lett. 42, 424-426 (1983).

[28] M. A. Cutter, P. Y. Key, and V. I. Little, "Temporal Development of Optically Etched Gratings: A New Method of Investigating Laser-Induced Damage," Appl. Optics 13, 1399-1404 (1974).

[29] J. C. Koo and R. E. Dusker, "Diffraction From Laser-Induced Deformation on Reflective Surfaces," Appl. Phys. Lett. 28, 614-616 (1976).

[30] D. L. Decker, M. J. Soileau, J. O. Porteur, and J. M. Bennett, "Surface, Optical and Laser Damage Characteristics of Diamond-turned Metal Mirrors," NBS #462, pp. 158-164 (1976).

[31] J. O. Porteur, C. W. Fountain, J. L. Jernigan, W. N. Faith, and H. E. Bennett, "Pulsed-Laser Stress Phenomena on Highly Reflecting Metal and Alloy Surfaces," NBS #509, pp. 204-214 (1977).

[32] N. R. Isenor, "CO_2 Laser-Produced Ripple Patterns in Ni_xP_{1-x} Surfaces," Appl. Phy. Lett. 31, 148-150 (1977).

[33] Clifton W. Draper, "Regrowth in Laser Initiated Elemental Metals and Alloys: Surface Nonuniformities and Coupling Phenomena," NBS #620, pp. 210-221 (1980).

[34] A. K. Jain, V. N. Kulkarmi, D. K. Lood, and J. S. Uppal, "Periodic Surface Ripples in Laser-Treated Aluminum and Their Use to Determine Absorbed Power," J. Appl. Phys. 52, 4882-4884 (1981).

[35] S. J. Thomas, R. F. Harrison, and J. F. Figueira, "Observation of the Morphology of Laser-Induced Damage in Copper Mirrors," Appl. Phys. Lett. 40, 200-202 (1982).

[36] S. R. J. Brueck and D. J. Ehrlich, "Stimulated Surface-Plasma-Wave Scattering and Growth of a Periodic Structure in Laser-Photodeposited Metal Films," Phy. Rev. Lett. 48, 1678-1681 (1982).

[37] A. I. Braunstein, V. Wang, M. Braunstein, J. E. Rudisill, and J. Wada, "Pulsed CO_2 Laser Damage Studies of Windows and Window Coatings," NBS #387, pp. 151-158 (1973).

[38] V. Wang, A. Braunstein, M. Braunstein, J. E. Rudisill, and J. Y. Wada, "Pulsed CO_2 Laser Damage Studies of Metal and Dielectric Coated Mirrors," NBS #387, pp. 157-169 (1973).

[39] T. T. Saito, G. B. Charlton, and J. S. Loomis, "10.6 Micrometer CW Laser Damage Studies of Metal Substrate Mirrors," Boulder, NBS #414, pp. 103-112 (1974).

[40] Susan D. Allen, Morris Braunstein, Concetto Ginliano, and Victor Wang, "Pulsed CO_2 Laser Damage Studies of RAP Grown KCl," Boulder, NBS #414, pp. 66-75 (1974).

[41] J. O. Porteur, M. J. Soileau, and C. W. Fountain, "Character of Pulsed Laser Damage in Al at 10.6 m Inferred From Single-Crystal Targets in Vacuum," NBS #462, pp. 165-172 (1976).

[42] H. M. van Driel, "'Universal' Laser-Surface Interaction," Laser Focus 19, 12 (1983).

[43] J. E. Sipe, J. F. Young, J. S. Preston, and H. M. van Driel, "Laser-Induced Periodic Surface Structure: I. Theory," Phy. Rev. B 27, 1141-1154 (1983).

[44] Zhou Guosheng, P. M. Fauchet, and A. E. Siegman, "Growth of Spontaneous Periodic Surface Structures on Solids During Laser Illumination," Phy. Rev. B 26, 5366-5381 (1982).

[45] E. W. Van Stryland, Arthur L. Smirl, William E. Williams, and M. J. Soileau, "Pulsewidth and Focal Volume Dependence of Laser-Induced Breakdown," Phys. Rev. B1, 23, 2144-2151 (1981).

[46] R. Ritchie, "Surface Plasmas in Solids," Surface Sci. 34, 1-19 (1973).

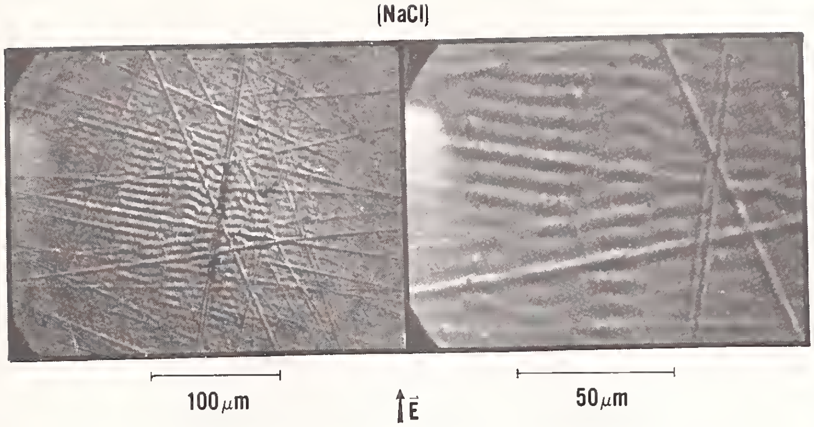

Figure 1. Laser Generated Ripple Patterns (LGRP) in NaCl. The above patterns were produced by normally incident 10.6 μm laser light on the exit surface of NaCl. The laser light was linearly polarized in the direction shown by $\bar{E}$. The higher power photo on the right illustrates that the ripples are associated with defects normal to $\bar{E}$ whereas scratches parallel to $\bar{E}$ have no ripples associated with them.

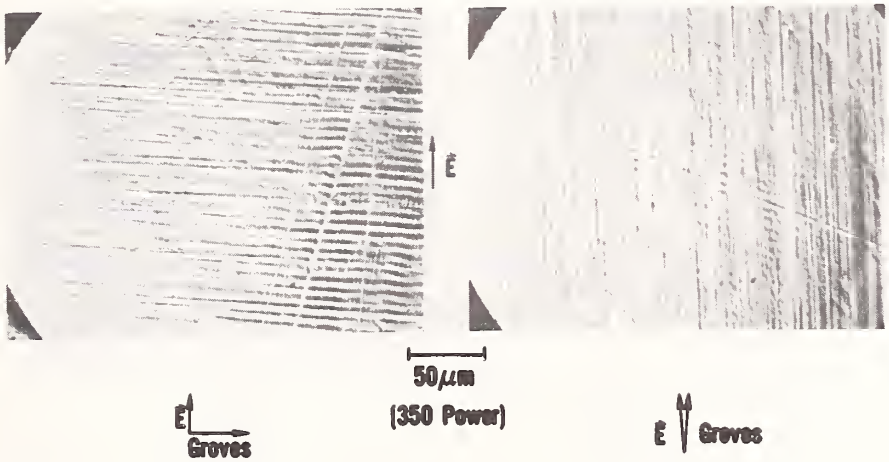

Figure 2. LGRP's on the exit surface of a NaCl specimen. The laser wavelength was 10.6 μm. The laser was linearally polarized in the direction indicated by the arrow ($\bar{E}$). Each site was irradiated only once.

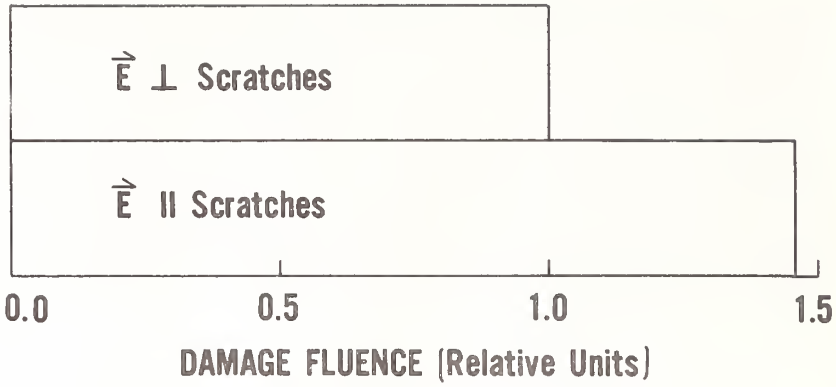

Figure 3. Threshold for Formation of LGRP's. The above is a plot (in relative units) of the fluence required to produce the LGRP for the cases where the linearly polarized electric field is parallel to and normal to the surface scratches. Measurements were made on a NaCl sample (exit surface) using 10.6 μm radiation.

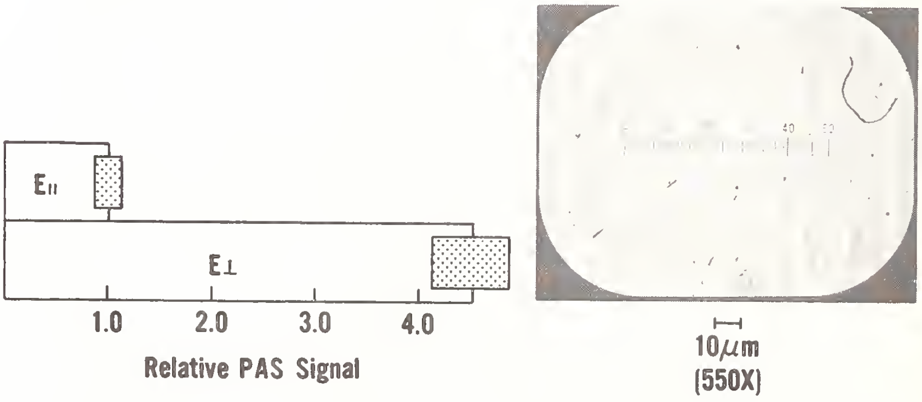

Figure 4. Grating Absorption. The bar graph on the right is the PAS signal (in relative sites) for normally incident, linearly polarized, 10.6 μm laser radiation. The micrograph on the right shows the surface of the Al grating.

Material	1.06μ	2.7μ	3.8μ	10.6μ
KCℓ	λ_o/n			λ_o/n
NaCℓ	λ_o/n		λ_o/n	λ_o/n
KBr	λ_o/n			λ_o/n
SiO_2 (fused)	λ_o/n			
BaF_2		λ_o/n	λ_o/n	
SrF_2		λ_o/n		
MgF_2			λ_o/n	
Si	λ_o			
CdTe	λ_o			
ZnSe	λ_o			λ_o
ZnS				λ_o
CdS	λ_o			
$Cd(S_{.25}Se_{.75})$	λ_o			
ZnTe	λ_o			
Aℓ	λ_o			λ_o
Cu				λ_o
Ag				λ_o

Table 1. The above is a listing of the materials, wavelength, and LGRP spacing observed in this work. Additional materials have been studied by other workers (see the references listed in the introduction).

In response to questions, the speaker stated (1) that he had not yet performed experiments at 532 nm because of a resolution limitation in the available microscope, and (2) that he did not believe the spacings in ripple patterns seen in damages could be explained by mechanisms which invoke surface plasmas or surface polaritons. A comment from the audience noted that damage to absorptive materials occurred at the entrance face, and involved superpositions of fields in air, whereas damage in transparent or thin samples occurred at the exit face and involved superposition of scattered and incident fields in the sample, and suggested this might account for some systematic differences in observed ripple spacings.

Charged Particle Exoemission From Silicon During Multi-Pulse Laser Induced Damage

M. F. Becker, Y-K. Jhee, M. Bordelon, and R. M. Walser

Electronics Research Center and Electrical Engineering Department
University of Texas, Austin, Texas 78712

The damage induced in silicon by multiple, picosecond Nd:YAG laser pulses at 1.06μm has been studied over the past few years. Observations of damage nucleation and growth, and the evolution of a spatially coherent damage structure led to an electronic model for the damage mechanism. To further understand the damage nucleation, we studied electron and ion emission by recording exoemission and laser intensity simultaneously. We found an incubation period for which we could not detect any laser damage. Initiation of damage was observed coincident with the initiation of exoemission. Furthermore, the length of the incubation period varied inversely with the laser intensity and diverged at a threshold intensity. The change in exoemission versus time and laser intensity was related to the damage morphology, as seen by SEM. For exoemission versus intensity, the emitted positive and negative charges are equal, and emission follows the fifth power of intensity. Excellent correlations are observed between all the experimental observations.

Key words: charged particle emission; exoemission; incubation; laser induced damage; multi-pulse laser damage.

1. Introduction and Background

The damage induced in silicon by multiple, picosecond Nd:YAG laser pulses at 1.06μm has been studied over the past few years. Observations of damage nucleation and growth, and the evolution of a spatially coherent damage structure led to an electronic model for the damage mechanism [1-2]. We characterize the damage process as a first order, non-equilibrium phase transition in which the nucleation and resulting multi-pulse damage is heterogeneous. The damage is not the result of uniform melting and resolidification; as would be observed at higher intensities or shorter wavelengths [3]. The damage has been shown to follow classical nucleation and growth behavior [4-5], including having an incubation period for which no detectable changes are observed. In phase transition theory, the incubation period in which the nucleation rate is not steady state is characterized strictly by reversible processes and not by microscopic irreversible events. Some evidence of reversibility in the incubation period has been reported as pulse repetition frequency (PRF) dependent multi-pulse damage [6-7].

In the experiments reported here, we use the exoemission of charged particles into vacuum as a probe of the energetics of the damage process. We have found charge emission to be a very sensitive indicator of the first appearance of surface damage on silicon, and is thus useful for measuring the duration of the incubation period. We have also correlated SEM observations with exoemission measurements to arrive at a sequence of events during the growth of multi-pulse laser damage.

The use of semiconductor grade silicon gives several advantages in material characterization and perfection. There is about one impurity atom for a cube of silicon 100A on a side. On the scale of the laser wavelength the material is homogeneous and well characterized. In addition, the 1.06μm wavelength is just beyond the band gap of silicon and the material is still somewhat transparent with an absorption length of 1mm. In this case, silicon has more in common with other semiconductor optical materials irradiated at or below their band gap. Their electron density can rise due to single or low order multi-quantum absorption. In silicon at 1.06μm, there is no problem obtaining a reasonable density of free electrons during the first instant of irradiation. A final point to consider is that regardless of the mechanism of damage, we have observed similar coherent multi-picosecond pulse damage morphology on widely dissimilar materials; such as amorphous silicon and single crystal aluminum.

2. Experimental Configuration

A block diagram of the experimental set-up is shown in Figure 1. A passively mode-locked Nd:YAG laser with a single pulse selecting switch produced 60-80ps, 250μJ pulses at PRFs up to

20Hz. The beam was directed to an ion pumped vacuum chamber (pressure < 10^{-5} torr) containing the silicon sample. The sample was placed at or somewhat in front of the focus of a lens which could be translated transversely to illuminate new regions of the target. The fluence was varied by using a multi-plate reflective attenuator. Using a micro-processor controlled data acquisition system, the energy and quantity of charge emitted could be collected for every laser shot. The size of the capacitor, C, in the charge collecting circuit was changed to vary the charge detection sensitivity. At its highest sensitivity, the detection limit was 10^{-13}C. The laser spot size at the sample was about 100µm and the PRF was kept at 13Hz.

The silicon samples were p-type <100> silicon wafers of high resistivity (35ohm-cm). They were prepared using standard semiconductor processing cleaning techniques before being placed in the vacuum chamber. The samples were examined optically and with a scanning electron microscope both before and after damage. The surfaces were always perfectly smooth and featureless before damage; and after damage, structures as smaller than .1µm could be easily seen.

3. Experimental Results

3.1 Incubation Period

It was first established that the initial exoemission event coincided with the first observable damage structures as seen by SEM. Numerous negative experiments were performed in which many near multi-pulse threshold laser pulses were incident on a sample location without either exoemission or observable damage. When damage occurred, it was always accompanied by exoemission and vice versa. Generally, when a damage event occurred, the amount of emitted charge correlated with the area of the damage pits. The smallest observed exoemission event was an order of magnitude larger than the instrumental detection sensitivity.

Using the first observed exoemission as an indicator of the end of the incubation period, we measured the number of pulses to the first emission event versus the laser fluence. The data is plotted in figure 2. The inverse of the number of pulses, N, is used in order to clearly show the linear dependence on 1/N and to show the intercept point where 1/N = 0 and N diverges. Sites which had pulses that were well above the average energy were discarded. Note that for $N < 4$ there are quantization steps in figure 2. No damage was observed below the intercept fluence, and no damage was observed for anomolously low numbers of pulses. This clearly indicates that the probability of damage is an increasing function of pulse number; and for these samples, damage does not proceed as the growth of "micro-damage."

3.2 Growth of Damage and Exoemission

After damage was initiated, the exoemission versus fluence was measured. The exoemission process after first damage is very nonlinear and noisy. The data in figure 3 shows average exoemission for the first 50 exoemission events at a given average fluence. As with all the observations, the emitted positive and negative charge was equal and gave equivalent information. The straight line drawn through the data in figure 3 represents a fifth power dependence. The good fit indicates that charge emission occurs through a five quantum process. Just below the lowest fluence in figure 3, was the infinite number of pulse threshold, and just above the highest fluence is the single pulse damage threshold.

The development of exoemission as a function of the number of laser pulses at a 13Hz PRF is shown in figure 4 for a relatively high fluence (upper curve) and for a low fluence (lower curve). Note that the vertical scale on the lower curve has been magnified 10 times. Both cases reach a stationary situation after a long enough time. These curves are correlated with SEM observations at the points on the curves marked with numbers. A sampling of these observations are shown in figures 5 and 6. Figure 5a shows an example of one of the smallest damage events observed after one exoemission event at a low fluence. A characteristic of lower fluence is that the pits are formed into rows of more than two pits each. The round spheres are ejected material and were not present before damage. Figure 5b shows the asymptotic form, and it is similar for all fluences where multi-pulse damage occurred. There is also evidence of material removal, transport, and redeposition in this region. As the density of pits decreases in the center of the spot, the exoemission also decreases. Figure 6a shows the result of one exoemission event at higher fluence. There are numerous pit pairs over the beam area. Figure 6b shows the higher fluence damage spot after 4 exoemission events. Already the coherent damage structure has filled in the beam spot. It is formed by the linking of the pits in chains and the subsequent generation of adjacent chains [1-2]. Note that in figure 6b there were some zero emission pulses after the damage began to initiate, and although damage initiated on the third pulse and there were four exoemission events, there were a total of 20 laser pulses incident on the site.

4. Conclusions

We observe that exoemission is coincident with the first observable damage morphology, which follows an incubation period. The length of the incubation period is inversely proportional to the laser fluence. These observations along with the findings in a related experiment [8] on the PRF dependence of the incubation period, strongly suggest that incubation represents a period of increasing damage probability. The accumulated quantity is not micro-damage or temperature in this case [8]. It appears that the excitation is reversable and not a morphological change.

When damage does nucleate, the accompanying exoemission appears as a five quantum process. It is tempting to correlate this observation with the photoelectric threshold of silicon which is between four and five photons in energy for both direct and indirect processes. This might indicate that the excitations in the exoemission process are from the valence band and not an excited state. The problem with this interpretation is that the positive charge emission is equal to the negative emission and can not be directly related to photo-electron emission.

The growth of multi-pulse damage and the exoemission rate correlate and show stationary behavior. The emission process correlates most closely with the pit structure on the damage surface. SEM reveals that material removed from the pits is ejected and some of it returns to the surface as small spheres. In addition, there seems to be a vapor phase growth of areas immediately adjacent to the pits indicating a complex vapor-liquid-solid material transport process.

This research was supported by the DoD Joint Services Electronics Program through AFOSR Contract F49620-77-C-0101.

5. References

[1] R. M. Walser, M. F. Becker, and D. Y. Sheng, "Laser Damage of Crystalline Silicon by Multiple 1.06μm Picosecond Pulses," in Laser Induced Damage in Optical Materials, November 1981, Nat. Bur. Stand. Spec. Publ. 621 (not yet in print).

[2] M. F. Becker, R. M. Walser, Y. K. Jhee, and D. Y. Sheng, "Picosecond Laser Damage Mechanisms at Semiconductor Surfaces," in Picosecond Lasers and Applications, January 1982, Los Angeles, CA, SPIE Vol. 322; pp. 93-98.

[3] J. M. Liu, R. Yen, H. Kurz, and N. Bloembergen, "Phase Transformation on and Charged Particle Emission from a Silicon Crystal Surface, Induced by Picosecond Laser Pulses," Appl. Phys. Lett. 39(9); 755-757, November 1, 1981.

[4] D. Y. Sheng, R. M. Walser, M. F. Becker, and J. G. Ambrose, "Heterogeneous Nucleation of Damage in Crystalling Silicon with Picosecond 1.06μm Laser Pulses," Appl. Phys. Lett. 39(1); 99-101, July 1, 1981.

[5] R. M. Walser, M. F. Becker, D. Y. Sheng, and J. G. Ambrose, "Heterogeneous Nucleation of Spatially Coherent Damage Structures in Crystalline Silicon with Picosecond 1.06μm and 0.533μm Laser Pulses," in Laser and Electron-Beam Solid Interactions and Materials Processing, T. J. Gibbons, W. Hess, and T. Sigmon eds., New York, Elsevier, 1981, pp. 177-184.

[6] S.-T. Wu and M. Bass, "Laser Induced Irreversible Absorption Changes in Alkali Halides at 10.6μm," Appl. Phys. Lett. 39(12); 948-950, December 15, 1981.

[7] S. K. Balitskas and E.K. Maldutis, "Bulk Damage to Optical Glasses by Repeated Laser Irradiation," Sov. J. Quantum Electron. 11(4); 541-543, April 1981.

[8] M. Bordelon, R. M. Walser, M. F. Becker, and Y-K Jhee, "Observations of Long-lived Metastable Excitations in Multi-pulse Laser Damage of Silicon," in these proceedings.

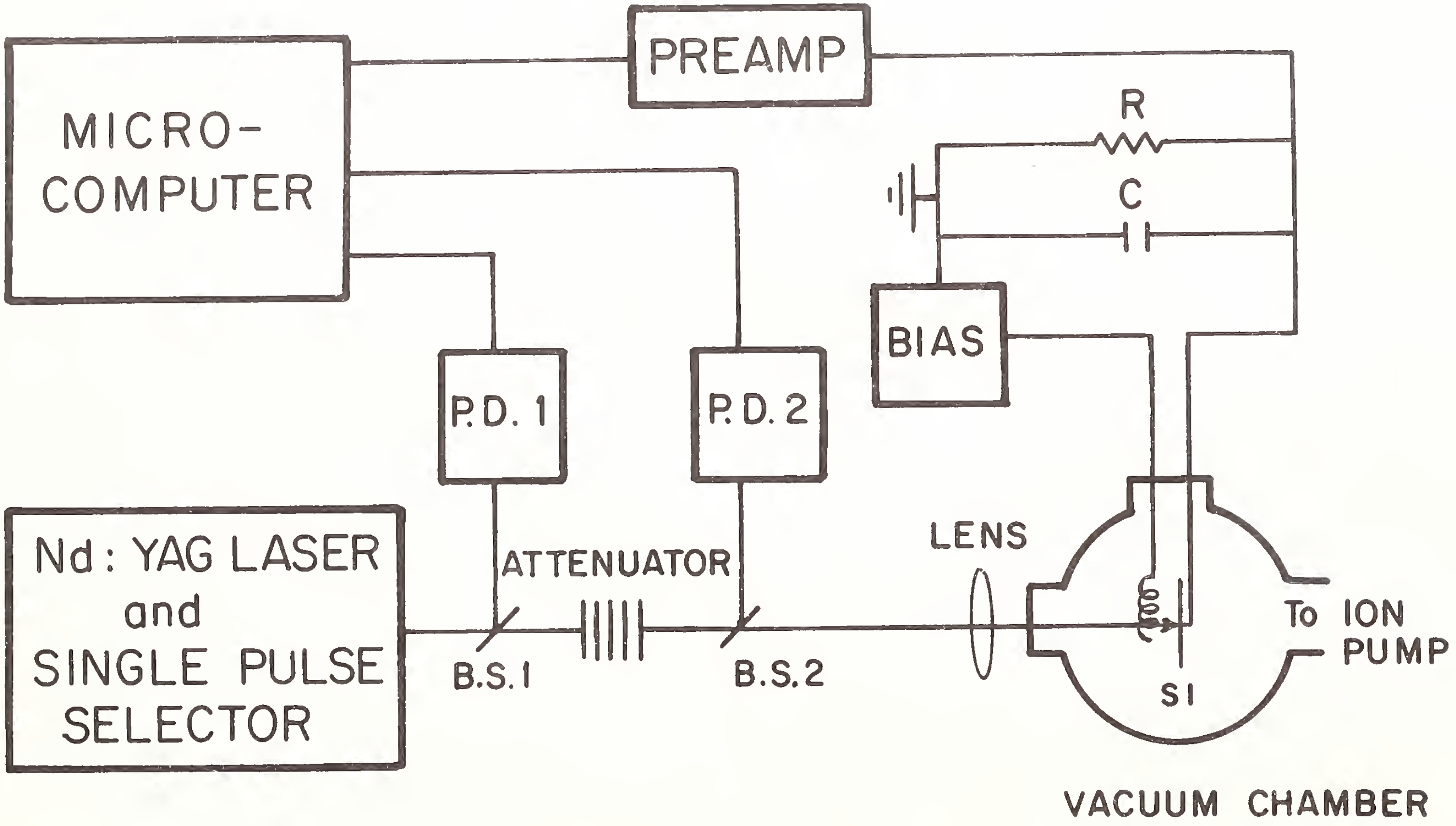

Figure 1. Experimental configuration, see text for details.

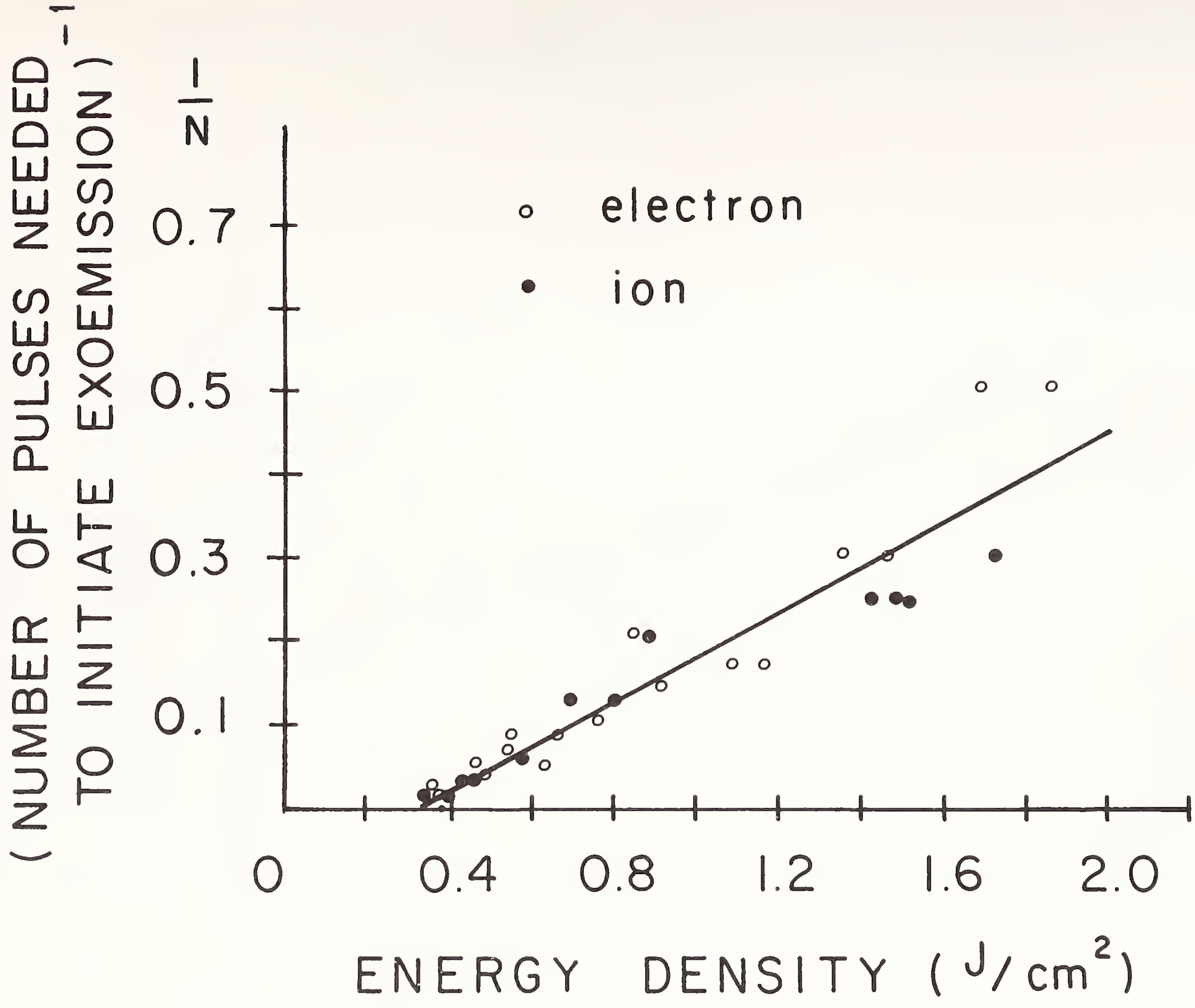

Figure 2. Inverse number of pulses to initiate exoemission and damage versus laser fluence. The line is a least squares fit to the data.

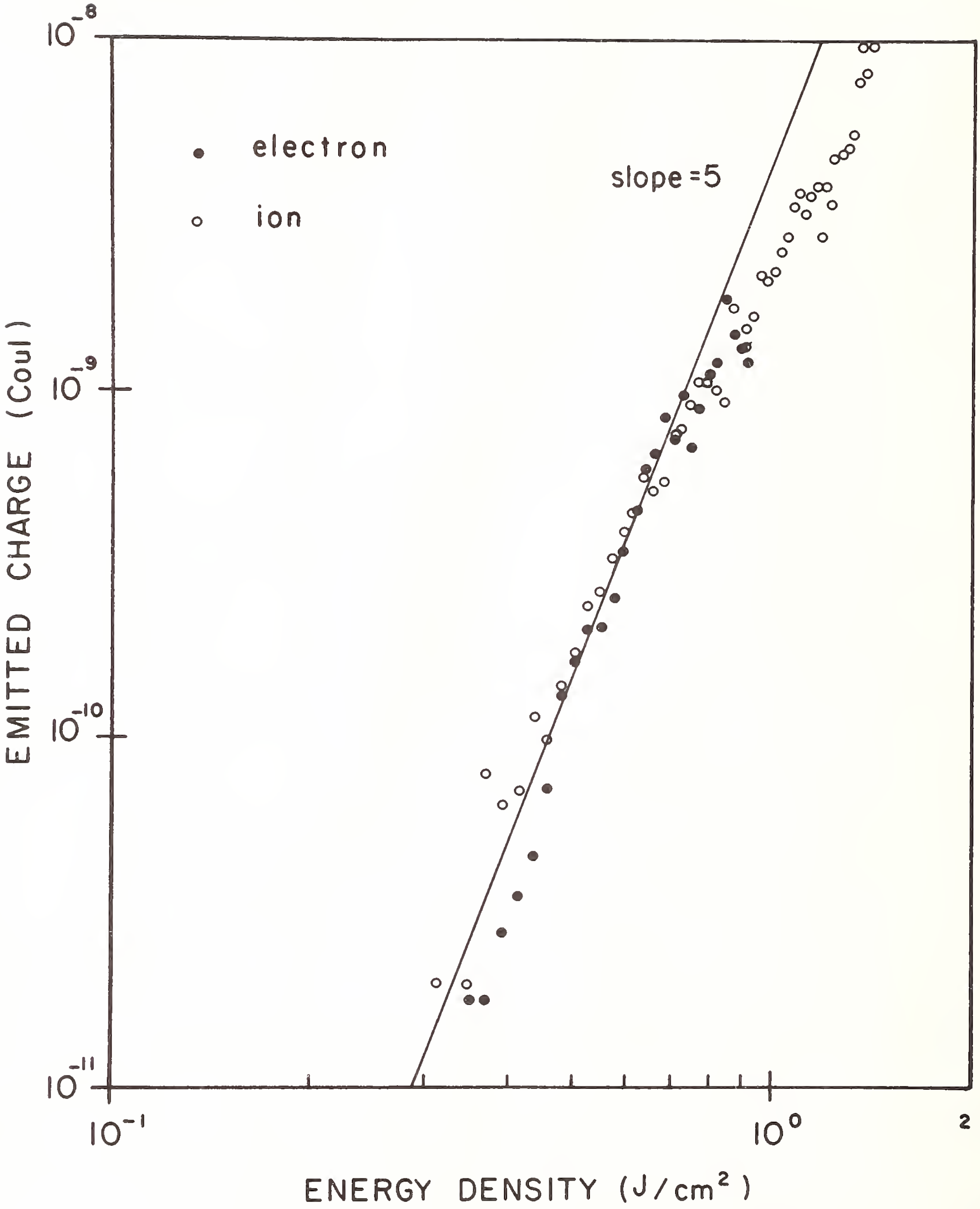

Figure 3. Exoemission versus laser fluence in the multiple pulse damage region. Each point represents the average of 50 exoemission events at a given damage site.

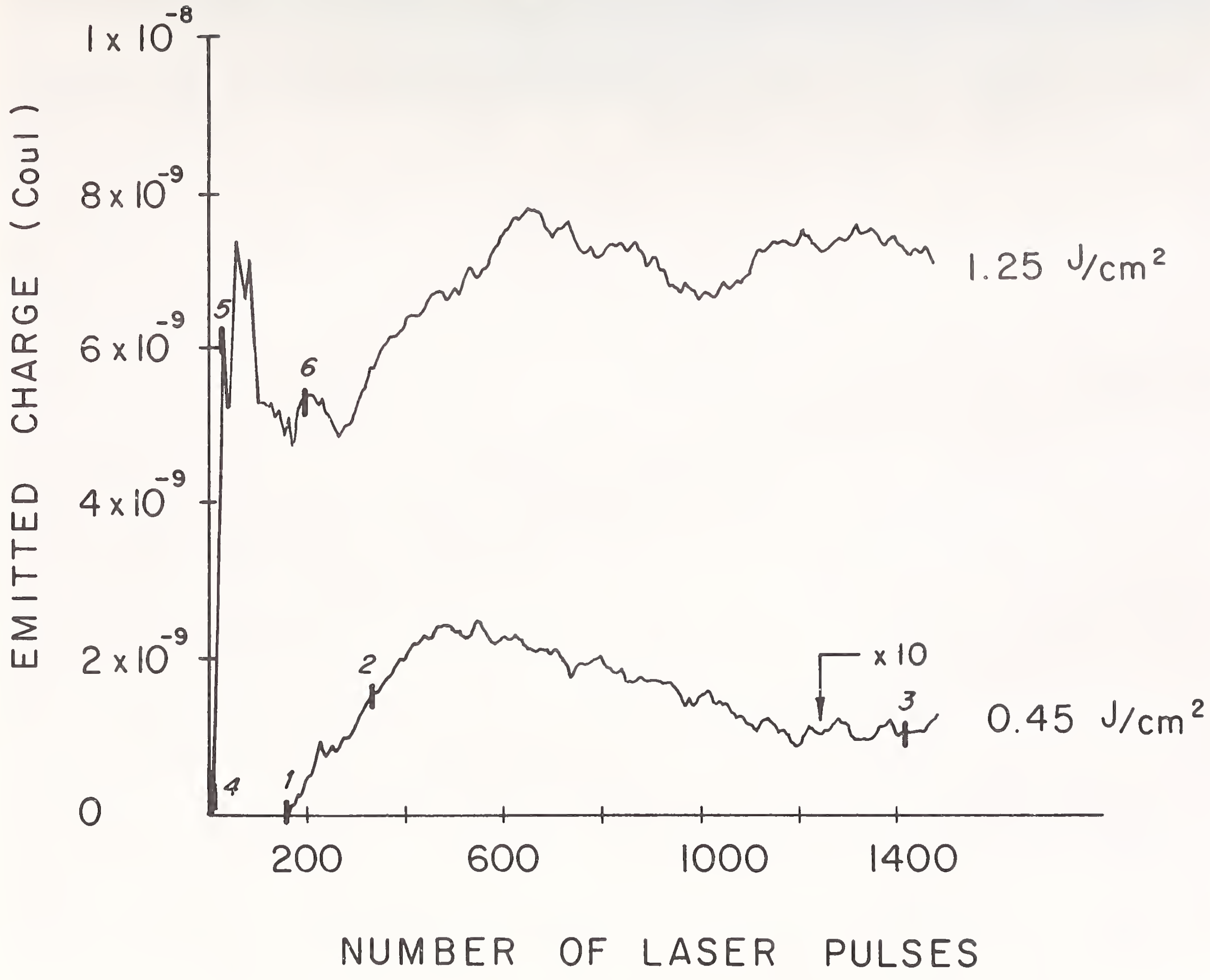

Figure 4. Exoemission versus number of laser pulses (time at a 13 Hz rep rate). The upper curve is for an energy density just below the single pulse damage threshold, and the lower curve is at an energy density just above the multi-pulse damage threshold (vertical scale 10x). Numbers on the curves are correlated with SEM observations of damage morphology development.

a. After first exoemission event or about 150 total pulses (point 1 on figure 4).

Figure 5. Damage morphology at .45J/cm^2.

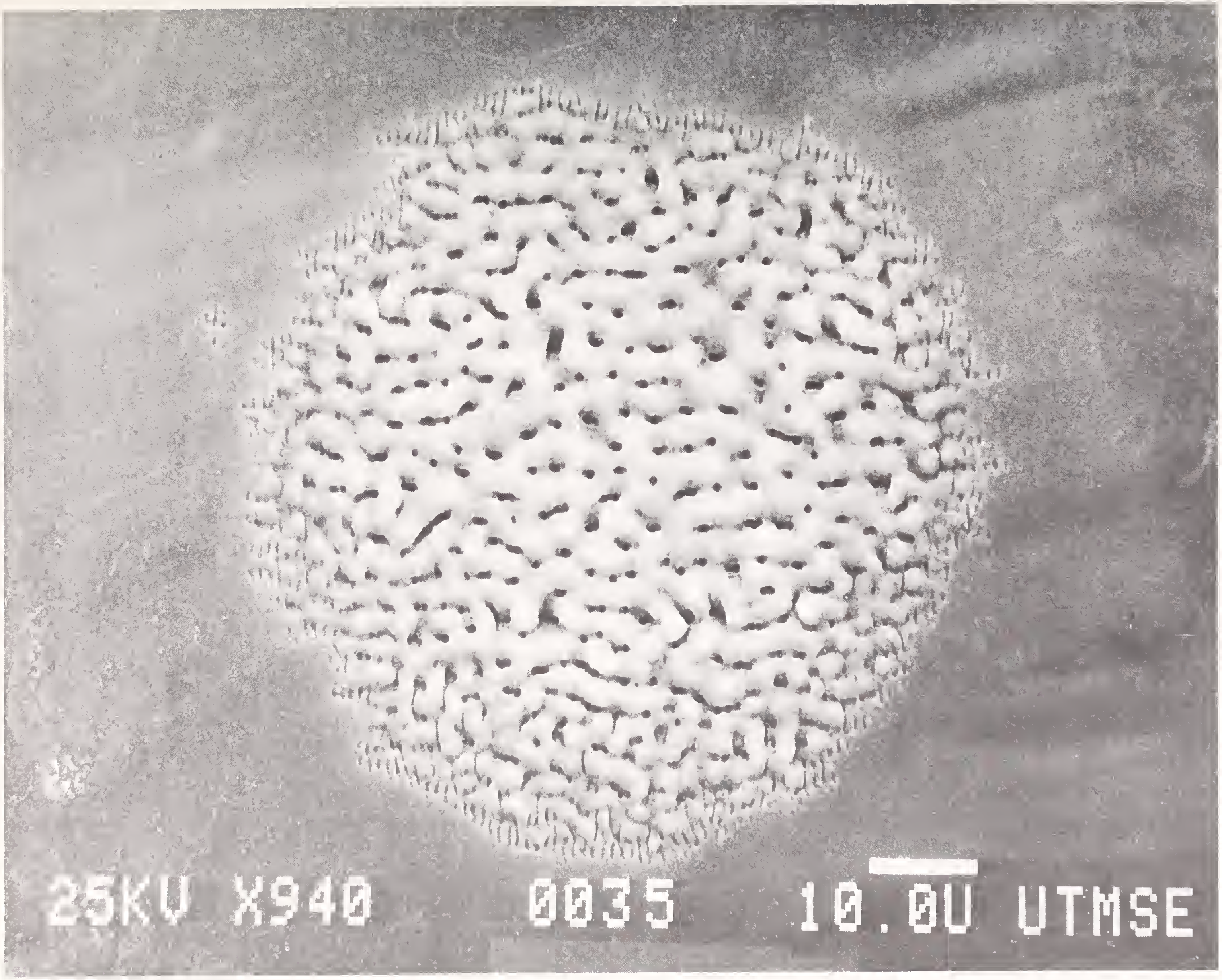

b. Asymptotic form, after about 1400 exoemission events (point 3 on figure 4).

Figure 5. Damage morphology at .45J/cm^2.

Figure 6. Damage morphology at 1.25 J/cm^2.
a. After first exoemission event on the third laser pulse (point 4 on figure 4).

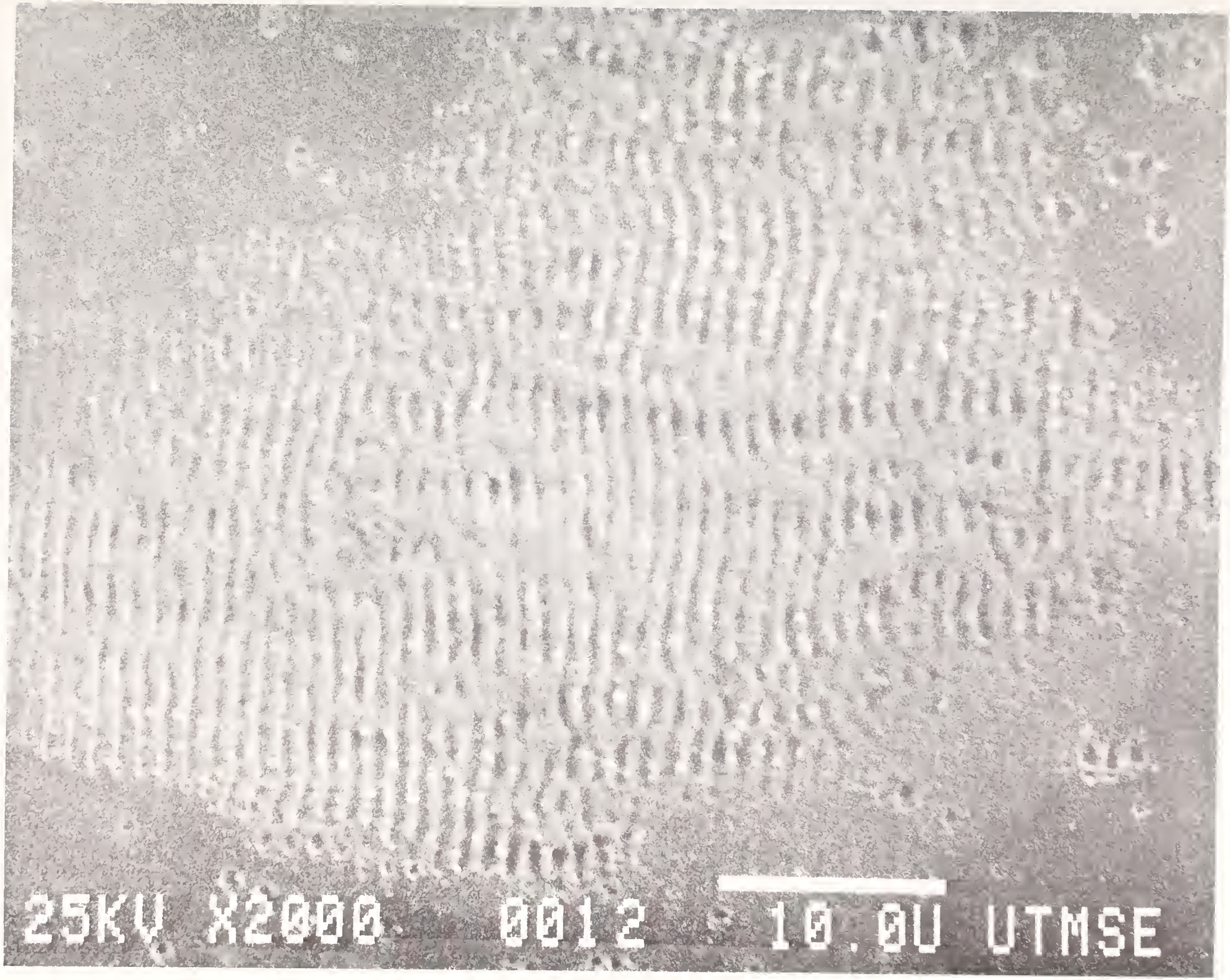

b. After 4 emission events or 20 laser pulses (point 5 on figure 4).

Figure 6. Damage morphology at 1.25J/cm^2.

In response to a comment that damage craters discussed here resembled the craters caused by unipolar arcing which was always associated with the presence of visible plasma, the speaker stated that visible plasmas were not observed during production of the least catastrophic of their damage sites. The speaker further commented that they had been unable to ascertain a relationship between the work function of silicon and the coefficient in the power law dependence of ion emission or intensity.

A Study of the PRF Dependence of the Accumulation Effect in Multiple Pulse Laser Damage of Silicon

M. Bordelon, R. M. Walser, M. F. Becker and Y-K. Jhee

Electronics Research Center
Electrical Engineering Department
The University of Texas at Austin
Austin, Texas 78712

We report on the effect of varying the laser pulse repetition frequency PRF (from 0.03 Hz to 15 Hz) on the accumulation effect in the multiple pulse damage of silicon by picosecond 1.06 μm pulses. When the laser intensity fluctuations are controlled on a pulse-to-pulse basis, no PRF dependence is observed. This implies that the precursors to damage are either characterized by very long reversible decays or are the result of irreversible processes. Our calculations show that thermal accumulation is negligible in these experiments for even the largest PRF.

Key words: picosecond, damage, silicon, nucleation, nonequilibrium phase change, multiple pulse, pulse repetition frequency.

1. Introduction

The objective of the experiments reported here was to study the thermodynamic reversibility of the subtle precursors to catastrophic damage of crystalline silicon irradiated by multiple, picosecond pulses of 1.06 μm radiation. The existence of difficult to detect precursors in multiple pulse laser damage is evidenced by an accumulation effect [1-5], the salient feature of which is an inverse relationship between the laser intensity and the number of pulses required to produce observable damage. Conventionally, a shift in this relationship with a change in the laser PRF is interpreted as evidence of reversibility on a time scale $\sim(\mathrm{PRF})^{-1}$.

Previous studies have, for example, revealed a PRF dependent accumulation effect in optical glasses for 7 ns pulses of both 1.06 μm and 0.533 μm radiation [4] and reversible, predamage, absorption changes in alkali halides [5] induced by 100 ns pulses of 10.6 μm radiation. Fauchet [7], however, in experiments nearly identical to ours, failed to observe a PRF dependence in the damage of crystalline silicon. Fauchet's data was, however, primarily taken for laser intensities for which $N >> 100$ pulses were required to observe damage. It is also not clear that the laser intensity fluctuations, which are critical in this region, were monitored on a pulse-to-pulse basis. Furthermore, the methods used to detect damage in these experiments increase the possible ambiguity of the results.

The time scale in which reversible precursors might occur in multiple pulse laser damage is an issue of crucial importance in understanding the accumulation effect. While irreversible precursors to multiple pulse laser damage will certainly occur in most cases, it is not clear that observable reversible processes may also occur, perhaps coincidentally. The latter is expected, for example, in a new perspective of this laser damage process as a nonequilibrium phase transition [6,13]. In this picture, the accumulation effect is associated with an incubation period, or induction time, characterized by the nonsteady growth of critically-sized embryos. Thus, nucleation and growth will occur simultaneously, and it is not clear that the prenucleation reversible fluctuations can be independently observed.

To answer this question and to attempt to verify the results of Fauchet [7], we conducted the experiments described in Section 2. If the laser-silicon energy transfer is reversible on time scales on the order of $\frac{1}{10}$ sec - 10 sec during the incubation period, it may be possible to observe a change in either the microscopic extent of damage, or in the damage threshold, by varying the PRF of a fixed number of laser pulses.

To reduce the ambiguity of these experiments, it is crucial to control or select the laser intensity fluctuation statistics and monitor these on a pulse-to-pulse basis. It is also important to use a high resolution technique to estimate the change in damage produced by varying only the PRF. In our experiments, this was done by inspecting the irradiated beam spot with high resolution electron microscopy.

2. Experimental

The laser used in these experiments was a passively mode-locked Nd:YAG operating at 1.06 μm with FWHM pulses of 60 to 80 picoseconds. The spatial and temporal distribution of intensity were both Gaussian and typical intensities used were between 2.0 and 4.0 GW/cm^2 (0.16 to 0.32 J/cm^2). The samples used were intrinsic <111> silicon wafers 15 mils thick. The samples were ultrasonically cleaned and boiled in a series of baths containing high purity trichloroethylene, acetone, and methanol. No defects or foreign particles were observed by optical microscopy with magnifications up to 1600X.

Single pulse damage experiments were conducted first, and a damage threshold of 6.0 ± 0.5 GW/cm^2 was determined for an irradiated area of 3.21×10^{-4} cm^2. As noted by others [8], we have observed that the single pulse damage thresholds are inversely proportional to the area irradiated. Next, the laser beam was attenuated so that the average intensity was between 3.0 and 4.5 GW/cm^2.

A mechanical shutter in the beam line was used to select 20 pulses for each damage spot. Damage produced by PRFs of 15 Hz, 10 Hz, 1 Hz, 0.1 Hz and 0.03 Hz was studied. The PRFs of 15 Hz and 10 Hz were produced by varying the frequency of the flash lamps. The lower frequencies were produced by switching out individual pulses with the shutter while the laser operated at 15 Hz. The energy of each pulse was recorded by a calibrated PIN photodiode interfaced with a microprocessor which calculated the average intensity and the standard deviation of the pulse train. The extent of damage and the damage threshold were determined by high resolution optical and electron microscopy.

When comparing the extent of damage for the different PRFs, the data was intentionally statistically biased by selecting damage spots such that the lower PRFs had a higher average intensity than the higher PRFs. This was done to ensure that the effect of positive laser intensity fluctuations, which are assumed to increase metastable lifetimes (if such states exist), would have a greater effect on the experiments with a lower PRF. Individual damage runs were rejected from the data when the standard deviation, σ, of the pulse train was greater than 20% of the average intensity, and whenever the absolute difference between the average intensity and any individual pulse intensity was greater than 2σ.

3. Experimental Results

When comparing the extent of the damage for any two PRFs, the result of the statistical bias was that slightly more damage occurred at the lower PRFs. Thus, for the same average intensity and pulse number, there was no difference in the extent of damage. The PRF independence of damage was further supported by the deterimination of the damage threshold, which was in the range of 3.3 to 3.6 GW/cm^2 for all PRFs.

The damage morphology observed was the same for all PRFs. As first reported by Sheng [3], the damage process induced by picosecond pulses of 1.06 μm radiation is a heterogeneous nucleation involving a first-order phase change to the liquid-like state. For each PRF, the first sign of damage was characterized by discrete damage sites that were shallow and elongated in shape with one or two small nipples within each depression. The depressions and resulting pits always formed with their long axis perpendicular to the electric field of the linearly polarized laser radiation. Both of these structures are evident in the SEM picture of figure 1 of damage initiated by 23 pulses at an average intensity of 3.74 GW/cm^2. Growth of the damage then occurs in a direction parallel to the electric field resulting from the interference between the wave scattered from the pits and the incident wave. This results in the formation of pit chains separated by the wavelength of the laser. This "ripple" structure is illustrated in Fig. 2.

4. Discussion

In the experiment presented here, the damage of silicon was not PRF dependent, which suggests that the mechanism of accumulation is not reversible on time scales less than 30 seconds. However, it can not be ruled out that over long periods, the mechanism is reversible. Reports of the optical properties of some amorphous semiconductors has shown reversibility on the order of hours and days [11].

To determine the effects of heating, calculations were made of the initial temperature profile (t=0) and for several t > 0. In previous work [6], it was shown that for intensities up to single pulse damage threshold, both one and two photon absorption occur in silicon with corresponding absorption coefficients of $\alpha = 10\ \text{cm}^{-1}$ and $\beta = 52$ cm/GW. If uniform illumination is assumed, the intensity relative to the surface is given by the differential equation

$$\frac{dI}{dx} = -(\alpha I + \beta I^2) \tag{1}$$

Rearranging and integrating explicitly gives

$$I(x) = \frac{\alpha(1-R)I_0 \exp(-\alpha x)}{\alpha+\beta(1-R)I_0\ [1-\exp(-\alpha x)]} \tag{2}$$

where I_o is the incident intensity and R is the reflectivity. Since silicon is not highly absorbing at 1.06 µm, the thermal diffusion length, $2\kappa t_p$, during the time of the pulse is $<< [\alpha+\beta I(x)]^{-1}$. This allows the initial temperature distribution to be approximated by

$$\Delta T(x) = \frac{-dI}{dx}\,\frac{t_p}{C_v\rho} = [\alpha+\beta I(x)]\ I(x)\ \frac{t_p}{C_v\rho} \tag{3}$$

where R is 0.3, the pulse length, t_p, is 80 psec (worst case), and the heat capacity, $C_v\rho$ is 0.56 Joules/cm^2°K [9]. The above gives a maximum surface temperature change, ΔT, of 62.2°C for an incident pulse of 4.0 GW/cm^2. This suggests that if only homogenous absorption were occurring, the sample would never damage unless thermal accumulation is significant. To check that possibility, the temperature decay was calculated assuming a one-dimensional semi-infinite sink with no radiative losses of heat at the surface [10].

A numerical solution of eq. (3) was obtained by a computer. Since the thermal diffusivity, k, is a function of temperature (decreasing with increasing temperature), a worst case approximation was obtained by assuming that k remains constant at its 100°C value, which is 0.536 cm^2/sec. The results of these calculations are shown in figure 3. These results show that thermal accumulation cannot be responsible for damage at any of the PRFs used, which is further supported by the experimental results. In the above calculations, free carrier absorption was assumed to be negligible since a charge carrier density of 10^{18} to 10^{19} cm^{-3} is produced for the intensities used [12].

Proposed mechanisms on the origin of damage of silicon surfaces by picosecond 1.06 μm radiation must explain (1) the inhomogenous absorption required to melt localized regions, (2) the symmetry breaking involved in the observation that damage is initially oriented perpendicular to the electric field of the laser, and (3) the mechanism of accumulation of microscopic change that allows many pulses with sub-single pulse threshold intensity to damage. A theory involving the resonant absorption of radiation by surface "particle" plasmas [6,13] gives an explanation for the inhomogeneity of damage and has predicted the orientation of the pit chains and the distance separating individual pits in each chain.

What has not been answered in this experiment is the mechanism of accumulation. An accumulated change is required to allow the localized region to have different absorption characteristics with respect to the bulk silicon. Experiments which would be beneficial to such a study would look for structural or electronic changes occurring during the incubation period before the onset of damage.

5. Conclusion

Multiple phase damage of silicon by picosecond 1.06 μm radiation has been shown to be independent of the pulse repetition frequency (PRF). Damage as a result of thermal runaway was incompatible with our calculated heating and cooling transients and with the observation of heterogeneous damage. For similar reasons, the presence of defects and impurities are not believed to be responsible for the accumulation of damage since localized heating would have a higher rate of cooling and could not begin to explain the consistently observed symmetry of the damage. The possibility of an avalanche ionization mechanism is neglected because of the low electron density assumed, and since the product of the excitation frequency and the electron-phonon collision time, $\omega\tau$, is greater than 100. Although the mechanism of accumulation could not be determined, this experiment clearly supports the perspective of the observed laser damage as a nonequilibrium phase transition involving precursor formation of long-lived excitation.

This research was supported by the DoD Joint Services Electronic Program through AFOSR Contract No. F49620-77-C-101.

References

[1] M. F. Becker, Y-K. Jhee, M. Bordelon and R. M. Walser, "Charged Particle Exoemission from Silicon During Multi-pulse Laser Induced Damage," these proceedings.

[2] R. M. Walser, M. F. Becker, D. Y. Sheng and J. G. Ambrose, "Heterogeneous Nucleation of Spatially Coherent Damage Structures in Crystalline Silicon with Picosecond 1.06 μm and 0.533 μm Laser Pulses," Laser and Electron Beam Solid Interactions and Material Processing, J. F. Gibbons, W. Hess and T. Sigmon, eds., Elsevier, New York, 1981, pp. 171-184.

[3] D. Y. Sheng, R. M. Walser, M. F. Becker and J. G. Ambrose, "Heterogeneous Nucleation of Damage in Crystalline Silicon with Picosecond 1.06 μm Laser Pulses," Appl. Phys. Lett., 39 (1), 19, 1981.

[4] S. T. Wu and M. Bass, "Laser Induced Irreversible Absorption Changes in Alkali Halides at 10.6 μm Laser Pulses," Appl. Phys. Lett., 39 (12), 948, 1981.

[5] S. K. Balitskas and E. K. Maldutis, "Bulk Damage to Optical Glasses by Repeated Laser Irradiation," Sov. J. Quantum Electronics, 11 (4), 541, 1981.

[6] M. F. Becker, R. M. Walser, Y-K. Jhee and D. Y. Sheng, "Picosecond Laser Damage Mechanism at Semiconductor Surfaces," in Picosecond Lasers and Application, Jan. 1982, Los Angeles, CA, SPIE, Vol. 322, pp. 93-98.

[7] D. M. Fauchet, Phys. Lett. 93A, 155 (1983).

[8] M. J. Soileau, M. Bass, P. H. Klein, "Frequency and Focal Volume Dependence of Laser-Induced Breakdown in Wide Bandgap Insulators," in Laser Induced Damage in Optical Materials: 1979, NBS Special Publication 568, p. 497 (1980).

[9] This value is reported by N. Bloembergen, Fundamentals of Laser Solid Interactions and Laser Processing, -1978, S. D. Ferris, et al., ed. AIP Conference Proceedings #50 (1979), p. 1. Other papers in the same proceedings use $C_p\rho$ = 1.6 J/cm^3°K. See M. von Allmen, et al., "Annealing of Silicon with 1.06 μm Laser Pulse," p. 43. The former should give a worst case approximation.

[10] H. S. Carslaw and J. C. Jaeger, Conduction of Heat in Solids, 2nd edition, p. 276, Oxford at the Clarendon Press, 1957.

[11] M. I. Korsunskii, Anomalous Photoconductivity (New York: Wiley, 1973).

[12] D. Y. Sheng, Ph.D. Dissertation, The University of Texas, 1981.

[13] R. M. Walser, M. F. Becker and D. Y. Sheng, "Laser Damage of Crystalline Silicon by Multiple 1.06 μm Picosecond Pulses," in Laser Induced Damage in Optical Materials: 1981, NBS publication of 1981 Boulder Damage Symposium.

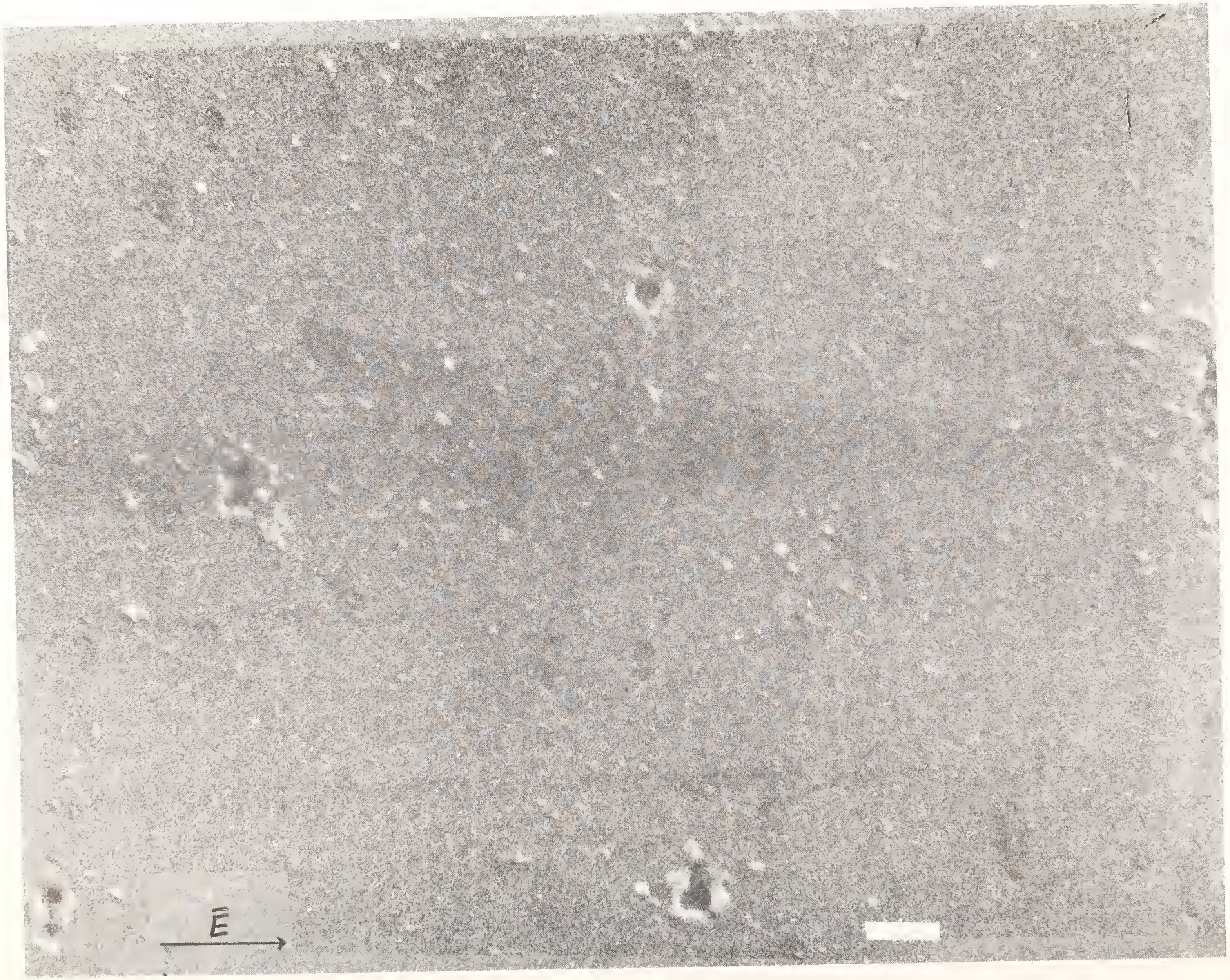

Figure 1. SEM photograph showing pits and shallow depressions. Note that the coupled pit pairs are perpendicular to the electric field of the laser. The bar equals 1 µm

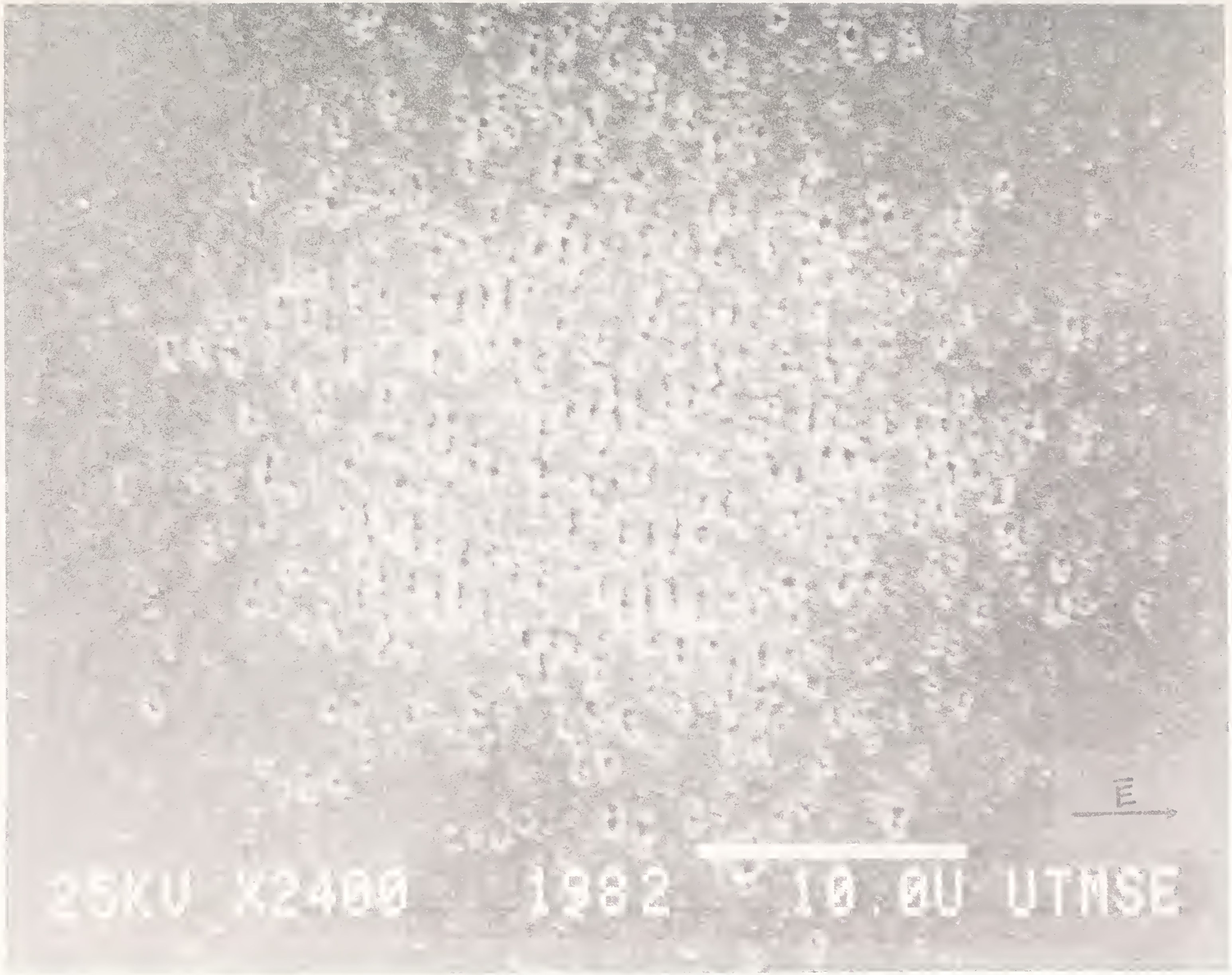

Figure 2. SEM photograph of damage showing ripple type structure caused by the formation of pit chains with a spacing of approximately 1μm.

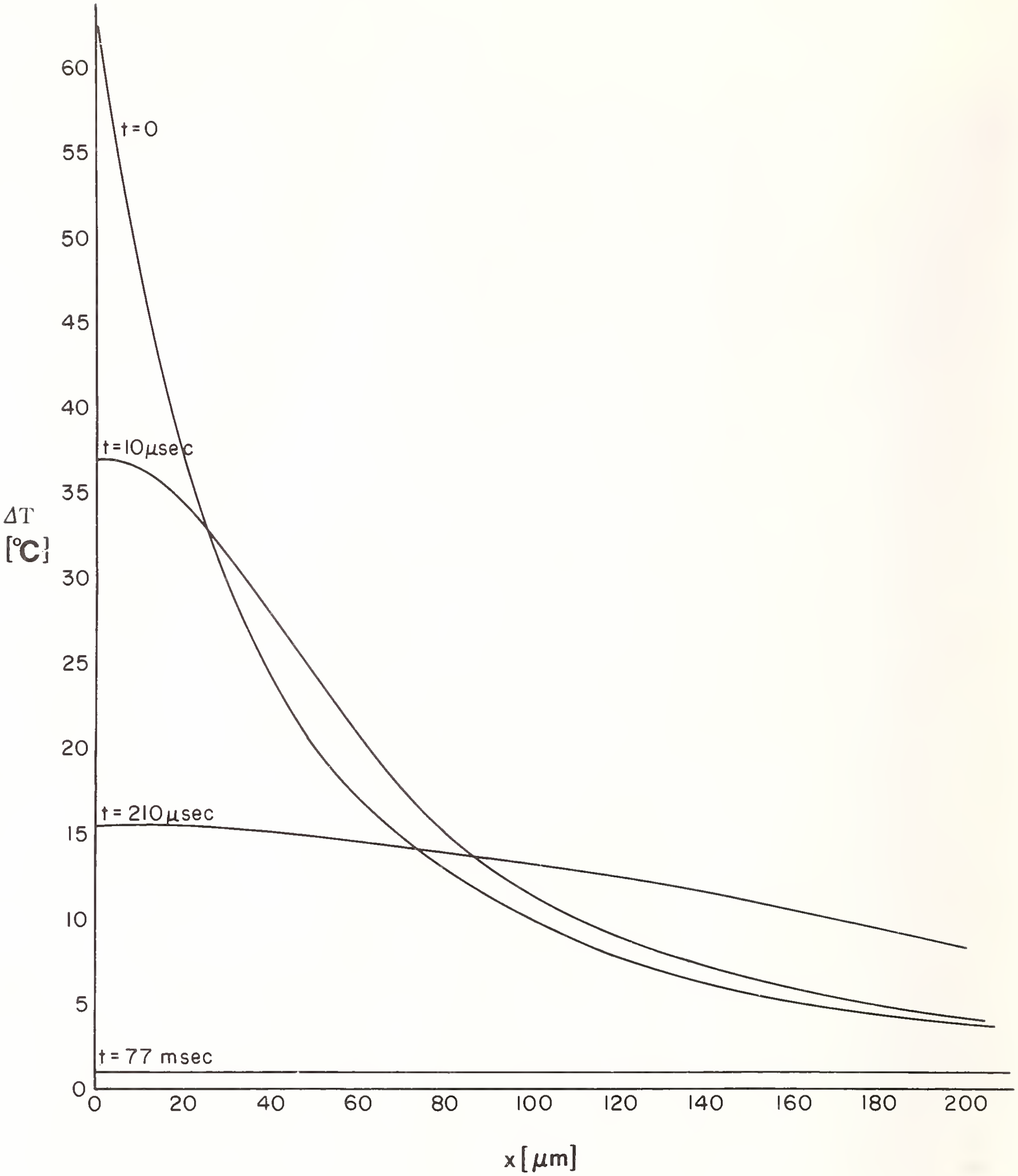

Figure 3. Calculated temperature profiles at four different times after a 4 GW/cm² 80 picosecond pulse.

In response to questions, the speaker said he was unable to specify whether the proposed long-lived excitation was an atomic state or a macroscopic effect. He further emphasized that the density of excited states ($<10^{19}$ cm^{-3}) and material temperatures (<100°C) reached in these experiments were much lower than those observed in annealing experiments which might produce 10^{21} to 10^{22} excited states/cm^3 and temperatures greater than one half the melting temperature.

On the Nature of Accumulation Effect in the Laser-Induced Damage to Optical Materials

A.A.Manenkov, G.A.Matyushin, V.S.Nechitailo,
A.M.Prokhorov and A.S.Tsaprilov

Lebedev Physical Institute of the USSR Academy of Sciences
Moscow 117924, USSR

Features of multiple-shot laser-induced damage to optical materials are analyzed. The methodology of studying the accumulation effect responsible for catastrophic damage, based on the statistical approach, is suggested and the basic characteristics of multiple-shot damage are introduced. Possible mechanisms of microdamage in materials under multiple laser irradiation are discussed. The experimental data on the laser-induced damage to optical polymer materials are presented, which demonstrate some basic properties of the accumulation effect. The ways of suppressing the accumulation effect in transparent polymers are proposed and realized which result in a considerable increase of laser damage resistance.

Key words: accumulation effect in laser-induced damage; laser-induced damage; laser-induced mechanochemical reactions; microdamage; macrodamage; optical polymers; single-shot and multiple-shot laser induced damage; statistics of damage.

1. Introduction

The resistance of optical materials to a high-power laser radiation in the multiple irradiation regime is known to be in many cases essentially lower than that at a single-shot. This fact has been established rather long ago 1, 2 , but systematic studying of multiple-shot damage has not been so far undertaken and the main attention in the problem of laser-induced damage was concentrated on the investigation of damage characteristics in the single-shot regime. However, taking into account the practical importance of the question of laser damage resistance of optical materials in the multiple-shot regime, we consider investigation of the causes responsible for the effect of multiple laser irradiation to be exclusively important.

In principle, the multiple irradiation effect may be connected with two essentially different processes: 1) the appearance of visible macrodamage at the N-th shot without any irreversible changes in all the previous shots (this process is associated with a random appearance of the so called "happy electron", resulting in an avalanche break-down 2 ; 2) accumulation of microdamages from shot to shot up to the formation of macrodamages at the N-th shot 3-7 . Note that the realization of the happy electron model in laser damage has not so far been experimentally confirmed. As to the model of gradual growth of microdamages up to macrosizes, the possibility of its realization has been demonstrated, probably for the first time, in 4, 5 , when investigating nonlinear light scattering by absorbing defects initiating laser-induced damage.

The dynamics of accumulation of irreversible changes in material under multiple laser irradiation can be studied using different techniques, i.e. by observation of the incident radiation scattering and the visible and near UV glow kinetics accompanying the damage process 4-17 , by the methods of electron spectroscopy 18 , IR-spectroscopy 19 , supersonic spectroscopy 20 and pulsed laser calorimetry 21 . As the experiments show, among these methods those of light scattering and visible and UV glow detection are the most simple and informative for studying the accumulation effect.

The accumulation effect has been so far revealed and investigated in the silicate glasses 4-7, 18-20 , alkali-halide crystals 11, 21 , ferroelectric crystals 17 , and polymers 8, 10, 12-16 . It was established that in the crystals and glasses the accumulation effect is revealed at the laser radiation intensities only several times below the single-shot damage threshold, whereas in the polymers it is observed in a much greater (up to 100 times) intensity range.

To account for the accumulation effect, different mechanisms have been suggested. For example, in silicate glasses it was interpreted as "the radiation-stimulated accumulation process of thermofluctuation decomposition of the intermolecular bonds" [22, 23], or it was associated with the accumulation of gases formed as a result of thermodestruction [24]. In the transparent polymer materials the accumulation effect was accounted for by a multi-quantum photolysis of macromolecules [25, 26], by the formation of absorbing products (like soot), due to high-temperature thermodestruction of the polymer [27-29], or by the mechano-chemical reactions initiated by thermoelastic stresses around the absorbing defects in a sample [14, 30, 31].

The analysis of the pointed works shows that despite a series of interesting experimental observations and suggested explanations, the accumulation effect hasn't yet been enough studied. Purposeful experimental and theoretical investigations are needed to elucidate its nature. In this connection we have made in the present paper an analysis of the basic regularities of the accumulation effect, their connection with the single-shot laser-induced damage characteristics and possible mechanisms of this effect. We present also some typical experimental results on the accumulation effect in organic glasses, where it is more pronounced as compared to the other optical materials.

2. The Basic Characteristics of the Accumulation Effect

The accumulation effect in the laser-induced damage is usually investigated as follows. The single-shot damage threshold for the surface or bulk of a sample is determined, the incident radiation intensity reduces to a definite level below the damage threshold, and the critical number of laser pulses N_{cr} resulting in visible macrodamage is determined. The experiments show [10], that a considerable variation of the N_{cr} values is observed (more than by a factor of 10) from site to site in the sample. This fact indicates a statistical nature of the accumulation effect and to describe it, it is apparently needed to introduce the main conceptions and characteristics similar to those used at statistical analysis of the single-shot damage. We suppose that such adequate characteristics are: an averaged over a great number of irradiated sites critical number of laser pulses $\bar{N}_{cr}(I)$, at which catastrophic macrodamages occur in the sample at fixed intensity level I; multiple-shot damage threshold I_N [16] defined as the intensity level at which a visible failure in the sample occurs at a fixed number of pulses N with a pregiven probability $W_N(I)$, the latter being determined by the ratio of the number of damaged sites in the sample to the total number of the irradiated sites at a fixed intensity I and number of laser pulses N; multiple-shot damage threshold distribution function $f(I_N)$ defined by the ratio of concentration Δn of defects in the sample having the N-shot damage thresholds in the interval $(I_N, I_N+\Delta I_N)$ to the value of interval ΔI_N. The function $f(I_N)$ makes it possible to calculate $W_N(I)$ by the formula:

$$W_N(I) = 1 - \exp[-\int_A dA \int_0^I f(I_N)\, dI_N] \qquad (I)$$

where A is the irradiated volume of surface of the sample.

In general, function $f(I_N)$ depends on the incident radiation parameters (wavelength, pulse duration, and so on) and on the sample characteristics (absorption coefficient and size of defects, thermoelastic properties of the material etc). Due to the statistical character of the damage described by the distribution function $f(I_N)$, a spot-size dependence of thresholds I_N should be observed, which is confirmed by the experimental results [15, 16]. It should be expected that at the multiple-shot damage, like at the single-shot damage, an unambiguous correspondence will be observed between the spot-size dependence of I_N and that of W_N upon I. More over, because of the same nature of the processes leading to damage at single and multiple irradiation, one can suggest that a difinite connection exists between the damage characteristics in these two cases. This connection can be expressed by the evolution of the single-shot damage threshold distribution function $f_o(I_1)$ usually introduced at statistical analysis of laser-induced damage in the single-shot irradiation regime (see review paper [33] and references threin), in the process of successive laser shots:

$$f_0(I_1) \rightarrow f_1(I_1) \rightarrow \ldots \rightarrow f_{N-1}(I_1) \equiv f(I_N)$$

or

$$f_1(I_1) = \hat{A}_1 f_0(I_1), \; \ldots, \; f_{N-1}(I_1) = \hat{A}_{N-1} f_{N-2}(I_1), \qquad (2)$$

$$f_{N-1}(I_1) = \hat{A} f_0(I_1),$$ where

$\hat{A} = \hat{A}_{N-1} \times \hat{A}_{N-2} \ldots \times \hat{A}_1$ is the evolution operator, whose form is determined by a concrete mechanism of the accumulation effect in different materials. Operator $\hat{A}$, generally being nonlinear, depends on the incident radiation parameters (wavelength, width and shape of the pulse and so on) and can be found solving an inverse problem, i.e. from the experimentally obtained dependences of the multiple-shot damage characteristics on the radiation parameters and sample characteristics.

Evolution of the distribution function may, in principle, lead to both the decreasing of the material laser damage resistance in the multiple-shot irradiation regime, compared to the single-shot damage resistance, and to its increasing (laser polishing and conditioning). In the experiments an effect of damage threshold decreasing is as a rule observed at multiple irradiation ($I_N < I_1$), though there is some opposite evidence ($I_N > I$) available in literature [34, 35].

3. Possible Mechanisms of the Accumulation Effect

The accumulation effect in laser-induced damage physically implies accumulation from shot to shot of irreversible changes in the interaction region of the sample up to the formation of visible macrodamage. Irreversible changes may occur due to photochemical, thermochemical and mechanochemical reactions and different phase transitions. The first process may be initiated both by direct laser radiation (due to multiphoton absorption), and by radiation of highly heated absorbing defects. Thermo- and mechanochemical reactions are most probably initiated in the vicinity of the absorbing defects because of the matrix heating and local thermoelastic stresses occuring in this case. Responsible for the accumulation effect in laser induced damage at multiple irradiation may naturally be only the reaction products, which absorb the incident radiation due to linear or nonlinear in intensity process.

The pointed mechanisms of irreversible changes at multiple laser irradiation were used in literature to account for the experimental results on the accumulation effect. Thus, in [25, 26] a model was discussed of gaseous product accumulation in microcavities (about 10^{-4}cm in size) as a result of multiquantum photochemical reactions, leading to destruction of polymer molecules. The formation of macrodamages in this model was considered as a result of a wedging effect of the gases. This model is not however in agreement with the available experimental data [15, 16] on laser-induced damage to polymers, indicating to the absence of any gaseous products in noticeable amount in macrodamages.

A similar "gas wedging model" of the accumulation effect was discussed to analyse the experimental data on laser-induced damage in silicate glasses [24]. According to this analysis the accumulation effect must not be observed at the laser pulse repetition rates $< 10^5$ Hz, which however contradict to many experimental observations [4-7, 18, 19, 36].

To account for the accumulation effect in silicate glasses a mechanism was also suggested in [22, 23] of thermofluctuational decomposition of intermolecular bonds, stimulated by laser radiation. But it remains unclear in this model how the electric field of the electromagnetic wave directly affects the intermolecular bonds leading to the decreasing of bond breaking activation energy.

In [27-29] a thermochemical mechanism was discussed of accumulation in polymer materials of strongly absorbing products (like soot) formed around the initial absorbing inclusions. Since the rate constants of thermochemical reactions exponentially depend on temperature T: $K_{tch} \sim \exp(-U_0/kT)$ (where U_0 is the activation energy usually being 2÷3 eV), and become noticeable only at very high temperatures, such an accumulation mechanism may be observed only in a very narrow interval of incident radiation intensities [28]. But in many materials (including silicate glasses [4-7, 18-20, 36], alkali-halide crystals [11, 21], ferroelectric crystals [17, 37], transparent polymers [8, 10, 12-16, 25-27, 29]) the microdamages occur at the incident radiation intensity several times (in the case of polymers up to 100 times) below the single-shot damage threshold, which cannot be explained on the basis of a "pure" thermochemical mechanism.

We assume that the most probable mechanism of accumulation of irreversible changes in materials at a multiple laser irradiation is associated with mechanochemical reactions [14, 30, 31] , whose rate constants $K_{mch} \sim \exp[-(U_0 - \gamma\sigma)/kT]$ essentially increase compared to K_{tch} at the expense of activation energy decreasing by elastic stresses σ (γ is the structure-sensitive factor). The latter occur in the vicinity of the absorbing defects due to their heating by laser radiation. In the process of mechanochemical reactions the excited active particles (radicals, ion-radicals, surface and solvated electrons, solitons, etc.) may appear, which absorb the laser radiation and lead to the chain reaction development and microdamage formation. As a result of such irreversible changes in the material, nonlinear absorption increases in successive laser shots, leading to catastrophic damage. Analysis of the mechanochemical mechanism of the accumulation effect [14, 30, 31] shows that it must be considerably different for optical materials with different thermoelastic properties (breaking strength, Young's modulus, expansion coefficient, etc.) and rate constants of mechanochemical reactions. In particular, one may expect an essential difference of the intensity range Δ I below the single-shot damage threshold, in which the accumulation effect may be observed. Indeed, the experiments confirm this expectation: to inorganic glasses this effect occur in a narrow range of Δ I [4-7, 18-20, 36], whereas in organic glasses (polymers) it is observed in a wide intensity range [8, 10, 12-16, 25-27, 29] .

Such a peculiarity of the polymer materials, compared to the other transparent dielectrics allows to study on this class of materials the main characteristics of the accumulation effect. In the next section we shall present some experimental data on the accumulation effect in the laser-induced damage of polymethylmethacrylate - a typical representative of organic glasses.

4. The Accumulation Effect in Transparent Polymers

The accumulation effect in laser-induced damage to polymer materials has been revealed and studied in many works [1, 2, 8, 10, 12-16, 25, 27-31]. Here we present some new results obtained for polymethylmethacrylate (PMMA) and modified polymethacrylate (MPMMA), widely used in conventional and laser optics, in particular for creation of solid-state dye lasers [38], bleachable filters [39], and optical elements for laser ophtalmology devices [40].

In the investigated specially purified samples [12], a pronounced accumulation effect has been observed in a wide intensity range:the 1-shot to N-shot damage thresholds ratio I_1/I_N is equal to 3 and 30 for MPMMA and PMMA, respectively (see fig. 1). The intensity dependence of $\overline{N}_{cr}$ has an asymptotic character: $\overline{N}_{cr} \rightarrow \infty$, at the intensity approaching some minimum value I_{min}, which is as much as $0.03 I_1$ for PMMA and $0.3 I_1$ for MPMMA.

We have studied the dynamics of the accumulation process by observing the incident laser radiation scattering and the glow in visible and near UV spectrum range, accompanying the damage. Fig. 2 shows the dependence of the light scattering intensity at $\lambda = 0.69 \mu m$ on the number of irradiation pulses N of a fixed site in the MPMMA sample at $I = 0.5 I_1''$. It is clearly seen that the scattering intensity monotonously increases from shot to shot up to N = 20, at which a sharp increasing of the scattering intensity is observed and a catastrophic damage occurs. A similar behaviour was observed for the dependence of glow intensity in the visible and UV spectrum range on the number of laser pulses ($\lambda = 1.06 \mu m$, $\tau = 20$ ns) with intensity $I = 0.5 I_1'$ irradiating a fixed site in the bulk of the PMMA sample (see fig. 3). It was observed in these experiments that the amplitude and the temporal shape of the glow pulses undergo essential fluctuations. This indicates a random character of the laser-induced damage process.

We have also investigated statistical properties of the laser-induced damage to polymers by studying the spot-size dependences of the damagethresholds I_1 and I_N at a fixed number of shots (N = 200) and probabilities W_1 and W_N (both equal to 0.5) for 1-shot and N-shot damage as well as the dependences W_1 and W_N on the incident radiation intensity. Fig. 4 shows these dependences for the PMMA sample irradiated by YAG.Nd laser pulses at $\lambda = 1.06 \mu m$. It is seen that the 1-shot damage threshold I_1 has a stronger dependence on the focusing lens focal spot diameter d_k, compared to that for N-shot damage threshold I_N. Such a behaviour of spot-size dependences of I_1 and I_N correlates with the intensity dependences of damage probabilities W_1 and W_N. Indeed, a more gently sloping dependence $W_1(I)$ corresponds to a steeper dependence $I_1(d_k)$ and, vice versa, a weak spot-size dependence $I_N(d_k)$ corresponds to a steeper dependence $W_N(I)$. These qualitative relationships were confirmed by a detailed analysis of the obtained experimental data on the basis of a statistical model of laser-induced damage, described by formula (I). In particular, it follows from this analysis that at successive laser irradiations the initial distribution function $f_0(I_1)$ of defects is transformed into the functions $f_{N-1}(I_1)$ having a more narrow distribution compared to $f_0(I_1)$ and shifted to smaller values of damage threshold I_1. Determination of a concrete form of these functions on the basis of experimental data will make it possible to clear up the form of the evolution operator $\hat{A}$, which, as it follows from section 2, is the basic characteristic of the accumulation effect.

Besides the statistical properties described above of the accumulation effect, we have also studied the dependence of the N-shot damage thresholds I_N on the laser radiation parameters (pulse width τ and wavelength λ) and physico-mechanical characteristics of the samples (temperature, visco-elastic parameters of the material, content of low-molecular-weight additives).

These studies have shown that, similar to the case of single-shot damage [41], the following relationship takes place in the multiple-shot irradiation regime: $I_N = B\lambda/\tau$ for $\tau = 3 \div 50$ ns and $\lambda = 1.06 \div 0.337 \mu m$ with B = const.

The temperature rise of the PMMA and MPMMA samples up to the glass-transition temperature and addition of plasticizers into polymers leads to a considerable (more than by a factor of 10) increase of their laser damage resistance in the multiple-irradiation regime, whereas both these factors relatively weakly affect the single-shot damage threshold [10, 14, 16, 42]. It was observed that the effect of the laser damage resistance increasing in multiple-shot irradiation regime essentially depends on the type of plasticizer [16] and its mole concentration. These results indicate that properly chosen additives in the polymer are able to suppress the mechnochemical reactions due to quenching of the excited active particles arising in the vicinity of the absorbing defects from thermoelastic stresses [14,30,31]. A similar suppression effect in the laser-induced microdamage accumulation can probably be attained in other optical materials by means of their structural modification resulting in the change of thermoelastic properties and decreasing of the rate constants of mechanochemical reactions.

5. Conclusion

Analysis of the laser-induced damage to optical materials in the multiple-irradiation regime shows that decreasing of their laser damage resistance in a series of successive shots is associated with accumulation of irreversible changes in the material. In other words, a catastrophic damage at the N-th shot is a result of accumulation of microdamages appearing at the previous N-1 shots.

In the present work we have developed the methodology of studying of the accumulation effect in the laser-induced damage, based on the statistical approach, and introduced the basic characteristics of multiple-irradiation damage: critical number of pulses $N_{cr}(I)$, the N-shot damage threshold I_N, N-shot probability for damage $W_N(I)$, N-shot damage threshold distribution function $f(I_N)$, evolution operator $\hat{A}$ of the single-shot damage threshold distribution function in a series of successive laser pulses. This methodology and the introduced characteristics allow to investigate purposefully the regularities of the accumulation effect.

The experiments conducted on laser-induced damage to optical polymer materials made it possible to establish specific properties of multiple-irradiation damage (weakening of spot-size dependence of I_N compared to that of I_1, narrowing of intensity dependence of W_N compared to that of $W_1(I)$), indicating a statistical character of the accumulation effect. Among the mechanisms of accumulation effect considered, the most probable is that associated with the irreversible changes in the material due to mechanochemical reactions under multiple laser irradiation.

The investigation of laser-induced damage to polymers in the multiple-irradiation regime permitted to find efficient methods of suppressing the accumulation effect (by variation of molecular-mass distribution of macromolecules and by introduction of additives quenching the excited active particles and preventing the development of chain mechanochemical reactions). One can expect that such methods can be efficient for suppression of the accumulation effect in the laser-induced damage to other optical materials.

6. References

1 Ashkinadze, B.M.; Vladimirov, V.I.; Likhachev, V.A.; Ryvkin, S.M.; Salmanov, V.M.; Yaroshetsky, I.D. JETP, 50, 1187, 1966.

2 Bass, M.; Barrett, H. JEEE J.Quant.Electr. QE-8, 338, 1972.

3 Likhachev,V.A.; Ryvkin S.M.; Salmanov, V.M.; Yaroshetsky, I.D. Solid State Physics, 8, 3432, 1966.

4 Nechitailo, V.S. Ph.degree dissertation, FIAN USSR, Moscow, 1974.

5 Danileiko, Yu.K.; Manenkov, A.A.; Nechitailo, V.S. Soviet Quantum Electr. 3, 538, 1976.

6 Danileiko, Yu.K.; Manenkov, A.A.; Nechitailo, V.S. FIAN Proceedings, 101, 31, 1978.

7. Danileiko, Yu.K.; Manenkov, A.A.; Nechitailo, V.S. Laser Induced Damage in Optical Materials. NBS Spec.Publ. 620, 369, 1980.

8 Aldoshin, M.I.; Gerasimov, B.G.; Mizin, V.M.; Nechitailo, V.S. Abstracts of the YIII All-Union Conference on Coherent and Nonlinear Optics, Tbilisi, Metsnieraba,I, 136, 1976.

9. Danileiko, Yu.K.; Manenkov, A.A.; Nechitailo, V.S. Soviet Quantum Electr. 5, 194, 1978.

10 Aldoshin, M.I.; Gerasimov, B.G.; Manenkov, A.A.; Nechitailo, V.S. Soviet Quantum Electr. 6, 1866, 1979.

11 Krutyakov, V.P.; Smirnov, V.N. JTP 49, 2647, 1979.

12 Manenkov, A.A.; Nechitailo, V.S. Soviet Quantum Electr. 7, 616, 1980.

13 Manenkov, A.A.; Nechitailo, V.S.; Tsaprilov, A.S. Izvestiya AN SSSR, Ser. physicheskaya, 44, 1771, 1980.

14 Dyumaev, K.M., Manenkov, A.A., Maslyukov, A.P.; Matyushin, G.A.; Nechitailo, V.S.; Prokhorov, A.M. Laser Induced Damage in Optical Materials. NBS Spec. Publ., 1981.
Dyumaev, K.M.; Manenkov, A.A.; Maslyukov, A.P.; Matyushin, G.A.; Nechitailo, V.S. Soviet Quantum Electr. 10, 3, 1983.

15 Manenkov, A.A.; Nechitailo, V.S.; Tsaprilov, A.S. Izvestiya AN SSSR, Ser.physicheskaya, 46, 1200, 1982.

16 Dyumaev, K.M.; Manenkov, A.A.; Maslyukov, A.P.; Matyushin, G.A.; Nechitailo, V.S.; Tsaprilov, A.S. Soviet Quantum Electr., 9, 1318, 1982.

17 Belyaev, N.N.; Bredichin, V.I.; Rubakha, V.I.; Freidman, G.I. JETP 83, 1065, 1982.

18 Tikhomirov, G.P.; Turovskaya, T.S. OMP, No5, 65, 1977.

19 Eron'ko, S.B.; Zhurkov,S.N.; Chmel, A.E. Solid State Physics 20, 3570, 1978.

20 Kogtina, I.G.; Kinber, B.E. Soviet Quantum Electr. 7, 2427, 1980.

21 Wu, S.T.; Bass, M. Appl.Phys.Lett., 39, 948, 1981.

22 Zhurkov, S.N.; Eron'ko, S.B.; Chmel, A.E. Solid State Phys. 22, 3040, 1980.

23 Zhurkov, S.N.; Eron'ko, S.B.; Chmel, A.E. Solid State Phys. 24, 733, 1982.

24 Novikov, N.P.; Novikova, N.N.; UFJ 27, 516, 1982.

25 Agranat, M.B.; Krasyuk, I.K.; Novikov, N.P.; Perminov, V.P.; Yudin, Yu.I.; Yampol'sky, P.A. JETP 60, 1748, 1971.

26.Novikov, N.P. UFJ 26, 1676, 1981.

27 Butenin, A.B.; Kogan, B.Ya. Soviet Quantum Electr. 3, 1136, 1976.

28 Liberman, M.A.; Tribelsky, I.I. JETP 74, 194, 1978.

29 Kovalev, A.A.; Makshantsev, B.I.; Pilipetsky, N.F.; Sidorin, Yu.V.; Stonik, O.G Soviet Quantum Electr. 7, 1287, 1980.

30 Manenkov, A.A.; Nechitailo, V.S.; Tsaprilov, A.S. Soviet Quantum Electr. 8, 838, 1981.

31 Nechtailo, V.S. Izvestiya AN SSSR, Ser. physicheskaya 46, 1194, 1982.

32 Manenkov, A.A.; Matyushin, G.A.; Nechitailo, V.S.; Prokhorov, A.M.; Tsaprilov, A.S. Soviet Quantum Electr. 10, No6, 1983.

33 Danileiko, Yu.K. Izvestiya AN SSSR, Ser. physicheskaya, 46, 1119 (1982).

34 Wang, V., Giuliano, C.R.; Garsia, B. Laser Induced Damage in Optical Materials. NBS Spec. Publ. 435, 216, 1975.

35 Bass, M.; Leung, K.M. JEEE. J.Quant.Electr. QE-12, 82, 1976.

36 Baliskas, S.K., Maldutis, E.K. Soviet Quantum Electr. 8, 902, 1981.

37 Zverev, G.M., Naumov, V.S.; Pashkov V.A.; Sidoryuk, O.E.; Skvortsov, L.A. Izvestiya AN SSSR, Ser.physicheskaya, 46, 1135, 1982.

38 Gromov, D.A.; Dyumaev, K.M.; Manenkov, A.A.; Maslyukov, A.P. Matyushin, G.A.; Nechitailo, V.S.; Prokhorov, A.M. Izvestiya AN SSSR, Ser. physicheskaya 46, 1956, 1982.

39 Gromov, D.A.; Dyumaev, K.M.; Manenkov, A.A.; Maslyukov, A.P.; Matyushin, G.A.; Nechitailo, V.S.; Prokhorov, A.M. Izvestiya AN SSSR, Ser.physicheskaya 46, 1959, 1982.

40 Akopian, V.S.; Berlin, A.A.; Vinogradov, A.P.; Gromov, D.A.; Danileiko, Yu.K.; Dyumaev, K.M.; Krasnov, M.M.; Krupnov, G.V.; Maslyukov, A.P.; Matyushin, G.A.; Naumidi, A.P.; Nechitailo, V.S.; Prokhorov, A.M. Izvestiya AN SSSR, ser.physicheskaya, 46, 1996, 1982.

41 Aldoshin, M.I.; Manenkov, A.A.; Nechitailo, V.S.; Pogonin, V.I. JTP 49, 2498, 1979.

42 Aldoshin, M.I.; Gerasimov, V.G.; Menenkov, A.A.; Maslyukov, A.P.; Nechitailo, V.S.; Ponomarenko, E,P. JTP 49, 2496, 1979.

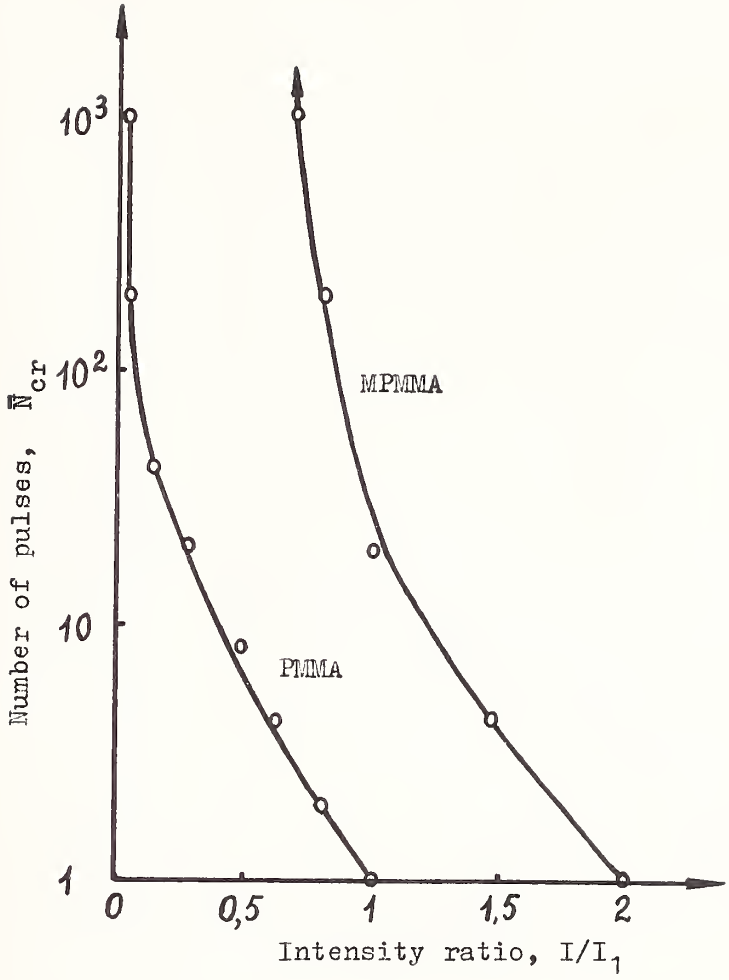

Figure 1. Mean critical number of pulses $\bar{N}_{cr}$ at which the damage in organic glasses PMMA and MPMMA occurs, versus the intensity I of incident radiation at the wavelength $\lambda = 0.69 \mu m$. I_1 is the single-shot damage threshold.

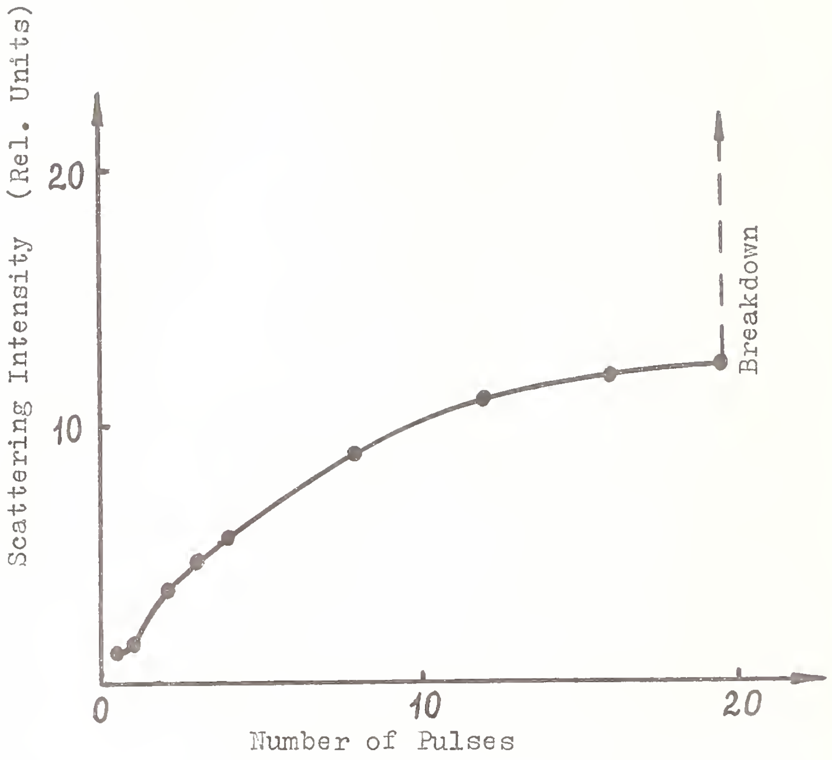

Figure 2. Scattering intensity of ruby-laser radiation versus the number of pulses at the multiple-shot damage in MPMMA at the incident intensity $I = 0.5I_1$.

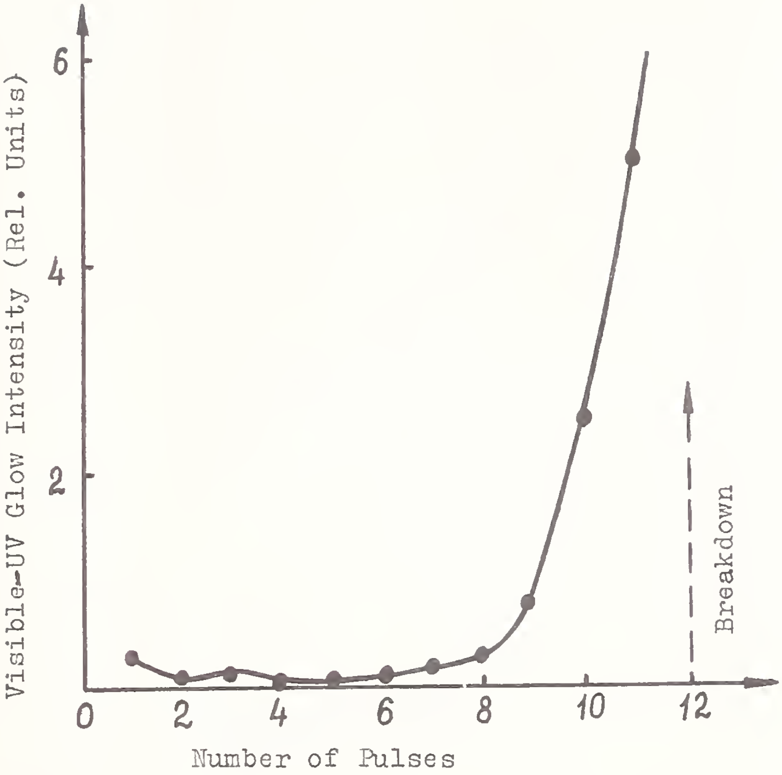

Figure 3. Intensity of the visible-UV glow accompanying the laser-induced damage in PMMA versus the number of pulses at 1.06 μm irradiation at the incident intensity $I = 0.5I_1$.

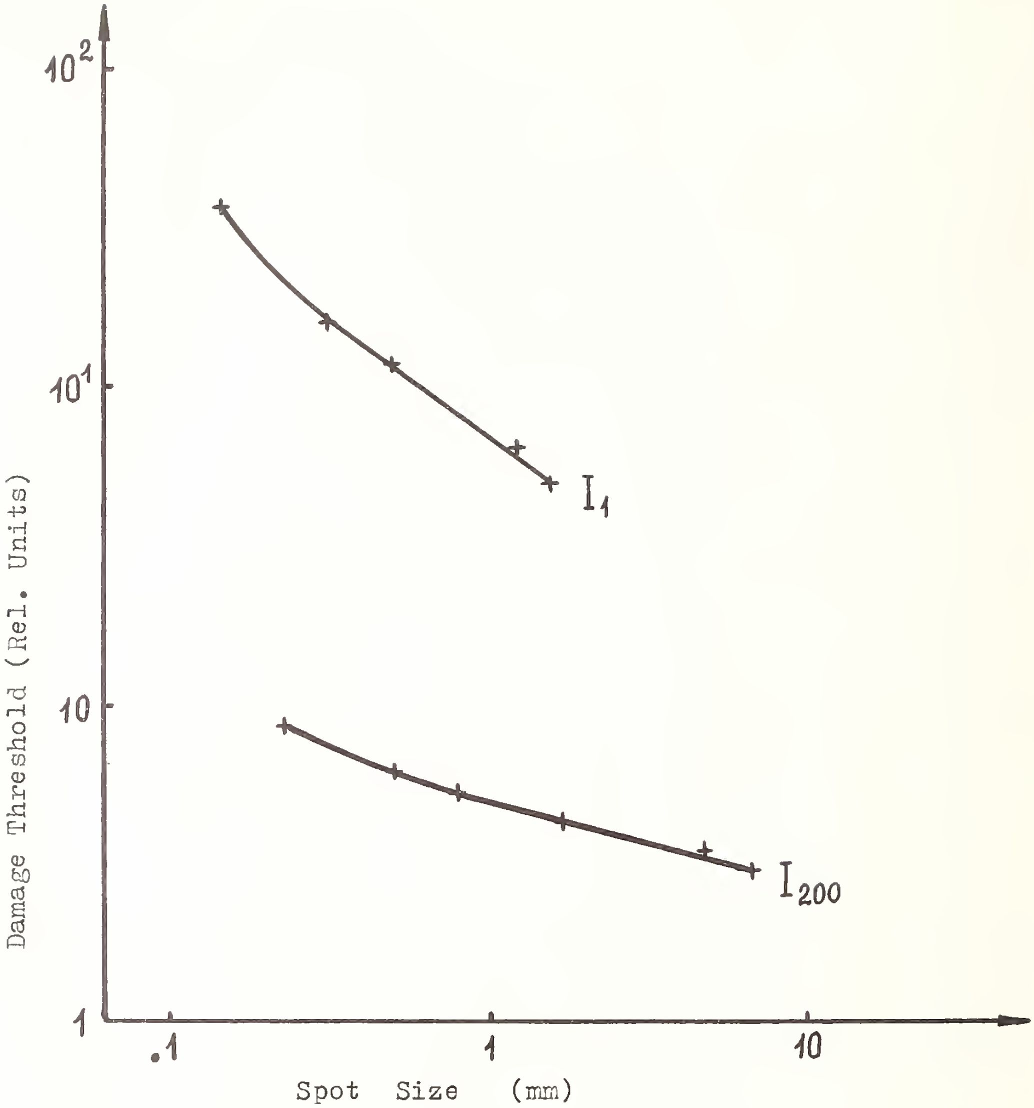

Figure 4. Spot-size dependence of the 1-shot and 200-shot damage thresholds (I_1 and I_{200} respectively) of PMMA at 1.06 μm irradiation.

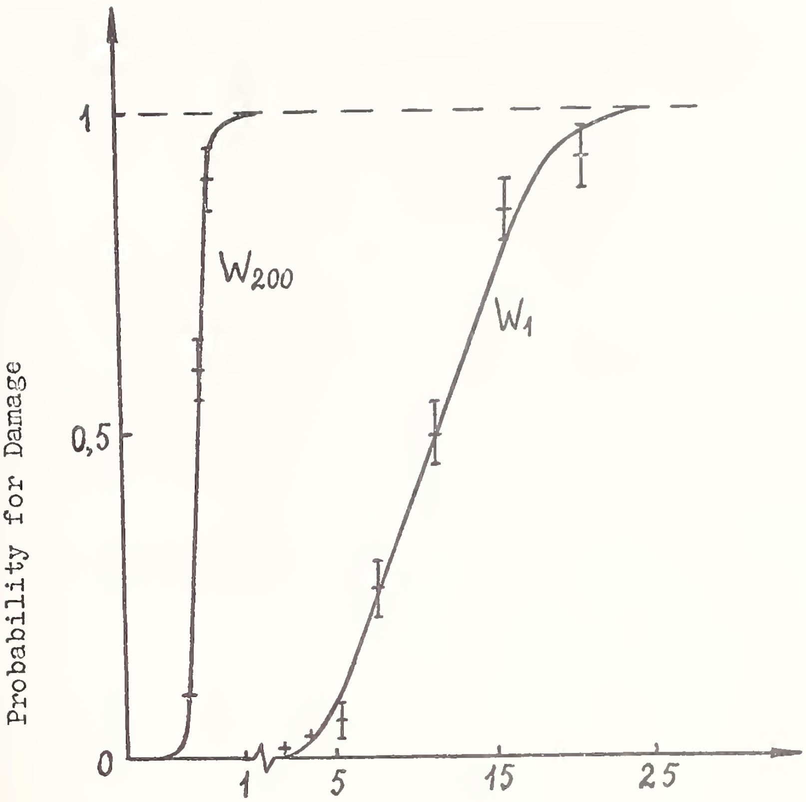

Intensity (Rel. Units)

Figure 5. Probabilities for single-and multiple-shot damage (W_1 and W_{200}, respectively) in PMMA versus the incident radiation intensity at the laser wavelength 1.06µm and the beam diameter 0.5 mm.

The speaker was asked if he had laser conditioned a site with repetitive low fluence shots and then tested to see if damage accumulated at that site during a set of repeated shots, as it did no nonconditioned sites. The speaker had not done this experiment. He further stated that plastics impregnated with dyes behave basically as undoped plastics provided the dyes were stabilize by adding an unspecified chemical. In comments from the audience, similar accumulation of damage was reported in plastics and in lithium niobate, and laser conditioning of KDP was mentioned. The speaker was asked whether the reports of damage accumulation arose from the inability to detect the first small damage induced, and agreed that this was the case and said that the lowest fluence to cause such micro damage was the real threshold for physical damage.

DISPERSION OF THE REFRACTIVE INDEX NEAR THE ABSORPTION EDGE IN COMPOUND SEMICONDUCTORS

B. Jensen, A. Torabi

Boston University
Boston, Massachusetts 02215

An analytical expression for the real part of the refractive index n near the fundamental absorption edge has been calculated for a semiconductor in terms of experimentally known quantities. It is derived from a quantum mechanical calculation of the complex dielectric constant which assumes the band structure of the Kane Theory. The expression obtained is a function of band gap energy, effective electron and heavy hole masses, the spin orbit splitting energy, the lattice constant, and the carrier concentration for n-type or p-type materials. The refractive index is given as a function of frequency and the basic material parameters listed above with no adjustable constants. Dispersion near the fundamental absorption edge, which has been observed experimentally for a number of III-V and II-VI compounds, is predicted and its calculation enabled. Comparison of theory with available experimental data is given.

Key words: Optical constants; optical materials; refractive index; semiconductors; wavelength dependence.

1. Introduction

An understanding of the spectral dependence of the refractive index of a semiconductor in the region near the fundamental absorption edge is a subject of considerable importance in integrated optics, as the refractive index plays a fundamental role in the guiding, coupling, and modulation of radiation.(1) Experimental data on the spectral dependence of refractive indices are available for a number of compounds.(2)-(7) However, there have been few theoretical analyses of the subject. The spectral dependence of n can be calculated using the general theory of dispersion and the Kramers-Kronig relationship, but this requires a knowledge of the complete spectrum of the imaginary part of the dielectric constant e_2. In practice, application of this method leads ultimately to the introduction of parameters whose relation to the experimentally available quantities, such as band gap energy, effective masses, and free carrier concentration, is more or less vague.(8)-(9) The spectral dependence of the refractive index is usually described by formal empirical relationships, involving several adjustable parameters.(10)-(11) It is known experimentally that at photon energies small compared with the band gap energy, the complex dielectric constant, from which the complex refractive index is derived, is given by the quasiclassical result of the Drude theory.(12)-(15) At frequencies close to the fundamental absorption edge however, the Drude theory result for the imaginary part of the complex refractive index is know to fail.(16)-(18) The experimentally observed result can be accounted for by a quantum calculation which reduces to the classical result at low frequencies.(19)-(21)

An analytical rexpression for the real part of the refractive index near the fundamental absorption edge has been calculated for a compound semiconductor in terms of experimentally known quantities.(22)-(24) It is derived from a quantum mechanical calculation of the complex dielectric constant(25) which assumes the band structure of the Kane theory.(26) We present theoretical results and give a comparison with experimental results for a number of compounds in Section III. A detailed derivation is given elsewhere.(22), (24)

2. Results

Near the fundamental absorption edge, the real part of the refractive index n is found as a function of the experimental parameters for a given semiconductor which are listed in Table I. The independent variable z is defined in terms of the photon energy $\hbar w$ in units of the band gap energy G as

$$z = \left(1 - (\hbar w/G) \right)^{\frac{1}{2}} \tag{1}$$

We define

$$n(0,0) = \left(1 + 2c_o Y_B \right)^{\frac{1}{2}} = \text{index of refraction at the absorption edge } (z = 0) \text{ for a pure material with zero carrier concentration.} \tag{2}$$

In (2), the constant c_o is given in terms of experimental quantities, specifically band gap energy, spin orbit splitting energy, and effective electron and heavy hole masses, in Table I. The quantity Y_B is a function of the lattice constant a (Å) of the form (24)

$$Y_B = m(a_o - a) = \frac{n^2(0,0) - 1}{2c_o} \tag{3}$$

where

$$m = \begin{cases} (3.04 \pm 0.08) \ \text{Å}^{-1} , & \text{III-V compounds} \\ (.346 \pm .020) \ \text{Å}^{-1} , & \text{II-VI compounds} \end{cases} \tag{4}$$

$$a_o = \begin{cases} (7.49 \pm 0.04) \ \text{Å} , & \text{III-V compounds} \\ (17.37 \pm 0.88) \ \text{Å} , & \text{II-VI compounds} \end{cases} \tag{5}$$

The real part of the refractive index is given as a function of frequency and carrier concentration, or z and y_F, near the fundamental absorption edge by (22), (24)

$$n^2(z,y_F) = 1 + 2c_o \left[(Y_B - y_F) - z\left(\tan^{-1}(Y_B/z) - \tan^{-1}(y_F/z) \right) \right] \tag{6}$$

where

$$y_F = 2 \left(n_e/N_v\right)^{1/3} , \quad \text{degenerate n-type materials} \tag{7}$$

$$y_F = \bar{\lambda}_r k_h , \quad \text{degenerate p-type materials} \tag{8}$$

where n_e is the free electron concentration for n-type materials and p is the free hole concentration for p-type materials and

$$\bar{\lambda}_r = (m_n/m_r)^{\frac{1}{2}} \quad (\bar{\lambda}_c/2) \tag{9}$$

$$k_h = (3 \pi^2 p)^{1/3} \tag{10}$$

In (7) through (10), N_v and m_r are functions of band gap energy and effective masses defined in Table I and m_n is the effective electron mass at the band edge. The concentration dependence of n occurs through the term y_F. Equation (6) applies to degenerate materials with non-zero carrier concentration where the Fermi level lies within the conduction band (for n-type materials) or the Valence band (for p-type materials). The expression for a pure material with negligable free carrier concentration is obtained from (6) by setting $y_F = 0$, and non-degenerate materials are discussed in Reference (22). Equation (6) contains no adjustable constants. If carrier concentration, band gap energy, lattice constant, effective electron and effective heavy hole mass, and spin orbit splitting energy are known, exact numerical results can be calculated from (6). Table II gives the experimental values of these material parameters and values of theoretical quantities which are functions of experimental parameters for GaAs, InP, InSb, CdTe, and ZnTe. We use the small spin orbit splitting limit if the spin orbit splitting energy is less than or equal to the band gap energy, and the large spin orbit splitting limit if the spin orbit splitting energy is greater than the band gap energy, as the calculation has been performed in these two limits only.

An attempt has been made to compare theory with experimental data from various sources. In Table III, theoretical results calculated as described above and experimental results are given for ZnTe. In Table IV, theoretical results calculated using the approximation discussed in Ref. (22), which involves replacing $\tan^{-1}(Y_B/z)$ by $\pi/2$, are given along with experimental results from sources listed in the References. Since Y_B ranges from around 4 to 6, while $z << 1$, the approximation is permissible for z sufficiently small. Theoretical results (solid lines) are plotted along with experimental results in Figures 1 and 5. Comparison for each of the five compounds considered is discussed in detail in the Figure Captions. It can be seen that overall, agreement between theory and experiment is quite reasonable, considering that no adjustable parameters are involved if Y_B is determined from the lattice constant. These results should be useful in technological applications, as they give a method of calculating the refractive index as a function of frequency in terms of measurable parameters for a class of important semiconductors.

This research was supported by the Department of Energy under contract # DE-AC02-79ER10444.A000.

References

[1] E. Garmire in "Integrated Optics," T. Tamir, Ed., Springer-Verlag (1979). pp 243.

[2] D.F.T. Marple, J. Appl. Phys. 35, 1241 (1964).

[3] H.C. Casey, D.D. Sell, M.B. Panish, Appl. Phys. Lett. 24, 63 (1974).

[4] D.D. Sell, H.C. Casey, K.W. Wecht, J. Appl. Phys. 45, 2650 (1974).

[5] D.F.T. Marple, J. Appl. Phys. 35, 539 (1964).

[6] E.G. Valyashko, Karin Gerrmann, Sov. Phys.-Semiconductors 1, 904 (1968).

[7] G.D. Pettit, W.J. Turner, J. Appl. Phys. 36, 2081 (1965).

[8] A.N. Pikhtin, A.D. Yas'kov, Sov. Phys.-Semiconductors 12, 622 (1978).

[9] F. Stern, Phys. Rev. 133, A1653 (1964).

[10] T. Tagaki, Japan. J. Appl. Phys. 21, L167 (1982).

[11] V. Gopal, Infrared Phys. 22, 255 (1982).

[12] J.K. Kung, W.G. Spitzer, J. Electrochemical Soc. 121, 1482 (1974).

[13] R.N. Zitter, K. As'Saadi, J. Phys. Chem. Solids 35, 1593 (1974).

[14] R.T. Holm, J.W. Gibson, E.D. Palik, J. Appl. Phys. 48, 212 (1977).

[15] S. Perkowitz, J. Phys. Chem. Solids 32, 2267 (1971).

[16] W.G. Spitzer, J.M. Whelan, Phys. Rev. 114, 59 (1959).

[17] W.P. Dumke, M.R. Lorenz, G.D. Pettit, Phys. Rev. B 1, 4668 (1970).

[18] R.M. Culpepper, J.R. Dixon, J. Optical Soc. Amer. 58, 96 (1968).

[19] E. Haga, H. Kimura, J. Phys. Soc. Japan, 18, 777 (1963); 19, 471 (1964); 19, 658 (1964).

[20] B. Jensen, Ann. Phys. 80, 284 (1973); J. Phys. Chem. Solids 34, 2235 (1973).

[21] B. Jensen, Ann. Phys. 95, 229 (1975).

[22] B. Jensen, A. Torabi, IEEE J. Quantum Electron. March (1983). To be published.

[23] B. Jensen, A. Torabi, J. Appl. Phys. April (1983). To be published.

[24] B. Jensen, A. Torabi, IEEE J. Quantum. Electron. May (1983). To be published.

[25] B. Jensen, IEEE J. Quantum Electron Q-18, 1361 (1982).

[26] E.O. Kane, J. Phys. Chem. Solids 1, 249 (1957).

[27] J.I. Pankove, in "Optical Processes in Semiconductors," Prentice-Hall, Englewood Cliffs, 1971. pp 412-413.

[28] D. Hennig, B. Strehlow, Phys. Status Solidi 107, 283 (1981).

Table 1.

Experimental parameters and theoretical quantities which are functions of experimental parameters.

G = band gap energy

m_n = electron effective mass at the band edge

m_p = heavy hole effective mass at the band edge

Δ = spin orbit splitting energy

a = lattice constant $(\overset{\circ}{A})$

n_e = free electron concentration for n-type materials

p = free hole concentration for p-type materials

$Y_B = m(a_o - a)$

$Y_B \cong 3.04(7.49 - a)$, III-V compounds

$Y_B \cong .346(17.37 - a)$, II-VI compounds

$$\eta = \begin{cases} 2/3 \;, & \Delta/G <<1, \quad \text{small spin orbit splitting unit} \\ 3/2 \;, & \Delta/G <<1, \quad \text{large spin orbit splitting unit} \end{cases}$$

$w_g = G/\hbar$ = frequency at fundamental absorption edge

$m_r = m_n m_p/(m_n + m_p)$ = reduced mass

$\alpha_o = (G/2m_n c^2)^{1/2}$

$\bar{\lambda}_c = \hbar/m_n \alpha_o c$

$\bar{\lambda}_r = (m_n/m_r)^{1/2} \; \bar{\lambda}_c/2$

$\dfrac{1}{V_c} = 2/\pi^2 \; \bar{\lambda}_c^3$

$N_v = (4/3) \; 1/V_c$

$N_v^* = N_v \; (m_r/m_n)^{3/2}$

$w_v^2 = 4 \; \pi e^2 N_v^*/m_n$

$k_h = (3 \; \pi^2 p)^{1/3}$

$c_o = (3/2) \; \eta \; (w_v^2/w_g^2)$

$n(0,0) = (1 + 2c_o Y_B)^{1/2}$ = index of refraction at absorption edge for a pure material ($n_e = p = 0$)

Table 2.

Values of experimental parameters and theoretical quantities which are functions of experimental parameters for various semiconducting compounds.

T = 300°K	GaAs	InP	InSb	CdTe	ZnTe
G(eV)	1.43	1.35	0.18	1.50	2.28
m_n/m	0.07	0.07	0.0133	0.11	0.15
m_p/m	0.50	0.40	0.18	0.35	0.663
a(Å)	5.653	5.869	6.479	6.477	6.101
Y_B	5.554	4.966	3.063	3.779	3.889
η	2/3	2/3	3/2	2/3	2/3
λ_c(Å)	12.4	12.7	80.0	9.63	6.68
$N_v^*(cm^{-3})$	1.18×10^{20}	1.03×10^{19}	4.76×10^{17}	2.01×10^{20}	6.66×10^{20}
$w_g(sec^{-1})$	2.17×10^{15}	1.95×10^{15}	2.73×10^{14}	2.28×10^{15}	3.47×10^{15}
$w_v(sec^{-1})$	2.31×10^{15}	2.16×10^{15}	3.37×10^{14}	2.41×10^{15}	3.76×10^{15}
c_o	1.133	1.114	3.422	1.118	1.175

Experimental parameters are taken from Reference (27) with the exception of m_p/m = .663 for ZnTe. A value of m_p/m = .6 for ZnTe is reported in Reference (28). There is a considerable amount of variation in reported values of m_p for many compounds, as discussed in Reference (23).

Table 3. Refractive Index of ZnTe

λ(um)	n(experiment)	n(theory)*	n(theory)$^{++}$
0.589	3.05	3.0247	3.042
0.620	3.00	2.9852	3.000
0.830	2.84	2.8614	2.863
1.240	2.78	2.7799	2.770
2.060	2.71	2.7260	2.710

* Calculated using Y_B = 3.982 ± 0.022 with m_p = 0.6m fixed. The variance is 3.99×10^{-4}.

++ Calculated using the approximation discussed in Reference (22), with m_p, treated as an adjustable parameter, found to be m_p = 0.663 ± 0.1414 compared with a reported experimental value of m_p = 0.6m.(28) The index of refraction at the absorption edge is n(0) = 3.2016 ± 0.0187 and the variance is 2.38×10^{-4}.

Table 4.

Sample	Wavelength (um)	Energy (eV)	n(exp)	n(theory)**
GaAs	1.89	0.654	3.346	3.334
	1.55	0.800	3.375	3.370
	1.37	0.900	3.400	3.396
	1.24	1.000	3.424	3.425
	1.12	1.10	3.453	3.458
	1.03	1.20	3.485	3.496
	0.95	1.30	3.540	3.543
	0.91	1.35	3.570	3.573
InP	2.06	0.60	3.126	3.105
	1.77	0.70	3.146	3.131
	1.55	0.80	3.166	3.159
	1.37	0.90	3.180	3.190
	1.24	1.00	3.220	3.224
	1.12	1.10	3.253	3.264
	1.03	1.20	3.300	3.312
	0.99	1.25	3.333	3.342
InSb	8.00	0.15	4.000	4.047
	9.00	0.13	3.930	3.961
	10.00	0.12	3.883	3.897
	11.00	0.11	3.866	3.846
	12.00	0.10	3.816	3.806
	13.00	0.09	3.800	3.773
	14.00	0.08	3.766	3.746
CdTe	0.903	1.37	2.91	2.916
	1.000	1.24	2.84	2.845
	1.10	1.12	2.81	2.798
ZnTe	0.589	2.10	3.05	3.042
	0.620	2.00	3.00	3.000
	0.830	1.49	2.84	2.863
	1.24	1.00	2.78	2.770
	2.06	0.60	2.71	2.710

** Theoretical values are calculated using the approximation discussed in Reference (22), which involves replacing $\tan^{-1}(y_B/z)$ by $\pi/2$ in Eq. (6).

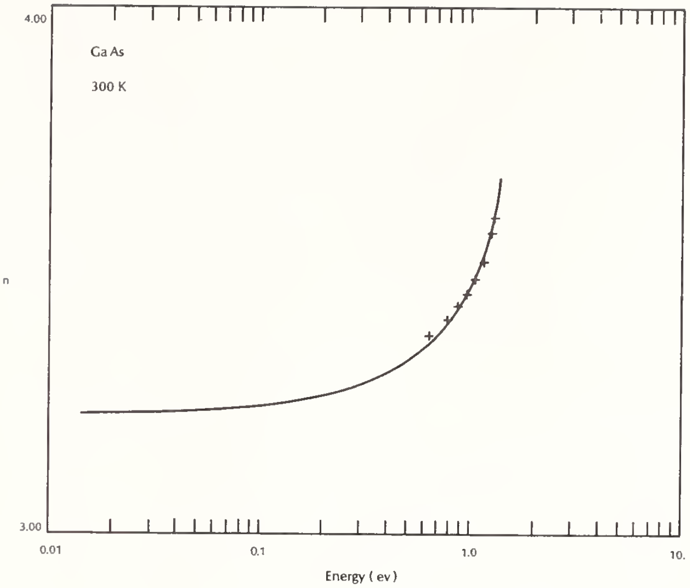

Figure 1. Theoretical results for n for GaAs with a carrier concentration of $n_e = 6\times10^{16}$ cm^{-3} (solid line) plotted together with experimental results for a sample of the same carrier concentration obtained from Reference (2) (+++++).

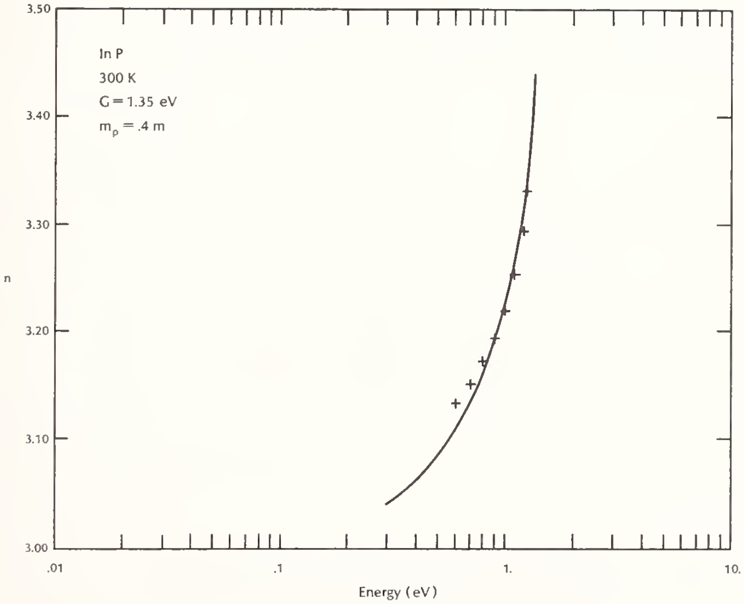

Figure 2. Theoretical results for InP for a sample with carrier concentration $n_e = 5\times10^{16}$ cm^{-3} (solid line) plotted along with experimental results on a sample of the same carrier concentration obtained from Reference (7) (+++++).

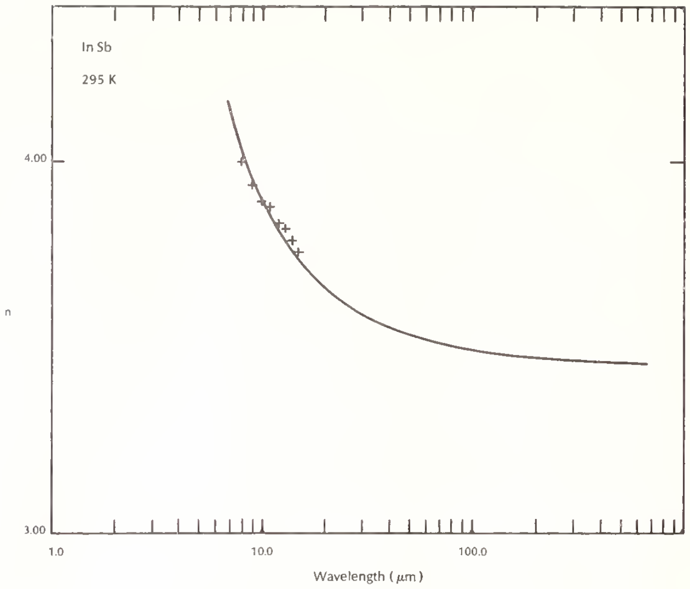

Figure 3. Theoretical results for InSb (solid line) for a sample with $n_e = 2.8\times10^{16}$ cm^{-3} are compared with experimental results (++++++) on samples 2n of Reference (6), which has an impurity concentration $N_i = 2.8\times10^{16}$ cm^{-3}. In making the comparison, we have assumed $n_e = N_i$.

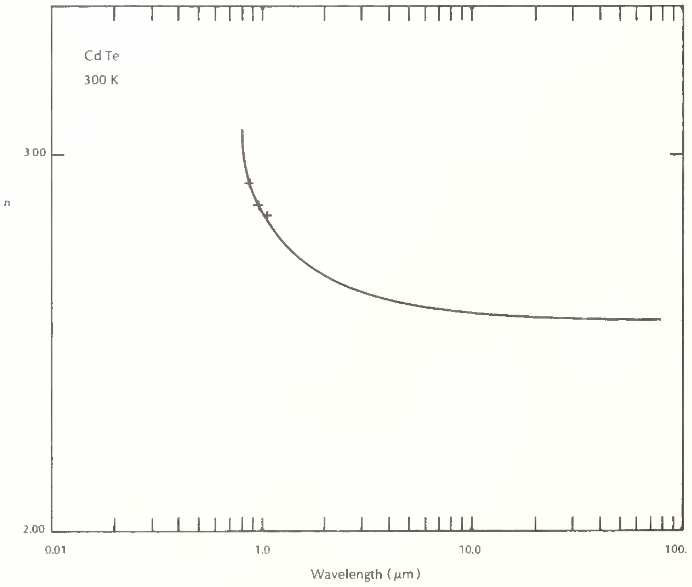

Figure 4. Theoretical results for CdTe (solid line) are compared with experimental results (+++) from Reference (5). An instrinsic sample, with $n_e = p = 0$, has been assumed.

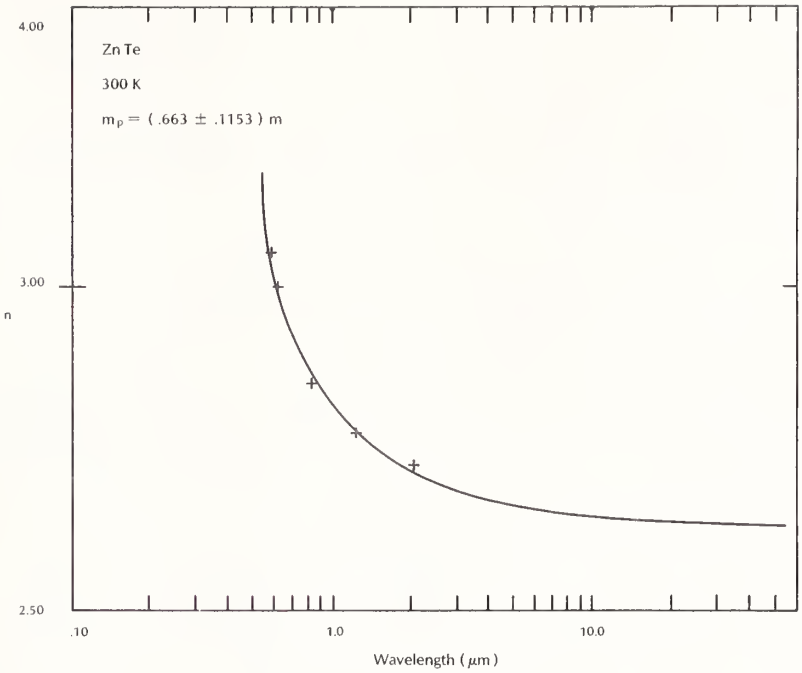

Figure 5. Theoretical results for ZnTe (solid line) are compared with experimental results (+++++) from Reference (5). An instrinsic material, with $n_e = p = 0$, is assumed.

UNIPOLAR ARCING, A BASIC LASER DAMAGE MECHANISM

F. Schwirzke

Naval Postgraduate School
Monterey, California 93940

Laser beams interact with surfaces by a variety of thermal, impulse and electrical effects. Energy coupling is considerably enhanced once surface electrical breakdown occurs. The laser heated plasma interacts then with the surface via three major interrelated damage mechanisms: thermal evaporation, ion sputtering, and unipolar arcing. While the first two are purely thermal and mechanical effects, unipolar arcing is an electrical plasma-surface interaction process which leads to crater formation, usually called laser-pitting, a process which was often observed but not well understood. Without any external voltage applied, many electrical micro-arcs burn between the surface and the laser heated plasma, driven by local variations of the sheath potential with the surface acting as both the cathode and anode. Unipolar arcing represents the most damaging and non-uniform laser-plasma-surface interaction process since the energy available in the plasma concentrates towards the cathode spots. This causes cratering of the surface. Unipolar arcing is the primary plasma-surface interaction process once breakdown occurs. The onset of arc damage is coincident with the onset of plasma formation. Never was there a plasma evident without attendant unipolar arc craters. At low irradiance there was no other laser damage (like melting) observed, all damage was in the form of unipolar arc damage.

Key Words: Laser damage mechanism; Laser-induced unipolar arcing; Unipolar arc model.

1. INTRODUCTION

Progress in pulsed power technology has been hampered by many plasma physics and technical problems not the least of which has been the problem area of plasma surface interactions. Surface breakdown by high power laser radiation leads to the formation of a plasma layer in front of the laser illuminated surface. Unipolar arcing then occurs at a sufficiently high plasma electron temperature.

The term unipolar arc was first used by Robson and Thoneman [1] in 1958. In their article they described the existence of an arc which "required only one electrode and is maintained by the thermal energy of the plasma electrons." The basis of their model is that at equilibrium there must be zero net current between an exposed conducting plate and a plasma. A retarding potential is established between plate and plasma. This floating sheath potential V_f prevents all but the higher energy electrons in the maxwellian distribution to reach the surface. Thus at equilibrium the net current becomes zero. The sheath potential depends on the electron temperature. If the electron temperature, T_e, is sufficiently large such that V_f exceeds the potential to initiate and sustain an arc, the authors argued that there will be strong local emission of electrons from a cathode spot on the plate into the plasma. Figure 1 represents this process. The plasma potential then lowers from V_f to the cathode fall potential V_c of the arc. With the plasma potential now lowered more electrons can return to the plate, thus closing the current loop and maintaining the plasma's quasi-neutrality. The circulating current is given by the increased

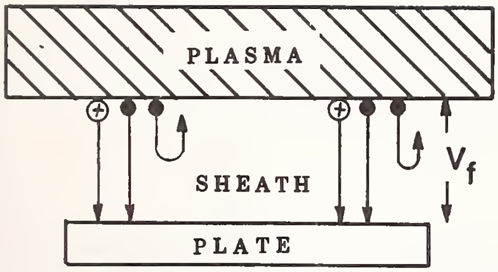

Figure 1a. Equilibrium flow of electrons and ions to isolated plate.

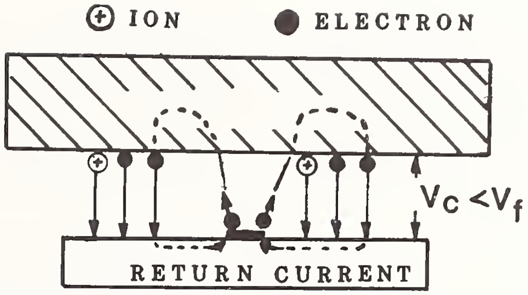

Figure 1b. Equilibrium flow of electrons and ions to isolated plate with electron emission from a cathode spot.

electron return current to the plate of area A due to the reduction of the sheath potential from V_f to V_c,

$$I_c = Aen_e \left[\frac{(kT_e)}{(2\pi m_e)}\right]^{1/2} \left\{ \exp\left(\frac{-eV_c}{kT_e}\right) - \exp\left(\frac{-eV_f}{kT_e}\right) \right\} \qquad (1)$$

n_e is the electron density, k the Boltzmann constant and e the elementary charge. The arc was sustained, they argued, until I_c fell below a minimum current I_a. The value of I_a depends on the material of the plate. The Robson-Thoneman mechanism implies a constant plasma electron density n_e contributing to the return current over a large area A of the wall.

The existence of unipolar arcs has been verified with extensive experimental evidence. Arc tracks have been observed on many tokamak surfaces [2-6].

2. UNIPOLAR ARC MODEL

While the Robson-Thoneman mechanism describes essentially the return current flow by eq (1), our model elaborates upon the electric fields which are set up in the plasma and drive the arc. The condition of plasma quasi-neutrality, $n_e = n_i$, leads to the formation of a sheath wherever the plasma is in contact with a wall. Since the electrons have a higher thermal velocity than the ions, an ion rich boundary layer is formed and the plasma potential is positive with respect to the wall. The magnitude of this sheath- or floating-potential is proportional to T_e, depends weakly on the ion/electron mass ratio M_i/m_e, and is independent of the plasma density,

$$V_f = (kT_e/2e)\ln(M_i/2\pi m_e) \qquad (2)$$

The sheath width is proportional to the Debye shielding length

$$\lambda_D = (kT_e/4\pi n_e{}^2)^{1/2} \qquad (3)$$

The plasma loss rate to the wall is controlled by the sheath potential. It accelerates the ions and electrostatically reflects most of the electrons such that electrons and ions reach the surface in equal numbers. Since the ions are much more effective than electrons in the desorption and sputtering of surface particles and the rates increase steeply with energy in the range of interest, sputtering and desorption of loosely bound particles [7] become worse if the sheath potential increases due to an increase of the electron temperature near the wall [8]. Electron and ion recombination on the surface contribute to surface heating.

Unipolar arcing, where the wall acts as both the anode and the cathode, occurs if the sheath potential increases sufficiently to ignite and sustain an arc. The Robson-Thoneman unipolar arc model implies a constant plasma density. However, for an arc to develop it is also necessary that the ion density increases above the cathode spot, in order to enable a larger electron current to flow into the plasma. Figure 2 shows schematically our unipolar arc model which takes into account the increase of plasma density due to ionization of neutrals released from the cathode spot.

The initial experiments were conducted on type 304 stainless steel targets [9] which had been highly polished. Surface protrusions, metallurgical inhomogenities, inclusions or whiskers from processing operations such as milling and grinding can serve as initial cathode spots. Furthermore, plasma waves and associated potential fluctuations in the sheath [10] can enhance electron emission and initiate cathode spots. The increased electric field strength on surface protrusions will also increase the ion flux from the plasma to these spots. Increased ion bombardment and recombination rates lead to a locally increased surface temperature. This results in desorption of neutral gas molecules and evaporation of metal atoms from the surface spot into the plasma. The ionization of a small fraction of the released neutral atoms results in a local increase in density of the plasma above the cathode spot.

The equation of motion for the electron fluid is given by

$$\rho_e \frac{\partial \vec{V}_e}{\partial t} = -en_e(\vec{E} + \vec{V}_e \times \vec{B}) - \nabla P_e + \frac{n_e e}{\sigma} \vec{j} = 0 \qquad (4)$$

Where $\rho_e = n_e m_e$ is the electron mass density, $\vec{V}_e$ the fluid velocity of the electrons, P_e the pressure, j the current density, and σ the electrical conductivity. The electron inertial term is insignificant for the characteristic time for arc evolution. Thus, setting eq (4) equal to zero and furthermore for $B = 0$, solving for E, one obtains,

$$\vec{E} = \frac{\vec{j}}{\sigma} - \frac{1}{n_e e} \nabla P_e$$

For $j = 0$, the ambipolar electric field becomes $E_o = -(1/e\ n_e)\nabla P_e$

For a weakly ionized plasma, the ratio $j/\sigma = \Delta E$ becomes independent of n_e and small in comparison to E_o:

$$\Delta E = \frac{j}{\sigma} = \frac{n_e e V_e (m_e \nu)}{(n_e e^2 \lambda_e)} = \frac{m_e V_e \nu}{e \lambda_e} < E_o = -\frac{\nabla P_e}{n_e} \approx \frac{kT_e}{ed} \approx \frac{m_e}{2} \frac{\bar{\nu}^2}{ed}$$

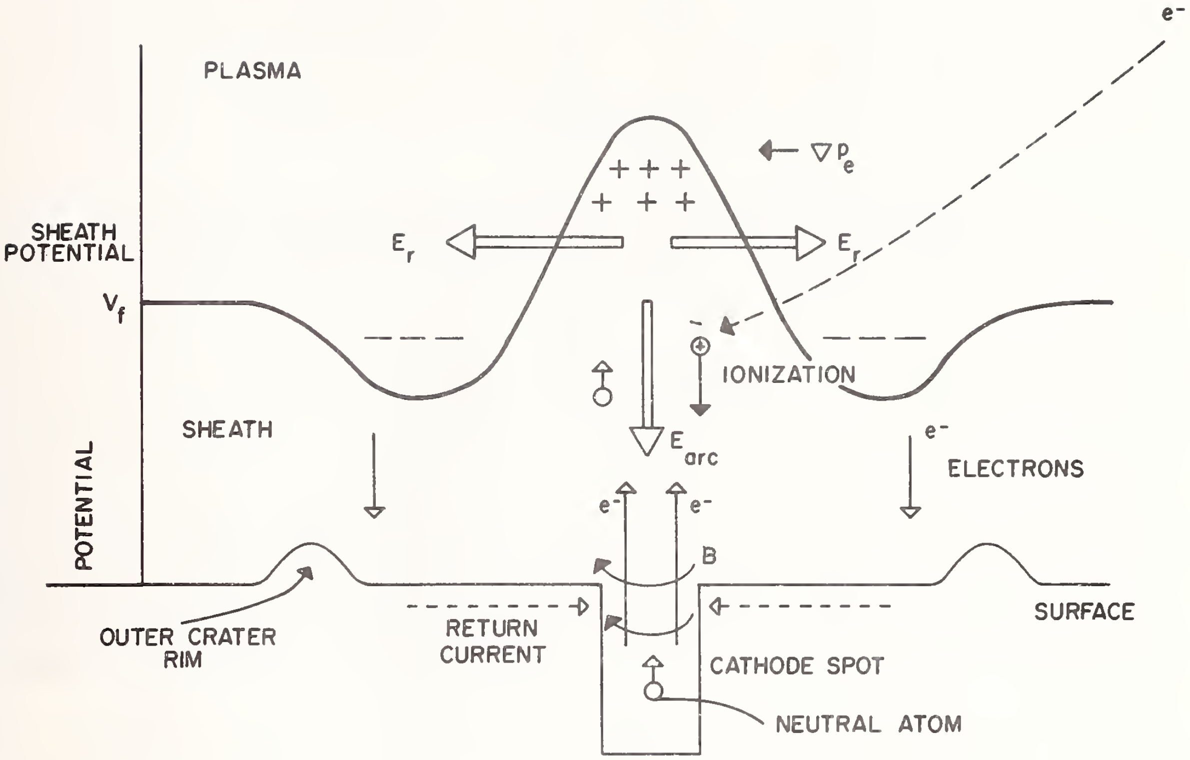

Figure 2. Unipolar arc model

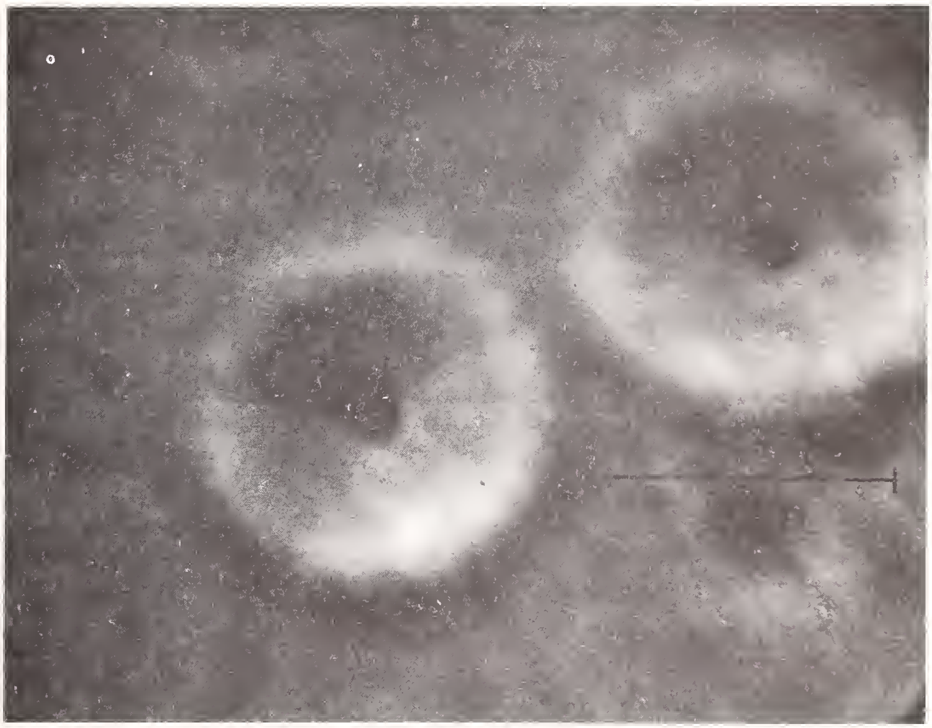

Figure 3. Unipolar arc craters. The outer rim diameter is 5.5 μm. The dark cathode spot at the center has a diameter of 0.7 μm, smaller than the laser wavelength of $\lambda = 1.06$ μm.

Our model implies that the mean free path length λ_e is larger than the dimensions of the neutral cloud above the cathode spot. Since the build-up of the plasma pressure gradient is caused by ionizing a fraction of the neutral particles, we assume $\lambda_e > d$, where d is the characteristic pressure gradient length. Even if $\lambda_e \lesssim d, E < E_o$ since the current associated drift velocity of the electrons $V_e << v$, where v is the electron thermal velocity.

The probability that a neutral atom is ionized in or near the sheath is of the order of the Debye length divided by the mean free path length. This ratio is much less than unity. For values of $n_e = 5 \times 10^{14}$ cm $^{-3}$ and kT = 10eV, which may be representative for an initial laser produced low density plasma layer, $\lambda_D = 10^{-4}$ cm. The electron mean free path for ionizing a neutral atom is $\lambda_e = 1/n_o\sigma_i$. Under vacuum conditions the neutral particle density n_o in the sheath depends on the desorption and evaporation rates from the surface. Iron atoms emitted at the melting temperature of 1526°C leave the surface with a thermal velocity of about 10^5 cm s $^{-1}$. Their time of flight to pass through the sheath would be 10^{-9} s. If, for example only one monolayer, i.e., 2×10^{15} particles cm^{-2} are released from a surface spot during this time, the neutral particle density within a Debye length will increase to $n_o = 2 \times 10^{19}$ cm^{-3}. (For comparison, atmospheric density at 0°C corresponds to 2.7×10^{19} cm^{-3}.) If we assume that the ionization cross section σ_i is 10^{-17}cm^2, λ_e becomes 0.005 cm. Thus a small fraction, $\lambda_D/\lambda_e = 2 \times 10^{-2}$, of the neutral atoms would be ionized within a Debye length from the surface. This, however, increases the plasma density from 5×10^{14} cm^{-3} to $n_i = (2 \times 10^{-2})\ n_o = 4 \times 10^{17}$ cm^{-3}, i.e., by a factor of 800 within 1 ns. Correspondingly, the local λ_D would rapidly decrease to 3.7×10^{-6} cm.

An ion produced in the sheath is driven back to the surface by the electric field which is of the order

$$E \approx V_f/\lambda_D \qquad (5)$$

The time of flight to return to the surface is proportional to the Debye length and the acceleration in the electric field $a = (eV_f)/(M_i\lambda_D)$. Thus

$$t = (2\lambda_D/a)^{1/2} = \lambda_D(2M_i/eV_f)^{1/2}$$

For the initially assumed Debye length of 10^{-4} cm an iron ion needs about 10ps to fall back to the surface. Since the Debye length decreases with build-up of the local plasma density above the cathode spot, later released neutrals which become ionized in the sheath need only picoseconds to return to the surface. The increased ion bombardment and release of recombination energy lead to a further increase in surface temperature. This in turn represents a feedback mechanism, leading to a further release of absorbed gases and material evaporation at a sufficiently high power deposition. Since the mean free path for electrons is much larger than the sheath width, the additional ionization of neutral atoms in (or near) the sheath and the acceleration of these ions in the sheath implies a concentration of available plasma energy towards the arc spot. Of course, most of the neutral atoms released from the surface become ionized within the plasma. The locally increased plasma density reduces λ_D and thus the sheath width. Correspondingly, the locally increased plasma pressure above the cathode spot leads to an increasing electric field E_{arc}(V/cm) to drive the arc current:

$$|E_{arc}| \approx V_c/\lambda_D \lesssim V_f/\lambda_D = 6.6 \times 10^{-3}(n_e\ kT_e)^{1/2} \qquad (6)$$

where kT_e is measured in electronvolts and n_e in reciprocal cubic centimeters. The high density plasma above the cathode spot is biased with respect to the surface via the cathode fall potential of the arc. The high density plasma dominates the surrounding lower density background plasma. The increased plasma pressure above the cathode spot thus also leads to an electric field E_r in the radial direction, tangential to the surface:

$$E_r = - \frac{kT_e}{en_e} \frac{dn_e}{dr} + \frac{j}{\sigma} \qquad (7)$$

Neglecting the j/σ term, this radial field reduces the plasma potential in a ring-like area surrounding the higher plasma pressure above the arc spot by

$$\Delta V(r) = \frac{kT_e}{e} \ell n \frac{n_e(r)}{n_{eo}} \qquad (8)$$

The ratio of the maximum plasma density above the cathode spot to the unperturbed plasma density can easily be of the order $(n_e/n_{eo}) \sim 10^3$ or larger. The reduced sheath potential in this ring area allows more electrons from the high energy tail in the maxwellian distribution to reach the surface, this closing the current loop of the unipolar arc, figure 2. In fact, equating ΔV with the sheath's floating potential, eq (2)

$$\Delta V = V_f$$

$$\frac{kT_e}{e} \ell n \frac{n_e}{n_{eo}} = \frac{kT_e}{2e} \ell n \frac{Mi}{2\pi m_e}$$

we find that independent of the electron temperature the sheath potential approaches zero when

$$\frac{n_e}{n_{eo}} = \left(\frac{Mi}{2\pi m_e} \right)^{1/2}$$

In this case, the electron return current to the surface is determined by n_e and the electron thermal velocity. This electron saturation current is

$$i_s^- = \frac{en_e v}{4} A \qquad (9)$$

Equation (9) can be used to estimate the order of magnitude of the surface area A needed for the electron return current. If the arc current is 10 Amp and $n_e = (M_i/2\pi m_e)\, n_{eo} = 130 n_{eo}$ for the mass M_i of iron ions and if we consider a laser produced plasma near the surface with initially $n_{eo} = 5 \times 10^{14}$ cm^{-3} and $kT_e = 10$ eV, the return current area is $A = \pi r^2 = 3 \times 10^{-9}$ m^2. Actually, $n_e(r)$ will rapidly increase above the assumed value, reducing A further. Thus the estimated value of the radius of $r \lesssim 30$ μm is of the same order as the radius of the outer crater rim. The location of the outer crater rim thus may indicate how far the return current area has expanded during the limited burntime of the arc.

3. EXPERIMENT

A plasma generated by a neodymium laser pulse was used to study unipolar arcing on solid material surfaces. A Korad K-1500 laser was operated in the Q-switched mode. Nominal beam pulse half width of the laser was 25 ns. Incident laser energy was varied by inserting neutral density filters of varying transmittance in the beam path. For low energy shots the laser amplifier was not fired. Laser energies on target between 0.0075 and 10 joules were obtained by these techniques. The beam was focused to various spot sizes on the target to provide further variation in power density at the target. Laser energy at each shot was measured using a Laser Precision RK-3200 Pyroelectric Energy Meter, with a RE 549 detector reading via an 8% splitter in the main beam.

The laser pulse was directed onto targets placed in a vacuum chamber. The vacuum system using an oil diffusion pump and a liquid nitrogen cooled baffle, was capable of providing chamber pressures of the order 10^{-6} Torr. To obtain a smooth surface the target disks were metallographically polished with a final polishing slurry of 0.05 µm Al_2O_3. Before being mounted in the test chamber, each specimen was cleaned with acetone. After one laser shot the damage on the polished surface was observed with an optical and a scanning electron microscope, Cambridge Stereoscan S4-10.

4. LASER-INDUCED UNIPOLAR ARCING

Laser induced unipolar arcing was studied over a wide range between two extreme, basically different laser-power and plasma-dynamic conditions on various metals and nonconducting surfaces.

1. High Irradiance

A high power laser pulse is focused onto the target. The laser produced plasma expands from the small focal spot over the target surface into areas which were not illuminated by the laser. The area damaged by the plasma is much larger than the laser focus area. The existence of unipolar arc craters in these areas proves that unipolar arcing is a plasma-surface interaction process, independent of the laser-plasma interaction processes, like self-focusing, filamentation, instability, etc. The laser just heats the electrons to a sufficiently high temperature.

2. Low Irradiance

A low power, defocused laser pulse is used to determine the laser power density threshold for onset of unipolar arcing. Laser intensity variations over the cross section (hot spots) cause breakdown and arcing only in areas where the power density was sufficiently high. The area damaged by the plasma is smaller than the laser illuminated area.

The high and the low irradiance experiments will be discussed in the following paragraphs and the results on conducting and non-conducting surfaces will be compared.

4.1 High Irradiance Laser Induced Arcing

In the Q-switched mode the range of energies on the target was selected as 3-5J, giving a power range of 100-200 MW. The laser focal spot diameter is approximately 0.5 mm. For a 200 MW pulse this gives a typical power density of 10^{11} W cm^{-2}. The temperature of the laser-produced plasma was measured spectroscopically, $kT_e \approx 100$eV. Time of flight measurements showed that the plasma expands rapidly with a velocity of about 10^7 cm/s from the focal spot on the target surface in the normal and radial directions.

The laser impact crater of about 0.75 mm diameter is surrounded by a plasma damaged surface area of about 6 mm diameter. Although no external voltage is applied, about 300,000 to 600,000 unipolar arc craters/cm^2 are observable on the stainless steel surface which was exposed to the radially expanding plasma but not to the laser radiation. Figures 4-6 show a sequence of SEM photos of the plasma-damaged surface for increasing distance from the laser focal spot. Close in, figure 4 shows a superposition of arc craters. The oldest one, burning for a longer time during the existence of the laser-heated plasma, have larger outer rim diameters of 30-50 μm. Smaller craters within larger ones are probably initiated towards the end of the laser pulse. They have smaller outer rim diameters. If not refilled by the liquid metal, craters show a dark spot of about 1 μm size at the center representing the cathode spot. The size of the outer rim craters also decreases with increasing distance from the focal spot (figures 5 and 6). Figure 6 shows the onset of crater formation near the edge of the expanding plasma.

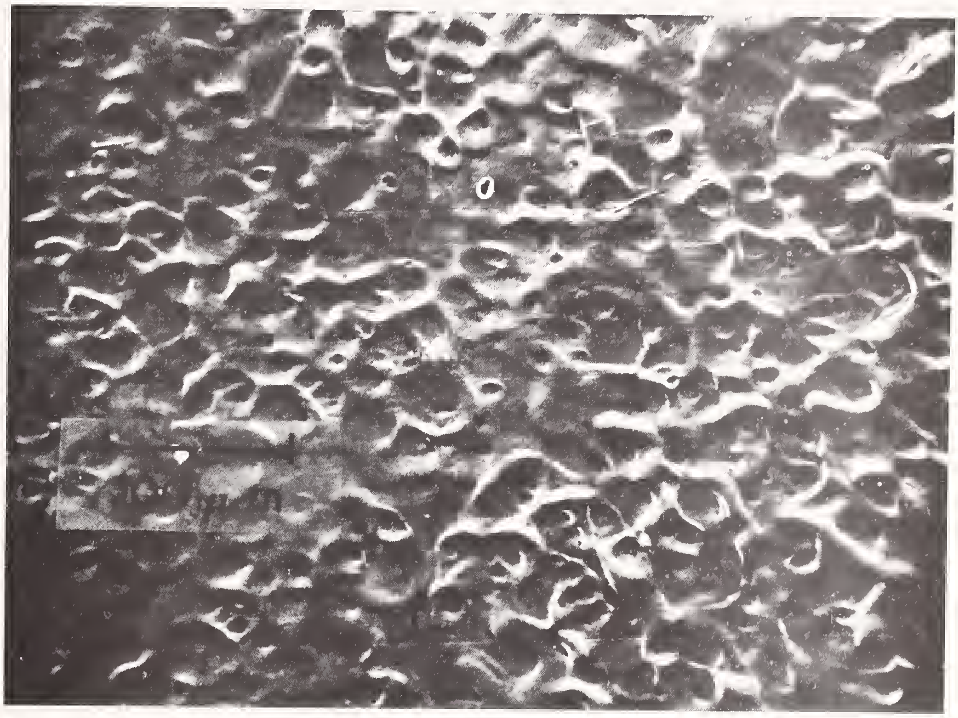

Figure 4. Overlapping craters near laser focal spot. Outer rim crater size depends on arc burn time.

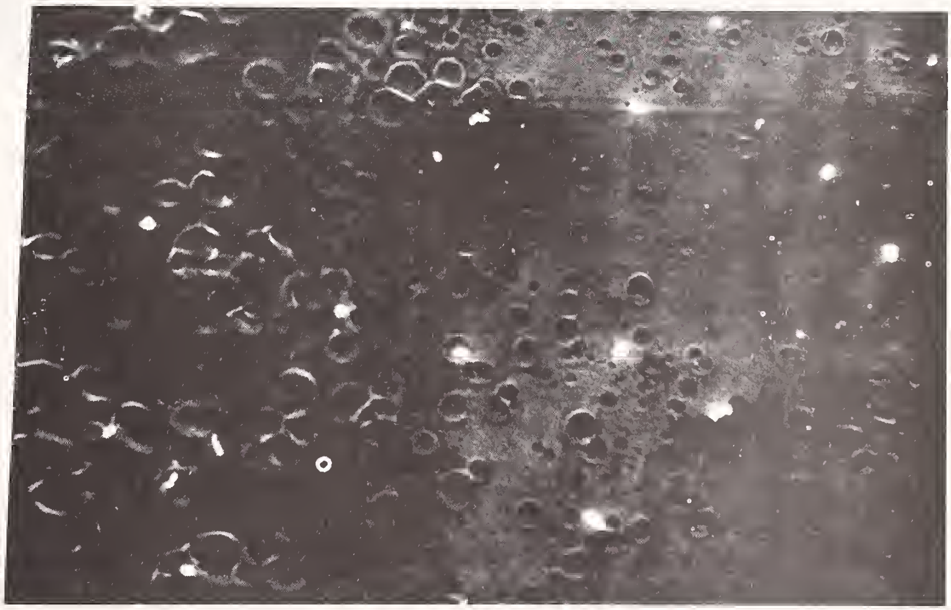

Figure 5. Crater formation at 1.5mm from laser focal spot which is located beyond the left side.

Figure 6. Onset of unipolar arc crater formation on highly polished stainless steel.

Deep cathode craters of 0.5 to 1 μm diameter are clearly visible with outer crater rim formation just barely beginning. The depth of these fully developed cathode craters is 3-6 μm.

The short lifetime of the laser-produced plasma allows the study of the temporal development of the arcs. The initial breakdown phase of unipolar arcing is documented by the small but deep cathode craters formed furthest away from the focal spot, figure 6, where the plasma conditions favorably for arc formations lasted only for a short time because after laser shut off T_e decreases rapidly in the expanding plasma. Further in, if allowed to burn long enough, the surface metal area A needed for the electron return current melts. The liquid is pushed outwards in the radial direction by the expanding dense plasma and an outer crater rim of 5-50 μm diameter is formed depending on the arc duration.

The depth of the initial arc crater of 3-6 μm, is larger than the diameter of 1 µm. This indicates that the pinch magnetic field of 40,000 Gauss for a current of 10A and r = 0.5 µm contributes to the concentration of the arc energy onto the small cathode spot, see figures 2 and 3. If kTe = 10eV, this field can confine a plasma with a density up to 4 x 10^{18} cm^2. At this density the Debye length λ_D = 10^{-6}<<1 µm and it is justified to assume that a high density plasma exists in the arc hole. This represents a hollow cathode configuration and the ionization rate should be high. The depth of the cathode spot craters corresponds to a removal of 10^4 to 10^5 monolayers.

Arcing continues only as long as the laser pulse is heating the electrons for 50-60 ns. The natural life time of a micro-arc seems to be of the order of 10 ns. Unipolar arcing on different materials has been studied. All metals show a very similar kind of arc craters. Evidence of unipolar arcing has been found on all targets irradiated at atmospheric pressure, that also arced in vacuum indicating that the metal vapor pressure near the surface is of the order or even larger than the atmospheric pressure.

4.2 Determination of Low Irradiance Threshold for Onset of Arcing

The incident laser power density for the onset of arcing was determined for type 304 stainless steel and type 2024 aluminum [11]. Since the energy output is more easily controlled by the introduction of filters than by adjusting laser power supply voltage, the incident power on the target was controlled in this manner. A polaroid camera was positioned above the target to note plasma formation by recording the attendant light. The beam spot size was measured by placing exposed polaroid film at the target position within the vacuum chamber and conducting a series of laser shots to find the average spot size area.

Using this experimental arrangement a series of laser shots were made to determine the power density threshold for breakdown and plasma formation and the power density threshold for unipolar arc formation. Surface breakdown and the formation of a visible plasma layer occur at a laser power density of about 10 MW/cm^2. Unipolar arcing has been shown to be then the primary plasma-surface interaction process once plasma formation occurs. Figures 7 and 8 provide a comparison of the extent of damage between 25.5 MW/cm^2 and 5.4 MW/cm^2. Figure 9, an enlargement of figure 8, shows the minimal damage observed at 5.4 MW/cm^2. The characteristic shape of unipolar arcs becomes clearly visible in the enlarged photo, a small dark cathode spot at the crater center surrounded by a pronounced rim.

A review of the target damage reveals that the damage was not evenly distributed across the laser illuminated area but rather was concentrated in one quadrant, due to non-uniformity in the laser beam, figures 7 and 8. The locations of the beam's hot spots coincide exactly in shape and location with the observed target damage. Since the area used in calculating power density assumed a uniform distribution of energy, the threshold density reported above can only be accurate as an order of magnitude power density for this particular laser.

The data thus obtained suggest that the power density threshold for the onset of breakdown and for the onset of unipolar arcing are the same. The onset of arc damage is coincident with onset of breakdown and plasma formation. Never was there a plasma evident without attendant unipolar arcs. At low power density there was no other direct laser damage (like melting) observed on the target. In fact, all damage was in the form of arc damage.

Figures 10 and 11 show patterns of micro-arc craters produced on polished stainless steel by an unfocused medium power Q-switched laser pulse. Arcing seems to follow the interference fringes of the laser output as clearly visible near the edge of the laser illuminated area. Breakdown and arcing occur in the regions of constructive interference. The expanding plasma pushes the liquid surface layers to form a rim in the region of destructive interference.

Figure 7. Arc damage on stainless steel, defocused laser pulse of 25.5 MW/cm^2 .

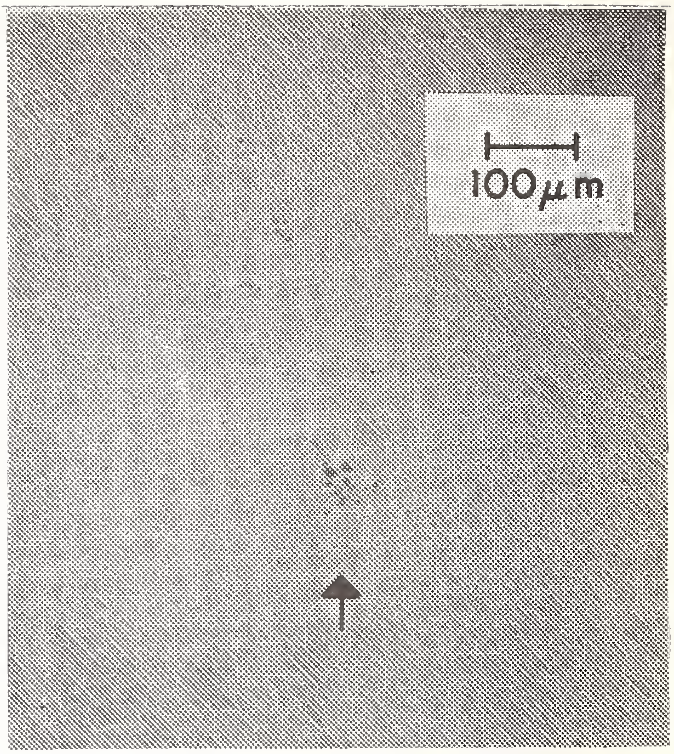

Figure 8. Onset of arcing on stainless steel at 5.4 MW/cm^2 . Same magnification as figure 7.

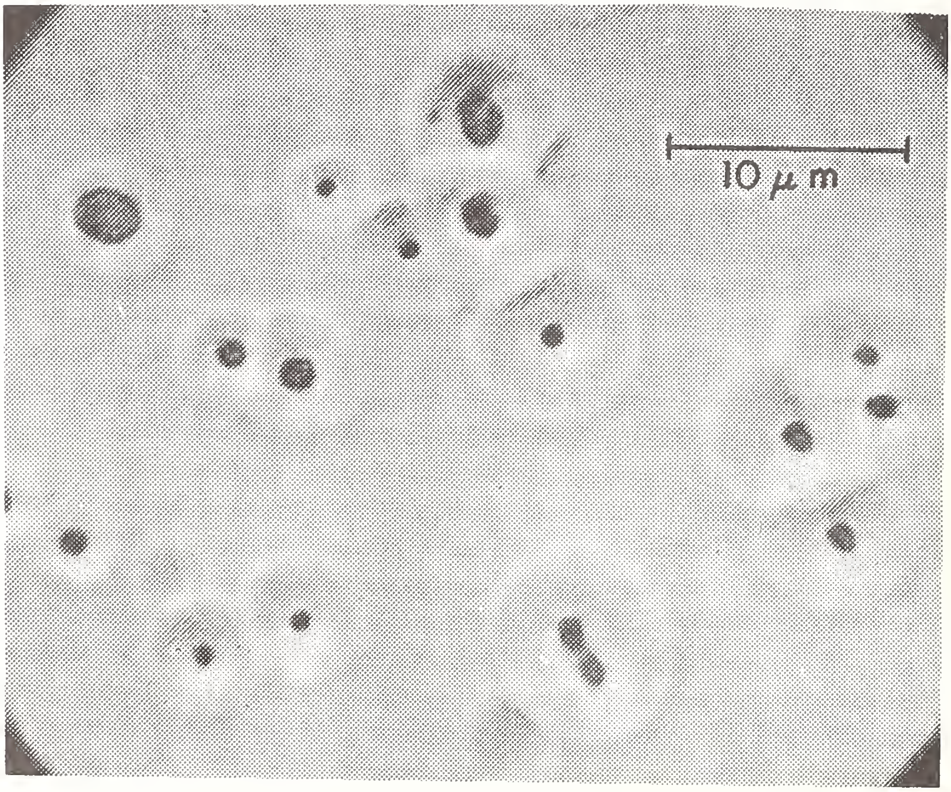

Figure 9. Further magnified view of figure 8. Onset of breakdown and arc formation at 5.4 MW/cm^2.

4.3 Comparison of Conducting and Non-Conducting Surfaces

Laser induced arcing on metal surfaces has been studied extensively. All metals investigated, stainless steel, copper, titanium, aluminum, molybdenum show similar arc damage, a cathode crater of about 1 μm diameter, 3-6 μm deep and an outer crater rim of 5-50 μm diameter. Evaporation of material from the cathode crater and the return current flow through the material are essential for the formation of a unipolar arc. A consequence of our unipolar arc model is that reduced surface conductivity and high melting point materials should influence the arc formation. The effect of unipolar arcing for various types of materials has been studied to determine whether material characteristics have any effect in reducing the arcing damage. Titanium carbide coatings were deposited by an activated reactive evaporation process on stainless steel surfaces. At 20°C the electrical conductivity of TiC is 1/15 the one of SS304, 1.4 x 10^5(ohm-cm)$^{-1}$. The melting temperature of TiC is 3410 K, roughly twice the value of SS304 at 1770 K. The large size characteristic unipolar arc craters for metals were not observed on laser illuminated TiC coatings [12]. Also, thermal energy and momentum coupling to various target materials was investigated to determine what effect unipolar arcing had on the coupling process [13]. Even though the heat conduction coefficient of TiC is about the same as the one of SS304, a 10 μm TiC coating on SS304 reduced the thermal coupling to about 1/3 of the SS304 value. This leads to the conclusion that large scale unipolar arcing on metal surfaces increases the coupling of energy from the laser heated plasma into the target.

A series of TiC-coated targets was irradiated at power densities ranging from 300 to 1000 MW/cm^2 and the targets were subsequently examined for surface damage. Figure 12 pictures the edge of the damage area. There are regions of apparent melting and resolidification in droplet form, cracking and arcing. Individual arc craters are clearly visible on the right hand side of the figure, in the transition zone to the undamaged area. This indicates again that unipolar arcing is the primary damage mechanism. However, crater sizes are considerably smaller. They range from 0.1 to 0.3 micron diameter, with crater densities of approximately 4.5 x 10^8 cm^{-2} in regions close to the melted material. Cracking occurs along a narrow band of arc craters, figure 13, indicating that large stress formation is associated with the cratering.

Silicon coatings of 1-2 micron thickness on SS304 and 2024 aluminum were also studied [14]. Figure 14 is a SEM photograph of a 1 micron silicon coating on polished aluminum prior to laser irradiation. This coating shows a bumpy structure. After irradiation at the power density for onset of plasma formation tiny spheres of various degrees of irregularity appear, but the coating does not appear to have melted through. Figure 15 shows the coating near the edge of the laser exposed region. Arc formation starts on the top of the bumps. The crater density is approximately 5 x 10^7 cm^{-2}, and the crater diameter is about 0.1 micron, again, about 1/10 of the crater size observed on metals.

5. DISCUSSION

The experimental results presented in this paper show that unipolar arcing is the primary laser-plasma-surface interaction mechanism which leads to a very non-uniform energy deposition and crater damage on the surface. Since the scale lengths are very small, typically 1 μm for the cathode spot on metals and the electrons provide the current flow, unipolar arcing should be considered as a fast evolving process with arcs forming within a nanosecond or less.

The initial absorption of laser radiation and plasma heating occur in the underdense plasma close to the surface. The release of material from a cathode spot leads to locally increased absorption of laser radiation and build-up of the plasma pressure until the critical density is reached. Heat conduction by electrons and short wave length plasma radiation provide the energy transport through the overdense plasma to the target surface. Many laser-plasma instabilities have been discussed which may cause non-uniformities near the critical density region. No attention has been

Figure 10. Laser-produced arc pattern near edge of laser illuminated area. Arrows show onset of arcing in ring pattern.

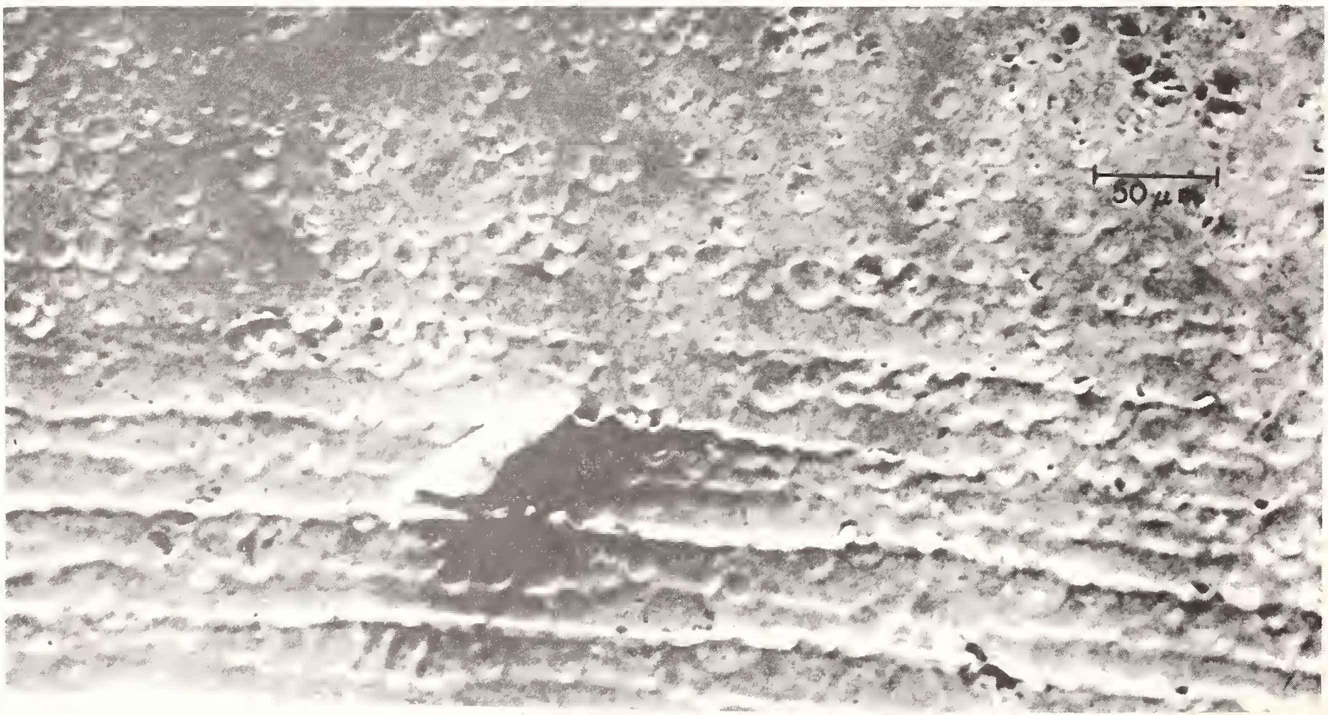

Figure 11. Laser-produced micro-arc pattern on SS304, defocused laser.

Figure 12. Unipolar arc craters on TiC coated SS304 after irradiation at 300 MW/cm^2.

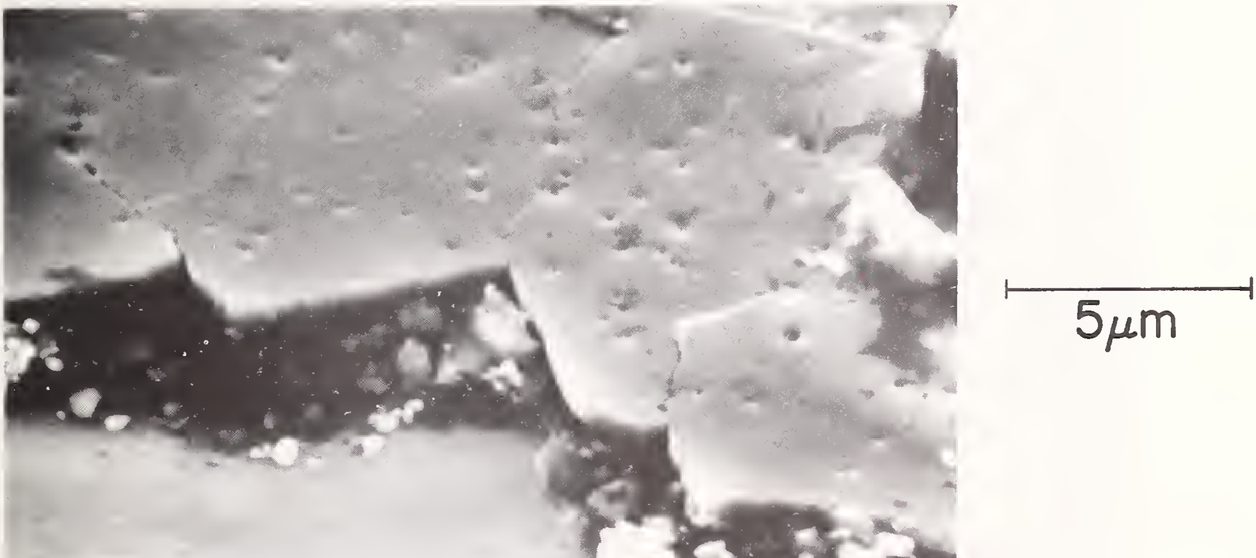

Figure 13. Cracked TiC coating on SS304 after irradiation with 1096 MW/cm^2. The bottom part shows removal of a surface layer. Along the edges of the removed TiC area, cracking follows a narrow band of arc craters.

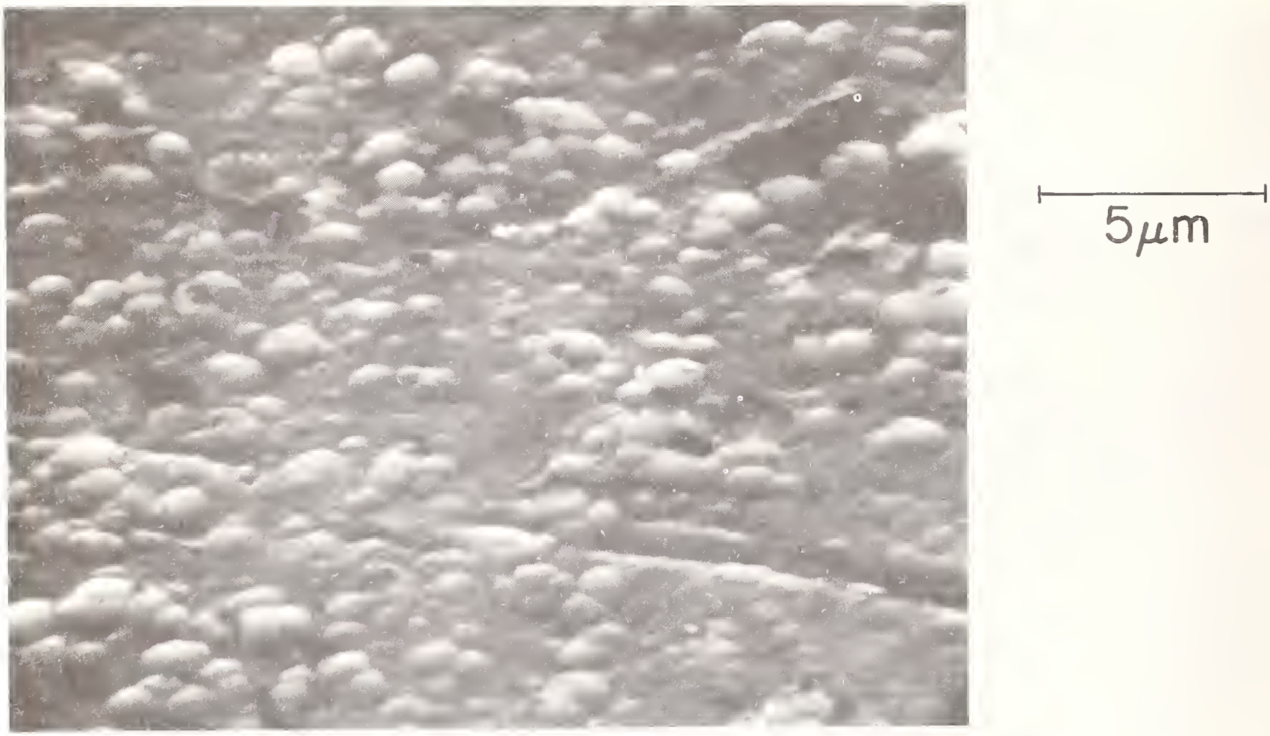

Figure 14. One micron silicon coating over polished 2024 aluminum before irradiation.

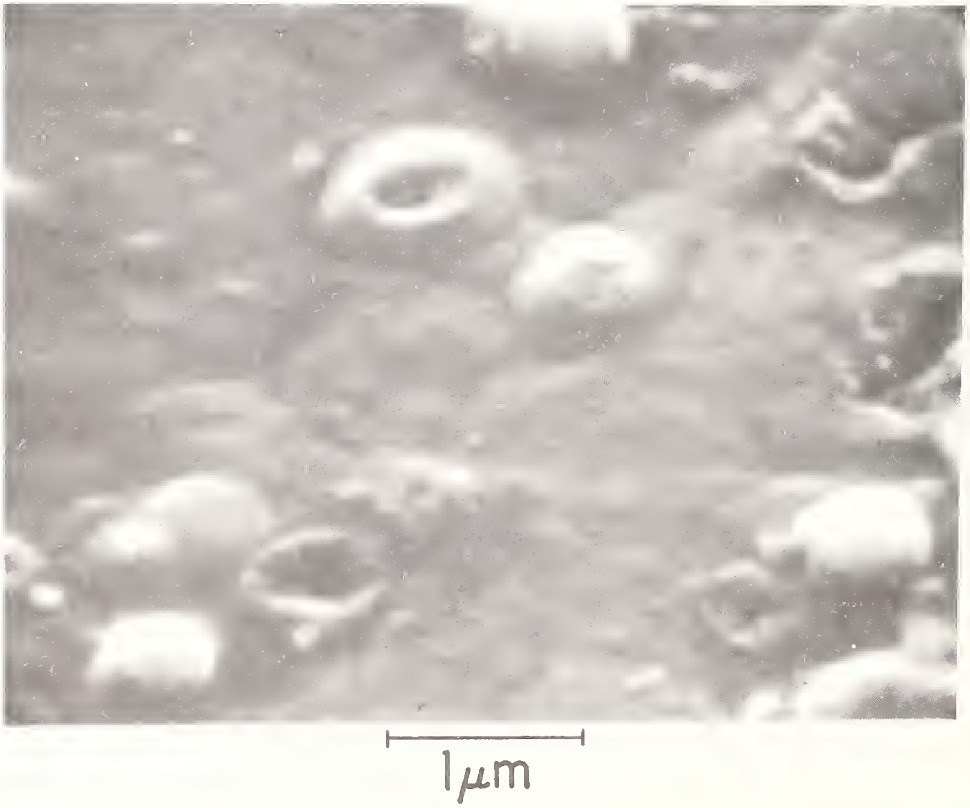

Figure 15. Silicon coating after irradiation with 400 MW/cm^2 near edge of irradiated area.

given to arcing which leads to non-uniform ablation of the material and thus also to a modulation of the critical density contour. The onset of arcing on conducting and non-conducting surfaces will be discussed in the following paragraphs.

5.1 Formation of Low Density Breakdown Plasma

The initial breakdown phase may be characterized by the build up of a low density plasma layer in front of the surface with a density $n_{eo} << n_{ec}$ where n_{ec} is the critical density. This initial plasma layer may be formed by photo electrons and ionization of neutral particles at a distance $\lambda/4$ from the surface where for normal incidence the first maximum in the electric field occurs due to the superposition of the incident wave and the wave reflected on a metal surface. A sheath will form immediately since the sheath potential V_f is independent of the plasma density. The electron temperature might be of the order of 5 to 20eV. Spatial variations of the laser intensity will produce density variations in this initial plasma layer. The electron density can be estimated from the laser produced arc pattern of figure 11. The ring width of about 30 micron is much larger than the laser wave length. The existence of the pattern of this size implies that the local sheath width should be smaller than 30 μm, otherwise the pattern would be "washed out." This assumption $\lambda_D << 30$ μm allows to estimate a lower limit of the plasma density. Assuming again an initial $\lambda_D = 10^{-4}$ cm and $T_e = 10$eV, we estimate $n_{eo} > 5 \times 10^{14}$ cm^{-3}.

In accordance with eq (6) the sheath electric field increases with the local build up of the plasma pressure as $E \propto P^{1/2}$. The dielectric strength of air at atmospheric pressure is 30 kV/cm. If we take this as a typical value for onset of sparking we find from eq (6) that a plasma layer of only $n_{eo} \geq 2 \times 10^{12}$cm^{-3} and $kT_e = 10$eV provides already a sheath electric field of $E \geq 30$ kV/cm to start spark formation at atmospheric pressure. As discussed previously, any release of neutral particles from the surface leads to a rapid build up of the local plasma pressure and this further increases the sheath electric field. Thermally enhanced field emission might begin at about 10^6 V/cm, that is at a plasma density of about $n_e = 1.25 \times 10^{17}$cm^{-3}.

Finally, thermionic electron emission from a cathode spot will lead to the formation of an arc. The local build up of the neutral and plasma density then also leads to non-uniform absorption of laser radiation.

5.2 Heating of a Surface Plasma Layer by Laser Radiation

Electrons change momentum through collisions with positive ions and neutral particles. The frictional force acting on the electron fluid is equal to the rate of change of momentum, and the equation of motion for a cold unmagnetized plasma becomes now

$$m_e \frac{\partial \vec{V}_e}{\partial t} = -e\vec{E} - m_e \vec{V}_e (\nu_{ei} + \nu_{eo})$$

where ν_{ei} and ν_{eo} are the collision frequencies for momentum transfer due to collisions with ions and neutral particles respectively. The collision frequency in a fully ionized plasma depends on n_i and T_e as

$$\nu_{ei} = 0.29 \times 10^{-6} (n_i Z^2 \ell n \Lambda)/(T_e)^{3/2}$$

where T_e is measured in eV and n_i in cm^{-3}, Z is the ionic charge and the Coulomb logarithm is of the order $\ell n\ \Lambda \approx 10$. Electron-neutral collisions dominate for a weakly ionized plasma, $\nu_{ei} << \nu_{eo}$, and ν_{eo} depends on the neutral particle density n_o the collision cross section σ_o (σ_o is of the order 5×10^{-16}cm^2) and the electron thermal velocity

$$\nu_{eo} = n_o \sigma_o v$$

Thus, assuming that ν_{ei} and ν_{eo} are independent of the fluid velocity V_e, we find for an electromagnetic wave of frequency ω for V_e the solution

$$\vec{j} = en_e\vec{V}_e = \frac{n_e e^2}{m_e(\nu_{ei} + \nu_{eo}) + i\omega}\vec{E} = \sigma\vec{E}$$

where the conductivity

$$\sigma = \frac{n_e e^2 \left[(\nu_{ei} + \nu_{eo}) - i\omega\right]}{m_e \left[(\nu_{ei} + \nu_{eo})^2 + \omega^2\right]}$$

The dispersion relation for transverse electromagnetic waves in a plasma can be written as $c^2 = \varepsilon\omega^2/k^2$ with the dielectric constant given by

$$\varepsilon = 1 + \frac{\sigma}{i\omega\varepsilon_o}$$

Thus the dispersion relation becomes

$$k^2c^2 = \omega^2 \left(1 - \frac{\omega_{pe}^2}{(\nu_{ei} + \nu_{eo})^2 + \omega^2} - \frac{i\omega_{pe}^2 \; (\nu_{ei} + \nu_{eo})}{\omega \; \left[(\nu_{ei} + \nu_{eo})^2 + \omega^2\right]} \right.$$

where the plasma frequency is defined as $\omega_{pe} = (n_e e^2/m_e\varepsilon_o)^{1/2}$

For the assumed initially weakly ionized plasma layer of $n_e = 5 \times 10^{14}$ cm^{-3} (which is many orders of magnitude below the critical density of $n_{ec} = 10^{21}$ cm^{-3} for Nd laser radiation) and a neutral density layer of $n_o = 2.7 \times 10^{19}$cm^{-3} (which corresponds to atmospheric density at 0°C and 760 Torr), we find $\omega_{pe}^2 << \omega^2$, and $\nu_{ei} << \nu_{eo} \approx 2 \times 10^{12} << \omega$ and eq (10) simplifies to

$$\frac{c^2}{\omega^2/k^2} = \left(1 - \frac{\omega_{pe}^2}{\omega^2}\right) - \frac{i\omega_{pe}^2 \; \nu_{eo}}{\omega^3} = n^2 = (n_R - in_I)^2 = n_R^2 - n_I^2 - 2in_R n_I \quad (11)$$

The refractive index $n^2 = \varepsilon$ is complex. Because of $(\nu_{eo}/\omega) << 1$ the real part of the refractive index becomes the familiar expression for an electromagnetic wave in a plasma

$$n_R \approx ck/\omega = (1 - \omega_{pe}^2/\omega^2)^{1/2}$$

The imaginary part of the complex wave vector k describes the damping of wave amplitude due to collisions. Since the intensity I is proportional to the square of the amplitude, we find that the absorption coefficient in the equation

$$I = I_o e^{-\alpha z}$$

becomes

$$\alpha = -2 \; \mathrm{Im}(k) = -2(\omega/c) \; n_I$$

From eq (11) also follows, $-2\, n_R n_I = \mathrm{Im}(\varepsilon)$. Thus α can be written

$$\alpha = (\omega/cn_R)\ \mathrm{Im}(\varepsilon)$$

The absorption length $\ell = 1/\alpha$ becomes

$$\ell \approx \frac{c\omega^2}{\omega_{pe}^2 \nu_{eo}} = \frac{3.3 \times 10^{31}}{n_e \lambda^2 \nu_{eo}}\ \mathrm{cm} \tag{12}$$

where n_e is measured in cm^{-3} and λ in micron.

Since $z/\ell << 1$ the intensity absorbed by the plasma becomes

$$I_o - I \approx I_o(z/\ell) \tag{13}$$

It is noteworthy from eq (12) and (13) that the absorption of laser energy per electron in a weakly ionized surface layer of depth z is independent of n_e

$$\frac{I_o z}{n_e z \ell} = \frac{I_o \omega_{pe}^2\ \nu_{eo}}{n_e c\omega^2} = \frac{I_o \lambda^2 \nu_{eo}}{3.3 \times 10^{31}} \tag{14}$$

Consequently, electron heating will occur for any initial electron density present near the surface and it will increase with the desorption of surface layers of absorbed gases (CO_2, H_2O, etc.) because ν_{eo} increases with the build up of the neutral particle density. For atmospheric pressure initially, the laser damage threshold is of the order $15 J/cm^2$ for short pulse Nd radiation. From eq (14) we estimate then that an electron absorbs 5.6eV. Ionization will occur if this energy becomes thermalized between the electrons. The existence of the sheath will enhance the electron-electron collision rate since most of the electrons will be reflected in the sheath and their velocity component v_z goes through zero, thus increasing the Coulomb collision cross section.

For a perfectly reflecting surface the time averaged value of a standing wave shows spatial intensity variations as

$$E^2 = 4E_o^2 \sin^2 \left(\frac{2\pi z}{\lambda}\right)$$

with maxima of 4 times increased intensity located at $z = \lambda/4, 3\lambda/4, \ldots$ This higher intensity and the release of neutral particles from the surface should considerably increase the electron heating in the $\lambda/4$ region. Figure 16 shows schematically this influence of the neutral density gradient on the preferential rapid electron heating, ionization and breakdown in a surface layer, near $z = \lambda/4$. The average speed of water molecules released from the surface at 25°C is 592m/s. For $\lambda = 1.06$ µm, the time for desorbed molecules to travel a distance of $\lambda/4$ is thus 0.4 ns. This time will be even shorter as rapid surface heating will occur. This discussion indicates that electrons can gain sufficient energy to ionize neutrals, thus further increasing the electron density and consequently the absorption coefficient. This feedback mechanism will lead to rapid ionization and build up of the local plasma pressure until the arc ignites. Furthermore, laser energy will be preferentially absorbed and less reflected where the arc burns since relative large amounts of material will be ejected from the cathode crater.

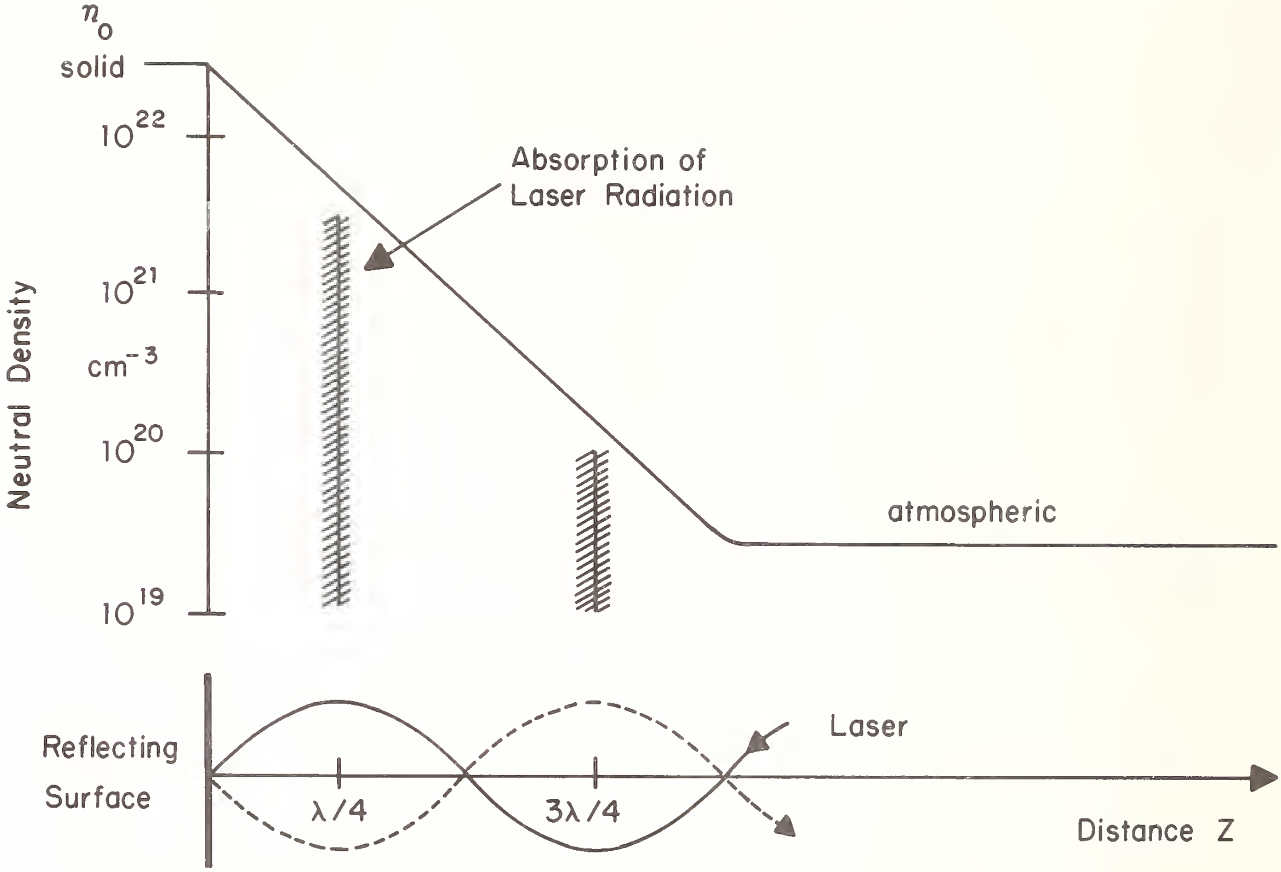

Figure 16. Absorption of short-pulse laser radiation near a reflecting surface. The neutral density gradient in front of the surface is caused by blow-off of surface material.

This contributes to a non-uniform laser energy deposition and plasma build up above the cathode spot until the critical density is reached.

5.3 Unipolar Arcing on "Non-Conducting" Materials

It is apparent that laser-target interaction with its attendant plasma-induced arcing is a dynamic process which must be described in terms of constantly changing variables. Such variables include, but are not limited to, plasma temperature and density, laser power and pulse duration, neutral particle density, absorbed gases, target material and surface preparation, physical properties of the target, like thermal and electrical conductivity and vapor pressure as function of surface temperature. The observed small scale cratering on non-metallic materials indicates that their surfaces exposed to a plasma require sufficient conductivity to provide the electron return current flow to the cathode spot. The modification of the sheath potential due to the radial pressure gradient, eq (7) and (8) provides an r-dependent electron flow from the plasma to the surface ring area $2\pi r\Delta r$

$$i^- = 2\pi r\Delta r n_e(r)e(kT_e/2\pi m)^{1/2} \exp -e[V_p(r)-V_w(r)]/kT_e \qquad (15)$$

where $V_p(r)$ is the plasma potential $V_w(r)$ the potential of the wall and the sheath potential is $V_s(r) = V_p(r)-V_w(r)$. The ion flow to the surface is determined by the number of ions entering the sheath, which corresponds to the ion saturation current [15] and it is independent of the sheath potential

$$i_s^+ = 0.4\ en_i(r)\ (2kT_e/M_i)2\pi r\Delta r$$

Differences between i^- and i^+ will charge the surface with a net charge. Since $n_i(r) = n_e(r)$ it is the exponential term in eq (15) which controls the net surface charge density. Electron and ion flows are equal when the sheath potential has the value of the floating potential, $V_s = V_f$. For $V_s(r) < V_f$ we find $i^- > i^+$. Since in accordance with eq (8) the plasma potential decreases with increasing distance r from the the high plasma pressure region above the cathode spot the surface areas $2\pi r\Delta r$ will be charged more negative with increasing r. The r-dependent net surface charge density causes then a surface radial electric field with the electron emitting cathode spot being more positive than the negatively charged surrounding ring areas. Electron surface mobility and diffusion will determine the electron-ion recombination rate on the surface and the electron return current flow to the cathode spot.

The small size observed for craters on silicon and TiC in comparison to the larger size cathode craters for metals may be qualitatively explained by the higher resistivity encountered by the surface electron return current which converges radially inward to the cathode spot. If ohmic heating is assumed to be the primary source for vaporization of material from the cathode spot, a smaller cathode spot diameter is required to achieve sufficient current density. The power dissipated per crater volume V_m is

$$P/V_m = j^2(r)/\sigma_s$$

where σ_s is the surface conductivity of the material. At the cathode spot we must have $j(r) \sim j_{arc}$. Neglecting differences in arc current densities and binding energy, dimensional analysis indicates that the crater size r_o should scale with conductivity roughly as $\sigma_s \propto r_o^2$ which is in qualitative agreement with the experimental observation that lower conductivity material show smaller crater size. In the case of TiC the resistivity is almost two orders of magnitude larger than the one for aluminum. The size of craters observed on TiC is 0.1 to 0.3 μm diameter while for metals the cathode crater is typically 0.7 to 1.5 μm. The actual size would depend also on the burn time of the arc. It is recommended that unipolar arcing on various non-conducting materials be further investigated.

SUMMARY

Unipolar arcing has been shown to be the primary plasma-surface interaction process when a laser produced plasma is in contact with a surface. Evidence of unipolar arcing was found on all targets irradiated at atmospheric pressure that also arced in vacuum, stainless steel, titanium, molybdenum, copper, and aluminum.

Cratering was observed even for a defocused and low-power laser pulse. The minimum laser power density required for the onset of breakdown on the surface is also sufficient to cause arc damage. Never was there a plasma evident without attendant unipolar arc craters. About 500,000 arc craters per cm^2 have been observed on laser illuminated metal surfaces although no external voltage is applied. Smaller size craters with a density of about $10^8/cm^2$ have been found on higher resistivity materials. The higher resistivity requires the radially inward surface return current to converge to a smaller cathode spot size to achieve sufficient power density to vaporize and ionize the material required for running the unipolar arc.

The local increase of the plasma pressure above the cathode spot leads to an electric field configuration which drives the arc current and also facilitates the return current flow to the surface and cathode spot.

Unipolar arcing concentrates the available laser-plasma energy towards the cathode spot. Large scale unipolar arcing on metal surfaces increases the coupling of energy from the laser heated plasma into the target. The ejection of a plasma jet from the cathode crater also causes highly localized shock waves to propagate into the target, softening it in the process. Thus, material erosion is much more severe than it would be the case for uniform energy deposition over a larger area.

This research has wide spread applications. Any situation in which a sufficiently hot surface plasma exists there will be unipolar micro-arcing. The physics relates to other forms of electrical breakdown on surfaces and electrodes.

ACKNOWLEDGEMENTS

This work was supported by the Naval Postgraduate School Foundation Research Program and in part by the Naval Research Laboratory.

REFERENCES

[1] Robson, A. E. and Thonemann, P. C., Proc. Phys. Soc. 73, 508(1959)
[2) McCracken, G. M., J. Nucl. Mater. 93/94, 3(1980)
[3] Clausing, R. E., Emerson L. C. and Heatherly, L. E., J. Nucl. Mater. 93/94, 150(1980)
[4] McCracken, G. M. and Goodall, D. H. J., Nucl. Fusion 18, 537(1978)
[5] Cohen, S. A., Dylla, H. F., Rossnagel, S. M., Picraux, S. T. and Magee, C. W., J. Nucl. Mater. 76/77, 459(1978)
[6] Staib, P. and Staudemaier, G., J. Nucl. Mater. 76/77, 78(1978)
[7] Schwirzke, F., Oren, L., Talmadage, S., and Taylor, R. J., Phys. Rev. Letters 40, 1181(1978)
[8] Oren, L., Taylor, R. J., and Schwirzke, F., J. Nucl. Mater. 76/77, 412(1978)
[9] Schwirzke, F. and Taylor, R. J., J. Nucl. Mater. 93/94, 780(1980)
[10] Gierke, G. V., Ott, W., and Schwirzke, F., Proc. Fifth International Conference on Ionization Phenomena in Gases, Munich 1961, p. 1412
[11] Schwirzke, F., Beelby, M. H., and Ulrich, H. G., "Basic Mechanisms that Lead to Laser Target Damage", Naval Postgraduate School Report NPS 61-82-002(1981)
[12] Schwirzke, F., Bunshah, R. F., and Taylor, R. J., Thin Solid Films 83(1981)117
[13] Metheny, R. M., An investigation of energy coupling in various arc susceptible and resistant conductors, M.S. Thesis, Naval Postgraduate School, Monterey, California, June 1982
[14] Jenkins, W. F., and Schmidt, W. R., Thermal coupling and damage mechanisms of 1.06 micron laser radiation and laser produced plasma on selected materials, M.S. Thesis, Naval Postgraduate School, December 1982
[15] Schwirzke, F., Phys. Fluids, 9, 2244(1966)

In response to questions, the author stated that his proposed damage mechanism did require existence of a continuous low-density plasma over the surface prior to initiation of a unipolar arc, but he believed that boil off of surface gases would provide the necessary plasma. He believed the predamage plasma density might be so low that the plasma was not apparent by simple visual inspection, and that his mechanism was consistent with the data of Kardach et. al. which was also presented at this meeting.

APPENDIX -- PARTICIPANTS

Dr. Joseph A. Abate
Laboratory for Laser Energetics
University of Rochester
250 East River Road
Rochester, NY 14623
(716) 275-5181

Dr. M. A. Archarekar
ILS
3404 N. Orange Blossom Tr.
Orlando, FL 32804
(305) 295-4010

N. Allen
Rutherford Appleton Laboratory
Chilton
Didcot
Oxon. OX11 0QX
England
235-21900

Susan D. Allen
Center for Laser Studies
Univ. of Southern California
Los Angeles, CA 90089-1112
(213) 743-6705

Joseph Apfel
Optical Coating Laboratory
2789 Griffen Ave.
Santa Rosa, CA 95402
(707) 545-6440

Tsuyoshi Asaeda
Canon U.S.A.
3191 Red Hill Ave.
Costa Mesa, CA 92626
(714) 556-1036

John F. Asmus
Maxwell Laboratories
Univ. of California
8239 Sugarman Dr.
La Jolla, CA 92037
(714) 279-5100

David S. Atlas
Eastman Kodak Company
D/177 Special Fabrication
901 Elmgrove Rd.
Rochester, NY 14650
(716) 588-5261

E. Douglas Baird (L-792)
Lawrence Livermore National
Laboratory
P.O. Box 808
Livermore, CA 94550
(415) 422-7633

Robert John Barton
Ministry of Defence
A.W.R.E.
Aldermaston
Reading, United Kingdom

William J. (Pat) Beauchamp
Optical Coating Lab
2789 North Point Parkway
Santa Rosa, CA 95401
(707) 525-7649

Michael F. Becker
Dept. of Electrical Engineering
The University of Texas at Austin
Engineering Science Bldg, Room 133
Austin, TX 78712
(512) 471-3628

Bernard Bendow
BDM Corp.
1801 Randolph
Albuquerque, NM 87106
(505) 848-5000

H. E. Bennett
Michelson Laboratory
Naval Weapons Center
Code 38101
China Lake, CA 93555
(714) 939-2869 or 939-2970

Jean Bennett
Michelson Laboratory
Naval Weapons Center
Code 38101
China Lake, CA 93555

Ralph R. Berggren
Avco Everett Research Lab., Inc.
2385 Revere Beach Parkway
Everett, MA 02149
(617) 381-4158

Lt. Col. Jerry R. Bettis
European Office of Aerospace R & D
(EOARD)
Box 14
FPO New York, 09510
London, England (01) 409-4505
Autovon 235-4505

E. C. Borsare
W. J. Schafer Assoc.
10 Lakeside Office Park
Wakefield, MA 01880
(617) 246-0450

Richard P. Bossert
Laboratory for Laser Energetics
University of Rochester
250 E. River Rd.
Rochester, NY 14623
(716) 275-3418

Theodore W. Broberg
Honeywell, Inc.
2600 Ridgway Parkway MN17-1622
P.O. Box 312
Minneapolis, MN 55413
(612) 378-5974

Richard R. Brown
The Boeing Company
M.S. 8C-23
P.O. Box 3999
Seattle, WA 98124

Charles K. Carniglia
Optical Coating Laboratory
2789 Griffen Ave.
Santa Rosa, CA 95402
(707) 545-6440

Michael Clancy
Rocketdyne Div. of
Rockwell International
6633 Canoga Ave., MS-FA40
Canoga Park, CA 91304
(213) 700-4908

Spencer D. Clapp
W. J. Schafer Assoc., Inc.
22222 Sherman Way, Suite 205
Canoga Park, CA 91303
(213) 704-1455

Garth Clarke
Westinghouse R & D
5180 Manont Road
Murrysville, PA 15668
(412) 256-7762

Joseph F. Connolly
CVD Incorporated
35 Industrial Parkway
Woburn, MA 01801
(617) 933-9243

Robert Culver
Aerojet Electro Systems
P.O. Box 296
MS Bldg. 160, Dept. 4344
Azuza, CA 91702

Frank Daly
Sundstrand Optical Technologies Inc.
2697 Lavery Court #8
Newbury Park, CA 91320
(805) 499-2636

Donald A. Dalton
UTRC/OATL
P.O. Drawer 4181
West Palm Beach, FL 33402
(305) 840-1052

Edward Danielewicz
Laser Power Optics Corp.
1211-V Sorrento Valley Rd.
San Diego, CA 92121
(619) 455-0751

Terry Deaton
Frank J. Seiler Research Lab
U.S. Air Force Academy
Colorado Springs, CO 80840
(303) 472-3502

Don Decker
Naval Weapons Center
China Lake, CA
(619) 939-3247

John A. Detrio
University of Dayton
Research Institute
300 College Park
Dayton, OH 45469
(513) 229-3527

T. M. Donovan
Naval Weapons Center
Code 3818 NWL
China Lake, CA 93555
(619) 446-2115

John Dugan
ITEK
10 Mcquire Road
Lexington, MA 02178

Richard Dyer
W. J. Schafer Associates
10 Lakeside Office Park
Wakefield, MA 01880
617-246-0450

Dr. Osama H. El-Bayoumi
U.S. Air Force
RADC/ESM
Hanscom AFB, MA 01737
617-861-5832

Ahmet Elci
University of New Mexico
Albuquerque, NM 87131

David Emmony
Dept. of Physics
University of Technology
Loughborough Leicestershire LE11 3TU
United Kingdom

Albert Feldman
National Bureau of Standards
A257 Materials Bldg.
Washington, DC 20234
(301) 921-2817

Dennis G. Fischer
Coherent, Inc.
2301 Lindbergh St.
Auburn, CA 95603
(916) 823-9550

Lawrence Fogdall
Boeing Aerospace
MS-2R-00, P. O. Box 3999
Seattle, WA 98124
(206) 773-2455

Stephen R. Foltyn
Los Alamos National Laboratory
MS-J 566, CHM-5
Los Alamos, NM 87545
(515) 667-1123

Neil Forbes
Ferranti PLC
Dunsinane Ave.
Iundee DD2 3PN
Scotland, United Kingdom

Venelsoa Foster
Optical Coating Laboratories, Inc.
2789 Northpoint Parkway
Santa Rosa, CA 95401
(707) 525-7652

Douglas L. Franzen
724.02
National Bureau of Standards
325 Broadway
Boulder, CO 80303
(303) 497-3346

Daniel Friart
CEA Limeil
BP 27
94190 Villeneuve - St. Georges
France

E. Joseph Friebele
DARPA/DSO
1400 Wilson Blvd.
Arlington, VA 22209
(202) 694-1346

David Gallant
Rocketdyne Div.
Rockwell International
P.O. Box 5670 KAFB
Albuquerque, NM 87185
(505) 846-0196

Robert L. Gallawa
724.02
National Bureau of Standards
325 Broadway
Boulder, CO 80303
(303) 497-3761

Victor Gamiz
Rocketdyne Div.
Rockwell International
P.O. Box 5670 KAFB
Albuquerque, NM 87185
(505) 844-4691

Paul Gilstrap
Physics Dept.
Colorado State Univ.
1799 S. College St. #17
Fort Collins, CO 80525
(303) 493-1425

Ann T. Glassman
Avionics Laboratory
AFWAL/AARI-2
Wright-Patterson AFB, OH 45433
(513) 255-5922/2698

Ms. Alison C. J. Glover
British Aerospace P.L.C.
Laser Systems Dept. F.P.C. 67
P.O. Box 5, Filton
Bristol BS12 79W
United Kingdom
(0272) 693831 x1012

William T. Goosey, Jr.
D/177 Special Fabrication
Eastman Kodak Company
901 Elmgrove Rd.
Rochester, NY 14650
(716) 588-5261

George Graves
University of Dayton
300 College Park
Dayton, OH 45469
(513) 229-2517

David L. Griscom
DARPA
Defense Sciences Office
1400 Wilson Blvd.
Arlington, VA 22209
(202) 694-1346

William Grossman
Mathematical Science N.W.
2755 Northup Way
Bellevue, WA
(206) 827-0460

Dr. Arthur H. Guenther
AFWL/ALO
Kirtland AFB, NM 87117
(505) 844-9856

Jayanta K. Guha
Rocketdyne
MS-FA42
6633 Canoga Ave.
Canoga, CA 91306
(213) 700-4841

Yu H. Hahn, President
CVI Laser Corporation
P.O. Box 11308
200 Dorado Place SE
Albuquerque, NM 87123
(505) 296-9541

Galen J. Hansen
Utah State University
Physics Dept. UMC 41
Logan, UT 84321
(801) 750-2846

Wilford N. Hansen
Utah State University
Logan, UT 84322
(801) 750-2852

James S. Harris
University of Dayton
Research Institute KL102
Dayton, OH 45469
(513) 229-3724

Richard Harris
University of Dayton
Research Institute
300 College Park Ave.
Dayton, OH 46469
(513) 254-2641

W. B. Harrison
Honeywell
5121 Winnetka Ave. North
New Hope, MN 55428
(612) 536-3156

James Harvey
Rocketdyne Div.
Rockwell International
P.O. Box 5670 KAFB
Albuquerque, NM 87185
(505) 846-2431

Gary L. Herrit
Two-Six Incorporated
Saxonburg Blvd.
Saxonburg, PA 16056
(412) 352-4455

W. C. (Bill) Herrmann, Jr.
Optic-Electronic Corp.
11477 Pagemill Road
Dallas, TX 75243
(214) 349-0190

Alan K. Hopkins
AFWAL/Materials Laboratory
WPAFB, OH 45433
(513) 255-4474

M. Huberman
R4/2135
TRW Inc.
One Space Park
Redondo Beach, CA 90278

Richard S. Hughes
Dept. of Physics and Computer
Science
Pacific Union College
Angwin, CA 94508
(707) 965-7269

Thomas Humpherys
U.S. Air Force
EOARD Box 14
FPO, NY 09510

Masahide Itoh
Optical Instrumentation Lab.
Inst. of Physical & Chemical
Research
2-1 Hirosawa Wako-shi, Saitama
351, JAPAN
0484-62-1111 x3243

Stephen D. Jacobs
Laboratory for Laser Energetics
University of Rochester
250 E. River Road
Rochester, NY 14623
(716) 275-4837

B. Jensen
Boston University
Dept. of Physics
111 Cummington St.
Boston, MA 02215
(617) 353-2610

Jerry Johnston
Dept. 441/2
OCLI
2789 Northpoint Parkway
Santa Rosa, CA 95401-7397
(707) 525-7148

Kenneth Jungling
University of New Mexico
EECE
Albuquerque, NM 87131
277-3317

John A. Kardach
AFIT/EN Box 4215
Wright-Patterson AFB, OH 45431
(513) 256-7348

Thomas A. Kardos
Broomer Laboratories, Inc.
3 Beech St.
Islip, NY 11751
(516) 277-0500

Ernest M. Kim
724.02
National Bureau of Standards
325 Broadway
Boulder, CO 80303

C. Klein
Aerospace Corp., MY 980
P.O. Box 92957
Los Angeles, CA 90009
(213) 648-6226

Claude A. Klein
Raytheon/Research
131 Spring St.
Lexington, MA 02173
(617) 831-5300

Walter L. Knecht
AFWAL/MLPO
Wright Patterson AFB, OH 45433
(513) 255-4474

Peter Koidl
Fraunhofer-Institute for Applied
Solid State Physics (IAF)
Eckerstrasse 4
D-7800 Freiburg
Fed. Rep. Germany
0761-27141-280

Nicholas Koumvakalis
Center for Laser Studies
University of Southern California
Denney Research Building, Rm. 17
Los Angeles, CA 90089-1112
(213) 743-5024

Dr. Valezi I. Kovalev
Lebedev Physical Institute
Academy of Sciences USSR
53 Leninsky Prospect
Moscow, USSR

Geoffrey C. Kung
Bldg E1, Mail Stop F112
Hughes Aircraft Company
P.O. Box 902
El Segundo, CA 90245
(213) 616-9802

M. R. Lange
University of New Mexico
Institute for Modern Optics
Albuquerque, NM 87131
(505) 277-6317

H. Le Bodo
Universite de Bretagne Occidentale
Laboratoire D'Energetique Laser
et de Thermophysique
10 rue Jean Zay
56100 Lorient
France

Dr. Keith L. Lewis
Royal Signals & Radar
Establishment
St. Andrews Rd.
Malvern, Worcs. WR14 3PS
England
(06845) 2733 x3062

Hui H. Li
CINDAS
Purdue University
2595 Yeager Rd.
West Lafayette, IN 47906
(317) 494-6300

Saukwan Lo
Honeywell, Inc.
2600 Ridgway Parkway
Minneapolis, MN 55432
(612) 378-4381

W. Howard Lowdermilk
Lawrence Livermore National
Laboratory
P.O. Box 5508, L-470
Livermore, CA 94550
(415) 422-5498

Y. Daines Lund
Utah State University
Logan, UT 84322
(801) 750-2853

Michael Lunt
Technical Optics
Second Avenue
Onchan, Isle of Man.
United Kingdom
0624 4443

Maj. Ronald L. Lusk
AFWL/ARAO
Kirtland AFB, NM 87117
(505) 844-1776

Malcolm J. MacFarlane
Rocketdyne Div.
Rockwell International
Box 5670
Kirtland AFB, NM 87185
(505) 846-2431

H. Angus Macleod
Optical Sciences Center
University of Arizona
Tucson, AZ 85721
(602) 626-3025

Myron T. Maclin
Air Force Weapons Laboratory
AFWL/ARAO
Kirtland AFB, NM 87117
(505) 844-1776

Alexander A. Manenkov
Lebedev Physics Inst.
Academy of Sciences USSR
Leninsky Prospect, 53
Moscow, USSR

Armen E. Mardiguian
U.S. Air Force Academy
Dept. of Physics
Colorado Springs, CO 80840
(303) 472-4570

Diane J. Martin
USAF
AFWL/ARAO
Kirtland AFB, NM 87117
(505) 844-1776

Cheryl R. Maxwell
Rocketdyne Div.
Rockwell International
KAFB East
Albuquerque, NM 87185
(505) 846-2433

Larry D. Merkle
Center for Laser Studies
University of Southern California
University Park, DRB 17
Los Angeles, CA 90089-1112
(213) 743-4379

David Merriman
Rocketdyne Div.
Rockwell International
P.O. Box 5670 KAFB
Albuquerque, NM 87185
(505) 846-0196

David Milam
Lawrence Livermore National
Laboratory
P.O. Box 5508, L-490
Livermore, CA 94550
(415) 422-5499

Perry A. Miles
Raytheon Company
Hartwell Rd.
Bedford, MA 01730
(617) 274-7100 X3553

Kent Moncur
KMS Fusion, Inc.
3621 S. State Rd.
P.O. Box 1567
Ann Arbor, MI 48106-1567
(313) 769-8500 X381

Dennis Morelli
Dept. 322/1
OCLI
2789 Northpoint Parkway
Santa Rosa, CA 95401-7397
(707) 525-7011

Donald Mullen
Rocketdyne Div.
Rockwell International
P.O. Box 5670 KAFB
Albuquerque, NM 87185
(505) 846-0196

Kathryn A. McCarthy
Dept. of Physics
Tufts University
Medford, MA 02155

J. K. McIver
University of New Mexico
Institute for Modern Optics
Albuquerque, NM 87131
(505) 277-5909

Capt. James F. McNally
United States Air Force
USAFA/OFP
USAF Academy, CO 80840
(303) 472-3355

Yoshiharu Namba
Univ. of New Mexico
800 Yale
Albuquerque, NM 87131
(505) 277-5625

Robert E. Nelson
724.00
National Bureau of Standards
325 Broadway
Boulder, CO 80303

Brian E. Newnam
Los Alamos National Laboratory
MS-J564, Group CHM-6
Los Alamos, NM 87545
(505) 667-7979 or -1991

Davis B. Nichols
Boeing Aerospace Company
M.S. 88-46
P.O. Box 3999
Seattle, WA 98055
(206) 773-8938

Bob O'Connell
Univ. of Missouri -
Columbia
2218 Ptarmigan Lane
Colorado Springs, CO
(303) 472-3122

Garl P. Owen
RARDE
Fort Halstead
Sevenoaks, Kent
United Kingdom

James R. Palmer
Doc Jim Enterprises
1250 N. Lynwood Dr.
Anaheim, CA 92807
(714) 779-0589

Roger A. Paquin
The Perkin-Elmer Corp.
Electro-Optical Div.
100 Wooster Heights Rd.
Danbury, CT 06810
(203) 797-6130

James L. Parham
Army Missile Command
Attn: DRSMI-RLM
J. L. Parham
Redstone Arsenal, AL 35898
(205) 876-3867
Autovon 746-3867

Alan Parker
Rockwell Int'l Science Center
P. O. Box 1085
Thousand Oaks, CA 91360
(805) 498-4545

Alexander Parker
M.I.T. Lincoln Laboratory
P.O. Box 73
Lexington, MA 02173
(617) 863-5500

Walter T. Pawlewicz
Battelle Northwest Laboratories
P.O. Box 999
Richland, WA 99352
(509) 373-2537

Winston K. Pendleton
Air Force Weapons Lab
AFWL/CA
Kirtland AFB, NM 87117
(505) 844-9856

John Peter
Hughes Aircraft Company
P.O. Box 902
El Segundo, CA

Alan B. Petersen
Spectra Physics Inc.
1250 W. Middlefield Rd.
Mountain View, CA 94042
(415) 961-2550 x2064

Roger Petty
Rocketdyne Div.
Rockwell International
P.O. Box 5670 KAFB
Albuquerque, NM 87185
(505) 846-0196

Major Bruce J. Pierce
USAF
AFWL/ARAO
Kirtland AFB, NM 87117
(505) 844-1776

Robert D. Poirier
Perkin Elmer Corp. S.E.G.
77 Danbury Rd.
MS 420
Wilton, CT 06897
(203) 834-4934

James O. Porteus
Naval Weapons Center
Code 3817
China Lake, CA 93555
(619) 939-3827

Tim Pottenger
Univ. of Dayton Research Inst.
KL 102
300 College Park
Dayton, OH 45469
(513) 229-3221

Frank Rainer
Lawrence Livermore National Lab
P.O. Box 5508, L-490
Livermore, CA 94550
(415) 422-4376

Max Reed
Los Alamos National Laboratory
MS S601
Los Alamos, NM 87545

Herman E. Reedy
II-VI Inc.
Saxonburg Blvd.
Saxonburg, PA 16046
(412) 352-4455

Stanley J. Refermat
Eastman Kodak Company
Kodak Apparatus Division
901 Elmgrove Road
Rochester, NY 14650
(716) 724-5426

Norman N. Richman
TRW S & TG
One Space Park
Redondo Beach, CA 90278
(213) 535-6709

Richard G. Roides
Laboratory for Laser Energetics
Univ. of Rochester
250 East River Rd.
Rochester, NY 14623
(716) 275-3418

Mehmet Rona
Physical Sys. Research Section
Arthur D. Little, Inc.
Acorn Park
Cambridge, MA 02140
(617) 864-5770

Lynn Ronsall
Rocketdyne
6633 Canoga Ave.
Canoga, CA 91304

J. Earl Rudisill
Laser Power Optics
11211/U Sorrento Valley Rd.
San Diego, CA 92121
(714) 455-0751

Rong Rujkorakarn
Dept. of Physics
Colorado State University
Fort Collins, CO 80523
(303) 491-5850

Lt. Col. Theodore T. Saito
FJSRL/NH
USAF Academy
Colorado Springs, CO 80840
(303) 472-3122

Aaron A. Sanders
724.02
National Bureau of Standards
325 Broadway
Boulder, CO 80303
(303) 497-5342

Virgil E. Sanders
(GE-14)
Rockwell International AMSD
3370 Miraloma
Anaheim, CA
(714) 632-1790

David Sandfort
Texas Instruments
P. O. Box 22547
Dallas, TX 75265

Albert C. Saxman
Los Alamos National Laboratory
P.O. Box 1663, MS E523
Los Alamos, NM 87545
(505) 667-7065

Erik Schwendeman
CVI Laser Corporation
P.O. Box 11308
200 Dorado Place SE
Albuquerque, NM 87192
(505) 296-9541

Fred R. Schwirzke
Naval Postgraduate School
Dept. of Physics & Chemistry
Monterey, CA 93940

Paul Scott
Rocketdyne Div.
Rockwell International
P.O. Box 5670 KAFB
Albuquerque, NM 87185
(505) 846-6178

Stuart K. Searles
Naval Research Lab.
Code 6545
Washington, DC 20375
(202) 767-2255

S. C. Seitel
Naval Weapons Center
Code 3817
China Lake, CA 93555
(714) 939-3049

C. Y. She
Physics Dept.
Colorado State Univ.
Fort Collins, CO 80523
(303) 491-6261

Jeffrey B. Shellan
W. J. Schafer Assoc., Inc.
2222 Sherman Way #205
Canoga Park, CA 91303
(213) 704-1455

Capt. Keith Shillito
Air Force Weapons Lab
Kirtland AFB, NM 87117
(505) 844-1776

Meyer Silver
TRW
One Space Park
Redondo Beach, CA 90266
(213) 535-6709

Robert A. Simms
Litton Industries
1215 S. 52nd St.
Tempe, AZ 85281
(602) 968-4471

James R. Sites
Physics Department
Colorado State University
Fort Collins, CO 80523
(303) 491-5850

David C. Skeen
19956 Lorne St.
Canoga Park, CA 91306

David H. Sliney
Laser Microwave Div.
U.S. Army Environmental Hygiene
Agency
Aberdeen Proving Ground, MD 21010
(301) 671-3932 or 3468

M. J. Smith
Avco Everett Research Lab.
2385 Revere Beach Parkway
Everett, MA 02149
(617) 381-4697

P. R. C. Smith
(P.B. 232)
British Aerospace Dynamics
Six Hills Way
P.O. Box 19
Stevenage, Herts, England
Stevenage 2422 x2531

M. J. Soileau
North Texas State University
Center for Applied Quantum
Electronics
P.O. Box 5368
Denton, TX 76203
(817) 565-3263

Ralph Somers
Mail Stop Bldg 160
Dept. 4344
Aerojet Electro Systems
P.O. Box 296
Azuza, CA 91702

Walter Spawr
Spawr Optical Research, Inc.
1527 Pomona Road
Corona, CA 91720

James L. Stanford
Naval Weapons Center
Code 3818
China Lake, CA 93555
(619) 939-2443

Alan F. Stewart
Air Force Weapons Lab.
AFWL/ARAO
Kirtland AFB, NM 87117
(505) 844-7368

Glen Stutz
810 S. Langley #103
Tucson, AZ 85711
(602) 748-2355

James E. Swain
University of California
Lawrence Livermore National
Laboratory
P.O. Box 5508, L-470
Livermore, CA 94550
(415) 422-5402

Orven F. Swenson
USAF/DFP
USAF Academy
Colorado Springs, CO 80840
(303) 472-2601

Paul Temple
Naval Weapons Center
Code 3816
China Lake, CA 93555

G. E. Titmuss
British Aerospace P.L.C.
Dynamics Group, Bristol Div.
Laser Systems Dept., F.P.C. 67
Filton
Bristol BS12 79W
United Kingdom
0272-693831

Howard C. Volkin
Rocketdyne Div.
Rockwell International
P.O. Box 5670 KAFB
Kirtland AFB, NM 87185
(505) 846-2441

Marc von Gunten
Spectra-Physics
1250 W. Middlefield
Mountain View, CA 94042
(415) 961-2550 X3008

Harshadrai Vora
Honeywell Corporate Technology
Center
10701 Lyndale Ave. South
Bloomington, MN 55420
(612) 887-4412

Thomas W. Walker
AFWL/ARAO
Kirtland AFB, NM 87117
(505) 844-0721

Rodger M. Walser
Dept. of Electrical Engineering
The University of Texas at Austin
Engineering Science Bldg, Room 404
Austin, TX 78712
(512) 471-5733

Anetta J. Weber
Air Force Weapons Lab/ARAO
Kirtland AFB, NM 87117
(505) 844-0721

James D. Weigner
Honeywell Ceramics Center
5121 Winnetka Ave. North
New Hope, MN 55428
(612) 536-3161

Frederic H. White III
Rocketdyne Division
Rockwell International
6633 Canoga Ave.
Canoga Park, CA 91304
(213) 700-4920

C. B. Willingham
Raytheon Company Research Div.
131 Spring St.
Lexington, MA 02173
(617) 863-5300, X3062

G. Richard Wirtenson
L-491
Lawrence Livermore National Lab.
7000 East Ave.
Livermore, CA 94550
(415) 422-0288

Steve S. Wiseall
Department of Physics
University of Technology
Loughborough, Leicestershire LE11
3TU
England
Loughborough (509) 263171 x5044

Frank Wodarczyk
Rockwell International Science
Center
P. O. Box 1085
Thousand Oaks, CA 91360
(805) 498-4545

Roger M. Wood
Hirst Research Centre
General Electric Company
East Lane, Wembley
Middlesex HA79PP
United Kingdom
01-904-1262 x205

Frank Woodberry
Rocketdyne MS FA 42
66310 Canoga Ave.
Canoga. CA 91303

Bulent Yoldas
Westinghouse R & D
1310 Beulah Road
Pittsburgh, PA 15235
(412) 256-3269

Matt Young
724.02
National Bureau of Standards
325 Broadway
Boulder, CO 80303
(303) 497-3223

Lawrence Zajac
W. J. Schafer Assoc., Inc.
22222 Sherman Way #205
Canoga Park, CA 91303
(213) 704-1455

Fred Zmarzly
Dept. 322/1
OCLI
2789 Northpoint Parkway
Santa Rosa, CA 95401-7397
(707) 525-7013

NBS-114A (REV. 2-80)

U.S. DEPT. OF COMM. **BIBLIOGRAPHIC DATA SHEET** *(See instructions)*	1. PUBLICATION OR REPORT NO. NBS SP 669	2. Performing Organ. Report No.	3. Publication Date January 1984

4. TITLE AND SUBTITLE

Laser Induced Damage in Optical Materials : 1982

5. AUTHOR(S) Harold E. Bennett (NWC), Arthur H. Guenther (AFWL), David Milam (LLNL) and Brian E. Newnam (LANL)

6. PERFORMING ORGANIZATION *(If joint or other than NBS, see instructions)*

NATIONAL BUREAU OF STANDARDS
DEPARTMENT OF COMMERCE
WASHINGTON, D.C. 20234

7. Contract/Grant No.

8. Type of Report & Period Covered

Final

9. SPONSORING ORGANIZATION NAME AND COMPLETE ADDRESS *(Street, City, State, ZIP)*

National Bureau of Standards (NBS)
American Society for Testing and Materials (ASTM)
Office of Naval Research (ONR)
Department of Energy (DOE)
Defense Advanced Research Project Agency (DARPA)
Air Force Office of Scientific Research (AFOSR)

10. SUPPLEMENTARY NOTES

Library of Congress Catalog Card Number: 83-600625

☐ Document describes a computer program; SF-185, FIPS Software Summary, is attached.

11. ABSTRACT *(A 200-word or less factual summary of most significant information. If document includes a significant bibliography or literature survey, mention it here)*

The Fourteenth Annual Symposium on Optical Materials for High Power Lasers (Boulder Damage Symposium) was held at the National Bureau of Standards in Boulder, Colorado, November 16-17, 1982. The Symposium was held under the auspices of ASTM Committee F-1, Subcommittee on Laser Standards, with the joint sponsorship of NBS, the Defense Advanced Research Project Agency, the Department of Energy, the Office of Naval Research, and the Air Force Office of Scientific Research. Approximately 200 scientists attended the Symposium, including representatives of the United Kingdom, France, Japan, West Germany, and the USSR. The Symposium was divided into sessions concerning Materials and Measurements, Mirrors and Surfaces, Thin Films and finally Fundamental Mechanisms. As in previous years, the emphasis of the papers presented at the Symposium was directed toward new frontiers and new developments. Particular emphasis was given to materials for high power apparatus. The wavelength range of prime interest was from 10.6 μm to the uv region. Highlights included surface characterization, thin film-substrate boundaries, and advances in fundamental laser-matter threshold interactions and damage mechanisms. Harold E. Bennett of the Naval Weapons Center, Arthur H. Guenther of the Air Force Weapons Laboratory, David Milam of the Lawrence Livermore National Laboratory, and Brian E. Newnam of the Los Alamos National Laboratory were co-chairmen of the Symposium. The Fifteenth Annual Symposium is scheduled for November 14-16, 1983 at the National Bureau of Standards, Boulder, CO.

12. KEY WORDS *(Six to twelve entries; alphabetical order; capitalize only proper names; and separate key words by semicolons)*

Laser damage; laser interaction; optical fabrication; optical materials and properties; thin film coatings.

13. AVAILABILITY

☒ Unlimited
☐ For Official Distribution. Do Not Release to NTIS
☒ Order From Superintendent of Documents, U.S. Government Printing Office, Washington, D.C. 20402.
☐ Order From National Technical Information Service (NTIS), Springfield, VA. 22161

14. NO. OF PRINTED PAGES

499

15. Price

NBS TECHNICAL PUBLICATIONS

PERIODICALS

JOURNAL OF RESEARCH—The Journal of Research of the National Bureau of Standards reports NBS research and development in those disciplines of the physical and engineering sciences in which the Bureau is active. These include physics, chemistry, engineering, mathematics, and computer sciences. Papers cover a broad range of subjects, with major emphasis on measurement methodology and the basic technology underlying standardization. Also included from time to time are survey articles on topics closely related to the Bureau's technical and scientific programs. As a special service to subscribers each issue contains complete citations to all recent Bureau publications in both NBS and non-NBS media. Issued six times a year. Annual subscription: domestic $18; foreign $22.50. Single copy, $5.50 domestic; $6.90 foreign.

NONPERIODICALS

Monographs—Major contributions to the technical literature on various subjects related to the Bureau's scientific and technical activities.

Handbooks—Recommended codes of engineering and industrial practice (including safety codes) developed in cooperation with interested industries, professional organizations, and regulatory bodies.

Special Publications—Include proceedings of conferences sponsored by NBS, NBS annual reports, and other special publications appropriate to this grouping such as wall charts, pocket cards, and bibliographies.

Applied Mathematics Series—Mathematical tables, manuals, and studies of special interest to physicists, engineers, chemists, biologists, mathematicians, computer programmers, and others engaged in scientific and technical work.

National Standard Reference Data Series—Provides quantitative data on the physical and chemical properties of materials, compiled from the world's literature and critically evaluated. Developed under a worldwide program coordinated by NBS under the authority of the National Standard Data Act (Public Law 90-396).

NOTE: The principal publication outlet for the foregoing data is the Journal of Physical and Chemical Reference Data (JPCRD) published quarterly for NBS by the American Chemical Society (ACS) and the American Institute of Physics (AIP). Subscriptions, reprints, and supplements available from ACS, 1155 Sixteenth St., NW, Washington, DC 20056.

Building Science Series—Disseminates technical information developed at the Bureau on building materials, components, systems, and whole structures. The series presents research results, test methods, and performance criteria related to the structural and environmental functions and the durability and safety characteristics of building elements and systems.

Technical Notes—Studies or reports which are complete in themselves but restrictive in their treatment of a subject. Analogous to monographs but not so comprehensive in scope or definitive in treatment of the subject area. Often serve as a vehicle for final reports of work performed at NBS under the sponsorship of other government agencies.

Voluntary Product Standards—Developed under procedures published by the Department of Commerce in Part 10, Title 15, of the Code of Federal Regulations. The standards establish nationally recognized requirements for products, and provide all concerned interests with a basis for common understanding of the characteristics of the products. NBS administers this program as a supplement to the activities of the private sector standardizing organizations.

Consumer Information Series—Practical information, based on NBS research and experience, covering areas of interest to the consumer. Easily understandable language and illustrations provide useful background knowledge for shopping in today's technological marketplace.

Order the **above** *NBS publications from: Superintendent of Documents, Government Printing Office, Washington, DC 20402.*

Order the **following** *NBS publications—FIPS and NBSIR's—from the National Technical Information Service, Springfield, VA 22161.*

Federal Information Processing Standards Publications (FIPS PUB)—Publications in this series collectively constitute the Federal Information Processing Standards Register. The Register serves as the official source of information in the Federal Government regarding standards issued by NBS pursuant to the Federal Property and Administrative Services Act of 1949 as amended, Public Law 89-306 (79 Stat. 1127), and as implemented by Executive Order 11717 (38 FR 12315, dated May 11, 1973) and Part 6 of Title 15 CFR (Code of Federal Regulations).

NBS Interagency Reports (NBSIR)—A special series of interim or final reports on work performed by NBS for outside sponsors (both government and non-government). In general, initial distribution is handled by the sponsor; public distribution is by the National Technical Information Service, Springfield, VA 22161, in paper copy or microfiche form.

U.S. Department of Commerce
National Bureau of Standards

Washington, D.C. 20234
Official Business
Penalty for Private Use $300